

Development Theories and Methods of Fracture-Vug Carbonate Reservoirs



Yang Li



Development Theories and Methods of Fracture-Vug Carbonate Reservoirs

Development Theories and Methods of Fracture-Vug Carbonate Reservoirs

Yang Li

China Petroleum & Chemical Corporation



ACADEMIC PRESS

An imprint of Elsevier

Academic Press is an imprint of Elsevier
125 London Wall, London EC2Y 5AS, United Kingdom
525 B Street, Suite 1800, San Diego, CA 92101-4495, United States
50 Hampshire Street, 5th Floor, Cambridge, MA 02139, United States
The Boulevard, Langford Lane, Kidlington, Oxford OX5 1GB, United Kingdom

Copyright © 2017 Yang Li. Published by Elsevier Ltd. All rights reserved.

No part of this publication may be reproduced or transmitted in any form or by any means, electronic or mechanical, including photocopying, recording, or any information storage and retrieval system, without permission in writing from the publisher. Details on how to seek permission, further information about the Publisher's permissions policies and our arrangements with organizations such as the Copyright Clearance Center and the Copyright Licensing Agency, can be found at our website: www.elsevier.com/permissions.

This book and the individual contributions contained in it are protected under copyright by the Publisher (other than as may be noted herein).

Notices

Knowledge and best practice in this field are constantly changing. As new research and experience broaden our understanding, changes in research methods, professional practices, or medical treatment may become necessary.

Practitioners and researchers must always rely on their own experience and knowledge in evaluating and using any information, methods, compounds, or experiments described herein. In using such information or methods they should be mindful of their own safety and the safety of others, including parties for whom they have a professional responsibility.

To the fullest extent of the law, neither the Publisher nor the authors, contributors, or editors, assume any liability for any injury and/or damage to persons or property as a matter of products liability, negligence or otherwise, or from any use or operation of any methods, products, instructions, or ideas contained in the material herein.

British Library Cataloguing-in-Publication Data

A catalogue record for this book is available from the British Library

Library of Congress Cataloguing-in-Publication Data

A catalog record for this book is available from the Library of Congress

ISBN: 978-0-12-813246-3

For Information on all Academic Press publications
visit our website at <https://www.elsevier.com/books-and-journals>



Working together
to grow libraries in
developing countries

www.elsevier.com • www.bookaid.org

Publisher: Glyn Jones

Acquisition Editor: Glyn Jones

Editorial Project Manager: Wing Yan K. Chan

Production Project Manager: Debasish Ghosh

Cover Designer: Vicky Pearson Esser

Typeset by MPS Limited, Chennai, India

Foreword

Continental clastic and marine carbonate reservoirs are two primary types of oil reservoirs. The Chinese oil industry originated from continental clastic reservoirs, and the theory of continental facies of petroleum and waterflooding technology played an important role in the rapid development of the Chinese oil industry in the last half-century. With Exploration & Production (EP) focus from the east to the west and the south, from continental to marine facies, marine carbonate reservoirs in western and southern China have become some of the main prospects for increasing reserves and production. The total oil and gas resources contained in marine carbonate reservoirs is greater than 300×10^8 t of oil equivalent, and oil resource is about 150×10^8 t, mainly found in the superimposed basins in the Tarim area and North China. These reservoirs are in deep High Pressure, High Temperature (HPHT) formations where the geological structures are very complicated and challenging to explore and develop. The discovery of the Tahe Oilfield opened a new field of study on marine carbonate reservoirs.

Generally marine carbonate reservoirs can be classified into three types including solution-pore, fracture-pore, and fracture-vug reservoirs. In China, the fracture-vug reservoir is the primary type of reservoir, which contains about 2/3 of proven reserves. The largest fracture-vug carbonate reservoir discovered in the Tahe Oilfield is buried in very deep and complicated HPHT formations.

The development of solution-pore carbonate reservoirs follows the same theory and technology as those in clastic reservoirs. The development of fracture-pore reservoirs is mainly based on dual-medium theory and methodology. However in the Tahe Oilfield where reservoir space is composed of caverns, caves, vugs, and fractures, the drilling success rate was very low, resulting in low reserves in development, but production declined quickly and recovery was very low in the early development stage due to lack of experience and mature development theory and methodology.

There are three kinds of difficulties in developing fracture-vug carbonate reservoirs:

1. It is hard to understand the development and distribution laws of fracture-vug reservoirs. After multistage tectonic movements, karst superposition and reformation and reservoir formation, reservoir spatial structure, lateral and vertical properties have changed significantly.
2. It is hard to understand the fluid flow laws in fracture-vug reservoirs. Generally the fracture-vug unit is a relatively isolated space where multiple flow patterns coexist, flow laws are very complicated, and fluid exchange mechanisms among different media are not clear.
3. Energy supplement is necessary so that it is difficult to enhance recovery.

In order to successfully develop a fracture-vug carbonate reservoir, it is necessary and very urgent to carry out studies on its forming mechanism, reservoir quantitative description, fluid flow law and other key points, thus to establish appropriate theory and technology for such reservoir development.

With the requirements above, two national “973” projects were initiated in 2006: *The Basic Study on the Development of Fracture-Vug Carbonate Reservoir* and *The Basic Study on How to Produce and Enhance the Recovery of Fracture-Vug Carbonate Reservoir*. In the process of these studies, many works have been performed involving investigation on the development formation and features, building geophysical and mathematical models, analyzing fluid flow law, conducting reservoir numerical simulation and performing effective production of fracture-vug reservoir in two stages for 10 years. Six major achievements have been made as follows.

1. Established a combination analysis method of karstification and dynamic actions, illustrated the relationship between karstification and the formation of fracture-vug systems, revealed the forming mechanisms and development laws of fracture-vug reservoirs;
2. Developed forward modeling, small-size, and high-fold 3D seismic survey, high-precision imaging and geophysical characterization methods and technologies for investigating super-deep fracture-vug reservoirs;
3. Expanded the geological modeling idea from continuous elastic medium to karstification and structure-controlling medium containing vugs and multiscale and discrete fractures, proposed nonseepage flow property parameters for describing caverns and established the modeling method for multiscale and discontinuous fracture-vug reservoirs;
4. Developed physical modeling experiment technology for analyzing fluid flow in the fracture-vug medium, which reveals the mechanisms and laws of single-phase flow, two-phase flow, and fluid exchange among media, and built a complex flow model;
5. Built coupled and equivalent continuous multimedium mathematical models, proposed numerically discrete and solving methods, and established three-dimensional (3D) two-phase reservoir numerical simulation based on coupled and equivalent continuous multimedium models;
6. Developed a performance indicator evaluation method, waterflooding and nitrogen-injecting technology especially for fracture-vug reservoirs.

This book summarizes the results of the “National 973” projects in six chapters in order to enrich and improve the development theory and technology for fracture-vug carbonate reservoirs. Chapter 1, Characteristics and forming mechanism of fracture-vug carbonate reservoirs describes the characteristics and forming mechanism of fracture-vug reservoirs by studying their development, evolution, and control mechanisms based on typical outcrop and well data. Chapter 2, Geophysical characterization of fracture-vug carbonate reservoirs introduces forward modeling, imaging, reservoir identification, and fluid detection using seismic data. Chapter 3, 3D geological modeling of a fracture-vug carbonate reservoir demonstrates 3D geological modeling, reservoir characteristics, reservoir unit division and evaluation. Chapter 4, Fluid flow law in a fracture-vug carbonate reservoir analyzes fluid flow mechanisms, single- and two-phase flow laws, and fluid exchange features in

fracture-vug reservoirs based on physical models and theoretical analysis. Chapter 5, Numerical simulation of a fracture-vug carbonate reservoir illustrates numerical simulation of fracture-vug reservoirs based on discrete and equivalent multimediuim models. Chapter 6, Development technology for fracture-cavern carbonate reservoirs concludes with technologies and their applications in developing fracture-vug reservoirs, focusing on reservoir engineering analysis, waterflooding nitrogen-injecting and, recovery enhancing processes.

The book is not only the scientific research result of the “National 973 projects,” but is also the embodiment of the efforts and wisdom of all experts and researchers who actively participated in the projects.

For help in preparation of this book, our thanks go to Li Yang, Yuan Xiangchun, Dou Zhilin, Qu Shouli, Xia Riyuan, Lu Xinbian, Hu Xiangyang, Yao Jun, Kang Zhijiang, Li Jianglong, Zhang Hongfang, Liu Zhongchun, Zheng Songqing, Hou Jiagen, Liu Huiqing, Wang Shixing, Zou Shengzhang, Zhong Jianhua, Gu Hanming, Guan Luping, Zhu Shengwang, Zhao Qun, Cao Huilan, Xiong Wei, Lv Aimin, Liu Xueli, Rong Yuanshuai, Jin Qiang, and Wu Feng, National 973 Basic Project Team; Academician Guo Shangping, Chinese Academy of Sciences; Academicians Han Dakuang, Luo Pingya, Kang Yuzhu, and Peng Suping, Professors Luo Zhibin, Huang Suyi and Zhang Liehei, and Doctor Yan Jinding, Chinese Academy of Engineering; and special thanks to Kang Zhijiang, Zheng Songqing, and Xue Zhaojie for their help in compiling and proofreading this book.

Characteristics and forming mechanism of fracture-vug carbonate reservoirs

1

Fracture-vug carbonate systems usually provide good reservoir space and play an important role in petroleum exploration and development. Affected by the combined effect of primary deposition and posttransformation, especially karstification and tectonism, the reservoir space in a carbonate reservoir is complex and diverse. The paleo-karstification process is a controlling mechanism for reservoir space, through which various complex fracture-vug systems have formed with the joint action of internal and external dynamics. A fracture-vug system refers to the composition of pores, fractures and vugs/caves/caverns formed during karstification under a unified recharge-flow-discharge hydrologic system.

Carbonate reservoirs in China are very old in geology, and after undergoing multiple stages of tectonic activities, karstification and hydrocarbon accumulation, have strong heterogeneity, with reservoir space composed of pores, fractures, vugs and caves, with poor connectivity; therefore, it is necessary to figure out their forming mechanisms and distribution laws.

In this study, we carried out detailed description and comparison of typical karstic outcrops and subsurface fracture-vug systems. Based on paleotectonic, paleogeomorphological, paleoclimatic, and paleohydrogeological analysis, we have identified paleo-karstification by integrating geochemical analysis, paleogeomorphological reformation, and geophysical survey. This enabled us to figure out the combinations of controlling factors of various karst features on micro- and macro-scales, outcrop-burial occurrences, and dissolution and filling conditions, and to get an insight into the karstification conditions and processes of the Ordovician reservoir in the Tahe Oil Field.

1.1 Characteristics of fracture-vug reservoirs

Affected by special deposition, lithology, diagenesis, tectonic destruction, and dissolution processes, carbonate reservoirs differ significantly from other types of reservoirs in reservoir space, distribution occurrence, and stability.

1.1.1 Classification criteria of karstic reservoir space

Pores, vugs, caves, and fractures are very common in carbonate rocks, and their contribution to hydrocarbon migration and accumulation are different because of their different forming mechanism, morphologic features, and developed scales.

How to classify karstic reservoir space has long been given different definitions and criteria. In this study, the following classification criteria were applied to define the reservoir space in a fracture-vug oil reservoir according to the *Glossary of Karstology* (Yuan, 1988) and reservoir characteristics.

1.1.1.1 Primary pore

Primary pores refer to intergranular pores in oolite and intragranular pores inside the body cavity of fossils. Due to only being several to tens of micrometers in diameter, these pores are insignificant reservoir space.

1.1.1.2 Secondary pore

There are seven types of secondary pores, including intercrystal pores, intercrystal and intracrystal solution pores, etc.

1. Intercrystal pore: pores between crystals, polygonal, tens to hundreds of micrometers in diameter.
2. Intercrystal solution pore: the product of dissolution and enlargement of intercrystal pores, tens to hundreds of micrometers in diameter.
3. Intracrystal solution pore: pores formed by dissolution within crystalline grains, over ten to tens of micrometers in diameter.

The primary (intergranular and intragranular) and secondary (intercrystal, intercrystal and intracrystal solution) pores discussed above constitute matrix pores in carbonate rock. After intense diagenetic reformation from the Caledonian to the Himalayan orogenies, most Paleozoic carbonate rocks in the China area have relatively low matrix porosity because most matrix pores suffered strong compaction or filling. For the Ordovician carbonate rock in the Tarim Basin, the average matrix porosity is 1.049%; the probability of porosity under 1% and 2% is 62% and 90%, respectively, and the permeability is generally lower than $1 \times 10^{-4} \mu\text{m}^2$.

4. Moldic pore: pores formed by selective dissolution of mineral or biologic crystal fragment, including gypsum and halite moldic pore, from hundreds of micrometers to several millimeters in length, and tens of micrometers in width. Generally formed during burial karstification, and low in filling degree and density, these pores provide good reservoir space.
5. Sandy moldic pore: small moldic pore formed by preferential dissolution of sand-sized grains, hundreds of micrometers in diameter.
6. Small-scale irregular pores: generated by dissolution, 0.01–2 mm in diameter, visible to the naked eye.
7. Solution cave (small cave): larger irregular vugs formed by dissolution, 2–20 cm in diameter.

1.1.1.3 Cave/cavern

In accordance with the criterion of modern karst classification, a cave/cavern refers to a vug greater than 20 cm in diameter.

In the Tahe Oil Field, about 86.67% of the wells drilled into paleokarstic fracture-vug systems (62.22% of the wells drilled into caves/caverns), indicate well-developed paleokarstic fracture-vug systems.

1.1.1.4 Fracture

Fractures can be classified into different types according to different classification principles and criteria. For specific tasks and study objectives, suitable criteria should be defined to avoid confusion or ambiguity.

1. Classification by origin
 - a. Tectoclase. The cracks directly formed by tectonic process, such as tension and shear cracks; in the Tahe Oil Field, early tectoclase formed during the Caledonian and early Hercynian orogenies have usually been filled. Later tectoclase formed from the Hercynian to Himalayan orogenies have only been partially filled and are mostly effective.
 - b. Solution-enlarged tectoclase. The tectoclase reformed (enlarged and filled) through dissolution. This kind of crack has an obvious enlarged crack surface and a wide opening, and they are filled or partially filled with calcite or calcareous mudstone. Partially filled solution-enlarged tectoclase makes a good seepage channel.
 - c. Diagenetic fractures. Such as desiccation cracks, collapsed fractures, and pressolved fractures, they provide good reservoir space and seepage channels.
2. Classification by filling degree
 - a. Unfilled fractures. With little filling inside, these kinds of fractures mainly include tectoclases and solution fractures formed during a late orogenic episode.
 - b. Partially filled fractures. Incompletely filled, this kind of fracture provides a little effective reservoir space.
 - c. Fully filled fractures. Such fractures have been fully filled with calcareous mud, calcite, and pyrite, etc.
3. Classification by occurrence and configuration
 - a. Vertical fractures. This kind of fracture is mainly characterized by near-vertical orientation. Some were originated tectonically with longer extension of over 2 m; others were originated during weathering and dissolution processes, and are usually found in the top part of weathered crusts, formed as perpendicular cracks by weathering-induced karstification and mechanical weathering. These fractures have slightly undulating fracture surfaces. Some fractures may merge to form a fracture bundle.
 - b. Obliquely intersected fractures. Fractures appear in groups and intersect one another at a given angle with the bed interface, and a dip angle of generally 40–50 degrees. The most common obliquely intersected fractures are X-shaped shear fractures formed separately during early and late tectonic episodes, with flat fracture surfaces, sometimes with scratches and steps on the fracture surfaces.
 - c. Bedding-parallel fractures. These fractures are parallel to the bedding interface. One of their origins is cracking along mechanically weak zones because of reduced field stress and stratal rebounding related to rock weathering, denudation, and unloading. Another origin is related to bedding and laminae slippage caused by tectonic stress. Most “cake” cracks produced by unloading in the process of coring are not natural fractures, or only represent a special stress setting not existing under natural subsurface conditions, so they should not be considered as fractures.

- d. Reticular fractures. These kinds of fractures are distributed irregularly, developed intensely, but without particular ordering. Reticular fractures have two types: one includes fractures generated by supergenetic weathering, such as karstic collapse, karstic brecciation, mechanical and physical weathering, etc.; the other type is of tectonic origin, developed in the crushing zone in the area of concentrated stress. Usually dense in distribution, interconnected, and connected with pores and vugs, this kind of fracture is important for hydrocarbon migration and accumulation.
 - e. Spall fractures. Found commonly in karst breccia, more chaotic in appearance than reticular fractures, the occurrence of spall fractures indicates intense tectonism or karstification.
 - f. Branching fractures. Microfractures in irregular distribution, with relatively short extension of 1–5 cm, and not intersecting one another, some branching fractures are wide at one end and narrow at the other, in pinch-out shape. They are formed by pressure cracking under burial conditions or expansion cracking caused by dissolution and filling.
 - g. Intersected branching fractures. Slightly longer than branching fractures, extending for 1–10 cm and intersecting each other, these cracks may be caused by karstification and weathering, as well as tectonism.
4. Classification by scale

Fractures can be classified according to fracture width, extension, and spacing (fracture density). Large fractures provide the flow channels or conduits for hydrocarbon migration, whereas small fractures serve as reservoir space.

- a. Microscale fractures. A microfracture may be a few micrometers to 0.01 mm wide, up to 10 cm long and about 10 cm in spacing.
- b. Middle-scale fractures. A middle-scale fracture may be 0.01–0.10 mm in width, 10–30 cm in length, and 20–30 cm in spacing.
- c. Large-scale fractures. A large-scale fracture may be 0.10 mm to several millimeters in width, more than 30 cm in length, and more than 30 cm in spacing.

1.1.2 Main types and characteristics

Fracture-vug carbonate reservoirs are usually strong in heterogeneity, and susceptible to the effects of subsequent tectonic activities. The reservoir space includes mainly secondary fractures and vugs, such as pores, vugs and fractures, and tectoclases which are different in shape, size and distribution. The porous space ranges from several micrometers to tens of meters (Zhihong and Liling, 2006), with strong spatial heterogeneity (Table 1.1) and variable lateral and vertical interconnectivity. Carbonate reservoir space can be classified into four types in terms of their configuration and scale: fracture type, fracture-vug type, vug type, and fracture-cave type. Different types of reservoirs have different reservoir properties, and their development and distribution are controlled by geological structures and karstification process.

Ordovician reservoirs in the Tahe Oilfield are typical fractured-vug reservoirs, undergoing four tectonic movements and three stages of palaeo-karstification, these reservoirs are buried deeply (deeper than 5300 m), strong in heterogeneity and complex and diverse in reservoir space, and complex in oil–water contact. Reservoir development proves fractured-vug reservoirs usually have several fracture-vug

Table 1.1 Fractured-vug reservoir versus sandstone reservoir

	Fracture-vug reservoir	Sandstone reservoir
Pore type	Pore, crack, fracture, pipe, vug	Intergranular pore
Pore size	From larger than several hundred meters to smaller than micrometers	Tens of micrometers to several micrometers
Porosity	Variable, mostly below 3%	15%–20%, relatively homogeneous
Pore geometry	Regular and irregular	Nearly equiaxial
Distribution	Along fractures and formation, in denudation zones, heterogeneous	Layered distribution
Genesis	Tectonism, karstification, geothermal fluids, etc.	Primary pore

systems, pressure systems, and flow units, which are caused by the variations of karsts and structures as well as multiphase karstification and tectonism.

Ordovician carbonate reservoirs in the Tahe Oilfield mainly concentrate in thick blocky micrite and grainstone in the Lower and Middle Ordovician Yijianfang Formation. Hydrocarbon mainly resides in caves formed along high-dip weathered fractures and tectoclasts. Scattered reservoirs differ greatly in volume. Different types of reservoir space form three types of reservoir in different combinations in the Oilfield, i.e., fractured reservoir, fracture-vug reservoir and fracture-cave reservoir. Vug reservoirs are very rare in this oilfield, and only occur in reef limestone zones.

1.1.2.1 Fracture reservoirs

Fracture reservoirs are further divided into fracture and vug-fracture types, which are characterized by extremely low matrix (rock mass) porosity and permeability and abundant fractures. These fractures act as both major migration pathways and reservoir space. In addition to fractures, pores and caves also exist in vug-fracture reservoirs. Reservoir porosity and permeability are closely related to the growth of fractures. Fractures differ greatly in size and distribution. Microfracture density may reach 100/m; large solution fractures may be 10 m from each other. Statistics show fractures are hierarchical; fractures at the same grade have similar intervals.

Fractured reservoirs in the Tahe field mainly concentrate in the Lower and Middle Ordovician carbonate rocks and the Upper Ordovician Lianglitage Formation. Laterally fracture reservoirs are mainly distributed in weathered zones with underdeveloped karsts. For example, karstic valleys in eastern and southern Tahe field or the areas where the Lower and Middle Ordovician limestone is covered by the Lower Carboniferous Series, but most solution fractures and caves are filled with sandy and muddy deposits. In spite of weak karstification, the areas, where the Lower and Middle Ordovician limestone is covered by the Upper Ordovician Series, are tectonically favorable for fracture growth. Vertically fractured reservoirs occur in infiltration and dissolution zones.

In accordance with petrophysical properties of limestone cores acquired from the Lower and Middle Ordovician pay zones in the Tahe field, fractured limestone reservoirs are generally less than 2% in porosity and less than $0.01 \times 10^{-3} \mu\text{m}^2$ in permeability.

Generally drilling break, lost circulation, or well kick would not occur during drilling this kind of reservoir.

1.1.2.2 Fracture-vug reservoirs

Fracture-vug reservoirs have various kinds of pores, vugs, and fractures as reservoir space, and microfractures as pore throats. Both small solution pores and vugs, and fractures are abundant in this kind of reservoir, and make comparable contributions to hydrocarbon migration and accumulation, giving this kind of reservoir typical features of dual-porosity medium. These reservoirs usually have good physical properties and high and stable productivity. With solution pores and vugs as the major reservoir space, the distribution of this kind of reservoir is closely related to palaeo-karstification.

In the Tahe Oilfield, this kind of reservoir has an average fracture porosity of 3.69%, average vug porosity of 2.67%, and matrix porosity of 2.17%. This kind of reservoir features abundant reticular fractures and small solution pores and vugs full of crude oil in core samples.

1.1.2.3 Fracture-cave reservoirs

Fracture-cave reservoirs, mainly developed in thick pure limestone, with secondary solution caves as main reservoir space, and featuring caverns, are very good oil and gas storage space, where fractures mainly act as seepage channels and links with caverns. There is no isolated cavernous reservoir. Drilling break, lost circulation, or well kick often occur during drilling. Oil and gas production in this kind of reservoir features high, stable, or fairly stable initial production, and a long stable production period.

Fracture-cave reservoirs are common in the Tahe Oilfield. The fracture-cave reservoirs drilled in by Well T402 are quite typical, where 242-m-thick Lower Ordovician of calcarenite and micrite was revealed, with a low matrix porosity of less than 1% on the average, and vugs and fractures as main reservoir space. Serious lost circulation of 997.19 and 940.6 m³ occurred at the intervals of 5370.0–5394.0 m and 5549.0–5587.0 m, respectively, and reduced drilling time and serious hole enlargement occurred at the intervals of 5373.0–5375.5, 5559.0–5560.5 m and 5566.0–5568.5 m in this well, indicating the existence of large caverns (with a diameter of 2.5, 1.5 and 2.5 m, respectively). Moreover, reservoirs in this well are rich in small vugs and fractures, 8–23 fractures/m, rich in macrofractures, 5–16 fractures/m from core statistics, and all macrofractures being unfilled effective fractures. In summary, caverns, caves and vugs constitute the majority of reservoir space, accounting for about 68% in this well.

1.1.3 Development conditions of the Ordovician reservoirs in the Taha Oilfield

The development of carbonate reservoir is dependent on tectonism, formation lithology, and palaeo-karstification.

1.1.3.1 Tectonism and rifting

Structurally located in the southwest of the Akekule salient, Xayar uplift, the Taha Oilfield experienced two phases of structural evolution (Figs. 1.1 and 1.2): craton basin phase in the Paleozoic Era when large gentle uplifts developed, and foreland basin phase in the Mesozoic Era and Cenozoic Era, when compressional, nappe and drag structures turned up at the margin of the foreland basin owing to the surrounding mountain system uplifting and thrusting into the basin.

As per the study of palaeostress field, regional principal stress in NW–SE trend in the middle and late Caledonian and early Hercynian (in South-Southeast (SSE) direction in the Early Hercynian) gave rise to the large NE–SW nosing salient inclined to the southwest in the Akekule salient; regional principal extrusion stress in N–S trend in the late Hercynian gave birth to nearly E–W reverse thrusts and local folded structures (Table 1.2). The Akekule salient is a large Lower Paleozoic Ordovician carbonate denuded and folded buried hill in anticline shape; With its top complicated by faults, the salient is divided by nearly E–W fracture sets into

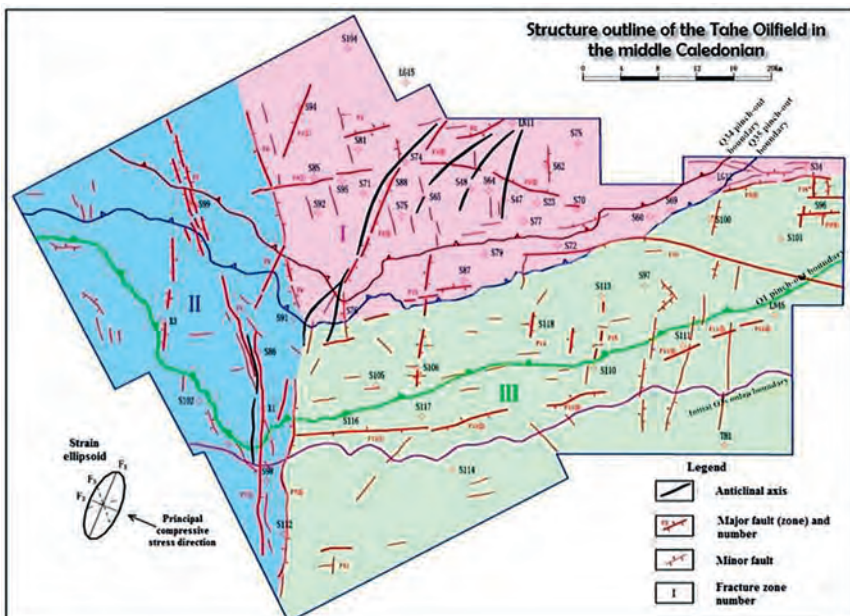


Figure 1.1 Structure outline of the Taha Oilfield in the middle Caledonian.

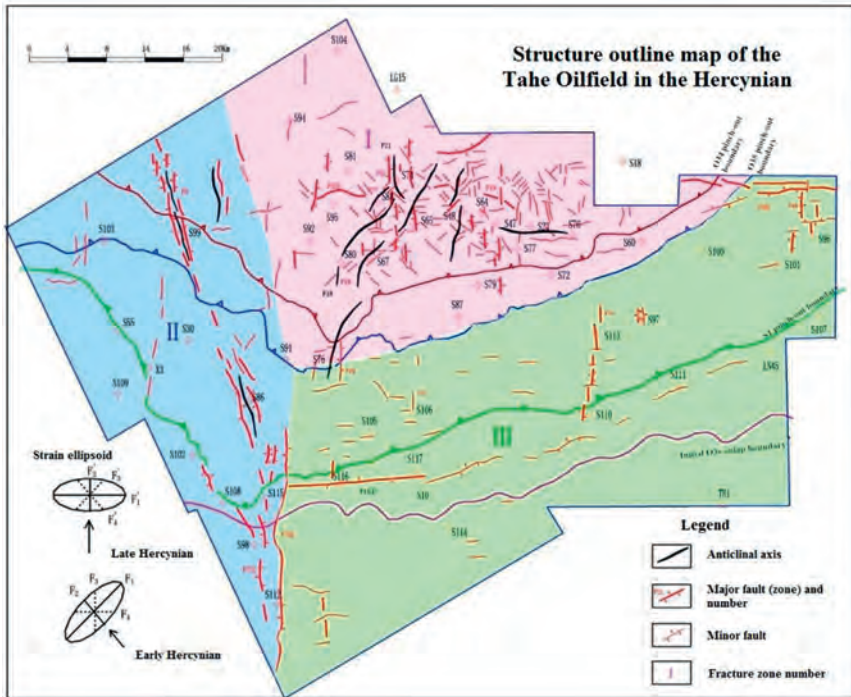


Figure 1.2 Structure outline map of the Tahe Oilfield in the Hercynian.

five zones, i.e., the north slope, Akkum faulted horst, central platform, Akekule faulted horst, and south slope. The Tahe Oilfield lies in the west of the south slope. A nosing salient inclined to the southwest formed in Akekule at the end of the Early Ordovician Epoch, in the early Hercynian, the salient further developed, together with nearly E–W Akkum and Akekule backthrusts and surrounding NE and NW shear fractures, due to the effect of NW–SE compresso-shear stress. In the late Hercynian, the salient was elevated above the water surface and faulting activities further continued.

Overall subsidence occurred in the Indosinian-Yanshanian. In the Himalayan, the Kuqa Foreland Basin subsided quickly; the area on the north of the Akkum fault subsided more due to differential settlement; thus the Lower Paleozoic top surface changed from the early nosing salient into a large anticline. Due to tectonic movements in the late Caledonian and early and late Hercynian, the structural high of the Akekule salient was denuded, losing the Middle and Upper Ordovician Series, Silurian and Devonian Systems, and Upper Carboniferous Series and Permian System. Due to Yanshan movement, the Middle and Upper Jurassic Series were lost in the south of the salient. During the uplifting in the Hercynian, a major part of the salient was exposed to weathering, denudation, leaching, and chemical erosion for a long time, giving birth to a mass of karstic fracture-vug reservoirs.

Table 1.2 Tectonic and stress field evolution in the Tarim Basin

Age			Stress field and tectonic deformation			Basin evolution	
Era	Period	Geologic time/Ma	Stress field	Tectonic deformation	Stress property		
Kz	Q	2.0	Compressive stress and compresso-shear stress	Tectonic axis at 45–135°	Axis of principal stress at 0°	Composite foreland basin	
	N	24.6					
	E	65					
Mz	E	65	Relaxation and adjustment	Tectonic axis: E: 64°-137° K: 80°-150° L: 75°-150°	Axis of principal stress: E: 11° K: 15° L: 17°	Fault basin	
	K	144					
Pz ₂	J	213	Two-way extrusion from south and north directions	Tectonic axis at 65°-110°	Axis of principal stress: T ₁ 365°, T ₂ 32°	Foreland basin	
	T	248					
	P	C	286	Compressive stress and compresso-shear stress	Tectonic axis at 25–145°	Axis of principal stress : P ₁ 39°, P ₂ 35°	Marginal craton depression and intra-craton rift
			360	Tensile stress	Tectonic axis at 40–150°	Axis of principal stress at 5°	
	Pz ₁	D	403	Compressive stress in the south and tensile stress in the north	Tectonic axis at 60–155°	Axis of principal stress : S:7°, D: 352°, D end: 348°	Foreland basin at craton margin
S		433					
O		505					
An	ε	590	Extrusion stress and compresso-shear stress in O ₂ –O ₃	Tectonic axis at 45–135°	Axis of principal stress at 2–12°	Aulacogen at craton margin	
							590
An	Z						

Source: Adapted from Jiajia, 1997.

Tectonism is the most fundamental factor controlling the development of reservoirs. The relationship between tectonism, faults, fractures, and karstification will be discussed as follows.

1. Control of faults over fracture development

a. Fractures dominated by and associated with faults

Tectoclasses are mechanically similar to adjacent faults because they formed in the same stress field. There are always one or several tectoclass sets near a fault extending in the same direction (Fig. 1.3—1). Examining the fracture directions and fault distribution shows the richer the faults in an area, the more fracture sets and more fractures in a set will be.

This phenomenon has also been observed in field survey. The area close to a fault is be more fractured than the area far away from the fault, which demonstrates the domination of faults on fracture development.

We found in the field study that the area with stress concentration was rich in fractures. NE fractures in the west and south of the study area converged southward of the area with stress concentration, where tectoclass tends to occur. In the study area, two conjugate shear fracture sets, one in nearly E–W trend and the other in nearly N–S trend, dominate the karstification in the Caledonian to some extent.

b. Faults dominate the growth of fractures in monadnocks and monadnock slopes.

Because the structural high of a monadnock penetrated by several faults is a stress concentration part, abundant fractures may also be generated by the same stress field (Fig. 1.3—3). A mass of tectoclasses formed in the early stage exist in the Ordovician System, but are densely filled later. Karstification is closely related to ancient landform. For example, the Akekule salient was a southwest plunged nosing anticline in the early Hercynian and the study area was in the southeast and northwest inclined slopes. At a karstic slope, the intensity of karstification is dependent on secondary ancient landform, the structural high, i.e., the buried karstic monadnock, generally experienced intense weathering and denudation, and thus might form a karst land feature rich in fractures and vugs. Therefore, karstic monadnocks at the slope usually have better petrophysical properties than those in the karst depression.

c. Faults in the folds are closely related to fractures.

Fracture development is closely related to faults and folds generated by tectonic movements. Fracture density is generally high around the structural axis and in the structural high, and low at the structural flank and in the structural low. In other words, tectoclass is most developed in fault zones and the areas with large tectonic curvature, and less developed in the areas with few faults or small tectonic curvature. Fractures usually occur in folds because of fault development and stress concentration in the top wall.

d. Branching faults in flower patterns may improve reservoir quality

The tectonism of thrusting and strike-slipping in the late Hercynian gave birth to backthrust blocks, en-echelon faults, and positive flower structures. A flower structure usually lies at the joint of several faults, where tectoclasses tend to form. Reservoir quality may be improved by small-scale branching faults in a positive flower structure, which indicates the area around branching faults in a flower structure would be rich in tectoclasses and oil and gas as well.

2. Relationship between faults and karstification

a. Earlier fault zones dominating later karstification.

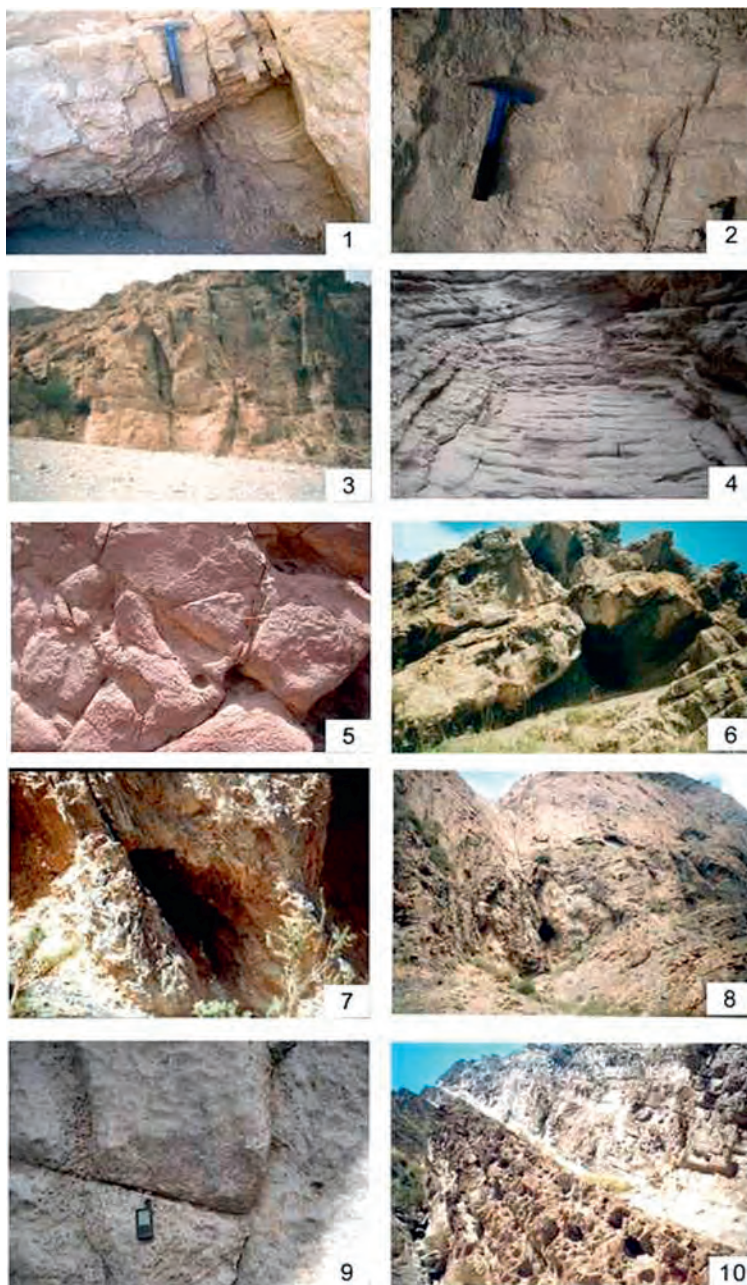


Figure 1.3 Relationship between fractures and karstification.

Fractures add contact area and dissolution scope between carbonate rock and surface water and groundwater, conducive to the dissolution. The water system of dissolution merging into major deep faults can be observed in field survey, which indicates surface water has infiltrated downward along faults, and karstification in the fault zone is also dominated by faults (Fig. 1.3—4).

b. Fractures and karst rich in fault zones

As per previous studies, drilling break and lost circulation often occur during drilling into a fault zone or near a fault; solution fractures have also been observed on core samples. Large fractures with fault gouge and sliding scratches can be observed in the field survey; these fractures are filled with unconsolidated calcite and carbonaceous and argillaceous deposits; thus lost circulation and reduced drilling time often occur during drilling.

c. Karstification occurring in ancient anticline structures.

Due to the effect of intense extrusion stress along the axis of an ancient anticlinal structure, a series of faults and extension joints in parallel with anticline strike form to provide necessary flow channels for groundwater; the junction of two fault sets may have more fractures (Fig. 1.3—5). Cavernous reservoirs mainly exist along the axis of the ancient structure, while fracture-vug reservoirs and fractured reservoirs appear at the flank, with reservoir properties deteriorating from the axis zone to the flank.

d. Consistent strike of dissolution and fault

Large solution fractures or unconformable surfaces show as bead-like reflections on seismic sections, or bead-like solution pores and vugs occur along a fault zone, indicating tectoclase dominated by the fault zone developed along the fault strike, and the process of karstification also occurred along the early fault strike (Fig. 1.3—6); therefore carbonate reservoir properties may be improved.

e. Consistent strike of fault and cave

Solution caves often occur along fault strike (Fig. 1.3—9) or at the junction of several fault sets (Fig. 1.3—6). Early faulted structures dominate the development of deep caves, and caves are mostly likely to occur at the structural axis or along the fault. Caverns (large-scale caves) tend to occur at the junction of several fault sets, where several fracture sets also intersect.

3. Relationship between fractures and vugs

a. Dependence of vug development on fracture shape

Vugs tend to occur at the junction of two or more fractures, especially at the junction of a number of fractures, where carbonate dissolution is faster (Fig. 1.3—5).

b. Control of fracture connectivity on vugs

Vugs are more developed in the area with good fracture connectivity, especially when several fractures are close to or connected with faults or unconformable surfaces.

c. Close relationship between bedding-parallel fractures and dissolution

Fractures are very common in carbonate rock. The carbonate rocks in descending order of fracture development degree are mudstone, muddy dolostone, dolostone, dolomitic limestone, limestone, sandstone, anhydrite, and gypsum. The study shows that Lower Ordovician reservoirs in the study area are mainly composed of pure limestone in stable distribution in the lateral direction, with lithology and rock fabric favorable for the development of fractures. Some isolated vugs occur above the sedimentary hiatus where the dissolution is weak; on the contrary, dense bedding-parallel vugs occur below the hiatus where the corrosion is strong (Fig. 1.3—10). Some vugs, 2–150 cm in size, are perpendicular to bedding surfaces.

1.1.3.2 Formation lithology

The Akekule salient is a palaeo-salient growing on pre-Sinian metamorphic basement, where formations drilled include the Cambrian and Ordovician Systems, Lower Silurian, Upper Devonian, Lower Carboniferous and Upper Permian (volcanic rocks) Series, Triassic System, Lower Jurassic Series, Cretaceous, Tertiary and Quaternary Systems (Table 1.3). The oldest formation ever drilled, in the Upper Cambrian Lower Qiulitage Group was 8408 m deep (Well Tashen 1). Due to the impacts of tectonic movements and crust uplifting in the late Caledonian, Hercynian and Yanshanian, Silurian, Lower and Middle Devonian, Upper Carboniferous, Permian, and Upper Jurassic, formations are lost in the major part of the Akekule salient and most of its southern slope; Upper, Middle and Lower Ordovician Series have been denuded to various degrees and are absent locally. Middle and Upper Ordovician and Lower Silurian formations are preserved only at the south margin of the salient; the Upper Devonian Donghetang Formation is preserved at the west margin of the salient.

The Ordovician System in the Tahe Oilfield is classified into six units (formations), i.e., the Lower Ordovician Penglaiba Formation, the Lower and Middle Ordovician Yingshan Formation, the Middle Ordovician Yijianfang Formation, and the Upper Ordovician Qrebake, Lianglitage and Sangtamu Formations, including 19 conodont zones, spanning over 69 Ma.

1.1.3.3 Karstification

Owing to the effect of tectonic movements, the Ordovician carbonate rock in the Tahe Oilfield experienced hypergenic karstification in the middle Caledonian, weathering karstification in the early Hercynian and stratifying karstification during burial.

The karstification in the middle Caledonian was affected by two factors: (1) Fracture growth along the axis of the Akekule salient in the middle Caledonian. On the one hand, after these fractures were dissolved and enlarged, reservoir space and seepage capacity increased, and on the other hand, atmospheric water flowing downward through these fractures may also intensify the karstification; (b) the rifting process in the middle Caledonian. Due to the effect of regional NWW–SEE principal stress in the first episode of the Caledonian movement, a mass of fractures in the Lower and Middle Ordovician Series were generated by conjugate shearing stress; thus a compresso-shear fault zone formed in nearly N–S trend. This fault zone has a great impact on the karstification in the middle Caledonian, which has improved Lower and Middle Ordovician reservoir properties.

The Akekule salient began to take shape in the Hercynian. Owing to the tectonic collision in northeastern and northwestern Tarim plate, consequent violent tectonic activities at the end of the Late Devonian Epoch and the end of the Permian Period gave birth to large folding structures characterized by great uplift and subsidence together with angular unconformities. Massive intense karstification in the salient was just caused by these tectonic activities. The salient was finalized by the tectonic movements in and after the Indosinian, when the alteration to karstification happened in the burial conditions.

Table 1.3 Formation column in the Tahe Oilfield

Stratigraphy						Thickness (m)	Lithology description
Erathem	System	Series	Fm. (Gr.)	Symbol	Reflection		
Cenozoic	Quaternary			Q	T ₁ ⁰	16–63	Khaki surface soil layer: grayish-yellow fine sand layers sandwiched with khaki cohesive soil layers
	Neogene	Pliocene	Kuqa Fm.	N ₂ <i>k</i>	T ₂ ⁰	1522–2009	Brown–yellow and brownish-gray mudstone and silty mudstone alternating with grayish-white and grayish-yellow fine-grained lithic arkose
		Miocene	Kangcun Fm.	N ₁ <i>k</i>	T ₂ ¹	732–1052	Grayish-white and light-yellow siltstone, fine-grained lithic arkose and gypseous feldspathic quartz sandstone alternating with yellow–gray and brown mudstone and silty mudstone with nearly uniform thickness
			Jidike Fm.	N ₁ <i>j</i>	T ₂ ²	349–694	Yellow–gray, chocolate-brown, gray and glaucous mudstone, light-gray pelitic siltstone and silty mudstone sandwiched with off-white and light-yellow fine-grained lithic arkose
	Eogene	Oligocene	Suweiyi Fm.	E ₃ <i>s</i>		38–306	Yellowish-brown and light-brown fine-grained arkose, fine-grained feldspathic quartz sandstone, light-brown and brown fine- to medium-grained feldspar lithic sandstone and pelitic siltstone sandwiched with brown silty mudstone
		Eocene					
	Paleocene	Kumugeliemu Gr.	E ₁₋₂ <i>km</i>	T ₃ ⁰	614–745	Brownish-red and brown fine-grained feldspar lithic sandstone, lithic arkose, feldspathic quartz sandstone, and brown and light-brown conglomeratic medium sandstone sandwiched with brown silty mudstone, siltstone and mudstone	

Mesozoic	Cretaceous	Lower	Kapushaliang Gr.	K_1kp	T_4^0	298–436	Chocolate-brown silty mudstone and mudstone alternating with grayish-green calcareous siltstone sandwiched with aphanite; light-gray and grayish-green fine-grained arkose and off-white conglomeratic sandstone sandwiched with gray silty mudstone at the bottom
	Jurassic	Lower		J_1	T_4^6	42–76	Gray fine-grained lithic arkose and feldspathic quartz sandstone alternating with gray mudstone, silty mudstone and siltstone with nonuniform thickness, usually contain 1–2 thin coal seams
	Triassic	Upper	Halihatang Fm.	T_3h		98–174	Dark-gray and gray mudstone and carbonaceous mudstone alternating with gray fine-grained arkose with nonuniform thickness in the upper section; gray fine-grained lithic quartz sandstone and arkose sandwiched with dark-gray mudstone and pelitic siltstone in the lower section
		Middle	Akekule Fm.	T_2a		176–298	Two cycles, lower coarse-grained cycle composed of glutenite, conglomeratic sandstone, finestone and medium sandstone sandwiched with dark-gray thin mudstone, upper fine-grained cycle composed of dark-gray and grayish-black mudstone sandwiched with pelitic siltstone, siltstone and thin finestone
		Lower	Ketur Fm.	T_1k	T_5^0	40–120	Gray and dark-gray mudstone with local brown and chocolate-brown mudstone sandwiched with gray silty mudstone, pelitic siltstone and some thin fine sandstone

(Continued)

Table 1.3 (Continued)

Stratigraphy						Thickness (m)	Lithology description
Erathem	System	Series	Fm. (Gr.)	Symbol	Reflection		
Paleozoic	Permian	Middle		P ₂	T ₅ ⁴	0–163	Grayish-black and greenish-black basalt and dacite, intercalated volcanoclastic rock and tuff in the southwest
	Carboniferous	Lower	Kalashayi Fm.	C _{1kl}	T ₅ ⁶	370–537	Thin interbeds of gray and chocolate brown mudstone and offwhite sandstone and siltstone in the upper section, dark-gray and gray mudstone and silty mudstone sandwiched with thin gray mudstone and marl in the lower section
			Bachu Fm.	C _{1b}	T ₅ ⁷	76–235	Gray micrite sandwiched with mudstone (dual-peak limestone) at the top; variegated mudstone sandwiched with thin marl in the middle and upper sections, thick gypsum rocks in the south; conglomerate and siltstone sandwiched with mudstone in the lower section, offwhite finestone sandwiched with mudstone in the southwest
Devonian	Upper	Donghetang Fm.	D _{3d}	T ₆ ⁰	0–80	Gray and off-white fine-grained quartz sandstone alternating with greenish-gray, chocolate-brown and dark-gray mudstone, pelitic siltstone, silty mudstone and calcareous mudstone with nonuniform thickness, more sandstone in the south	

	Silurian	Lower	Kepingtage Fm.	S_{1k}	T_7^0	0–222.5	Grayish-green mudstone, brown and gray mudstone and silty mudstone sandwiched with light-greenish-gray lithic quartz sandstone
	Ordovician	Upper	Sangtamu Fm.	O_{3s}		0–600	Grayish-green and dark-brown silty mudstone sandwiched with dolomitic mudstone or dolostone and local bioclastic limestone and oolitic limestone in the upper section, gray micrite alternating with silty mudstone in the lower section
			Lianglitage Fm.	O_{3l}		0–120	Gray, dark-gray and brownish-gray micrite, calcirudite and oolitic limestone with local small organic reefs
			Qrebake Fm.	O_{3q}	T_7^4	0–25	Grayish-red, purple–red and light-gray marl and bioclastic limestone sandwiched with brownish-red mudstone
		Middle	Yijianfang Fm.	O_{2yj}		0–80	Gray and brownish-gray calcarenite and bioconstructed limestone sandwiched with bioclastic limestone or oolitic limestone, micrite and finely crystalline and crystalline powder limestone, small organic reefs occur locally
			Lower	Yingshan Fm.	O_{1-2y}		600–900
				Penglaiba Fm.	O_{1p}	T_8^0	250–400

1.2 Developmental and evolutionary mechanism of palaeo-karst

Palaeo-karst refers to the karst formed in geological history stage in general (Riyuan et al., 2011). However, as for the definition of geological history stage, there is no unified criterion. Referring to the practices of geology and other disciplines, the karst formed before the Pleistocene can be called palaeo-karst, and the karst that has been developing from the Holocene to the present is called the contemporary karst (there was the Taihang (Yunnan) Movement from the Holocene to Pleistocene). It is noteworthy that the karst generally experienced a long period of evolution, especially for the soluble rock layers exposed to the surface, the karstification generally has experienced a longer period of time span, namely, the incessant reformation from the late stage to present. Therefore, whether it was formed in a geological history period and the occurrence of preserved signs of karst should be taken as the basis in judging whether it is palaeo-karst. If the signs of karst in the past were completely changed in a later period, despite the possibility of karstification happening in a geological period, the karst should be categorized as contemporary karst.

The generation of palaeo-karst is closely related to the relative eustasy and tectonic movements. Because of the relative drop in sea level and regional tectonic uplift, carbonate formations might be uplifted and exposed to the surface, suffering weathering denudation and leaching karstification, thus substantial solution pores, vugs, and fractures are formed, turning the carbonate formation into karst reservoir in palaeo-weathered crust, which provides favorable conditions for the formation of oil and gas reservoirs; organic acid dissolution, thermal dissolution, composite dissolution, dissolution of pressure-releasing water, hydrothermal dissolution, and the like, in the late burial hydrocarbon-generation stage combined, causing the formation of secondary pores and recombination of previous fracture-vug systems. The multiple periods of superposition and alteration of karstification and burial dissolution in palaeo-weathered crust is the optimal combination pattern for palaeo-karst reservoir formation, and is also one of the key factors affecting carbonate reservoirs.

The Middle-Lower Ordovician carbonate in the Tahe Oilfield, with a large number of palaeo-karsts formed in the exposure stage and preserved in the late burial stage, including caves, solution pores and vugs, and solution fractures, has become a good reservoir space for hydrocarbons.

1.2.1 Karst dynamic mechanism

The karst geochemical system is an open system that can be elucidated using the conceptual model of the karst dynamic model (Fig. 1.4).

It is composed of three parts, solid, gas, and liquid phases, in which the solid phase mainly comprises carbonate rock and the fracture networks in them; the liquid phase mainly comprises water with Ca^{2+} (Mg^{2+}), HCO_3^- , CO_3^{2-} , H^+ and dissolved CO_2 ; the gas phase is dominated by CO_2 engaged in the karstification. Its operation mechanism is as follows: CO_2 from the air dissolves into the water,

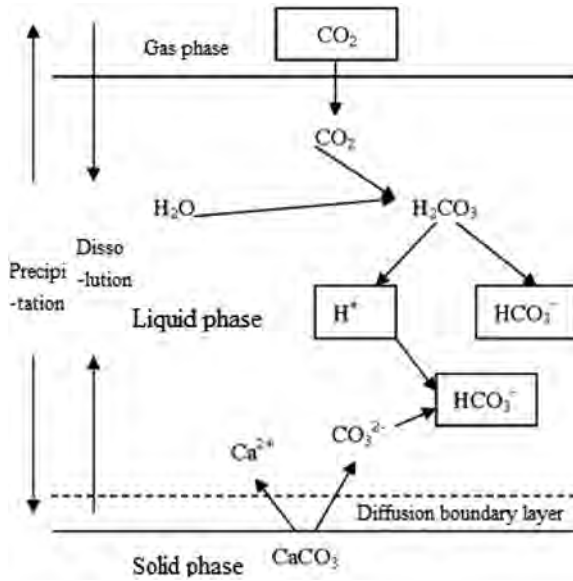


Figure 1.4 Conceptual model of karst dynamics (Yuan et al., 2002).

wherein, a portion reacts with water molecules to form H₂CO₃, which then ionizes into HCO₃⁻ and H⁺, or the liquid phase CO₂ converts into gas and escapes, the chemical reaction formula is:



In water, the carbonatite dissolves into Me²⁺ (Ca²⁺ or Mg²⁺) and CO₃²⁻, the reverse process is the precipitation of carbonatite, the chemical reaction formula is given by:



Then in the solution, the H⁺ generated in reaction Eq. (1.1) combines with the CO₃²⁻ generated in reaction Eq. (1.2), making the dissolution reaction continue Eq. (1.2) or precipitation to occur. This is a reverse reaction, the chemical reaction formula is given by:



In this process, gas, liquid, and solid phases are all involved, and the exchange, conversion, and equilibrium of material and energy take place on different interfaces in an open system.

1.2.2 Formation condition and controlling factors

Rock and water are the basic material conditions for karstification. Specifically, there are four basic conditions: rock solubility and permeability, water erosiveness and fluidity. In fact, karstification is the combined result of internal and external geological agents—regional natural environment, such as climate, vegetation, soil, topography, also have significant effects on karstification. Among the above factors, structure, hydrodynamic, and geomorphologic conditions are nonzonal, while climate, vegetation, and soil are zonal. Also, the above-mentioned internal and external factors have different effects on karstification in different times and places. Therefore, analysis on the factors controlling and affecting the formation and development of regional karst should be specific, rather than general, isolated, and absolute. Evidently, karstification and development process of karst and the karst phenomenon, as a whole, should be considered as systematic engineering.

1.2.2.1 Relationship between carbonate rock properties and karstification

Soluble rock is the material base of karstification. Of the host factors controlling and affecting karstification, mineral composition and texture are the foremost. It is found by field survey that different lithologies in carbonatite have significant effects on the intensity of karstification. Generally, the karst developmental scale and karstification degree in pure carbonatite are higher than that in impure carbonatite, limestone, and dolomite.

A previous study (Weng, 1987) shows that limestone has the highest specific solubility in various kinds of carbonatite, dolomite is in second place, limy (dolomitic) siliceous rock is in the third place, and pure siliceous rock has the lowest solubility; under the same physical and chemical conditions, the solubility of dolomite in any aqueous medium is greater than that of limestone, the solubility of muddy carbonatite decreases because of the increase in insoluble substances, but the siliceous rock still has the lowest solubility. The difference is determined by the mineral composition and crystal structure of carbonate rock.

1. Relationship between rock mineral composition and karstification

The solubility of carbonate can also be judged by the relative content of calcite and dolomite, the relative dissolution rate of carbonate varies with the CaO/MgO ratio (Table 1.4). Dolomite has a CaO/MgO ratio of 1.44–3.74, and limestone has a CaO/MgO ratio of 10.94–150.75. The relative dissolution rate of various dolomites is less than 1.0% (the dissolution rate of standard marble is 1.0), comparatively, various limestones have a dissolution rate greater than 1.0%.

Clearly, karstification has obvious selectivity. In the exposed environment, the karstification intensity of limestone is generally higher than that of dolomite (Table 1.5); in this situation, for the formation with limestone and dolomite interbeds, the underground water flow and dissolution are more and more concentrated in the limestone layers because of the higher dissolution rate of limestone, leading to more and more obvious differential dissolution. In the limestone layers, a series of layered caves often occur, while large layered caves rarely occur in dolomite.

Table 1.4 Test results of erosiveness

Carbonate rock	Horizon	Chemical composition (%)				Mineral composition (%)		Porosity (%)	Relative dissolution rate (mean)
		CaO	MgO	CaO/MgO	Acid insoluble	Calcite	Dolomite		
Mudstone	O ₂	53.18	0.87	61.12	2.99	93.0	4.0	1.9	1.03
Mottled dolomitic limestone	O ₂	49.49	4.52	10.94	2.08	77.2	20.7	0.5	1.03
Bioclast limestone	O ₂	54.1	0.54	100.2	2.03	95.5	2.5	0.4	1.03
Dolomitic and muddy limestone	O ₁	50.17	2.36	21.26	5.19	84.1	10.7	/	1.09
Limy dolomite	O ₂	36.92	15.12	2.44	3.48	27.4	69.1	4.6	0.82
Dolomicrite	O ₂	3.07	18.18	1.66	5.36	10.1	84.5	7.9	0.80
Fine crystal dolomite	O ₁	28.83	19.36	1.48	7.33	4.2	88.5	3.1	0.77
Mudstone	O ₂	54.27	0.36	150.75	2.25	95.0	/	/	1.09
Muddy micritic biolithite	O ₂	53.70	1.19	45.13	1.99	98.0	1.0	/	1.11
Gypsum-dissolved limy dolomite	O ₂	34.63	15.41	2.24	6.06	75.0	68.0	/	0.93
Micritic limy dolomite	O ₂	41.00	10.93	3.74	3.09	38.0	60.0	/	0.93
Microcrystal dolomite	O ₂	32.19	15.87	2.03	9.17	5.0	85.0	/	0.96
Fine crystal dolomite	O ₁	28.96	20.15	1.44	5.62	2.5	95.0	/	0.51

Table 1.5 Comparison of chemical dissolution and mechanical damage

Carbonate rock	Specific solubility (K_{cv})	Specific corrodibility (K_v)	Mechanical damage amount (%)
Mudstone	0.93	0.91	0.004
Muddy dolomitic limestone	0.83	1.15	24.93
Medium-fine crystal dolomite	0.46	0.62	27.95
Dolomitic limestone	0.99	1.14	14.65
Dolomite	0.39	0.49	20.11
Mudstone	1.12	1.10	1.19
Breccia dolomite	0.80	1.73	54.86

In impure carbonate rock, the higher the content of insoluble components, the less developed the karst would be. The influence of shale content on solubility has the following rule: when less than 10%, shale content has little effect on karstification. According to indoor dissolution test results, the relative dissolution rate is slightly higher than that of pure limestone; but when the shale content is greater than 10%, karstification gradually decreases.

2. Relationship between rock texture and karstification

The effect of rock texture on karst development mainly depends on the size and texture of mineral crystals in rock. Generally speaking, the coarser the crystal grains, the more developed the karst would be. This is because the carbonate rocks with different textures have different porosity and intergranular binding forces. The coarser the grain size, the higher the porosity between grains, and the weaker the intergranular binding force is, which is conducive to the formation of hydraulic-rock interaction space, and the karstification degree will be much higher. Therefore, the carbonate rocks of bioclastic texture, pellet texture, nonuniform texture with complex compositions have higher karstification degree than carbonate rocks of micritic texture, crystal grain texture, and uniform texture with monotonous composition.

Rocks with different types of textures have certain differences in denudability. Theoretically, the finer the rock grains, with the higher total porosity and denudation surface, the stronger the denudability of the rock should be, but most of the total porosity and total corrodible amount scatter in micropores, thus not favoring the intensive development of karst; while coarse rock although with lower total porosity, is conducive to the intensive development of karst. When there are dolomite patches in rock, uneven denudation could occur. Mechanical damage in the patches could occur when calcite matrix is dissolved, thus facilitating the overall denudation and damage of the rock body. As shown in Table 1.5, the dolomite has a relatively low dissolution rate but larger mechanical damage; in contrast, limestone has a higher dissolution rate but smaller mechanical damage. Under the condition of identical solution properties and temperature, the major factor affecting chemical dissolution amount is rock composition, and the major factor affecting physical damage amount is rock texture.

3. Mechanism of differential denudation

In the process of karstification, carbonate rocks with different mineral compositions and textures have differential denudation because of different dissolution rates. According to theoretical chemistry studies, in pure water without CO₂, the solubility of natural dolomite is 320 mg/L (18°C), but the solubility of natural calcite is 14 mg/L (25°C), which indicates that in pure water at normal temperature dolomite has higher solubility than calcite, but there is almost no pure water without CO₂ in nature. The CO₂ partial pressure has a significant effect on the dissolution-precipitation of carbonate rock. Under the conditions of 25°C and CO₂ partial pressure of 1 atm, the solubility of calcite reaches up to 800 mg/L and the solubility of dolomite is 599 mg/L; obviously, with the increase of CO₂ partial pressure, the solubility of calcite increases much faster than that of dolomite; namely, under normal temperature and high CO₂ partial pressure, the solubility of calcite is greater than that of dolomite.

The small amount of Mg²⁺, Na⁺, and other ions in water can speed up the dissolution of carbonate rock. In the process of simultaneous dissolution of calcite and dolomite, the small amount of Mg²⁺ occurring in the solution will increase the solubility of calcite, which is also one of the reasons leading to differential denudation when dolomite and calcite coexist.

Due to differential denudation of calcite and dolomite, special microkarst topography often forms on the surface of weathered crust, for example, the criss-crossing “chopping” marks formed on the outcrop surface of dolomite are the result of the faster dissolution rate of calcite in dolomite fractures; differential denudation often leads to “pits” and “granular sugar shapes” on the rock surface; the former are pitted dimples, and the latter rock surface shows granular sugar-shaped embossment.

When the rock is mudstone with even structure, even dolomitization would occur. Since dolomite has even grain size and distribution, its denudation pattern mainly depends on the relative content of calcite and dolomite. If the rock has a dolomite content higher than calcite content, after differential denudation, calcite will leave small pits between dolomite; if the rock has dolomite content lower than calcite content, after differential denudation, the dolomite will be sugar-grain shaped between calcite grains.

Additionally, when dolomitization happens in carbonate rock, the intercrystal pore will increase as a result of replacement; therefore, uniform karstification is frequently seen in the dolomite formations.

1.2.2.2 *Relationship between carbonatite structure and fracture-vug system*

Because of the variation of sedimentary environment and the differences of epidiagenesis, carbonate rocks in an area have complex lithological changes in vertical and lateral directions, thus forming different lithostratigraphic assemblages. Different lithostratigraphic assemblages have different denudation features, for example, limestone with good continuity has denudation along joint fractures, forming uneven karst pipes in larger scale; relatively homogenous pore-fracture networks on a small

scale often occur in thick massive dolomite due to percolation and leaching through pores; the limestone intercalated with dolomite and limestone–dolomite interbeds are in between the two, forming a small pipe–fissure–pore interactive karst system. [Table 1.6](#) shows the controlling features of lithology and karst formation types on karst topography and morphology.

1.2.2.3 Relationship between geological structure and karstification

The Earth's surface has always been in motion due to the influence of celestial bodies and the movement of the Earth itself. The source of force varied in geological history periods and the geological structure features in different regions also vary. The crustal deformation features are controlled by regional crustal structure and strain conditions. Therefore, in certain geological history periods and in certain regions, the field state variance of structural stress created the regional structural features. However, in different geological periods, the stress field was applied on the structural plane of geological bodies, making the deformation situation and scale presented on the same structural plane a superimposed reflection of different mechanical properties in different periods. The change in mechanical properties on the structural plane had significant influences on the circular condition of underwater and development of karst system.

Under the influence of structural stress, the crust could rise, strata fold and rift, laying the foundation for karst development. On the one hand, the crustal uplift led to the exposure of carbonatite massif to the surface or the denudation of overlying sealing, making the carbonatite strata exposed in an open karst system closely linked with atmosphere–hydrosphere–lithosphere; the precipitated carbonatite formed intensive karstification; on the other hand, the uplift and subsidence of crust controlled the circulation and migration of water flow, drainage base level, and depth of karst development. Geological structures also have certain effects on the development of epikarst. In the zones where structures are developed, the tectoclasses are generally more developed, providing infiltration pathways for the surface precipitation to the surficial rock bodies. Thereby, in the structure developed zones, the zonation degree of epikarst is higher.

In a karst system, the fold structure leads to tensional fracture of rock strata, favorable for circulation and migration of water. When there is infiltration of soluble water, tectoclasses could become solution fracture-vug system through hydraulic-rock interaction and solute migration.

1.2.2.4 Effect of topographic and geomorphic conditions on karstification

Topography and geomorphy control the karst development mainly by hydrodynamic conditions and distribution pattern of groundwater field. For the gentle slope and depression, local water circulation in the epikarst zone is likely to occur ([Fig. 1.5](#)); the epikarst zone is most developed in topographic conditions such as inter-river massif, valley slope, peak cluster valley, peak cluster depression, and margin of karst basin.

Table 1.6 Relationship of karst topography and karst formation types in a typical karst zone

Karst formation type			Karst topography and morphology	
Classification	Type	Subtype	Individual morphology	Karst topography
Homogenous pure carbonatite rocks	Continuous limestone	Mudstone Oosparite	Bucket-shaped, tower-shaped, screen-shaped pinnacle and gallery-type, hall-type large caves	Peak cluster depression
	Limestone intercalated with dolomite	Mudstone intercalated with dolomite	Cuesta, screw-shaped mountain and caves developed along the bedding plane	Peak cluster valley Peak forest valley
	Interactive limestone-dolomite	Patched dolomitic limestone or limy dolomite		
Inter-layered impure carbonatite rocks	Interlayered limestone-dolomite	Microcrystallized limestone interbedded with dolomite	Coned, screw-shaped pinnacle and maze-type caves	Peak forest plain
	Interrupted impure carbonate	Lentiform muddy limestone Muddy limestone with siliceous nodules	Hummocky mountain and small springs	Cluster mound valley Gentle mound valley



Figure 1.5 Morphology of karst in regions with different topography and geomorphology (Riyuan et al., 2011).

In the recharging zone, the carbonate outcrops in the topographically high location, due to long-term weathering and erosion, weathered fractures are relatively developed on the rock surface, forming favorable hydrodynamic conditions. Groundwater with relatively high erosiveness and denudability seeps down the surface zone, eroding and altering the originally existing weathered fissures, giving rise to the epikarst zone. With the lengthening of runoff pathway of groundwater in the epikarst zone and the decreasing of hydraulic slope, the erosiveness of water decreases, saturation of carbonate increases, and denudability decreases accordingly, therefore, the development of epikarst in the low-lying areas is relatively weak.

In geomorphologically different locations, karst development degree differs widely, main manifestations are as follows:

1. In the steep zones such as mountain tops, mountain ridges and steep slopes, as infiltration conditions are poor, rain water mainly emerges as slope flow and is lost on the surface, thus diminishing the chance of water–rock contact and dwindling the karstification time, so these areas have low karst developmental levels.
2. At replenishment acceptance locations of groundwater such as mountain tops, karst platforms, periphery slopes of depression, upper slopes on both sides of the valley, and bulges of mountain body slope zones, etc., where the hydraulic gradient is higher, and the weathered fissures on the carbonate rock surface are fairly rich, with favorable hydrodynamic conditions, the immediate-infiltration of precipitation forms underground runoff with higher erosiveness and denudability, so the karstification is stronger, and the epikarst zone is strongly developed.
3. The bottom of the hill, and lower parts of the periphery slopes in the depression and bottom depression, and the bottom of inter-slope valley, etc., are often the discharging zone of groundwater, where with the lengthening of groundwater pathways, the continuous increase of carbonate saturation and the diminishing of hydraulic dynamic gradient, the erosiveness and denudability of underground runoff decrease, so the karstification gets weaker and the development degree of epikarst is lower.
4. In the replenishment area near groundwater watershed at the higher ground, with higher terrain elevation differences, the karst is larger in developmental depth, and mainly shown as vertical dissolved cracks and small caves; in the runoff zone of groundwater, the karst decreases in development depth accordingly with the decrease of terrain elevation, and is in the form of doline on the surface and a pipe-type underground stream under surface; in the

discharging zone, with relatively low terrain and gentle topography, the karst is in low developmental level, large-scale karst is rare, but continuous karst collapse is frequently seen.

1.2.2.5 Relationship between underground hydrodynamic circulation and karst development

Water is one of the basic material conditions for the development of karst, only in the water circulation system, can karst develop. Fig. 1.6 shows the formation process of a fracture-vug system by continuous enlarging dissolution along joints and bedding plains of soluble rock bodies with secondary pores. Fig. 1.6A shows that the enlarging dissolution in the bottom of earth layer leads to the permeability increase of the vertical joints in the upper part of rock bodies, at this point there is no direct hydraulic connection between the water in the upper earth and that in the lower horizontal passage; with the development of karstification, the dissolution enlarges from vertical joints to bedding planes (Fig. 1.6B), but there is no horizontal hydraulic connection between the vertical joints yet, and the water level is almost constant; when there is connection between individual joints and lower horizontal passages (Fig. 1.6C), and when the water flow rate of the connecting parts

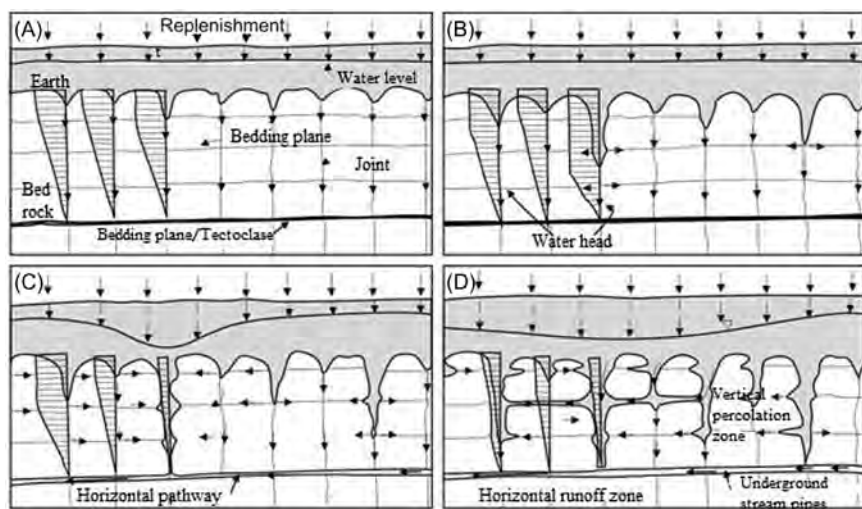


Figure 1.6 Denudation of karst underground water. (A) enlarging dissolution in the bottom of earth layer leads to the permeability increase of the vertical joints in the upper part of rock bodies; (B) with the development of karstification, the dissolution enlarges from vertical joints to bedding planes; (C) when the water flow rate of the connecting parts increases, there is direct hydraulic connection between the water in earth layer and that in the lower horizontal passage, and the water-level-drop funnel is formed; (D) when there is connection between vertical joints in network shape and lower horizontal passage, and there is hydraulic connection between the bedding planes as well.

Source: Adapted from Cooley, T. (August 2002). Engineering approaches to conditions created by a combination of karst and faulting at a hospital in Birmingham, Alabama (in Engineering and environmental impacts of karst). Eng. Geol. 65, (2–3) 197–204.

increases, there is direct hydraulic connection between the water in earth layer and that in the lower horizontal passage, and the water-level-drop funnel is formed there; meanwhile, the dissolution along the bedding plane continuously enlarges as well, but there is still no hydraulic connection between vertical joints; at last, when there is connection between vertical joints in network shape and lower horizontal passage, and there is hydraulic connection between the bedding planes as well (Fig. 1.6D), the overall water level in earth decreases, and in the narrower portion of soluble gas in the vertical joints, partial infiltration water is frequently entrapped because of bottleneck effect, forming water in epikarst zone; while in the lower part, with the enlarging dissolution, the underground stream system forms.

The movement of groundwater is one of crucial conditions for the development of karst, from the surface to deep underground, the movement of groundwater gradually slows down; accordingly, the karst development strength gradually weakens. Despite immense differences in development scale and extremely complex spatial structure of individual fracture-vug systems, under the control of factors such as layered lithologies, hydraulic conditions, and structures, karst development strength follows certain rules vertically, showing zonal distribution (Yubin, 1991; EЖOB, 1992). Different karst developmental zones have different hydrologic and engineering properties, and different types of reservoir structures, so different exploration and development techniques are taken for them.

In the book *China Karst Study*, compiled and published by the Karst Group in the Geology Institute of the Chinese Academy of Sciences, the hydrodynamic section of uniform thick limestone is divided into four zones: vertical infiltration zone, seasonal variation zone, horizontal runoff zone, and deep slow-flow zone (Fig. 1.7),

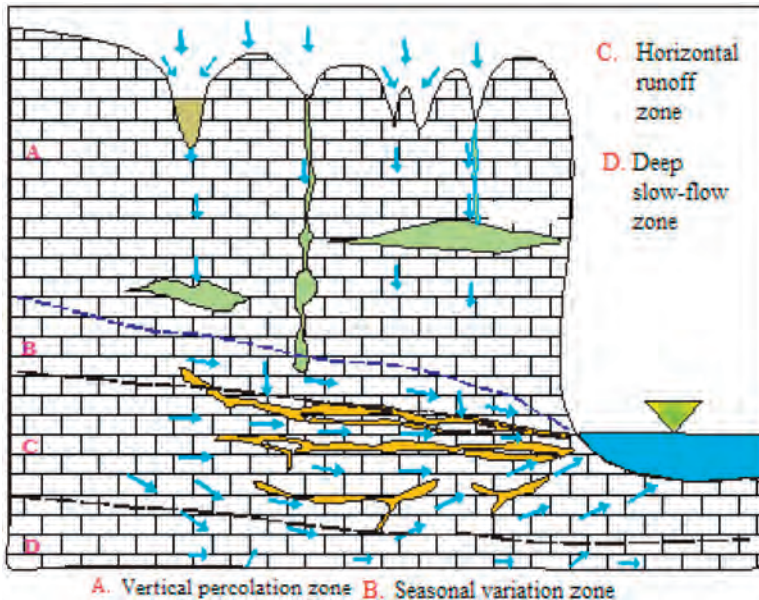


Figure 1.7 Vertical hydrodynamic zonation of karst water in homogenous thick limestone formation.

and the division was widely acknowledged in national Hydrology and Karst circles before the 1990s. However, this zone division and nomenclature only considers one aspect, karst hydrodynamic, and has no universality in multidisciplines; furthermore, there is overlap between the seasonal variation and vertical percolation zone above, and horizontal runoff zone below.

According to the development strength of a fracture-vug system, movement behavior of groundwater, and karstification mode, Xia Riyuan et al. divided the karst section into four zones, epikarst zone, vertical percolation dissolution zone, runoff dissolution zone, and undercurrent dissolution zone in the vertical direction (Fig. 1.8).

1. Epikarst zone

The concept of “epikarst zone” was first found and proposed in the thinly layered mudstone by a French scholar in the early 1970s through the establishment of a karst hydrogeological field testing site. In 1974, Mangin applied it to karst hydrology, and distinguished the water-rich part in the upper part of the aeration zone in the karst hydrodynamic zonation, thus making the karst hydrodynamic zonation more perfect.

The epikarst zone is a karst developmental zone with stronger surficial karstification and a higher degree of karstification in soluble rock bodies and is often bounded by a bottom interface of relatively intact soluble rock. It is usually shown as a strong karstification layer (zone) composed of the assemblage of individual karst forms such as karst groove, lapie, solution fracture, solution fissure, karren, solution cave, solution pipe, and fractures. Its bottom boundary is a plane where multiple-intensity indicators of karstification show abrupt change from big to small (Riyuan et al., 2003).

2. Vertical percolation dissolution zone

In the vertical percolation dissolution zone, the carbonate rock is leached and dissolved by groundwater percolating (or infiltrating) downward along faults or fissures, giving rise to a

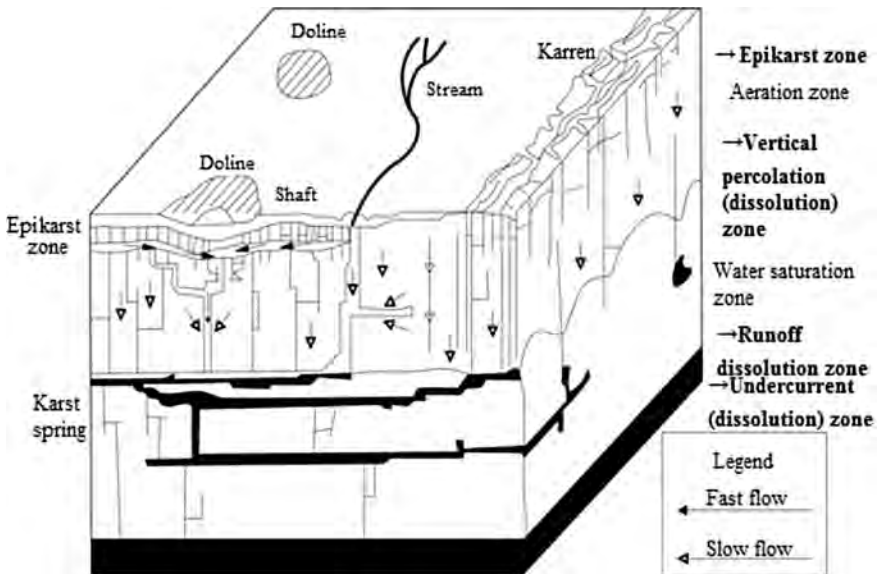


Figure 1.8 Development model of karst vertical zone.

Source: Adapted according to Doerfliger.

series of vertical or high-dip solution fractures or caves and solution space with weaker connectivity. Different geomorphic units have apparent differences in zonal thickness; generally, groundwater replenishment zone > runoff replenishment zone > runoff zone > discharging. The top boundary is the waterproof floor in the epikarst zone and the bottom part is bounded by a large nearly horizontal fracture-cavernous (especially karst pipe) ceiling.

3. Runoff dissolution zone

The runoff dissolution zone is located in the runoff zone of groundwater, where the groundwater flows fast along faults or radially along fissures, dissolving carbonate rock and forming a series of nearly horizontal solution fractures, solution caves, or karst pipeline systems. The zone is characterized by: relatively large scale of dissolution space and stronger connectivity of karst space in the same system; extremely heterogeneous karst development; unobvious differences of zonal thickness in geomorphic units.

4. Undercurrent dissolution zone

The undercurrent dissolution zone is located under the groundwater runoff zone, where groundwater flow along slowly faults or fractures to dissolve carbonate rock. It is characterized by relatively small scale of dissolution space, heterogeneous karst development, relatively weak mechanical filling in late period, relatively strong chemical illuviation, and overall not developed karst.

1.2.3 Developmental and evolutionary mechanisms of paleo-karst in the Tahe region

1.2.3.1 Geological background

Carbonate rock in the Tahe area mainly includes the Middle-Lower Ordovician limestone and dolomite, in which the earliest paleo-karst was formed after the Silurian. Affected by the Caledonian and Hercynian Movement, the Lower Silurian and Ordovician were strongly denudated, with large denudation thickness and expansive erosion area (Xiaoguang et al., 1996). At that time, the climate there was a warm–humid subtropical climate (Dengfa, 2001), and the karst was strongly developed and large in scale; what is left now includes residual paleo-karst halls hundreds of meters in diameter and paleo-underground stream pipes hundreds of meters long. Transgression occurred from the late Carboniferous in the region, and early paleo-karst was buried, filled, and altered. Under the effect of the Himalayan Movement, the margin of the Tianshan massif continuously uplifted, causing partial exposure of the Ordovician carbonate rock to the surface, but the Ordovician carbonate rock was still buried inside the basin (Institute of Xinjiang Geography, Chinese Academy of Sciences, 1986; Chunfang, 1997; Qidong, 2000).

1. Paleoclimate

According to previous studies, in the Devonian and Silurian Period, the paleo-continent of Tarim located in the latitude range of 5 degree south–30 degree north, belonged to a tropical and subtropical marine climate, with plentiful precipitation; from the Upper Devonian to the Middle Carboniferous, the warm–humid and arid–semi-arid tropical–subtropical climate occurred alternately; from the Upper Permian, it was dominated by an arid oxidizing environment.

2. Regional structure

The Tarim Basin is a large multicycle superimposed basin (Desheng, 1995). The Akekule bulge is located in the central Shaya uplift of the uplift zone in the northern Tarim Basin, and

Table 1.7 Statistics of fracture length

Well	Fracture length (%)				Maximum length (cm)
	$L \leq 8$ cm	$8 < L < 13$ cm	$13 \leq L \leq 30$	$L > 30$	
S65	0.2037	0.3333	0.3704	0.0926	110
T415	0.0000	0.0000	0.3333	0.6667	120
S47	0.1154	0.3462	0.5385	0.0000	22
T401	0.0238	0.2143	0.6667	0.0952	57
T402	0.0000	0.3077	0.3077	0.3846	58
T403	0.0152	0.2424	0.6515	0.0909	162
S64	0.0000	0.2308	0.6923	0.0769	50
S88	0.1111	0.1667	0.6667	0.0556	50
T444	0.0000	0.0000	1.0000	0.0000	13
TK406	0.0000	0.0000	1.0000	0.0000	15
TK404	0.4375	0.1875	0.3750	0.0000	15
TK407	0.2000	0.0000	0.8000	0.0000	15
TK409	0.2000	0.2000	0.6000	0.0000	13
S80	0.0000	0.5556	0.3333	0.1111	70
T417	0.1923	0.3462	0.3077	0.1538	99
TK427	0.2778	0.2778	0.4444	0.0000	15

was formed in the late Caledonian, and finalized in the Hercynian period. It is a nose convex trending NE and dipping SW. Due to denudation in the Silurian–Devonian and the Middle–Upper Ordovician in this region, the Silurian–Devonian and the Middle–Upper Ordovician and part of Lower Ordovician are absent, on this basis, the Lower Carboniferous marine mudstone sealing overlapped, forming a wedge-shaped distribution of hiatus, thinning from north to south on the section.

3. Carbonate sequence and lithologies

The formations revealed by drilling wells in the Tahe area include the Cambrian, Ordovician, Lower Silurian, Upper Devonian, Lower Carboniferous, Upper Permian (volcanic rocks), Triassic, Lower Jurassic, Cretaceous, Tertiary, and Quaternary. The lithology of all formations is shown in Table 1.7 in detail.

1.2.3.2 Formation conditions and controlling factors

Identical to contemporary karst, the development of paleo-karst, which is the joint result of internal and external agents, is controlled by rock properties such as solubility, permeability, and fluid erosiveness and fluidity. Rock, structure, geomorphology and hydrodynamic conditions are intrinsic formation conditions, and climate, vegetation and earth are extrinsic influential factors.

1. Lithological feature

The Ordovician carbonate rock in the Tahe area include eight types: mudstone, muddy grainstone, oosparite, microcrystal limestone, and biosparite, limy dolomitic and dolomitic limestone with residual structure, granular crystal dolomite, and mudstone bearing siliceous nodules, in which mudstone is the major type, and limy dolomite and organic reef limestone in local area. The chemical components of the Lower Ordovician medium-thick layered and massive carbonate

rock are 50%–54.27% of CaO, 0.96% of MgO, 1.18% of SiO₂, 0.09% of Al₂O₃, and 0.015% of Fe₂O₃. The chemical components of dolomite are 29.55%–36.57% of CaO, 15.01%–20.92% of MgO, and 0.91%–4.0% of acid insoluble. The palaeo-karst fracture-vug systems mainly occur in limestone, and reef limestone in the local area has the highest developmental level of palaeo-karst, while in the dolomite, there mainly developed solution pores and vugs.

2. Type of formation structure

The combinations of lithology of Ordovician carbonate rocks in the Tahe area mainly contain four types: (1) combination of carbonate and noncarbonate rock, mainly the combination of the Middle-Lower Ordovician carbonate rock and the Upper Ordovician noncarbonate rock—mudstone; (2) combination of pure carbonate and impure carbonate rock—impure carbonate rock is mainly distributed in the upper part of the Yijianfang Formation, and in other carbonate formations, the proportion of impure carbonate rock is all less than 10%; (3) combination of limestone and dolomite—interbeddings of grayish powdery mudstone and powdery crystal dolomitic limestone, limy dolomite and dolomite in local area; (4) combinations of different types of rock structures—including combination of mudstone, microcrystalline limestone, dolomitic limestone and limy dolomite with residual structure, granular crystal dolomite and mudstone bearing siliceous nodules. Among them, the karst formation type of the Yingshan Formation can be divided into one class, three types, and five subtypes (Table 1.8).

Different rock combinations occur alternately in the Yingshan Formation, so the karst developmental level also changes alternately, forming multiple karstified intervals. The three major karstified intervals in this formation are: O_{1y}², O_{1y}⁴ and O_{1y}⁵, among which, the lower part of O_{1y}⁵ and O_{1y}² are thick mudstone and microcrystalline limestone, algae coagulated pellet mudstone intercalated with algae calcarenite, with the strongest karst development degree, and most of large fracture-vug systems occur in these intervals; weaker in

Table 1.8 Division of Karst formation type the Ordovician carbonate rock

Classification	Type	Subtype	Interval	
I Homogenous carbonate rocks	I-1 Continuous limestone	I-1-A Sparitic calcarenite, microcrystalline limestone	O _{1y} ⁵	
		I-1-B Interbedded microcrystalline and sparitic calcarenite	O _{1y} ⁴	
		I-1-C Interbedded mudstone and microcrystalline limestone	O _{1y} ²	
	I-2 Limestone intercalated with dolomite	Mudstone and microcrystalline limestone intercalated with lime dolomite	O _{1y} ¹	
	I-3 Interactive limestone and dolomite	Interbedded mudstone, microcrystalline limestone and dolomitic		O _{1y} ³

the O_{1y}^4 , the karst includes some small–medium fissured caves and vugs; karst is not developed in the O_{1y}^1 and O_{1y}^3 , and karst of certain scale is rarely seen.

3. Geological structure

The evolution of the tectonic stress field in the Tahe area has multistage features, and a variety of structural deformations have formed with the variation of major stress direction. The tectonic evolution of Tabei uplift and Akekule bulge mainly manifested as the formation of uplift prototype in the middle Caledonian period; during this period, multiple movement stages occurred, including the end of Middle Ordovician, the Upper Ordovician, the end of Upper Ordovician, and the end of Silurian, and the tectonic movements were characterized by small-amplitude fluctuation, and the lower and upper formations of the hiatus were in unconformable contact. The Hercynian was the shaping period of the Akekule bulge, because the tectonic stress was derived from the tectonic collision in the northeast and northwest parts of the Tarim Basin, the tectonic movements were strong at the end of the Upper Devonian and the end of the Permian, characterized by the formation of large folds, overall large fluctuation, and angular unconformity. This period was the tectonic period causing the large-scale, strong karstification in the Akekule bulge. The structural movements in and after the Indosinian period intensified or finalized the structural development of the Akekule bulge, when the alteration of the karst system was under burial conditions.

4. Palaeogeomorphological conditions

According to the results of geomorphologic research, the second-order geomorphologic type of the pre-Carboniferous in the Tahe Oilfield can be divided into three types, karst platform, karst gentle slope, and karst intermountain basin (Fig. 1.9), and the third-order geomorphological types include peak cluster depression, karst groove, mound peak

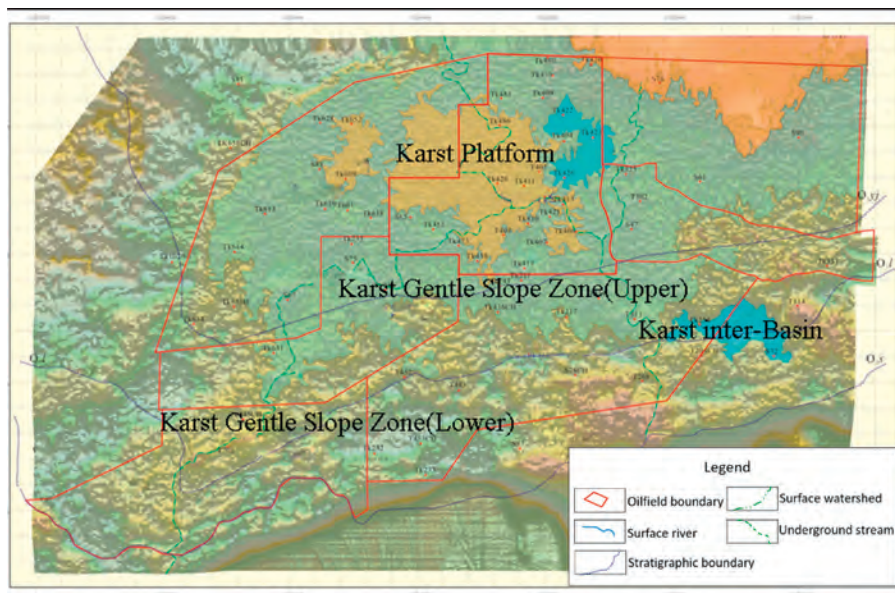


Figure 1.9 Geomorphological map of pre-Carboniferous palaeo-karst in the Tahe Oilfield region (second-order geomorphological division).

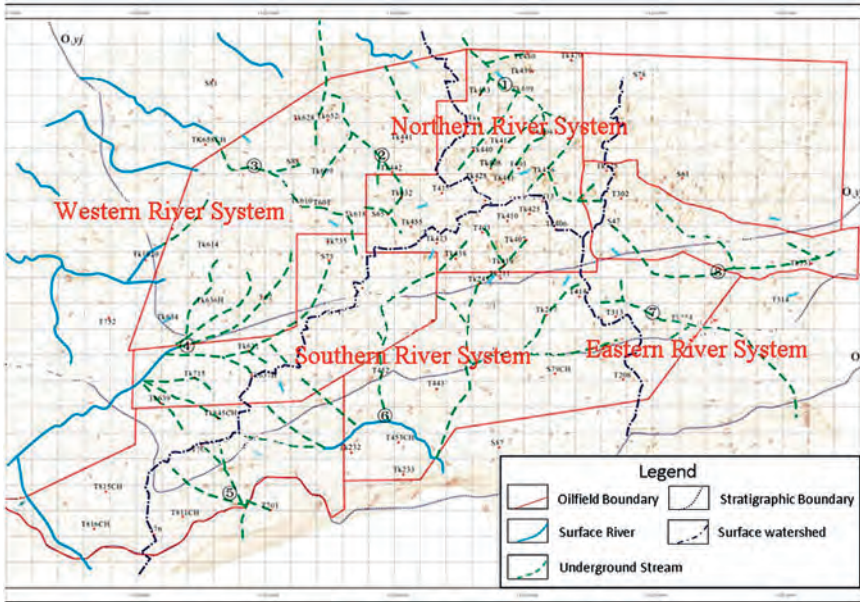


Figure 1.11 Pre-Carboniferous palaeo-drainage distribution of the major body in the Tahe Oilfield.

The $\delta^{13}\text{C}$ and $\delta^{18}\text{O}$ value of carbonate can be used as indicators of depositional environment (Tingyu, 2004). The marine and freshwater limestones can be distinguished according to the empirical formula:

$$Z = a(\delta^{13}\text{C} + 50) + b(\delta^{18}\text{O} + 50)$$

where, $\delta^{13}\text{C}$ and $\delta^{18}\text{O}$ are the values in Program database file (PDB) standard, $a = 2.048$, $b = 0.498$.

In the equilibrium fractionation of isotopes (Hendy and Wilson, 1986), $\delta^{18}\text{O}$ value is mainly controlled by changes in ambient temperature. The hydraulic-rock reaction controlled by temperature leads to a temperature gradient of about $-0.24\text{‰}/\text{C}$. Under isotopic equilibrium conditions, the $\delta^{18}\text{O}$ involved with hydraulic-rock reaction reflects the annual average value of atmospheric precipitation; and the $\delta^{18}\text{O}$ of atmospheric precipitation is also affected by the factors such as source of water evaporation, and migration pathway of water evaporation, condensation temperature and precipitation (Gascoyne, 1992). Therefore, $\delta^{18}\text{O}$ of fracture and cave fillings mainly reflects the environmental temperature and atmospheric precipitation information in its forming stage.

Compared with $\delta^{18}\text{O}$, $\delta^{13}\text{C}$ is more susceptible to factors such as evaporation, dynamic fractionation, and previous deposition of carbonate rocks, making its values positive-prone. Therefore, when the $\delta^{13}\text{C}$ is used to reconstruct paleoclimate, it should be examined whether it was disturbed. Also, there are some karstification processes that can cause $\delta^{13}\text{C}$ to deviate from the equilibrium value. Related studies show that the fast flow of infiltration water through the earth zone due to high levels of precipitation could lead to imbalanced dissolution of intergranular CO_2 in earth, thereby, an increase in the $\delta^{13}\text{C}$ value from -12‰ to -2‰ in the travertine deposits (Bar-Matthews et al., 1999, 2000);

the addition of carbon from bedrock and surficial earth zone can also deviate $\delta^{13}\text{C}$ from its equilibrium value (Genty et al., 2001).

a. Carbon–oxygen isotope characteristics in the Ordovician karst fillings in the outcrop area of the northern Tarim Basin

In the outcrop area of the northern Tarim Basin, the carbon–oxygen stable isotope characteristics of the Ordovician karst fillings evidently show the abundance feature of secondary minerals (Table 1.9). Compared with isotope abundance of marine carbonate rock ($\delta^{13}\text{C}$, PDB, generally -1 to 2% , a varying amplitude of 3 – 5%), most of the fracture and cave fillings have a $\delta^{13}\text{C}$ value of less than -1.0% , with a varying amplitude of up to 7.28% . The lower $\delta^{13}\text{C}$ values indicate that the minerals were formed in shallow layers, and during the forming stage, they were affected by the oxidation of organic matter introduced by the infiltration of surficial water. In general, the $\delta^{18}\text{O}$ value of marine and fresh-water carbonate rocks are -1.5% to -10% and -5% to -10% , respectively. $\delta^{18}\text{O}$ of fracture and cave fillings is -6.46% to -14.54% , much lower than that of bedrock, which indicates its forming environment is more complex, and hydrothermal effect and isotope metasomatism cause $\delta^{18}\text{O}$ depletion.

Table 1.9 Stable carbon-oxygen isotope test results of palaeo-karst fillings in the outcrop area of the Tarim Basin

Location	Sample no.	Mineral name	$\delta^{13}\text{C}$ (PDB)%	$\delta^{18}\text{O}$ (PDB)%
Sulfur Mine No.1 Valley	2	Infilled muddy	-2.64	-12.47
S314 Road 1133 km Sulfur Mine	Kb001	calcareous, muddy filling material	-3.23	-15.05
Sulfur Mine No.4 Valley 7 cave	KT004	Gypsum intercalated with calcite	-1.19	-13.32
Sulfur Mine No.4 Valley 9 cave	KT005	Gypsum paragenetic calcite	-2.7	-14.86
Sulfur Mine No.4 Valley 9 cave	KT006-2	Calcite vein	-2.55	-14.96
Yijianfang No.2 groove	KT011	Calcite	-0.19	-6.63
Yijianfang No.2 groove	KT012	Cave deposits	-0.49	-11.64
Yijianfang No.2 groove	KT013	Calcite	-2.21	-10.79
Sanchakou 1232.5 km	KT017	Calcite vein	0.94	-8.94
Sanchakou 1234 km	KT019	Early period calcite	-1.24	-12.26
Sanchakou 1257.5 km	KT019-2	Calcite	-1.9	-10.26
Sanchakou 1276-km ³ gully	KT022-1	Calcite	-2.1	-12.16
Sanchakou 1276-km ³ gully	KT022-2	Mud of cave deposits	1.29	-8.99
Xike'er 1282 km	KT023-1	Mud deposited in fracture	0.18	-8.28
Sulfur Mine No.1 gully	KT038	Crystallized travertine	-4.33	-15.86

The analysis of the $\delta^{13}\text{C}$ – $\delta^{18}\text{O}$ relationship diagram shows that the Ordovician karst filling minerals in the Tarim Basin were formed in five different environmental conditions: type 1, the mud-rich calcareous, muddy sedimentary filling, is the carbonate deposits formed under the condition of fluviation by mechanical filling in relatively dry and hot conditions, with a $\delta^{18}\text{O}$ of -8.99‰ to -6.63‰ and a $\delta^{13}\text{C}$ of -0.19‰ to 1.29‰ ; type 2 is the infilled calcite in earlier period with a $\delta^{18}\text{O}$ of -13.32‰ to -11.46‰ and a $\delta^{13}\text{C}$ of -1.24‰ to 0.49‰ , which has a baking rim caused by magma invasion in field survey; type 3 is the chemical precipitation formed in a later period, which mainly fills in the karst fissures or solution tectoclases, the infilling process was slow, showing multilayered features; type 4 is also chemical precipitation formed in a later period, mainly seen in the wall of caves and paragenetic with gypsum; type 5 is the recrystallization of early karst fillings with a $\delta^{18}\text{O}$ of -15.86‰ to -15.05‰ and a $\delta^{13}\text{C}$ of -4.33‰ to 3.23‰ , much lower than other types (Fig. 1.12).

b. Carbon–oxygen isotope characteristics of the Ordovician karst fillings in the Tahe Oilfield region

According to the $\delta^{13}\text{C}$ – $\delta^{18}\text{O}$ relationship (Fig. 1.13), the carbonate minerals in the karst fillings were mainly formed in two different environmental conditions. Type I was formed by the mechanical deposition process in the period of weathered crust karstification, the fillings are mud-rich calcareous, muddy sedimentary filling, and were the carbonate deposits formed by the mechanical deposition under the condition of fluviation, the environment was relatively dry and hot with higher $\delta^{18}\text{O}$ value of -9.88‰ to -6.60‰

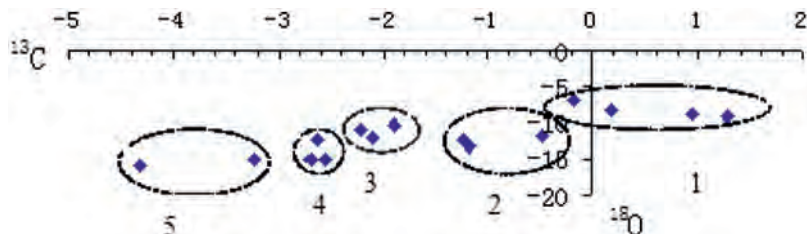


Figure 1.12 $\delta^{13}\text{C}$ – $\delta^{18}\text{O}$ relationship of the palaeo-karst fillings in the Tarim Basin.

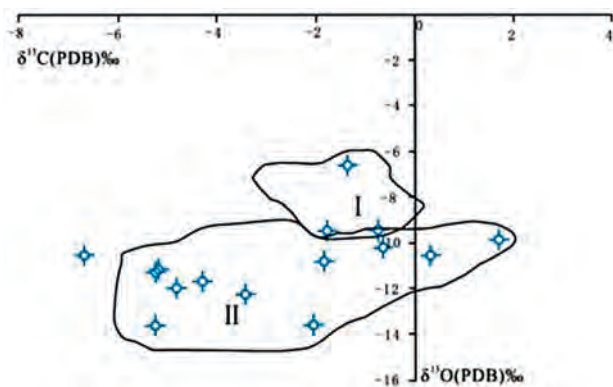


Figure 1.13 $\delta^{13}\text{C}$ – $\delta^{18}\text{O}$ relationship of the palaeokarst fracture-vug system fillings in the Tahe region.

and higher $\delta^{13}\text{C}$ value of -0.74‰ to -2.05‰ ; type II is the chemical precipitation fillings formed in a later stage, in which calcite has a strongly negative $\delta^{18}\text{O}$ value, indicating the obvious relationship between the formation of calcite fillings and hydrothermal process; the $\delta^{18}\text{O}$ values of calcareous, muddy material are also negative, reflecting that the calcareous cementation was formed by the late hydrothermal alteration of early infilled mud, with a $\delta^{18}\text{O}$ value of -12.27‰ to -10.17‰ . Mainly filled in caves, karst fissures or solution tectoclasts, they underwent a slow infilling process over a long period of time, with multilayers, indicating multiple actions in the same period.

The forming environments of carbonate minerals in type I, II karst fillings were relatively universal, respectively belonging to the major stage of infilling and alteration of the palaeo-karst fracture-vug system.

The $\delta^{13}\text{C}$ and $\delta^{18}\text{O}$ values of fillings in the palaeokarst fracture-vug system of the Ordovician carbonate rock in the Tahe region have a wide range (Table 1.10) with a $\delta^{13}\text{C}$ value of 1.70‰ to -6.67‰ and a $\delta^{18}\text{O}$ value of -6.60‰ to -12.27‰ . The $\delta^{18}\text{O}$ value of fillings in the palaeokarst fracture-vug system is uniformly negative, indicating that the formation of fillings in the palaeokarst fracture-vug system was affected by atmospheric freshwater, and the depositional environment was weathered crust at that time.

Overall, the illuviation products formed in the karstification process of freshwater leaching, lixiviation, and organic acid obviously have negative $\delta^{18}\text{O}$ values. Among them, the karst fillings produced in the environment of early epidiagenesis and exposure have relatively rich $\delta^{18}\text{O}$, and obviously negative $\delta^{18}\text{O}$ and little variation of $\delta^{13}\text{C}$ value; the precipitant produced after the introduction of organic acid in the pressure-released water in the burial environment has a high content of CO_2 , obviously a negative $\delta^{13}\text{C}$ value, and a lower $\delta^{18}\text{O}$ value; under the hydrothermal process, the organic

Table 1.10 Carbon-oxygen isotope characteristics of the palaeo-karst fracture-vug system fillings in the Tahe region

Sample no.	Sampling depth (m)	Sample rock	$\delta^{13}\text{C}$ (PDB) ‰	$\delta^{18}\text{O}$ (PDB) ‰
S161 8(23/35)	5523.1	Calcite + rock	-3.42	-12.27
S165 7(49/56)	5468.3	calcite	-4.82	-11.98
S165 17(5/7)	5723.3	Gray calcite	-1.84	-10.78
S170 12(71/71)	5434.0	calcite	-0.65	-10.17
S174 15(1/49)	5720.1	calcite	-2.05	-13.58
S180 12(10/39)	5711.8	Gray sand and mud + calcite	-5.25	-13.67
S190 8(29/58)	5655.8	calcite	0.33	-10.57
S191 7(20/27)	/	calcite	1.70	-9.88
T403 6(26/26)	5488.9	Mottle calcite	-1.36	-6.60
T417 4(4-8/29)	5506.5	calcite	-5.21	-11.22
T417 6(25/55)	5663.0	calcite	-5.12	-11.10
T501 11(37/43)	5628.1	calcite	-4.29	-11.70
T601 4(26/39)	5576.4	calcite + lime calcareous mud	-6.67	-10.55
S147 11(2-3/51)	5442.8	calcite	-0.74	-9.43
S147 14(9/14)	5467.8	calcite	-1.79	-9.49

matter decomposed and methanized, and there was a heavy isotope enrichment in water, causing a higher $\delta^{13}\text{O}$ value, and some higher positive values.

2. Indication of filling inclusions to paleo-karstification

The shape, composition, and homogenous temperature of filling inclusions can intuitively reflect the fluid properties and environmental conditions when they were formed (Shaobo and Jiayu, 1997), and the features of inclusions are also indicative to the environment and stage of palaeo-karst (Huanzhang, 1990; Riyuan and Jiansheng, 2004; Riyuan et al., 2006).

a. Features of filling inclusion in Ordovician palaeo-karst fillings in the outcrop region of the northern Tarim Basin

The test and analysis (Tables 1.11–1.13, Figs. 1.14–1.17) of calcite and fluorite inclusions in the Ordovician palaeo-karst filling minerals in the outcrop region of the northern Tarim Basin indicate that the fluid characteristics and environmental conditions reflected by all eigenvalues are as follows:

Physical characteristics. Individual inclusions in the regional palaeo-karst filling minerals are generally small, 0.1–150 μm , generally 3–35 μm , rice-shaped, rectangular, polygonal, diamond, and other irregular shaped, occurring in bead-like or free distribution, and a small amount are distributed along microfissures. There are two types of typical inclusions: saline mono-liquid ($\text{L}_{\text{H}_2\text{O}}$) phase and saline gas–liquid ($\text{L}_{\text{H}_2\text{O}} + \text{V}_{\text{H}_2\text{O}}$) phase. In addition, fluorite inclusions have another CO_2 -rich gas–liquid phase ($\text{L}_{\text{CO}_2} + \text{V}_{\text{CO}_2}$ or $\text{L}_{\text{H}_2\text{O}} + \text{L}_{\text{CO}_2} + \text{V}_{\text{CO}_2}$).

Chemical phase. The chemical equilibrium system of calcite inclusions has three types: $\text{NaCl-H}_2\text{O}$, $\text{NaCl-H}_2\text{O-MgCl}_2$, $\text{NaCl-H}_2\text{O-CaCl}_2$. Besides the three types, fluorite inclusion has $\text{CO}_2\text{-NaCl-H}_2\text{O}$, indicating fluorite is hydrothermal and hydrothermal metasomatism genesis. Early-filled calcite was recrystallized by hydrothermal process or was converted into fluorite by hydrothermal metasomatism.

Salinity. The salinity of calcite inclusions can be divided into three levels: low-salinity, 1.0–3.0 wt.% NaCl, medium salinity, 5.0–8.0 wt.% NaCl, and high salinity, 22.0–23.0 wt.% NaCl. The salinity of fluorite inclusions has a wide range, mainly 1.0–8.0 wt.% NaCl, and a small number of them reach up to 22.0–24.0 wt.% NaCl.

Homogenous temperature. Calcite gas–liquid inclusions have a homogenous temperature range of 40–180°C, mainly 105–135°C; fluorite inclusions have a homogenous temperature range of 90–285°C, which can be divided into four sections: namely, 90–110°C, 110–130°C, 130–170°C, and 250–285°C. The high-temperature inclusions belong to the $\text{CO}_2\text{-NaCl-H}_2\text{O}$ system, and are the result of hydrothermal processes and alterations in the deep formations.

Chemical composition. According to the chemical composition of inclusions, gas is mainly composed of H_2O and CO_2 . Compared with the composition of paleo-karst filling inclusions from the deep Ordos Basin, they have much lower content of CH_4 and CO ; liquid components are dominated by HCO_3^- , Ca_2^+ , with lower content of Cl^- and K^+ than those in the Ordos Basin, reflecting that the paleo-karst fillings were formed in a freshwater karstification environment with lean organic matter.

Combination type. Due to differences in formation environment, comprehensive chemical characteristics of calcite and fluorite inclusions in this region can be divided into four types: low-temperature and low-salinity $\text{NaCl-H}_2\text{O}$; low-temperature and high-salinity $\text{NaCl-H}_2\text{O-CaCl}_2$; medium-temperature and medium-salinity $\text{NaCl-H}_2\text{O-MgCl}_2$; and high-temperature and medium-salinity $\text{CO}_2\text{-NaCl-H}_2\text{O}$.

b. Features of inclusions in Ordovician palaeo-karst fillings in the Tahe Oilfield. The test and analysis of inclusions in the precipitated calcite in the palaeo-karst fracture-vug system (palaeo-cave, solution fracture-vug,) of the drilled wells in the Tahe Oilfield (Table 1.14) show the inclusions are mainly water inclusions and a small number of

Table 1.11 Features of calcite inclusions in the Ordovician palaeo-karst in the Tarim Basin

Sample no.	Inclusion type	Homogenous temperature (°C)	Forming pressure ($\times 10^5$ Pa)	Density (g/cm ³)	Salinity (wt.% NaCl)	Freezing point (°C)	Chemical equilibrium system
KT011-1	Single-liquid phase Gas-liquid phase	118-146	320-395	0.971-0.979	6.2-6.6 6.2-7.0	-3.8 to -4.1 -3.8 to -4.4	NaCl-H ₂ O
KT013	Single-liquid phase Gas-liquid phase 1 Gas-liquid phase 2	105-125 95-115	285-340 267-325	0.975-0.988 1.11-1.114	6.2-6.7 21.5~22 6.4-6.7 21.9-22.67	-3.8 to -4.2 -18.5~ -19.1 -4.0 to -4.2 -19 to -20	NaCl-H ₂ O NaCl-H ₂ O-CaCl ₂
KT014	Single-liquid phase Gas-liquid phase	160-180	433-492	0.932-0.954	6.2-7.2 6.2-7.6	-3.5 to -4.5 -3.8 to -4.8	NaCl-H ₂ O
KT018-1	Single-liquid phase Gas-liquid phase Gas-liquid phase	40-60 105-135	86-148 280-360	0.968-0.978 0.971-0.995	1.4-2.6 0.9-2.0 4.6-5.5	-0.8 to -1.5 -0.5 to -1.2 -2.8 to -3.4	NaCl-H ₂ O NaCl-H ₂ O
KT022-1	Single-liquid phase Gas-liquid phase 1 Gas-liquid phase 2	110-130 120-140	310-365 335-385	1.112-1.115 1.029-1.035	22.3-23.0 22.67-23.36 13-13.5	-19.5 to -20.2 -20 to -21 -9.9 to -11	NaCl-H ₂ O-CaCl ₂

Table 1.12 Features of fluorite inclusions in the Ordovician palaeo-karst in the northern margin in the Tarim Basin

Sample no.	Inclusion type	Homogenous temperature (°C)	Forming pressure ($\times 10^5$ Pa)	Density (g/cm ³)	Salinity (wt. % NaCl)	Freezing point (°C)	Chemical equilibrium system
KT009	Gas–liquid phase 1	120–140	322–380	0.963–0.979	5.2–6.4	–3.2 to –4.0	NaCl–H ₂ O
	Gas–liquid phase 2	90–110	245–301	0.997–1.007	6.7–7.6	–4.2 to –4.8	NaCl–H ₂ O
	Gas–liquid phase 3	115–135	308–364	0.968–0.979	4.9–5.7	–3.0 to –3.5	NaCl–H ₂ O
KT011-2-1	Single-liquid phase				7.2–7.9	–4.5 to –5.0	
	Gas–liquid phase 1	125–155	340–425	0.968–0.975	7.3–8.0	–4.6 to –5.1	NaCl–H ₂ O–MgCl ₂
	Gas–liquid phase 2	110–120	305–430	1.014–1.022	10.2–12	–6.8 to –8.2	NaCl–H ₂ O–MgCl ₂
KT011-2-4	Single-liquid phase				21.2–23.02	–18.0 to –20.5	
	Gas–liquid phase	120–146	335–410	1.098–1.101	22–24.04	–19 to –21	NaCl–H ₂ O–CaCl ₂
KT041-1	Single-liquid phase				6.4–6.7	–4.0 to –4.2	
	Gas–liquid phase	130–170	350–465	0.962–0.978	6.4–7.6	–4.0 to –4.8	NaCl–H ₂ O
KT041-2	Single-liquid phase				5.0–5.2	–3.0 to –3.2	
	Gas–liquid phase	105–135	280–360	0.981–0.987	5.1–5.7	–3.1 ~ –3.5	NaCl–H ₂ O–MgCl ₂

Table 1.13 Chemical composition of inclusions in infilled minerals in solution pores and fractures

Item		Gas phase (ppm)								
Sample no.		H ₂ O	CO ₂	CO	CH ₄	H ₂				
KT019 (calcite)		417.20	187.85	0.10	0.15	0.16				
KT036 (fluorite)		431.47	2.15	0.05	0.02	0.17				
KT038 (crystal travertine)		305.76	81.60	0.06	0.05	0.12				
Liquid phase (ppm)										
Sample No.	K ⁺	Na ⁺	Ca ²⁺	Mg ²⁺	Li ⁺	F ⁻	Cl ⁻	SO ₄ ²⁻	HCO ₃ ⁻	pH
KT019 (calcite)	0.96	12.41	319.47	8.282	0.005	0.21	15.51	5.00	187.50	7.20
KT036 (fluorite)	0.94	8.22	55.06	1.059	0.010	44.22	12.35	0.00	0.00	5.80
KT038 (crystal travertine)	4.28	2.09	51.85	1.901	0.005	0.33	5.11	0.00	41.50	6.90

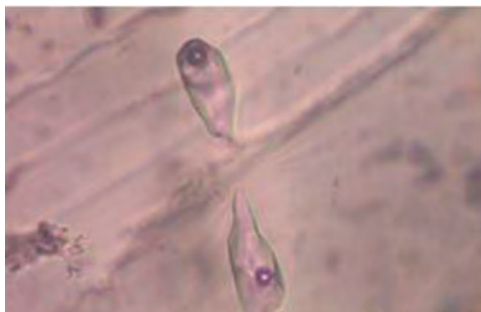


Figure 1.14 Microscopy of inclusion KT009. The two-phase saline oval inclusion in the amatista is 20–30 μm .

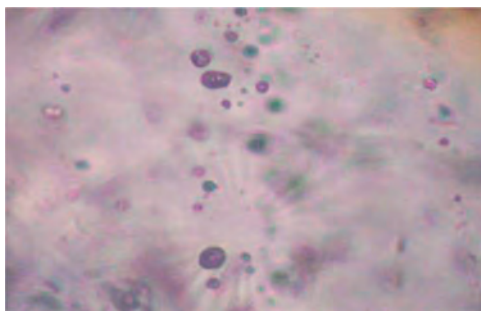


Figure 1.15 Microscopy of inclusion KT018. In the fluorite, the CO_2 -rich two-phase inclusions ($L_{\text{CO}_2} + V_{\text{CO}_2}$) distributed in small groups and 20 μm in size.

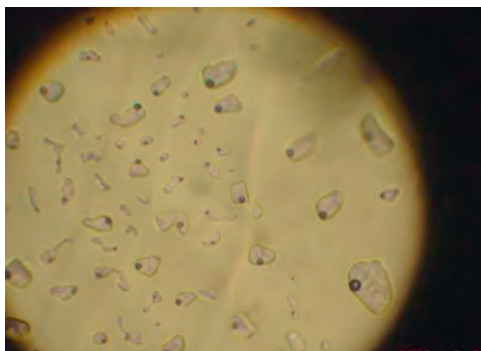


Figure 1.16 Microscopy of inclusion KT041. Light-colored fluorite two-phase inclusion in group distribution, 4–14 μm in size.

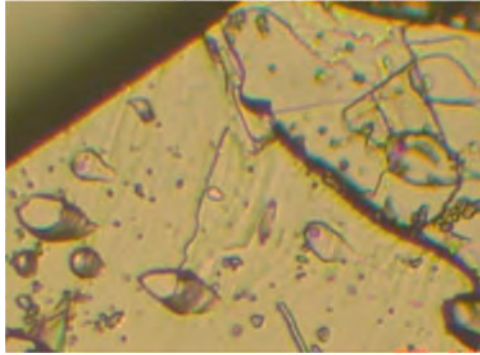


Figure 1.17 Microscopy of inclusion KT022. Saline inclusions in calcite in small group distribution, 4–14 μm in size.

hydrocarbon inclusions (more in the local area), and liquid hydrocarbon-bearing inclusions in the local area (mainly in the buried karst area). The water-inclusions have two types, single-phase and two-phase saline inclusions; the hydrocarbonaceous inclusions have three types, single-phase gaseous hydrocarbonaceous inclusion, single-phase and two-phase hydrocarbonaceous inclusions. Individual inclusions are generally small, 1–30 μm , mainly 2–15 μm , and rice-shaped, rectangular, polygonal, diamond, and irregular-shaped, occurring in small groups or freely distributed, and a small number of them are distributed along microscopically healed fissures.

The chemical equilibrium system of calcite inclusions has three types, namely, $\text{NaCl-H}_2\text{O}$, $\text{NaCl-H}_2\text{O-MgCl}_2$, and $\text{NaCl-H}_2\text{O-CaCl}_2$, mainly $\text{NaCl-H}_2\text{O-CaCl}_2$ type, reflecting the recrystallization of early-infilled calcite by hydrothermal process, which is similar to the Lungu region.

The homogeneous temperature of calcite hydrocarbonaceous inclusions is 102–105°C, 65–75°C, and 75–95°C.

In the two-phase brine inclusions of calcite water inclusions, different inclusion groups in the same sample differ widely in salinity, freezing temperature and chemical equilibrium phase system, reflecting the differences of different genetic environments and the chemical evolution in the precipitation of minerals; in the same sample, inclusion groups have the same chemical equilibrium phase system but certain differences in freezing temperature and homogenous temperature, also reflecting certain differences in their forming environment and chemical evolution in the precipitation of minerals.

The calcite water inclusions can be comprehensively divided into: low-temperature and low-salinity ($\text{NaCl-H}_2\text{O}$ or $\text{NaCl-MgCl}_2\text{-H}_2\text{O}$); low-temperature and high-salinity $\text{NaCl-CaCl}_2\text{-H}_2\text{O}$; medium-temperature and medium-salinity $\text{H}_2\text{O-MgCl}_2$ or $\text{NaCl-MgCl}_2\text{-H}_2\text{O}$; medium-temperature and high salinity $\text{NaCl-CaCl}_2\text{-H}_2\text{O}$ or $\text{NaCl-H}_2\text{O-CaCl}_2$; high-temperature and medium salinity $\text{NaCl-H}_2\text{O}$ or $\text{H}_2\text{O-NaCl-CaCl}_2$.

The characteristics of inclusions show that the fillings in the major body of the Tahe Oilfield were formed in three or four different environments, representing karstification in different periods, which correspond to different karst evolution stages: low-temperature, low-salinity freshwater karst environment; low-temperature, high-salinity offshore karst environment; medium-temperature, medium-salinity shallow

Table 1.14 Inclusion characteristics of palaeo-karst fracture-vug system fillings drilled in typical wells in the main body of the Tahe Oilfield

Sample no.	Tested minerals	Type and its proportion	Inclusion size (μm)	Morphology	Distribution feature	Initial melting temperature and system	Freezing point (°C)	Salinity (wt.%, NaCl)	Homogenous temperature (°C)/ (inclusion number)	Homogenous temperature range (°C)	Density(g/cm ³)
BT403	Calcite	Single-phase gaseous hydrocarbonaceous inclusions and a few hydrocarbonaceous inclusions	5–25	Oval, polygon, a few irregular shapes	Most distributed in calcite crystals, in free distribution linear distribution along microfractures						
		Single-phase saline inclusions	1–25	Rice-shaped, small diamond, polygon, oval	Most of them in calcite crystals, in free distribution or linear distribution along microfractures						
		Two-phase saline inclusions	mainly 3–35	Motally rectangular and polygon	Most in calcite crystals, in free or small group distribution, a few in linear distribution along microfractures	–49 to –52–21°C (NaCl-H ₂ O-CaCl ₂ system)	–17.5 to –16.8	18.6–19.2	101.25(12)	95–110	1.101–1.08
						–20.8 to –21°C (NaCl-H ₂ O-CaCl ₂ system)	–5.8 to –6.2	9.0–9.5	136.25(12)	130–145	1.003–0.987
						–52to –53°C (NaCl-H ₂ O-CaCl ₂ system)	–18.5 to –17.9	20.0–19.5	149.25(12)	145–155	1.071–1.059
BT417	Calcite	Single-phase gaseous hydrocarbonaceous inclusions	3–30	Oval, polygon, a few irregular shape	Most in calcite crystals, in free distribution or a few of in linear distribution along microfractures						
		Single-phase saline inclusions	1–15	Rice-shaped, small diamond, polygon, oval, a few of irregular	Most in calcite crystals, in free distribution or a few of them in linear distribution along microfractures of calcite						

(Continued)

Table 1.14 (Continued)

Sample no.	Tested minerals	Type and its proportion	Inclusion size (μm)	Morphology	Distribution feature	Initial melting temperature and system	Freezing point ($^{\circ}\text{C}$)	Salinity (wt.%, NaCl)	Homogenous temperature ($^{\circ}\text{C}$)/ (inclusion number)	Homogenous temperature range ($^{\circ}\text{C}$)	Density(g/cm^3)
		Two-phase saline inclusions	mainly 5-20	Major rectangular and polygon, secondary diamond, oval, and a few irregular shape	Most in calcite crystals, in free distribution or a few of them in linear distribution along microfractures of calcite	-20.5 to -20.6°C (NaCl-H ₂ O system)	-0.1 to -2.1	0.2-3.5	102 (10)	85-98	0.970-0.969
						-20.8 to -21°C (NaCl-H ₂ O system)	-5.1 to -4.8	8.0-7.6	119.87 (8)	120-125	1.00-0.993
						-52 to -53°C (NaCl-H ₂ O-CaCl ₂ system)	-19.0 to -18.0	20.3-19.6	115.55 (18)	145-155	1.094-1.090
BT417	Calcite	Single-phase gaseous hydrocarbonaceous inclusions	1-20	Oval, polygon, and a few irregular shape	Most in calcite crystals, appearing in small groups or a few of them in linear distribution along microfractures of calcite						
		Single-phase saline inclusions	5-25	Rice-shaped, small diamond, polygon, oval, rectangular, a few of irregular	Most in calcite crystals, appearing in free distribution or small groups or a few of them in linear distribution along microfractures of calcite						
		Two-phase saline inclusions	mainly 5-15	Major rectangular and polygon, secondary diamond, oval, and a few of irregular shape	Most in calcite crystals, in free or small group distribution or a few of them in linear distribution along the microfractures of calcite	-20.5 to -20.6°C (NaCl-H ₂ O system)	-1.0 to -1.2	1.7-2.0	91.11 (17)	89-95	0.98-0.975
						-20.8 to -21°C (NaCl-H ₂ O system)	-2.8 to -3.3	4.6-5.4	89.46 (15)	85-92	1.006 - 0.996

burial karst environment; medium-temperature, high-salinity shallow burial brine karst environment; high-temperature, medium-salinity deep burial hydrothermal karst environment. Homogenous temperature, salinity, and organic matter components of inclusions indicate that most of the carbonate fillings were formed in an environment with low level of organic matter.

The discussion above shows that the homogenous temperature of water inclusions generally have two to three magnitude segments, with slight differences among them, but they can be divided into three sections, namely, 60–90°C, 90–120°C, 120–155°C, and there is no high-temperature inclusion. Different from the palaeo-karst fracture-vug fillings in the northern margin of the Tarim Basin, (such as multiphase and multiple morphologies of fluorite inclusions, the homogenous temperature with a large variation range, from 98 to 285°C, generally in three to four sections, namely, 98–115°C, 110–140°C, 130–170°C, and 248–285°C). The high-temperature inclusions are the CO₂-NaCl-H₂O system, indicating the alteration of karst fillings and karst space by the hydrothermal fluid from the deeper crust, and also the relatively weak alteration of karst fillings and karst space by the hydrothermal fluid from the deeper crust.

1.2.3.4 Evolution features

The evolution of palaeo-karst in the Ordovician carbonate rock in the Tahe Oilfield mainly experienced multiple periods of karstification process, namely, the epikarstification in the Middle Caledonian, exposed weathered karstification in the early Hercynian, and layered karstification in the burial stage. The epikarst in the Middle Caledonian mainly developed in the Middle Ordovician Yijianfang Formation, when tectonic movements led to oscillation and uplift of the depositional platform, resulting in smaller terrain elevation and shallower water circulation depth, so in the shallow surface, the karst, mainly small caves and fracture-vug systems developed. The exposed weathered karstification in the early Hercynian was mainly developed in the Middle-Lower Ordovician Yingshan Formation, and altered the epikarst in the Yijianfang Formation. Tectonic movements caused substantial uplift of the depositional platform, and formation of rich folds and faults, long exposed to the surface expansively, subjected to denudation, the carbonate suffered strong karstification, forming large-scale exposed weathered karst, mainly caves and wide solution fractures; the burial karst is the product of continuous dissolution and filling alteration of Ordovician carbonate rock caused by the burial. The tectonic movements after the Carboniferous period led to continuous subsidence of the basin, and the early karst was dominated by sedimentary filling. Meanwhile, the deep hydrothermal process led to the formation of solution vugs in layered distribution.

1. Development and evolution of the Yijianfang Formation karst

At the end of the Yijianfang Formation period, the study area was semi-restricted, or intra-platform lacustrine, or open sea depositional system (Fig. 1.18A). Affected by tectonic movements in the Middle Caledonian, the eustasy made the northern semi-restricted platform and the platform margin near the mean low tide level, the freshwater or brackish water from precipitation dissolved calcite through intra- and inter- micropores in grainstone and contracted microfractures from the consolidation and dehydration of carbonate depositional layers (Fig. 1.18B), the major signs are open upward microsolution fractures filled with filtrated limy sandstone on the surface and in the shallow part of the

2. Development and evolution of exposed weathered karst in the Devonian–Early Carboniferous

Early Hercynian tectonic movement in the Devonian–Early Carboniferous period led to considerable uplift of this area, and profuse development of folds and faults in this area; as a result, the Ordovician carbonate rock was widely exposed to the surface, and subject to strong karstification.

Seismic exploration and drilling show that the Ordovician and Carboniferous in the Akekule bulge are in unconformable contact ($T7^0$ interface). From the analysis of tectonic evolution, before the carbonate rock exposed to the surface, the overlying Silurian and Devonian were considerably denudated. In the main body of the Tahe area, the carbonate rock overlying the Yingshan Formation was denudated completely, and the denudated thickness of Yingshan Formation is greater in the axial of the Akekule bulge and the northern platform, reaching up to 250 m; while in the northern part and periphery of the bulge, part of the Yijianfang Formation and Lianglitage Formation outcrop is circular in shape.

a. At the end of the Devonian, the Middle-Lower Ordovician, carbonate rock in the Akekule region was buried by clastic-dominant layers of Upper Ordovician Sangtamu Formation, Silurian, and Devonian. Affected by the Caledonian tectonic movement, the prototype of nose-shaped bulge was formed (Fig. 1.19A).

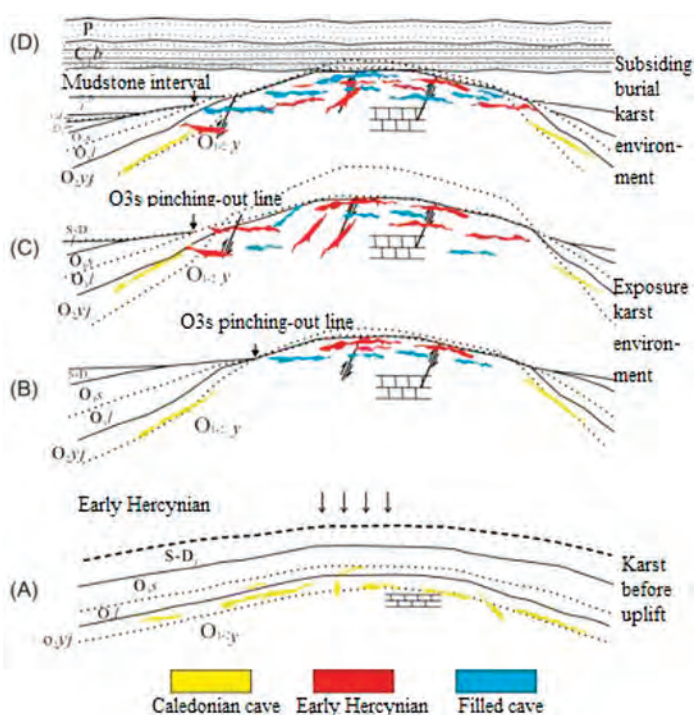


Figure 1.19 Developmental and evolutionary features of exposed weathered karst at the end of Devonian–early Carboniferous. (A) Affected by the Caledonian tectonic movement, the prototype of nose-shaped bulge was formed. (B) In early Hercynian, the Akekule area was dramatically uplifted, accompanied by the generation of faults. (C) With further uplift, the Yijianfang Formation in the bulge highs were completely denudated, and part of the upper member of the Yingshan Formation was denudated as well. (D) In Early Carboniferous, the Tarim block started to subside and the paleo-karst surface was gradually submerged, the fracture-vug system was locally filled by chemical illuviation.

- b. In early Hercynian, the Akekule area was dramatically uplifted, accompanied by the generation of faults. Apart from the overlying clastic layer on the Middle-Lower Ordovician carbonate rock, the Middle Ordovician Yijianfang Formation was also denudated substantially. The pinching-out line of this layer mainly occurs in the eastern, southern, and western marginal zone of the bugle body, outcropping in a circle-shape between the pinching-out line of the Sangtamu Formation and the Yijianfang Formation. The early karst in the Yijianfang Formation was severely reworked and recreated, with the karst developmental depth and the scale of fracture-vug system increased, and connectivity improved too. Within the flow field of groundwater in the burial karst section, affected by the water conductivity of faulted structures, deeper fault dissolution zone developed in places adjacent to the exposed zone (Fig. 1.19B).
 - c. With further uplift, the Yijianfang Formation in the bugle highs were completely denudated, and part of the upper member of the Yingshan Formation was denudated as well. The circulation depth of surface water increased, thereby, the dissolution increased as well. Controlled by the base level of groundwater, stronger karst developmental zones distributed in different elevations were formed, and in the seasonal groundwater variation zone, the underground stream cave developmental zone was formed. In the development process of solution solution fractures and vugs, collapsed cave top, residual solution breccia and clasts entrapped by water flow, and sedimentary filling of mud and sand occurred in places where the water flowed slowly or was in poor circulation (Fig. 1.19C).
 - d. In Early Carboniferous, the Tarim block started to subside and the paleo-karst surface was gradually submerged, thereby, the water head difference of groundwater field decreased, and the potential energy of water decreased, the fracture-vug system was locally filled by chemical illuviation, the fractures and vugs/caves in the transgression basin margin and the offshore surface drainage were liable to be filled with sediments in a later period, the early syphon pipe developmental zone, the steep karst slope zone with greater elevation difference, and the distributary caves in the downstream of groundwater level transformation zone had a relatively lower filling degree (Fig. 1.19D).
3. Karst development and evolution in the early coverage of Hercynian period

In the northern Akekule bulge, the early coverage of the Hercynian period referred to the periphery of the Middle-Lower Ordovician exposed zone, the place covered by the Upper Ordovician impure carbonate rock and clastic rock, and the overlapping area of the Devonian, Silurian in the eastern part of the bugle. In the shallow covered area and burial zone downstream of the karst water system, affected by deep circulation of water flow, especially near the fault structural zone, deep karst was still better developed.

Controlled by palaeogeomorphological conditions, the distribution of the karst water system in the Akekule bugle took the central highs as the replenishment boundary, and developed to the southeast, southwest, and south. The first-order discharging level of groundwater was the Lake Baikal, and the second-order discharging level was located near the pinching-out line of the Upper Ordovician. Locally segmented by structure and topography, groundwater discharging occurred between the first- and second-order discharging level, thus it can be seen that, in the circulation of water flow, despite the different exposure conditions of the carbonate rocks, there was a storage and migration space for karst water from the self-replenishment zone to the discharging zone. In the covered zone, the Caledonian palaeo-karst became the base for the early Hercynian karst development, and the storage and migration space for underground pressure water, meanwhile, and expanded in space and was reworked further (Fig. 1.20).

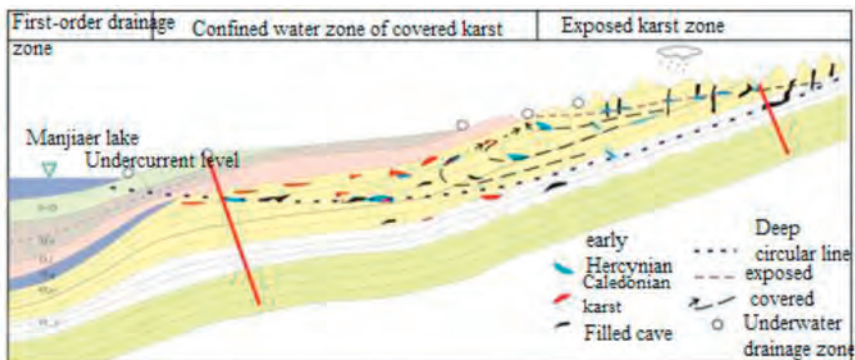


Figure 1.20 Karst development and evolution features of the early covered area of the Hercynian period.

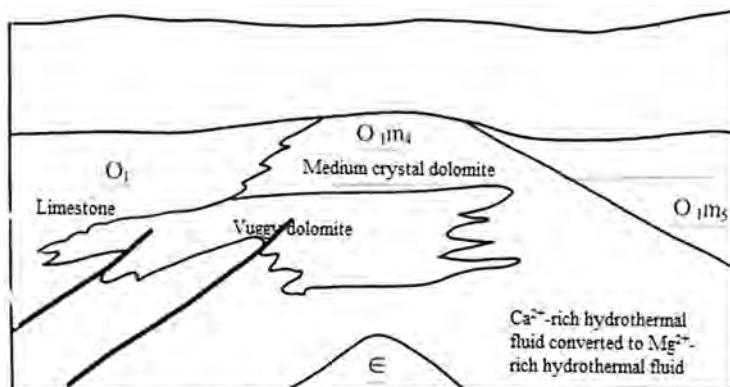


Figure 1.21 Schematic of hydrothermal dissolution and dolomitization.

The development of burial karst had constructive significance for the formation of karst reservoir space. Under burial conditions, the previous caves and fractures could expand in volume and improve in connectivity. Meanwhile, distant from the provenance of mechanical fillings bearing the strong dynamic of pressure water, the preservation chance of formed karst space in the buried karst zone was far greater than that of exposed karst zone, thus good karst reservoirs could form in the groundwater runoff zone.

4. Layered karstification in the burial stage

Buried karstification refers to dissolution and filling and reworking on Ordovician palaeo-karst. The tectonic movements in late Carboniferous led to the continuous subsidence of the basin. The early karstification in this period was dominated by depositional filling, meanwhile, the deep hydrothermal fluid action gave rise to solution pores and caves in layered distribution.

The hydrothermal karstification is the dissolution of soluble rock by deep circulating hydrothermal water flowing upward or downward at high pressure (Fig. 1.21), and the

Table 1.15 Classification of Ordovician carbonate fracture-vug system in the Tarim Basin

Type of fracture-vug system		Main morphological characteristics	Vug scale	Remarks
Type	Subtype			
Underground stream system type	Single-pipe type	The main body of the cave is sub-circular, and the underground stream is in linear distribution	The main cave is 2–10 m in diameter, and 1–30 km long	The underground stream pipeline only has one main water inlet and one main outlet, and the main body of the pipeline and the zone of influence around the cave formed the fracture surface structure, in “strip dual structure”
	Pipe network type	The main body of the cave is sub-circular, and the underground stream is in network distribution	The main cave is 2–10 m in diameter, and 10 to hundreds of kilometers long	It is composed of one main pipeline and many single pipelines with two or more main water inlets or outlets; in dendroid distribution on the plane, with multiple layers in vertical profile. Besides the main body of the river, the secondary karst forms between pipeline networks are also quite rich, and therefore its structure is called “the network multiple structure”
	Tectonic corridor type	The main body of the cave is canyon shape in fold distribution	It is 1–10 m wide, 5–50 m high, and 0.5–5 km long	It generally winds and extends along fracture tectonic zones on the plane, and huge in vertical space; the zones of influence on both sides of the cave, especially secondary tectonic fractures are well developed, therefore such kind of fracture-cave system is called “fold ternary structure”

Cave type	Hall-like type	The cave has a flatter ceil or arch shape, in scattered distribution	The cave/cavern may be 50 to hundreds of meters in diameter at bottom, and 10–50 m high	The caves are equivalent in width and length, or less than five-times between width and length; huge in internal space, and high in karstification degree
	Solution cave type	Their section are diverse in shape, mostly irregular oval shape; and they are in scattered distribution	0.2–50 m in diameter	The cave is the secondary or third order structure in the fracture-cave system; in the preliminary stage of karst development, most caves are isolated, forming independent small-scale fracture-cave system together with solution fractures; in the middle and late stage of karstification, the caves are connected with adjacent caves or the cave system of the upper class by the fracture network system, becoming a part of a large-scale fracture-cave system
	Shaft-like type	Simple in shape, they are oval or sub-circular in the main part; and distributed along the trend of underground stream in scattered dots	2–20 m in diameter, and 10–100 m in depth	Big in elevation change, they often have near-vertical steep scarps of more than ten or tens of meters high at the shaft; and are usually associated with fractured caves; and there are usually vertical karst grooves on the wall of the caves
Vug type		Irregular pores or caves, in layers or strips	0.2–20 m in diameter	Mainly formed by dissolution, they form lamellar or strip-shaped fracture-cave systems with the adjacent solution fractures

(Continued)

Table 1.15 (Continued)

Type of fracture-vug system		Main morphological characteristics	Vug scale	Remarks
Type	Subtype			
Solution-enlarged fracture type		Relatively flat and straight fracture surface, mainly inclined fractures, in network shape	Class-I fractures are 10–50 cm wide, 8–15 m in spacing and over 50 m in extension length; class-II fractures are 2–10 cm wide, 1–5 m in spacing and 10–50 m in extension length; class-III fractures are 1–5 cm in width, 0.1–0.3 m in spacing and 1–10 m in extension length	Fractures are the base for karst development, as well as the main passage between karst pores (caves), including karst collapse fractures and solution fractures; the distribution and development scale of solution fractures is mainly controlled by regional tectonism; fractures are classable, and fractures of the same class have similar spacing
Reef shoal type		Irregular cycle shape, in layer or strip distribution	Pores are 0.5–10 cm in diameter, 5–30% in porosity, fractures are 1–5 mm wide and 10–50 mm in extension length	The reef shoal solution pore system is composed of solution pores and adjacent solution fractures with strong karstification, low filling degree, high porosity, relatively uniform pore distribution and good connectivity between pores
Dolomite pore type		Regular cycle shape, in layer or strip distribution	The pores are 0.01–5 mm in diameter	Mainly including cellular solution pores and small caves, without medium to large-scale underground caves; composed of interconnective microfractures and solution pores

dissolution products are dominated by solution pores and fractures filled with medium-low temperature hydrothermal minerals and dolomite of hydrothermal metasomatic genesis.

- a. The slowly rising hot brine rich in Ca^{2+} percolated along pores and fractures in relatively stable environment, conducting persistent and weak penetration dissolution on soluble rock, forming a karst developmental zone dominated by solution pores and fractures along the layers. The solution pores were mostly pellet-shaped, 2–5 mm. After enlarging dissolution, they were mostly arch and irregular. The fillings were dominated by dolomite, calcite, quartz, and clay minerals, and sphalerite, galena crystals were also seen occasionally.
- b. With the proceeding of dissolution, the Ca^{2+} -rich hydrothermal brine gradually converted into the Mg^{2+} -rich hydrothermal brine, which converged with upward infiltrated Mg^{2+} -rich groundwater from the above layer, causing dolomitization in the upper part of the slope.

1.3 Development pattern of carbonate fracture-vug system

A fracture-vug system refers to the reservoir containing pores, fractures, vugs, and caves/caverns formed in a unified hydrological system of supplement, runoff and drainage. According to the morphological structure, they are classified into 10 types, underground stream network system, hall-type cave system, and solution fracture system, etc. (Table 1.15), and 10 kinds of fracture-vug system patterns have been correspondingly established, of which eight typical geological-geophysical models have been established and seven of these models have been applied to the test area in the Tahe Oilfield, including single-pipe underground stream system, pipe network underground stream system, hall-like cave system, shaft-like cave system, solution cave system, and vug system and solution fracture system.

1.3.1 *Single-pipe underground stream system*

The single-pipe underground stream system is an underground stream channel with one main inlet and one main outlet. Its fracture structure consists of the main body of the pipe and the influence zone around it, like a “strip dual-structure” (Fig. 1.22 and Table 1.16). There is a single-pipe underground stream system across TK424–TK476–T403–TK419 in Block 4 in the Tahe Oilfield (Fig. 1.23).

The forward modeling of the seismic wave field of the single-pipe reservoir shows that the small-scale vugs show the bead-like reflection character, and the large-scale vugs show quasi-lamellar reflection character; the interface reflection at the top of the fracture-vug unit is relatively clear; and the reflection event at the bottom of the fracture-vug unit shows a pull-down phenomenon in time. The reflection event inside the fracture-vug unit of the corridor-type reservoir shows continuous reflection character (Fig. 1.24).

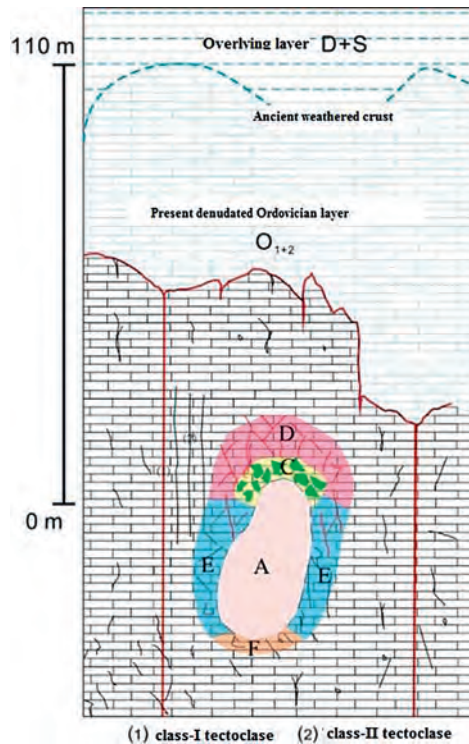


Figure 1.22 Structural model of single-pipe underground stream system (cross-section). A, the vug is 1–3 m high and 1–75 m wide; C, the fracture zone of collapse dissolution at the top of the vug is 0.8–2.5 m high and 2.5–4.2 m wide; D, the fractured dissolution influence zone at the top of the vug is 1.0–2.5 m high and 1.0–1.5 m wide; E, the dissolution influence zone at the side of the vug is 1.8–4.2 m high and 4.1–10.3 m wide; F, the dissolution influence zone at the bottom of the vug is 3–6.9 m wide and 1–2.0 m high.

1.3.2 Pipe network underground stream system

The pipe network underground stream system is composed of the main pipe and the surrounding zone of dissolution influence (Table 1.17), of dendroid shape, with the main pipe and at least one branch, and a large amount of karst in ponor, shaft, and skylight forms. It is dendroid on the plane and multilayered in vertical profile. Besides the main body of the stream, the secondary karst formed between pipe networks is also quite rich, and therefore its structure is called “the network multistructure”. The underground stream is generally at the runoff dissolution zone, with the main pipe usually more than 10 km long, and the branch usually >1 km long; in terms of scale, the main pipe is larger than the branch, and the branch of the upper class is always larger and longer than that of the lower class (Fig. 1.25).

There is one pipe network underground stream system around Well TK422–TK472 in Block 4 in the Tahe Oilfield (Fig. 1.26), the main pipe of which

Table 1.16 Characteristic parameters of single-pipe underground stream system

	Height (m)	Width (m)	Shape and distribution characteristics	Filling characteristics	
				Paleo-karst	Modern karst
Vug	2–10	1–8	The main body of the vug is sub-circular and the underground stream is in linear distribution	Fully filled with chemical or mechanical sediments	There are collapse deposits at the bottom of the vug and fluvial sediments such as rubbles in the river
Height of fracture zone of collapse dissolution at the top of the vug	1–3	2–4	Upper convex falcate	Fractures are fully filled with calcite	Solution fractures are partially filled with chippings such as sand and clays
Zone of fractured dissolution influence at the top of the vug	1–3	1–2	Near-horizontal upper convex arch	Fractures are fully filled with calcite	
Dissolution influence zone at the side of vug	2–5	4–10	Near-vertical arch wide in the middle and narrow at both ends	Fractures are fully filled with calcite	
Dissolution influence zone at the bottom of the vug	3–7	1–2	Near-horizontal lower convex arch	Fractures are fully filled with calcite	
Length of underground stream	1–30 km				

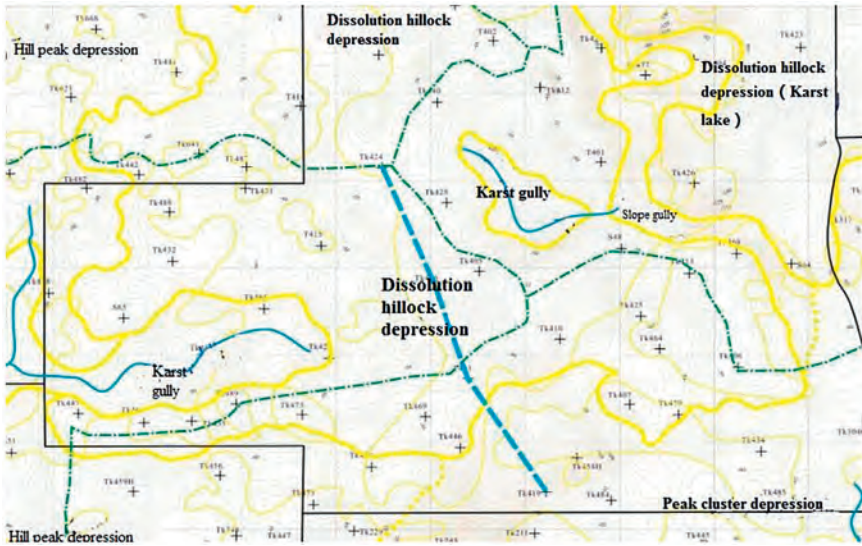


Figure 1.23 Single-pipe underground stream system across TK424–TK476–T403–TK419 in Block 4 in the Tahe Oilfield.

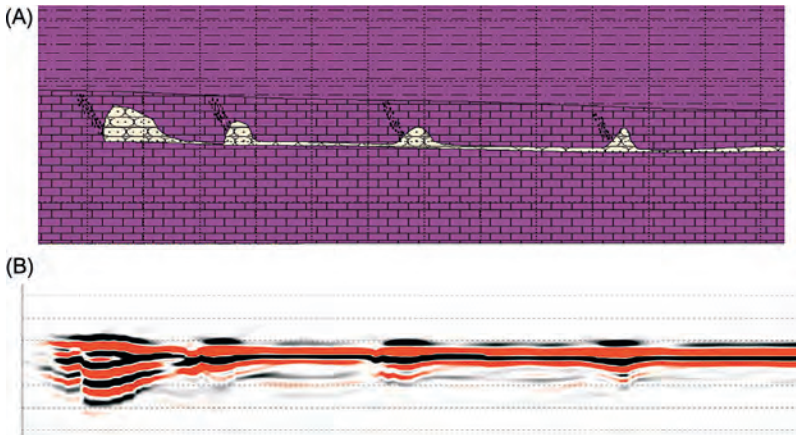


Figure 1.24 “Bead-like” underground stream pipe system model and seismic response characteristics. (A) seismic-geological model of fracture-vug unit; (B) forward modeling record of numerical model.

is located around Well TK423–TK422–TK417–TK472, in near NW trend, the distance between the top of the pipe and double peak limestone is about 180–240 m, the pipe is 20–75 m high; there are three branch karst systems 2–20 m high.

Table 1.17 Characteristic parameters of pipe-network underground stream system

	Main pipe of underground stream		Branch		Shape and distribution characteristics	Filling characteristics	
	Height (m)	Width (m)	Height (m)	Width (m)		Paleo-karst	Modern karst
Main cave body	Diameter 2–10 m				The main body of the cave is quasi-circular and the underground stream is in network distribution	Fully filled with sand shale sediments or chemical sediments such as gypsum Half or fully filled with calcite and calcium clay	There are collapse deposits at the bottom of the cave and mechanical sediments of fluvial-facies sand-pebbles in the riverbed Unfilled or half filled with calcite and sand clasts
Fracture zone of collapse dissolution at the top of the cave	0.5–5	2–3	0.5–2	0.5–1	Upper convex falcate		
Fractured dissolution influence zone at the top of the cave	4–6	3–6	0–0.5	1.0–2.0	Near-horizontal upper convex arch		
Dissolution influence zone between caves	3–4 m wide, five zones/m ² in density				Strips with similar width at both ends		
Zone of dissolution influence at edge of the cave	10–15	6–7	5–8	1.0–2.0	Near-vertical arch wide in the middle and narrow at both ends		
Zone of dissolution influence at the bottom of cave	2–4	20–25	0.5–1	3–5	Near-horizontal lower convex arch		
Development length of underground stream	10 to hundreds of kilometers		1–5 km, always smaller than the main pipeline of underground stream				

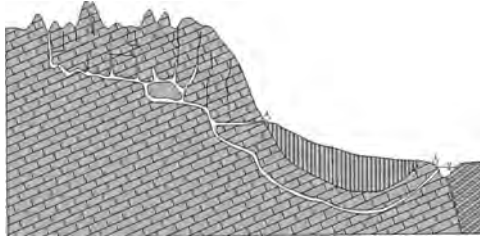


Figure 1.25 Pipeline-network underground stream system (cross-section).

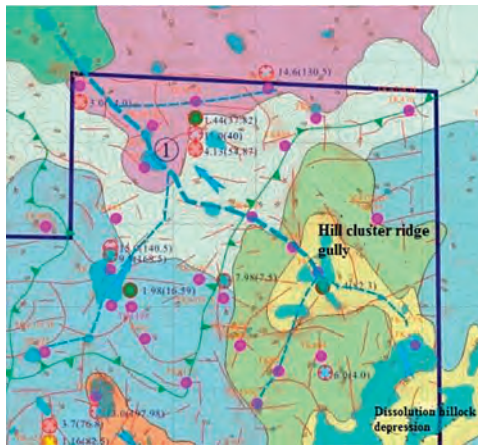


Figure 1.26 Paleo-pipe-network underground stream system at the test area in the Tahe Oilfield.

Forward modeling shows that the pipe-network underground stream system has obvious “bead-like” reflection characteristics and can be compared with the reflection characteristics of underground karst. In terms of amplitude, due to the absorption of high-frequency energy by cave reflection, the energy is strong at lower frequency (30 or 40 Hz) and is weak at higher frequency (60 or 80 Hz).

1.3.3 Tectonic corridor underground stream system

With an aspect ratio of more than 5, the pipe of an underground stream system usually winds along a faulted structure zone, with a huge vertical space (Fig. 1.27); the influence zones on both sides of the pipe, especially the secondary tectoclasses are well developed, belonging to the “folded ternary structure”.

The corridor underground stream is composed of the main pipe, influence zone around the pipe, and class-I tectoclasses, and between the class-I fractures there are also class-II fractures; its extending distance on the plane is obviously affected by

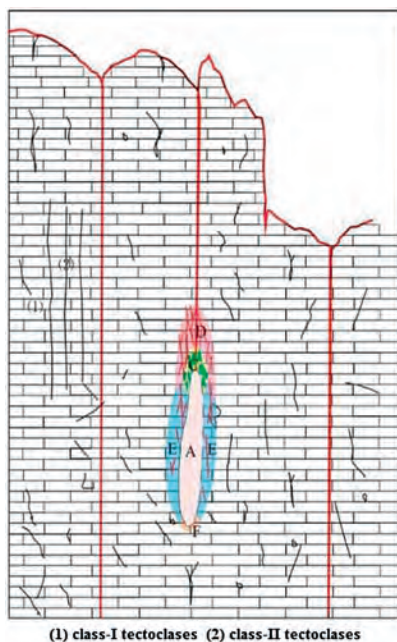


Figure 1.27 Development mode of corridor-like underground stream system.

tectonism, and is 1–5 km long. The height of the main pipe is 5–50 m and it is 1–10 m wide; the influence zone around the pipe and thickness of dissolution influence zone at the bottom of the pipe are small, while the fractured zone by the pipe is fairly wide (Table 1.18).

1.3.4 Hall-like cave system

The hall-like cave system includes halls, ponors, or solution fractures etc. (Fig. 1.28F). The hall can reach 50 to hundreds of meters in diameter, and 10–50 m high; the cave has a fairly flat or arch-shaped ceiling, and a lot of collapse deposits and secondary chemical sediments inside. Distributed discretely (Table 1.19), they have obvious “bead-like” reflection characteristics on seismic profiles.

Wells T403, Tk409, S48 and TK471X in Block 4 in the Tahe Oilfield have obvious characteristics of a hall-like cave system, and the caves are 3–72 m high, and located at the slope near the hilltop or at the top of small dissolution hillocks in karst depressions. In the mountainous areas with peak clusters, large-scale hall-like caves with high storage capacity are likely to occur in areas where the pipe-like underground stream system in the runoff dissolution zone in the early phase overlaps with the epikarst zone in the last phase, for example, both Well S48 and Well TK471X are high-production wells; while the hall-like caves developed in the

Table 1.18 Characteristic parameters of corridor underground stream system

	Cross-section of the main pipe of underground stream		Filling characteristics	Shape and distribution characteristics
	Height (m)	Width (m)		
Main cave body	5–50	1–10	There are mainly collapse deposits at the bottom of the cave Half or fully filled with calcite and calcium clay	The main body of the cave is canyon type in fold distribution
Fracture zone of collapse dissolution at the top of the cave	1–3	1–10		
Fractured dissolution influence zone at the top of the cave	1–4	1–3		
Dissolution influence zone at edge of the cave	3–5	5–10		
Dissolution influence zone at the bottom of the cave	0.5–1	1–3		
Development length of underground stream	1–5 km			

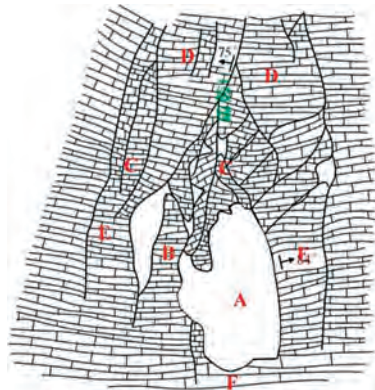


Figure 1.28 Development mode of hall-like cave system (cross-section). A, main cave body; B, solution fracture zone between caves; C, fractured zone of collapse at the top of the cave; D, dissolution influence zone at the top of the cave; E, dissolution influence zone at the side of cave; F, dissolution influence zone at the bottom of the cave.

Table 1.19 Development characteristics of hall-like cave system

	Height (m)	Width (m)	Shape and distribution characteristics	Filling characteristics	
				Paleo-karst	Modern karst
Main cave body	50 to hundreds of meters in diameter; 10–50 m in height		With relatively flat ceiling or arch-shaped ceiling, these caves are dispersive	Fully filled with karst breccia	Collapse deposits and secondary chemical sediments
Dissolution influence zone between caves	10–50	5–35	Strip shape similar width at both ends	Fractures are fully filled with calcite and calcium clay	Solution fractures are half filled with chippings such as sand and clay
Height of fractured zone of collapse dissolution at the top of the cave	1–5	2–15	Upper convex falcate		
Fractured dissolution influence zone of at the top of the cave	3–10	50 to hundreds of meters	Near-horizontal upper convex arch		
Dissolution influence zone at the side of the cave	10–50	2–5	Near-vertical arch wide in the middle and narrow at both ends		
Dissolution influence zone at the bottom of the cave	0.5–5	50 to hundreds of meters	Near-horizontal lower convex arch		
Ponor	2–20 m in diameter; 10–50 m in depth		Nearly vertical in shape, and dispersive in distribution		
Solution fracture	Dominated by class-I fractures, with extending length of 10 to more than one hundred meters		Nearly vertical, and in network pattern	Fully filled with calcite and calcium clay	Half filled with calcite and calcium clay or unfilled

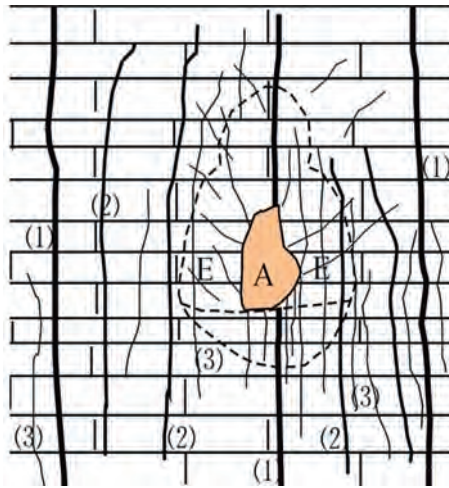


Figure 1.29 Development mode of cave system. (1) Class-I solution fracture; (2) class-II solution fracture; (3) class-III small-scale solution fracture; A, main body of solution cave; E, dissolution influence zone around the cave.

runoff dissolution zones in the last phase, connected with the earth's surface by large-scale ponors, are mostly fully filled with mechanical sediments or are high in water content, and can hardly become good reservoirs.

1.3.5 Solution cave system

Caves refer to the solution caves except caverns such as halls, and they are mainly small- and medium-sized with a diameter of 0.2–50 m. This kind of system centers on the main body of a cave (A) with different classes of solution fractures on both sides (Fig. 1.29). Except small-scale caves, there are fractured collapse dissolution zones (C) and dissolution collapse influence zones at the top of larger caves (D), fractured dissolution zones on both sides of the caves (E) and dissolution zones at the bottom of the caves (F). For scattered caves, Zone C is 0–3 m thick, Zone D is 0–5 m thick, Zone E 0–5 m thick, and Zone F 0–2 m thick (Table 1.20).

In Block 4 in the Tahe Oilfield, most caves identified by well log are small and medium, 2–8 m high, and filled with sand and clay or calcite, and some are half filled or unfilled.

1.3.6 Shaft-like cave system

Shaft-like caves refer to the karst forms dominated by downward development, including shafts, ponors, and skylights; they usually occur in areas with relatively big thickness such as the epikarst zone and vertical percolation zone, and mostly occur in mountainous areas with peak clusters and are seldom seen in peak

Table 1.20 Characteristic parameters of solution cave system

	Height (m)	Width (m)	Shape and distribution characteristics	Filling characteristics	
				Paleo-karst	Modern karst
Main cave body (A)	0.2–10	0.2–10	Sub-circular shape in main body, and distributed in layer or strip	Fully filled with chemical or mechanical sediments	With collapse deposits at the bottom, the caves are half or fully filled with loose clay
Fractured collapse dissolution zone at the top of the cave (C)	0–3	0–10	Upper convex falcate	Fractures are fully filled with calcite	Solution fractures are half filled with chippings such as sand and clay
Dissolution collapse influence zone at the top of the cave (D)	0–5	0–10	Near-horizontal upper convex arch	Fractures are fully filled with calcite	
Dissolution influence zone on both sides of cave (E)	0–5	0–10	Near-vertical arch wide in the middle and narrow at both ends	Fractures are fully filled with calcites	
Dissolution influence zone at the bottom of the cave (F)	0–2	0–10	Near-horizontal lower convex arch	Fractures are fully filled with calcites	
Extending length	0.5–50 m				

forest-plain areas. Large-scale shafts with diameter and depth both larger than 100 m are called “sinkholes”.

The shaft-like cave system is composed of the main cave of the shaft (A) and the surrounding zone of dissolution influence (E). This kind of cave is 2–20 m in main body diameter, and 10 to hundreds of meters in depth (Fig. 1.30 and Table 1.21).

There is a large ponor at Well TK422 (5539.5–5553.0 m) in Block 4 in the Tahe Oilfield. This well is located at the bottom of a peak cluster depression at the edge of Karst Lake, with good impoundment conditions, a favorable position for the development of ponors.

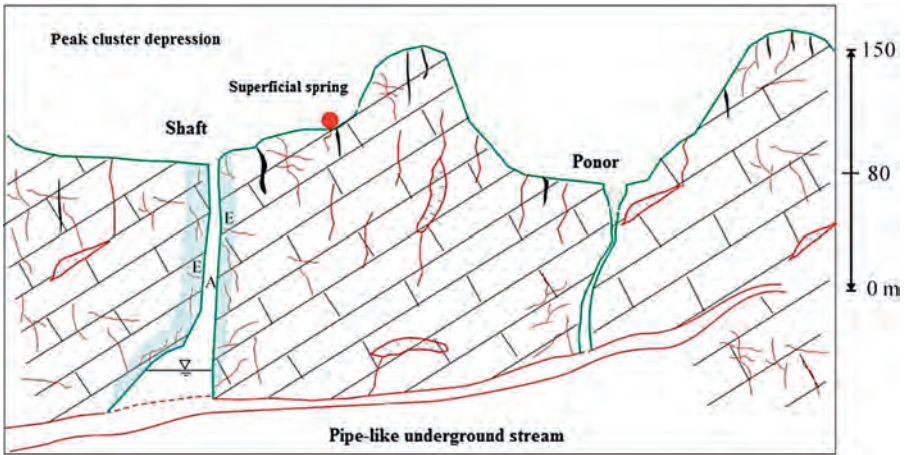


Figure 1.30 Development mode of shaft-like cave system. A, the main body of the cave; E, dissolution influence zone around the cave.

Table 1.21 Characteristic parameters of shaft-like cave system

	Main pipeline of underground stream		Shape and distribution characteristics	Filling characteristics	
	Height (m)	Width (m)		Paleo-karst	Modern karst
Main body of cave	Diameter 2–20 m, depth 10 to hundreds of meters		Oval or sub-circular, and distributed along the trend of underground stream in dots	Fully filled with mechanical sediments such as sand clays and collapse deposits	There are a lot of collapse deposits only at the bottom of the cave
Dissolution influence zone around the cave	The same height as the ponor, 10 to hundreds of meters	2–5 m	Developed around the ponor in near cylinder shape	Half or fully filled with calcite and calcium clay	Unfilled or half filled with calcite and sand cuttings

1.3.7 Fault-karst system

Various irregular fracture-cave units are formed along large-scale solution fracture zones (Fig. 1.31). The forms and scales of a fault-karst system are related to the fault class, karst active phases, and structure pattern; and different fracture combination styles result in very different fault-karst; according to the distribution form, they are classified into strip type, layered cake type, and panel type.

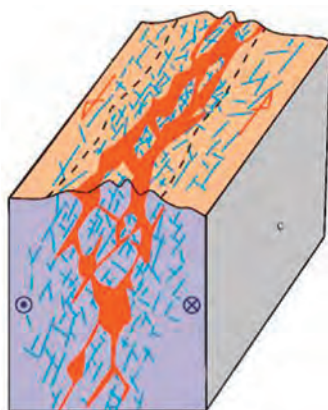


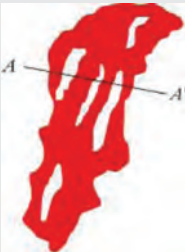
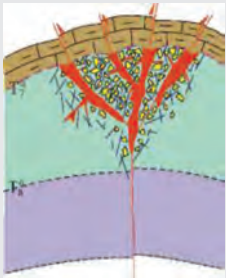
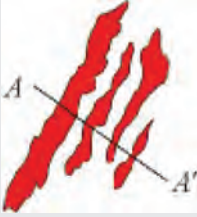
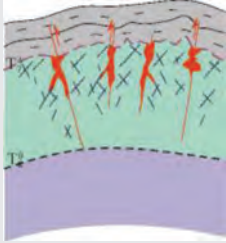

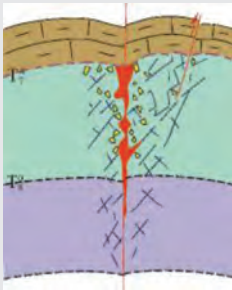
Figure 1.31 Structural mode of fault-karst system.

A strip-type fault-karst system is controlled by a large-scale main fault and the fault style is dominated by a “Y” shape (Table 1.22). The upper part of this kind of fault-karst on cross-section is mostly funnel shaped, and distributed in irregular strip shape along the trend of the fault laterally. Large-scale main fractures are usually main fractures that control the regional tectonic framework with a long distance of horizontal extension of up to 50 km, and they are compression-torsion and high-dip strike-slip faults and are successively developed. They are fracture-cave reservoirs dominated by large-scale caves formed under the enlarging dissolution action of metrical water flowing along the fractures in the karst stage, also the favorable positions for oil and gas accumulation when the oil and gas migrated upwards along the fractures. So far, oil wells drilled into caves in actual drilling of strip-type fault-karst reservoirs take up 46.2%, with an average productivity of single well of up to 37.4 t/day, showing strong energy and long stable production period in production.

An en echelon-type fault-karst system is controlled by the secondary fractures associated with the main fractures, and distributes in en echelon shape or in parallel with the main fractures. This kind of associated fracture, formed at a later stage, with smaller vertical depth of cut, has smaller dissolution scale, smaller horizontal reservoir control range, and poorer oil and gas accumulation degree than the main fractures. The fault-karst traps formed by this series of parallel or en echelon-type associated fractures are mainly en echelon shape and distributed in a group of narrow strips of the same direction along the trend of the fracture. The karstification at the fracture surface is strong, and the fracture degree between secondary fractures is poorer, and there the fracture-type reservoirs mainly develop, and the karstification becomes weaker too, therefore oil and gas mainly gather near the associated fracture surfaces. In the layer cake-type fault-karst reservoir in the Tahe Oilfield, 37 wells have been put into production, and 32 have been completed for production, with an average productivity of 20.2 t/day a well.

In an isolated narrow strip shape laterally, single linear fault-karst is controlled by deep and large fractures; when the fracture is low in activity intensity, karstification will be weaker, large caves would only occur near the deep fracture surface,

Table 1.22 Classification characteristics of fault-karst systems

Type	Plane mode	Profile mode	Type of fracture-cave
Strip			Cave reservoir and vug reservoir
En echelon			Vug reservoir and fracture-vug reservoir
Single line			Fracture-vug reservoir and fractured reservoir

and oil and gas would only enrich in the local area. The production wells in this kind of reservoir have an average productivity of 16.5 t/day, but experience a fast drop of tubing pressure during blowing after being put into production, showing the characteristic of constant volume.

1.3.8 Solution fracture system

Solution fractures can be divided into four classes at macro-level (Fig. 1.32): class-I solution fractures are 10–50 cm wide, spaced 8–15 m, and up to hundreds of meters long; they can grow into large valleys at the earth's surface, and they also usually develop small-scale caves along the class-I solution fractures; class-II fractures are 2–10 cm wide, spaced 1–5 m, and up to several meters to tens of meters long. They grow into branch gullies at the earth's surface with a width of 5–20 m and a depth of

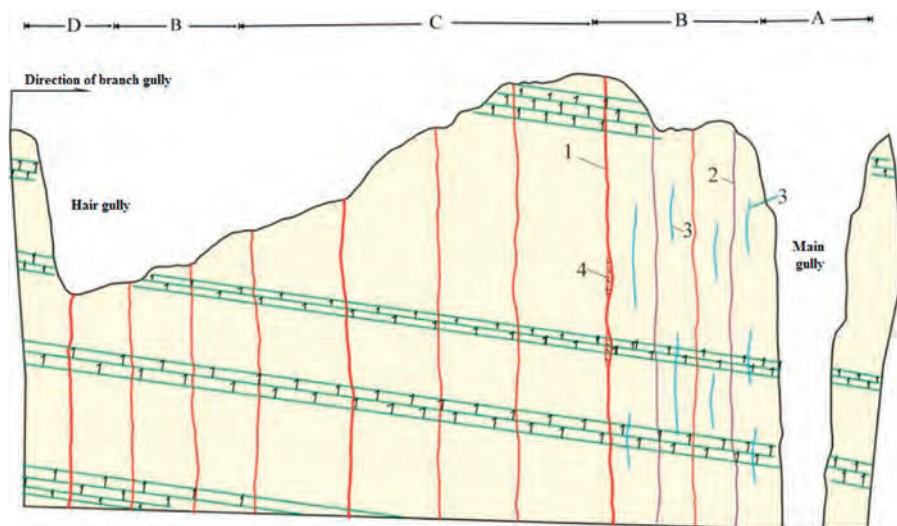


Figure 1.32 Classified development mode of large solution fractures. 1, class-I fracture; 2, class-II fracture; 3, class-III fracture; 4, solution cave developed along class-I fracture; A, main gully; B, solution fracture zone along the ridge of gully; C, solution fracture zone between gullies; D, hair gully.

Table 1.23 Characteristics of large solution fractures

Class of solution fracture	Width (cm)	Spacing (m)	Length (m)	Shape and distribution characteristics	Filling characteristics	
					Paleo-solution fracture	Modern solution fracture
Class I	10–50	8–15	50 to hundreds of meters	Inclined fracture or near-vertical fracture, distributed in similar intervals	Fully filled with chemical or mechanical sediments	Unfilled or half or fully filled with clay and sand cuttings
Class II	2–10	1–5	Several meters to tens of meters			
Class III	0.1–2	0.1–0.3	1–10			
Class IV	0.01–0.1	0.01–0.05	0.1–0.5			

40–100 m, most of which are gap intensive belts or fractured zones; class-III fractures, located between two class-II fractures, are 1–5 cm wide, spaced 10–30 cm and 1–10 m long; class-IV fractures in similar spacing are between class-III fractures, with a width of 0.1–1 mm, a spacing of 1–5 cm and an extension length of 10–50 cm in different lithologies (Table 1.23).

The fairly abundant fractures are the main flowing channels and reservoir space in the paleo-karst reservoir in Block 4 in the Tahe Oilfield, where solution fractures and caves usually form complete fracture-cave systems, of which the system with medium or low filling degree provides good reservoir space.

1.3.9 Reef shoal system

The reef shoal system is composed of solution pores and surrounding solution fractures, with strong karstification, low filling degree, high porosity, relatively uniform pore distribution, and good connectivity.

In a reef shoal system (Fig. 1.33 and Table 1.24), solution pores are mostly irregular circle-shaped with a diameter of 0.5–10 cm and porosity of 5%–30%. The solution pores are usually in layers or strips, in “cellular shape” in the local area and are denuded strongly and filled less. The solution fractures are 1–5 mm wide and 10–50 mm long, directional and in network in local area.

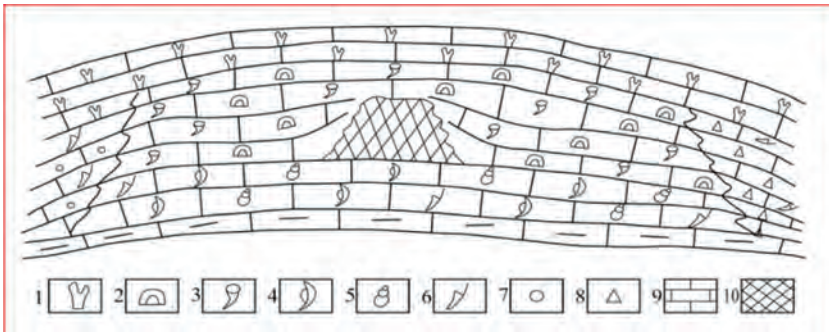


Figure 1.33 Development and evolution mode of organic reef (cross-section).

1, stromatoporoids in dendritic layer; 2, stromatoporoids in spherical or semi-spherical layer; 3, coral; 4, brachiopoda; 5, gastropods; 6, biotritus; 7, spherulite; 8, breccia; 9, mudstone; 10, patch reef.

Table 1.24 Structural parameters of reef shoal system

	Thickness (m)	Width (m)	Porosity (%)	Filling characteristics
Reef shoal-facies reservoir	5–100	10–1000	5–30	Unfilled or half or fully filled with calcite
	Diameter 0.1–10 mm		5–30	
Solution fracture	Width 1–5 mm, length 10–50 mm			

1.3.10 Dolomite system

Dolomitization is the product of metasomatism of carbonate rock, the mechanism of which is quite complicated. Dolomitization may occur at any stage of the formation of dolomite, including penecontemporaneous dolomitization and backflow and permeation dolomitization in sedimentation and diagenesis stage; mixed water dolomitization in dissolution and failure stage; dolomitization of various karst breccia in dissolution filling and cementation stage; and buried dolomitization in dissolution transformation stage.

Pores in dolomite are mostly cellular solution pores and small caves, with few medium- and large-scale cave systems. A dolomite system is composed of solution pores and adjacent interconnected microfractures (Fig. 1.34 and Table 1.25). The

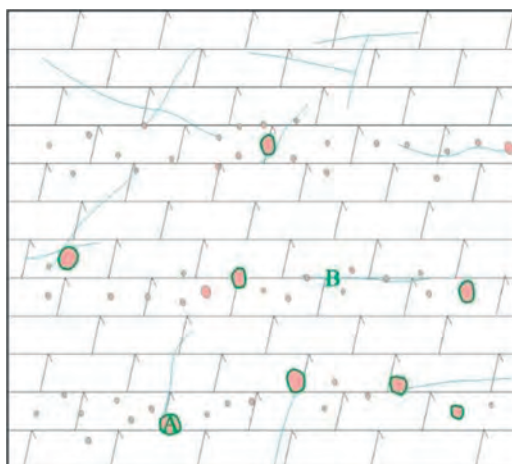


Figure 1.34 Development mode of vug dolomite system. A, dis; B, micro-fracture.

Table 1.25 Characteristics of the development mode of dolomite system

	Pore diameter/width (mm)	Length (mm)	Porosity (%)	Shape and distribution characteristics	Filling characteristics
Microfracture	0.01–5	2–10	4–19	In sub-circle shape, cellular shape in local area	Unfilled or half or fully filled with dolomite and calcite
	0.01–1	10–50		With certain directionality, in network in local area	Unfilled or half or fully filled with calcite

solution pores are smaller, and sub-circular, with a diameter of 0.01–5 mm and porosity of 4%–19%. They are usually distributed in layers or strips, in “cellular shape” in local strongly denuded areas, and low in filling degree. The microfractures are 0.01–1 mm in width, 10–50 mm in extension length; directional to some extent, and in the network in the local area.

1.4 Plane distribution features of fracture-vug systems in the Tahe Oilfield

The Ordovician carbonate rock in the Tahe Oilfield experienced tens of millions of years of weathering and erosion from late Caledonian to early Hercynian, forming paleokarst geomorphology of various forms, and leading to the spatial distribution differences of the paleokarst fracture-vug systems. In this section, by analyzing the correlation between the upper and lower formations of the Ordovician ancient weathered crust in the main area of Tahe Oilfield, taking the regional Carboniferous marker bed (double peak limestone) as the datum, by using the genetic combination identification method of the paleokarst geomorphology, the Ordovician paleokarst geomorphology was restored, secondary and tertiary geomorphic units were classified, and plane distribution features of fracture-vug systems in various geomorphic units were summarized.

1.4.1 Combined identification of the genesis of paleokarst geomorphology

Using moldic and residual thickness methods, the palaeogeomorphology in the Tahe Oilfield was restored by seeking palaeogeomorphic relic traces on ancient weathered crust, such as the type, thickness and distribution of erosion forms and residual deposits (breccia, ferro-aluminium layer, etc.), and erosion forms (karst valleys and funnels, etc.) etc., on the top of the crust.

1. Moldic method

During the process of continuous subsidence and receiving deposits, when tectonic movements are vertical rises and falls, or chiefly vertical (no lateral compression), the relative relief differences of the weathered crusts could be preserved, though they might be covered by sea water and buried by overlying deposits. Then, the paleokarst geomorphology can be restored by the moldic method, that is firstly to find a formation interface that can represent the ancient sea level in the formation overlying the ancient weathered crust, then calculate the relative thickness of the layers on the weathered crust by the formation thickness between this depositional interface and the weathered crust, and finally to restore the geomorphology (Fig. 1.35). The depositional interface that can represent the datum must meet the following conditions:

- a. It is a chronohorizon distributed in the whole area, and can represent the sea level at that time.

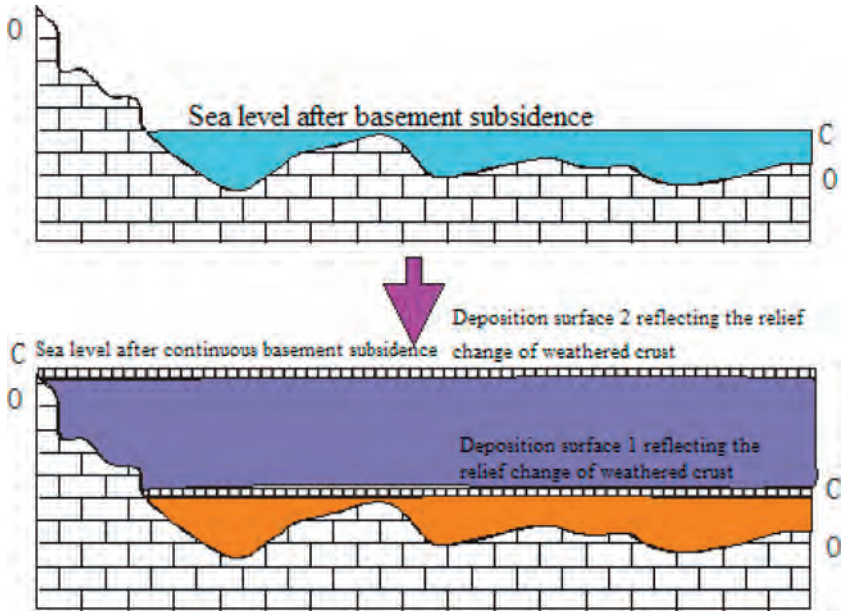


Figure 1.35 Schematic diagram of restoring palaeogeomorphology using the moldic method. Source: Adapted from Xiaote, 2002.

- b. It is closer to the weathered crust surface, as the closer to the weathered crust, the smaller the influence of later tectonic movements on the weathered crust, and the smaller the change in the relative relief of the palaeogeomorphology.
- c. This interface must be a strong acoustic impedance boundary, with apparent features of seismic reflection wave. The stable correspondence between reflection events and geologic boundaries can ensure the identification and correlation of such boundaries on seismic sections.

The deposits between depositional interface and weathered crust were unconsolidated at the beginning of deposition, with high porosity and high water content, thus there would be apparent formation water release and formation compaction during diagenesis, resulting in very big changes in formation thickness before and after diagenesis. Hence, when restoring palaeogeomorphology by the moldic method, we should also consider the compaction change of compactible formations, and calculate the compaction quantity. The calibration procedure is as follows:

- a. Calculate ancient formation thickness:

$$\int_0^S [1 - \varphi(Z)]dZ = \int_Z^{Z+h} [1 - \varphi(Z)]dZ \tag{1.4}$$

where Z is the present depth of formation top (m), h is present formation thickness (m), S is ancient formation thickness (m), $\varphi(Z)$ is a relation function between porosity and depth.

Assuming that the formation matrix volume is constant, the ancient formation thickness (S) can be calculated by Eq. (1.4) through iteration.

b. Calculate compaction quantity

Compaction quantity ($H_{\text{compaction}}$) refers to the difference between ancient and present formation thicknesses (h): $H_{\text{compaction}} = S - h$.

2. Residual thickness method

Restoring palaeogeomorphology by the residual thickness method is based on the marker bed below the weathered crust, that is first to find a depositional interface that can represent the ancient sea level in the formation underlying the ancient weathered crust, then to obtain the residual thickness between this depositional interface and the weathered crust top from seismic data, and to calculate the relative thickness of the layer on the weathered crust to restore the palaeogeomorphology.

The depositional interface that can represent the datum taken in this method must meet the same conditions as those used in the moldic method. Compaction calibration must be carried out to the compactible deposition formations when using the residual thickness method to restore palaeogeomorphology too.

3. Combined genesis identification method

This method is to restore paleokarst geomorphology based on moldic and residual thickness methods, by seeking palaeogeomorphic relic traces on ancient carbonate weathered crust, such as the type, thickness and distribution of erosion forms and residual deposits (breccia, ferro-aluminium layer, etc.), and erosion forms (karren, funnel, etc.) on the top of ancient weathered crust.

The main bases for restoring palaeogeomorphology with combined genesis identification method include: (1) the thicknesses and distribution trends of the overlying (or underlying) marker beds of the weathered crust; (2) residual thickness and characteristics of the weathered crust; (3) erosion and dissolution characteristics and deposit properties on the weathered crust surface; (4) ancient hydrodynamic field features; (5) seismic response features of the topographic relief.

According to field survey, core observation and test identification results, the analysis of paleokarst conditions, karst form combination and development features in exposed weathering environment, we have established the index system for restoring paleokarst geomorphology with a combined genesis identification method (Tables 1.26, 1.27 and 1.28).

According to regional geomorphic features, the secondary geomorphic types of Ordovician weathered crust in the Tarim Basin can be divided into six types: karst platform, karst highland, karst gentle slope, karst steep slope, karst peak cluster valley, and karst intermontane basin. The specific division indexes include topography and terrain features, total restored thickness of the overlying Carboniferous marker bed, and the relative residual thickness of the Ordovician weathered crust relative to Carboniferous marker bed (double peak limestone) pinching surface. On the basis of individual forms and combination features of karst topography, we have divided the tertiary topography into 11 types (karst hill, karst peak, depression, etc.), and the division indexes include topographic slope gradient and mountain height difference etc.

Table 1.26 Index system for dividing secondary geomorphic types of Ordovician weathered crust in the Tarim Basin

Secondary geomorphic types	Major indexes
Karst platform	Topography is flatter, without apparent terrain downslope, $H_c < 60$ m, $H_e \geq 150$ m
Karst highland	Terrain is overall higher, $H_c < 20$ m, $H_e \geq 200$ m
Karst gentle slope	Topography and terrain distribution is gentle, and terrain has slow downslope trend, $60 \text{ m} \leq H_c < 150 \text{ m}$, $H_e \geq 150 \text{ m}$; terrain downslope $< 20\%$
Karst steep slope	Topographic relief is bigger, $100 \text{ m} \leq H_c < 250 \text{ m}$, $H_e \geq 100 \text{ m}$; terrain downslope $> 20\%$
Karst peak cluster valley	Topography and terrain distribution is gentle, topographic slope gradient is smaller, mountains are smaller, and karst depressions, karst valleys and karst peaks are alternately distributed; $100 \text{ m} \leq H_c < 200 \text{ m}$, $H_e \geq 100 \text{ m}$
Karst intermontane basin	Surrounding topography is closed, with bigger area and surface runoff and confluence feature, $100 \text{ m} \leq H_c < 200 \text{ m}$, $H_e \geq 100 \text{ m}$

Note: H_c is the total restored thickness of the overlying Carboniferous marker bed (the thickness from the Carboniferous double peak limestone bottom to Ordovician top); H_e is the relative residual thickness of the Ordovician weathered crust relative to Carboniferous marker bed (double peak limestone) pinching surface.

1.4.2 Paleokarst geomorphology types and distribution features

Based on ancient topography and terrain distribution during Pre-Carboniferous in the Tahe Oilfield, the thickness from Ordovician top to Carboniferous “double peak limestone”, and regional topography feature of Akekule bulge in Shaya uplift, we divided the secondary geomorphology into three types: karst platform, karst gentle slope, and karst intermontane basin (Fig. 1.9). On the basis of division of secondary geomorphology units, according to the microgeomorphology combination forms of Pre-Carboniferous in this Oilfield, we divided the tertiary geomorphology into 11 types: peak cluster depression, karst trough, hill peak depression, hill cluster ridge valley, hill cluster valley, karst hill depression, peak cluster ridge valley, and peak cluster valley, etc. (Fig. 1.10 and Table 1.29).

Different geomorphology units have different features of karst development (Table 1.30). Among six kinds of tertiary geomorphology units in Block 4 of Tahe Oilfield, peak cluster depressions and hill peak depressions have the most fractures, vugs and caves drilled (60 and 46, respectively); drilled wells show the biggest cave in Well TK409 is 75 m high, located in a ridge trough region, but fully filled with breccia (at well depth of 5584–5659 m, 165 m away from Ordovician top). The second largest one, 70 m high, is in Well T403 in peak cluster depression,

Table 1.27 Index system for dividing tertiary geomorphic types of Ordovician weathered crust in the Tarim Basin

Type	Major indexes	Description
Karst hill	Mountain is less than 25 m high, less than 0.5 in height/base diameter ratio; usually rounded shape (with mountain side slope generally $< 30^\circ$)	Belonging to elongated corrosion valley; with relatively flat bottom terrain, dipping to one side; the cross-section is generally "U" shape; with relatively flat terrain slope gradient on both sides, and relatively open upper part.
Karst peak	The mountain is more than 25 m high, more than 0.5 in height/base diameter ratio, usually conical shape; and steep in mountain side slope (generally $> 30^\circ$)	
Karst trough	Slope gradient at valley bottom $< 15^\circ$, width > 5 m, length > 50 m. If the terrain slope gradient on two sides is steeper (generally $> 60^\circ$), and height/valley bottom width with terrain slope gradient change at two sides > 2 , it is called "karst peak valley"; if karst trough is more than 100 m long, and more than 10 m wide, it is called "karst valley"	
Karst valley	Slope gradient at valley bottom $> 15^\circ$, width < 5 m, length > 50 m; slope gradient on two sides of valley $> 30^\circ$	
Depression	Bottom diameter < 200 m; if the relative height difference between the karst peak and depression bottom < 25 m, it is called "shallow depression" (or "dished" depression); if the relative height difference > 25 m, it is called "deep depression" (or "funnel" depression)	

(Continued)

Table 1.27 (Continued)

Type	Major indexes	Description
Karst intermontane basin	Bottom diameter > 200 m	Generally evolved from karst depression; its bottom terrain is flat, with smaller topography relief, and often has covering layer; its periphery is often peak cluster depression or karst hill depression
Peak cluster	Mountain base bottom diameter > 200 m	Karst peak mountains have connected base (including three or more karst peaks), in irregular arrangement
Peak cluster ridge	Mountain base bottom diameter > 200 m, length > 250 m	Karst peak mountains have connected bases, and three or more karst peaks in arrangement of a certain direction; ridge strike direction is wavy and flat, hill crests are smaller in relief, or decline to one side
Hill cluster ridge	Mountain base bottom diameter > 200 m, length > 250 m	Karst hills and karst peak mountains have connected bases (including three or more karst hills or karst peaks), with arrangement in a certain direction; ridge strike direction is wavy and flat, the hills have small relief, or decline to one side
Karst hill depression	Relative height difference between karst hill top and depression bottom < 25 m	Including karst hills and depressions
Peak cluster depression	Relative height difference between karst peak top and depression bottom often > 25 m	Including karst hills and depressions; karst peak mountains have connective base, and there is generally depression between peaks

also filled with breccia (at well depth of 5488.0–5558.0 m, 83.0 m away from Ordovician top).

The paleokarst caves in peak cluster depressions are generally high; the filling degree of paleokarst fractures, vugs, and caves in karst troughs and intermontane basins are higher than those in peak cluster depressions and ridge troughs, etc.; the development depth of paleokarst is the biggest in peak cluster depressions and hill

Table 1.28 Identification indexes for palaeogeomorphology restoration of Ordovician weathered crust in the Tarim Basin

Type	Category	Identification index	Remarks
Surface karst forms	Karst trough	Generally cut 20–30 m deep and dozens or hundreds of meters wide	Dendritic distribution, filled with chaotic breccia
	Solution fracture	Class I fracture is 10–50 cm wide, 8–15 m spaced, 50-hundreds of meters long. Class II fracture is 2–10 cm wide, 1–5 m spaced and several-dozens of meters long. Class III fracture is 1–5 cm wide, 0.1–0.3 m spaced and 1–10 m long	Fractures have classes; fractures of the same class have near equal spacing; and they have chemical or mechanical fillings
	Funnel, sinkhole, vertical shaft	Diameter: 0.2–10 m, length <50 m	Filled with chaotic breccia
Subsurface karst forms	Hall-like cave	Diameter: 50-hundreds of m, height: 10–50 m	Filled with chemical or mechanical deposits; cavern floors have collapse deposits, and channels have fluvial sediments (such as breccia).
	Middle-small cave	Diameters: 0.2–50 m, heights: 0.2–10 m	In lamellar and zonal distribution; with chemical or mechanical fillings
Residual material		pore diameters: 0.5–10 cm	In lamellar and zonal distribution
	Solution-deposited breccia	Thickness: <10 m	In lamellar and zonal distribution
Filling material	Ferro-aluminium layer	Thickness: 3–5 m	In lamellar, zonal and nodular distribution
	Filling material type	Mechanical fillings	Sandy mudstone and collapse breccia with fluvial sediment property
		Chemical deposits	Calcite, dolomite, kaolinite and quartz etc. with fresh water karstification feature
	Filling degree	Unfilled, semi-filled, fully filled	
	Geochemical property	Isotope, inclusion, palynology and chemical component	

Table 1.29 Classification of Pre-Carboniferous paleokarst geomorphy in the Tahe Oilfield

Geomorphic types				Distribution location	Geomorphic genesis type		
Primary geomorphic unit	Secondary geomorphic unit	Tertiary geomorphic unit	Major individual form				
Southern slope belt	Karst platform (I) Upper karst gentle slope (II)	Karst hill depression (II1)	Karst hill, depression	Southern Block 5	Denudation		
		Monadnock plain (II2)	Karst hill, karst plain	Northern Block 5	Denudation and erosion		
		Hill peak depression (II1)	Karst peak, karst hill, depression	Major in Blocks 6, 5 and 2, and minor in Blocks 4 and 7, the most important Pre-Carboniferous geomorphic unit	Denudation		
		Peak cluster depression (II2)	Karst peak, karst hill, depression	In middle-west Block 4 and 6	Denudation		
		Hill cluster ridge valley (II3)	Karst hill, depression, ridge, karst valley	Mainly in Blocks 5, 3 and 4, with more surface drainage system and valley	Denudation and erosion		
	Lower karst gentle slope (III)	Hill cluster ridge trough (II4) Karst trough (II5)	Hill cluster ridge trough (II4)	Karst hill, ridge, trough	Block 4 and northern Block 6	Denudation and erosion	
			Karst trough (II5)	Karst hill, trough, depression	Block 4 and northern Block 6	Denudation and erosion	
			Hill peak depression (III1)	Karst peak, karst hill, depression	Mainly in Blocks 3 and 2	Denudation	
			Hill cluster valley (III2)	Karst hill, depression, karst valley	Mainly in Block 3	Denudation and erosion	
			Karst hill depression (III3)	Karst hill, depression	Mainly in Blocks 2 and 8	Denudation	
		Karst intermontane basin (IV)	Peak cluster ridge trough (III4) Hill cluster ridge valley (III5) Peak cluster valley (III6) Peak cluster valley (IV1) Karst lake (IV2)	Peak cluster ridge trough (III4)	Karst peak, depression, karst trough	Mainly in western Block 2, Block 8 and western Block 6	Denudation and erosion
				Hill cluster ridge valley (III5)	Karst hill, depression, karst valley	Mainly in western Block 6	Denudation and erosion
				Peak cluster valley (III6)	Karst peak, depression, karst valley	Mainly in western Block 8 and western Block 6	Denudation and erosion
				Peak cluster valley (IV1)	Karst peak, depression, karst valley	Block 4 and Block 2	Denudation and erosion
				Karst lake (IV2)	Funnel, sink hole	Blocks 4 and 2	Denudation and erosion

Table 1.30 Development features of fracture-vug systems in various geomorphic units in Block 4 in the Tahe Oilfield

Geomorphic unit	Number of drilled fractures and caves	Number of paleokarst caves		Scale of paleokarst caves (m)		Thickness of corroded-fractured section (m)		Depth of fractures and caves from O top (m)		Development position	Filling features
		Semi-filled	Fully filled	Min	Max	Min	Max	Min	Max		
Peak cluster depression	60	14	14	0.3	70.0	0.6	50.0	0.0	338.5	Side slopes of karst peaks (hills) mainly have large caves; major areas of karst peaks (hills) mainly have various dis-vug-fracture systems; there are fewer karst in depression.	The overall filling degree is lower; filling material in caves is mainly gray-green mud and a small amount of calcite; filling material in solution fractures is equivalent in gray-green mud and calcite; filling material in caves is mainly calcite.
Hill peak depression	46	3	24	0.37	36.5	6.5	99.0	4.0	273.7	Solution fracture-vug systems are all in side slopes of karst peaks (hills).	The overall filling degree is higher; filling material is gray-green mud and calcite.

Ridge valley	12	4	1	0.3	25.5	1.0	34.50	0.0	61.7	Side slopes of karst hills and valleys mainly have caves; ridge edges mainly have fractures and caves.	The overall filling degree is lower; major filling material is gray—green mud.
Ridge trough	22	8	2	1.0	75.0	1.44	72.0	0.0	167.0	Side slopes of ridges have caves; side slopes of depressions have dissolution caves and fractures; karst peaks have solution fractures.	The overall filling degree is higher; filling material is gray—green mud and calcite.
Karst trough	20	0	3	2.0	29.0	2.0	29.0	0.0	142.0	Karst hills and their side slopes all have solution fractures, with few caves.	The overall filling degree is higher; filling material is silt and gray—green mud.
Karst lake	14	0	10	1.0	19.5	1.0	19.0	0.0	92.5	Caves occur in side slopes of karst hills and depressions.	Karst fracture-vug system is basically fully filled; filling material is gray—green mud.

peak depressions (338.5 m and 273.7 m, respectively). Paleokarst is best developed in side slopes of various peaks and karst hills.

1. Paleokarst geomorphology and development conditions of karst platform

Karst platforms (I): they are situated in middle-west of Block 4, and Well TK609–TK652 and TK442–TK441 regions in Block 6. In Block 6 and Block 4, they are near-round in shape, with a diameter of about 5–6 km and outline area about 30–35 km²; in Well TK609–TK652 and TK442–TK441 regions in Block 6, they are in the SN direction, with an area of about 3–4 km². The ancient thickness between Ordovician top to Carboniferous “double peak limestone” was around 60–100 m. The Ordovician top relief is smaller, generally 10–20 m (30–50 m in some local regions), being the primary karst platform in the Tahe Oilfield. The topography in the platform is flatter, with well-developed surface karsts. The major phenomena are karst peak (local gentle hill), depression (shallow depression), sink hole, and karst trough, etc. Higher in topography, the region was regional water dividing ridge and major subsurface water recharge area in the paleokarst area.

According to microgeomorphology combination forms, karst platforms in Block 6 and Block 4 can be divided into three types of tertiary paleokarst geomorphology: peak cluster depression, karst hill depression, and karst trough.

a. Peak cluster depressions (I1)

Mainly distributed in middle Block 4 (TK432–TK428–TK440–TK486, and TK406–TK413 in the middle west), peak cluster depressions are the most important geomorphology and cover about 40% of Block 4. This kind of region has flat topography, undulating terrain, and relative height differences of 30–50 m, mountains in gentle conform, and superimposed depressions and small valleys between karst peaks. Small funnels and sink holes are universally developed in these depressions and small valleys. This kind of geomorphology is situated in the water dividing ridge region of three major water systems, where as there were only a few surface drainage systems, atmospheric precipitation gathered and flowed to subsurface depressions, funnels, and sink holes mainly through vertical percolation or laminar flow; subsurface water moved mainly in vertical style, and finally discharged to surrounding lower mesas or valleys in divergence style. Therefore, there are more karsts in shallow layers, with deeply developed karst; however, because of limited confluence and runoff conditions, the shallow karst is relatively small in scale. The karst is mainly in the form of vertical solution fractures and caves. As rainfall generally gathered to funnels and sink holes in depressions and valleys in laminar flow, the solution fractures and caves in depressions and valleys are more likely to be filled during a later period than those in karst peaks. For instance, Well TK424 is located in microtopographic karst peak, its cave system at 5536.0–5537.16 m is unfilled; Well TK440 is located in a microtopographic depression, its cave system at 5575.98–5596.85 m is fully filled.

b. Karst hill depressions (I2)

Karst hill depressions are distributed mainly in Well area TK609–TK652 and TK641–TK441 in Block 6 and Well area TK469–TK405 in Block 4. This kind of geomorphologic region has undulating topography, with relative height differences of 15–20 m; mountains generally are gentle hill shape, and depressions and small valleys are superimposed between karst hills. Small funnels and sink holes are universally developed in these depressions and small valleys. This kind of geomorphology is situated on two sides of the water dividing ridge region, with few surface drainage systems, so atmospheric precipitation gathers and flow to subsurface depressions, funnels, and sink holes mainly through vertical percolation or laminar flow; subsurface water

moved mainly in vertical style, and finally discharged to the surrounding lower mesas or valleys in divergence style. Karstification is chiefly in the forms of vertical solution fractures and dissolution caves. As rainfall generally gathers into funnels and sink holes in depressions and valleys in laminar flow, the solution fractures and caves in depressions and valleys are more likely to be filled during a later period than those in karst peaks.

c. Karst troughs (I3)

Karst troughs in karst platforms are principally situated in Well area TK408–TK411 in Block 4. This type of geomorphologic region has undulating topography, relative height differences between karst hill and karst trough of 10–20 m; flat trough bottom dipping to one side; small funnels and sink holes, depressions in bead-like in local area. This kind of geomorphologic region is the precipitation confluence and runoff area in karst platforms, where there are more karsts in shallow layers, but they are likely to be filled in a later period. The lower part belongs to the runoff and drainage section of subsurface water in karst platforms to karst intermontane basin in eastern Block 4. There may be karst conduit systems along karst troughs, but they are probably filled in a later period. For example, in Well TK411 in this geomorphologic unit, the cave system at 5466.0–5470.0 m is fully filled with sandy mud.

2. *Paleokarst geomorphology and development conditions of upper karst gentle slopes*

Upper karst gentle slope (II): on the boundaries of Blocks 4 and 6, upper karst gentle slopes are mainly extensive in Blocks 6, 7, 3, and 5 where the ancient thickness between Ordovician top and Carboniferous “double peak limestone” is 60–110 m. This kind of geomorphologic region has undulating topography and terrain of gentle distribution, with apparent slow terrain slope gradient (generally <2%–3%); the mountains are not at the same elevation, with relative height differences of generally <50–60 m; the terrain overall dips in all directions from Block 4, with few surface valleys and water systems. This kind of geomorphologic region was recharged and runoff areas of ancient water systems, where karsts, very developed, are mainly complex peak clusters, hill clusters, karst depressions (or sink holes), karst channels (valleys), and local karst intermontane basins (karst hill depressions), particularly, deep and long karst valleys are most developed near karst troughs; the relative height elevation between depression bottom and peak cluster top is about 20–80 m; the strike direction of the valleys are generally parallel to the slope dip direction, with many irregular geomorphologic forms (mostly hill peak depressions, hill cluster ridge valleys or troughs).

According to microgeomorphology combination forms, they can be further divided into six types of tertiary paleokarst geomorphology: hill peak depression (II1), karst hill depression (II2), hill cluster ridge valley (II3), hill cluster ridge trough (II4), karst trough (II5), and karst lake (II6).

a. Hill peak depressions (II1)

These are located mainly in southern Block 4 and northern Block 2 (TK425–K419 and TK210–TK213), middle Block 6 and northern Block 7 (TK628–K610 and TK735–TK714), and Well S78–S90 in middle-northern Block 5. They are the most important Pre-Carboniferous paleokarst geomorphic units of Tahe Oilfield. This type of tertiary paleokarst geomorphology belongs to the border area of karst platform and upper karst gentle slope, where the ancient thickness between Ordovician top and Carboniferous “double peak limestone” was 60–110 m (relative height differences of about 50–60 m). This kind of geomorphologic region has undulating topography, and flatter terrain, slow drop trend of terrain slope gradient and small relative height elevation, mountains in coniform or gentle hill form, shallow cut depressions and small troughs superimposed between hill peaks, and small funnels and sink holes universally developed on these depressions and small troughs. This region was the decline and

transition part of Block 4 to its periphery, and also confluence and runoff area of meteoric water, where underground runoff discharged to its periphery. Thus the karstification was stronger and water–rock interaction cycle was longer, resulting in fairly rich subsurface caves and karst conduits, but this region was near the water dividing ridge of the paleokarst drainage area, with limited convergence conditions, thus the development scale of the karst space is smaller; some local areas were regional water dividing ridges, thus shallow solution fractures and caves in depressions and troughs are not likely to be filled during a later period. For instance, Well TK447, Well TK480, and Well TK434 in this geomorphic unit, all encountered drilling break and lost circulation, indicating there are unfilled ancient fracture-vug systems.

b. Hill cluster ridge valleys (II3)

These are mainly located in Block 5, Block 3, and part of Block 4. Eastern Block 4 belongs to the transition belt between karst platform and karst intermontane basin, where the terrain dips to the karst intermontane basin, and surface valleys are well-developed. Block 5 and Block 3 with terrain dipping to southwest, have better-developed surface water systems and valleys. In this kind of geomorphologic region, the ancient thickness between Ordovician top and Carboniferous “double peak limestone” was 60–90 m (with relative height differences of about 30–50 m), the mountains are connected in base into ridges, most of the mountains are coniform, some are gentle-hill-shaped; the ridge, wavy in strike, dips and declines to the karst intermontane basin, or dips in the southwest direction, with a bigger terrain slope gradient. Karst valleys or troughs in the same strike direction as the ridges developed between these ridges, associated with bowl-shaped depressions and sink holes, and the valleys or troughs open to the downstream at one end. Dissolution depressions and funnels of various scales usually occur between hill clusters, but the depressions are often smaller. Similar to the whole terrain, these karst valleys, troughs or depressions dip and decline to the karst intermontane basins or southwestern direction. In this kind of geomorphologic region, meteoric water seeped down vertically or conflowed to valleys in laminar flow, then discharged to karst intermontane basins by runoff. Because of big runoff slope gradient and limited catchment area, though the surface valleys were well-developed, their scales were smaller; in shallow layers, the karst is mainly in the form of vertical solution fractures, while large-scale cave systems are rare. The lower part is the discharge and runoff area of the groundwater in karst platforms to the karst intermontane basin or southwest direction, where small karst conduit systems may exist.

c. Hill cluster ridge troughs (II4)

These are mainly located in Block 4 and northern Block 6, with terrain dipping north, and well-developed surface drainage systems, troughs, and valleys. In this kind of geomorphologic region, the ancient thickness between Ordovician top and Carboniferous “double peak limestone” was 60–90 m (with a relative height difference of about 30–50 m); the mountains, connected at the base, form ridges, and are mostly buninoid, some are coniform; the ridge is wavy trend, with a bigger terrain slope gradient. Karst valleys or troughs in the same strike with the ridges developed between these ridges, associated with bowl-shaped depressions and sink holes. Dissolution depressions and funnels of various scales usually exist between hill clusters, but the depressions are often smaller. In this kind of geomorphologic region, meteoric water infiltrated vertically or conflowed to valleys in laminar flow, resulting in well-developed surface troughs; in shallow layers, vertical solution fractures, and small scale caves are dominant, and large scale cave systems are rarely formed; the lower part is the discharge and runoff area of the groundwater in karst platform to the north direction, where large scale karst conduit systems may exist. For example, Well TK481 and Well TK483,

etc., are near the karst trough, the paleokarst fracture-vug systems at 5513–5536 m in Well TK481 and 5677–5691 m in Well TK483 are filled with sandy and muddy rock with features of underground stream deposits, which indicates there are karst conduit systems in this region.

d. Karst troughz (II5)

These are mainly located in Well S65-TK453 region of Block 4, Well T601 region of Block 6, and north of Well TK419 in southern Block 4. In this kind of geomorphologic region, the terrain is undulating, with relative height differences between karst hills and troughs of 10–20 m; the bottoms of the troughs are flat, there are small funnels and sink holes in these troughs in general, and depressions in the local area are bead-like in shape. This kind of geomorphologic region is confluence and runoff area of precipitation in the karst platform, shallow karst is well-developed, and there may be karst conduit systems along lower karst troughs, but they are likely to be filled in a later period. For instance, fracture-vug systems at 5480–5488 m (29–34 m away from Ordovician top) in Well S65 are well-developed but filled with calcareous and argillaceous materials; the fracture-vug systems at 5724.67–5727.77 m (273 m away from Ordovician top) in this well are fully filled with muddy silt with features of underground stream deposits.

3. Paleokarst geomorphology and karst development conditions of lower karst gentle slopes

Lower karst gentle slope (III): these are situated in the south and west of the major part of Tahe Oilfield, i.e., Block 2, Block 7, Block 8, and western Block 6, where the ancient thickness between Ordovician top and Carboniferous “double peak limestone” was 110–300 m. This kind of geomorphologic region has larger fluctuation in topography and terrain, with apparent slow terrain slope gradient (generally 3%–5%); the mountains are not at the same elevation, with relative height differences of generally less than 50 m; the terrain in Blocks 2, 7, and 8 dips toward the south on the whole, while the terrain of western Block 6 dips toward the west, and the surface valleys and water systems are well-developed. This kind of geomorphologic region was the recharge and runoff area of ancient water systems, where karsts are very developed, featuring complex peak clusters, hill clusters, karst depressions (or sink holes), karst troughs and karst valleys, karst troughs and karst valleys are better developed, with greater depth and extension; the relative height elevation between the depression bottom and peak cluster top is about 20–80 m, the geomorphologic forms, very irregular, are mostly hill peak depressions, karst hill depressions, hill cluster valleys or peak cluster valleys.

According to microgeomorphology combination forms, they can be further divided into eight types of tertiary paleokarst geomorphology: hill peak depression (III1), hill cluster valley (III2), peak cluster depression (III3), peak cluster ridge trough (III4), hill cluster ridge valley (III5), karst trough (III6), peak cluster valley (III7), and karst lake (III8).

a. Hill peak depressions (III1)

These are located in Well T314 and Well TK331 regions in Block 3, and southwestern Well T208 in Block 2. This type of tertiary paleokarst geomorphology is in the local border of runoff discharge area, where the ancient thickness between Ordovician top and Carboniferous “double peak limestone” was 60–110 m (with relative height difference of about 50–60 m); the topography has bigger fluctuation, and the terrain has a slow slope gradient drop to its vicinity (in isolated island state); the mountains are coniform or in gentle hill form; shallow cut depressions and small troughs are superimposed between karst hill and karst peaks, and small funnels and sink holes are universally developed on the depressions and small troughs. As the local watershed area, it had limited water supply and confluence conditions, and it is also the distribution region of the Ordovician Lianglitage Formation with poorer lithology and karstification conditions, thus the karst space is smaller in scale, and the shallow karsts are mainly solution fractures and small caves.

b. Peak cluster depressions (III3)

These are mainly distributed in Well T314 and Well T204CH–T208–T209CH regions in Block 2, and Well TK845CH–T815CH region in Block 8, where the ancient thickness between Ordovician top and Carboniferous “double peak limestone” was 150–120 m (with a relative height difference of about 20–30 m). This kind of geomorphic area has fluctuating topography, small relative height difference, terrain dipping and declining to southeast and south, mountains of gentle mound shape, shallow cut depressions and small troughs superimposed between gentle hills, and bigger karst valleys include those occurring along Well TK258–TK221. There are small funnels and sink holes universally in the depressions and small troughs. This kind of geomorphic region is located in confluence and runoff areas of the paleokarst drainage area, or in a local watershed area, with undeveloped surface drainage systems (developed surface drainage system in some local regions), where meteoric water mainly infiltrated in the vertical direction or conflowed to underground depressions, funnels and sink holes in valleys in laminar flow, groundwater mainly moved in the vertical direction, and finally discharged to karst valleys and troughs in disperse state, with better hydrodynamic conditions of karstification. However, this kind of geomorphologic area is mainly the distribution region of the Ordovician Lianglitage Formation with poorer rock-karstification conditions, so in this kind of geomorphologic area, shallow karsts are fairly developed, and the karsts are mostly vertical solution fractures and smaller caves with poorer connectivity. Moreover, as the precipitation principally conflowed to funnels and sink holes in depressions and valleys in laminar flow, the solution fractures and caves in depressions and valleys are more likely to be filled than those in karst hills in a later period.

c. Peak cluster ridge troughs (III4)

Mainly distributed in Well TK226CH–TK232 area in western Block 2, Well T703CH–T811CH area in Block 8, and western Block 6, they were the discharge regions of runoff in the paleokarst drainage area of the Tahe Oilfield, where the ancient thickness between Ordovician top and Carboniferous “double peak limestone” was 110–250 m (with a relative elevation difference of 100–150 m); the Ordovician top has bigger fluctuation, with apparent terrain slope gradient (generally <5%–10%); the terrain in Well TK226CH–TK232 in western Block 2 and Well T703CH–T811CH in Block 8 dips toward the south, with big topography fluctuations; the western Block 6 dips toward the west. This kind of geomorphologic area is composed of karst peaks, depressions, valleys, or troughs; the karst peak mountains are connected at their bases to form ridges; most of them are coniform, and some are in gentle mound shape. The ridges are in wavy strike, and karst valleys or troughs in the same strike direction as the ridges exist between these ridges, associated with bowl-shaped depressions and sink holes; one end of the valleys or troughs opens to the downstream. Karst depressions and funnels of various scales usually develop between peak clusters, but these depressions are generally smaller. Overall, karst troughs and valleys are better-developed, with apparent surface runoff.

This kind of geomorphologic area, situated in the runoff, confluence, and discharge region of the paleokarst drainage area, had stronger karstification and longer water–rock interaction cycle, thus shallow karst fracture-vug systems are better-developed there; moreover, this kind of area is the major runoff and discharge region of underground runoff, thus there may be more underground karst caves and conduits.

d. Peak cluster ridge troughs (III5)

These are distributed in western Block 6 (Well T752–TK0145–TK658CH–S81), where the ancient thickness between Ordovician top and Carboniferous “double peak limestone” was 110–180 m, the terrain dips toward the west overall, and the surface valleys are well-developed, most of the mountains are rounded karst hills with their bases connected,

forming ridges; these ridges with wavy strike direction, dip and decline toward the west, with relatively flat terrain slope gradients. Karst valleys or troughs in the same strike direction as the ridges develop between these ridges, associated with bowl-shaped depressions, the valleys or troughs have one end opening to the downstream. Similar to the whole terrain, these karst valleys, troughs, and depressions dip and decline toward the west.

This kind of geomorphologic area is situated in the slope belt in western Block 6, where the major developed water systems are karst valleys; because of the limited water catchment area, the groundwater mainly seeped vertically, and the runoff slope gradient is big, which is favorable for forming hill clusters, karst valleys, troughs or depressions; therefore, shallow karsts are well-developed, and the karst spaces are unlikely to be filled in a later period, but because of short precipitation retention time and short karstification cycle, the caves in this area are smaller than those in other areas. Its lower part was the runoff region of the paleokarst drainage area, except for the areas with more karst valleys where karst conduit systems might exist, other areas had no unified confluence or runoff, and poorer karst development conditions, thus cave systems (or karst fracture-vug systems) are not well-developed.

e. Hill cluster valleys (III2) and peak cluster valleys (III7)

Hill cluster valleys are mainly distributed in Well TK333–TK331 in Block 3, and peak cluster valleys are located in western Block 6 (western Well S92). The ancient thickness between Ordovician top and Carboniferous “double peak limestone” in wells TK333–TK331 of Block 3 and western Block 6 of Tahe Oilfield (western well S92) were 150–200 m and 270–300 m respectively. With bigger terrain relief, big relative elevation height difference, this kind of geomorphologic area contains karst peaks, deep depressions and valleys, and dissolution depressions and valleys of various scales between peak clusters. There are more karst valleys with a “U”-shaped cross-section, with a length of 3–8 km, width of 100–300 m, and depth of 30–60 m.

4. Paleokarst geomorphology features and karst development conditions of karst intermountain basins

Located in Well TK423–TK422 in Block 4 and Well S72–TK254 in Block 2, karst intermountain basins (IV) have closed topography around, bigger area, and features of surface runoff and confluence. According to microgeomorphologic combination forms, they can be further divided into two types of tertiary paleokarst geomorphology: peak cluster valley (IV1) and karst lake (IV2).

On the east of Block 4, the ancient thickness between Ordovician top and Carboniferous “double peak limestone” was 90–150 m, with sealed terrain area of about 6 km²; in Well S72–TK254 in Block 2, the ancient thickness between Ordovician top and Carboniferous “double peak limestone” was 180–220 m, with sealed terrain area of about 3–5 km². Evolving from peak cluster depression, this kind of geomorphologic region has undulating terrain, flatter topography, small relative height difference, gentle-hill-shaped mountain bodies, shallow cut depressions and small troughs superimposed between gentle hills, and small funnels and sink holes universally in depressions and small troughs. Located in the local low of Tahe Oilfield, this area is a confluence area of meteoric water, where the gathered water is discharged outwards in underground runoff, thus this region has better-developed karsts, and the lower part may have underground stream karst conduits. Moreover, as the water supply was sufficient, and the water–rock interaction cycle was longer, the karst space is larger in scale in this kind of area. But as it was in the lower position of this area, the shallow solution fractures and caves in depressions and valleys are more likely to be filled in a later period.

1.4.3 Storage properties of paleokarst geomorphic units

Paleogeomorphic forms have apparent controlling effects on hydrocarbon enrichment (Table 1.31). In the Tahe Oilfield, peak cluster depressions are the geological structures providing the highest productivity, accounting for 69.8% of total oil and gas production. Although karst intermontane basins have abundant fracture-vug systems, located in the low position in this Oilfield, they have higher oil/water contact and poorer reservoir conditions. The side slopes of karst hills and residual peaks with better-preserved karst space are potential exploration targets in the future.

1. Peak cluster depression

There are 28 production wells in this area, accounting for 35.4% of the total wells in the Tahe Oilfield. Its cumulative oil production was 407.596×10^4 t (by the end of 2008, and similarly hereinafter), accounting for 69.8% of the total oil production, ranking it the best production block. In this area, Well T401 had a cumulative oil production of 45.09×10^4 t, and Well TS48 71.69×10^4 t; some wells have extraordinary high productivity (TK427, TK412, TK410, and TK407, etc). The producing intervals are mainly in surface karst zones and vertical percolation dissolution zones; the wells (S48 and T401, etc.) in karst hills, karst peaks or their side slopes have higher cumulative productivity, which indicates that the fracture-vug systems have some connectivity and better reservoir conditions; while the wells (such as T415 and TK405) in depression side slopes, valley side slopes, and depressions have lower cumulative productivity, and although they might have substantial productivity in the initial period, they witnessed a rapid rise of water cut.

2. Hill peak depression

This region, bigger in area, includes three well areas (TK470–TK439, etc.), and 28 production wells (accounting for 35.4% of the total wells in the Tahe Oilfield). Its productivity is only less than that in peak cluster depression: with a cumulative oil production of 145.113×10^4 t, accounting for 21.5% of total oil production. There are seven wells with total oil production of more than 10×10^4 t, among which, Well TK439 and Well TK474 had a cumulative oil productions of 21.97×10^4 t and 20.288×10^4 t, respectively. Except that some produced intervals in Well TK480 are in the zones with runoff corrosion zones, other produced intervals are generally in the surface karst zone and the vertical

Table 1.31 Oil and gas production performance in paleogeomorphic units in the pilot area in the Tahe Oilfield

Geomorphic type	Production well		Cumulative oil production of single well ($\times 10^4$ t)				Total oil production	
	Well number	%	>10	10-5	5-1	<1	$\times 10^4$ t	%
Peak cluster depression	28	35.4	9	4	12	13	407.596	69.8
Hill peak depression	28	35.4	7	1	8	12	145.113	21.5
Ridge valley	6	7.6	3	0	3	0	48.497	7.2
Ridge trough	9	11.4	2	0	4	3	43.933	6.5
Karst trough	3	3.8	1	2	0	0	27.687	4.1
Intermontane basin	5	6.3	0	0	1	4	1.501	0.2
Total	79	100	22	7	28	32	674.327	100

percolation dissolution zone. The wells at the side slopes of karst hills and karst peaks had higher initial daily production from the surface karst zone and the vertical percolation dissolution zone, longer water-free periods and higher single-well cumulative production.

3. Hill cluster ridge valley

This region, including six production wells, had a cumulative oil production of 48.497×10^4 t (accounting for 7.2% of total oil production). The oil productivity in this region is apparently uneven: three wells had cumulative production of more than 10×10^4 t; wells (such as TK429 and TK404) at ridges or their side slopes had higher cumulative production (Well TK429 and Well TK404 had a cumulative oil production of 14.441×10^4 t and 13.224×10^4 t, respectively); while wells (such as TK477) at the side slopes of valleys had lower total production.

4. Hill cluster ridge trough

This region has nine production wells, with a cumulative oil production of 43.933×10^4 t (accounting for 6.5% of total oil production). The wells (such as TK409) at the side slopes of karst hills and ridges have higher productivity; while the wells (such as TK483) at the side slopes of depressions, valleys or troughs have lower productivity. Well TK409 had a cumulative oil production of 18.206×10^4 t, and Well TK471 had a cumulative oil production of 15.102×10^4 t.

5. Karst trough

This region has only three production wells, with a cumulative oil production of 27.687×10^4 t (accounting for 4.1% of total oil production). All the three wells (TK455, etc.) are located on the side slopes of karst hills in troughs, with higher productivity and long water-free periods. Well TK455 and Well TK411 had cumulative oil production of 8.103×10^4 t and 11.279×10^4 t, respectively; other regions had poorer productivity conditions.

6. Intermontane basin

This region has five production wells, with a cumulative oil production of 1.501×10^4 t. Except for Well TK426 in a karst hill with considerable productivity, the other wells have low productivity. Though higher in initial productivity, they had short water-free periods, and high water cut, indicating that oil/water contact of this geomorphic unit is higher, thus the oil reservoir conditions are worse.

1.5 Vertical distribution of fracture-vug systems in the Tahe Oilfield

The development of karst has vertical zonation, which dictates vertical distribution of the fracture-vug system. The systems, similar in the development strength of the palaeo-karst and the flow manner of palaeo-groundwater and spatially interconnective intervals, are divided into a karst developmental zone.

The basic information on which the vertical distribution zone of the palaeo-karst is divided include: (1) downhole vertical distribution of palaeo-karst system; (2) vertical zonation correlation between palaeo- and modern karst systems; (3) geochemical markers of fillings in the palaeo-cave system; (4) features of the palaeo-karst geomorphic unit; (5) palaeo-hydrodynamic and palaeo-hydrologic conditions; (6) drilling and well-logging interpretation results; (7) seismic interpretation results.

1.5.1 Vertical zonation type in the Tahe Oilfield

According to the development features of the primary production blocks in the Tahe Oilfield and the development theory of modern karst, the fracture-vug system in the Tahe Oilfield has been divided into four zones vertically: (1) epikarst zone; (2) vertical percolation dissolution zone; (3) runoff dissolution zone; (4) undercurrent dissolution zone.

The epikarst zone is the karst developmental zone near-surface soluble formation, where the acting CO₂ in the internal dissolution process was from soil or atmosphere, karstification is stronger and higher, resulting in karren, solution groove, fracture, vestige, vug and pipe and pore below the soluble formation.

In the vertical percolation zone, underground water seeps downward along faults or fractures, leaching and dissolving carbonate, forming a series of perpendicular or high-dip solution fractures or karst vugs. The dissolved space has comparatively weak lateral connectivity, and caves are partially filled with mechanical collapse material. This zone is thicker in underground water supply regions.

The runoff dissolution zone is the runoff zone of groundwater, with faster flow rate of underground water, where a series of nearly parallel solution fractures and caves, and karst pipe systems are formed, as well as considerable mechanical or chemical filling or semi-filling materials. The features of this zone are that the scale of dissolved space is comparatively larger, the karst space has better lateral connectivity, and the karstification development is very uneven.

The undercurrent dissolution zone is located below the groundwater runoff zone where the groundwater flows quite slowly along faults or cracks, dissolving carbonate, the dissolution space is smaller, the karst development is very uneven, the mechanical postfilling is relatively weak, the chemical deposition is relatively strong, and the overall karst is not developed.

The vertical palaeo-karst zones have obvious differences in logging responses, drilling rate, groundwater runoff behavior, karstification type, filling features, and shape of individual karst (Table 1.32).

The vertical palaeo-karst zonation in different geomorphologic units in Block 4 (Table 1.33) have some differences: the epikarst and vertical percolation dissolution zones in peak cluster depressions and mound peak depressions are thicker; the vertical percolation dissolution zone in solution grooves and karst lakes are thinnest; the runoff dissolution zone in different geomorphologic units do not vary much in thickness.

1.5.2 Vertical distribution features of the fracture-vug system

The vertical development features of the palaeo-karst in different geomorphic units are different (Table 1.34, Figs. 1.36 and 1.37). The epikarst zone in mound cluster ridge and peak cluster areas is thicker; while the vertical percolation dissolution zone in peak cluster depression areas is thicker, in the lower parts such as karst lake

Table 1.32 Vertical plaeokarst zonation in different geomorphologic units in Block 4

Vertical zonation				
Third-level Geomorphologic unit	Epikarst zone thickness (m)	Vertical percolation dissolution zone thickness (m)	Runoff dissolution zone thickness (m)	Undercurrent dissolution zone (below Ordovician top)
Peak cluster depression	20–30	50–150	20–35	Below 85–180 m
Mound peak depression	10–30	60–140	15–30	Below 105–270 m
Ridge cheuch	10–25	45–120	20–30	Below 80–190 m
Ridge groove	10–25	60–100	20–35	Below 70–190 m
Dissolution groove	10–20	60–85	15–25	Below 110–120 m
Karst lake	5–15	50–55	20–30	Below 85–115 m

and lower land, all vertical zones are thinner. Taking peak cluster depression as an example, the features of different zones are as follows (Figs. 1.38 and 1.39):

1. Epikarst zone: located 0–30 m below the Ordovician top, it is 20–30 m thick, containing main palaeo-karst forms such as solution fractures and caves, palaeo-caves are developed commonly, with a size of 0.3–26.0 m (the scale of nonfilled caves is 1–5 m), the infillings are mainly mud and calcareous material; the solution fractures are mostly fully filled or semi-filled with mud. Overall middle to strong in karst development level, it is a composite strong karst development zone of a fracture-cave system.
2. Vertical percolation dissolution zone: located 30–160 m below the Ordovician top, and 50–150 m thick, it mainly contain solution fractures and few palaeo-caves, the solution fracture system is completely or partially filled with mud and calcite. Medium to weak in overall karst developmental level, it is a medium karst developmental zone of the solution fracture type.
3. Runoff dissolution zone: located 80–180 m below the Ordovician top, 20–35 m thick (locally up to 70 m, such as Well T403), this zone has widespread palaeo-caves, and sparse unfilled caves, the solution caves are 1.0–70.0 m in size (unfilled caves are 3–13 m). The primary fillings are breccia, calcareous and muddy sandstone, some are underground stream depositions. The solution fractures are mostly fully filled or semi-filled with calcareous and muddy material. Showing overall strong development with local karst pipes, it is a strong karst developmental zone with solution fractures and karst pipes.
4. Undercurrent dissolved zone: located 105–270 m below the Ordovician top, it mainly contains tectoclases, microsolution fractures, and a small amount of solution pores, but no caves. Overall not developed, it is a weak karst development zone with solution fractures.

Table 1.33 Feature indicators of vertical palaeo-karst zones in Block 4 in the Tahe Oilfield

Vertical zone	Well logging response			Drilling velocity	Runoff behavior of groundwater	Karstification type	Feature and type of fillings	Shape features of individual karsts
	Natural gamma	Caliper log	Resistivity					
Epic-karst zone	Serrated logging curve, filled fracture-vug systems are generally 20–60 API; the unfilled fracture-vug systems are generally less than 10 API	Hole enlargement	Generally low in dual-lateral resistivity (lower than that of vertical percolation dissolution zone, and higher than that of overlying Carboniferous mudstone), in serrated shape. When the solution fractures and caves are developed, $R_D > R_S$	Accelerated	Containing surface runoff, vertical percolation, and horizontal runoff	dissolution scouring weathering	Mainly mechanical fillings, some karst eluvial or chemical fillings, the filling materials are mainly grayish-green, taupe gray calcareous and muddy rock, some solution fractures are filled with calcite, the filling materials are mixed and of poor sorting	Surface dolines, depressions, solution grooves are strongly developed, underground caves, solution fractures are better developed, and small karst pipes are developed in local areas. The caves and karst pipes are smaller in scale
Vertical percolation dissolution zone	Similar to tight limestone, logging curve is nearly parallel or in serrated shape; the filled fracture-vug systems are generally 20–50 API;	No hole enlargement or slight hole enlargement	Fairly high dual-lateral resistivity, and positive differences, generally $R_D < R_S$; serrated shape in local part, when the solution fractures and caves are abundant, dual-lateral resistivity is generally low	Not accelerated or slightly accelerated	Mainly vertical percolation	Dissolution	Mainly mechanically infilled, some infilled by chemical precipitation, the fillings are mainly grayish-green calcareous and muddy rock	Mainly contains vertical solution fractures and caves, the caves are larger in vertical scale and small in lateral scale in general. The system connectivity is relatively poor. The solution fracture-vug systems are average in development degree on core samples

Runoff dissolution zone	<p>Unfilled solution fracture-vug systems (vug, karst pipe)</p> <p>Filled solution fracture-vug system</p> <p>Breccia-filled solution fracture-vug system</p>	<p>Generally low</p> <p>High GR value, generally ranging 45–100 API, larger in fluctuation</p> <p>Higher than that of tight limestone, generally ranging 30–60 API, the curve in slightly serrated shape</p>	<p>Severe hole enlargement</p> <p>Hole enlargement</p> <p>Hole enlargement</p>	<p>Low resistivity</p> <p>Low dual-lateral resistivity, in serrated shape, with positive differences</p> <p>Obviously lower than that of tight limestone, in severe serrated shape, with positive differences</p>	<p>Accelerated drilling velocity, drill break</p> <p>Accelerated</p> <p>Not accelerated</p>	Mainly horizontal runoff	Dissolution scouring	<p>Mainly mechanically filled, showing deposition features of underground stream, locally filled by collapse stacking and chemical precipitation. The filling materials are mainly grayish-green silty mudstone, sandstone, and breccia, with sedimentary beddings and up-fining depositional sequence</p>	<p>Mainly composed of large karst pipes or horizontal caves. The same karst pipe system has certain connectivity, while different karst pipes have poor connectivity. Large cave systems can be seen in core samples</p>
Undercurrent dissolution zone	<p>Very similar to that of tight limestone, nearly straight and slightly serrated in curve shape; values of infilled fracture-vug systems are 20–50 API</p>	No hole enlargement	Dual-lateral resistivity is generally high, with positive differences	Not accelerated	Mainly undercurrent (laminated current)	dissolution	<p>Mainly filled by chemical precipitation, fillings are mostly calcite, and some grayish-green calcareous mud</p>	<p>Solution pores and fractures take the majority, and caves are not developed. The karst is not developed in core samples</p>	

Table 1.34 Structural features of vertical zones in typical geomorphologic units of Block 4 in the Tahe Oilfield

	Peak cluster depression	Mound peak depression	Mound cluster ridge cheuch	Karst lake
Epic-karst zone	Mainly composed of solution fractures and caves, and palaeo-caves are widely developed in the size of 0.3–2.6 m (the unfilled caves are 1–5 m.), the fillings are mainly muddy, calcareous material; the solution fractures are mostly completely or semi filled with mud and calcareous material; overall strong to medium in karst development, it is composite solution fracture-cave type karst developmental zone.	Palaeo-karst fractures and caves are relatively developed; the caves are mostly completely filled or semi-filled with calcareous cemented breccia and calcareous mud. The solution fractures are mostly completely filled with mud and a small number of them are semi-filled with calcite. Stronger in overall karst development degree, it is composite solution fracture-vug type medium karst developmental zone.	Palaeo-karst fracture systems are relatively developed, with a cave scale of 1.5–13.0 m. There exist semi-filled caves mainly located in the mound cluster ridge region; the fillings are mainly mud, located in the grooves and low land; the solution fractures are mostly completely filled or semi-filled with mud and calcite; Overall medium in karst development degree, it is the solution fracture-vug composite type medium karst developmental zone.	Palaeo-cave systems are fairly developed, with a cave scale of 1.0–5.0 m. The caves are completely filled or semi-filled with calcareous mud, the solution fractures are mostly fully filled with mud. Medium to strong in karst development degree, it is the composite solution fracture-vug zone.
Vertical percolation dissolution zone	Mainly contains solution fractures, and few caves. The solution fracture systems are completely filled or semi-filled with mud and calcite. Weak to medium in overall karst development degree, it is solution fracture type medium karst development zone.	Solution fractures or caves abundant in local areas, are completely filled or semi-filled with mud and calcite; it is solution fracture type medium karst developmental zone.	Mainly contains solution fractures and pores, small scale palaeo-caves are locally developed with a scale of 0.3–2.0 m. The caves are mostly completely filled with mud; the unfilled caves are few. Overall medium in karst development degree, it is the solution fracture type medium karst developmental zone.	Palaeo-cave systems are smaller. The caves are completely filled or semi-filled by calcareous and muddy rock. The solution fractures are mostly completely filled with mud. Overall medium in karst development degree, it is the solution fractures and caves zone.

<p>Runoff dissolution zone</p>	<p>Palaeo-caves are widely developed, and unfilled caves are sparse with a scale of 1.0–70.0 m (unfilled caves are 3–13 m). Fillings of the caves are cave breccia, calcareous and muddy sandstone, with depositional features of underground stream. It is solution fracture-karst pipe composite type strong karst developmental zone.</p>	<p>Mainly contains solution fractures and caves; the cave systems are mostly completely filled or semi-filled, and unfilled caves exist in local areas. Some cave fillings have depositional features of underground stream. Overall medium in karst development degree, it is solution fracture-karst pipe composite type medium karst developmental zone.</p>	<p>Karst pipe systems are locally developed. Unfilled caves are substantial too. The infillings are mainly cave breccia or sandy and muddy stone, with depositional features of underground stream. Overall strong in karst development degree in core samples, it is the composite solution fracture-karst pipe type medium karst developmental zone.</p>	<p>Both solution fractures, palaeo-karst pipe systems are relatively developed. The caves are completely filled with grayish pyrite-bearing muddy siltstone and the solution fractures are completely filled with muddy materials, and the fillings have depositional features of underground stream. Medium and strong in local areas in overall karst development degree, it is the composite solution fracture-karst pipe zone.</p>
<p>Undercurrent dissolution zone</p>	<p>Mainly contains tectoclases, microsolution fractures, and a small number of s, with no caves. Overall not developed in karst fracture-vug systems, it is solution fracture type weak karst developmental zone.</p>	<p>Mainly contains tectoclases and microsolution fractures, with a small number of solution pores, but no caves. Undeveloped in fracture-vug system, it is solution fracture type weak karst developmental zone.</p>	<p>Solution pores are locally developed and palaeo-caves are not seen. The solution fractures are mainly network micrfractures, and interlayer solution fractures in local area, fillings in the fractures are mainly calcite and mud. Overall weak in karst development degree, it is -vug type weak karst developmental zone.</p>	<p>Solution fractures are developed, but palaeo-caves are not. With overall weak karst development, it is the solution-fracture zone.</p>

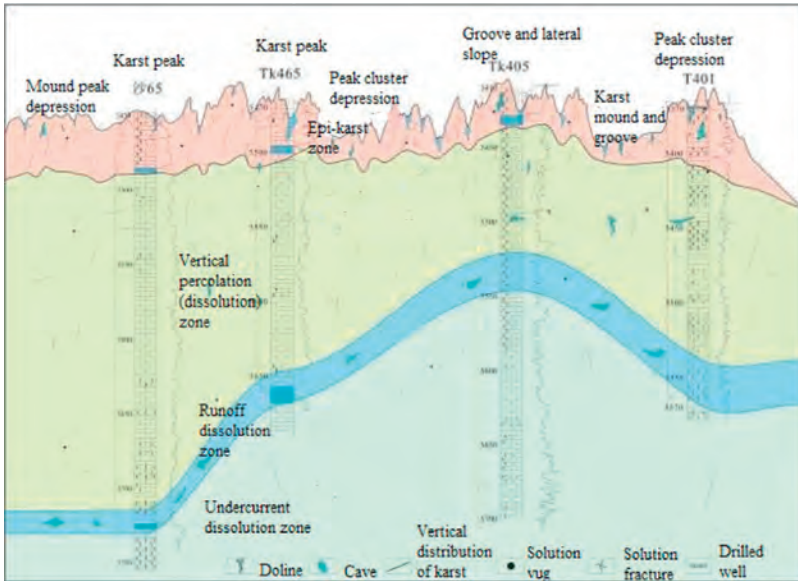


Figure 1.36 Palaeo-karst vertical structural mode of peak cluster depression geomorphologic unit.

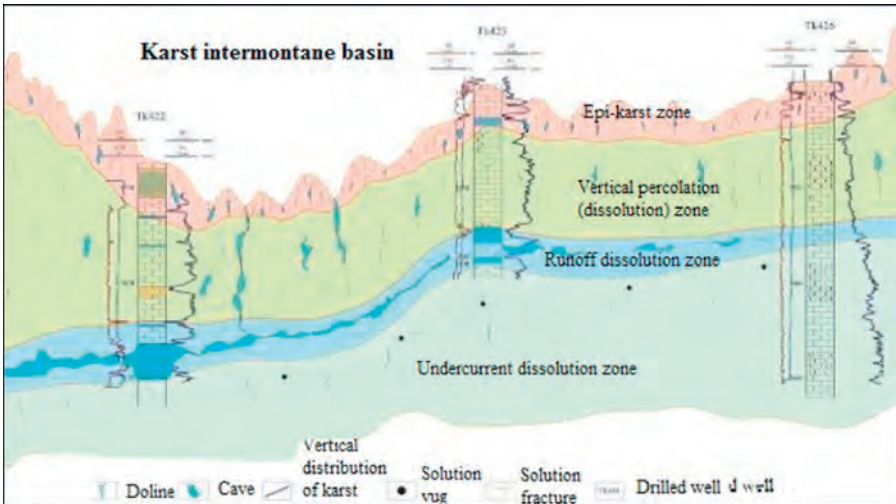


Figure 1.37 Palaeo-karst vertical structural mode of karst lake.

1.6 Forming mechanism and development characteristics of fracture system

Block 4 in the Tahe Oilfield was selected to study fracture systems including drilling-induced, diagenetic, syndepositional and structural fractures. Core observation shows

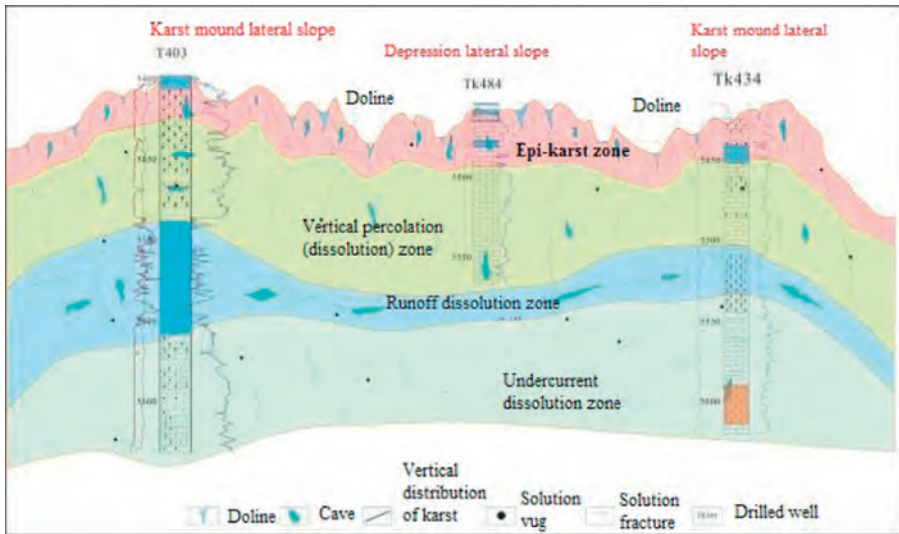


Figure 1.38 Palaeo-karst vertical structural mode of mound peak depression geomorphologic unit.

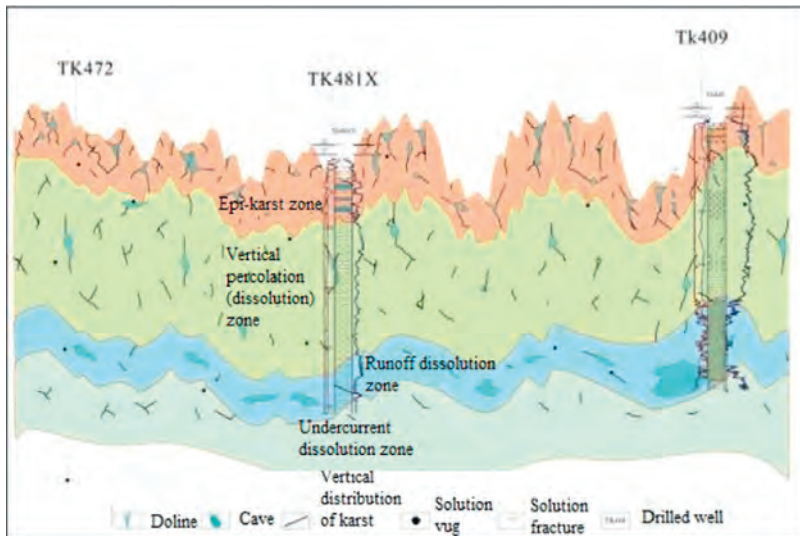


Figure 1.39 Palaeo-karst vertical structural mode of mound cluster ridge and groove.

structural fractures/tectoclases are the most important and most common kind. Core description and analysis of well logging imaging data from 17 wells show that the Ordovician fractures and microfractures have developed densely, which are intersective and highly dipped. Due to denudation at later stages, most fractures were filled with crude oil, providing effective reservoir space and flowing channels.

1.6.1 Forming mechanisms

The Akekule salient where the Tahe Oilfield is located experienced multiple stages of tectonic movements from Caledonian to Himalayan. Since tectonic movements in different stages produced different regional stress fields, faults and fractures in different directions have been formed. As a result of superimposed deformations induced by tectonic stresses in different stages, well-developed fracturing systems have been formed in Ordovician carbonate formations. Laterally, these faults and fractures occur in rows and belts in three predominant directions: NE, near WE and near NS, forming a complicated network including faults, fractures and microfractures.

Most fractures in the study area are shear, and few are tensile. There are more tensile fractures in Well T402 and Well T401 at the structural high. Large high-dip fractures are abundant in this area. Large amounts of data show this area was in a relatively stable period prior to Caledonian (Changquan, 2000; Guorong, 1997; Yongchang et al., 2000), when uplift did not occur, and many diagenetic fractures were formed after sedimentation. During the Caledonian Period, a large number of horizontal conjugate shear joints were created on the originally peaceful plate under the force from NW to SE, which were re-constructed and filled at later stages to form Stage II fractures in the area. The plate remained not uplifting until the end of movements at this stage.

The early Hercynian Period is very important for tectonic movement, when most major structures formed. During this period, the Akekule salient experienced Caledonian movements and gradually came into being. Under the ongoing effect of the NW–SE squeezing force of Caledonian, the formations further cracked and uplifted, forming a large number of vertical original conjugate shear fractures trending near WE and NS. Since the uplift was mild in amplitude, these shear fractures with original dip angle of up to 90 degrees were still mostly high-dip fractures though with some changes in dip angles. Associated with the formation of the salient, a large number of tensile fractures in the northeast direction were formed due to the regional tensile stress produced by bending formations on structural highs. These tensile fractures, with strike consistent with the direction of the long axis of the structure, and high-dip angle too, are the Stage III fractures in this area. These fractures also experienced continuous reformation and filling due to the forces at later stages, especially tectonic stress causing the Sangtamu Formation weathered and denuded. As a result the green mudstone in the Sangtamu Formation entered these fractures, making them partially filled.

As mentioned before, the majority of fractures formed in this period are in NNW and NEE trends, which are slightly different from the near south–north and near east–west fractures formed in Early Hercynian. Since fractures formed during Early Hercynian are major fractures in this area, why are there differences between them? Research results show the following potential factors.

1. Impact of regional structures. The strike of fractures is controlled by tectonic stress, and the impact of early structural faults. Often associated with structural faults, fractures are inevitably subject to the impact of regional tectonic stress, so their development direction

is closer to regional structures, but slightly different from that of regional tectonic stress. Though the fracture strikes described here are statistical, this only reduces the impact to some extent, but can not thoroughly remove such impact.

2. Reformation at later stages. Later reformation by tectonic stress is inevitable, especially structural movements in Late Hercynian during which the South Tianshan Ocean was closed, the Tarim Plate collided with the Yili Plate, and the study area in the north Tarim Plate was subject to intensive northward squeezing, forcing existing structures in this area to deform more or less. In terms of tectonic trace, Tabei Piedmont Faults all have a rotation in arch (included angle of tangent on tip of the arch), and the rotation angle decreased from piedmont to the basin, which indicates that the squeezing stress originated from the north. The fault on the border of the study area is also an arch fault with radian coinciding with the Tabei Fault. Statistics on fracture strike show NEE and NNW relative to NE and NW is 15–20 degrees, consistent with the rotation of piedmont faults and boundary faults of the study area. Therefore, it can be inferred that deviations in fracture strike may be related to the rotation of the Tabei Area due to NW squeezing in Late Hercynian.

Multistage structural movements in Indochina Period, Yanshanian Period, Himalayan Period turned the top interface of Upper and Lower Paleozoic formations from earlier nose-like uplift into large-scale gentle anticline with relatively mild dip. Block 4 in the Tahe Oilfield is at the center of the anticline with not much variation in formation dip, so the dip of fractures would not change much—only forming new fractures in weak places, or enlarging dissolution of existing fractures.

Core observations have fully verified this point—high-dip fractures are widespread. High-dip shaft-like fractures are common in gentle-slope zones, while in steep slope zones, middle-dip fractures formed more, middle-high-dip shaft-like fractures are developed; accordingly, solution fractures are very developed.

1.6.2 Development characteristics

1. Dip angle of fracture

According to core observation, fractures are classified into three groups by dip angle: low-dip fractures, 0–30 degrees; middle-dip fractures, 30–70 degrees; and high-dip fractures, 70–90 degrees. High-dip fractures are predominant in the Tahe Oilfield.

Wells in Block 4 are classified into two types according to the number of fractures at different dips (Fig. 1.40, Table 1.35):

- a. Wells drilling into high-dip fractures: this kind of well mainly has high-dip fractures of over 60%, or even up to 100%. Thirteen such wells are in Block 4 as T401, T402, T415, and TK406.
 - b. Wells drilled into middle-high-dip fractures: middle-dip and high-dip fractures in these wells are comparable. Some wells have a little more middle-dip fractures, such as K407, TK409, and S88; others have a little more high-dip fractures, such as TK404.
2. Length of fracture

Vertical extension is an important parameter characterizing fractures. In fact, lengths of fractures have a significant impact on vertical migration of hydrocarbons. Fracture length observed on cores is limited to some extent, but as the majority of fractures observed are high-dip fractures, or even vertical fractures, fracture length is highly reliable.

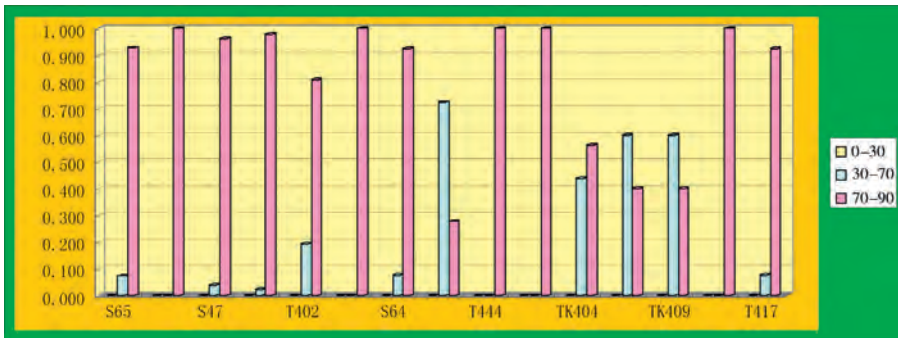


Figure 1.40 Statistics of fracture dip.

Table 1.35 Statistics of fracture dip

Well	0–30°	30–70°	70–90°	Well	0–30°	30–70°	70–90°
S65	0.000	0.074	0.926	T444	0.000	0.000	1.000
T415	0.000	0.000	1.000	TK406	0.000	0.000	1.000
S47	0.000	0.038	0.962	TK404	0.000	0.438	0.563
T401	0.000	0.024	0.976	TK407	0.000	0.600	0.400
T402	0.000	0.192	0.808	TK409	0.000	0.600	0.400
T403	0.000	0.000	1.000	S80	0.000	0.000	1.000
S64	0.000	0.077	0.923	T417	0.000	0.077	0.923
S88	0.000	0.722	0.278	TK427	0.056	0.333	0.611

According to core observation findings, fractures can be categorized into the following groups according to vertical extension length.

- a. Small vertical fractures: with a length of less than 1 cm, these fractures are usually vertical and in parallel with each other, at a spacing of about 0.8 cm. Fully closed and not containing oil, these fractures are generally meaningless because they are neither conductive nor capable of storing hydrocarbons.
- b. Small fractures: $1 < L \leq 8$ cm, these fractures account for a small proportion in general, usually no more than 20% (Fig. 1.41), but the Well TK404 is an exception where this kind of fracture dominates.
- c. Medium-sized fractures: $8 < L < 13$ cm, this kind of fracture takes up a slightly higher proportion, 20%–40% on average in most of wells. These fractures are secondary fractures, rather than dominant ones.
- d. Large fractures: $13 \leq L \leq 30$ cm, highest in proportion, and mostly high in fracture angle, these fractures are the most important channels for oil and gas migration. They may connect suture lines and other horizontal structures, generating a network of conductive systems. More details will be discussed in later chapters.
- e. Super-large fractures, $L > 30$ cm, this kind of fracture takes up a small proportion of no more than 10% often. Only in Well T415 super-large fractures take dominance. Super-large fractures have a wide range of length from 30 cm to up to 165 cm (Table 1.7).

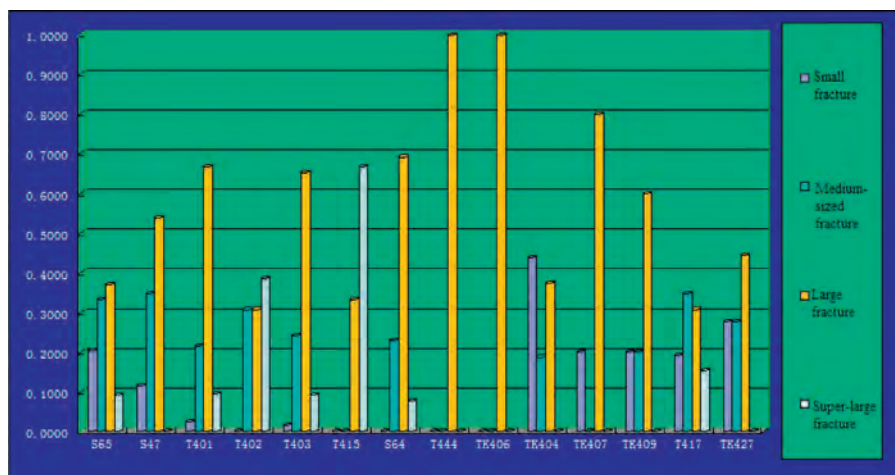


Figure 1.41 Histogram of frequency of fracture length.

3. Strike of fracture

Fracture strike is of great significance in determining the development mechanism and stage of fractures. Since there is no directional coring data available at present, borehole acoustic televiewing and Formation microscanner image (FMI) logs provide primary data to find out fracture dip.

According to the borehole acoustic televiewing and FMI data from over 20 wells evenly distributed throughout the study area, a rose map of fracture strike has been plotted, which shows the fracture strike of major fractures in the study area (Fig. 1.42).

It is worth noting that in Well TK457 and Well TK458, FMI data were acquired in horizontal intervals, so the fracture strike demonstrates the fracture development trend in the lateral direction, other than local phenomena found in a vertical well, these fractures are very representative.

It can be seen from this figure that the fracture strikes mainly concentrate in three groups: NE, NEE, and NWW; there are some fractures of south–north direction in all wells, but they are not dominant. Different wells have dominant fractures of different strikes: in Well TK458, the dominant fractures are NEE, while in Well TK457, the dominant fractures are NE. Core observation results coincide well with field observation results in the Tabai Area. Based on comparability between field observation results and core data (Fig. 1.43), limitations in wells selected, and differences in dominant fractures in each well, it is inferred that fractures in the study area can be classified into three groups: NE–SW, NEE–SWW, and NWW–SEE, with another secondary group in the south–north direction. These features are in agreement with the basic fault features in this area, with similar strikes and groups with the faults in this area.

4. Different stages of fractures

Fractures in the study area are characterized by genesis, re-construction and filling of multiple stages. Based on observation of conventional thin sections, cast thin sections and cores, and according to occurrence of fractures, filling materials, and cutting of fractures with different fillings, filling compositions and sequence, logging data, regional tectonic stress, structural evolution of the study area and surrounding zones, and with reference to buried history and diagenetic evolution maps of the Tahe Oilfield (Fig. 1.44), fractures in the study area are classified into four stages in accordance with their specific features (Table 1.36).

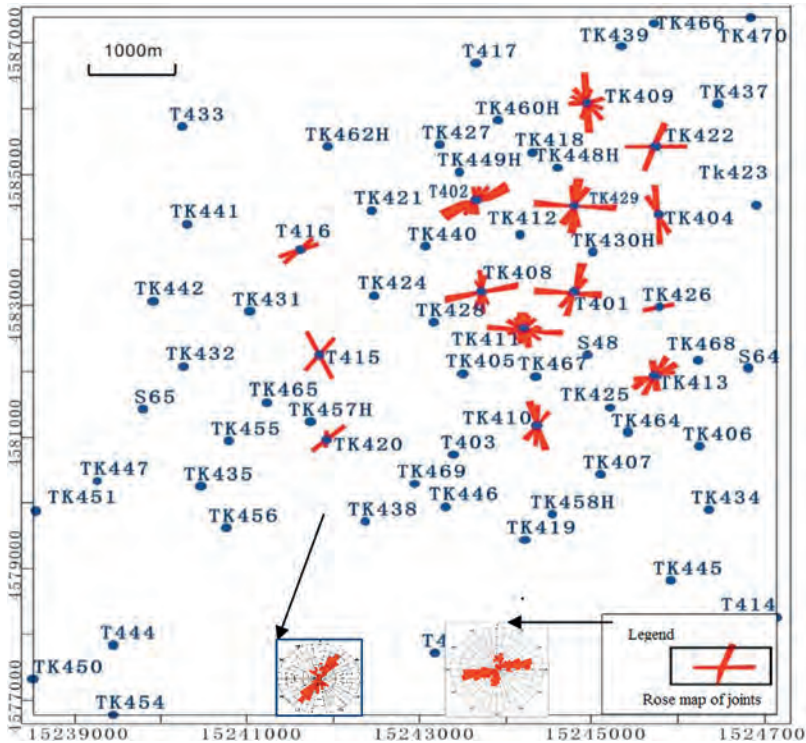


Figure 1.42 Rose map of fracture strike.

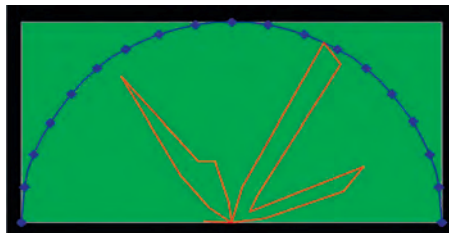


Figure 1.43 Rose map of fracture strike in the field.

Stage I fractures are tiny fractures fully filled with calcite. These fractures are irregular in extension, strike and dip; some are vertical, others are horizontal; and these fractures have different lengths, approximately 80% of them are less than 5 cm long, and the longest can be 10 cm. Filled with creamy calcite, these fractures generally have cross-cuttings in later stages (Fig. 1.45—1, —2), and are probably diagenetic shrinkage fractures formed in Pre-Caledonian.

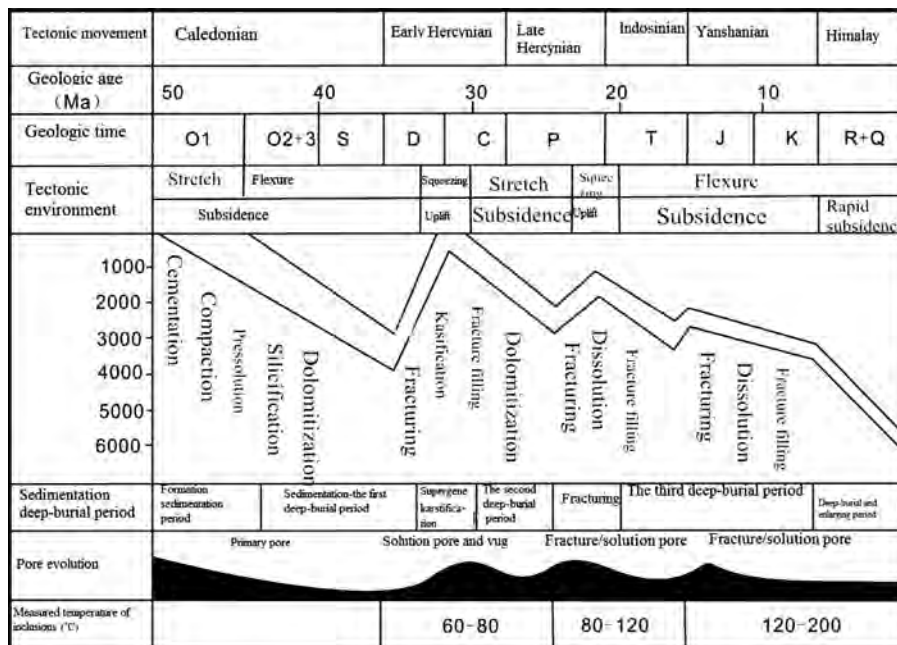


Figure 1.44 Burial history and diagenetic evolution of Ordovician Formations in the Tahe Oilfield (Xingbian, 2003).

Stage II fractures are tectoclasses filled with calcite, including vertical fractures, high-dip fractures and horizontal fractures, predominantly high-dip fractures with shearing features. Calcite filling these fractures is transparent–semi-transparent, and coarse in grain size. Crossing in X shape can be observed occasionally (Fig. 1.45–4). These fractures are generally over 10 cm long, or even up to 1 m. These fractures have features of continuous reformation at later stages; calcite filling the fractures occasionally has bending solution fractures formed by reconstruction at later stages; a majority of these fractures are plane conjugate shear joints formed under structural pressure in the Caledonian Period; due to impacts of tectonic movements at later stages, these fractures became wider and wider, and were reformed in a denudation process after being filled (Fig. 1.45–3).

Stage III fractures are tectoclasses partially filled with calcite (Fig. 1.45–5), partially or fully filled with green mud (Fig. 1.45–6), or not filled. Most of these fractures are high-dip fractures with shearing features and long extension, and large fractures or super-large fractures. These fractures have features of chemical filling and physical filling. Physical fillings are predominantly green mud with clear signs of reformation in later stages. There are also some partially filled fractures. Most unfilled fractures are open shear fractures with good oil bearing and conductivity. Stage III fractures cross Stage II fractures (Fig. 1.45–7); according to Fig. 1.44, it is concluded these fractures were formed in Early Hercynian–early stages of Late

Table 1.36 Features of fractures formed in different stages in Block 4 of the Tahe Oilfield

Characteristic parameters	Stage I fractures	Stage II fractures	Stage III fractures	Stage IV fractures
Filling materials	Calcite	Calcite	Calcite or mudstone	No
Filling degrees	Fully filled	Fully filled	Fully, SEMI or no filled	No
Length of extension	<5 cm	>10 cm	>13–20 cm	<10 cm
Shape	Irregular, tiny	Flat, straight, larger in scale	Bending or flat and straight in relatively large scale	Predominantly flat and straight with average scale
Occurrence	Uncertain	Variable	Predominantly in NE, some in NWW	Network or individual
Dynamic properties	Shrinkage fractures	Shear fractures	Shear fracture	Shear fractures
Timing of formation	Early Caledonian	Caledonian	Early Hercynian–Late Hercynian	Late Hercynian–Himalayan Period
Effectiveness	No	No	Yes	Yes

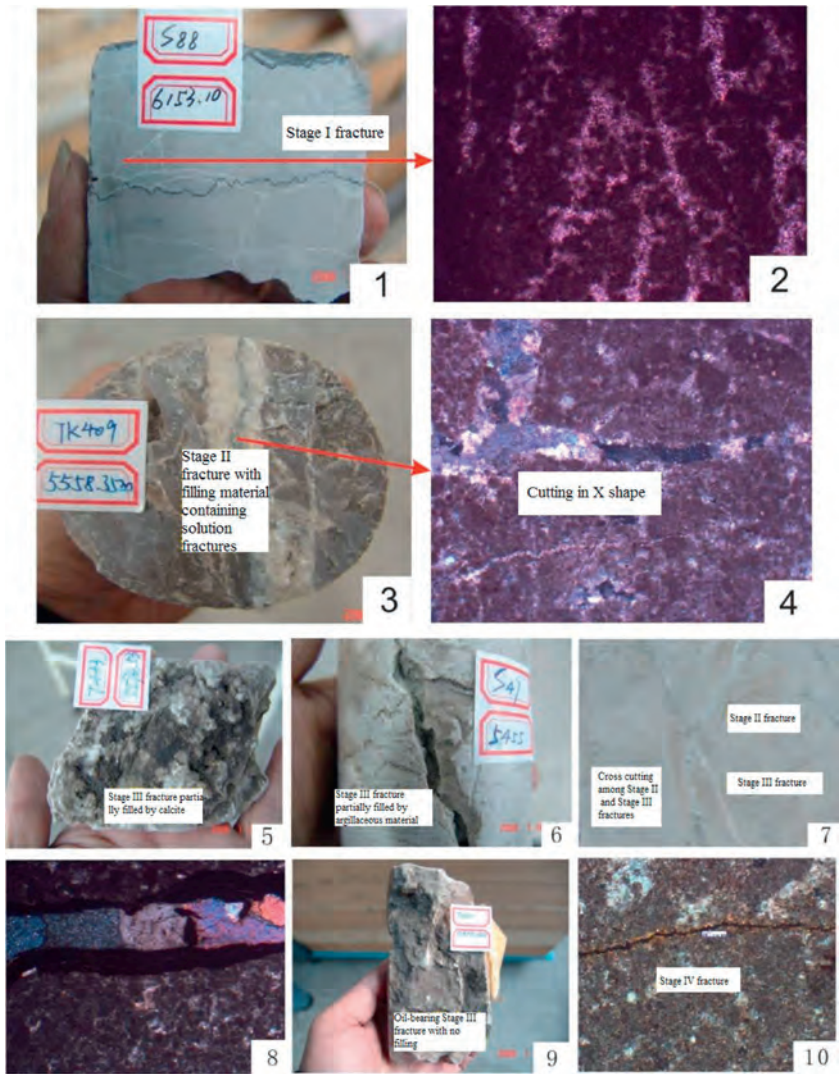


Figure 1.45 Features of fractures formed in different stages.

Hercynian, after Caledonian movements due to continuous Hercynian tectonic stress. These fractures include plane conjugate shear joints formed in early stages of uplifting and tensile joints during the uplifting. Upon sedimentation of Sangtamu green mudstone, partially filled muddy fractures were formed as the green mudstone was squeezed into these fractures (Fig. 1.45—6). Stage III fractures are characterized by a large number, and high proportion of effective fractures and common oil-bearing (Fig. 1.45—8 or Fig. 1.45—9), or impregnation by oil, so these fractures are the most important fractures in this area.

Stage IV fractures are microscale tectoclasses not filled with solid minerals. They are fewer, small and short, may be the fractures of the first two stages, which were sheared and cut and filled with calcite, as a result of tectonic movements in later stages of Late Hercynian–Himalayan. Some of these fractures contain crude oil, or are impregnated with oil (Fig. 1.45–10).

1.7 Filling materials and characteristics

1.7.1 Filling materials

Both outcrop survey and core observation show that primary filling materials in palaeokarst fractures, caves, and vugs include four kinds of filling materials: mechanical deposition, collapsed deposition, chemical deposition, and weathered residual. In different karst periods, different karst development and filling conditions resulted in different types, properties, and structures of filling materials.

1. Mechanical deposition

Filling materials from mechanical deposition were carried into karst space by flowing water and deposited under gravity. It has beddings produced by alluvial, gravitational differentiation, and sorting structure. Complicated in composition, this kind of material mainly contains calcareous-argillaceous and carbonate breccia, or rock fragments, sometimes debris of foreign rock, sand and muddy material (Figs. 1.46–1.49).

Mechanical deposition is apparently different from matrix. In addition to calcareous-argillaceous and carbonate breccia, this kind of filling material also contains large amounts of sand, mud, and rock fragments with microbedding, and is often found in the caves in underground stream systems and associated interlayer solution fractures, or solution fracture systems, and was formed in the exposed karst stage and the early burial karst stage. For example, the filling material in the caves under No. 3 Valley west of Sulfur Mine in the Tabei outcrop area contain calcareous-argillaceous and carbonate breccia and large amounts of sand, mud, and rock fragments originating from Silurian shale with microbedding.



Figure 1.46 Features of filling material in caves in No. 3 Trench of Sulfur Mine West.



Figure 1.47 Features of filling material in caves (limestone and siltstone).



Figure 1.48 Calcareous-argillaceous filling material in fractures and caves.



Figure 1.49 Breccia in caves.

2. Collapsed deposition

Formed by collapsed rocks from top fragmental zones, this type of filling material is mainly filled in cave systems. Residual rock beddings can be observed in large rock pieces, the upper section of the collapsed structure is mostly filled with calcareous-argillaceous material, while the lower section contains calcareous-argillaceous material with large amounts of matrix breccia. For example, in the major part of No. 1 Cave in No. 1 Valley of Yijianfang Area, well-developed collapsed filling material can be found in the top section (Fig. 1.50). The cave encountered by Well S49 is filled with grayish-green, brown limestone breccia with calcareous-argillaceous cementation and siltstone with grayish-green calcareous cementation which show clear collapsed deposition signs (Fig. 1.51).



Figure 1.50 Colluvial filling material in a cave south of Yijianfang.



Figure 1.51 Fractures and vugs filled with light-green calcareous-argillaceous siltstone in Well S79.

3. Chemical deposition

Chemical deposition was formed in hydrodynamic environments with stagnant water flow, and is different in composition because of different source materials. In the area west of the Sulfur Mine in the Tabei Outcrop Area, the material source of karst systems was mainly Silurian siltstone with abundant sulfates, as precipitation and filtration water brought sulfates into karst spaces, and concentrations of dissolved materials increased, filling materials of calcite and gypsum deposited along sidewalls of such caves, the central part of the sedimentation body is composed of relatively pure gypsum; with climate becoming drier, the depositional environment turned into reduction conditions, sulfate deposits differentiated into elemental sulfur, filling fractures, vugs, and solution fractures at later stages.

In the southern part of Yijianfang in the Tabei Outcrop Area, the karst systems were subject to impacts of regional major faults and invasion of lava; accordingly, chemical deposition in the karst-cave systems are composed of predominantly gigantic crystal calcite, purple fluorite and iceland spar, the tight and crystallized filling material formed reflects the impact of geothermal activities at later stages (Fig. 1.52).

Core observation shows chemical depositions include calcite or calcareous cement predominantly formed in middle or later stages of filling of such caves. Filling materials in such systems can be summarized as follows: mechanical deposition such as calcareous-argillaceous, rock fragment breccia, and other materials under high hydrodynamic conditions in the early filling stage experienced dissolution or erosion in the middle stage, and part or all original filling material was replaced by chemical deposition material at a later stage.

In solution fractures in near-surface weathered crust, chemical depositions usually occur in secondary fractures and microfractures, and the filling material is mainly calcite

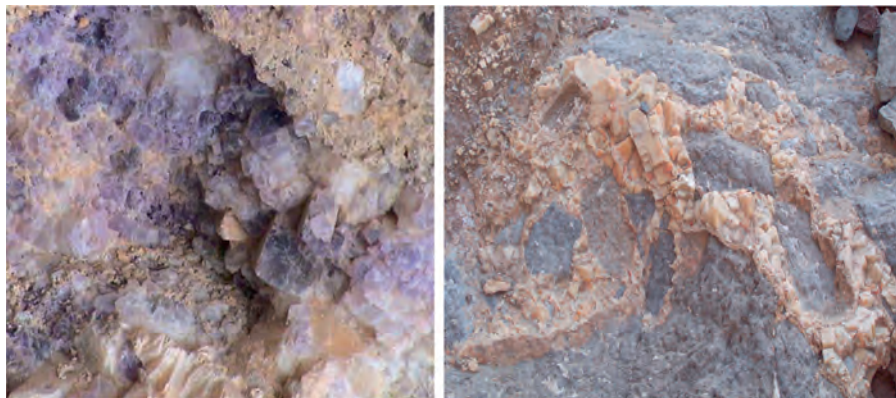


Figure 1.52 Purple fluorite and calcite fillings in a cavern in Yijianfang.



Figure 1.53 Fillings in solution fractures. *Grayish-yellow* calcareous-argillaceous filling materials in earlier stages and calcite in later stages.

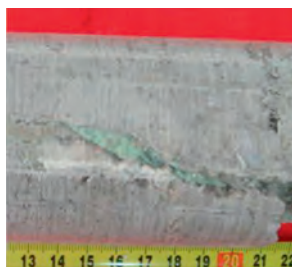


Figure 1.54 Filling in solution fractures. Solution fractures were filled with *grayish-green* calcareous-argillaceous material, with less calcite and pyrite.

(with some calcareous-argillaceous material); big solution fractures are dominated by mechanical deposition fillings, some are filled with chemical deposition fillings, which is demonstrated by the small amount of calcite and pyrite in calcareous-argillaceous material (Fig. 1.53, Fig. 1.54).

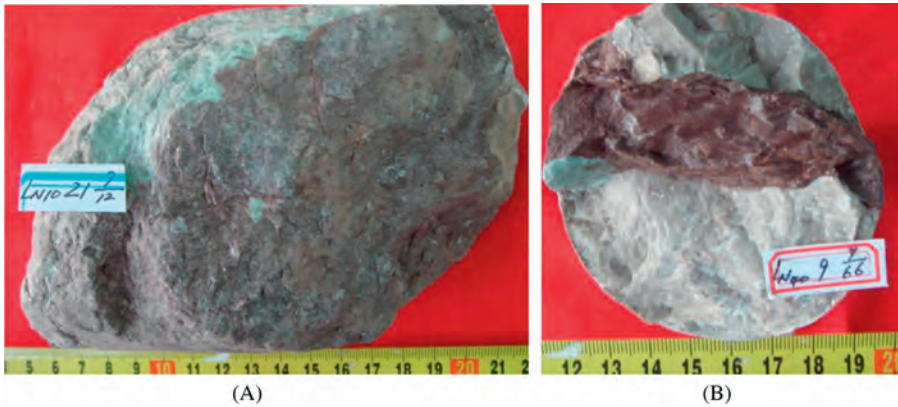


Figure 1.55 Weathered residuals. (A) brownish-red weathered residual materials on the top of karst, which were formed mostly in oxidizing environments; (B) brownish-red weathered residual materials in the solution pipe.

4. Weathered residual materials

Weathered residual material is mostly found in the solution trenches, grooves, or sinkholes in near-surface weathered crust, on the bottom of vertical wells, or in the solution fractures in shallow formations. Usually brownish-red (Fig. 1.55), this kind of material was formed mostly in oxidizing environments, and is the residual left by matrix dissolution and weathering.

1.7.2 Filling space

Filling space in fracture-vug systems is affected by multiple factors, and can be classified into the following three types:

1. Open space (inflow and outflow)

Inflow fracture-vug systems are mostly in supply or supply runoff sections in epikarst zone or vertical seepage dissolution zone, with good connectivity with ground surface, this kind of system is mostly filled at later stages, with mudstone or silty mudstone, breccia, and a small amount of calcite through mechanical deposition. Their primary spaces (caves) include sinkhole and shaft in moderate scale.

Outflow fracture-vug systems are mostly distributed in runoff or drainage sections in runoff dissolution zones or vertical seepage dissolution zones; these systems are mostly filled at later stages, with bedded mudstone, silty mudstone, or sandy mudstone with calcite cementation through mechanical deposition. Their primary spaces (caves) include pipes and halls that are in large size.

2. Partially open/closed space (fractured reservoir)

This kind of reservoir system is distributed in the epikarst zone or the vertical seepage dissolution zone; it is generally small and connected by solution fractures. Caves in such a system are poorly connected to the ground surface. They might not be filled at later stages (mostly partially filled) with filling material like mudstone or calcareous cement (chemical deposition). The primary space includes small bead-like or isolated caves. Isolated caves are dominant.

3. Enclosed space (isolated caves)

Distributed mostly in vertical seepage, runoff or undercurrent dissolution zones, caves in this kind of system are mostly enclosed. They were formed through source invasion, so

they poorly connect to the ground surface, and weakly connect to runoff belts by solution fractures. Such caves might be filled by chemical deposition at later stages. The primary space is composed of solution pore and fractures.

1.7.3 Filling degree

Statistics show reservoir spaces including pores, fractures, vugs, and caves in the Tahe Oilfield have been filled with various filling materials more or less. According to the ratio of filling volume to total reservoir volume, the reservoir can be divided into the following three types: lowly filled (<30%), moderately filled (30%–70%) and highly filled (>70%).

In the Tarim Basin, early underground stream system, karst pipes and solution tectoclasses were filled highly, but microfractures were filled moderately or lowly due to late denudation. Statistics indicate that the solution fractures in the Ordovician palaeo-weathered crust were filled lowly (very small proportion of fully filled fractures): Class I fractures filled by about 70%, Class II by 50%, Class III by 30%.

1.7.4 Filling characteristics

Field outcrop survey and core observation in the Tarim Basin show that filled karst space is composed of underground stream systems, karst pipes, solution tectoclasses, and solution joint cracks in weathered crust. In the Tabei Outcrop Area, large-scale underground stream systems are mainly distributed in No. 3 Valley and No. 4 Valley of Sulfur Mine West and No. 1 Valley in Yijianfang. These filled cave systems have multiple branches and multiple layers. On the dense exposed area, the cave extends to 120–200 m, the filled-up belt extends to 500–1000 m, relative elevation difference between upper and lower layers is 17–35 m, and predicted extension length is over 2000 m. Filling materials in the caves in No. 3 Valley and No. 4 Valley of Sulfur Mine West feature large amounts of gypsum, sulfur, and noncarbonate debris, whereas filling materials in No. 1 Valley of Yijianfang is dominated by calcareous-argillaceous calcite with gigantic crystals, purple fluorite, and iceland spar.

The solution joints in Ordovician weathered crust are filled mostly at their tips with calcareous-mud and calcite, 2–50 m deep and 2–20 mm wide.

Downhole solution fractures are fully or partially filled with calcareous-mud, some by calcite. But karst pipes in the runoff dissolution zone are mostly unfilled or partially filled, and filling materials in these caves are mostly calcareous-argillaceous rock, and a small amount of calcite.

1. Filling characteristics in different geomorphologic units

Quite different hydrodynamic conditions in different geomorphologic units lead to different karstification strength and filling degree. Generally speaking, troughs, grooves, and other lower parts have higher degrees of mechanical fillings, whereas slopes have lower degrees of mechanical filling. Different sections of the karst pipes in underground stream systems also have different filling degrees: inlets and outlets of the pipes, and intervals connective to the ground surface through sinkholes or shafts have relatively higher

degrees of mechanical fillings; whereas other locations are dominated by chemical fillings.

a. In the karst mound depression

In karst mound depressions with relatively high elevation, although subject to long denudation, fracture-vug systems in the epikarst zone in low lands or karst valleys may be connected with the ground surface, and susceptible to filling at later stages. Most of residual karst fracture-vug systems in the vertical seepage dissolution zone are isolated with relatively poor connectivity. In addition, these fracture-vug systems are poorly connected with the ground surface in general, so these systems are unlikely to be filled at later stages. Fracture-vug systems in the runoff dissolution zone are composed of bead-like karst pipes where the hall-like caves have poor connectivity, which may be out-flow karst systems, and unlikely to be filled at later stages.

b. In the peak-cluster ridge valley

In the ridge section with relatively steep slopes and fast surface runoff speeds, karst fracture-vug systems are poorly connected with the ground surface, so they are unlikely to be filled at later stages; while fracture-vug systems in confluence locations like lowlands or troughs are connected well with the ground surface, and susceptible to filling at later stages.

The epikarst zone in the ridge section has greater thickness than that in the trough section, and better-developed karst, where the karst forms are dominated by vertical solution fracture-vug systems and small solution vugs, with relatively poor lateral connectivity; these systems are mostly chemically filled rather than mechanically. In the vertical seepage dissolution zone, the karsts, being relatively weak, are dominated by vertical solution fracture-vug systems, with caves developed locally; these caves are mostly isolated, with poor connectivity, and are mostly chemically filled, rather than mechanically. The majority of karsts in the runoff dissolution zone occur in troughs, and mostly in pipe form. These relatively small karst formations are likely to be filled mechanically.

c. In the karst lake

Distributed in structural lows, with standing water all year round, karst lakes have less-well-developed epikarst zones, and main karst forms like the vertical solution fracture-vug system and small solution vugs, and there are usually sinkholes and other vertical solution systems connecting with the underground stream systems in the lake bottom, which are susceptible to mechanical filling at later stages. The runoff dissolution zone is mostly in large pipe form, which is more susceptible to mechanical fillings.

2. Filling characteristics in different karst belts

From the vertical distribution of karst belts, palaeokarst fracture-vug systems in different geomorphologic units in the Tahe Oilfield have very different filling features.

a. In the epikarst zone

This zone has a filling degree of 50%–95%, and mechanical filling of up to 40%–80%; the filling materials include mainly grayish-green calcareous-argillaceous rock, and some breccia with calcareous-argillaceous cement locally. Chemical filling accounts for 10%–40% on average, and the main filling materials include calcite, calcareous materials, and a small amount of pyrite. The epikarst zone with a higher degree of chemical filling is predominantly in karst gentle slope-hilllock depressions and karst peak-cluster valley-peak-cluster depressions. The epikarst zone with lower degree of chemical filling is in the karst gentle slope-hilllock depressions and karst mound depressions. The epikarst zone with high filling degree

is distributed in the karst platform-peak-cluster depressions, karst peak-cluster valleys, karst gentle slope-karst valleys, karst ridges and peak-cluster ridge valleys; the epikarst zone with low filling degree is distributed in karst platform-karst mound depressions and karst gentle slope-peak-cluster ridge valleys, hillock depressions, and karst mound depressions.

b. In the vertical seepage dissolution zone

This zone has a filling degree of 60%–95%, and a mechanical filling degree of 50%–85%. The filling materials include grayish-green calcareous-argillaceous rock in the majority, and breccia with calcareous-argillaceous cement in the local area. This zone has a chemical filling degree of 10%–50%, and the filling materials are calcite, calcareous layers, and a small amount of pyrite. The zone with higher chemical filling degree is distributed predominantly in karst platform-peak-cluster depressions, karst gentle slope-peak-cluster ridge valleys, and peak-cluster ridge valleys; the zone with lower degree of chemical filling is distributed predominantly in karst platform-karst mound depressions, karst gentle slope-hillock depressions, hillock depressions, and karst ridges. The zone with higher filling degree is distributed in karst platform-peak-cluster depressions, karst peak-cluster valley-peak-cluster valleys, karst gentle slope-karst valleys, hillock depressions, and peak-cluster ridge valleys; the zone with lower filling degree is distributed in karst platform-karst mound depressions, karst gentle slope-peak-cluster ridge valleys, and hillock depressions.

c. In the runoff dissolution zone

This zone has a filling degree of 60%–95%, and a mechanical filling degree of 50%–85%. The filling materials include grayish-green calcareous-argillaceous rock and siltstone in the majority, and breccia with calcareous-argillaceous cementation in the local area; some depositions have features of underground streams. Chemical filling at a degree of 10%–50% in general, is dominated by materials such as calcite, calcareous materials, and a small amount of pyrite. The zone with higher chemical filling degree is distributed predominantly in karst platform-peak-cluster depressions, karst gentle slope-karst mound depressions, peak-cluster ridge valleys, and karst peak-cluster valleys; the zone with lower chemical filling degree is distributed predominantly in karst platform-karst mound depressions, karst gentle slope-peak-cluster ridge valleys, and hillock depressions. The zone with high filling degree is distributed predominantly in karst platform-peak-cluster depressions, karst peak-cluster valley-peak-cluster valleys, karst gentle slope-karst valleys, hillock depressions and peak-cluster ridge valleys; the zone with lower filling degree is distributed in karst platform-karst mound depressions, and karst gentle slope-karst mound depressions.

d. In the undercurrent dissolution zone

This zone has a filling degree of over 90% on average, and chemical filling of over 50%. The main filling materials include calcite, calcareous layers, and a small amount of pyrite; mechanical filling of 10%–50% on average is dominated by grayish-green and gray mudstone. The zone with lower chemical filling degree is distributed predominantly in the karst gentle slope-karst valley. Overall the filling degree is over 90%. Generally, the entire karst zone has lower mechanical filling and higher chemical filling.

3. Filling characteristics in the same geomorphologic unit

Even in a geomorphologic unit, the vertical filling degree may be dramatically different:

- a.** Epikarst and runoff dissolution zones have higher mechanical filling degrees and low chemical filling degrees; vertical seepage and undercurrent dissolution zones have lower mechanical filling degrees, but higher chemical filling degrees. From epikarst

zone→vertical seepage dissolution zone→runoff dissolution zone→undercurrent dissolution zone, the mechanical filling degree reduces and the chemical filling degree increases.

- b. Filling degree also shows a similar trend: from epikarst zone→vertical seepage dissolution zone→runoff dissolution zone→undercurrent dissolution zone, the filling degree increases significantly.

Generally, different filling degrees in different geomorphologic units and different karst zones are closely related to hydrodynamic conditions and underground runoff zones at specific positions. In general, water in shallow formations and underground runoff zones has relatively high hydrodynamic force, so fracture-vug systems there have relatively high connectivity, the water carries more mechanical matter, and these systems usually have higher degree of mechanical filling; while vertical seepage and undercurrent dissolution zones have relatively weak hydrodynamic conditions, and fracture-vug systems there have poor connectivity, so their mechanical filling is weaker, chemical filling is likely to happen at later stages.

Consequently, karst platform-peak-cluster depression, karst gentle slope-karst mound depression, peak-cluster ridge valley, and karst peak-cluster valley have higher chemical filling degree; karst platform-karst mound depression, karst gentle slope-peak-cluster ridge valley, hillock depression, and hillock depression have lower chemical filling degree.

References

- Bar-Matthews, M., Avner, A., Kaufman, A., 1999. The Eastern Mediterranean paleoclimate as a reflection of regional events: Soreq cave, Israel". *Earth Planet. Sci. Lett.* 166, 86–95.
- Bar-Matthews, M., Ayalon, A., Kaufman, A., 2000. Timing and hydrological conditions of Sapropel events in the Eastern Mediterranean, as evident from speleothems, Soreq Cave, Israel. *Chem. Geol.* 169, 146–156.
- Changquan, L., 2000. A discussion on the geological model of carbonate seam-cavern type gas pool in Chishui region. *Guizhou Geol.* 17 (2), 71–78.
- Chunfang, C., 1997. Study on fluid-rock interactions in the Tarim Basin. Geological Publishing House, Beijing.
- Cooley, T., 2002. Engineering approaches to conditions created by a combination of karst and faulting at a hospital in Birmingham, Alabama (in Engineering and environmental impacts of karst). *Eng. Geol.* 65 (2–3), 197–204.
- Daoxian, Y. (Ed.), 1988. Dictionary of karstology. Geological Publishing House, Beijing.
- Daoxian, Y., Zaihua, L., Yushi, L., et al., 2002. Dynamic system for Karst in China. Geological Publishing House, Beijing.
- Dengfa, H., 2001. Structural evolution and hydrocarbon accumulation in the Tarim Basin. Geological Publishing House, Beijing.
- Desheng, L., 1995. Theory and practice of petroleum geology in China. *Earth Sci. Front.* 2 (3–4), 15–19.
- EЖOB et al., 1992. Vertical zoning of karst development. Mo Yuezhi (trans): Selection of Translation Works for hydrological geology and engineering geology, No. 6, 30–35.

- Gascoyne, M., 1992. Palaeoclimate determination from cave calcite deposits. *Quat. Sci. Rev.* 11, 609–632.
- Genty, D.D., Baker, A., Massault, M., 2001. Dead carbon in stalagmites: Carbonate bedrock paleodissolution vs. ageing of soil organic matter: Implications for ^{13}C variations in speleothems. *Geochim. Cosmochim. Acta.* 20, 3443–3457.
- Guorong, L., 1997. Discussion on the genetic mechanism of stylolites in carbonate rocks and their significance for storage. *Mineral Petrol.* 17 (2), 49–54.
- Hendy, C.H., Wilson, A.T., 1986. Palaeoclimatic data from speleothem. *Nature.* 216, 48–51.
- Huanzhang, L., 1990. Geochemistry study for inclusions. Geological Publishing House, Beijing.
- Jiajia, W., 1997. Petroleum system analysis of the permo-carboniferous of the Southwest depression in the Tarim basin. *J. Xinjiang Pet. Inst.* 9 (1), 7–11.
- Jintao, W., 1987. Karst and carbonate in Guilin. Chongqing Publishing House, Sichuan.
- Mangin, A., 1974. Contribution a l'étude hydrodynamique des aquifers karstiques. *Ann Spéleol.* 29, 283–332.
- Qidong, D., 2000. Tectonic movements of the Tianshan Mountain. Seismological Press, Beijing.
- Riyuan, X., Jiansheng, T., 2004. Features of mineral inclusions and performances as indicators for palaeokarst activities. *Acta Geosci Sinica.* 25 (3), 373–377.
- Riyuan, X., Hongfeng, C., Shengzhang, Z., Bin, L., 2003. Methodology and significance of study of epikarst zones: Study for karst underground water and desertification in China. Guangxi Science and Technology Press, Nanning, pp. 141–147.
- Riyuan, X., Jiansheng, T., Shengzhang, Z., Bin, L., 2006. Features of inclusions in filling materials of palaeokarst on northern edges of the Tarim Basin. *China Karst.* 25 (3), 246–249.
- Riyuan, X., Shengzhang, Z., Bin, L., et al., 2011. Study on the Patterns and Forming Mechanism of Fracture-Cravity Systems. In: Ordovician Carbonate, Tarim Basin, Geological Publishing House, Beijing.
- Shaobo, L., Jiayu, G., 1997. Analytical methods of fluid inclusions and applications to the study of oil and gas. *Pet. Explor. Dev.* 24 (2), 29–33.
- Tingyu, L., 2004. Geochemistry processes and their environmental significance of evolution of stable carbon isotope in karst vug systems. Doctoral Dissertation. Graduate University of Chinese Academy of Sciences, Beijing.
- Xiaoguang, T., et al., 1996. Progresses in petroleum geology studies in the Tarim Basin. Beijing Science Press, Beijing.
- Xiaote, H., 2002. An approach on the development technologies of fissure-karst cave-typed hydrocarbon pools in carbonate rock. *Pet. Geol. Exp.* 24 (5), 446–448.
- Xingbian, L., 2003. Heterogeneity of karst-vuggy carbonate reservoir rocks. *Xinjiang Pet. Geol.* 24 (4), 360–362.
- Xinggong, K., 2009. Advance in study of oxygen and carbon isotope variations in cave stalagmites as palaeo-climate proxies. *Geol. J. China Univ.* 15 (2), 165–170.
- Xinjiang Institute of Geography and Chinese Academy of Science, 1986. Evolution of the Tianshan Mountain. Beijing Science Press, Beijing.
- Yongchang, Z., Xinwei, W., Guolong, Y., et al., 2000. Oil and gas pool forming condition and exploration prospects of Ordovician carbonate rocks in Akekule region, Tarim basin. *Oil Gas Geol.* 21 (2), 104–109.
- Yubin, H., 1991. Hydrodynamic profiles and significance of evenly distributed thick limestone formations. *China Karst.* 10 (1), 1–12.
- Zhihong, K., Liling, W., 2006. Evaluation of fractured vuggy reserves in Tahe with dynamic production data. *Nat. Gas Ind.* 26 (8), 53–55.

Further reading

- Desheng Y., Ordovician palaeokarst in Akekule Upheaval, Tarim Basin and the Tahe Oilfield. In: Proceedings of the 2001 China National Conference of Sedimentology.
- Komtine, A.M.A., Jianhua, Z., Yang, L., Fuping, Z., Yufei, G., 2008. Carbonate fractures and karstification. *Geol. Rev.* 4, 76–82.
- Liangjie, T., 1996. Evolution and structural patterns of the Tarim Basin. Geological Publishing House, Beijing.
- Riyuan, X., 2001. Progresses in researches related to palaeokarst and karst in oil and gas fields. *China Karst.* 20 (1), 76.
- Riyuan, X., Shengzhang, Z., Bin, L., et al., 2011. Study on patterns and genesis of Ordovician carbonate fracture-vug system in the Tarim Basin. Geological Publishing House, Beijing.
- Xishuang, W., Huizhen, S., Jie, L., 1999. Numerical simulation for tectonic stress field in the Tarim Basin and its significance on hydrocarbon accumulation. *Seism Geol.* 21 (3), 268–273.

Geophysical characterization of fracture-vug carbonate reservoirs

2

Geophysical characterization of a fracture-vug carbonate reservoir involves how to identify and delineate the reservoir distribution, and detect the filling and fluid properties of the reservoir. Fracture-vug carbonate reservoirs are usually characterized by multiple types, multiple scales, strong heterogeneity, and irregular geometries; and particularly in the Tahe oilfield, karstic carbonate reservoirs related to unconformities are buried in deep formations (mostly below 5600 m). This makes it difficult to accurately image the reservoir, makes seismic response complex, and makes it hard to distinguish the geometry and properties of reservoir rocks, and accordingly makes it hard to identify the reservoir and detect the fluid in it.

Accurate characterization of fracture-vug carbonate reservoir rocks and fluids is based on the understanding of relevant seismic responses of various reservoir types and seismic imaging through target-oriented acquisition and processing. Seismic techniques should be integrated with multidisciplinary information to characterize such complicated fracture-vug carbonate reservoirs; prestack and poststack seismic attributes are used for reservoir delineation and multiattribute fusion for the description of spatial reservoir rock and fluid distribution.

2.1 Seismic forward modeling

Seismic forward modeling plays an important role in fundamental research. Its objective is to establish seismic response features for fracture-vug reservoir rocks and internal fluids. These features may be used as the references for seismic data acquisition, processing, and reservoir prediction.

2.1.1 Physical modeling

Physical modeling of subsurface structures and fracture-vug reservoirs is a complicated process. Physical modeling is more realistic than numerical simulation because a physical model is the reproduction of a real application. If the similarity criterion is satisfied, actual spatial configuration of geologic structures and reservoirs can be reproduced; thus it is possible to simulate seismic wave propagation in an environment equivalent to a subsurface geologic setting. Physical modeling and numerical simulation may complement each other and therefore could be used together in the analyses of data acquisition and processing, seismic responses of subsurface formations and rocks, technical feasibility, etc.

2.1.1.1 *How to make physical models*

In deeply buried karstic reservoir rocks in the Tarim Basin, pore space mainly composed of dissolved vugs/caverns and fractures are connected by channels of various geometries, sizes, and origins. The diameter of single vugs/caverns may change from several centimeters to over a hundred meters. We need to have some prior information about vug/cavern occurrences so as to generalize some typical fracture-vug reservoir features; it is then possible to make physical models and examine the most typical seismic responses.

Geologic features of physical models

The fracture-vug systems include six types: underground streams (flow-in caves/caverns and flow-out caves/caverns), karstic caves/caverns, vugs, solution fractures, reef-related solution pores, and vuggy dolostone. Vugs may be unfilled, partially filled or fully filled. Unfilled vugs mainly contain fluids and therefore have low-velocity and density. Vugs partially or fully filled may have relatively high-velocity and density. The filling degree in vugs has a notable impact on seismic responses.

Model materials and model making

Knowing how to select model materials and make a good model similar to actual scenarios is essential to a successful physical simulation. The physical model may be designed as per the similarity criterion. The results are directly dependent on the materials used. In addition to the similarity criterion, actual scenarios should also be taken into consideration in the processing of model making.

There are two types of materials for model making; one is homogeneous industrial materials which could be processed and the other is new composite materials. As per the experiments, new composite materials are more applicable to the modeling of fracture-vug units with different velocities, densities, and attenuation.

One kind of new material is high molecular polymer mixtures constituted of epoxy resin and rubber through an interpenetrating polymer network (IPN) and a copolymer network. Some accessory materials, e.g., diluent, hardener, crosslinker, flexibilizer, coupling agent, defoamer, plasticizer, softener, and filling material, may be added to generate the mixtures for model making.

The technique of in situ synthesis is the combination of in situ crystallization and in situ polymerization. The second phase or reinforced phase in the composite material is a newcomer created during material preparation; thus the process of preparing the second phase in advance could be avoided to simplify the process and reduce costs. In addition, this technique could be used to produce some special microstructures or properties. Some problems with conventional material preparation, such as inhomogeneous dispersion of the second phase, loose interfacial adhesion, deficiencies of design performance caused by physical or chemical reactions, may also be avoided through in situ synthesis. [Fig. 2.1](#) shows the micropores produced by in situ synthesis.

Blending modification is a technique of producing a new polymer physically or chemically by adding modified monomers or modifiers into basic materials. Chemical modification involves the methods of improving basic material properties through

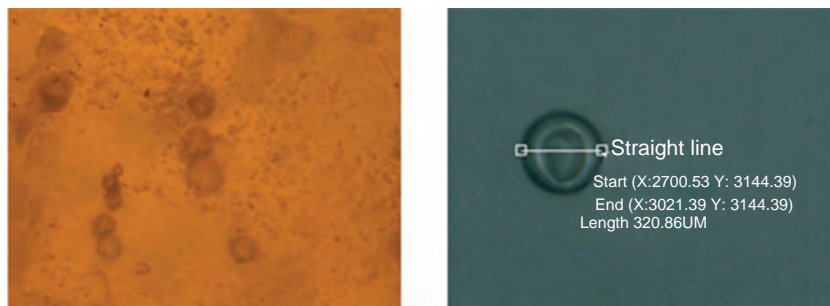


Figure 2.1 Microscopic view of a model sample.

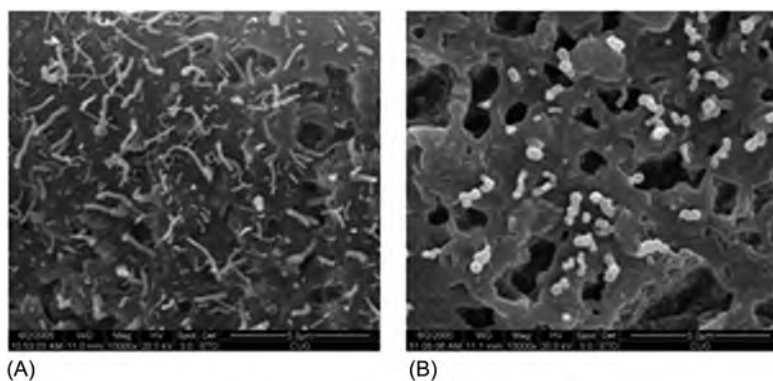


Figure 2.2 SEM photos of polyblend cross-sections (10000 \times). (A) Original dispersive palygorskite/natural rubber; (B) modified dispersive palygorskite/natural rubber.

polymerization reaction of two monomers or grafting reaction of two monomers with a third monomer. Physical modification involves the techniques of blending some modifiers and basic materials, which is called blending modification.

Fig. 2.2 shows scanning electron micrograph (SEM) photos of amorphous polyblend samples with continuous single-phase structures. Fig. 2.3 shows SEM photos of samples prepared through compatibilization processes; the phase state of the polyblend varies with the content of the compatibilizer. Fig. 2.4 shows SEM photos of toughened elastomer samples.

After IPN and copolymer network modification, the crosslinking degree of the solidified polyblend is improved. The range of velocity in the model has been expanded from 2000–2700 m/s to 1000–4500 m/s. High molecular polymers could be used to make a 2-dimensional (2D) or 3-dimensional (3D) model with a single structure or complicated shape-variant multilayer structure.

Model size and medium velocity are two important considerations in model making. As per the experiments, it is suggested to scale the model to be one 10000th of the actual size in view of the buried depths and geometries of vugs; thus a model of 1 mm is equivalent to an actual vug of 10 m. A single vug over 10 m

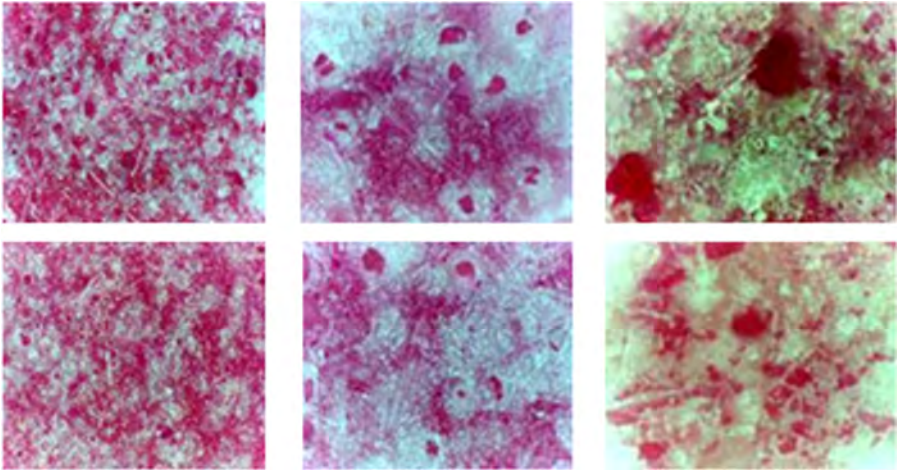


Figure 2.3 SEM photos of polyblend samples. Compatibilizer content of 15% (top); Compatibilizer content of 25% (bottom).

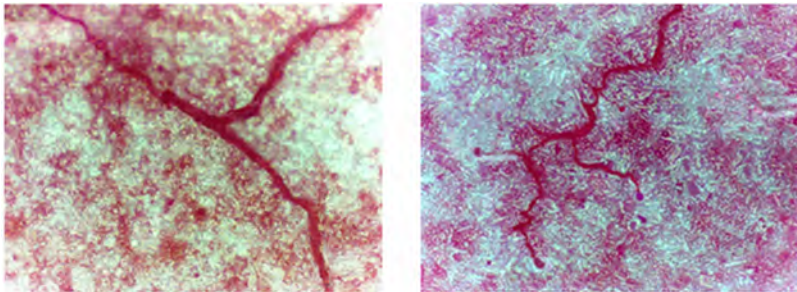


Figure 2.4 Scanning electron micrograph (SEM) photos of toughened elastomer samples.

may not occur frequently underground, but a vug system or vuggy zone (or belt) composed of numerous vugs may be larger than 10 m or reach several hundred meters. These vug models are embedded into a high-velocity package representing high-velocity carbonate formations. The package is made of epoxy resin, a kind of solidified fluid material ideal for model making. The appropriate velocity in model is 1/2 of that in formation, which means for an actual velocity of 4000 m/s, modeled velocity is 2000 m/s.

In view of the scale limit and seismic wavelength, shape-variant caverns have to be abstracted as some simple shapes, e.g., sphere, line (stick), or column, in dissolved cavern modeling. A cavern less than 3 mm (30 m) may be approximated with a sphere, flake, stick, column, or a small randomly shaped unit. For a stick-shaped cavern, another issue concerns 2D or 3D observations. For a 2D survey of a line-shaped cavern, the energy along its extension is usually neglected because the model is 3D.

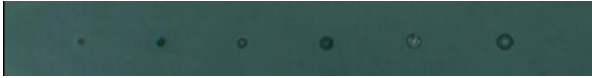


Figure 2.5 Cavern models of various sizes.

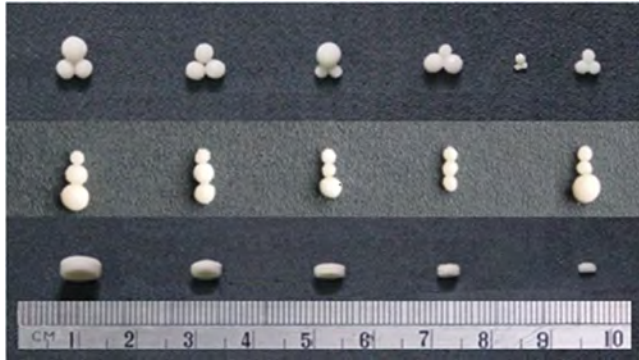


Figure 2.6 Polyblend sculptured cavern models.

Cavern shape and internal velocity are two considerations in model making; the latter is the first consideration in accordance with actual geologic conditions. Fig. 2.5 shows various 3D cavern models created with in situ synthesis techniques. Fig. 2.6 shows several groups of cavern models made of polyblend with variable velocity and microstructure; the minimum size is 0.5 mm.

For fracture model design and preparation, vertical fractures are simulated by gaps between a stack of parallel plexiglass sheets. Fracture density can be adjusted by inserting additional plexiglass sheets into the gaps. Epoxy resin has been used in the experiments because it has some flowability before being mixed with a hardening agent and also has good elasticity after being solidified. Processing fracture model materials is the most difficult step in fracture model making. A large piece of polyblend is cut into thin strips, which are then fabricated into disks of equal diameters. These disks are then implanted into the model with in situ techniques.

Carbonate vugs/caverns have various shapes and sizes ranging from several millimeters to dozens or hundreds of meters. It is impossible to build a vug structure model identical to the actual scenario. Some knowledge of the regional geologic conditions is required before modeling and then these conditions should be simplified into a generalized model to make the features of interest stand out.

2.1.1.2 Physical modeling experiments

The large 3D high-precision positioning and observation instrument (Fig. 2.7) designed for geophysical experiments is equipped with an automatic high-speed data acquisition system. The built-in miniaturized analog transducers with



Figure 2.7 3D high-precision positioning and observation instrument.

floating-point gain control are designed to receive weak signals from an object smaller than 10 mm within a frequency range of 200–500 kHz. The central component in this real-time ultrasonic system is a computer preset with high-speed real-time data acquisition, storage, and digital imaging packages. The system comprises a computer (or industrial personal computer), ultrasonic pulse emitter, ultrasonic signal receiver, high-speed data acquisition unit, transducers, dual 3D coordinate axes automatic location and control system for probe movement, a model tank, data processing and analysis software packages, etc.

Data acquisition is usually conducted underwater with P-wave. Water is treated as the first medium layer. The solid vug model is fixed on the mount and survey lines are laid out above the vugs.

For vertical fracture observation, a series of fracture models with different azimuths and densities may be made for multiazimuth surveys so as to record anisotropic reflections. There are three recording geometries used in the experiments. The first is a constant-offset layout; the distance between shot point and receiver point remains constant, but the angle between survey line and fracture changes. The second is a variable-offset layout in which the angle between the survey line and the fracture is varied; the common midpoint (CMP) recording is employed for azimuthal amplitude versus offset (AVO) analysis. The third is transmission survey for shear wave splitting across vertical fractures. One trace is acquired every 10 degree and altogether 19 traces make a group. The polarized direction of the S-wave is parallel to the fracture strike.

2.1.2 Numerical simulation

Numerical simulation has been widely used because it allows for simulation and modification with great convenience and low cost. For fracture-vug carbonate units, the issues which should be addressed in numerical simulation include how to characterize a complicated model, meshing induced heavy computation, and how to merge the wave fields of large-scale models and small-scale fractures and vugs.

2.1.2.1 *Random medium description*

It is hard to image a fracture-vug reservoir in detail due to the limitation of seismic resolution, but its heterogeneity and sporadic distribution may be statistically reconstructed with seismic information. A stochastic model, instead of deterministic model, would then be used to correlate seismic attributes with geostatistical features. If such correlation is found, it is possible to describe vuggy reservoirs with seismic attributes. With more and more discussions on the geostatistical behavior of 2D random-media models, it is possible to correlate vug size and density with model parameters so as to analyze the seismic responses of stochastic vuggy models.

A stochastic fracture-vug model could be generated with a distribution density function. In a random-media model, pores and vugs are different only in size and thus could be described with similar mathematical methods. Geophysical parameters of porous and vuggy media are spatially variable; for example, internal velocity and density are usually much lower than wall rock velocity and density. Fracture-vug reservoir characterization involves the following parameters, e.g., background parameters, the size and distribution density of fractures and vugs, and internal media parameters.

The size and distribution density of fractures and vugs are two important parameters for reservoir description. In random-media modeling, fracture-vug distribution could be statistically defined. The autocorrelation length of an elliptic autocorrelation function represents the average size of fractures and vugs and then could be used to define their sizes. The normal distribution of parameter values could be used to define a fracture-vug model; its porosity is defined as the volumetric proportion of fractures and vugs to the model.

The objective of stochastic modeling is to describe the reservoir model statistically and locate fracture-vug zones for exploratory drilling. Model parameters are defined in accordance with drilling, logging, and seismic data. A single small fracture or vug (smaller than a wavelength) would not cause detectable responses in low-resolution seismic reflections, but the changes in fracture-vug size and distribution density may lead to notable seismic attribute variations; thus it is possible to define space-variant parameters with seismic attributes. In turn, the stochastic model could be evaluated through correlating seismic attributes extracted from synthetic seismogram with the analogs extracted from actual data; if necessary, the model could be modified iteratively until the final product represents actual fracture-vug distribution.

2.1.2.2 *Variable-grid finite difference using elastic wave equation*

Numerical simulation is usually performed for a specified geologic target (or reservoir) which accounts for a small volumetric proportion of the model. Therefore variable grid size, small inside the target region and large outside the target region, is employed to reduce the number of grid nodes and consequent computational workload.

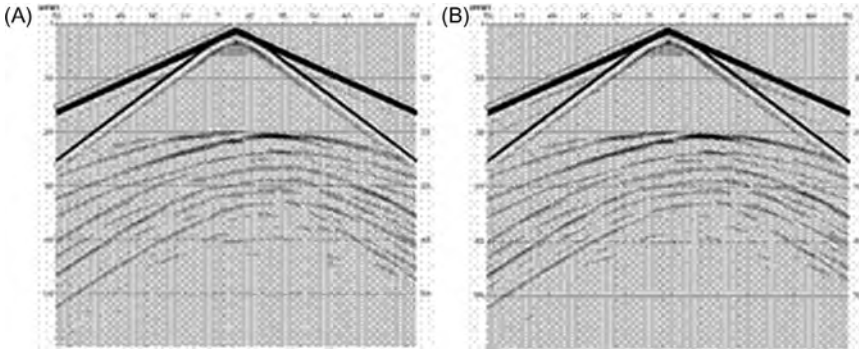


Figure 2.8 Single-shot gathers from variable-grid and constant-grid modeling. (A) Seismogram from variable grid modelling; (B) seismogram from small constant-grid modelling.

In order to reduce computational workload and improve efficiency, Jastram and Tessmer presented a modeling scheme on a grid with vertically varying spacing. The point is how to merge wave fields at internal interfaces aligned with grids to avoid noises. In forward modeling by solving the elastic wave equation, the first derivative is computed by high-precision finite difference operators on a nonuniform staggered grid. Wavefield interpolation is performed by a high-precision algorithm. In addition, the nodes at interfaces between coarse grids and fine grids should be carefully selected. Using this method we obtain accurate results without additional noise at internal interfaces.

Two single-shot gathers are compared as follows. Fig. 2.8A shows the seismogram from variable-grid modeling with the source set in the center of the model. Fig. 2.8B shows the record of 1×1 m grids. Few discrepancies in these two plots indicate similar precision of the variable-grid scheme and constant-grid scheme, but the former reduced computational workload by 14-times compared with the latter. This improvement is especially significant for the simulation of a large model with continuous sources.

2.1.2.3 Variable-grid numerical simulation using acoustic wave equation (VS&T)

Numerical simulation by solving an acoustic wave equation is also performed on variable grids to ensure both efficiency and precision. Small grids are used in a region with substantial changes or low-velocity zone, whereas large grids used in a homogeneous medium or high-velocity zone with subtle changes. A small sampling interval is first used throughout the model, and then those regions filtered out by a specified threshold value are resampled with a large interval. A large time-step is used in the region with large grids, and a small time-step is used in the region with small grids. Using this scheme in the case of integral sampling interval ratio and time-step ratio improves efficiency and flexibility.

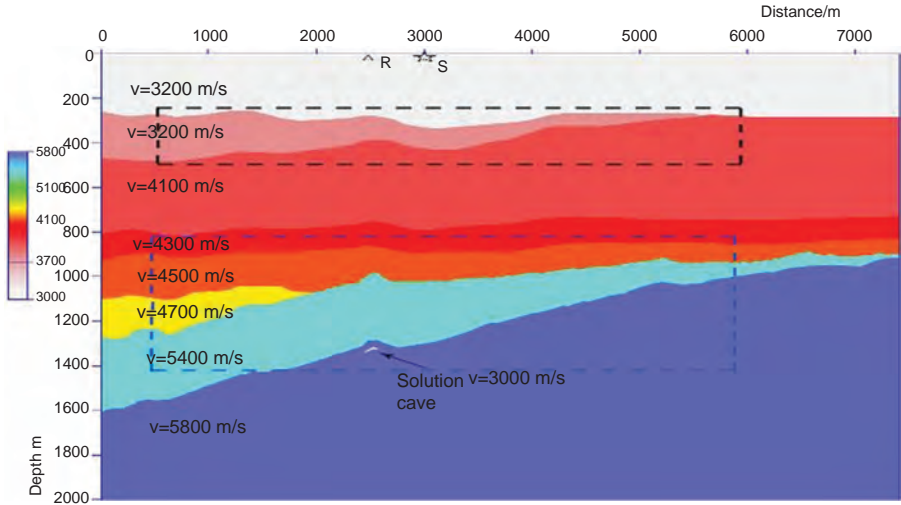


Figure 2.9 Complicated structural model with some internal solution caves (the detector R is positioned at the source S).

The VS&T technique avoids ghosting and improves efficiency. For a simulation with a grid of 10×10 m and a time-step of 0.5 ms, the computing time of VS&T is almost one-third that of a conventional method with uniform large grids and a large time-step. For a simulation with a grid of 2×2 m and time-step of 0.1 ms, the computing time of the conventional method is more than 100-times greater than the method for large-grid modeling; the computing time of the conventional method with variable grids and the same time-step is more than two-times that of VS&T. Thus it can be seen that the VS&T technique improves efficiency and guarantees precision at the same time.

Small grids (less than 1 m) must be used in microscale fractures and vugs, when the simulation by a conventional method is very time-consuming and it is necessary to use VS&T to improve efficiency. Fig. 2.9 shows a model which is designed for testing computational efficiency. Three scenarios are tested. The first is constant-grid modeling with a uniform grid of 10×10 m and time-step of 0.25 ms; the second is constant-grid modeling with a uniform grid of 2×2 m and a time-step of 0.1 ms; the third is VS&T modeling with a grid of 1×1 m and time-step of 0.05 ms inside dashed rectangles and a grid of 10×10 m and time-step of 0.25 ms elsewhere.

VS&T reduces shallow diffractions caused by discretized staircase corner points in the shallow zone and deep diffractions by using small grids to highlight the reflections of small caves in the deep zone, as shown by single-shot records in Fig. 2.10. As per Table 2.1, VS&T has much better efficiency than constant-grid modeling using uniform small grids. VS&T guarantees precision and improves efficiency at the same time by using small spatial sampling intervals in the region with subtle changes.

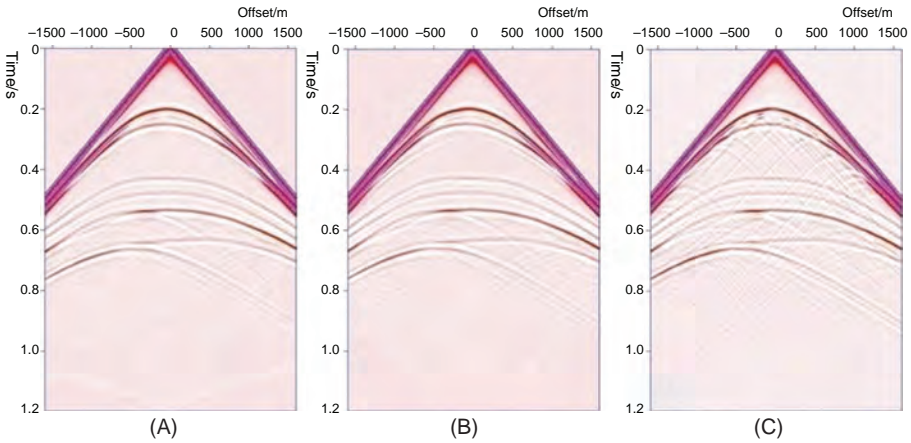


Figure 2.10 Single-shot records from (A) constant-grid modeling using uniform small grids, (B) VS&T modeling and (C) constant-grid modeling using uniform large grids.

Table 2.1 Efficiencies of three methods

Model 3	Computing time (ms)
Constant grid 10×10 m, time-step 0.25 ms	2213.94
Constant grid 2×2 m, time-step 0.1 ms	123755.90
VS&T modeling, large grid 10×10 m, small grid 1×1 m, large time-step 0.25 ms, small time-step 0.05 ms	16642.68

2.1.2.4 Staggered-grid high-order finite difference using elastic wave equation with variable grid and time-step (VGTS)

Variable grid and time-step (VGTS), modeling with variable grids and variable local time-steps, is similar to VS&T to ensure precision and improve efficiency.

Fig. 2.11 shows a cavern model for VGTS testing. Constant-grid modeling uses a grid of 10×10 m and a time-step of 0.25 ms. VGTS modeling uses a grid of 2×2 m and time-step of 0.05 ms inside dashed rectangles and a grid of 10×10 m and a time-step of 0.25 ms elsewhere. The cave radius which is modeled decreases from 5 m for a grid of 10×10 m to 1 m for a grid of 2×2 m; thus the responses of small caves are precisely modeled.

As shown in Figs. 2.12 and 2.13, the cave with a radius of 1 m is not sampled with only one point and thus cannot be identified on the large-grid record. In contrast, the cave is sufficiently sampled and precisely modeled on VGTS record; besides multiples from caves have also been precisely simulated on VGTS record.

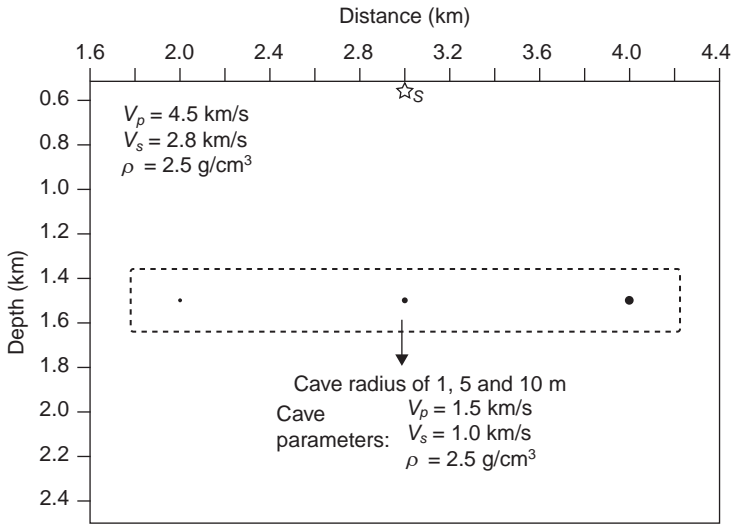


Figure 2.11 Model with varied caverns (source *S*).

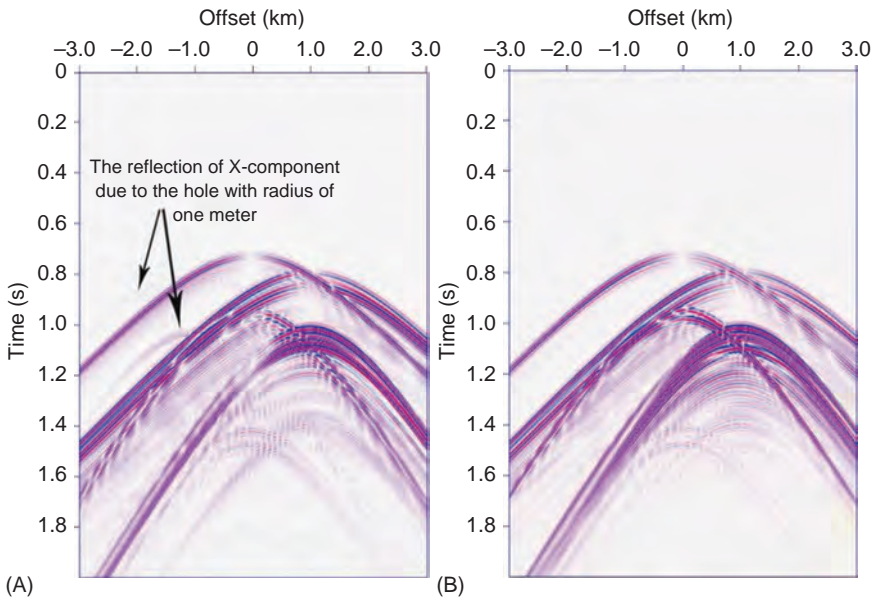


Figure 2.12 X-components on single-shot gathers generated for the model in Fig. 2.11. (A) VGTS modeling, (B) constant-grid modeling with a large grid.

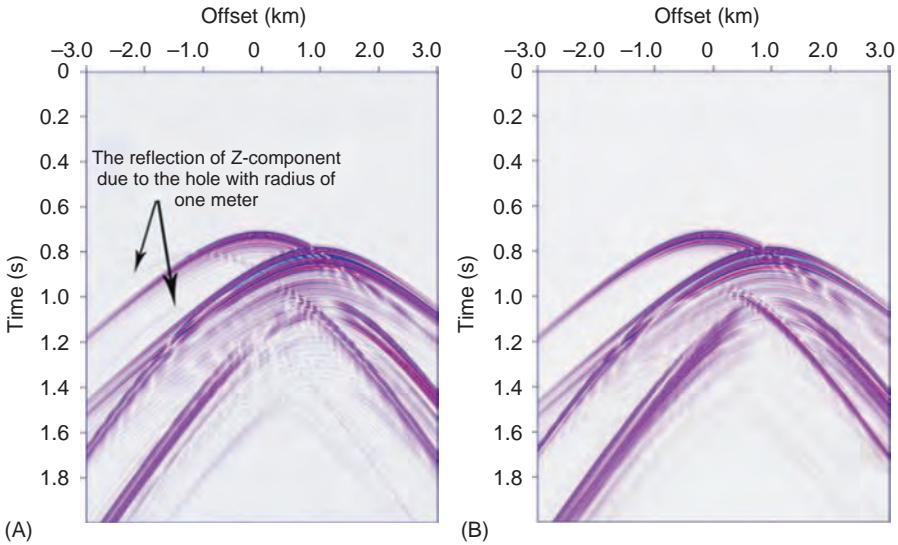


Figure 2.13 Z-components on single-shot gathers generated for the model in Fig. 2.11. (A) VGTS modeling, (B) constant-grid modeling with a large grid.

2.2 Seismic responses of fracture-vug carbonate units

Seismic responses are closely related to fracture-vug reservoir size, geometry, internal fluids and configuration. It is necessary to understand seismic responses generated by physical and numerical simulations to reveal the relationships between fracture-vug reservoir properties and seismic attributes.

2.2.1 Seismic responses of isolated caverns

In the Tahe oilfield there are isolated caverns which may occur anywhere at any size, and are relatively independent heterogeneous reservoirs. Their seismic responses should be identified first before tackling more complicated fracture-vug units.

2.2.1.1 Theoretical analysis of scattered seismic waves in a single cavern

Intensely heterogeneous carbonate reservoirs cause scattered waves which contain information on geologic properties. Thus it is important to study the relationships between scattering attributes and geologic properties.

Seismic waves striking an acoustic impedance contrast or series of contrasts are reflected; this process is generally described by the Zoeppritz equations which relate the amplitude of reflected and transmitted waves with the angle of incidence. Obviously reflection methods are not suitable for the analysis of scattered waves.

Here we use the Born approximation to solve the acoustic wave equation and derive an analytic solution for a single scattering object.

Vertical scale (thickness) variation causes a tuning effect observed on surface seismic sections. On a seismic profile with coincident source and receiver, (1) if the scattering object is small (less than $\lambda/8$, for example), the amplitude of scattered wave is nearly linear with the volume of the object, which means the amplitude increases with the volume; (2) the impact of lateral extension (in x and y directions) on scattered wave amplitude is dominated by the radius of the Fresnel zone; amplitude variation with lateral extension is also related to vertical scale; (3) vertical scale (in the z -direction) variation causes a tuning effect; the amplitude of the scattered wave reaches a peak at tuning thickness. For an object with a small lateral extension, amplitude variation with vertical scale is basically independent of lateral extension.

As per the analysis of scattered wave amplitude, the lateral extension of a simple scattering object may be estimated using the zero-offset seismogram; the thickness may be estimated using tuning amplitude. The interference between reflected and scattered wave fields has not been taken into consideration. The lateral extension may be precisely estimated provided that: (1) relative amplitude has been preserved in data processing, otherwise erroneous results would be obtained; (2) scattered wavefield has been separated from reflected wavefield at each spatial point. But in fact it is difficult to satisfy these two conditions; therefore scattered signals are not utilized in seismic prospecting unless the issues related to data processing are addressed. On the other hand, the analytical methods and conclusions may be used to deepen the understanding of scattered responses of fracture-vug units.

2.2.1.2 Seismic responses of single caves with varied sizes

Single-cavern responses

The models shown in Fig. 2.14 were designed with some single caves of 3 m in diameter in a homogeneous horizontal layer of 800 m thick. Background velocity and cave velocity are 2370 and 1800 m/s, respectively. The underlying formation of 5 m thick has a velocity of 2700 m/s.

The cave in Fig. 2.14 model A is 480 m apart from the top; two caves in the same horizontal position in model B are buried at 320 and 480 m, respectively; two caves 200 m apart in model C are buried at 320 and 480 m, respectively. Fig. 2.15 shows the results of 2D physical simulation with distinct diffractions on horizontal stacked sections. Diffractions generated by a single cave appear to be hyperbolic on a zero-offset section and the vertex of the hyperbola coincides with the location of the cave. Diffracted energy reaches a peak at the center of the cave and declines on both sides. The convexity of diffraction hyperbolas decreases with buried depth.

Model A Vp = 2370 m/s	Model B Vp = 2370 m/s	Model C Vp = 2370 m/s
--------------------------	--------------------------	--------------------------

Figure 2.14 Physical models.

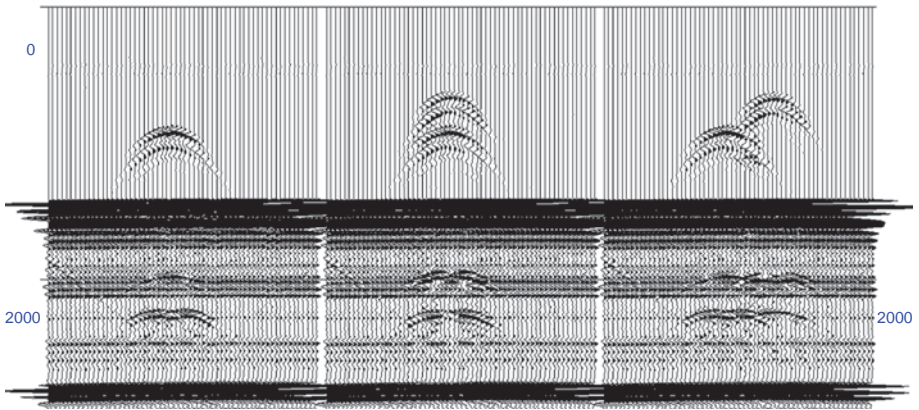


Figure 2.15 Horizontal stacked sections for single cave modeling.

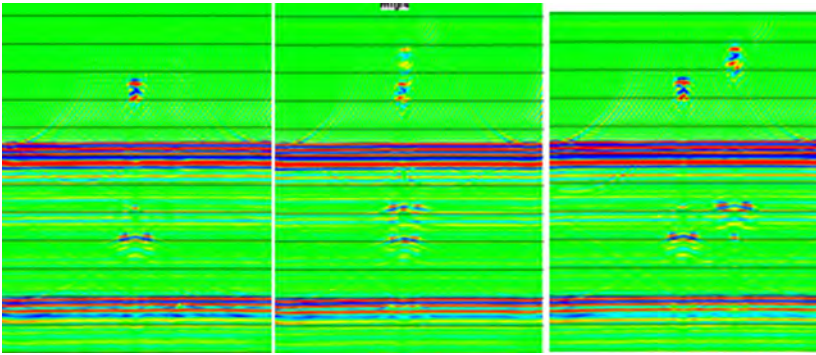


Figure 2.16 Migrated sections for single cave modeling.

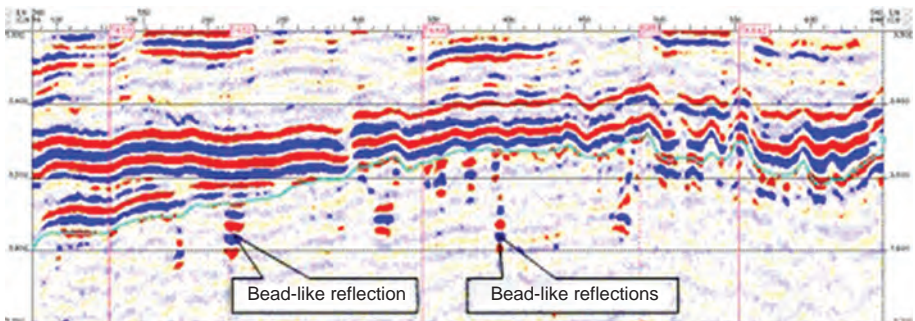


Figure 2.17 Bead-like reflections on an actual seismic profile.

Fig. 2.16 shows corresponding migrated sections; diffraction events converge into a series of strong bead-like short events, the top of which coincides with the top of the cave. These phenomena are quite similar to that which has been observed on actual seismic profiles (shown in Fig. 2.17).

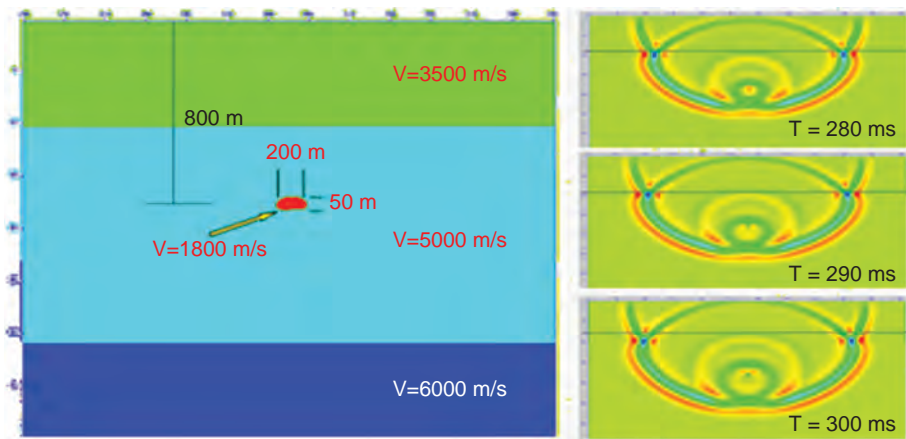


Figure 2.18 Model parameters and wavefield snapshots.

Fig. 2.18 shows model parameters on the section view and wavefield snapshots of numerical simulation at different times. These snapshots further demonstrate that diffractions are generated by multiple reflections from the top and bottom and thus exhibit a bead-like form.

Amplitude analysis

The following part deals with seismic attribute extraction and analysis to understand the relationships between seismic responses and fracture-vug units.

The maximum amplitude corresponding to different dominant frequencies and buried depths has been extracted from numerical simulated data (Fig. 2.19). A trend similar to the tuning effect is observed; reflection amplitude first increases and then decreases with cave diameter; finally the amplitude becomes relatively consistent.

As shown in Fig. 2.19, the maximum amplitude first increases with cave diameter at different dominant frequencies and reaches a peak at the diameter equal to $1/\pi$ of the wavelength. And then the amplitude decreases with cave diameter and hits bottom at the diameter equal to the wavelength. Afterward the amplitude again increases with diameter and then becomes relatively consistent. It is explained as follows. For a circular cave with a diameter less than the wavelength, incident waves are mostly diffracted. The maximum amplitude first increases and then decreases with cave diameter and reaches a peak when wavelength–perimeter ratio is equal to 1. For the diameter larger than the wavelength, incident waves are dominantly reflected by the cavern. The maximum amplitude again increases with cave diameter until the diameter approaches infinity, when the cave changes into a horizontal layer and the maximum amplitude becomes consistent.

Time-frequency spectra derived by the Gabor transform are shown in Figs. 2.20 and 2.21. The dominant frequency decreases with cave diameter. A small cave has a wide band and strong energy at high frequencies; the dominant frequency is higher than wavelet frequency. A large cave has a narrow band and strong energy at low frequencies; the dominant frequency is basically equal to wavelet frequency.

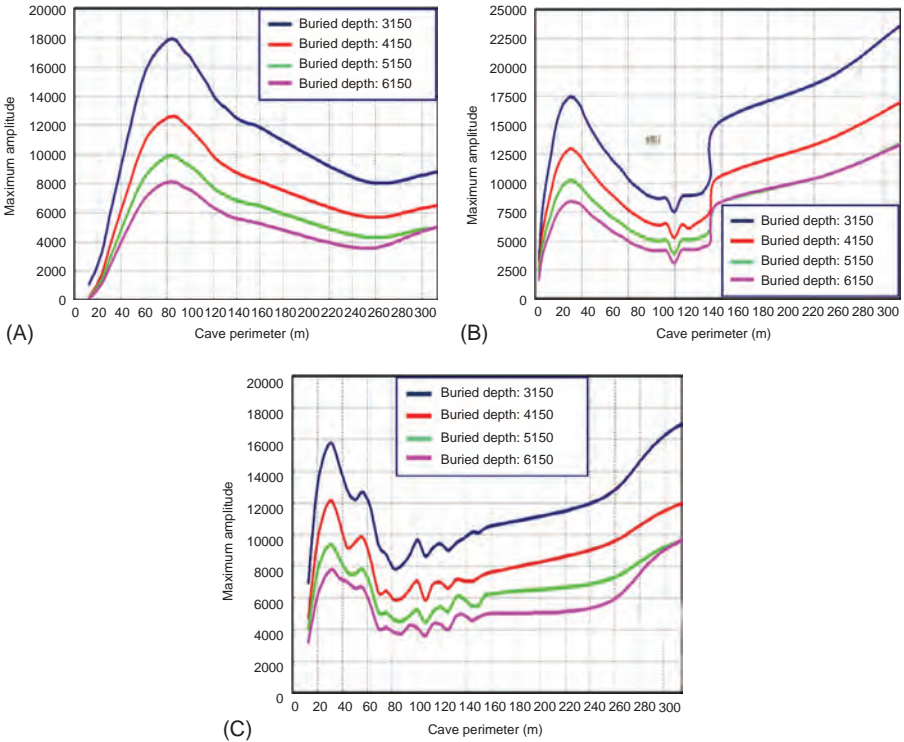


Figure 2.19 Maximum amplitude variation with cave perimeter (or diameter) at different buried depths. (A) Dominant frequency 20 Hz and wavelength 75 m; (B) dominant frequency 40 Hz and wavelength 37.5 m; (C) dominant frequency 60 Hz and wavelength 25 m.

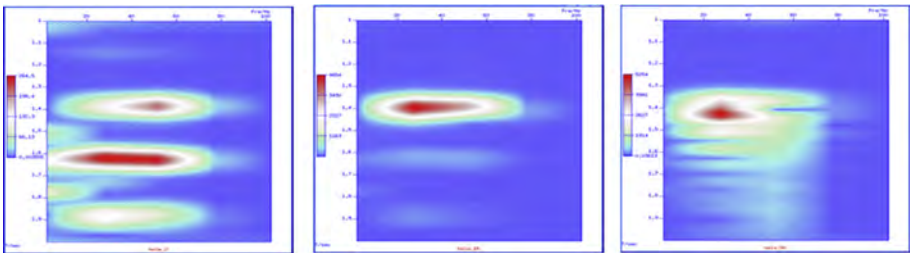


Figure 2.20 Time-frequency spectra for caves (with the diameter of 2, 15 and 50 m, respectively) at buried depth of 3150 m.

Single-cave physical modeling experiment

Ten physical models were designed with varied single caves/caverns (of 5, 10, 20, 35, 45, 60, 80, 120, 140, and 180 m, respectively) at the depth of 5200 m. Cave velocity is 3250 m/s and cave density is 1.2. Wall rock velocity is 4800 m/s. The dominant frequency is 25 Hz and wavelength is 130 m. The photos of physical

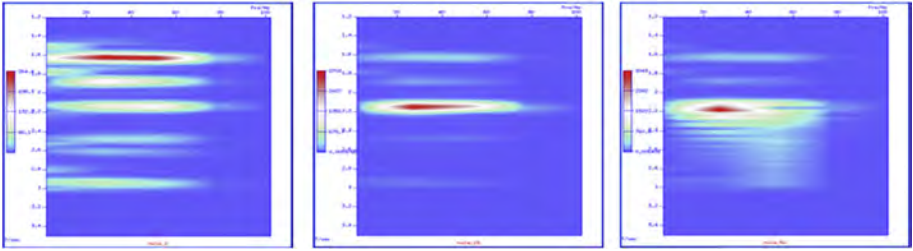


Figure 2.21 Time-frequency spectra for caves (with the diameter of 2, 15 and 50 m, respectively) at buried depth of 5150 m.

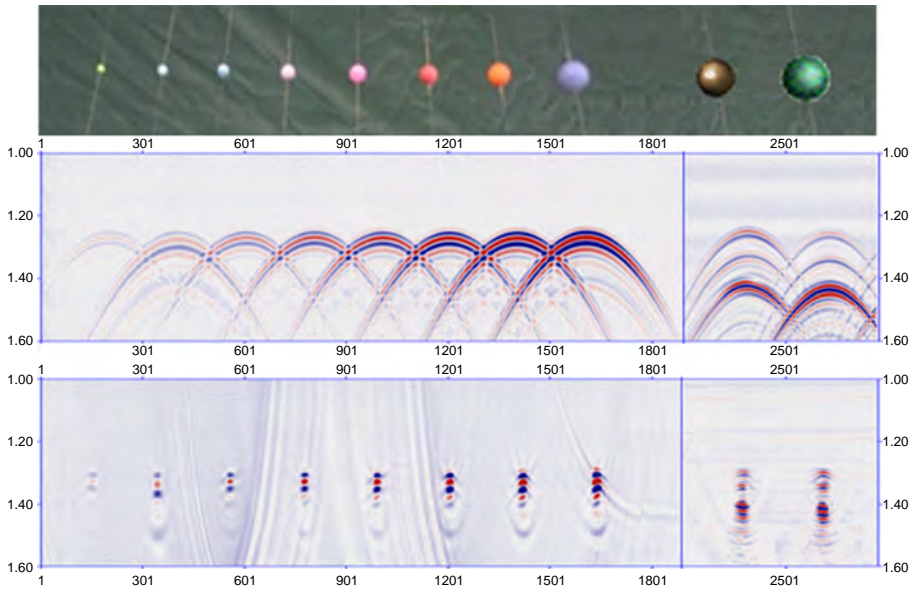


Figure 2.22 Physical models with varied single caves.

models are shown above in Fig. 2.22 and corresponding stacked and migrated sections shown below.

On stacked and migrated sections, diffracted energy decreases with decreased cave size. If a cave is smaller than $\lambda/20$, it is hard to identify it on reflection waveform and thus image it by conventional processing. A cave larger than 20 m generates bead-like reflections, the interval and lateral span of which increase with cave size. For a cavern with a diameter larger than 80 m, the top and bottom reflections can be separated on the sections and bottom reflections are stronger than top reflections.

Fig. 2.23A–E show time-frequency spectra for five caves/caverns (of 20, 35, 45, 60 and 80 m, respectively); z -axis is time and x -axis is frequency. Frequency band widens at the interval from 2000 to 2400 ms. A wide band could be observed when

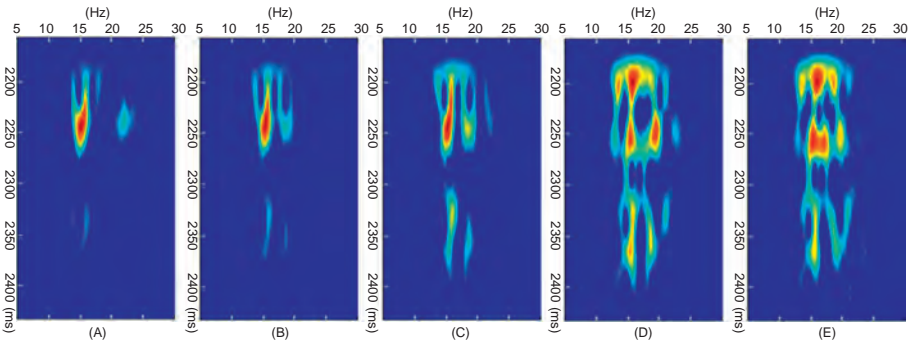


Figure 2.23 Time-frequency spectra for varied caves (A) is time-frequency spectra for cave with 20 m diameter (B) is time-frequency spectra for cave with 35 m diameter (C) is time-frequency spectra for cave with 45 m diameter (D) is time-frequency spectra for cave with 60 m diameter (E) is time-frequency spectra for cave with 80 m diameter.

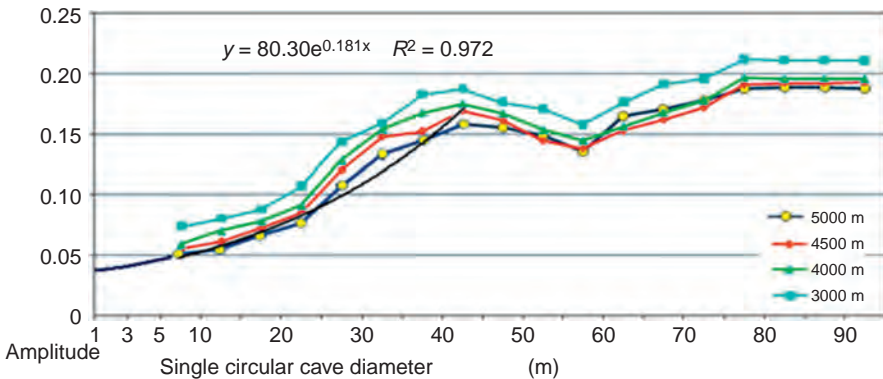


Figure 2.24 Maximum reflection amplitude variation with cave diameter.

seismic waves penetrate a large cavern, especially at the interval from 2300 to 2400 ms, which is related to cavern geometry and structure. As per the analysis, it is possible to distinguish between a large cave and a small cave through time-frequency analysis of bead-like reflections.

Fig. 2.24 shows four curves of reflected energy variation with cave size at different depths. The curve of maximum diffraction amplitude variation with cave diameter for small caves is plotted with a black line; the square of correlation coefficient is 0.972. Exponential increase, instead of linear increase, of diffracted energy with cave diameter indicates that the relationship between reflected energy and cave diameter could be formulated as $A = A_0e^{Cx}$. In addition, a trend similar to tuning effect could be observed for reflection amplitude variation with cave diameter.

Cave models discussed above with the diameter of 20 m at least are relatively large compared with the wavelength of 77 m; therefore they may be identified on the sections. Reflected energy decreases rapidly with cave diameter when the



Figure 2.25 Physical model with pipe-like caves of different lengths.

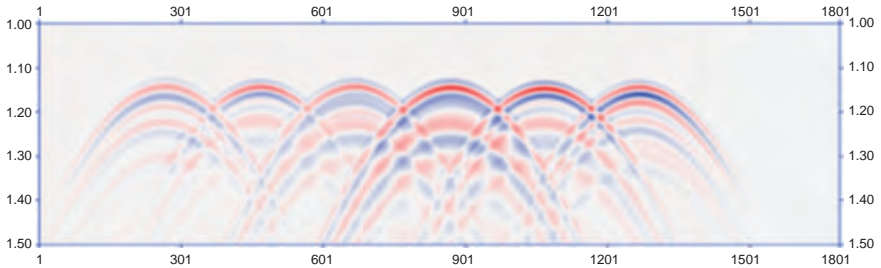


Figure 2.26 Stacked section of physical simulation.

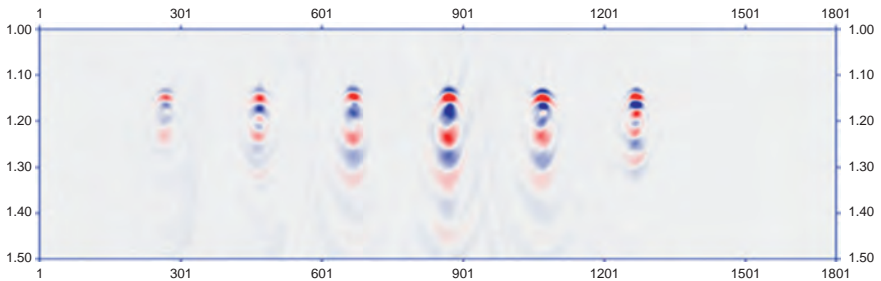


Figure 2.27 Migrated section of physical simulation.

diameter is smaller than $\lambda/4$. A cave with its diameter less than $\lambda/25$ could not be directly identified on the reflection profile.

2.2.1.3 Seismic responses of single caves with varied geometries

Fig. 2.25 shows a model with pipe-like caves (of 10, 15, 20, 30, 40 and 50 m long, respectively; the diameter is 10 m). All the caves are buried at the same depth of 5200 m. Cave velocity is 2500 m/s and wall rock velocity is 4150 m/s. As shown on corresponding stacked and migrated sections in Figs. 2.26 and 2.27, the precision of imaging, as well as reflected energy and length of bead-like reflections, decreases with decreased pipe length. Reflected energy reaches a peak when pipe length is equal to the radius of the Fresnel zone; afterward the energy decreases with pipe length and finally becomes consistent.

As per quantitative analysis of physical simulation data, it is difficult to identify or detect a pipe-like cave equal to or less than $\lambda/25$ and a spherical cave equal to or less than $\lambda/20$ on reflection profiles.

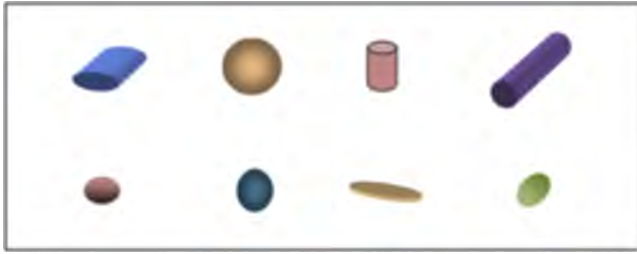


Figure 2.28 Cave models with varied geometries.

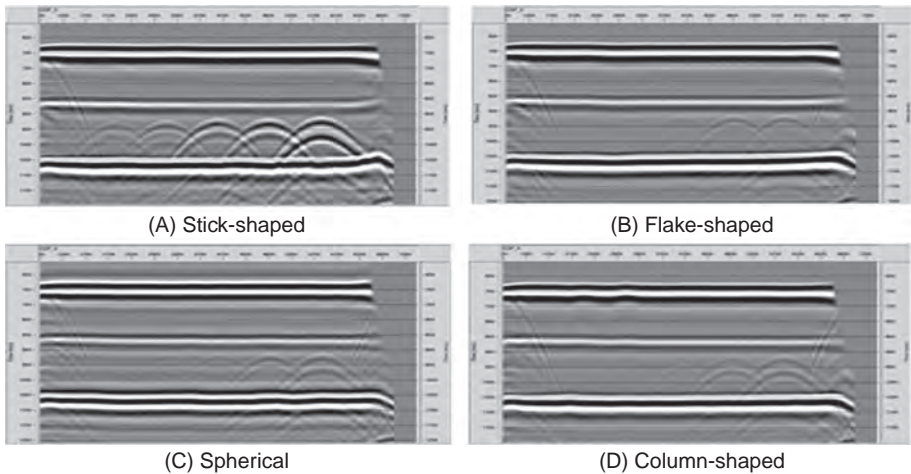


Figure 2.29 2D stacked sections for four geometries (A) is 2D stacked sections for stick-shaped cave (B) is 2D stacked sections for flake-shaped cave (C) is 2D stacked sections for spherical cave (D) is 2D stacked sections for column-shaped cave.

Fig. 2.28 shows four types of cave models with varied geometries and Fig. 2.29 shows corresponding stacked sections of physical simulation data. Each group of models has similar profiles and different sizes (of 10, 20, 30, 40 and 60 m). As shown on stacked sections, different caves have different seismic responses. Five stick-shaped caves generate the strongest diffracted energy compared with other geometries. The strength of diffracted energy is dependent on the horizontal projected area of the reflector, i.e., the proportion of projected area to the Fresnel zone. For example, the vertical projection of a stick-shaped or spherical cave is a circle; but in the horizontal direction, the projection of a spherical cave is a circle and that of a stick-shaped cave is a long belt much longer than the Fresnel zone, which means the whole belt contributes to the diffraction or reflection from the stick-shaped cave.

Fig. 2.30 shows the curves of diffracted amplitude variation with trace interval (or number of common depth point (CDP) points) at the time window from 1800 to 1900 ms. For cave size of 40 or 60 m, the amplitude of a stick-shaped cave at least

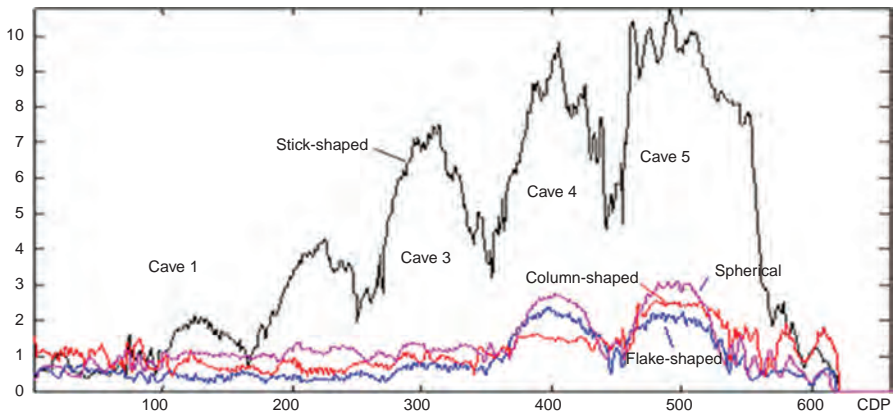


Figure 2.30 Diffracted amplitude variations for four cave types.

triples that of other geometries. The difference in amplitude is greater for cave sizes below 30 m. As shown in Fig. 2.30, diffracted amplitude decreases with decreased cave size for all geometries. It is hard to observe diffracted waves from a 10-m cave except the stick-shaped one. The horizontal projection of a spherical or column-shaped cave must reach 20 m, otherwise diffracted waves could not be observed. In terms of diffraction events, stick-shaped, spherical and column-shaped caves appear to have two similar parallel events in the vertical direction with the time difference increasing with vertical scale. For the fifth cave type (of 60 m), two groups of diffractions occur in parallel; it is diagnosed that the second group of diffractions comes from cave bottom. A flake-shaped cave, independent of size, only generates one group of diffractions and less “beads” on the migrated section. For a flake-shaped cave with top-bottom height difference less than 10 m, top and bottom diffractions coincide with each other; thus only one group of diffractions could be observed.

2.2.1.4 Seismic responses of single caves with different filling materials

The strength of scattered signals is dependent on cave size, shape, and extension as well as the properties of internal materials. Signal strength increases with the impedance contrast between fluids and rocks. As per numerical simulation, an oil-bearing cave generates the weakest signals due to small impedance contrast between oil and rocks and a gas-bearing cave has the strongest scattered signals because of large gas–rock impedance contrast; a water-bearing cave falls in between. Frequency analyses show that the dominant frequency of the scattered wave from the gas bearing cave is close to the dominant frequency of the reflected wavelet, but lower than that from the liquid-bearing cave. In the frequency–space domain, the energy for gas bearing concentrates in the center.

Five equally sized cave models designed with different filling materials are embedded at the same depth into a background model with the velocity of 3000 m/s,

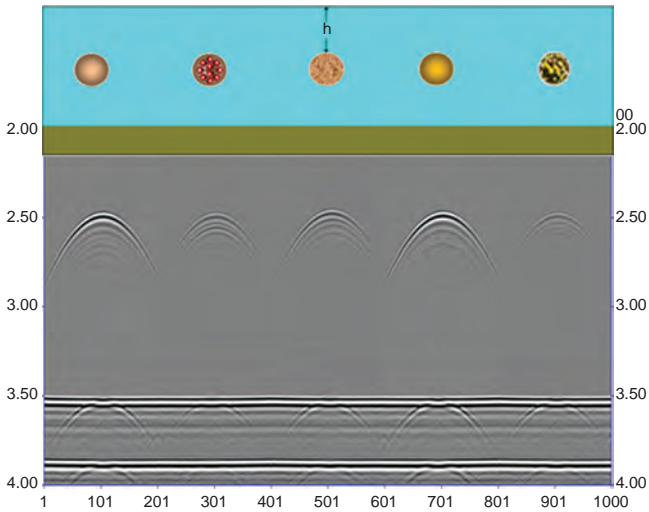


Figure 2.31 Cave models with different filling materials and stacked sections.

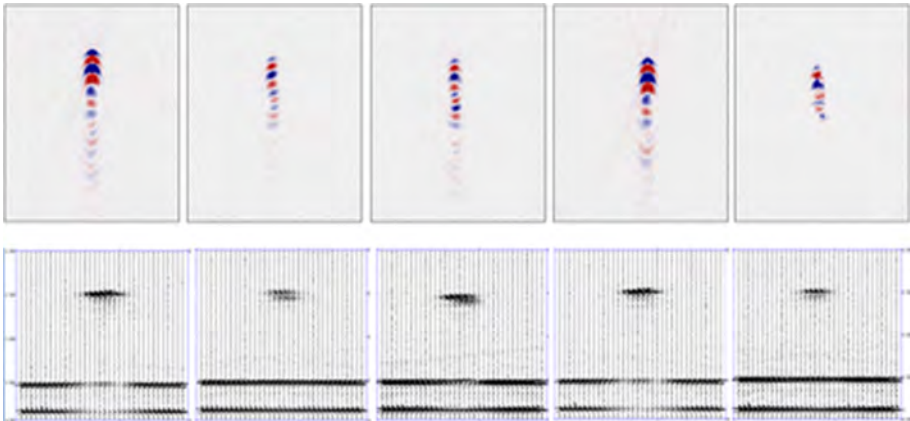


Figure 2.32 Migrated sections.

as shown in the upper plot in Fig. 2.31. Caves A, B, C, D, and E from left to right are filled with air, small balls, homogeneous porous medium, viscous crude oil, and heterogeneous porous medium. The average interval velocity of filling materials, except air, is 1800 m/s. A cave with a diameter of 4 mm and buried to a depth of 360 mm corresponds to an actual cave of 20 m at a depth of 1800 m as per the scale of 1:5000. Wall rock velocity is 3000 m/s and cave velocity is 1800 m/s. The lower plot in Fig. 2.31 shows the stacked section of physical simulation data. Fig. 2.32 shows the corresponding migrated section. Bead-like reflections from caves filled with air and crude oil are strong and symmetrical with long tails at both sides.

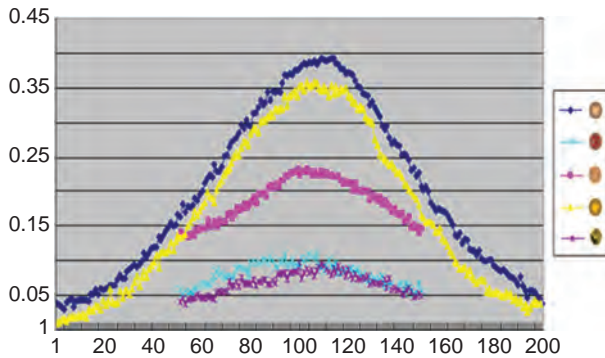


Figure 2.33 Amplitude variation with offset.

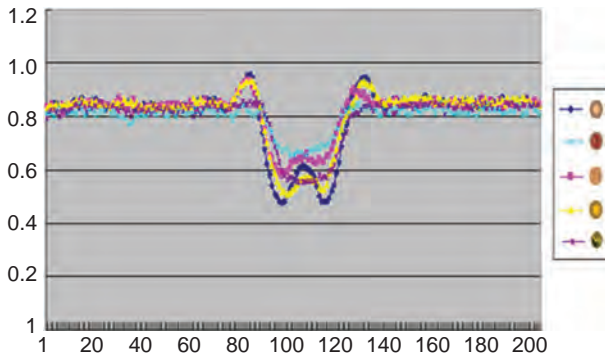


Figure 2.34 Amplitude variation with offset for underlying formations.

The strength of bead-like reflections is related to the heterogeneity of filling materials; a highly heterogeneous medium generates asymmetrical bead-like reflections with short tails. Fig. 2.32 shows a wiggle display of migrated data at the bottom; the reflection configuration for air and crude oil is simpler than that for heterogeneous media.

Fig. 2.33 shows the maximum amplitude variation with offset for different filling materials. For the caves filled with air and crude oil, the amplitude is large and decreases quickly with offset. For the cave filled with a heterogeneous medium, the amplitude is small and decreases slowly with offset. The magnitude of reflection amplitude is directly related to heterogeneity; the cave filled with a homogeneous medium generates a stronger amplitude than an analog filled with a heterogeneous medium.

Fig. 2.34 shows amplitude variation with offset for underlying formations below the cave. The cave has a great impact on underlying reflections. The interval of influence (about 275 m) is much larger than cave size and varies with filling materials.

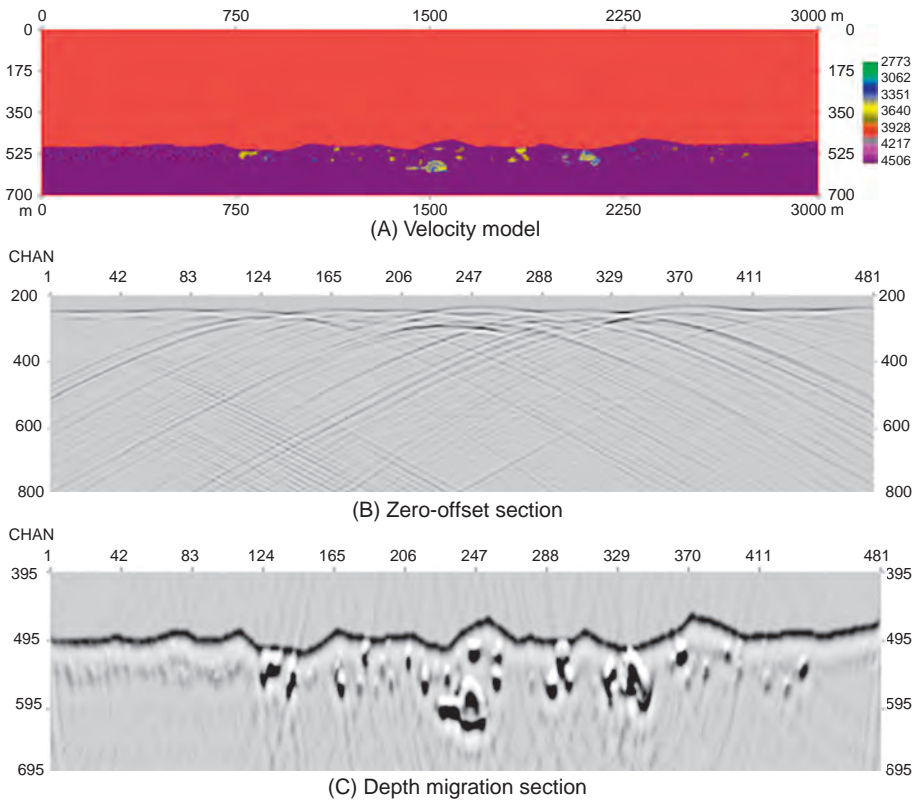


Figure 2.35 Numerical simulation for random caves. (A) Velocity model; (B) zero-offset section; (C) depth migration section.

2.2.2 Seismic responses of a complicated cave system

An actual cave system usually comprises a number of caves with varied sizes, geometries, and internal fluids. It is hard to quantitatively correlate geologic properties with seismic attributes in view of a cave system's complex seismic responses. The following part deals with forward modeling to obtain some qualitative knowledge.

2.2.2.1 Seismic responses of random caves

Fig. 2.35 shows a numerical model with random caves embedded in two-layer media separated by a velocity interface which is equivalent to an unconformable surface. These caves within an interval of 70 m at the depth of 500 m randomly scatter in three horizontal zones from left to right; cave velocity is also randomly defined, as shown by the color bar. In forward modeling, the dominant frequency of the wavelet is 40 Hz; P- and S-velocity ratio is 0.6; the density is transformed from

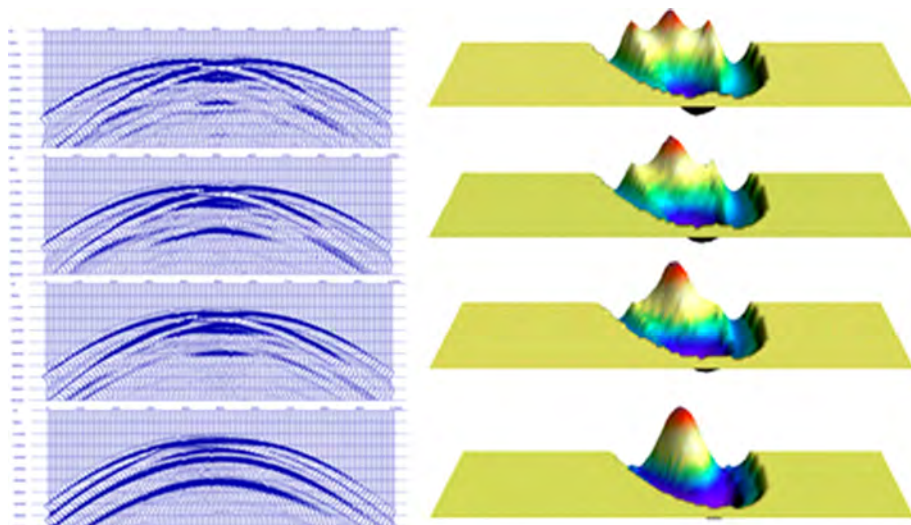


Figure 2.36 Physical simulations for two separated caves and corresponding 3D analyses.

P-velocity by an empirical formula. The seismic survey has been designed to be a multifold acquisition with a shot interval of 6.25 m, a trace interval of 6.25 m, and 481 shots in total. Fig. 2.35B and C show the zero-offset section extracted from shot gathers and the depth migration section of the zero-offset section.

Bead-like reflections of large caves could be clearly identified and interpreted one-to-one on the migrated section, whereas chaotic reflections of small caves are locally confused by the strong event of the unconformity; thus it is hard to differentiate high-frequency scattered waves from small caves. This means that it is challenging to predict those small caves immediately beneath a fossil basal surface unless the strong unconformity reflection could be suppressed while the cave reflections were preserved.

2.2.2.2 Seismic responses of cave group

Fig. 2.36 shows zero-offset seismograms (with CDP spacing of 10 m) for two equally sized physical cave models at a depth of 2000 m; the horizontal cave interval is set to be 150, 100, 50, and 20 m, respectively. The Fresnel radius is 243 m. Three-dimensional analyses are shown on the right (with trace interval in the x -direction, time in the y -direction, and energy in the z -direction). Two caves with an interval larger than 50 m could be separated and two caves less than 50 m apart could not be identified individually.

Fig. 2.37 shows stacked sections, model photos, and migrated sections for three cave groups. In Fig. 2.37B, the model comprises three vertical caves of 15, 20, and 35 m; total vertical height is 60 m and the largest lateral width is 35 m. The model in Fig. 2.37C comprises three equally sized caves (of 20 m) disposed in a triangular configuration; total vertical height is 43 m and the largest lateral width is 40 m. The

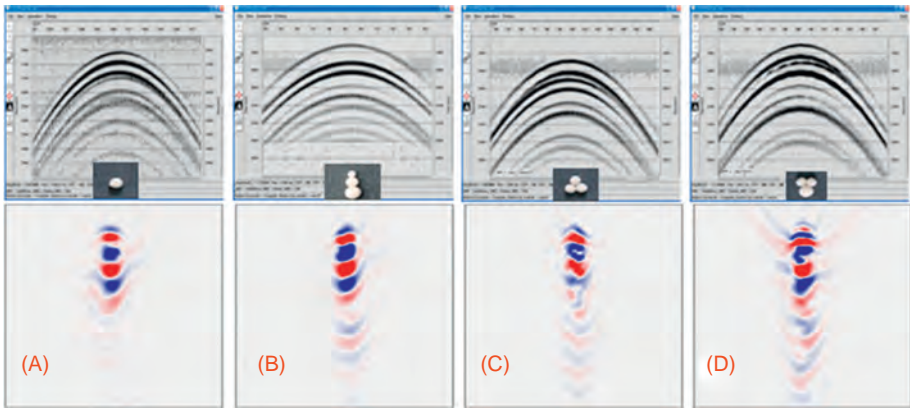


Figure 2.37 Stacked sections, model photos, and migrated sections for a single cave and three cave groups (A) is stacked sections, model photo, and migrated section for single cave (B) is stacked sections, model photo, and migrated section for three caves with different size (C) is stacked sections, model photo, and migrated section for three caves, one cave is above and two are below (D) is stacked sections, model photo, and migrated section for three caves, two caves are above and one is below.

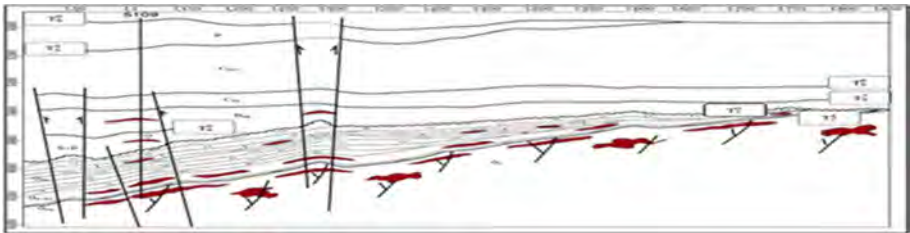


Figure 2.38 Schematic reservoir section in the NE direction.

model in Fig. 2.37D comprises two equally sized caves (of 20 m) and a large cave of 35 m in an inverted triangular configuration; total vertical height is 53 m and the largest lateral width is 40 m. The single model (of 20 m) shown in Fig. 2.37A is designed for comparison. Four stacked sections exhibit different reflected wave fields and hyperbolas. On migrated sections, the single-cave image features homogeneous bead-like reflections with short tails, while the image of a cave group is characterized by distorted bead-like complex reflections with long tails, multippeak frequency spectra and varied dominant frequencies, which are caused by wave interference.

2.2.2.3 Numerical simulation of an actual geologic model

Fig. 2.38 shows a cave model established based on a cross-well reservoir section in the Tahe oilfield. The simplified numerical model is shown in Fig. 2.39. Lateral cave width changes from 5 to 150 m. Cave diffractions break the continuity of

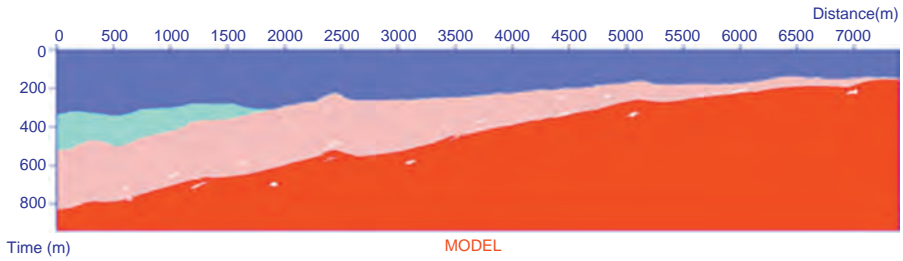


Figure 2.39 Simplified numerical cave model.

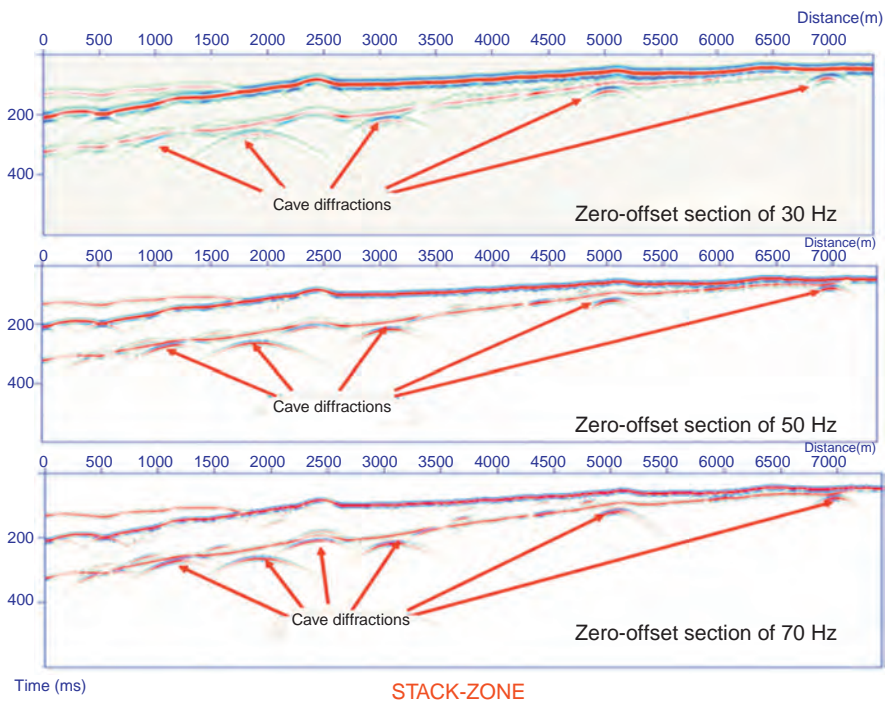


Figure 2.40 Zero-offset sections with dominant frequencies of 30, 50, and 70 Hz.

interface reflections, as shown on zero-offset synthetic seismograms with dominant frequencies of 30, 50 and 70 Hz in Fig. 2.40.

Figs. 2.41–2.45 show the sections after poststack depth migration with different frequency ranges; the dominant frequencies are 30, 50, and 70 Hz, respectively. More distinct bead-like reflections could be observed on a narrow band section; but a wide band section also has bead-like reflections. If cave-induced diffractions have abundant high frequencies which have been preserved in data processing, the cave may be well imaged without obvious bead-like reflections and long tails.

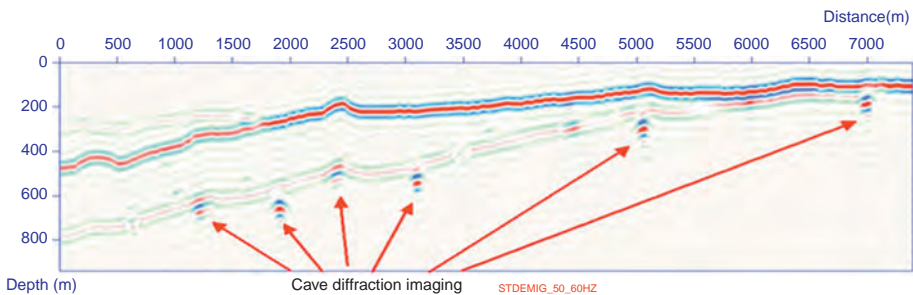


Figure 2.41 Poststack migrated section of 30 Hz (5–50 Hz).

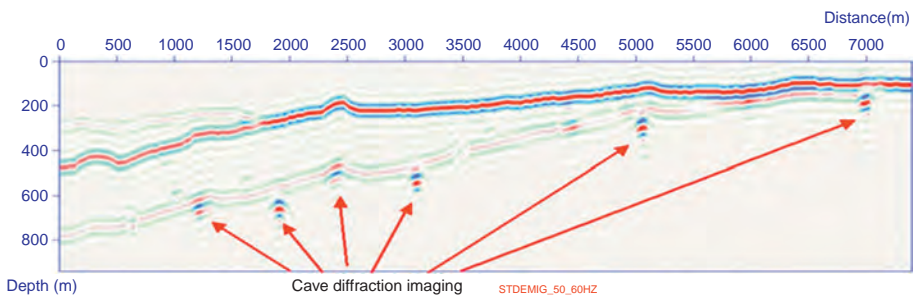


Figure 2.42 Poststack migrated section of 50 Hz (5–90 Hz).

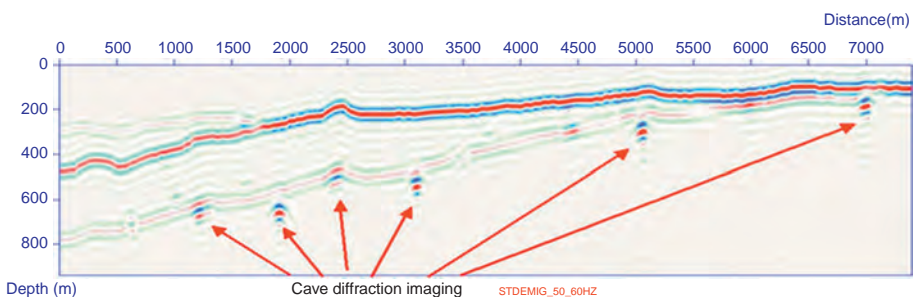


Figure 2.43 Poststack migrated section of 50 Hz (5–60 Hz).

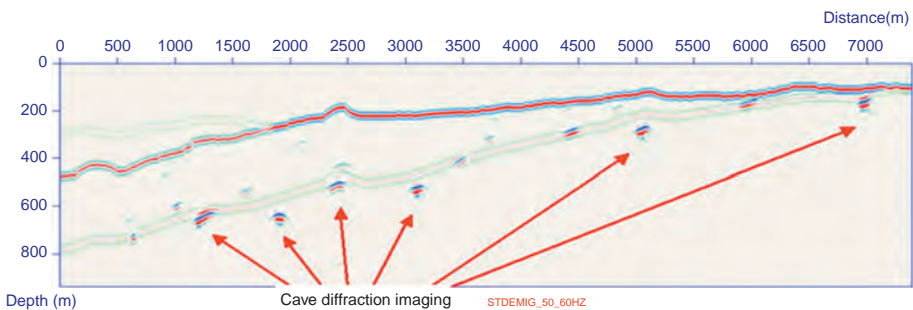


Figure 2.44 Poststack migrated section of 70 Hz (5–120 Hz).

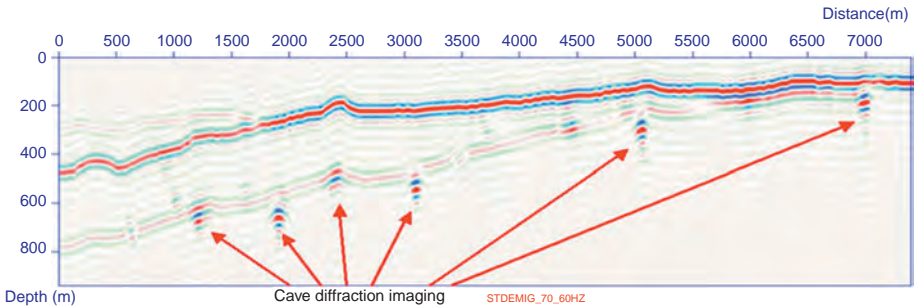


Figure 2.45 Poststack migrated section of 70 Hz (5–60 Hz).

2.2.3 Seismic responses of fractures

2.2.3.1 P-wave azimuthal anisotropy in a vertically fractured medium

As per the study, reflected P-waves exhibit azimuthal anisotropy when traveling through a fractured medium. Reflection amplitude and velocity reach the maximum when survey lines are parallel to the fracture strike (with the included angle of 0 degree) and then decrease with included angle; minimum amplitude and velocity appear at the included angle of 90 degree. Afterward the amplitude and velocity increase with included angle and once again reach the maximum at the angle of 180 degree. Periodic changes occur within the range from 0 to 180 degrees. Reflection time reaches the minimum at the included angle of 0 degree and then increases with the angle before it reaches the maximum at 90 degree; afterward the time decreases with the included angle. Periodic changes of reflection time also occur within the range from 0 to 180 degrees. Thus seismic amplitude or velocity could be simplified as

$$F(a) = A + B \cos 2a \quad (2.1)$$

where a is the azimuth angle of the shooting direction against the fracture strike; A is a bias factor related to offset; B is an offset- and fracture-related tuning factor of amplitude or velocity; $F(a)$ is azimuthal anisotropy of amplitude or velocity. Eq. (2.1) is schematically approximated by an ellipse (as shown in Fig. 2.46).

Analysis of experimental results

An annular layout with a constant offset was designed for a vertical fracture model (with six to seven fractures per wavelength, as shown in Fig. 2.46). Beginning with an angle of 0 degree when the survey line runs parallel to the fracture strike, a trace was recorded every 15 degree up to 25 traces within 360 degree, which constitute a complete profile, as shown in Fig. 2.47. As indicated on the time section, the reflection time of the model top (indicated by A in the figure) remains consistent in all azimuths.

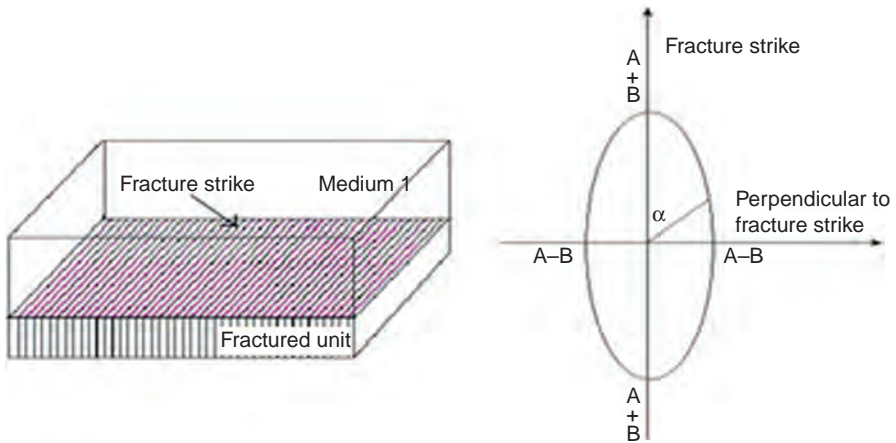


Figure 2.46 P-wave azimuthal anisotropy in a vertically fractured medium.

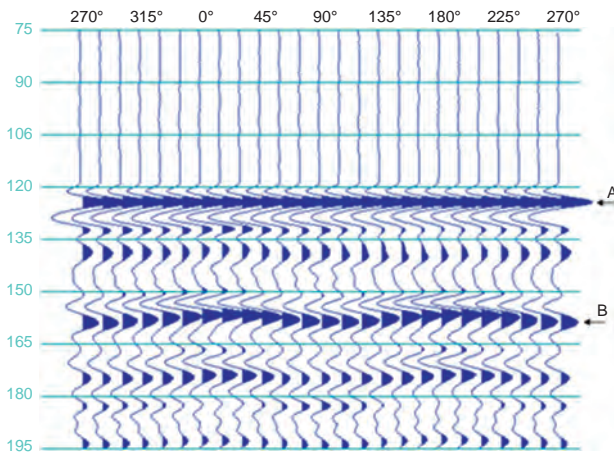


Figure 2.47 Vertical fracture observation through an annular layout with a fixed offset.

Both travel time and reflection amplitude exhibit azimuthal anisotropy for reflected waves from the bottom of the fractured unit (as indicated by B in the figure). Fig. 2.48 shows amplitude, time, and velocity variations with azimuth angle for event B. P-wave velocity and amplitude reach the maximum when the survey line runs parallel to the fracture strike; the lowest velocity and amplitude take place when the survey line is perpendicular to the fracture strike. Wavy variations of amplitude and velocity are approximate to sine or cosine curves with the period of 180 degree. The difference of first arrivals between reflected waves parallel with

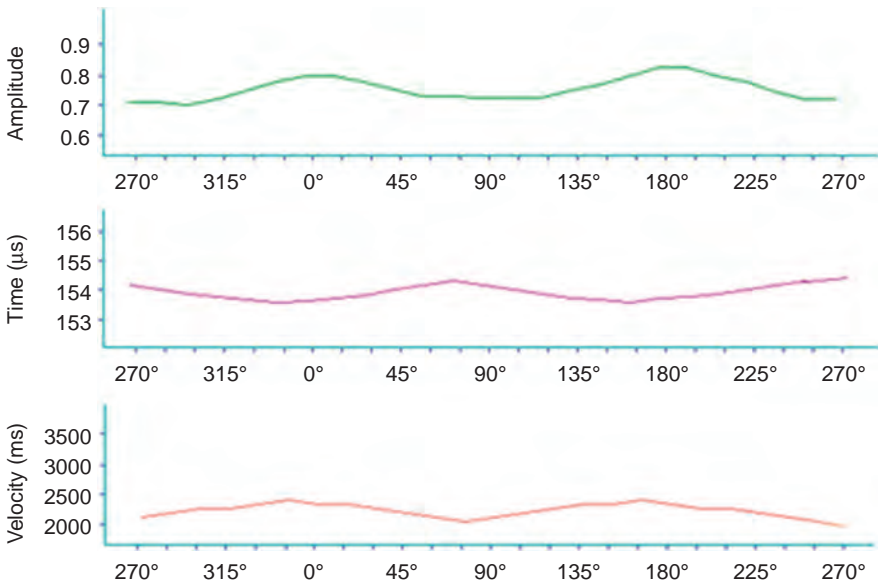


Figure 2.48 Amplitude, time, and velocity variations with azimuth for a fixed offset.

and perpendicular to the fracture strike is $2.7 \mu\text{s}$. P-velocity is 2492 m/s when the survey line runs parallel to the fracture strike and 2298 m/s when the survey line is perpendicular to the fracture strike; percentage difference of anisotropic velocity is 7.8%. The difference between maximum and minimum amplitude is about 20%.

Azimuthal AVO responses

Five CMP gathers (five survey lines) have been acquired for the above vertical fracture model at the included angle between each survey line and the fracture strike being 90, 60, 45, 30, and 0 degrees, respectively. To compare with the records of the five lines, an isotropic model (made of a plexiglass standard block) was built with the same material and thickness as the fracture model, and a line was acquired. The six seismic time sections acquired with the same recording geometry are shown in Fig. 2.49.

Let us see how top and bottom reflection time and amplitude vary with offset. Reflection amplitude at the model top slightly varies with azimuth; the amplitude reaches the maximum at the included angle of 0 degree between the survey line and the fracture strike and then decreases with the angle until it reaches the minimum at the angle of 90 degree. Amplitude difference between survey lines is very small and each profile exhibits similar AVO trend (Fig. 2.50). This means the top reflection is not sensitive to azimuthal anisotropy. In addition, the amplitude of the standard block without fractures is larger than that of the fractured model. AVO curves of reflections from the model bottom (Fig. 2.51) exhibit remarkable variations compared with top AVO curves. Reference amplitude of the standard block is the largest at near offsets. The amplitude reaches the maximum when the

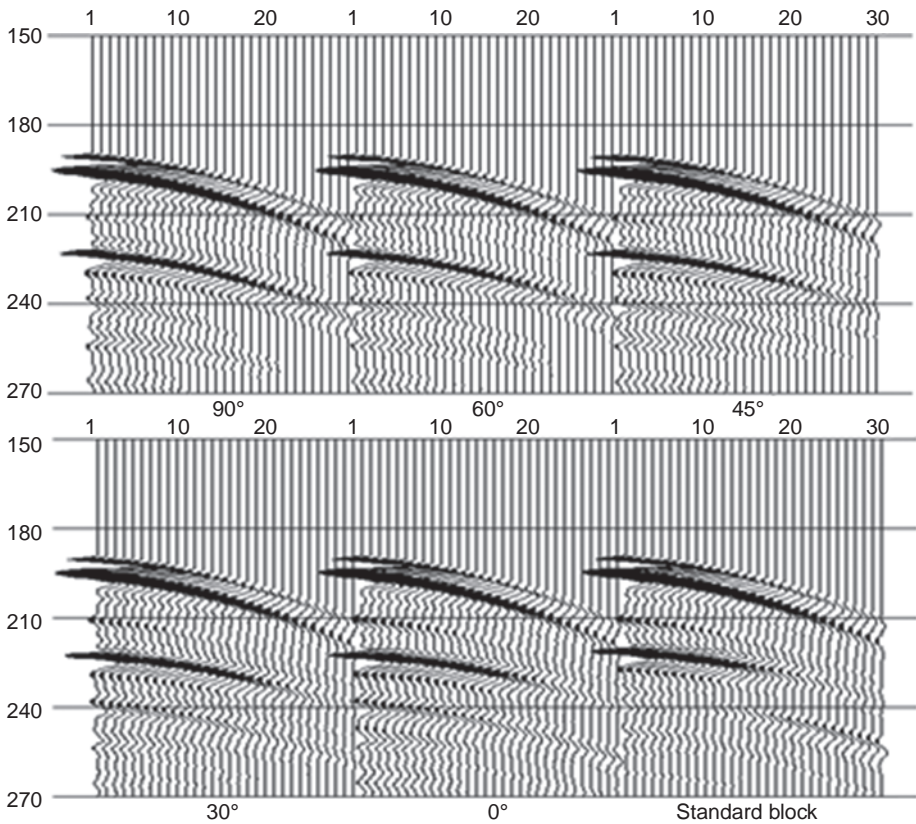


Figure 2.49 CMP gathers at different azimuths.

survey line runs parallel with the fracture strike (with the included angle of 0 degree) and then decreases with the included angle from 30, 45 to 60 degrees until it reaches the minimum at 90 degree (here only the curves of 0, 45, and 90 degrees and reference curve of the standard block were plotted for comparison; AVO curves of 30 and 60 degrees lie between them). Reference amplitude decreases with offset with the largest gradient, followed by the curves of 0, 30, 45, 60, and 90 degrees; the curve of 90 degree shows the smallest gradient. Therefore the amplitude of 90 degree is larger than that of 0 degree at far offsets. Far-offset amplitude may be somewhat affected by transducer performance in view of its directional property of signal emission and reception; but in terms of completely uniform surveying conditions, relative amplitude relationships have been preserved. In the above curves, the bottom amplitude has been compensated to correct transducer directivity, but the spherical spreading and other amplitude inconsistency have not been corrected.

The curves of the top reflection time changing with offset acquired by the six lines indicate that identical travel time, meaning consistent surveying conditions in

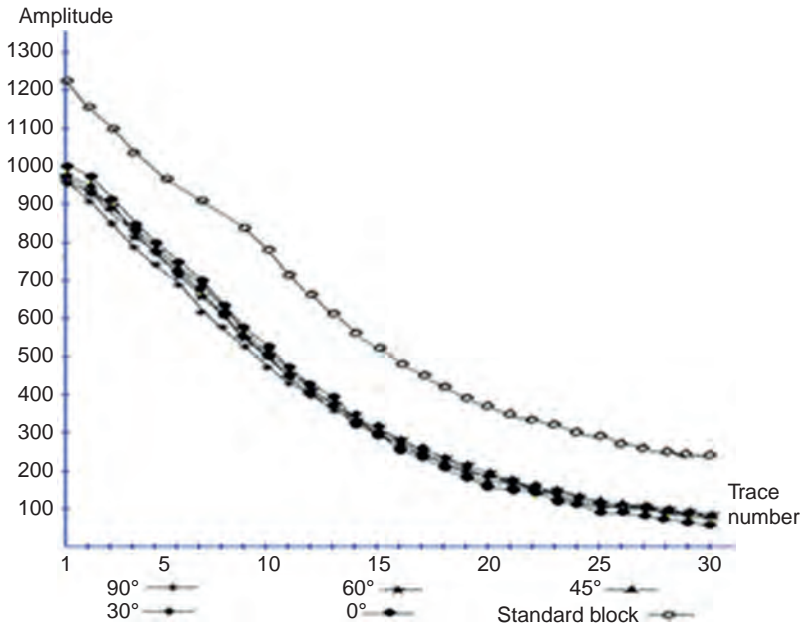


Figure 2.50 AVO curves of top reflections at different azimuths.

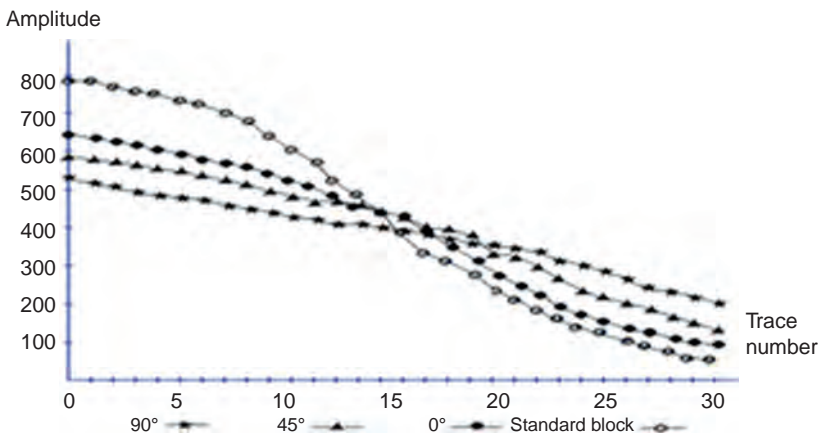


Figure 2.51 AVO curves of bottom reflections at different azimuths.

the experiment. For the bottom reflections, the travel time in the standard block is the smallest; the time for parallel propagation (of angle 0 degree) in the fractured model is smaller than that for perpendicular propagation (of angle 90 degree). Time difference between survey lines increases with offset, which means velocity anisotropy increases with offset.

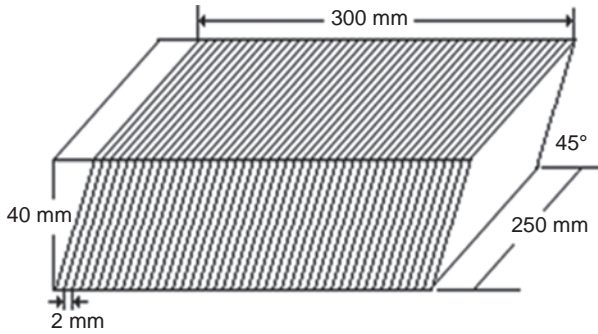


Figure 2.52 Schematic titled fracture model.

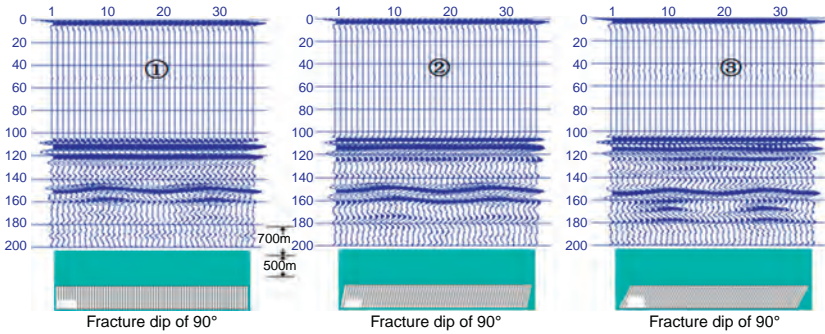


Figure 2.53 Azimuth variant seismograms for a high-dip fracture model.

2.2.3.2 *P-wave azimuthal anisotropy in a fractured medium with varied fracture dips*

The scenarios discussed above deal with the simplest case in azimuthal anisotropy, i.e., vertical fractures with a horizontal symmetry axis (HTI medium). But as per core data and ultrasonic imaging logging data, high-dipping fractures, instead of vertical fractures, occur in most cases in real reservoirs. There are also some low-dip oblique cracks in, for example, structural fold belts or tilted sandstone and shale units. A fractured medium with a tilted axis has much more complicated azimuthal anisotropic properties than a vertically fractured medium.

The physical model with titled fractures is composed of a stack of 150 aligned plexiglass sheets of $250 \times 57 \times 2$ mm individually, gaps between which are used to simulate fractures (Fig. 2.52). Fracture density is 6–7 per wavelength. Fracture dip could be adjusted randomly. The results show that a titled fracture model has more complex reflection signatures at different azimuths and consequent azimuthal anisotropic properties, which are remarkable but difficult to characterize.

A series of simulation experiments have been made to understand anisotropic properties for different fracture dips. Fig. 2.53 shows P-wave seismograms for a

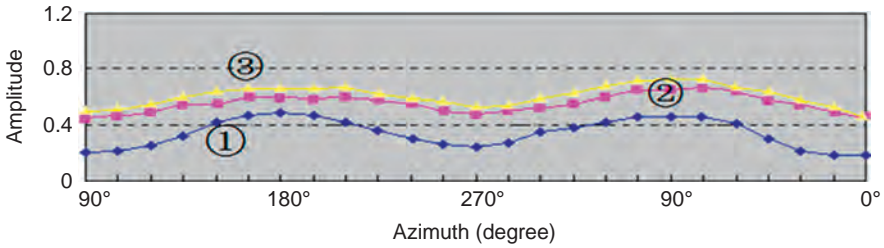


Figure 2.54 Bottom reflection amplitude variation with azimuth.

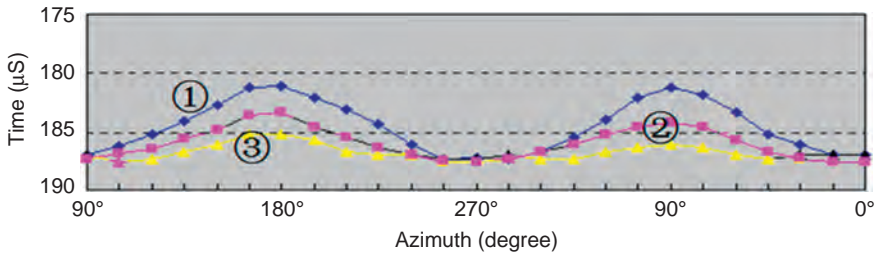


Figure 2.55 Bottom reflection time variation with azimuth.

high-dip fracture model. The offset is 300 m; the velocity of the fracture unit is 2500 m/s and the fracture density is 0.02; fracture dip is 90, 80, and 70 degrees, respectively. As shown in the figure, curves 1, 2, and 3 demonstrate similar variations; that is reflection time is small for a survey line parallel to fracture strike and large for a line perpendicular to fracture strike.

Amplitude and time variations with azimuth for bottom reflections are shown in Figs. 2.54 and 2.55. Periodic changes of time from large to small and of amplitude from small to large occur twice for the azimuth changing from 0 to 360 degrees. The percentage of time change is 3.37%, 2.08%, and 0.91%, respectively, at 90, 80, and 70 degrees; the percentage of amplitude variation is 59%, 21%, and 17%, respectively, at 90, 80, and 70 degrees. In terms of the percentage of change, amplitude is more sensitive to azimuth than velocity. As shown on the seismograms, second arrivals are stronger on the low-angle section; therefore, the impacts of fracture dip should be taken full account of in azimuthal anisotropy detection.

2.2.3.3 P-wave responses for varied fracture densities

Fig. 2.56 shows nine equal-volume models with different fracture densities from 0% to 12%, which are controlled by inserting a number of cracks into the model. The amplitude and travel time of ultrasonic pulses penetrating the model are recorded by four-frequency P-wave transducers in x and z directions. All the transducers with four frequencies feature wide band and short pulse, but are different in sensitivity and band width.



Figure 2.56 Model photos with different fracture densities.

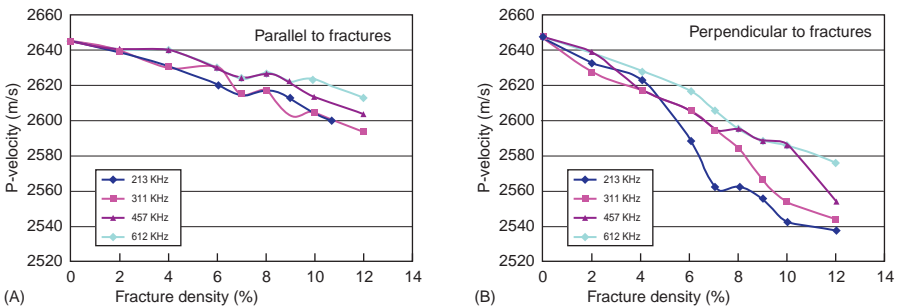


Figure 2.57 P-velocity variations with fracture density. (A) P-wave propagation parallel to fractures; (B) P-wave propagation perpendicular to fractures.

Fig. 2.57 shows velocity variations with fracture density in x and z directions. For P-wave propagation parallel to fractures, velocity change with frequency may reach 30–50 m/s; P-velocity decreases by 2% at most when fracture density increases from zero to 12%. It is noted that in view of P-wave testing error less than 0.8%, i.e., $\pm 0.1 \mu\text{s}$, a velocity difference of 2% demonstrates the influence of fracture density.

Wave propagation perpendicular to fractures witnesses more rapid velocity decrease with fracture density compared with parallel propagation. P-velocity decreases by more than 3% and 4.2% at most when fracture density increases from 0% to 12%. Velocity decrease doubles that for parallel propagation. Therefore, velocity drop is mainly related to fracture density for perpendicular propagation.

As shown in Fig. 2.57, velocity drop with fracture density varies with frequency. Velocity drop with fracture density is more quick at low frequencies than that at high frequencies, which means high-frequency velocity is higher than low-frequency velocity for a same fracture density. This phenomenon is unique for these kinds of media.

Normalized P-wave amplitude variations with fracture density in x - and z -directions are shown in Fig. 2.58. P-amplitude drop with fracture density varies greatly

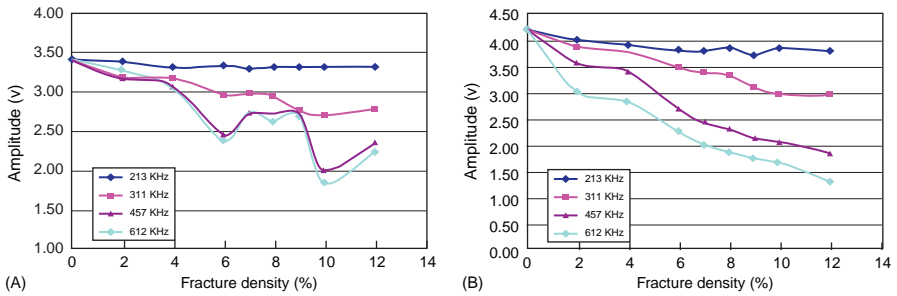


Figure 2.58 P-amplitude variations with fracture density. (A) P-wave propagation parallel to fractures; (B) P-wave propagation perpendicular to fractures.

with frequency. Amplitude drop is small at the low frequency (of 213 kHz) and large at high frequencies, especially for wave propagation perpendicular to fractures. This means P-wave attenuation is sensitive to frequency in a fractured medium.

As per the above tests, P-velocity decreases with fracture density for both parallel propagation and perpendicular propagation. For parallel propagation which is common in field surveys, P-waves are considered to travel in the matrix because fracture interval is (14.3-times) much larger than fracture thickness. For perpendicular propagation, P-velocity drop with fracture density is only 4%, which is smaller than what is expected. P-wave anisotropy is only 2.3% from parallel propagation to perpendicular propagation for a same fracture density (of 12%). In spite of small velocity drop with fracture density, velocity dispersion occurs in the experiments; velocity drop with fracture density decreases with frequency. This is difficult to explain by conventional fracture-induced dispersion and may be explained by the ratio of wavelength to fracture interval. More fractures occur within one wavelength at low frequencies, which indicates the large effect of fractures on wave propagation.

P-amplitude drop with fracture density may be explained by P-wave dispersion caused by fractures. At low frequencies, dispersion has little impact on amplitude even for a large fracture density. But at high frequencies, P-amplitude decreases rapidly with fracture density due to increased impact of dispersion. Amplitude anomalies at fracture densities of 6% and 10% for parallel propagation in Fig. 2.58A may be explained to be dependent on fracture thickness. The impacts of fracture thickness have been observed in another experiment.

In summary, P-wave amplitude and frequency are more sensitive to fracture density than velocity provided that other parameters remain constant.

2.2.4 Physical simulation of a 3D fracture-vug model

Fig. 2.59 shows the photo of a cave model which is designed to comprise three parallel fault blocks with different top and bottom depths and thicknesses; the velocity of fault blocks is uniformly set to be 2300 m/s. Five uplifted low-velocity units are disposed every 500 m in the middle block; the velocity is 1230 m/s. Five sags with a velocity of 1000 m/s are designed every 500 m in each block on both sides.

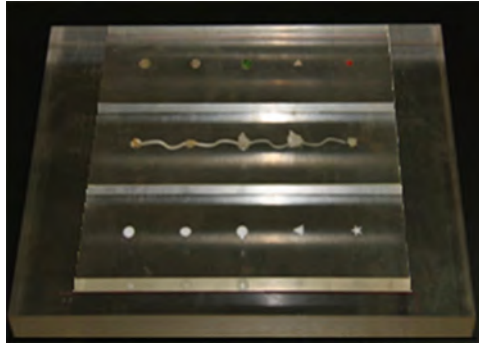


Figure 2.59 3D physical model.

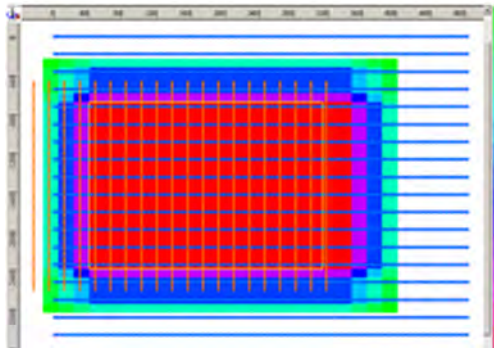


Figure 2.60 Recording geometry.

Velocity anomalies run parallel with survey lines. The velocity of the underlying layer is 2400 m/s; the top depth of the underlying layer is 1800 m. The model is embedded into a homogeneous medium (water) with the velocity of 1545 m/s. Three blocks are 150, 200, and 200 m thick, respectively. Water thicknesses between fault blocks and underlying layer are 50, 30, and 10 m, respectively. Top depths of fault blocks are 1600, 1570, 1590 m, respectively. The model is 3000 m long along the survey line and 2600 m wide.

Fig. 2.60 shows the recording geometry with six swaths, eight lines/swath, 12 shots, 48 traces, and 20 shot lines for the 3D physical simulation. The bin size is 15×15 m. Shot points lie on one side of the spread. The minimum offset is 270 m. The number of sampling points is 4000 and the sampling interval is 1 ms.

Fig. 2.61 shows eight gathers for one shot, on which cave reflections could be observed. Fig. 2.62 shows two sections across cave units after prestack time migration and prestack depth migration, respectively. The targets (with low velocities) are clearly imaged after prestack depth migration with an accurate interval velocity model. In contrast, prestack time migration uses a route mean squared (RMS) velocity model which needs to be further improved for accurate imaging.

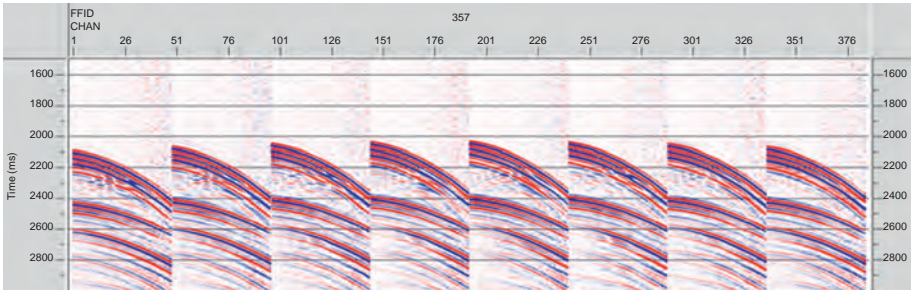


Figure 2.61 Raw gathers of 3D physical simulation.

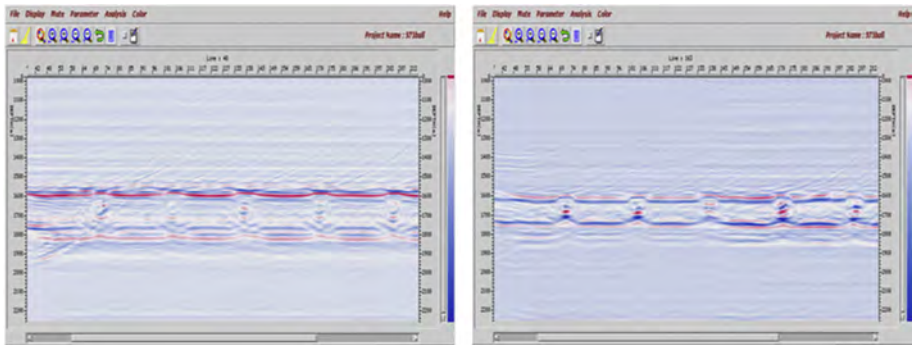


Figure 2.62 Migrated sections across cave units.

As per data recorded, each cave unit, regardless of shape, size, and filling materials, generates bead-like reflections. A large regular cave with homogeneous filling materials generates clear bead-like reflections with strong amplitude. Cave reflections vary with cave size, shape, and filling materials. It is hard to locate and describe different cave units unless their dynamic properties and attributes in different domains are carefully examined.

2.3 Seismic imaging

Fracture-vug carbonate reservoirs usually exhibit strong heterogeneity and large lateral lithologic changes. Accurate migration and imaging is challenging due to the impacts of diffracted waves, strong reflections from unconformities and high-velocity rock matrix. In order to improve the accuracy of migration and imaging, great efforts have been made on algorithms and techniques. This section deals with time-shift depth migration and velocity analysis in angel domain, offset plane-wave prestack time migration, and equivalent offset prestack time migration to improve the resolution of diffraction imaging.

2.3.1 Offset plane-wave finite-difference prestack time migration

Kirchhoff prestack time migration has been widely used in seismic data processing due to its high computational efficiency and adaptability to various recording geometries, but it cannot generate a good result if lateral velocity variation is abrupt because it uses an RMS velocity field. Hong et al. (2009) developed an algorithm for asymmetric travel time calculation, which allows velocity change in the lateral direction and thus improves the focusing of Kirchhoff migration. But it is hard to obtain an accurate amplitude weighting factor if the velocity is varied laterally. Compared with Kirchhoff prestack time migration, wave equation migration by extrapolation operators is more amplitude preserved and more computationally efficient. It is easy to generate imaging gathers for velocity analysis. Mosher et al. (1996) presented an approach of offset plane-wave depth migration in common ray parameter domain, which is similar to poststack zero-offset migration except for an additional dip term related to stratigraphic dip. Pestana and Stoffa (2000) proposed 2D plane-wave prestack time migration which includes two steps, slant stacking of shot gathers followed by time migration in common ray parameter domain. A correction term related to ray parameter was included. Wang et al. (2009, 2011) proposed an algorithm of offset plane-wave time migration which allows for the relationship between incident angle and offset wavenumber in the plane-wave equation. Wavefield extrapolation is computed by finite difference operators. This algorithm is applicable to the media with gentle lateral velocity changes due to the utilization of an interval velocity field in time domain. The use of finite difference operators based on wave equation improves amplitude preservation.

2.3.1.1 3D offset plane-wave decomposition

Slant stacking within a limited range

Offset plane-wave decomposition may be realized by slant stacking of CMP gathers in view of the predictability of CMP events, but plane waves may be contaminated by noises after τ - p transform. These noises may be generated in the process of slant stacking or result from an irregular layout (including irregular azimuths and offset sampling points) and limited acquisition aperture. A τ - p transform restricted within a limited range would remarkably reduce aliasing in slant stacking to generate a data set with high signal to noise ratio (S/N).

A τ - p transform of CMP gathers is formulated as follows.

$$\Phi(\tau, \vec{y}, \vec{p}_h) = \sum_{|\vec{h}|=H_{start}}^{H_{end}} \Psi(t - \vec{p}_h \cdot \vec{h}, \vec{y}, \vec{h}), \quad (2.2)$$

where τ is intercept time; $\vec{y} = (m_x, m_y)$ is CMP coordinates; \vec{p}_h is a ray parameter of offset plane wave; $\vec{h} = (h_x, h_y)$ is semi-offset; H_{start} and H_{end} are the minimum and maximum offsets, respectively; $\Phi(t, \vec{y}, \vec{p})$ is the result of offset plane waves; $\Psi(t, \vec{y}, \vec{f})$ is a CMP gather.

The hyperbolic time–distance curve for a CMP gather is mapped to an elliptical curve after τ - p transform. Noises are generated by tangential stacking along the time–distance curve in the process of slant stacking. In order to reduce noises, slant stacking is restricted in the neighborhood of the tangent. The time–distance curve for a CMP gather is expressed as follows.

$$t = \sqrt{t_0^2 + 4 \frac{\vec{h}^2}{v^2}}, \quad (2.3)$$

where t_0 is two-way time; v is stacking velocity. Traveltime t , intercept time τ , and ray parameter \vec{p}_h have the following relationship.

$$t = \tau + \vec{p}_h \cdot \vec{h} \quad (2.4)$$

The offset ray parameter is defined as

$$\vec{p}_h = \frac{dt}{d\vec{h}} = \frac{4\vec{h}}{v^2 t}. \quad (2.5)$$

Therefore \vec{h} is expressed as the function of offset ray parameter \vec{p}_h , intercept time τ and RMS velocity v .

$$\vec{h} = \frac{v^2 \vec{p}_h \tau}{4 - v^2 \vec{p}_h^2} \quad (2.6)$$

Eq. (2.6) describes the relationship between a seismic trace in midpoint–offset domain and that in τ - p domain. Summation of seismic traces in a tangential direction necessarily gives rise to noises in the process of slant stacking. If seismic traces included in the stacking are restricted within a range defined by Eq. (2.6), noises generated may be reduced. In view of inaccurate velocity in field data processing, the offset calculated by Eq. (2.6) is necessarily restricted in a limited range.

$$|\vec{h}| \in [h - A_\tau, h + A_\tau] \quad (2.7)$$

where A_τ is a time variant range which is small in shallow zones and large in deep zones. Only those seismic traces in the neighborhood of the tangent are included in slant stacking; thus we obtain a less noisy plane-wave data set (Fig. 2.63).

Azimuth-independent 3D slant stacking

Theoretically 3D slant stacking would not generate aliasing, but this problem is very common in field data processing. For example, for synthetic plane-wave shot gathers (synthetic plane-wave shot records), spatial sampling points are usually insufficient. CMP gathers usually have irregular azimuths and offset sampling

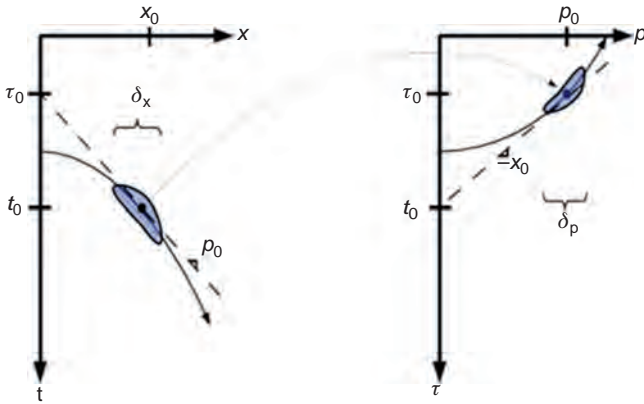


Figure 2.63 Schematic slant stacking within a limited range.

points. A CMP gather $\Psi(t, \vec{y}, \vec{h})$ is transformed into $\Phi(\tau, \vec{y}, \vec{p}_h)$ by τ - p transform, where the plane-wave vector is expressed as $\vec{p}_h = (p_{hx}, p_{hy})$ in the Cartesian coordinate system or as $\vec{p}_h = (p_{hr}, \theta)$ in the polar coordinate system. The hyperbolic time–distance curve for a CMP gather is mapped to an elliptical curve after τ - p transform. For a layout with irregular azimuths or narrow azimuth, aliasing occurs after 3D plane-wave decomposition of CMP gathers by τ - p transform. Azimuth-independent 3D slant stacking may address the issue caused by irregular azimuths and offset sampling points. The first step is to calculate the projection P_{hr} of the plane-wave vector (P_{hr}, θ) to exclude the effect of azimuth angle θ ; the second step is to stack all plane-wave vectors $(P_{hr} = \text{const}, \theta)$, which have equal absolute values and different azimuths, into a plane-wave scalar $(P_{hr} = \text{const})$, thus the amplitude is preserved and the azimuth is neglected. Azimuth-independent 3D plane-wave decomposition generates a data set similar to the analog produced by 2D plane-wave decomposition; signal to noise ratio is also improved by azimuth stacking so as to reduce aliasing after τ - p transform.

2.3.1.2 3D offset plane-wave migration

As shown in Fig. 2.64, an offset plane-wave ray parameter is defined as follows.

$$\vec{p}_h = \vec{p}_r - \vec{p}_s = \frac{\sin \theta_r}{v} - \frac{\sin \theta_s}{v} \tag{2.8}$$

where \vec{p}_r and \vec{p}_s are receiver-point and shot-point ray parameters, respectively; \vec{p}_h is expressed as the function of the half-opening angle γ between the incident ray and reflected ray and the apparent dip α of the reflecting boundary, i.e., $|\vec{p}_h| = 2 \sin \gamma \cos \alpha / v$; α is the apparent dip of the reflecting boundary in the inline direction. For a small α , \vec{p}_h is approximated as $|\vec{p}_h| \approx 2 \sin \gamma / v$, which is allowed for prestack time migration.

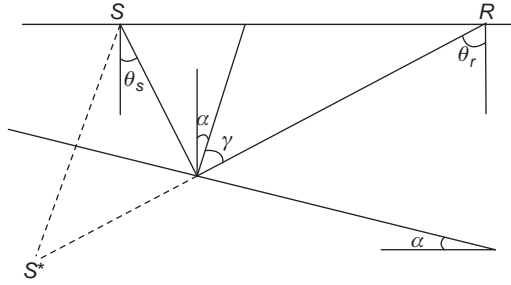


Figure 2.64 Shot–receiver geometric relationship.

In quasi-depth domain, the dispersion relation of a double square root operator (DSR) is

$$2k_{\tau} = \sqrt{\omega^2 - \frac{v^2}{4}(\vec{k}_m - \vec{k}_h)^2} + \sqrt{\omega^2 - \frac{v^2}{4}(\vec{k}_m + \vec{k}_h)^2} \quad (2.9)$$

where $\vec{k}_m = (k_{m_x}, k_{m_y})$, $\vec{k}_h = (k_{h_x}, k_{h_y})$; ω is angular frequency; v is a constant velocity. Eq. (2.9) is modified as

$$\omega = -k_{\tau} \sqrt{\left(\frac{1 + v^2 \vec{k}_m^2}{4k_{\tau}^2}\right) \left(1 + \frac{v^2 \vec{k}_h^2}{4k_{\tau}^2}\right)} \quad (2.10)$$

For a small apparent dip, γ is expressed as the function of offset wavenumber (Weglein, 1999).

$$\tan \gamma = -v \vec{k}_h / 2k_{\tau} \quad (2.11)$$

The dispersion equation of an offset plane-wave is derived by substituting Eq. (2.11) into Eq. (2.10).

$$\frac{4}{v^2} k_{\tau}^2 + \vec{k}_m^2 - 4 \frac{\omega^2}{v^2} \cos^2 \gamma = 0 \quad (2.12)$$

Eq. (2.12) is expressed as follows in the frequency–space domain.

$$\left(\frac{4}{v^2} \frac{\partial^2}{\partial \tau^2} + \frac{\partial^2}{\partial x^2} + \frac{\partial^2}{\partial y^2}\right) \tilde{U} + 4 \frac{\omega^2}{v^2} \cos^2 \gamma \tilde{U} = 0 \quad (2.13)$$

The 3D offset plane-wave equation for a constant-velocity medium is derived by replacing $\cos \gamma$ in Eq. (2.13) with the offset plane-wave vector \vec{p}_h .

$$\left(\frac{4}{v^2} \frac{\partial^2}{\partial \tau^2} + \frac{\partial^2}{\partial x^2} + \frac{\partial^2}{\partial y^2}\right) \tilde{U} + 4 \frac{\omega^2}{v^2} \left(1 - \frac{v^2 \vec{p}_h^2}{4}\right) \tilde{U} = 0 \quad (2.14)$$

Eq. (2.14) is valid for the media with gentle lateral velocity changes. The single-square-root (SSR) approximate expression of Eq. (2.13) is

$$\frac{\partial \tilde{U}}{\partial \tau} = -i\omega \sqrt{1 - \frac{v^2 \bar{p}_h^2}{4}} \cdot \sqrt{1 + \frac{v^2}{4\omega^2 \left(1 - \frac{v^2 \bar{p}_h^2}{4}\right)} \left(\frac{\partial^2}{\partial x^2} + \frac{\partial^2}{\partial y^2}\right)} \tilde{U} \quad (2.15)$$

After continued fraction expansion of the right term in Eq. (2.15) and Laplace operator splitting in x and y directions, the following equation is derived based on the approach of finite difference proposed by Clearbout (1985).

$$\frac{\partial U(x, y, \tau; \omega)}{\partial \tau} = -i\omega \sqrt{1 - \frac{v^2(x, y, \tau) p_{hx}^2}{4}} U(x, y, \tau; \omega) \quad (2.16a)$$

$$\begin{aligned} & \frac{\partial}{\partial \tau} \left[1 + \gamma_x \Delta x^2 \frac{\delta^2}{\delta x^2} + \gamma_y \Delta y^2 \frac{\delta^2}{\delta y^2} + \frac{bv^2(x, y, \tau)}{4\omega^2 \left(1 - \frac{v^2(x, y, \tau) p_{hx}^2}{4}\right)} \left(\frac{\delta^2}{\delta x^2} + \frac{\delta^2}{\delta y^2}\right) \right] U(\omega, x, y, \tau, p_{hx}) \\ & = -i \frac{av^2(x, y, \tau)}{2\omega \sqrt{1 - \frac{v^2(x, y, \tau) p_{hx}^2}{4}}} \left(\frac{\delta^2}{\delta x^2} + \frac{\delta^2}{\delta y^2}\right) U(\omega, x, y, \tau, p_{hx}) \end{aligned} \quad (2.16b)$$

Eq. (2.16a,b) is the fundamental equation for offset plane-wave extrapolation and is solved by finite difference operators.

2.3.1.3 Method testing

Two sections after 3D Kirchhoff-PSTM (realized by OMEGA system) and 3D offset plane-wave pre-stack time migration (PSTM) are shown in Figs. 2.65 and 2.66, respectively. The latter exhibits a great improvement in diffracted wave convergence (*red circles*) and lateral resolution compared with the former; thus fractures are imaged more clearly.

2.3.2 Time-shift depth migration and velocity analysis in angle domain

The biggest challenge to image a complex structure is how to build a velocity model. Velocity analysis is usually made on angle-domain common-image gathers

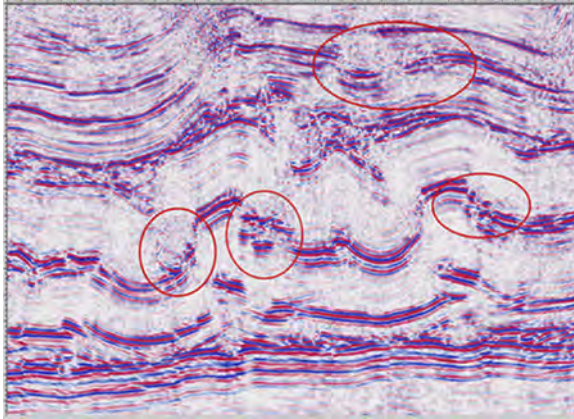


Figure 2.65 Section by Kirchhoff integral migration.

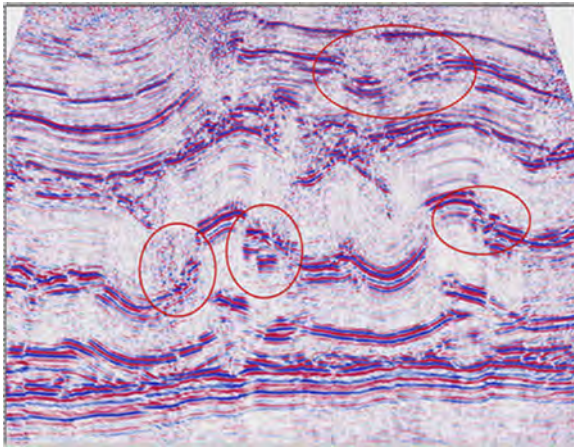


Figure 2.66 Section after 3D offset plane-wave migration.

(ADCIGs) because they contain information on elastic parameter variations and migration velocity. If the images after migration achieve the most coherent display, migration velocity is judged to be accurate. Doherty and Claerbout (1974) presented an approach for depth focusing analysis (DFA), which uses the difference between the depth of focusing and imaging depth after nonzero-time imaging to update the velocity model. Theoretically sorting ADCIGs from preimaging data or postimaging data is essentially the process of extracting reflection coefficients corresponding to different incident directions, although these angle-related reflection coefficients are not completely equal to actual coefficients. If migration velocity is not correct, the events in ADCIGs could not be flattened; thus residual curvature of the event is used to update the velocity model.

There are some problems related to focusing analysis and residual curvature analysis. In focusing analysis, the velocity field is diagnosed based on diffracted energy focusing and the difference between depth of focusing and imaging depth. If signal to noise ratio is low, it is difficult to judge energy focusing on imaging gathers and thus to determine the depth of focusing. Residual curvature analysis only concerns event flattening in imaging gathers. Residual curvature is related to the error of migration velocity. It is necessary to integrate focusing analysis with residual curvature analysis on time-shift angle-domain imaging gathers to improve the accuracy of migration velocity.

2.3.2.1 Imaging conditions for velocity analysis

The image of migration is reflection amplitudes extracted from seismic records in accordance with the imaging condition in the process of wavefield extrapolation. For the SSR equation, the imaging condition is

$$\mathbf{u}(\mathbf{x}, z, t) = \mathbf{u}_s(\mathbf{x}, z, t) * \mathbf{u}_r(x, z, t) \quad (2.17)$$

$$\mathbf{I}(\mathbf{x}, z) = \mathbf{u}(\mathbf{x}, z, t = 0) \quad (2.18)$$

where $\mathbf{u}(\mathbf{x}, z, t)$ is the wavefield at (\mathbf{x}, z) and time t ; $*$ denotes cross-correlation; $\mathbf{I}(\mathbf{x}, z)$ is the imaging result at (\mathbf{x}, z) .

Similarly, the imaging condition for the DSR equation is expressed in the frequency–wavenumber domain.

$$\mathbf{I}(\mathbf{x}, z) = \int d\omega \int d\mathbf{k}_h \tilde{p}(\omega, \mathbf{x}, \mathbf{k}_h; z) \quad (2.19)$$

where $\tilde{p}(\omega, \mathbf{x}, \mathbf{k}_h; z)$ is the wavefield in the frequency domain. The integral with respect to ω and \mathbf{k}_h expresses the imaging condition for the DSR equation: $t = 0$ and $\mathbf{h} = 0$.

The imaging condition is expanded to $t \neq 0$ (conventional DFA uses the results of wavefield focusing at $t \neq 0$) or $\mathbf{h} \neq 0$ (residual curvature analysis uses the results of wavefield imaging at different offsets) for velocity model update. Offset-domain common-image gathers (ODCIGs) are first derived from nonzero-offset imaging and then converted into ADCIGs through slant stacking. The imaging conditions for SSR and DSR migration to obtain ODCIGs are expressed in frequency domain as follows.

$$\mathbf{I}(\mathbf{x}, \mathbf{h}, z) = \int d\omega \tilde{\mathbf{u}}_s(\mathbf{x} - \mathbf{h}, z, \omega) * \tilde{\mathbf{u}}_r(\mathbf{x} + \mathbf{h}, z, \omega) \quad (2.20)$$

$$\mathbf{I}(\mathbf{x}, \mathbf{h}, z) = \int d\omega \int d\mathbf{k}_h e^{i\mathbf{k}_h \mathbf{h}} \tilde{p}(\omega, \mathbf{x}, \mathbf{k}_h; z) \quad (2.21)$$

where the superscript $*$ denotes the conjugate. ODCIGs \mathbf{I} are then converted into ADCIGs through slant stacking. The parameter h here does not refer to land offset; in fact it involves the angle of wave incident upon the reflecting boundary and is entitled local offset.

The wavefield at $\mathbf{h} = 0$ is extracted for DFA imaging, followed by searching for the time or depth (of focus) corresponding to the point with the largest energy. The time-shift imaging condition is given by introducing a time-shift τ in the SSR equation.

$$\mathbf{u}(\mathbf{x}, z, t, \tau) = \mathbf{u}_s(\mathbf{x}, z, t - \tau) * \mathbf{u}_r(\mathbf{x}, z, t + \tau) \quad (2.22)$$

$$\mathbf{I}(\mathbf{x}, z, \tau) = \mathbf{u}(\mathbf{x}, z, t = 0, \tau) \quad (2.23)$$

The gathers calculated by Eqs. (2.22) and (2.23) are entitled TSCIGs here. Through slant stacking of Eq. (2.23) by

$$\tan \gamma = -k_h/k_z$$

pseudo-ADCIGs are obtained. The time-shift focusing condition expressed by Eqs. (2.22) and (2.23) is simply formulated in frequency domain.

$$\mathbf{I}(\mathbf{x}, z, \tau) = \sum_{\omega} \tilde{\mathbf{u}}_s(x, z, \omega) * \tilde{\mathbf{u}}_r(x, z, \omega) e^{2i\omega\tau}, \quad (2.24)$$

Following imaging condition for DSR migration is equivalent to Eq. (2.24).

$$\mathbf{I}(\mathbf{x}, z, t) = \int d\omega \tilde{p}(\omega, \mathbf{x}, ; z) e^{2i\omega t} \quad (2.25)$$

The time-shift imaging condition with τ is essentially a depth focusing condition for nonzero-time migration. A zero time shift $\tau = 0$ indicates energy focusing at $t = 0$, which means migration velocity is correct.

The time-space-shift imaging condition for SSR migration is formulated as follows to diagnose migration velocity at different τ .

$$\mathbf{u}(\mathbf{x}, z, t, \mathbf{h}, \tau) = \mathbf{u}_s(\mathbf{x} - \mathbf{h}, z, t - \tau) * \mathbf{u}_r(\mathbf{x} + \mathbf{h}, z, t + \tau) \quad (2.26)$$

$$\mathbf{I}(\mathbf{x}, z, \mathbf{h}, \tau) = \mathbf{u}(\mathbf{x}, z, t = 0, \mathbf{h}, \tau) \quad (2.27)$$

$\mathbf{I}(\mathbf{x}, z, \mathbf{h}, \tau)$ in Eq. (2.27) is termed time-shift offset-domain common-image gathers (TSODCIGs). For DSR migration, the time-space-shift imaging condition is expressed as

$$\mathbf{I}(\mathbf{x}, \mathbf{h}, z, \tau) = \int e^{2i\omega\tau} d\omega \int d\mathbf{k}_h e^{i\mathbf{k}_h \cdot \mathbf{h}} \tilde{p}(\omega, \mathbf{x}, \mathbf{k}_h; z) \quad (2.28)$$

TSODCIGs $\mathbf{I}(\mathbf{x}, z, \mathbf{h}, \tau)$ are converted into time-shift angle-domain common-image gathers (TSADCIGs) through slant stacking $\gamma = -k_h/k_z$.

$$\mathbf{I}(\mathbf{x}, z, \mathbf{h}, \tau) \Rightarrow \mathbf{I}(\mathbf{x}, z, \gamma, \tau) \quad (2.29)$$

Wave equation prestack migration involves reverse-time extrapolation of the receiver wavefield and the application of the imaging condition to extract zero-time and zero-offset images. If migration velocity is incorrect, zero-time and zero-offset conditions cannot be satisfied simultaneously at the depth of wavefield extrapolation. Migration velocity is diagnosed in accordance with reflection events in imaging gathers. Velocity analysis uses the imaging condition and judging criterion of velocity error to update the velocity model with appropriate correcting methods and strategies. Two criteria have been used to verify the velocity model. One is consistent depths for zero-time imaging and zero-offset focusing presented by Doherty and Claerbout in DFA velocity analysis; the other is flattening of common-imaging-point (CIP) gathers proposed by Al-Yahya (1989) in residual curvature velocity analysis. As per the former, the depth (of imaging) for zero-time imaging condition is consistent with the depth (of focusing) for zero-offset imaging condition if migration velocity is correct. A higher velocity results in the depth of imaging being larger than the depth of focusing, whereas a lower velocity results in the depth of imaging being smaller than the depth of focusing. As per the latter, CIP gathers are flattened if migration velocity is correct. A higher velocity results in decurved events and a lower velocity in upcurved events.

2.3.2.2 Velocity update

A higher or lower velocity could be diagnosed through observing TSADCIGs; in addition we need a formula to update the velocity field. For horizontally layered media, extrapolating to a wrong depth with correct velocity is equal to extrapolating to a correct depth with inaccurate velocity.

$$\frac{Z_f}{v} = \frac{Z}{v_m} \quad (2.30)$$

where Z_f , Z , v and v_m are depth of focusing, true depth, true velocity, and migration velocity, respectively.

The depth of focusing and true depth have the following relation.

$$\frac{Z - Z_f}{v_m} = \tau \quad (2.31)$$

τ is the time shift at focusing resulting from incorrect migration velocity. If migration velocity is correct, τ is equal to zero. The following equation is obtained by substituting Eq. (2.30) into Eq. (2.31).

$$\frac{Z_f}{v} = \frac{Z}{v_m} + \tau \quad (2.32)$$

The velocity of horizontally layered media is then updated by the following equation.

$$v = \frac{Z_f v_m}{Z_f + \tau v_m} \quad (2.33)$$

The dip of reflecting boundary is included in velocity updating. Assume the focusing reflector is parallel to the imaging focusing reflector.

$$\cos \alpha = \frac{v_m \tau}{Z - Z_f} \quad (2.34)$$

Integrate the above equation with Eq. (2.30).

$$\frac{Z_f}{v} = \frac{Z}{V_m} + \frac{\tau}{\cos \alpha} \quad (2.35)$$

Migration velocity for the nonhorizontal reflector is updated by the following equation.

$$v = Z_f v_m / \left(Z_f + \frac{\tau v_m}{\cos \alpha} \right) \quad (2.36)$$

z, α, γ are true reflector depth, true reflector dip, and actual incident angle, respectively; z_m, α_m, γ_m are imaged depth, dip and incident angle, respectively; z_f, α_f, γ_f are focused depth, dip and incident angle, respectively. Assuming $\alpha_m = \alpha_f = \alpha$, $\gamma_m = \gamma_f = \gamma$, if velocity error is small,

$$\cos \alpha = \frac{\tau \cdot \bar{v}}{(z_f - z_m(\gamma)) \cos \gamma} \quad (2.37)$$

where τ is the focusing time shift and \bar{v} is the average velocity from the imaging point to focusing point. Use Eq. (2.37) to calculate reflector dip. For a monocline with constant velocity,

$$t = t_m = \frac{2z}{v} \frac{\cos \alpha \cos \gamma}{\cos^2 \alpha - \sin^2 \gamma} \quad (2.38)$$

For migration velocity $v_m \neq v$, the focusing time is

$$t_f = \frac{2z_f}{v_m} \frac{\cos \alpha_f \cos \gamma_f}{\cos^2 \alpha_f - \sin^2 \gamma_f} \quad (2.39)$$

Assuming velocity error and dip angle are small, if $\alpha_m = \alpha_f = \alpha$, $\gamma_m = \gamma_f = \gamma$,

$$\tau = \frac{1}{2}(t_f - t) = \frac{\cos \alpha \cos \gamma_f}{\cos^2 \alpha - \sin^2 \gamma} \left(\frac{z_f}{v_m} - \frac{z}{v} \right) \quad (2.40)$$

In view of one-way time in Eq. (2.39) and two-way time in Eqs. (2.38) and (2.39), the right term in Eq. (2.40) is multiplied by 1/2. Substitute Eq. (2.40) into Eq. (2.37), then we get

$$v = \frac{z \cdot v_m}{z_f - (z_f - z_m(\gamma)) \cdot (\cos^2 \alpha - \sin^2 \gamma)} \quad (2.41)$$

When $\gamma = 0$, above expression is simplified to be

$$v = \frac{z \cdot v_m}{z_f - (z_f - z_m(\gamma)) \cdot \cos^2 \alpha} \quad (2.42)$$

Eq. (2.42) is applied to velocity updating on TSCIGs. Assuming $\alpha = \gamma = 0$,

$$v = \frac{z}{z_m} v_m \quad (2.43)$$

Eq. (2.43) is used for depth focusing for horizontally layered media.

v_m, z_f, γ in Eq. (2.41) are known and dip angle α may be derived by ray-based depth migration scanning; only true depth z is unknown. Assume

$$z \approx \frac{z_m(0) + z_f}{2} \quad (2.44)$$

Substitute Eq. (2.44) into Eq. (2.41), then we get

$$v = \frac{1}{2} \frac{(z_m(0) + z_f) \cdot v_m}{z_f - (z_f - z_m(\gamma)) \cdot (\cos^2 \alpha - \sin^2 \gamma)} \quad (2.45)$$

Eq. (2.45) is still based on DFA velocity analysis to update velocity. Next we discuss whether or not the updating function (2.45) is applicable to a complex structure. A relative velocity Δv is defined for the convenience of discussion.

$$\Delta v = v - v_m = \frac{(z_f - z_m(\gamma)) \cdot (\cos^2 \alpha - \sin^2 \gamma) - \frac{(z_f - z_m(0))}{2}}{(z_f - (z_f - z_m(\gamma)) \cdot (\cos^2 \alpha - \sin^2 \gamma))} v_m \quad (2.46)$$

Assume without loss of generality that migration velocity is small; thus Δv has to be greater than zero to stabilize Eq. (2.46). $\cos^2 \alpha - \sin^2 \gamma > 0$ or $\alpha + \gamma < \pi/2$ in the equation is determined by land layout; it is always true if the reverse branch is not taken into account. The depth of imaging is smaller than the depth of focusing, i.e., $\Delta z > 0$, if migration velocity is small. For a Δv greater than zero, the numerator in Eq. (2.46) has to be greater than zero; this means the dip angle would not exceed 45 degree in Eq. (2.46). In addition, in view of the convergence of velocity analysis, the dip angle in field data processing should not exceed 40 degree.

This limitation of dip angle is induced by the assumption of small angle in velocity updating. In fact for a large dip angle, angle-domain gathers derived from slant stacking discussed above also have large errors.

In order to get stable velocity updating at a large dip angle, assuming velocity error is small and true depth is equal to the depth of focusing, Eq. (2.40) can be modified to be

$$v = \frac{z_f \cdot v_m}{z_f - (z_f - z_m(\gamma)) \cdot (\cos^2 \alpha - \sin^2 \gamma)}. \quad (2.47)$$

This equation may ensure velocity updating in the right direction when dip angle is large.

2.3.2.3 Velocity analysis workflow

The above formulas are derived for velocity updating under the assumption of a single dipping formation. Therefore velocity updating is realized by layer stripping. The workflow is detailed as follows.

1. Interpret all velocity horizons on the whole dataset after stacking or time migration. Select enough control points on each velocity horizon for velocity analysis. In order to reduce the workload of gather sorting and velocity updating, only those gathers on control points are extracted for velocity analysis. Gathers on other points are derived from interpolation and smoothing.
2. Calculate the initial interval velocity field using a conventional method.
3. Convert a horizon, as well as control points, from time domain into depth domain. Scan dip angle on the horizon in depth domain. Extract TSCIGs and TSADCIGs at control points on the horizon; TSCIGs are displayed in energy. Extract relevant parameters (time shift τ , depth of imaging and depth of focusing on TSCIGs and depth of imaging corresponding to different incident angle on TSADCIGs) for velocity analysis on TSCIGs or TSADCIGs.
4. Use Eq. (2.47) to update velocity on all control points on the horizon, followed by interval velocity interpolation and smoothing.
5. Repeat steps (3) and (4) until the interval velocity for this horizon is good enough. Begin velocity analysis for the next horizon. Repeat this process until all horizons are analyzed. The output is the updated velocity model.

2.3.2.4 Method testing

Fig. 2.67A and B show migrated sections using the initial velocity model and the updated model, respectively. The latter exhibits more distinct reflections than the former. Fig. 2.68 shows ADCIGs extracted using the initial model and the updated model. The latter exhibits more horizontal events than the former.

2.3.3 How to improve resolution of diffraction imaging

In equivalent offset prestack time migration based on the scattering theory, each subsurface point is taken as a scatter point and seismic traces that involve the same

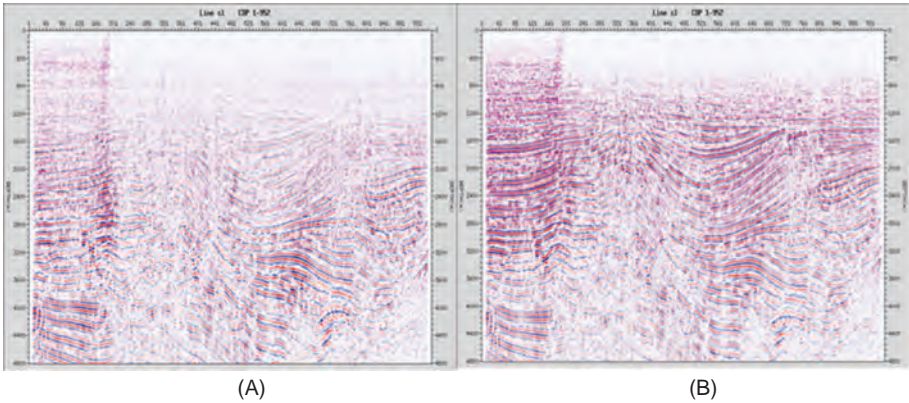


Figure 2.67 Migrated sections using the initial velocity model (A) and the updated model (B).

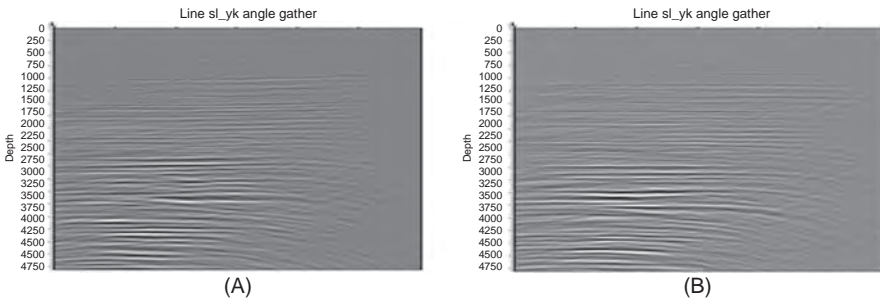


Figure 2.68 ADCIGs extracted using the initial velocity model (A) and the updated model (B).

scatter point within an offset range are collected to form a common-scatter-point (CSP) gather; Kirchhoff migration is then performed on CSP gathers. A CSP gather involves all offsets within the migration aperture; thus the fold and signal to noise ratio may be large. This technique is practical for imaging complicated heterogeneous structures resulting in abundant diffracted and scattered waves and low S/N. Due to better energy focusing on velocity spectra, velocity analysis on CSP gathers may yield a more accurate velocity model. Junjie et al. (2010) and Wang et al. (2007) used equivalent offset prestack time migration in imaging low S/N data to improve the accuracy of migration and minor-fault imaging.

The objective of seismic migration is to improve lateral resolution which is particularly important for fracture-vug carbonate reservoir description because it determines the accuracy of the size and geometry for delineating fracture-vug reservoir. Here we present an approach of diffraction imaging based on equivalent offset prestack time migration, which improves lateral resolution by using signal decomposition to suppress mapping noises from neighboring diffraction points.

2.3.3.1 Diffracted waves on CSP gathers

Bancroft et al. (1998) and Margrave et al. (1999) discussed equivalent offset pre-stack time migration. CMP gathers are mapped to CSP gathers by DSR equation and then Kirchhoff migration is performed on CSP gathers.

For a diffraction point with vertical two-way time of τ , the travel time t is expressed by the following DSR equation.

$$t^2 = \tau^2 + \frac{4h^2}{v^2} + \frac{4x^2}{v^2} - \frac{16h^2x^2}{v^4t^2} \quad (2.48)$$

x is the coordinate of shot-receiver midpoint; h is semi-offset; v is velocity. Using the equivalent offset transform,

$$h_E^2 = x^2 + h^2 - \left(\frac{2xh}{tv}\right)^2 \quad (2.49)$$

CMP gathers in (h, t) domain are mapped to CSP gathers in (h_E, t) domain, where h_E is the equivalent semi-offset. The travel time is then expressed by following the SSR equation instead of the DSR equation after the transformation by Eq. (2.49).

$$t = \sqrt{\tau^2 + \frac{4h_E^2}{v^2}} \quad (2.50)$$

A CSP gather has a hyperbolic time–distance curve.

Assuming that the projection of the diffraction point is x_0 on the ground, the travel time t observed is described as follows:

$$t^2 = \tau^2 + \frac{4h^2}{v^2} + \frac{4(x-x_0)^2}{v^2} - \frac{16h^2(x-x_0)^2}{v^4t^2} \quad (2.51)$$

After the equivalent offset transform, the travel time t of the diffracted wave observed at $x = 0$ in the CSP gather is expressed by the following equation:

$$t^2 = \tau^2 + \frac{4h_E^2}{v^2} - \frac{4x_0}{v^2}(2x-x_0)\left(1 - \frac{4h^2}{v^2t^2}\right) \quad (2.52)$$

As per Eq. (2.52), diffracted energy from neighboring diffraction points is mapped to noises in the CSP gather; these noises are not random and entitled mapping noises. If $h \ll vt/2$, Eq. (2.52) is approximated to be

$$t^2 = \tau^2 + \frac{4(h_E - x_0)^2}{v^2} \quad (2.53)$$

Near-offset energy from the diffraction point is mapped onto the hyperbola with its vertex at $h_E = x_0$. As per theoretical calculation, coherent mapping noises are mainly composed of near-offset energy.

Fig. 2.69 shows the results for a theoretical model. The velocity model with eight velocity anomalies in the homogeneous background is shown in Fig. 2.69A. Fig. 2.69B shows gathers of CDPs 32, 40 and 48 (whose locations are indicated in Fig. 2.69A) from forward modeling. Fig. 2.69C shows corresponding CSP gathers. CSP gathers exhibit more distinct diffracted waves than CMP gathers. Diffracted waves from the common scatterpoint on the CSP gather exhibit a hyperbolic event, while those from neighboring diffraction points behave as mapping noises, which are demonstrated by a hyperbolic event with its vertex deflecting from zero-offset.

The existence of mapping energy from neighboring diffraction points may blur the images of migration and reduce lateral resolution. In order to improve lateral resolution of diffraction imaging, mapping noises from neighboring diffraction points should be suppressed before imaging CSP gathers.

2.3.3.2 Mapping noise suppression

Diffracted waves from the common scatterpoint form hyperbolic events on the CSP gather after the equivalent offset transform, whereas diffraction energy from neighboring diffraction points behaves as coherent mapping noises. After normal moveout (NMO) correction, hyperbolic events become horizontal and coherent mapping noises appear as tilted events, which may be eliminated by dip filtering. There are some methods of dip filtering, of which the least-squared dip decomposition (by the Radon transform, Nowak and Imhof, 2004) is the most effective. The key point is how to separate signals and noises with small moveout.

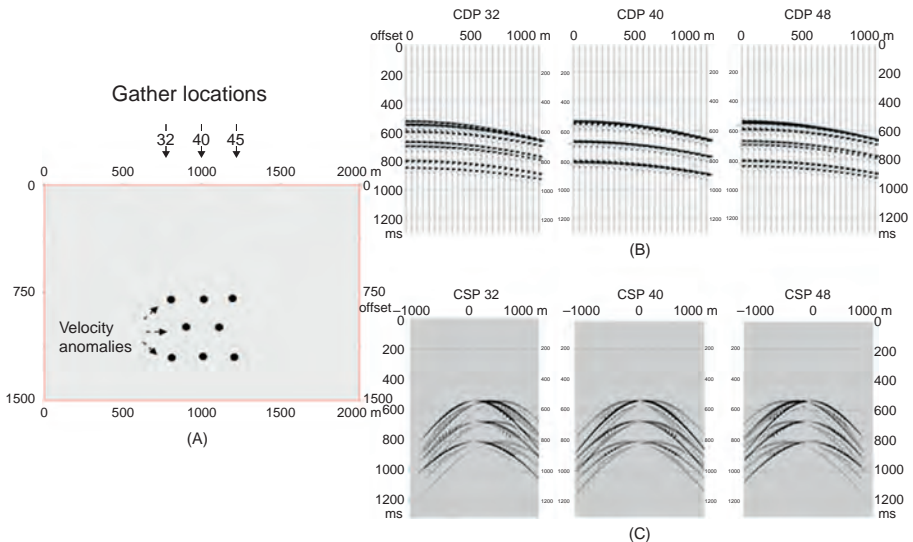


Figure 2.69 Velocity anomalies induced diffracted waves on CMP and CSP gathers. (A) Velocity model; (B) CMP gathers; (C) CSP gathers.

2.3.3.3 Theoretical modeling

A velocity model is designed to test lateral resolution improvement by suppressing mapping noises generated after the equivalent offset transform. The model shown in Fig. 2.70A contains 11 circular caverns with diameter of 200, 180, 160, ... 40, 20 and 10 m. Shot gathers are calculated by acoustic wave equation. The recording geometry is designed with a trace interval of 20 m, 360 active traces, 90 folds, and 220 shots.

Fig. 2.70B and C compare the results of CSP imaging before and after noise suppression. Coherent noise suppression improves cavern imaging and lateral resolution.

2.3.3.4 Field data testing

Fig. 2.71 compares the result from Kichhoff prestack migration and that from CSP imaging after mapping noise suppression with the same migration aperture, velocity model, bin size, and folds. Diffracted waves have not been migrated entirely by Kichhoff migration; some residual arcs could be observed on the section. CSP imaging by the equivalent offset transform after mapping noise suppression generates the result with good continuity and lateral resolution; fault points and caverns have been imaged clearly.

2.4 Reservoir description and fluid detection

Physical and numerical simulations indicate that the seismic responses of fracture-vug reservoirs vary with the size and shape of fractures and vugs, the filling material and degree in vugs, the spatial configuration and extension of reservoir, and the properties of wall rock. In order to improve the accuracy of prediction, target-oriented techniques are used to predict different types of reservoirs. Geologic and logging data are used to constrain sensitive attribute analysis. Comprehensive description of a fracture-vug reservoir is finally realized by integrating the results derived from different methods.

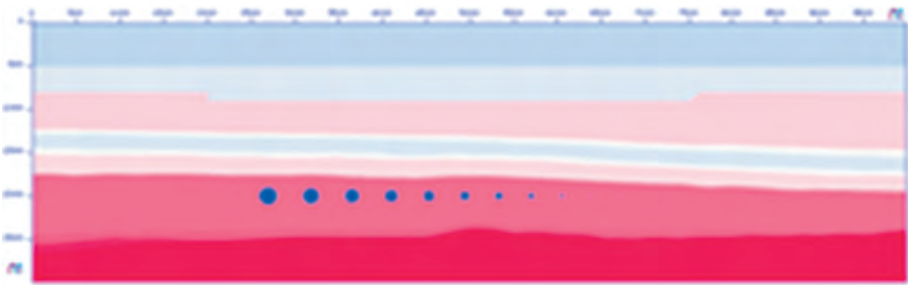
2.4.1 Reservoir prediction

2.4.1.1 Cave prediction

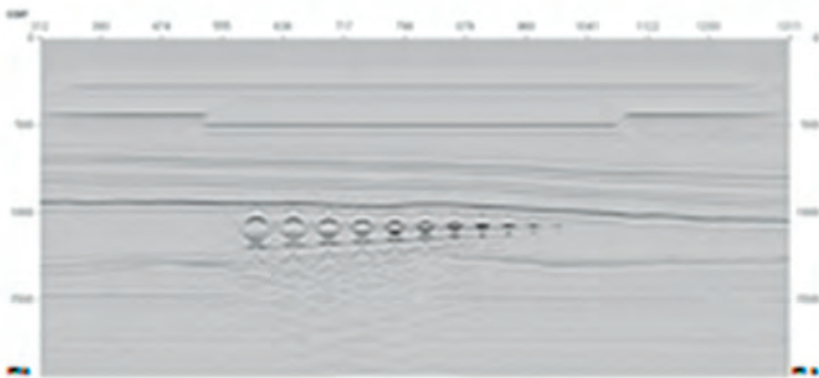
The existence of caves in a reservoir may result in amplitude anomalies and changing reflection configuration on seismic section. Due to limitation of resolution and imaging, seismic techniques should be target-oriented. Some techniques, e.g., reflection configuration analysis, strong amplitude clustering, and discontinuity detection, have been proved to be effective for cave prediction.

Reflection configuration analysis

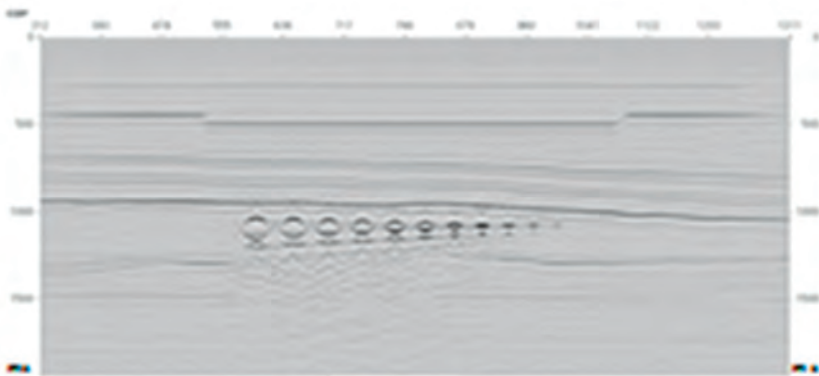
Reflections from near-surface weathering crust and internal structures may be classified into two types. One is strong short reflections (i.e., bead-like



(A)



(B)



(C)

Figure 2.70 CSP imaging before and after mapping noise suppression. (A) Velocity model; (B) CSP imaging; (C) CSP imaging after mapping noise suppression.

reflections) from a relatively intact cave, which are caused by large impedance contrast between cave top and bottom and wall rocks. The other is chaotic reflections from a cave system which is composed of several caves and complicated by faults.

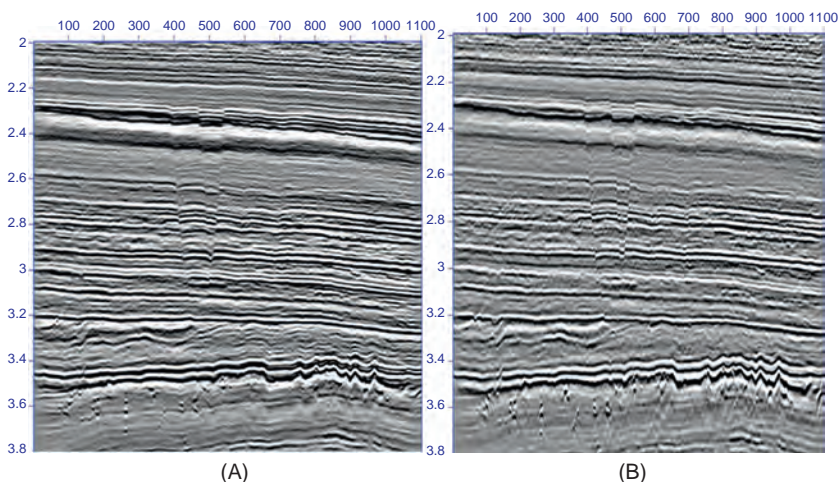


Figure 2.71 Imaging results. (A) CSP imaging after mapping noise suppression; (B) Kichhoff prestack time migration.

Large amounts of drilling and seismic data reveal that the large cave system in the Tahe prospect exhibits three reflection configurations, i.e., varied configuration at the top, blank reflections in the middle part, and strong discontinuous reflections in the lower part. Relatively stable configuration with strong amplitude occurs above the zone with underdeveloped vugs (Fig. 2.72). Target signatures are highlighted after data processing (by extracting instantaneous amplitude, average amplitude and threshold amplitude, scaling up and scaling down, waveform boxing, frequency division filtering, amplitude modulated carrier, etc.) (Fig. 2.72). Upper, middle, and lower reflection configurations may be overlaid, followed by pattern extraction, to predict fracture-vug units.

Strong amplitude clustering

According to the well and seismic data acquired in the Tahe prospect, caverns/caves/vugs, solution channels, and underground streams in this area usually appear as strong short reflections (i.e., bead-like reflections) on seismic sections, which could be detected by strong amplitude clustering. The principle of strong amplitude clustering (Fig. 2.73) is extrapolation from strong amplitude to weak amplitude and extraction of bead-like reflections by various methods, such as threshold interception, voxel aggregation, neighboring-point search and connection, eliminating geologically irrelevant aggregate, to identify potential karst cave/vug units.

Discontinuity detection

Discontinuity detection is used to highlight weak reflections, chaotic reflections, and dissimilarities which may be caused by pores, fractures, and solution channels.

Multiwindow edge preservation and dip correction use the eigen structure of multitrace covariance matrix to accentuate dissimilarities in the data. There are several advantages. (1) The technique of multiwindow edge preservation enhances

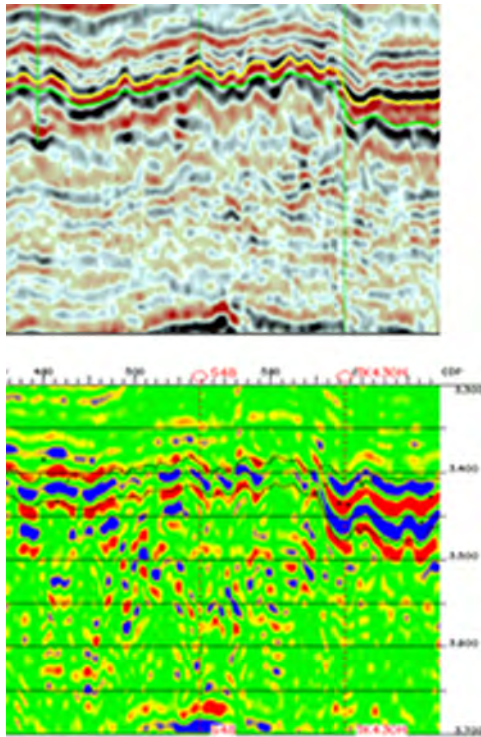


Figure 2.72 Seismic section across Well S48 and reflection signatures.

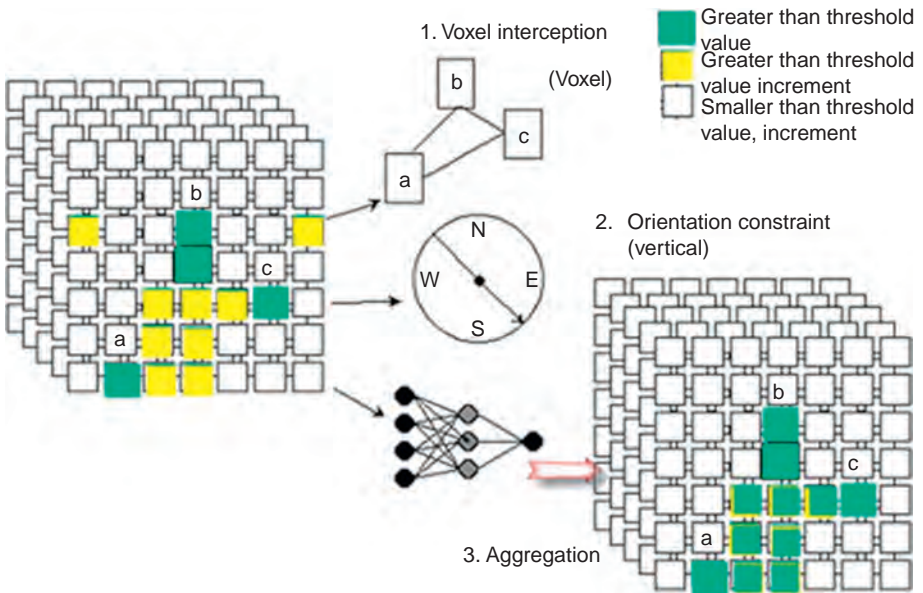


Figure 2.73 Principle of strong amplitude clustering.

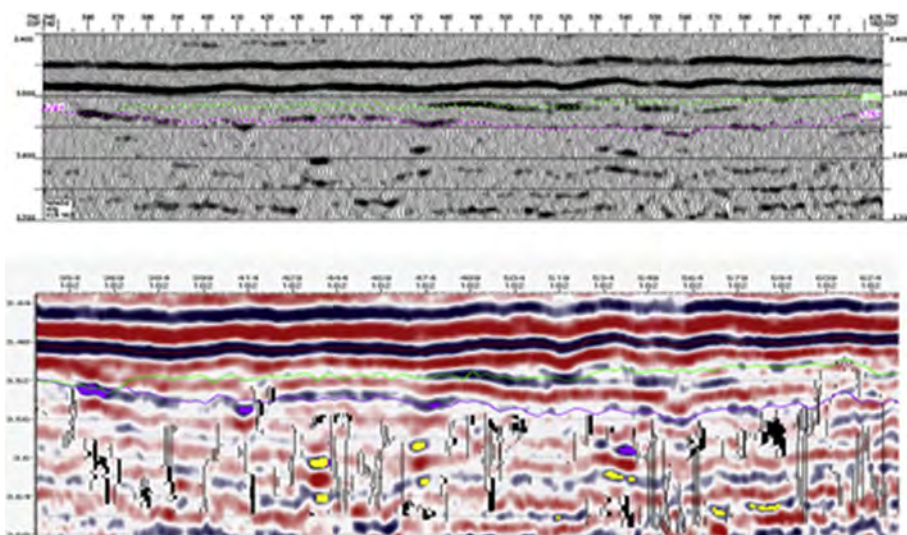


Figure 2.74 Seismic section of INLINE180 (upper) and strong amplitude clustering overlaid by the result of discontinuity detection.

boundary reflections in the data. (2) Dip correction eliminates the effect of stratigraphic dip. (3) Multitrace covariance matrix is used to improve credibility and S/N. (4) Spatial weighting coefficients in multitrace cross-correlation are not assigned manually; thus the technique is more applicable to low S/N data. (5) Face and volume clustering eliminates the effect of horizontal or low-angle data to highlight vertical minor faults inside carbonate rocks. (6) These techniques enhance vertical continuity of anomalies and eliminate local scattered anomalies less relevant or irrelevant to targets; thus the accuracy of detection is improved.

Fig. 2.74 shows abnormal reflections at 10–120 ms below T74, a time horizon of the Ordovician weathering crust. Upper and lower strong amplitude reflections (*purple* and *yellow*) appear as dot and line shapes (filtered by different threshold values). Vertical discontinuous belts (*black*) and potential high-energy absorption units (*black* blocks) are superimposed upon strong amplitude reflections. These results demonstrate reflection variations caused by the existence of fractures and minor faults and high-energy absorption related to cave groups which are complicated by fractures.

2.4.1.2 Fracture prediction

Curvature

As per large-scale plate experiments, microfractures tend to occur at the top of an anticline, the bottom of a syncline, and both sides of a fault, where tectonic deformation reaches a maximum. The density of microfractures is related to the curvature of deformation (Price and Cosgrove, 1990).

Coherence tomography is used to calculate dip, azimuth, and curvature attributes with high-precision. Multiwindow edge-preserved plane scanning combined with curved surface scanning improves the credibility of dip estimation. Reflection signatures on both sides of a fault could be detected more accurately by multiwindow scanning.

The maximum positive curvature in a set of orthogonal curvature volumes corresponds to convex events, where abundant unfilled extensional microfractures tend to occur. The maximum negative curvature corresponds to concave events, where abundant extensional cracks which have already been filled tend to occur (Fig. 2.75).

Neural networks

Attributes (e.g., coherence, amplitude gradient and azimuth) extracted from the traces across faults or fractures are taken as the samples for training the network. A neural network may solve the problems of effective sample clustering and effective attribute (dominant attribute) prediction (confidence probability) so as to predict fractured zones (Fig. 2.76).

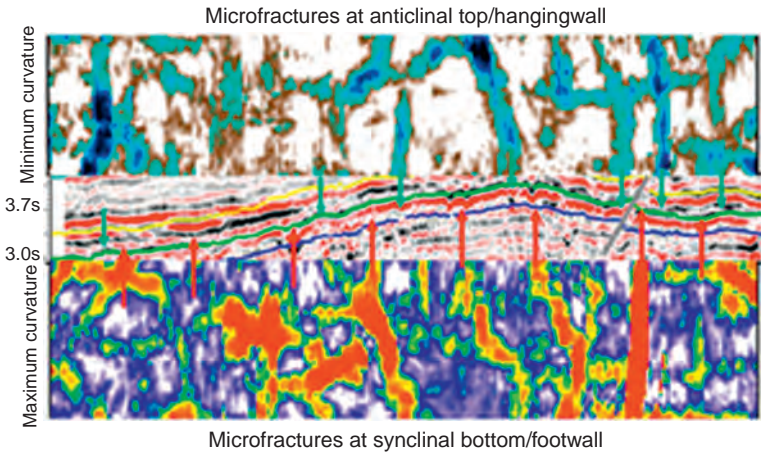


Figure 2.75 Correspondence between curvature-detected microfractures and convex and concave events.

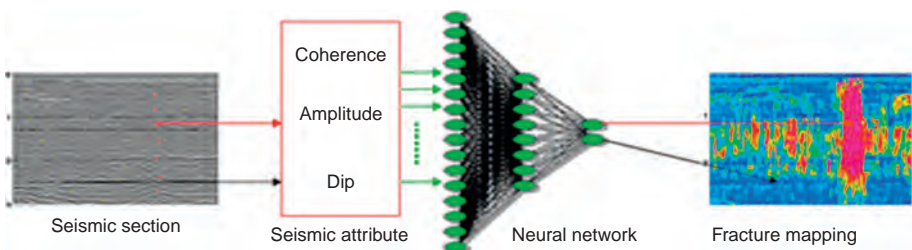


Figure 2.76 Schematic semi-automatic fracture detection by neural network.

2.4.2 Prestack azimuthal anisotropy-based fracture detection

The study of fracture-induced azimuthal anisotropy is usually based on several kinds of models, e.g., transverse isotropy with a vertical symmetry axis (VTI), transverse isotropy with a HTI, orthotropy, and monoclinic anisotropy. These models often differ greatly from actual scenarios. A model of transverse isotropy with a tilted axis (TTI) is more feasible compared with the above models.

2.4.2.1 Fracture prediction based on residual P-wave NMO for TTI media

Residual NMO for TTI media

Taylor expansion of two-way time t^2 is

$$t^2 = A_0 + A_2X^2 + A_4X^4 \quad (2.54)$$

X is source-to-receiver distance.

$$A_0 = t_0^2; \quad A_2 = \left. \frac{d(t_0^2)}{dX^2} \right|_{X=0}; \quad A_4 = \left. \frac{1}{2} \frac{d}{dX^2} \left[\frac{d(t_0^2)}{dX^2} \right] \right|_{X=0} \quad (2.55)$$

where $t_0 = t(0)$ is zero-offset time; A_2 is related to NMO velocity and $A_2 = V_{nmo}^{-2}$. The quadratic term at the right side of Eq. (2.54) corresponds to the hyperbolic time-distance curve and the quartic term describes the nonhyperbolic time-distance curve.

A hyperbolic time-distance curve based on NMO velocity is incorrect for offset-to-depth ratio of 1.5–2.0, while Eq. (2.54) better describes time-distance relation at far offsets.

Andres Pech and Ilya Pech et al. (2003) developed the formula of quartic moveout coefficient for TTI media.

$$A_4^{TTI} = -\frac{2\eta}{t_{p0}^2 V_{p0}^4} F(\alpha, \phi, \nu) \quad (2.56)$$

where t_{p0} is zero-offset two-way time for P-wave; α is the azimuth of the CMP gather from direction of dip; ϕ is reflector dip and $\phi = 0$ corresponds to a horizontal boundary. The quartic moveout coefficient for TTI media is expressed as follows.

$$\begin{aligned} A_4^{TTI} &= \frac{-2\eta}{t_{p0}^2 V_{p0}^4} F(\alpha, \nu) \\ &= \frac{-1}{64 t_{p0}^2 V_{p0}^4} [(18 - 24 \cos 2\alpha + 6 \cos 4\alpha)x_1 \\ &\quad + 8(5 - 4 \cos 2\alpha - \cos 4\alpha)x_2 + (70 + 56 \cos 2\alpha + 2 \cos 4\alpha)x_3] \end{aligned} \quad (2.57)$$

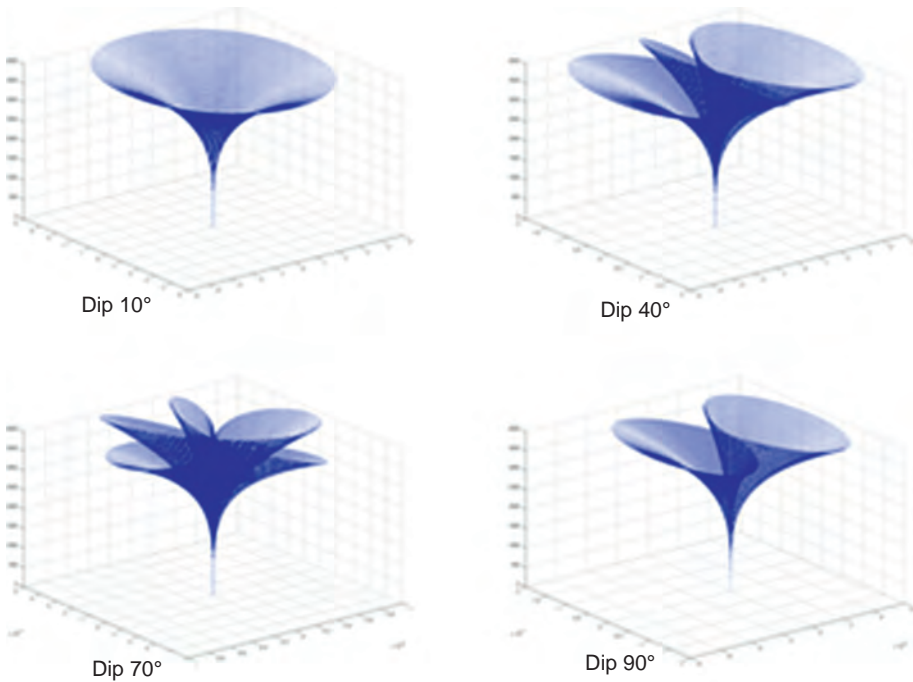


Figure 2.77 Theoretical computations of quartic moveout coefficient.

Fig. 2.77 shows theoretical computations of quartic moveout coefficient for TTI media at different dip angles. At the dip of 10 degree, TTI media are similar to VTI media; thus the curve is nearly circular. A lemniscate curve appears at a larger dip and three complicated lemniscate curves appear at the dip of 70 degree. When the angle increases to 90 degree, TTI media degrade to HTI media and the lemniscate curve appears once again.

Fracture detection based on residual P-wave NMO for TTI media

We use a model-based fracture parameter inversion to demonstrate the workflow and results. **Fig. 2.78** shows a three-layer model with TTI media intercalated in isotropic media. Two recording geometries have been employed to acquire prestack P-wave data for HTI media; one is changing azimuth but maintaining a constant offset and the other is varying azimuth with offset. Acquisition parameters include unilateral shot, 525 active traces, trace interval of 20 m, and azimuth increasing from 0 to 165 degrees on a step of 15 degree. Each CDP gather has 525 traces with trace intervals of 20 m. The offset ranges from 0 to 10,480 m. Data processing involves extracting macro-bins, sorting regularized azimuthal gathers, selecting reference traces with azimuthal residual NMO, calculating azimuthal residual NMO, 2D interpolation of azimuthal residual NMO in the polar coordinate system, and azimuthal residual NMO inversion.

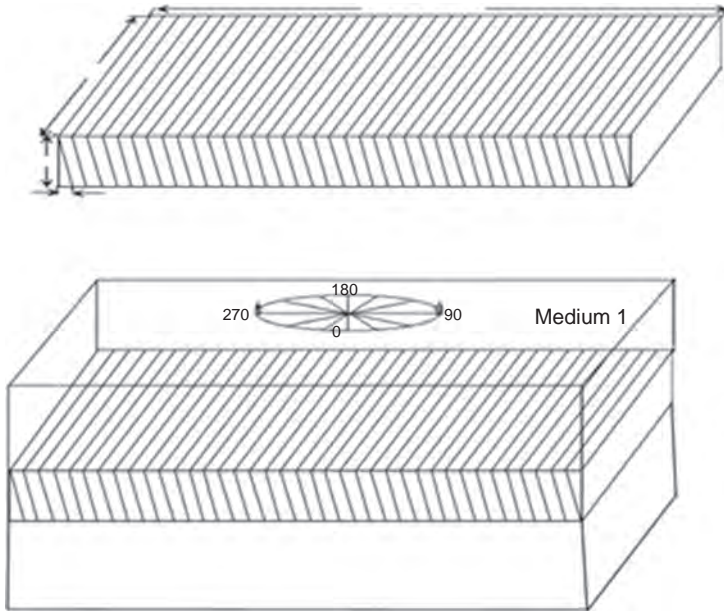


Figure 2.78 Prestack acquisition for a model with vertical fractures. Upper layer: 3800 m thick, $V_p = 3800$ m/s, $V_s = 2760$ m/s, $\rho = 2100$ g/cm³; Middle layer: 2000 m thick, $V_p = 4500$ m/s, $V_s = 2900$ m/s, $\rho = 2300$ g/cm³, $\varepsilon = 0.11$, $\delta = -0.0453$, $\gamma = 0.280$, dip 60 degree, strike 0 degree; Lower layer: 4000 m thick, $V_p = 5500$ m/s, $V_s = 3200$ m/s, $\rho = 2500$ g/cm³, azimuth 0 degree.

The objective function of inversion is

$$F(x_1, x_2, x_3) = \sum_{i=1}^n \left\{ \frac{X_{\max}^4}{64t_{p0}^3 V_{p0}^4} [(18 - 24 \cos 2\alpha_i + 6 \cos 4\alpha_i)x_1 + 8(1 - 4 \cos 2\alpha_i - \cos 4\alpha_i)x_2 + (70 + 56 \cos 2\alpha_i + 2 \cos 4\alpha_i)x_3] + \Delta t \right\}^2 \quad (2.58)$$

where Δt is actual residual moveout. Inversion parameters are derived by solving x_1 , x_2 and x_3 .

$$\eta = x_1; \quad v_1 = \frac{1}{2} \cos^{-1} \frac{x_2}{\eta}; \quad v_2 = \frac{1}{4} \cos^{-1} \frac{x_3}{\eta} \quad (2.59)$$

ν is expressed as follows.

$$\nu = \frac{v_1 + v_2}{2} = \frac{1}{4} \cos^{-1} \frac{x_2}{\eta} + \frac{1}{8} \cos^{-1} \frac{x_3}{\eta} \quad (2.60)$$

Table 2.2 Inversion results and model parameters

		Random error	Fracture intensity	Fracture dip
Model parameter			0.1708	15
Inversion	Random noise	0	0.1742901	15.00259274
		5%	0.1795501	15.04835967
		10%	0.18959	15.11335928
		20%	0.2077001	15.18491022
	Bottom reflection angle	40%	0.2413201	15.0472155
		0°		
		5°	0.1747	11.7284285
	10°	0.1771801	9.289958747	
	20°	0.17711	9.226814669	

where η is the anellipticity of anisotropy parameters and indicates fracture intensity; v is fracture dip. Inversion results are basically reconciled with model parameters (as shown in Table 2.2); thus the method is demonstrated to be effective.

Random errors and bottom reflection times (Table 2.2) have been included in theoretical computation to test the robustness of the inversion. As per the results, random error of azimuthal residual NMO has a great impact on inverted fracture intensity and small impact on inverted fracture dip. Bottom relief of TTI media has a great impact on fracture dip inversion and small impact on fracture intensity inversion.

2.4.2.2 Fracture prediction based on P-wave AVO for TTI media

Theoretical basis

Ranjit developed a formula to describe reflection coefficient at the boundary between an isotropic medium and TTI media.

$$R_{PP}^{TTI}(i, \phi) = {}^{iso}R_{PP}^{TTI}(i) + {}^{ani}R_{PP}^{TTI}(i, \phi) \quad (2.61)$$

The isotropic component is

$${}^{iso}R_{PP}^{TTI}(i) = \frac{1}{2} \frac{\Delta Z'}{Z'_0} + \frac{1}{2} \left[\frac{\Delta \alpha'}{\alpha'_0} - 4 \left(\frac{\beta'_0}{\alpha'_0} \right) \frac{\Delta G'}{G'_0} \right] \sin^2 i + \frac{1}{2} \frac{\Delta \alpha'}{\alpha'_0} \sin^2 i \tan^2 i \quad (2.62)$$

The anisotropic component is

$${}^{ani}R_{PP}^{TTI}(i, \phi) = \left[\frac{\delta}{2} (\cos^2 \psi - \cos^2 \theta) - (\varepsilon - \delta) (\cos^2 \psi + \cos^2 \theta) \cos^2 \theta + 4 \frac{\beta_0^2}{\alpha_0^2} \gamma \cos^2 \psi \right] \sin^2 i + \frac{1}{2} [\delta (\cos^2 \psi - \cos^2 \theta) + (\varepsilon - \delta) (\cos^4 \psi - \cos^4 \theta)] \sin^2 i \tan^2 i \quad (2.63)$$

where $\cos \psi = \sin \theta \cos \phi$; θ and ϕ are incident angle and azimuth angle, respectively.

For $\theta = \pi/2$, $\cos \psi = \cos \phi$, Eq. (2.63) is degraded for HTI media.

For $\theta = 0$, $\cos \psi = 0$, Eq. (2.63) is degraded for VTI media.

$${}^{ani}R_{PP}^{VTI}(i, \phi) = \frac{1}{2} [(\delta - 2\varepsilon)\sin^2 i - \varepsilon \sin^2 i \tan^2 i] \quad (2.64)$$

There is no anisotropy then and $\delta^v = \delta - 2\varepsilon$, $\varepsilon^v = -\varepsilon$ are Thomsen parameters to describe VTI media with weak anisotropy.

Model-based AVO inversion

The anisotropic component in Eq. (2.63) is expressed as

$$R_{PP}^{ANI}(i, \varphi) = F(\theta, \varepsilon, \delta, \gamma) \quad (2.65)$$

The objective function is derived to be

$$\Phi(\theta, \varepsilon, \delta, \gamma) = \left\| F(\theta, \varepsilon, \delta, \gamma) - R^{OBS,ANI} \right\| \quad (2.66)$$

where $R^{OBS,ANI}$ is the anisotropic component of reflection coefficient. Eq. (2.66) is usually solved through simulated annealing, a nonlinear inversion method, in view of its nonlinearity. Here we conduct a model-based inversion to verify this method.

The model is shown in Fig. 2.79 and model parameters are listed in Table 2.3.

In accordance with forward modeling, azimuthal anisotropy becomes less distinct with decreased fracture dip; but fracture strike may still be identified by azimuthal anisotropy at fracture dip of 60 degree. Fig. 2.80 shows the inversion results with 5% noises added. This percentage of noises has little impact on the inversion, which means the method is robust.

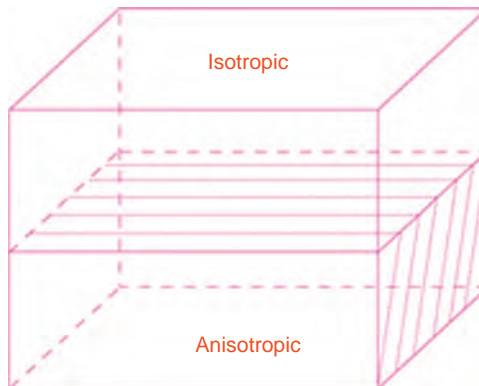
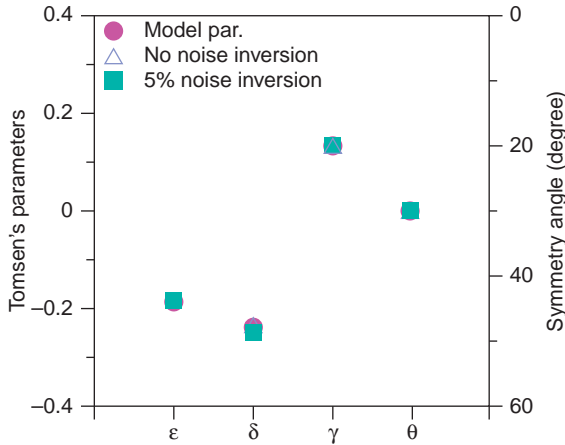


Figure 2.79 TTI model.

Table 2.3 Model parameters

Medium	V_p (m/s)	V_s (m/s)	ρ (kg/m ³)	ϵ	δ	γ
ISO	4000	2310	2650	0	0	0
TTI	3070	2060	2600	-0.191	-0.238	0.127

**Figure 2.80** Anisotropic inversion for TTI media.

2.4.3 Comprehensive description of fracture-vug units

Various types of attributes are integrated to delineate fracture-vug units. The workflow is shown in Fig. 2.81.

2.4.3.1 Logging and seismic responses

In accordance with well drilling, logging, core and seismic data, carbonate reservoirs in the Middle and Lower Ordovician Yingshan Formation in the Tahe area are classified into four types based on pore space, including unfilled caves, partially/fully filled cave, fractures-vugs, and fractures, respectively.

Different carbonate reservoirs have different seismic responses, so such seismic prediction features can be established: (1) fracture-vug carbonate reservoirs generally feature chaotic reflections on amplitude preserved migrated sections; (2) fracture-vug reservoirs close to Lower Ordovician weathering crusts feature weak amplitude, strong discontinuity and small impedance; (3) fracture-vug reservoirs inside the Lower Ordovician Series feature strong amplitude, abrupt amplitude variation, strong discontinuity, heavy attenuation, and small impedance.

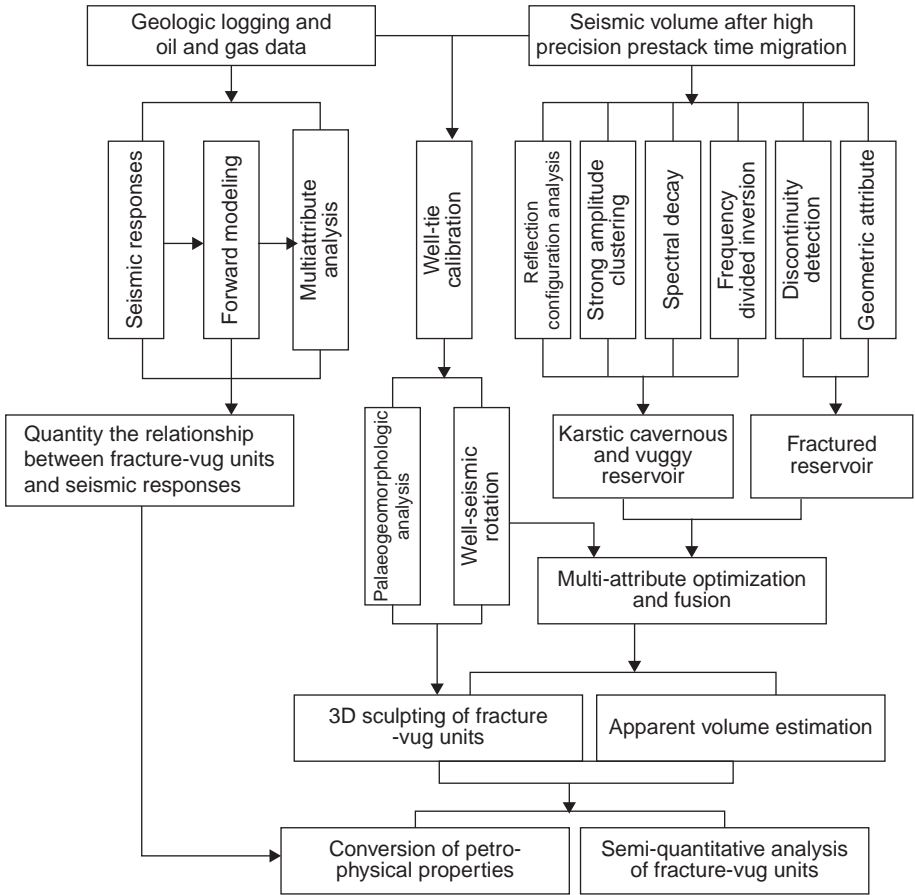


Figure 2.81 Workflow of comprehensive prediction.

2.4.3.2 Nonlinear reconstruction of log curves

Drilling break and serious lost circulation usually take place when drilling into large fractures or caverns, resulting in serious deformation on well logging curves so that they could not be used in seismic prediction. We adopt two methods to reconstruct deformed or lost curves in line with the principle of the good match between synthetic seismogram and field data near the wellbore. Acoustic and density logs may be reconstructed by the fitting formulas derived at the intervals with good downhole conditions in the well or other wells. Reconstructed pseudo-acoustic curves may point out the differences between reservoirs and non-reservoirs (Well TK429, Fig. 2.82). After nonlinear log curve reconstruction, the correlation between synthetic seismogram and field data has also been improved (Well TK429, Fig. 2.83).

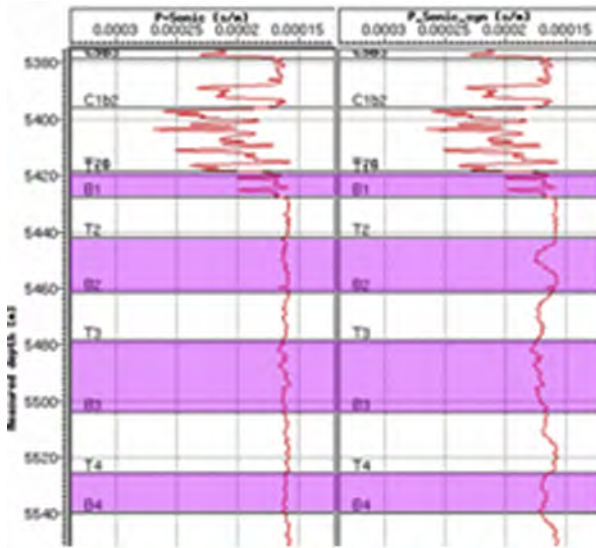


Figure 2.82 Raw (left) and reconstructed (right) acoustic curves at the fractured interval, Well TK429.

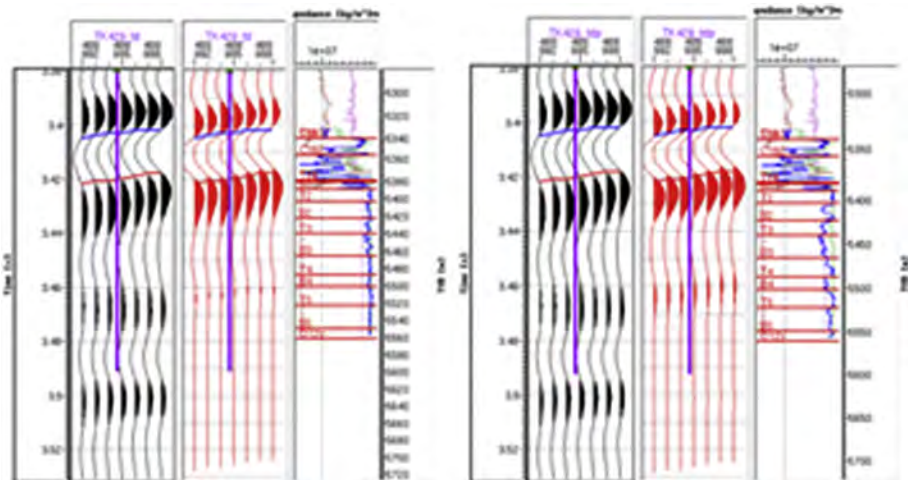


Figure 2.83 Well-tie calibration before (left) and after (right) acoustic curve reconstruction, Well TK429.

2.4.3.3 Well-controlled frequency-divided inversion

Well-controlled frequency-divided inversion is a kind of seismic-constrained low-frequency sparse spike inversion aiming at delineating the outline and extension of fracture-vug units; log-constrained high-frequency stochastic inversion is used to describe the heterogeneity and petrophysical properties inside the units. Two results are integrated in frequency domain to combine well and seismic information in reservoir prediction.

Frequency-divided inversion involves deterministic inversion and geostatistical inversion. The former establishes a deterministic relation between impedance parameters and seismic responses. The result is credible, but the resolution is low due to the limitation of seismic band width. The latter establishes a geostatistical relation between well log and seismic responses; the resolution is high. Full-band inversion is accomplished by integrating the results of deterministic and geostatistical inversions so as to improve the accuracy and credibility of prediction.

2.4.3.4 Multiattribute optimization and fusion

Dimensionality reduction approaches try to find a useful subset of the original attributes. The simplest method is linear combination based on principal component analysis, which relates seismic attributes with reservoir properties by a least square method. The workflow is shown in Fig. 2.84.

For the overdetermined equations containing various seismic attributes extracted at each well site, attribute weighting factors are calculated by the least square method to discriminate between those attributes sensitive to reservoir properties and those less relevant to reservoir properties. The attributes sensitive to the properties

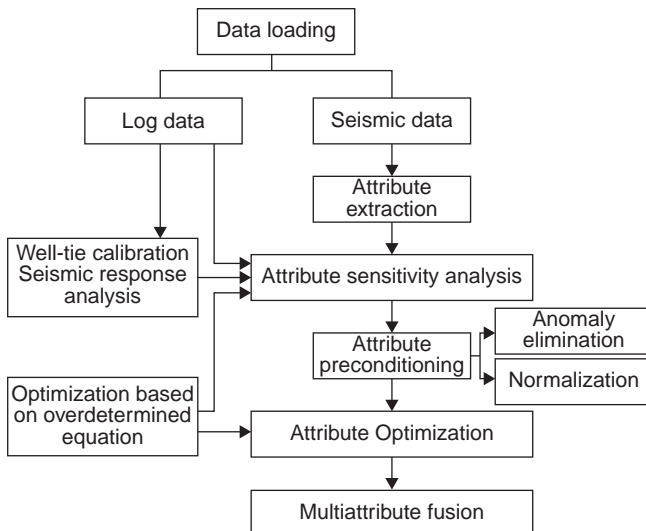


Figure 2.84 Workflow of multiattribute optimization and fusion.

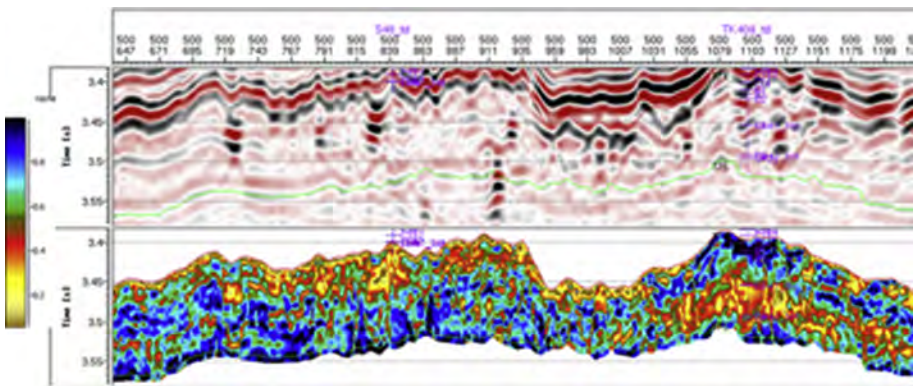


Figure 2.85 Multiattribute fusion of inline500: seismic section (top) and multiattribute fusion section (bottom).

of cave-vug reservoir are selected first, followed by those sensitive to fractured reservoir, as shown in Fig. 2.85.

2.4.3.5 Palaeogeomorphology-controlled sculpting

After seismic attribute optimization, we use 3D sculpting technique to delineate fracture-vug carbonate units in accordance with the relationships among epikarst, palaeogeomorphology, and palaeo-drainage pattern. The geometric shape of fracture-vug units is described quantitatively by apparent volume estimation. The final results are spatial extension and apparent volume of each fracture-vug unit.

Palaeogeomorphologic study

A bed boundary (dual-peak reflections at limestone top as a key bed) in overlying formations of fossil weathering crusts is selected to represent ancient sea level. As per the principle of filling and leveling up in the sedimentary process, estimate the formation thickness between the boundary and weathering crusts for compaction correction, then recover sedimentary thickness and palaeogeomorphology of weathering crusts before deposition (Fig. 2.86).

Palaeogeomorphology-controlled sculpting

Studies show secondary pore space in carbonate reservoirs is dominated by palaeogeomorphology. Corroded fracture-vug reservoirs occur most frequently in residual hill tops and slopes which have experienced intense leaching processes. On the contrary, reservoir units with good properties seldom occur in karst depressions, i.e., collection areas.

We use logging and production performance data to analyze the correlation between reservoir properties and seismic attributes to determine the threshold values for reservoir description.

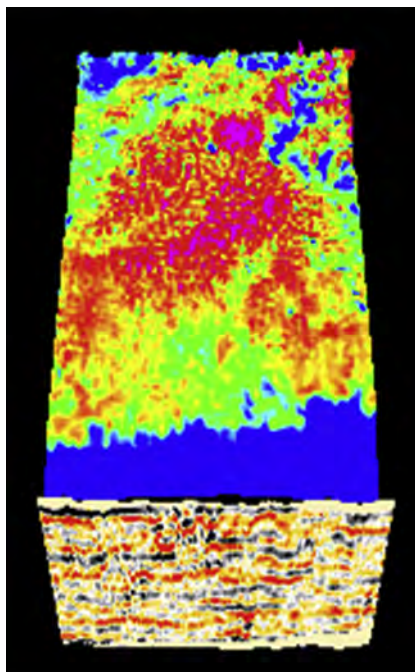


Figure 2.86 Karst palaeogeomorphology in the early Hercynian in S48 well field.

Attribute fusion is subject to the constraints of data visualized as graphics and images. Face-to-face connected values are preserved and point-to-point connected values are eliminated by link constraint. Extension constraint is used to keep the samples being connected out of the low-lying areas in recovered palaeogeomorphology or to limit the samples with low values within the restricted areas.

Different sculpting methods (restricted time window sculpting, seeds controlled sculpting, and horizon sculpting) are used to identify the top and bottom boundaries of fracture-vug units.

Fig. 2.87 shows two seismic sections in inline and crossline directions across Well S48 and sculpting results. The fracture-vug units identified occur immediately beneath T74 horizon. Time thickness is 50 ms, which is equivalent to a cavern height of 150 m in accordance with the velocity of 6000 m/s. According to the results of well drilling and testing, lost circulation of 2318 m³ and drilling break of 1.56 m occurred at 1.24 m penetration into the Lower Ordovician carbonate formations in Well S48. Daily oil and gas outputs were 458.4 m³ and 1.45 × 10⁴ m³, respectively, using 9 mm choke, and cumulative oil production has been over 60 × 10⁴ t. These results demonstrate the existence of fracture-vug units predicted in Well S48.

Fig. 2.88 is the final result of a prediction showing lateral distribution of fracture-vug units in S48 well field, which is in agreement with the result of performance monitoring (Fig. 2.89).

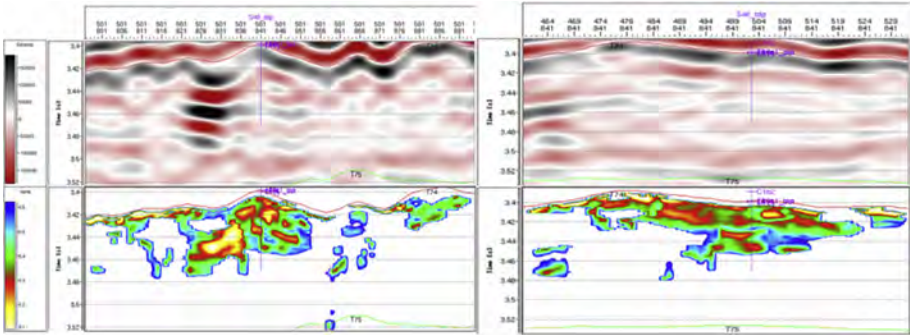


Figure 2.87 Seismic sections across Well S48 and sculpting results of fracture-vug units: inline section (left) and xline section (right).

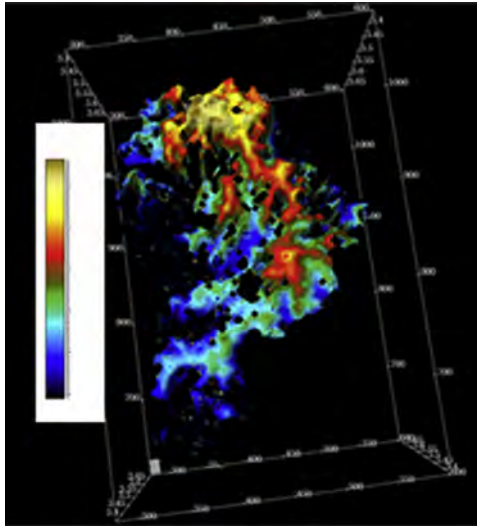


Figure 2.88 t_0 map of fracture-vug units top in S48 well field.

2.4.3.6 Petrophysical properties inversion

Reservoir description involves reservoir properties in addition to geometric shape in the process of oilfield development. Porosity, an important parameter for reservoir modeling, is inverted from seismic data with the constraint of porosity curve derived from logging interpretation.

Probabilistic simulation of porosity is realized by geostatistical inversion involving constrained sparse spike inversion (CSSI) and probabilistic simulation. The probability density function and variogram function of porosity are derived from logging data analysis. A probabilistic model of porosity is built for probabilistic

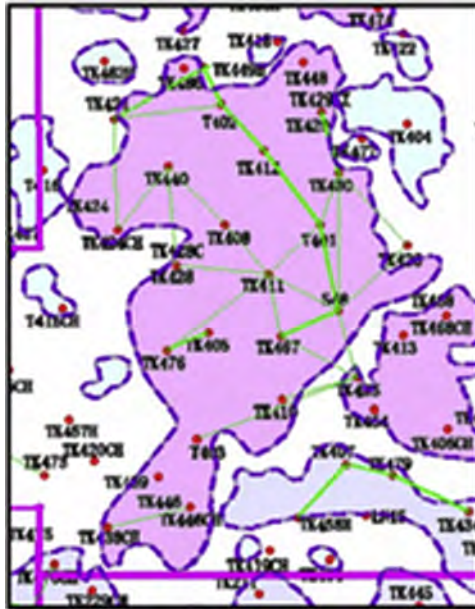


Figure 2.89 Lateral distribution of fracture-vug units (determined by production performance data) in S48 well field.

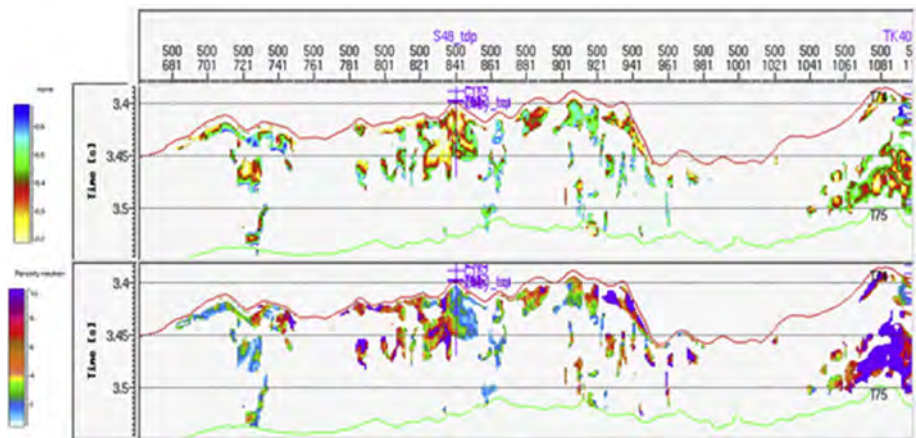


Figure 2.90 Porosity section derived from probabilistic simulation. Fracture-vug unit distribution (top) and corresponding porosity (bottom).

simulation based on correlation coefficient or correlation function of impedance and porosity at well sites (Fig. 2.90).

The process of probabilistic simulation is constrained by sparse spike inversion, tectonic framework model and log data. Thus the heterogeneity and variations of reservoir properties could be characterized by the results of simulation.

2.4.4 Fluid detection

Seismic reflection signatures contain information on pore fluids, which could be predicted by inverting dynamic information into elastic parameters.

2.4.4.1 Sensitivity analysis

Elastic parameters are correlated with reservoir properties (lithology, petrophysical property, and hydrocarbon) by petrophysical analysis, which involves fluid substitution and prestack inversion. The former is used to understand the variations of elastic parameters caused by the changes in fluid properties and analyze fluid-related AVO effects and seismic attributes; the latter (including AVO inversion and elastic parameters inversion) is used to obtain elastic parameters for reservoir characterization.

Petrophysical model

Knowing how to build an accurate petrophysical model is crucial to S-velocity prediction and fluid substitution. Assuming there are $N-1$ log curves and M mineral contents (including pore volume) to be solved, then N equations, including the equation of equilibrium, compose a linear overdetermined system, Eq. (2.67).

$$\begin{pmatrix} L_1 \\ L_2 \\ \dots \\ L_{N-1} \\ 1 \end{pmatrix} = \begin{pmatrix} P_{11} & P_{12} & \dots & P_{1,M-1} & P_{1\phi} \\ P_{21} & P_{22} & \dots & P_{2,M-1} & P_{2\phi} \\ \dots & \dots & \dots & \dots & \dots \\ P_{N-1,1} & P_{N-1,2} & \dots & P_{N-1,M-1} & P_{N-1,\phi} \\ 1 & 1 & \dots & 1 & 1 \end{pmatrix} \cdot \begin{pmatrix} V_1 \\ V_2 \\ \dots \\ V_{M-1} \\ V_\phi \end{pmatrix} \quad (2.67)$$

L_i is the response of the i^{th} log curve; P_{ij} is the response of the i^{th} log curve for the j^{th} mineral; V_j is the volume fraction of the j^{th} mineral. The volume fracture of each essential mineral, including pore volume, would be calculated by Eq. (2.67) for petrophysical modeling.

For the reservoirs of interest in the S48 test area in the Tahe oilfield, seven log curves, i.e., acoustic impedance, density, neutron porosity, deep resistivity, shallow resistivity, natural GR, and caliper, were selected as the input parameters into Eq. (2.67) to solve calcite, dolomite, and clay contents and porosity. Altogether 101 wells have been included in the test. Fig. 2.91 shows petrophysical modeling results for the Ordovician formations in Wells T402 and TK214. Track 4 displays porosity estimation and track 5 displays calcite, dolomite, and clay contents.

P- and S-velocities have been modeled using the Gassmann equation for nearly 100 wells. Modeled results correlate well with actual measurements.

Fluid substitution

Fluid substitution has been performed using the Biot–Gassmann equation. Fig. 2.92 shows P- and S-velocity curves in the left and right tracks, respectively,

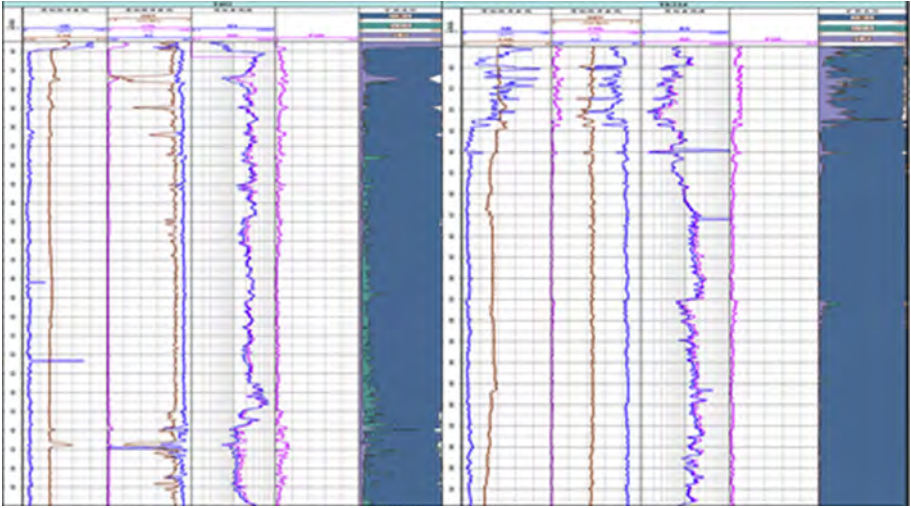


Figure 2.91 Petrophysical modeling results for the Ordovician formations in Wells T402 (left) and TK214 (right).

and density curve in the middle track for Well TK410 after fluid substitution. Original, water saturated, oil saturated, and gas saturated log curves are plotted in *black, blue, red, and yellow*, respectively. The results show that S-velocity is basically irrelevant to fluid content, while P-velocity is greatly affected by fluid content. Different fluid contents lead to different AVO effects on CMP gathers.

Feasibility study

The change in fluid content leads to the variations of elastic parameters. The point is whether or not these variations could be detected.

Angle-dependent elastic impedance (EI) curves, as shown in Fig. 2.93 for Well T207, have been generated by integrating Aki–Richards integration results with low-frequency components of back propagation (BP) EI. The existence of oil and gas in reservoir rocks leads to large EI difference between near and far offsets, as indicated by the black arrow at the depth of 5580 m, where lost circulation occurred during drilling the well. Daily oil and gas yields were 156 and 6525 m³, respectively; water cut was 15%.

The cross-plot of angle-dependent EIs is used to examine EI sensitivity to the existence of oil and gas (Fig. 2.94). In spite of some overlapping, the difference between far-angle (27 degree) EI and near-angle (5 degree) EI is somewhat sensitive to fluid properties. The far-angle EI is larger than near-angle EI (with the trend deflecting from the line of 45 degree) at the interval containing oil and gas; this result is similar to that shown in the above figure.

In addition to EI, V_p , V_s , and lambda-mu-rho (LMR) (λ , μ and ρ) are also sensitive to fluid properties. The cross-plots of $\lambda\rho$ - $\lambda\mu$ and V_p - σ may also be used for fluid detection.

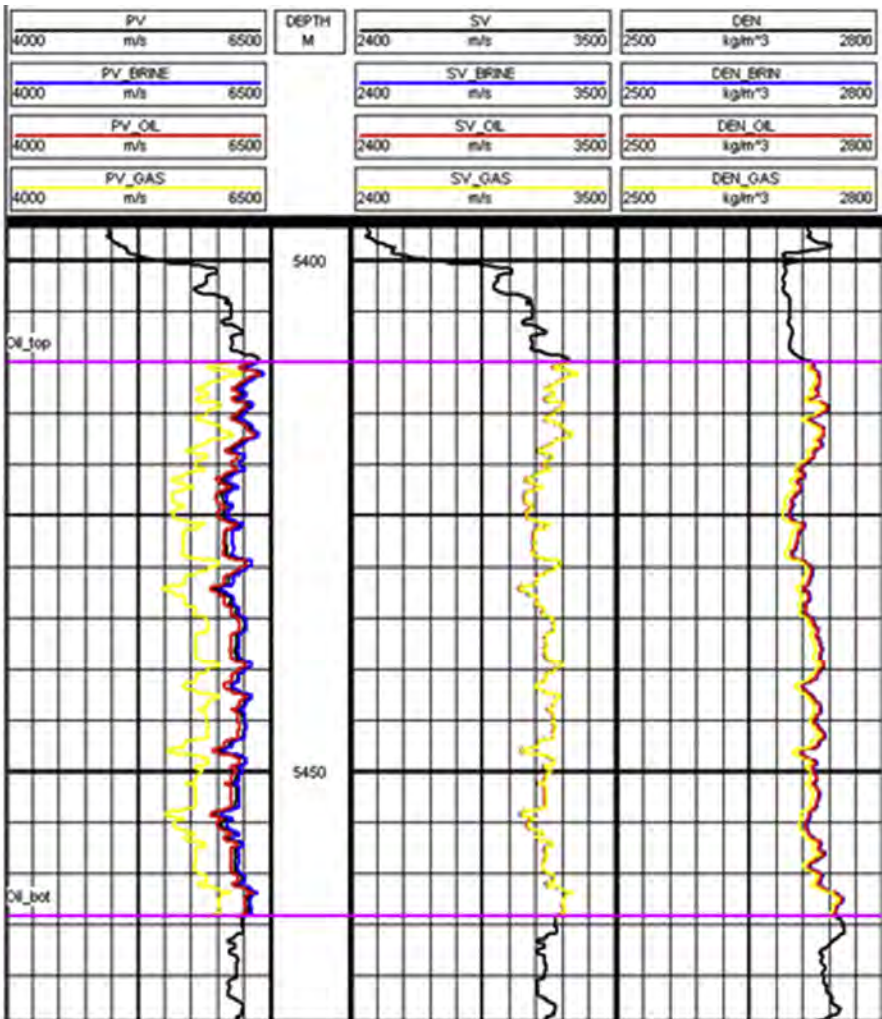


Figure 2.92 Log responses before and after fluid substitution, Well TK410.

2.4.4.2 Prestack fluid detection

Prestack EI inversion uses seismic trace gather and well logging data such as density and dipole acoustic to invert elastic parameters (e.g., EI, P-impedance, S-impedance, density, and Lamé coefficients) which are related to lithologies and hydrocarbon properties. Prestack EI inversion is more credible than poststack acoustic impedance inversion because a mass of seismic and logging information is integrated.

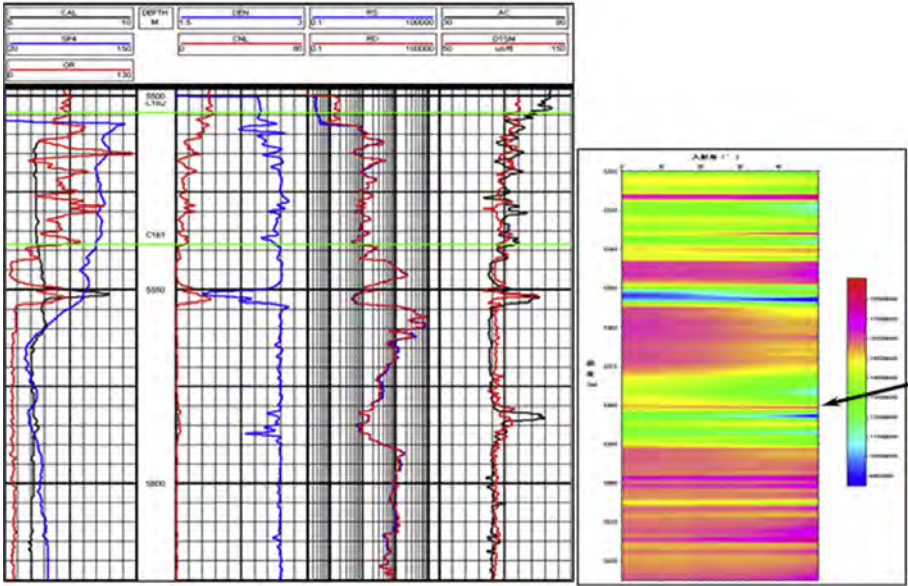


Figure 2.93 Log curves (left) of Well T207 and angle-dependent EI curves (right).

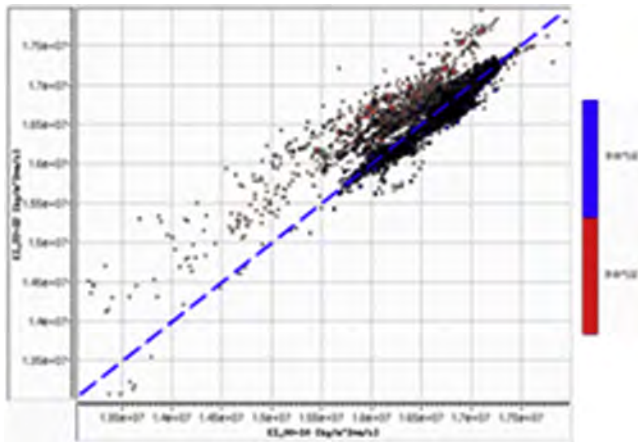


Figure 2.94 Fluid detection by cross-plotting far-angle EI with near-angle EI. The line of 45 degree is plotted as a *blue dashed line*.

Prestack elastic impedance inversion

EI was developed by Connolly in accordance with the Aki–Richards approximation to the Zoeppritz Equations; $EI(\theta)$ is the function of P-velocity V_p , S-velocity V_s , density ρ , and incident angle θ .

$$EI(\theta) = V_p^{1+\sin^2 \theta} V_s^{-8K \sin^2 \theta} \rho^{1-4K \sin^2 \theta} \tag{2.68}$$

EI inversion involves the information of converted shear wave. It has several advantages: EI correlates well with lithology; accurate reflection coefficient could be calculated; EI has specific units and could be normalized; and EIs at different angles could be used to estimate Poisson's ratio.

EI inversion is realized through following steps: (1) generate partial angle stacked volumes in accordance with AVO responses; (2) calculate angle-related EIs using P-velocity, S-velocity, and density logs; (3) analyze EIs sensitivity to lithologies and fluids through cross-plotting; (4) extract seismic wavelets for different angle stacks; (5) perform CSSI on angle stacks; (6) extract inverted EIs along well-bore track for cross-plotting; (7) convert EIs into reservoir properties to identify lithologies and fluids.

LMR inversion

LMR inversion, which was proposed by Pickfort, is based on gradient and intercept analysis and inversion to extract rock parameters from prestack seismic data by first inverting P- and S-impedance and then calculating elastic parameters using the equations $V_p = \frac{I_p}{\rho}$, $V_s = \frac{I_s}{\rho}$, $\lambda\rho = I_p^2 - 2I_s^2$, $\mu\rho = I_s^2$ and $\delta = \frac{\lambda}{2(\lambda + \mu)}$, where I_p and I_s are P- and S-impedance, respectively; V_p and V_s are P- and S-velocity, respectively; μ is shear modulus; λ is Lamé coefficient; and δ is Poisson's ratio.

Compared with EI inversion, (1) LMR inversion generates P-velocity, S-velocity, P-impedance, S-impedance, density, and Lamé coefficients, which are of physical significance and related to reservoir properties; (2) LMR inversion is less affected by noises; (3) S-impedance is a good lithology indicator; (4) V_p - V_s ratio is a good fluid indicator; (5) reservoirs and nonreservoirs could be identified on the cross-plot of P-impedance and S-impedance; and (6) LMR inversion excludes the ambiguity of EI. Therefore elastic parameters derived from LMR inversion may better describe petrophysical and fluid properties.

LMR inversion is realized through following steps: (1) generate partial angle stacks in accordance with AVO responses; (2) perform residual moveout correction to align different angle stacks; (3) calculate P-impedance and S-impedance using P-velocity, S-velocity and density logs; (4) analyze P-impedance and S-impedance sensitivity to reservoir properties through cross-plotting; (5) extract seismic wavelets for different angle stacks; (6) establish low-frequency models of P-impedance, S-impedance (or velocity) and density; (7) perform AVA CSSI on angle stacks; (8) calculate elastic parameters including V_p/V_s , $\lambda\rho$, $\mu\rho$, and Poisson's ratio using inverted P-velocity, S-velocity, impedance, and density; and (9) identify lithologies and fluids through cross-plotting of elastic parameters.

2.4.4.3 Fluid probabilistic analysis based on AVO inversion

A Monte Carlo probabilistic model can be built for forward modeling in accordance with log-based elastic parameters analysis. Based on the model and using fluid substitution by the Biot-Gassman equation, synthetic seismograms for oil, gas, and water will be obtained, and accordingly intercept and gradient attributes will be extracted using the Shuey approximation. These attributes extracted from field data

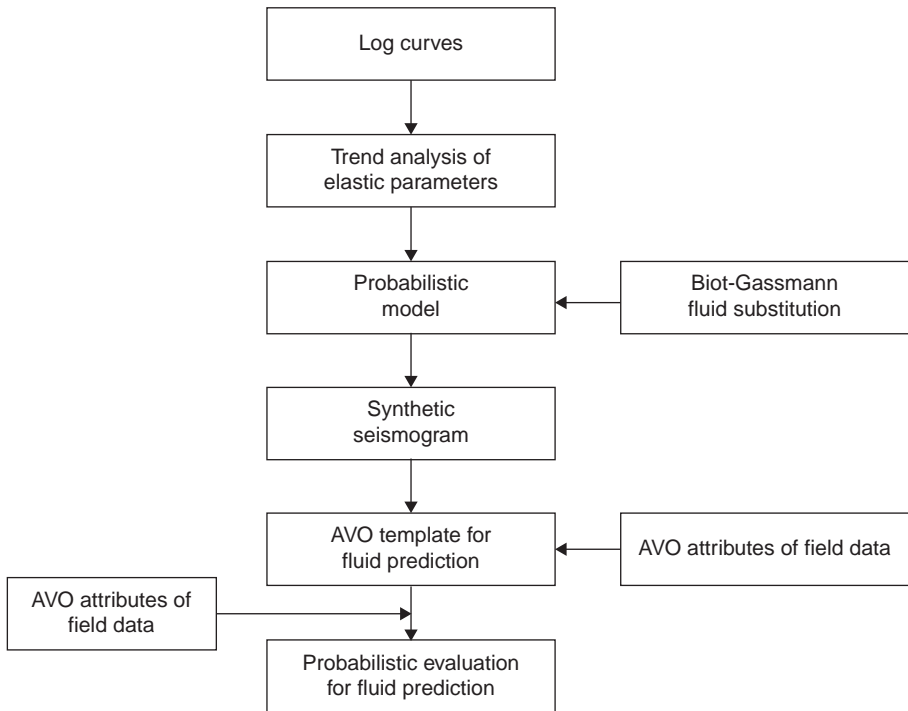


Figure 2.95 Workflow of fluid probabilistic analysis.

are then compared with those from the model to assess the probabilities of oil, gas, and water by the Bayes' theorem. The workflow is shown in Fig. 2.95.

Some reference wells were selected to calculate the mean values and standard deviations of the velocity and density at reservoir and nonreservoir intervals through the analysis of velocity and density trends. Probabilistic models at different depths were built by Monte Carlo methods. Fluid substitution and the Shuey approximation were then used to establish the cross-plots of intercept and gradient at different depths (Fig. 2.96) for fluid prediction.

Fluid probability for a point on the intercept-gradient plot is calculated by the Bayes posterior probability formula.

$$P(\tilde{F}|I, G) = \frac{P(I, G|\tilde{F})P(\tilde{F})}{\sum_k P(I, G|F_k)P(F_k)} \quad (2.69)$$

where $P(\tilde{F}|I, G)$ is the fluid probability for a point on the intercept-gradient plot; $P(I, G|\tilde{F})$ is the distribution density of a fluid on the intercept-gradient plot; $P(\tilde{F})$ is the probability of a fluid; $P(I, G|F_k)$ is the distribution density derived from probabilistic simulation; $P(F_k)$ is the probability of oil, gas, or water; \tilde{F} is the sampling

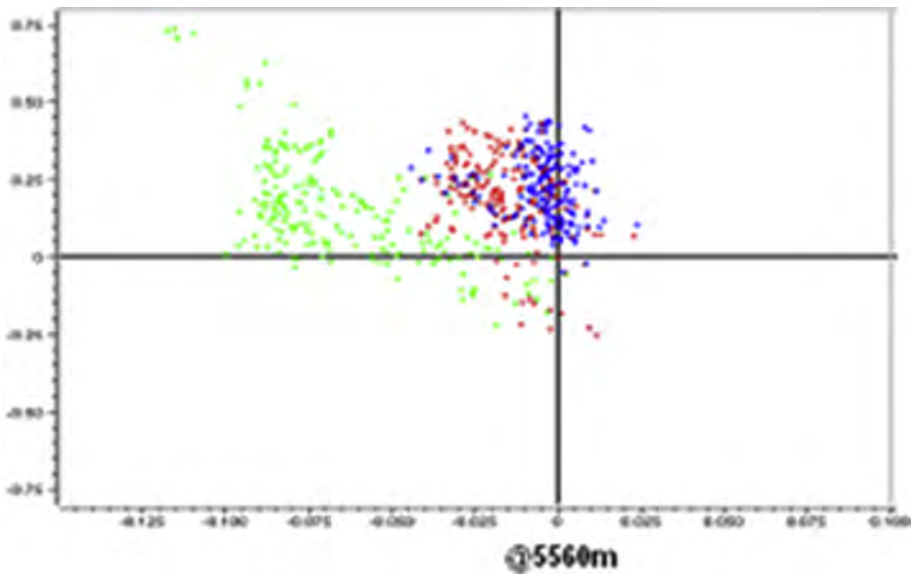


Figure 2.96 Cross-plot of intercept and gradient at 5560 m. Water, oil, and gas points are plotted in *blue*, *red*, and *green*, respectively.

point on the intercept-gradient plot for field data; k stands for a fluid of oil, gas, and water; F_k is the modeled sampling point on the intercept-gradient plot.

2.5 Comprehensive application of geophysical technology

As the 3D high-density seismic survey area, the S48 well field in the Tahe oilfield was selected as the test area for seismic data acquisition and processing, and fracture-vug reservoir prediction.

2.5.1 Data quality and acquisition

The credibility of reservoir prediction is greatly dependent on how to preserve and image complicated reflection signals and how to migrate diffracted waves. In order to improve imaging and migration, it is necessary to optimize recording geometry and acquisition parameters. In addition, diffracted waves should be preserved and migrated accurately in data processing.

2.5.1.1 High-density seismic acquisition

Lateral resolution is important for accurate description of fracture-vug units, especially small reservoir units. How to improve seismic resolution is crucial to reservoir description.

Lateral resolution

Seismic band width and spatial sampling rate are the most crucial factors which affect lateral resolution.

Lateral resolution is essentially dependent on seismic wavelength or band width for a constant velocity, which could be demonstrated by numerical simulation. Take a $14,000 \times 4100$ m homogeneous model as an example (Fig. 2.97): At 4000 m deep, there are five groups of rectangular caves/caverns of 5, 10, 20, 50, and 100 m wide, respectively, distributing within the range of 6500–7500 m in the middle of the model; the cave/cavern height is 10 m; cave/cavern interval inside a group doubles the cave width; the background velocity is 3500 m/s and the cave velocity is 2000 m/s. In forward modeling, CDP spacing is 10 m; the dominant frequency of zero-phase Ricker wavelet varies from 25, 50, to 100 Hz, respectively. Imaging results are shown in Fig. 2.98.

The results show that lateral resolution is closely related to the dominant frequency of wavelet. In other words, seismic band should be wide enough to identify small units.

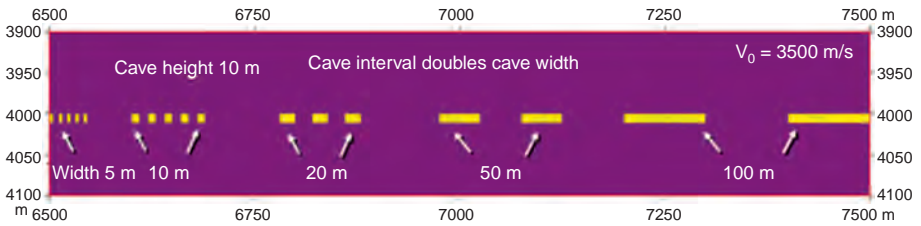


Figure 2.97 Velocity model.

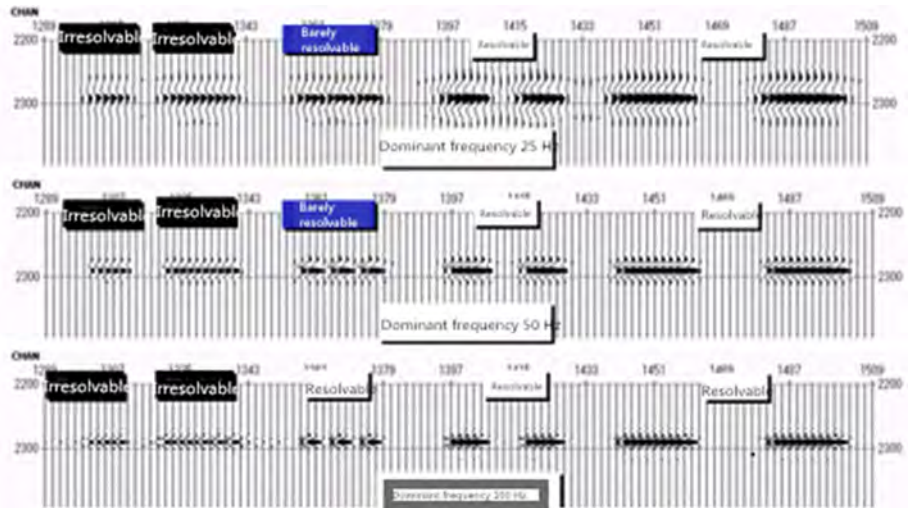


Figure 2.98 Migrated sections for CDP spacing of 10 m at different dominant frequencies.

Spatial sampling rate also affects lateral resolution. The sampling rate should be large enough to ensure accurate imaging. This will be demonstrated by the following two physical modeling tests.

The first model is designed with a single cave at the depth of 5300 m. Cave velocity is 2500 m/s and background velocity is 4500 m/s. The recording geometry is designed to be 10–100–2500. The dominant frequency is 30 Hz. Cave diameter varies from 50, 30, 40, 10, 25, 15, to 20 m. Fig. 2.99 shows the results. Amplitude increases with cave diameter and decreases with CDP spacing. The energy increases by about 30% if CDP spacing decreases by a half. According to the tests, data resolution increases with decreased CDP spacing. Thus high-density acquisition is necessary for high-precision exploration.

Another model is designed for testing the impact of CDP spacing on cave imaging. The model comprises three groups of small caves (Fig. 2.100).

Cave	Diameter 50 m	Diameter 40 m	Diameter 30 m	Diameter 25 m	Diameter 20 m	Diameter 15 m	Diameter 10 m
CDP	Amplitude	Amplitude	Amplitude	Amplitude	Amplitude	Amplitude	Amplitude
5 m	9.34	8.01	6.96	4.89	3.56	2.94	2.23
10 m	6.44	5.15	3.77	2.94	2.57	2.21	1.47
15 m	6.20	4.01	3.12	2.35	2.06	1.21	0.63

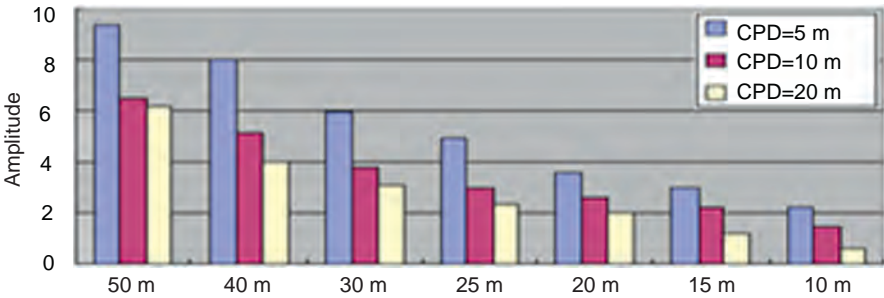


Figure 2.99 Maximum amplitude values and histogram for different CDP spacings.

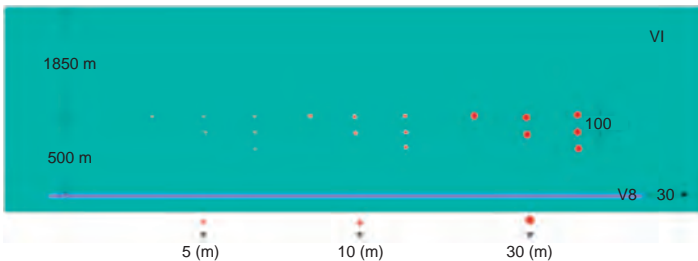


Figure 2.100 Schematic cross-sections of three groups of small caves.

Table 2.4 Recording geometries

	Geometry 1	Geometry 2	Geometry 3
Trace interval	10 m	20 m	30 m
Shot spacing	20 m	40 m	60 m
Channel/shot	96	80	80
Number of shots	230	120	75
Time sampling rate	2 ms	1 ms	1 ms
Number of sampling points	3000	6000	6000
Fold	24	20	20
Shooting	Unilateral shot	Unilateral shot	Unilateral shot

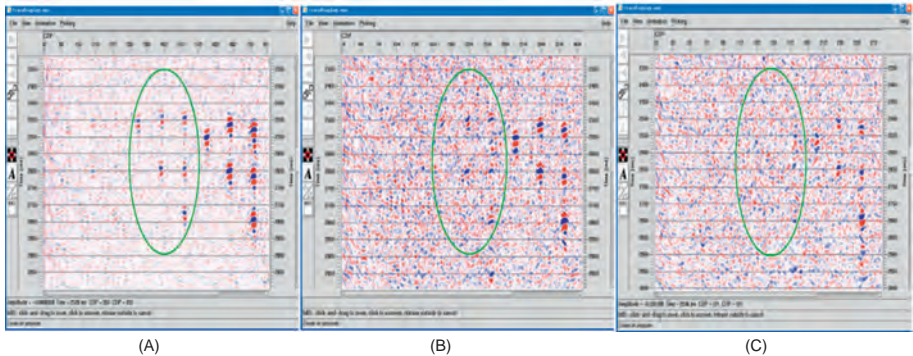


Figure 2.101 Migrated sections for three recording geometries (A) is migrated section for Geometry 1 (B) is migrated section for Geometry 2 (C) is migrated section for Geometry 3.

Background velocity is 1500 m/s and cave velocity is 1100 m/s. The parameters of three recording geometries are shown in [Table 2.4](#).

[Fig. 2.101](#) shows migrated sections for three recording geometries. The energy of short cave reflections decreases with increased trace interval. The decrease in the number of traces has a negative impact on data resolution. Thus using a small trace interval is helpful to improving cave description.

Bin size

Empirically the side length of the bin should be equal to a half or one-third of the size of the geobody so that it could be identified. Studies show if a small geobody is covered by three to five bins, diffracted waves could be migrated accurately with preserved amplitude. In view of the Ordovician cave of 10–30 m, basic bin size is 15×15 m and then reduced to 7.5×7.5 m; therefore a fracture-vug/cave unit of 15 m in lateral direction is covered with two bins; a unit of 25 m is covered with three bins. Thus fracture-vug/cave units of 15 m could be imaged and units above 25 m could be better imaged and identified.

Azimuth

Wide-azimuth acquisition may be helpful to better imaging and fluid detection based on prestack P-wave azimuthal anisotropy. In order to facilitate prestack P-wave AVO analysis and avoid strong noises induced by wide-azimuth migration, the aspect ratio is finally set to be 0.5.

Maximum offset

Some factors, e.g., NMO stretch, precision of velocity analysis, buried depth of the zone of interest, stability of reflection coefficient and noises, have been taken into consideration. In view of time window analysis of shot gathers for field data in Tahe, forward modeling results required offsets for velocity analysis, NMO stretch clipping and stability of reflection coefficient, the maximum offset of 6000 m is feasible in this prospect.

Fold

Increasing the fold is a way to S/N enhancement. In the Tahe prospect, signal attenuation in shallow and middle zones leads to low S/N in the deep zone of interest. In order to suppress noises, broaden band width, and improve S/N, the number of folds for a 3D survey should be 80 at least as per 2D tests with different folds.

Recording geometry

Fold: $320 (40 \text{ inline} \times 8 \text{ crossline})/80 (20 \text{ inline} \times 4 \text{ crossline})$

Bin size: $15 \times 15 \text{ m}/7.5 \times 7.5 \text{ m}$

Trace spacing: 30 m

Receiver line interval: 225 m

Shot point spacing: 30 m

Shot line interval: 135 m

Swath interval: 1800 m

Inline layout: 5317.5–7.5–30–22.5–5452.5 or 5452.5–22.5–30–7.5–5317.5

Maximum offset: 6029 m

Maximum noninline offset: 2572.5 m

Aspect ratio: 0.47

Total of shots: 33,600 (five shotlines)

Full-coverage area: 81.48 km²

Multiwave recoding geometry:

Recording spread: 12L4860S-4320P (bin partition)

Total of receiver points: 4320 (360 × 12)

Maximum fold: 960/240

Bin size: $15 \times 15 \text{ m}/7.5 \times 7.5 \text{ m}$

Trace spacing: 30 m

Receiver line interval: 165 m

Shotpoint spacing: 30 m

Shot line interval: 135 m

Maximum noninline offset: 1792.5 m

Maximum offset: 10940.34 m

Total of shots: 4860

Full-coverage area: 14.31/5.89 km² (more than 80 folds)

2.5.1.2 High-density data processing

Fig. 2.102 shows the workflow of data processing designed in terms of raw data quality and requirements of processing. An accurate near-surface velocity model is obtained by first arrival tomographic inversion for static correction. Noise reduction uses target-oriented techniques to improve S/N. The iteration of velocity analysis and residual static correction improves the accuracy of velocity analysis. More control points both in vertical and lateral directions improve velocity picking. Based on elaborate velocity analysis, prestack time migration is used for better imaging.

The S/N and resolution of 3D high-density seismic data have been greatly improved. Ordovician fracture-vug reservoirs (Fig. 2.103), karstic unconformities, local structural highs at the Ordovician top, and bead-like reflections inside the Ordovician System have been better imaged. Fault-point reflections inside the Ordovician System have been further focalized.

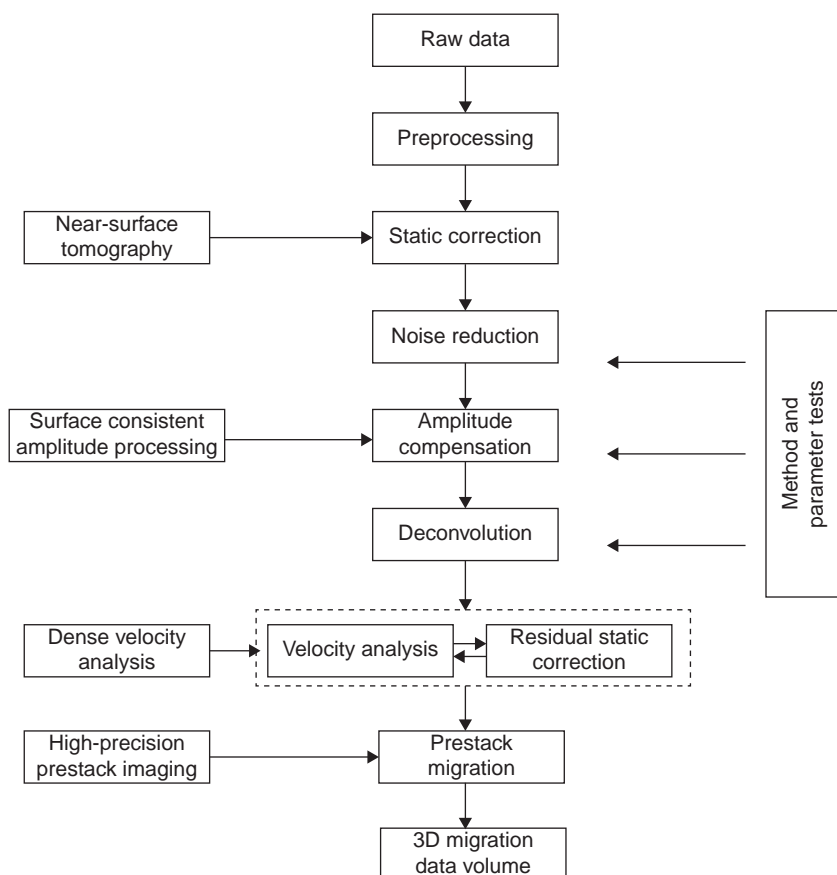


Figure 2.102 Processing workflow.

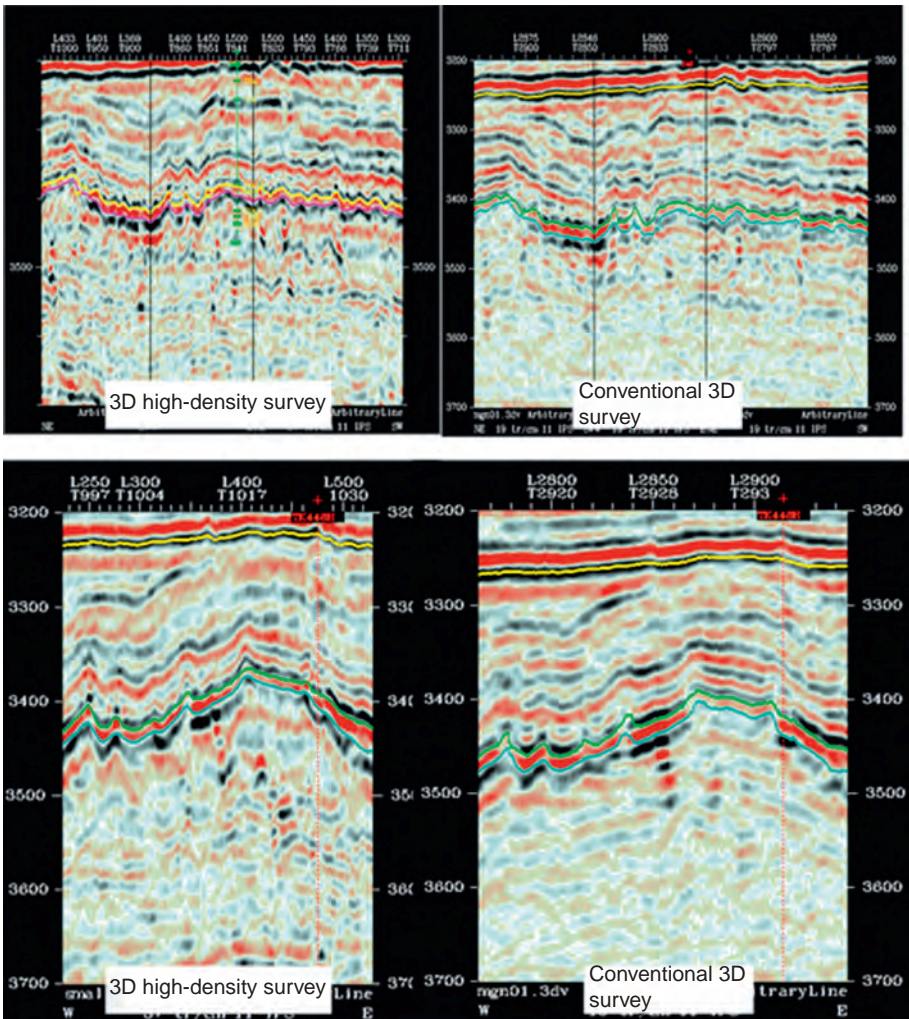


Figure 2.103 Comparison between old and new sections.

2.5.1.3 Discussions of 15-m cave identification

As per that which is discussed above, resolving power of high-density seismic data is dependent on two key factors, band width and spatial sampling rate. As shown in Fig. 2.98, it is challenging to improve the accuracy of cave description by doubling the dominant frequency for a survey with thick desert or deeper than 5400 m in the Tahe oilfield. As shown in Figs. 2.99–2.101, a decrease in spatial sampling rate by a half leads to an increase by 30% in cave reflection energy. Effective reflections and resolution increase with decreased CDP spacing. According to physical simulation shown in Fig. 2.101, CDP spacing should be less than 30 m to identify caves

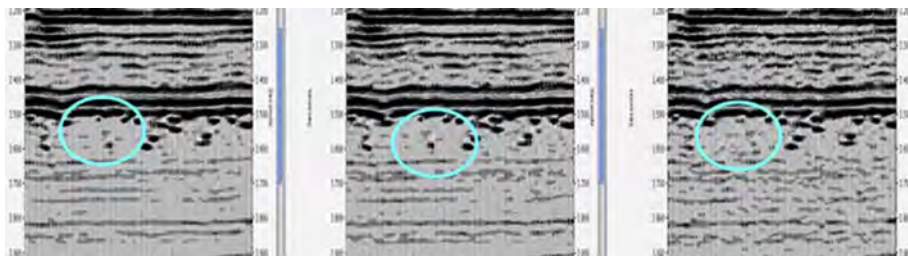


Figure 2.104 Migrated sections for different CDP spacing. Left, 7.5×7.5 m; middle, 15×15 m; right, 30×30 m.

of 30 m (right) and less than 20 m or close to 10 m to identify caves of 10 m (middle and left). In the following part, we use energy difference instead of geometric resolution to discuss small cave description.

In a pilot test of high-density survey with small CDP spacing and subdividable bins in the Tahe oilfield, three recording geometries have been dealt with, i.e., the original layout with CDP spacing of 15×15 m and 320 folds, layout with CDP spacing of 7.5×7.5 m and 80 folds, and layout with CDP spacing of 30×30 m and 320 folds. Uniform processing workflow and parameters have been employed in prestack time migration. The results are shown in Fig. 2.104. Bead-like reflections of the cave imaged by more than two traces (larger than 30 m) on the section with CDP spacing of 30×30 m can also be observed on the additional two sections, while the reflections imaged by two traces (about 15 m) on the sections with CDP spacing of 15×15 m and 7.5×7.5 m could not be identified on the section of 30×30 m. The sections with CDP spacing of 15×15 m and 7.5×7.5 m have similar energy of bead-like reflections, which indicates these two layouts generated similar results of migration for caves of 15 m. Thus it is inferred that a layout with CDP spacing smaller than 10 m and 300 folds is necessary to identify the caves of 10 m.

Accurate description also relies on energy preservation and cave boundary migration, which may be realized through amplitude-preserved processing and accurate velocity modeling. In view of velocity complexities induced by pore fluids, a coarse grid of 400×400 m for routine velocity analysis has been reduced to 150×150 m to establish an accurate velocity model for better migration and imaging (Fig. 2.105). Anisotropic migration (VTI-PSTM) has been used to address the issue of insufficient NMO correction at far offsets, which is common in a seismic survey with large spreads for ultra-deep observation, so as to ensure signal enhancement for diffracted waves (Fig. 2.106).

According to outcrops observation and well drilling data, there are seldom isolated fractures or caves/vugs; most caves/vug occur in a cluster with complicated configuration (Fig. 2.107). For a cave outcrop of 6.8×2.3 m, the whole system is 3.1-times wider and 4.2-times higher than the cave; the area is 7.7-times greater than that of the cave. Generally a fracture-vug unit of 15 m which could be identified on seismic data refers to a complex composed of a cave/vug, surrounding pores and fractures and internal fluids.

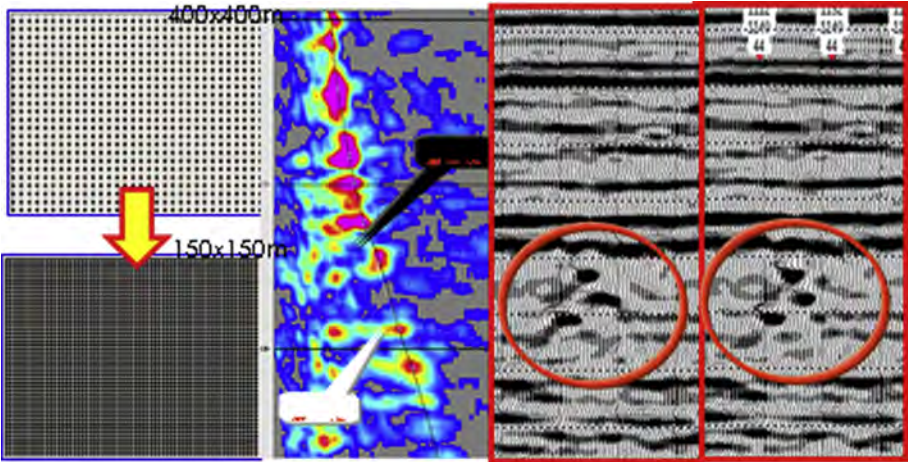


Figure 2.105 Improved boundary imaging by dense velocity analysis.

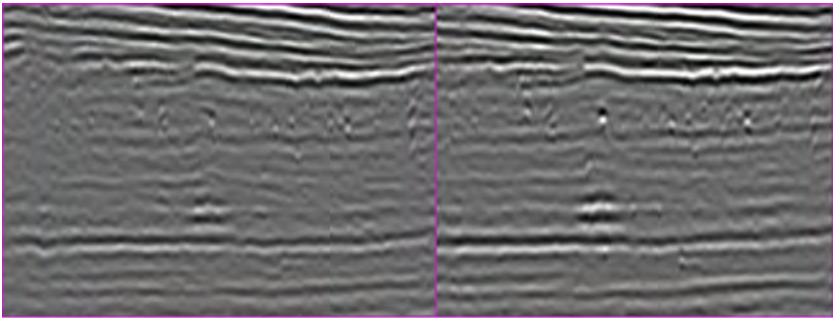


Figure 2.106 Enhanced diffraction energy by anisotropic (VTI) migration.

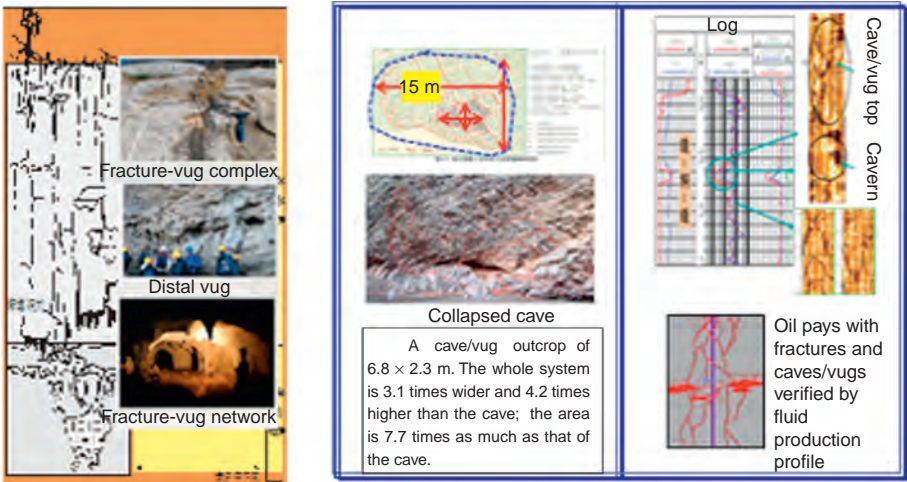


Figure 2.107 Fracture-vug complex with different types of pore space and complicated configuration.

2.5.2 Fracture-vug units prediction

The prediction of fracture-vug units was based on 3D high-density seismic data. The techniques used include forward modeling, seismic responses analysis, multiattribute analysis, and fluid detection.

2.5.2.1 Fracture-vug units prediction

Poststack seismic attributes

We extracted reflection configuration to predict the cave/vug system in S48 well field, in the Tahe oilfield (Fig. 2.108). Well S48 is an oil producer with the longest natural flow and stable production periods in the Tarim Basin; the pay formation is the Ordovician System. Lost circulation of 2318 m³ and drilling break of 1.56 m took place after penetration of 1.24 m into the Lower Ordovician carbonate formations. Daily oil and gas outputs were 458.4 m³ and 1.45×10^4 m³, respectively, using 9 mm choke. Fig. 2.108 shows reflection signatures on an inline section across Well S48. The events between CDP490 and CDP580 at 3.4 seconds feature strong discontinuity and weak energy. It is inferred that sunken discontinuous reflections below correspond to the lower boundary of the cave system; blank reflections correspond to the cave system.

The analyses of drilling and seismic data demonstrate that the producers and stringers or dry holes exhibit different reflection configurations on seismic sections (Fig. 2.109). At the drilling sites of producers with stably high yield, seismic reflections usually feature upper weak (and discontinuous) events at the Ordovician top, middle blank reflections (compared with those on both sides), and lower strong discontinuous reflections (which may not be observed at some well sites) or upper weak (and discontinuous) events at the Ordovician top, middle strong bead-like reflections, and lower strong discontinuous reflections (which may not be observed at some well sites). At the drilling sites of stringers or dry holes, seismic reflections feature relatively stable configuration or local concave events with stable or strong internal amplitude, which indicates karst caves are underdeveloped or filled. These wells usually have no or low productivity.

Abnormally strong amplitude (Fig. 2.110) mainly occurs in various shapes within a time window of 100 ms beneath the unconformity. Drilling break, lost circulation, well kick and small drilling time occurred at some well sites with strong amplitude on seismic sections. For example, drilling break of 1.16 m occurred at 5536–5537.16 m in Well TK424, which yielded commercial oil flow. Wells TK404 and TK412 are located within or close to the regions with strong amplitude. Wells TK427, TK440, T416, S65, and T444 drilled in the belts with strong amplitude, which may be the response of ancient underground streams, in the northwest of the test area had production capacity over 10,000 tons.

Fig. 2.111 shows a seismic section across Well T404 and corresponding discontinuity detection result. These vertical belts with intense discontinuity correspond to discontinuous, weakened, undulating, or faulted reflections under the Ordovician weathering crust, which are related to complicated cave complexes,

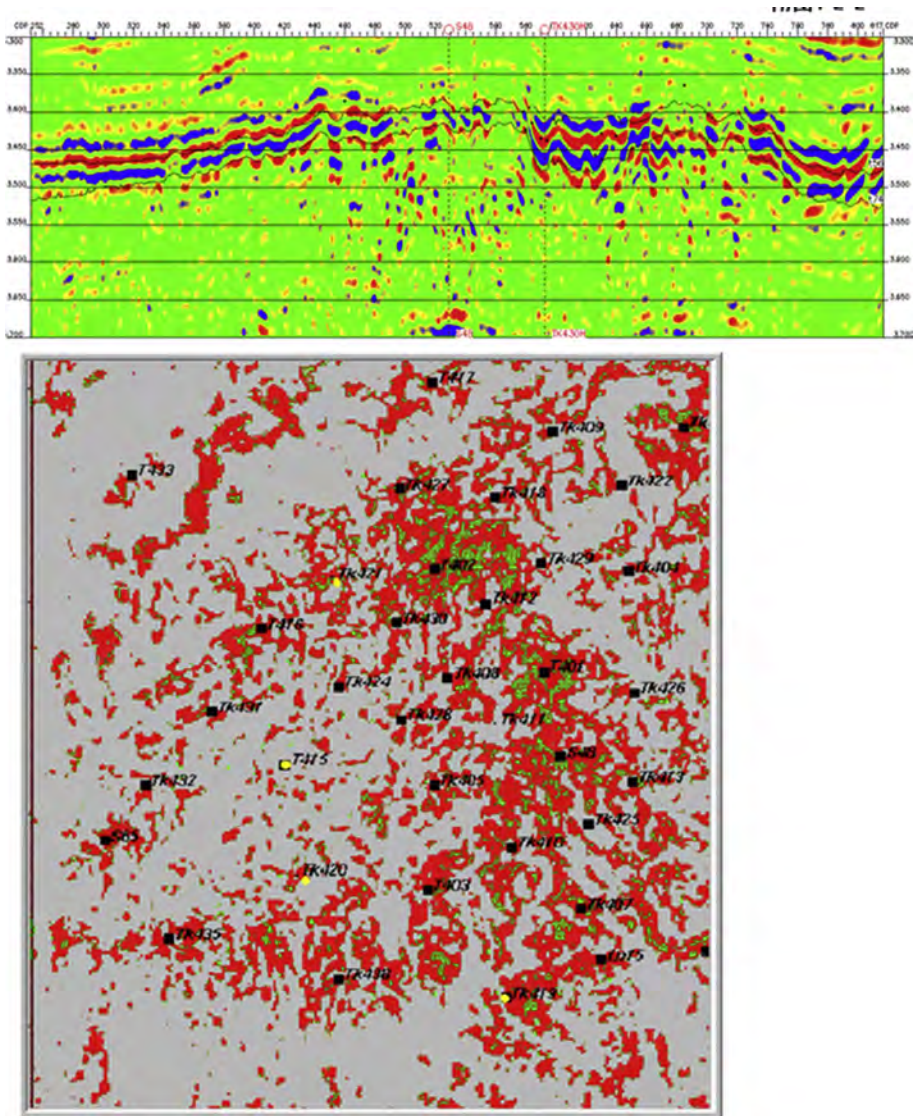


Figure 2.108 Seismic reflection signatures on an inline section across Well S48.

fracture-complicated caves, fractured zones, single faults, and fault groups. Fig. 2.112A–C show a fracture map overlaid with coherence attribute, fracture map overlaid with discontinuity attribute, top structure map of Ordovician buried hills overlaid with discontinuity attribute, respectively. The attribute of discontinuity is superior to coherence in fracture detection. In general, fracture-cave/vug units detected by discontinuity attribute extend in the same trend as regional palaeostructures. Strong belt-shaped discontinuities in *red* and *yellow* correspond to discontinuous

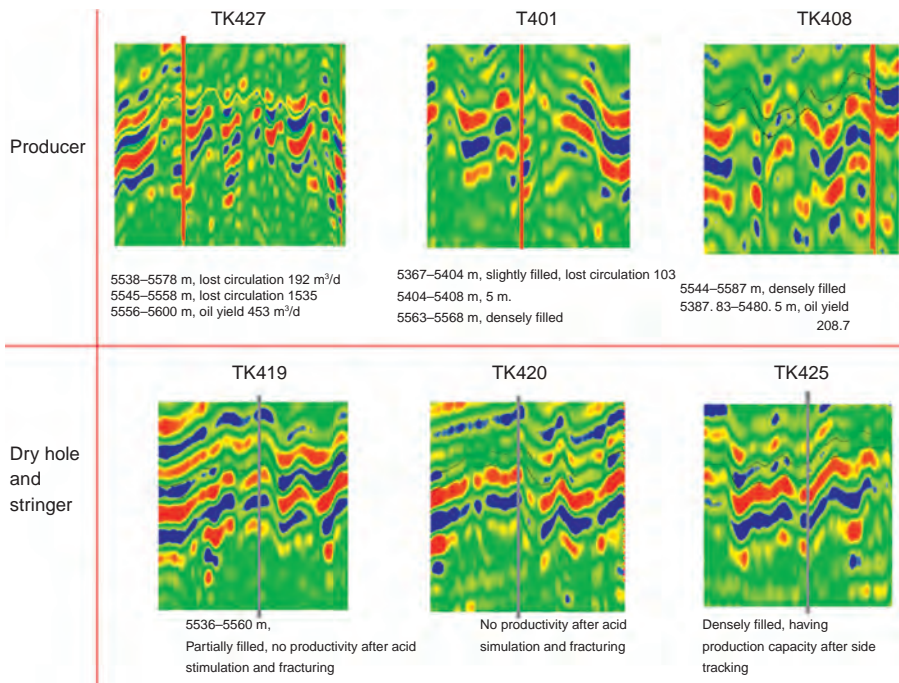


Figure 2.109 Reflection configurations for producers and nonproducers in S48 well field.

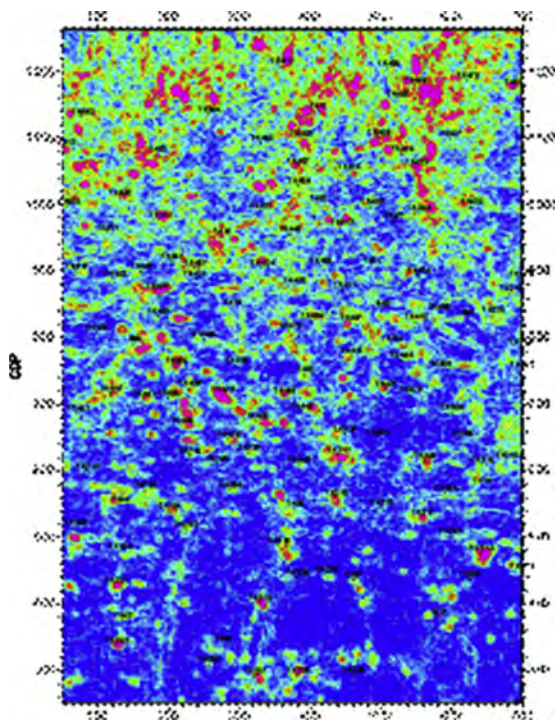


Figure 2.110 Strong amplitude clustering map within the time window from 40 to 60 ms beneath T_7^4 in S48 well field.

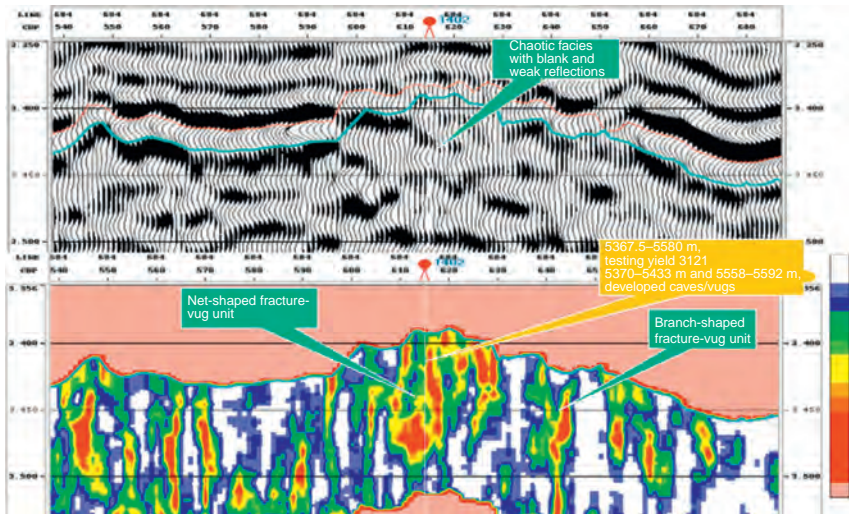


Figure 2.111 Discontinuity detection for blank and weak reflections across Well T404.

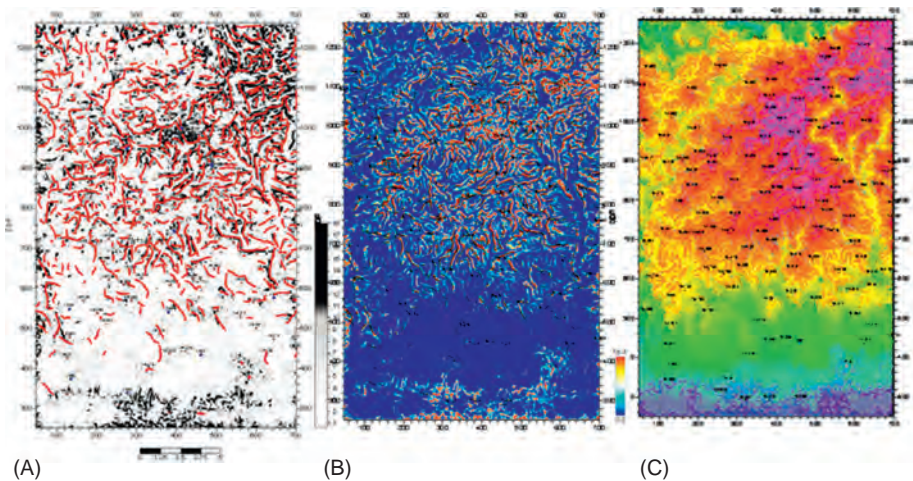


Figure 2.112 Attributes overlaid with discontinuity detection results in S48 well field. (A) Fractures overlaid with coherence; (B) fractures overlaid with discontinuity detection result; (C) top structure of Ordovician buried hills overlaid with discontinuity detection result.

reflections on seismic sections and indicate the existence of fracture-cave/vug units. Block-shaped discontinuities in *red*, *yellow*, and *blue* correspond to weak seismic reflections and indicate the occurrence of karst corrosion. Branch- or net-shaped discontinuities indicate karsts overlaid with fracture-cave/vug reservoirs.

Prestack azimuthal anisotropy-based fracture detection

A routine 3D amplitude-preserved processing workflow (including trace editing, bandpass filtering, amplitude recovery, static correction, velocity analysis, residual static correction, surface consistent amplitude compensation, prestack deconvolution, and NMO correction) was employed for P-wave azimuthal anisotropy-based fracture detection in S48 well field, the Tahe oilfield. After preprocessing, macro-bin generation, azimuth/azimuthal angle gather sorting, prestack azimuth gather envelope and normalization were used to generate high-precision 3D seismic data for fracture detection based on residual NMO and AVO analyses.

1. P-wave residual NMO-based fracture detection

We conducted some tests for fracture detection based on P-wave residual NMO in TTI media. In view of complex seismic reflections and horizons, the method of calculating residual moveout based on a reference trace is not feasible. Here a new approach was used: obtain the horizon on azimuthal gathers at an offset after offset-azimuth stacking and the horizon on near-offset gathers; subtract the second horizon from the first one to yield the moveout at different azimuths; invert the moveout by a genetic algorithm to generate the parameter related to fracture growth in the area.

The result of fracture detection was verified by formation microscanner image (FMI) data of Wells T443 and TK429. Fig. 2.113 shows FMI images of Well T443 on the left. Anisotropic responses at 5512.0–5526.0 and 5595.0–5600.0 m indicate high-dip fractures in the formation, including two intervals with vertical fractures of 8.2 m and four groups of obliquely intersectant fractures of 4.3 m. The result of fracture prediction in T443 well field in Fig. 2.113 on the right is in agreement with the result of FMI imaging.

Matrix porosity by sonic log interpretation for Well TK429 is very low (about 2%). FMI images and cross-multipole array acoustilog (XMAC) fracture analysis show that secondary pores in this well mainly consist of dissolved caves/vugs, dissolved pores, and open fractures. As per azimuthal anisotropy analysis by XMAC multipole array acoustic logging, there are no obvious anisotropic responses in this well, which indicates homogeneous isotropic formations with few high-dip fractures. This interpretation is in agreement with the result of seismic prediction shown in Fig. 2.114 on the right.

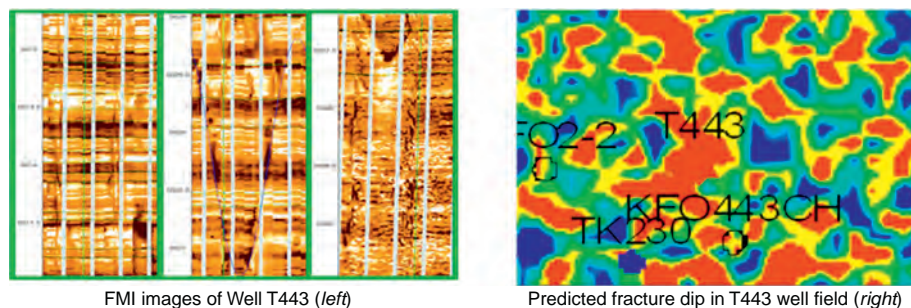


Figure 2.113 FMI images of Well T443 and fracture prediction result.

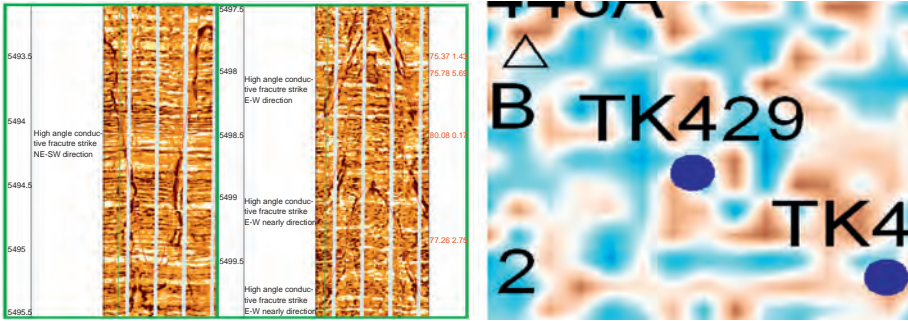


Figure 2.114 FMI images of Well TK429 and fracture prediction result. FMI images of Well T429 (left); predicted fracture intensity in T429 Well (right).

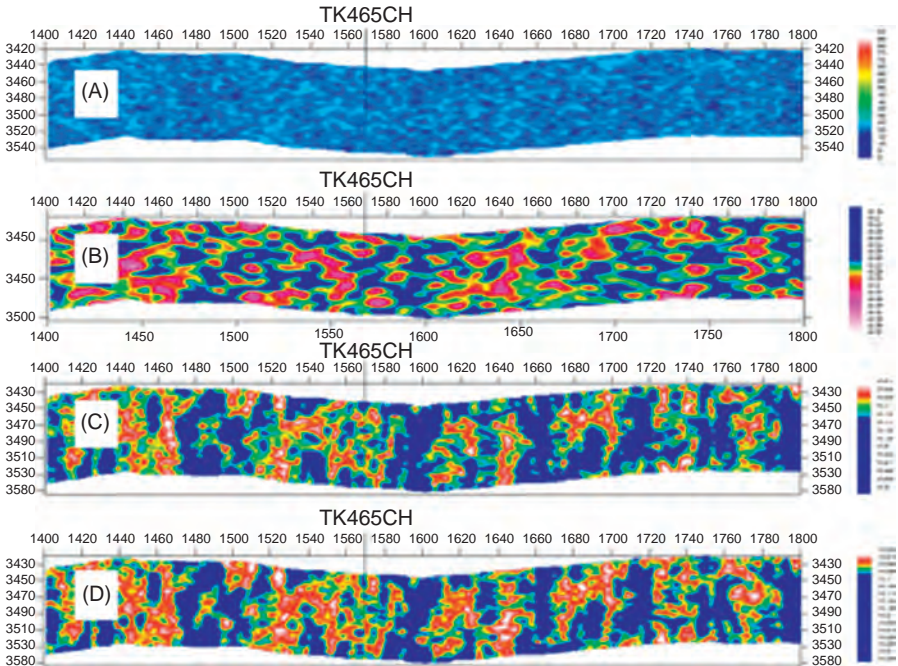


Figure 2.115 Sections across Well TK465CH showing fracture-related features.

2. P-wave AVO-based fracture detection

A seismic section across Tahe4 block has been inverted to derive fracture dip θ and Thompson parameters ϵ, δ, γ based on the theory for TTI media. Fig. 2.115 shows the results across Well TK465CH. Panel (A) shows the result of fracture dip θ and vertical fractures are plotted in blue. Panel (B) shows P-wave anisotropy ϵ ; a large ϵ indicates strong anisotropy. Some vertical belts could be observed on the section. Panel (C) shows

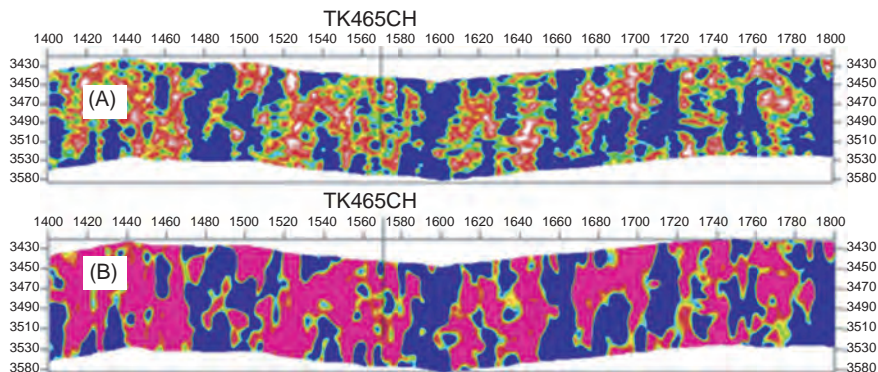


Figure 2.116 Results based on HTI and TTI assumptions.

the coefficient of variation δ , which indicates the variation of P-wave anisotropy in vertical direction. In an area with vertical fractures, this parameter denotes fracture intensity. The vertical belts on the section correlate with the result of discontinuity detection at the Ordovician top in Tahe 4 block. Panel (D) shows S-wave anisotropy γ , an indicator of S-wave anisotropy or S-wave splitting. This parameter correlates well with fracture intensity because the existence of fractures has more impact on S-wave than on P-wave. In the case of weak anisotropy, this parameter approximates to fracture density. Some vertical belts could also be observed on the section. The similarities between panels (C) and (D) indicate the dependence of these two parameters on fracture intensity and also demonstrate the credibility of inversion.

Fig. 2.116 compares the results based on HTI and TTI assumptions. The two results have some similarities related to fracture density, but the result based on TTI assumption exhibits more details.

2.5.2.2 Comprehensive description of fracture-vug reservoir

Detailed description

Comprehensive description was constrained by single-well analysis and the relationships among epikarst, palaeogeomorphology, and palaeo-drainage pattern. Reservoir sculpting within a limited time window was realized by threshold and spatial boundary constraints and 3D visualization. Fig. 2.117 shows the distribution of fracture-vug reservoirs in S48 well field. This prediction is in agreement with the result of production performance monitoring. Cave/vug systems and reservoirs with good properties occur at ancient structural highs; this result is reconciled with the occurrence of fossil karsts and also demonstrates the credibility of palaeogeomorphology-controlled multiattribute fusion.

As per the production data of Well T402, an open hole in the middle part of S48 well field, the interval at 5358.5–5602 m yielded oil at 209 t/day and water at 0.6 t/day. Cumulative oil production is 7.16×10^4 t. There are five fractured reservoir beds of 127 m thick in Well T402 according to testing and logging interpretation. Unfilled caves/vugs were interpreted to exist at the intervals of 5372–5376.5 m and

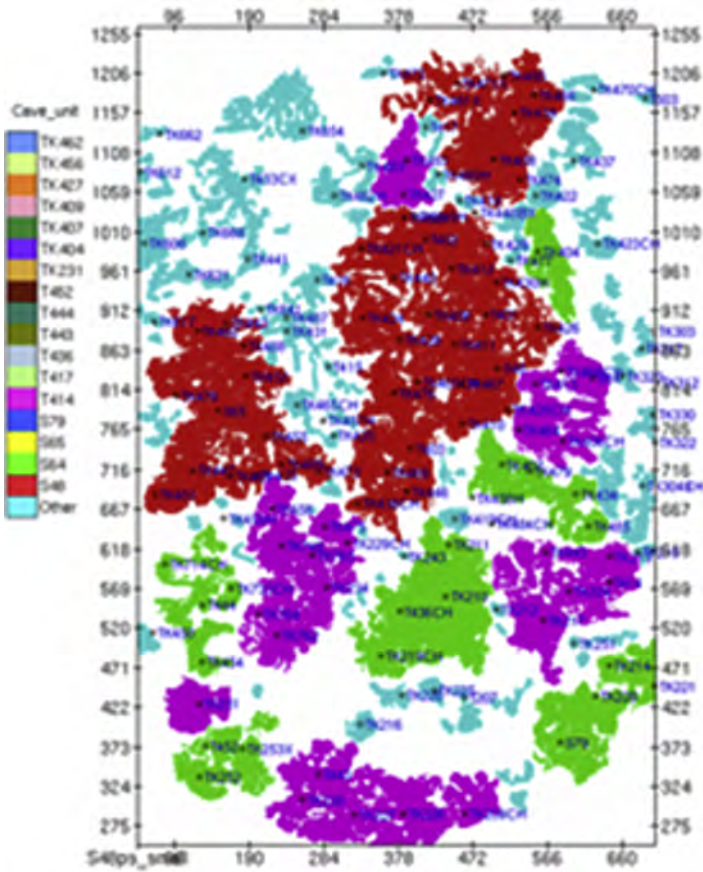


Figure 2.117 Distribution of fracture-vug reservoirs in S48 well field.

5566–5568.5 m. The prediction of fracture-vug reservoirs by multiattribute fusion is in agreement with testing and logging interpretation results for Well T402 (Fig. 2.118).

Apparent volume estimation

The result of logging interpretation is in good agreement with seismic prediction. But due to limited seismic resolution, it is hard to correlate logging interpreted reservoir beds one-to-one with seismic predictions.

The technique of 3D visualization was used. Pixel (voxel) size is related to bin size and sampling rate. The bin size is 15×15 m and vertical sampling rate is 1 ms in S48 well field; thus the apparent volume of a voxel is 1267 m^3 . The volume of a fracture-vug reservoir is the sum of all voxel volumes. The results of 17 fracture-vug units in S48 well field are shown in Table 2.5.

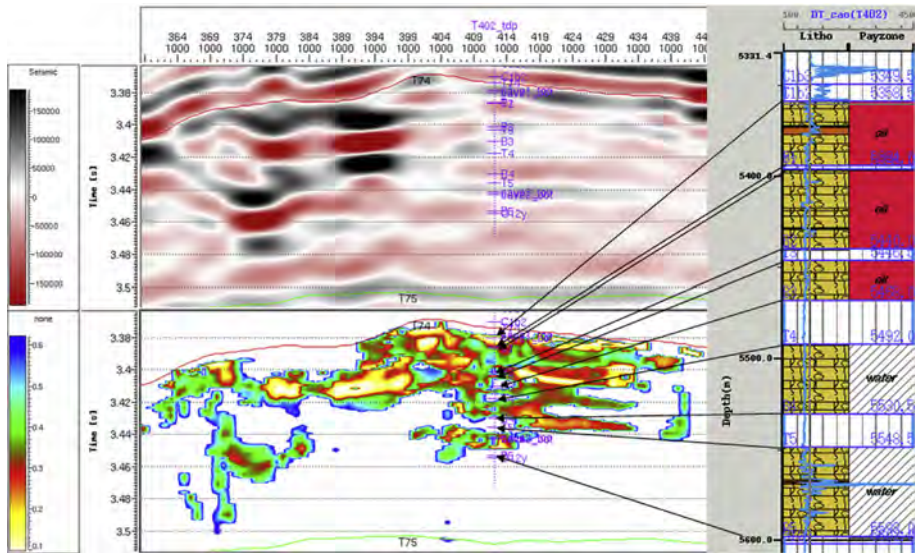


Figure 2.118 An xline seismic section across Well T402, distribution of predicted fracture-vug reservoir (left) and logging interpretation (right).

Table 2.5 Apparent volumes of 17 fracture-vug reservoirs in S48 well field

No.	Unit	Apparent volume ($\times 10^5 \text{ m}^3$)	No.	Unit	Apparent volume ($\times 10^5 \text{ m}^3$)
1	S48	8.139	10	T452	1.198
2	S64	1.459	11	TK231	0.443
3	S65	5.25	12	TK404	0.7381
4	S79	2.463	13	TK407	1.048
5	T414	2.102	14	TK409	2.53
6	T417	9.289	15	TK427	0.789
7	T436	4.84	16	TK456	2.943
8	T443	2.64	17	TK462	0.1482
9	T444	1.166			

Goodness of fit

In order to analyze the accuracy of reservoir description and apparent volume estimation, production data and logging data were used in qualitative and semi-quantitative analyses. Logging sampling rate is dozens of times as much as seismic sampling rate and vertical seismic resolution is much less than logging resolution; the most direct and simple way is to verify seismic prediction by log interpretation. The standards are shown in [Table 2.6](#).

Table 2.6 Standards of verifying seismic prediction by log interpretation

High goodness of fit (grade A)	Medium goodness of fit (grade B)	Low goodness of fit (grade C)
Seismic prediction larger than log interpretation	Deflecting downward	Seismic prediction not interpreted on log data
Seismic prediction close to log interpretation	Deflecting upward	Log interpretation not predicted on seismic data
Seismic prediction in agreement with log interpretation	Bias ≤ 5 ms (vertical)	Bias > 5 ms (vertical)
	Smaller value predicted	
	Bias of 2-CDP (lateral)	

The fracture-vug unit, S65, is taken as an example. S65 is a grade-I interconnected unit. Original oil in place (OOIP) is 560.6×10^4 t; recoverable reserves are 90.83×10^4 t; cumulative production is 80.635×10^4 t (Fig. 3.7). The apparent volume is 183,000 m³s. The distribution and thickness of fracture-vug units are shown in Fig. 2.119. Cumulative reservoir thickness at ancient structural highs and karstic slopes, for example drilled in Wells S65, TK447, TK435, TK451, and TK432, mostly exceeds 6 ms, or 18 m. These wells also have the largest productivity. Reservoir rocks are less developed or thin at ancient structural lows.

Fig. 2.120 shows the seismic section across Well S65 and the result of reservoir description. Seismic reflections at Well S65 feature weak amplitude. Two 3-m high

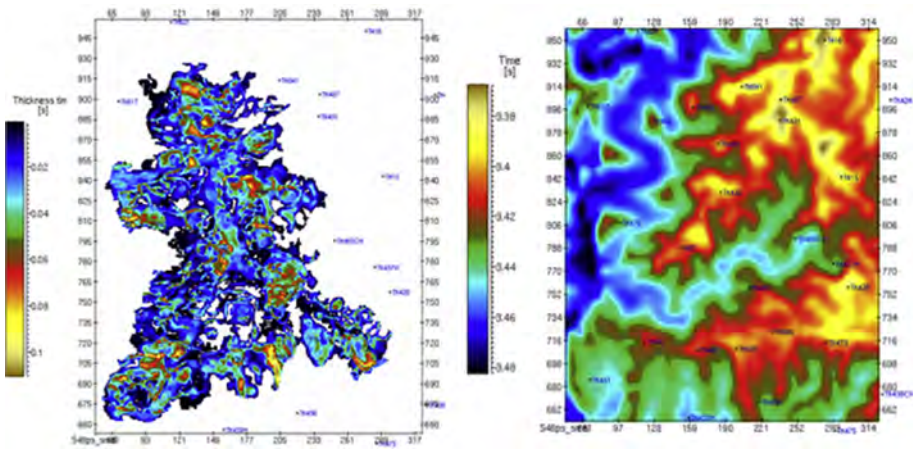


Figure 2.119 Thickness map of fracture-vug units (left) and T_0 map of Ordovician top (right).

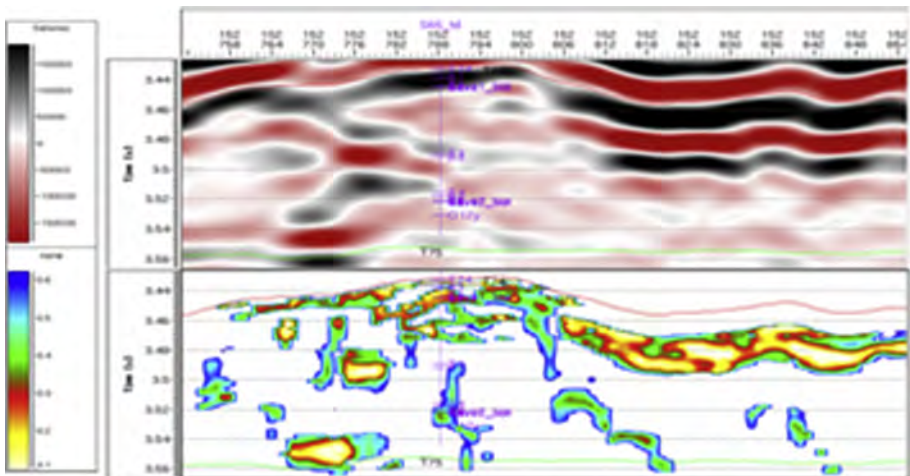


Figure 2.120 Seismic section across Well S65 and predicted fracture-vug units.

caves and three reservoir beds drilled in the Ordovician System correspond to seismic predictions except for slightly larger reservoir thickness predicted. Similarly bead-like reflections at Well TK488 are in excellent agreement with three reservoir beds as per log interpretation (Fig. 2.121). Another cross-well section (Fig. 2.121) shows the distribution of S65 unit across six wells. There are 25 reservoir beds drilled; except for three grade-III reservoirs, 88% of reservoirs have been successfully predicted (Fig. 2.122) (Table 2.7).

There are 118 vertical wells in the test area. Except for eight wells drilled at the boundaries with small folds and two wells with insufficient log data, the additional 108 wells were included to verify seismic prediction in accordance with the standards listed in Table 2.6. Seismic predictions correlate well with log interpretations at 68 well sites, accounting for 62.96% of the total. Seismic predictions basically correlate with log interpretations at 32 well sites, accounting for 29.63% of the total. In summary, seismic predictions correlate with log interpretations at 100 well sites, accounting for 92.59% of the total. Seismic predictions are not in agreement with log interpretations at eight well sites, accounting for 7.41% of the total (Fig. 2.123).

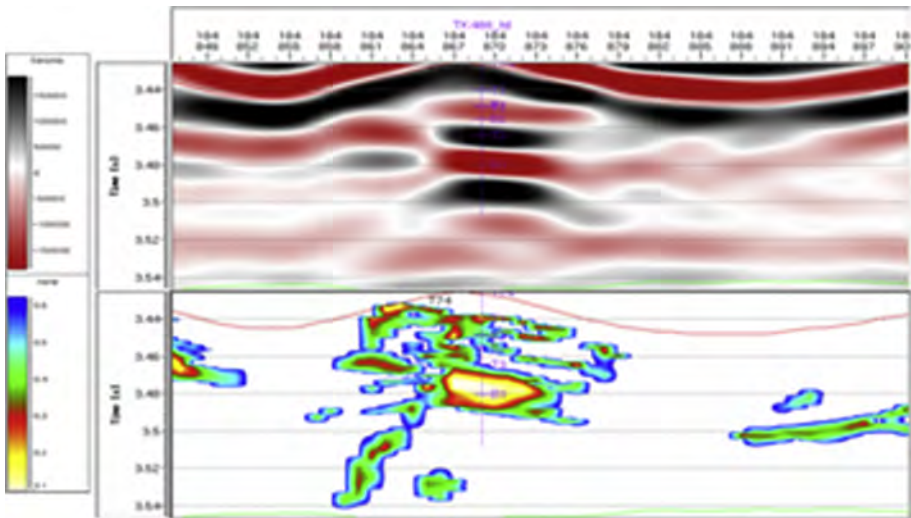


Figure 2.121 Seismic section across Well TK488 and predicted fracture-vug units.

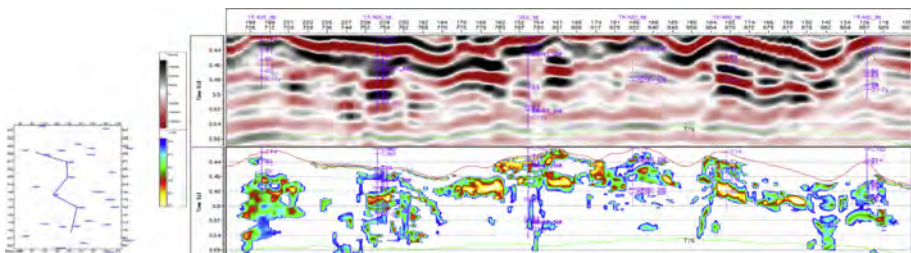
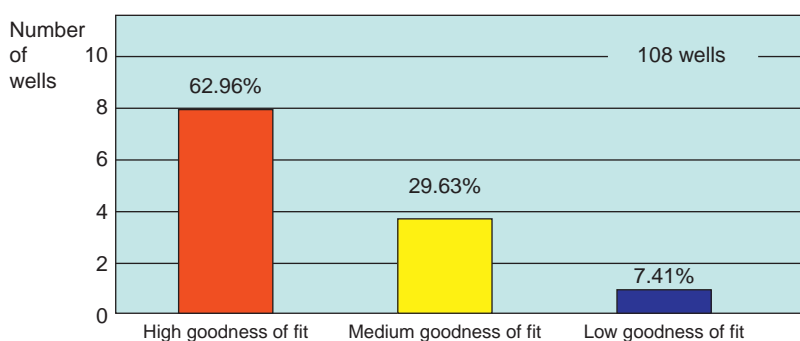


Figure 2.122 Cross-well seismic section and predicted fracture-vug units (the location of the section is shown on the left).

Table 2.7 Reservoir parameters of S65 unit

Unit	Well name	Fracture-vug interval (m)		Pay interval (m)	Cumulative production ($\times 10^4$ t)	
		Depth	Thickness		Oil	Water
S65	S65	5485–5488	3	5460.5–5476.7	17.16	3.51
		5724–5727	3	5485.0–5488.0		
				5503.2–5520.0 (water layer)		
	TK447	5474.7–5485	10.3	5467–5485.0	11.6	1.46
	TK432	5571.5–5585	13.5	5438.5–5456.0	7.4	6.97
				5483.0–5529.5		
	TK461	5594–5596	2	5530.0–5539.0	5.05	2.68
				5585.0–5604.6		
	TK435	No		5440.0–5500.0	11.3	1.48
	TK455	5535–5539	4	5486.4–5488.7	7.02	0.32
	TK451	5521–5525		5504–5560.0	8.164	1.58
	TK478	5503.5–5505	1.5	5497–5595	0.74	1.28
	TK442	5518.8–5533.6	14.8	5461–5533.55	6.4	3.33
	TK473	No		5424.5–5480	4.67	1.84
				5497.92–5580.25		
	TK488	No		5450.65–5521.36	0.39	0.54
				5562.0–5666		
TK482	No		5490–5530	0.291	0.46	
			5570–5660			
TK489	5450–5461	11	5443–5549.54	0.45	0.06	

**Figure 2.123** Goodness of fit.

As per the results of reservoir sculpting, the volume of 17 fracture-vug units delineated in S48 field were calculated by a topological algorithm based on threshold values of reservoirs and reservoir boundaries (in time domain) (Table 2.8).

According to the analyses of production data, estimated reserves, recoverable reserves, OOIP and apparent volume, the dependence of recoverable reserves and

Table 2.8 Apparent volume of fracture-vug units in S48 well field

No.	Unit	Apparent volume (m ² s)	Recoverable reserves (×10 ⁴ t)	OOIP (×10 ⁴ t)
1	S48	289,000	500.35	3068.7
2	S64	51,700	28.42	148
3	S65	183,000	90.83	560.6
4	S79	87,900	28.6628	206.9
5	T414	74,400	89.8554	402.78
6	T417	3150	4.5262	35
7	T436	174,000	33.25	428.87
8	T443	95,900	26.62	225.3
9	T444	40,900	30.2289	133.3
10	T452	43,800	18.3239	139.78
11	TK231	16,500	8.78	35.9
12	TK404	25,600	18.59	105.7
13	TK407	37,800	38.88	317.54
14	TK409	93,900	99.27	630
15	TK427	30,300	48.08	265
16	TK456	104,000	39.96	324.6
17	TK462	5250	22.8529	153.6

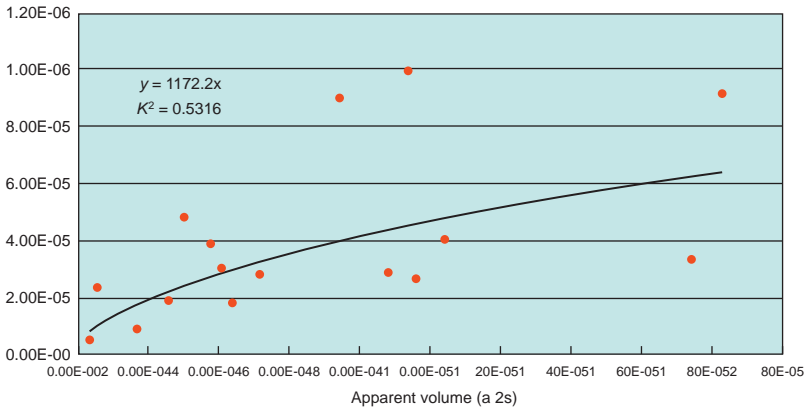


Figure 2.124 Dependence of recoverable reserves on apparent volume.

OOIP on apparent volume is shown in Figs. 2.124 and 2.125, respectively. OOIP correlates with apparent volume (correlation coefficient R_2 of 0.6).

2.5.2.3 Fluid detection

Fluid detection based on prestack elastic inversion

1. Fluid detection based on EI inversion

Fracture-vug carbonate reservoirs in S48 field feature strong heterogeneity. There are some relationships between angle-related EIs derived from CSSI and fluid properties.

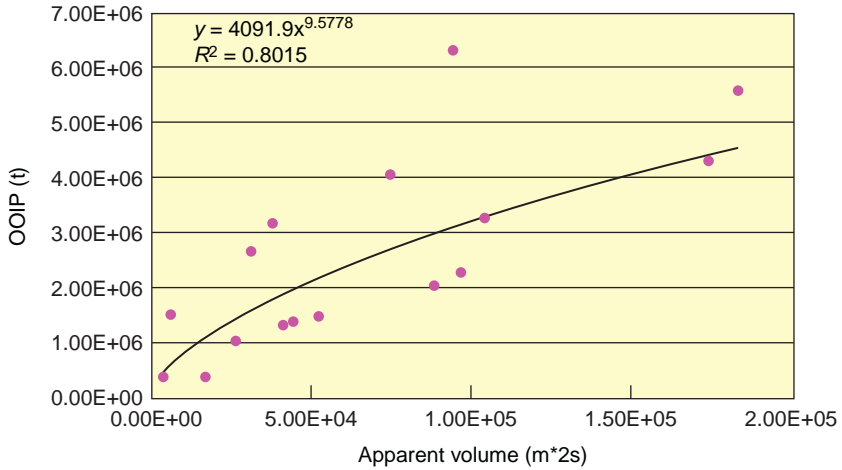


Figure 2.125 Dependence of OOIP on apparent volume.

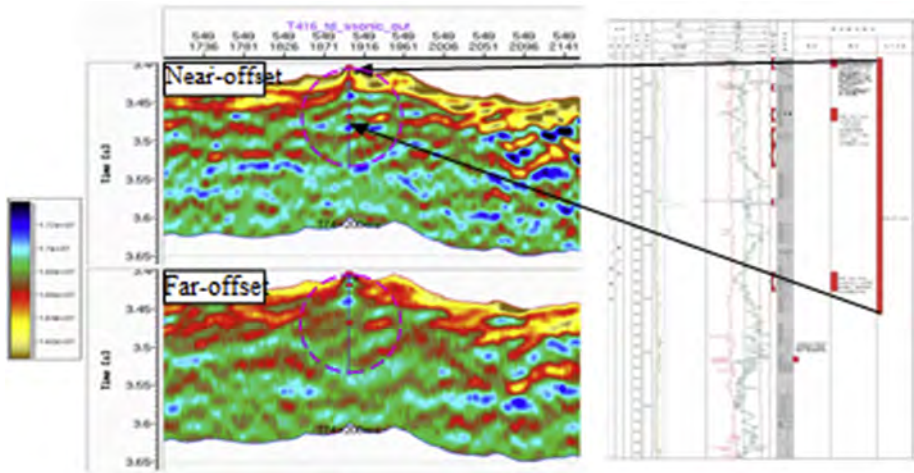


Figure 2.126 EI sections across Well T416: EI (left) and production test (right).

Fig. 2.126 shows the results of EI inversion across an oil producer T416. Differences between near-offset and far-offset EIs are related to reservoir properties.

Fluid detection was based on the cross-plotting of log-based near-offset and far-offset EIs. Fig. 2.127 shows the results across Wells T402 and T416. These results have some correlation with the result of production test, which means EI-based fluid detection is feasible.

2. Fluid detection based on LMR inversion

Four partial stacks corresponding to different incident angles (0–10, 8–16, 16–24, and 22–32 degrees) were used in LMR inversion to obtain P-velocity, S-velocity, $\lambda\rho$, $\mu\rho$, $\lambda\mu$, V_p/V_s and σ . Fig. 2.128 shows inverted sections across Well T402 (the upper two plots are $\lambda\rho$ and $\lambda\mu$; the lower two plots are σ and V_p/V_s). As per the production tests, low $\lambda\mu$, low V_p/V_s and low σ indicate good reservoir beds.

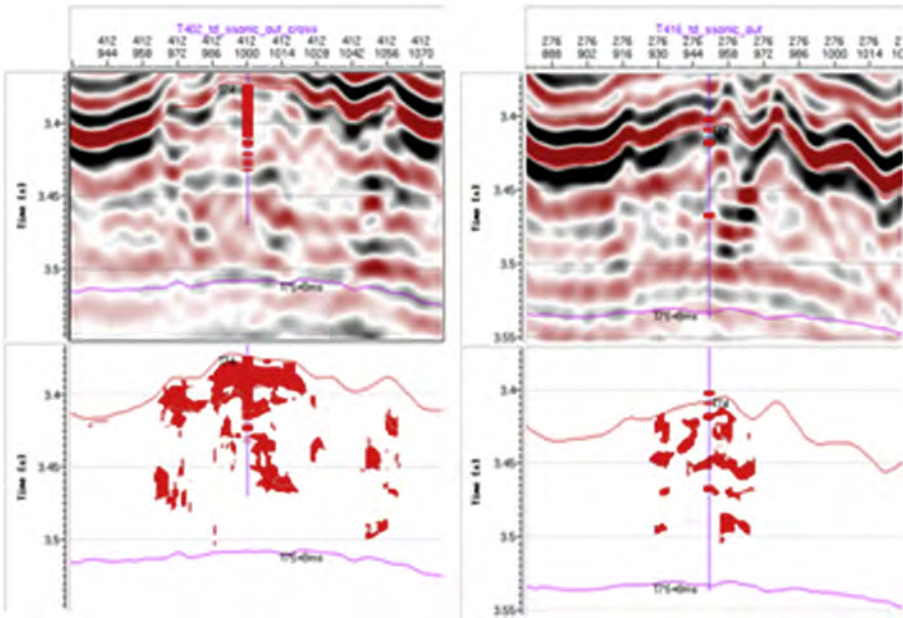


Figure 2.127 EI-based fluid detection: pay zones (red block), Well T402 (left), and Well T416 (right).

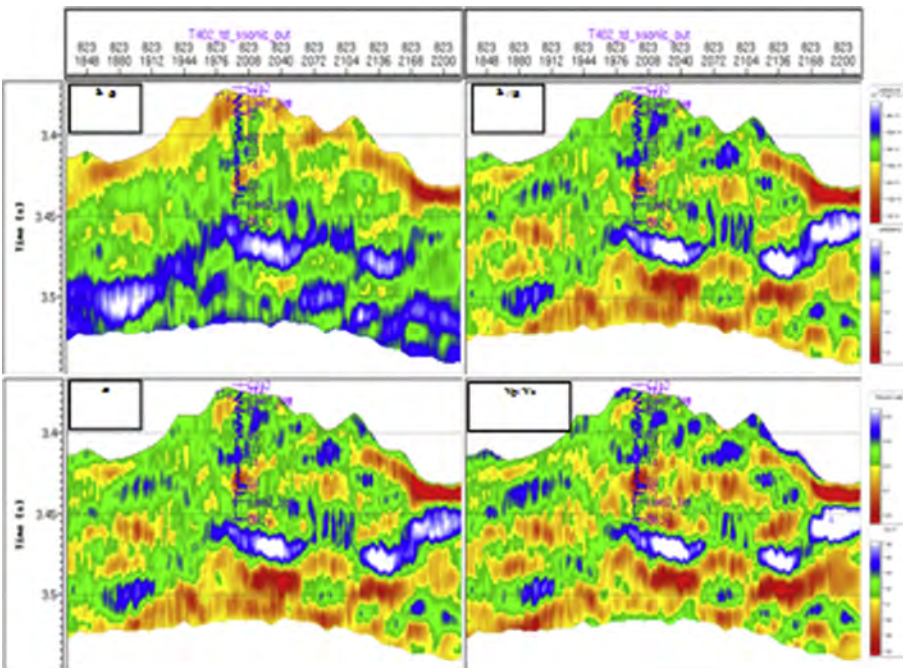


Figure 2.128 Inverted sections across Well T402.

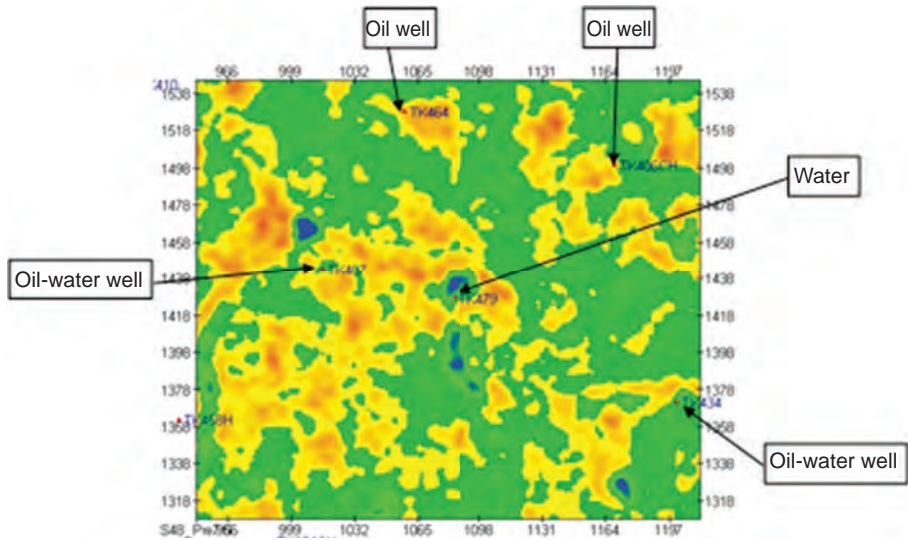


Figure 2.129 Fluid probability in TK479 well field and well performance.

Fluid probability analysis

Fluid probability models at different depths built by Monte Carlo methods were used to predict fluid probability. In view of the differences between gradient and intercept values obtained by forward modeling and those fitted with field seismic data, it is necessary to perform well-tie calibration.

This method and the scale factor derived from well-tie calibration were used to predict fluids distribution in the upper part of the Yijianfang Formation (20 ms below T74). Fig. 2.129 shows inverted fluid probability around Well TK479. As per the results, fluid probability is usually above 0.5 at oil and gas well sites and below 0.5 at water well sites.

3D geological modeling of a fracture-vug carbonate reservoir

3

Reservoir geology models are the basis for reservoir numerical simulation, preparation for oil field development plans, and making development decisions. In fracture-vug carbonate reservoirs, oil can be hardly found in the matrix but is mainly found mainly in caverns, fractures, and vugs developed during tectonism and paleokarstification. Knowing how to build a geological model which can quantitatively depict the 3-dimensional (3D) characteristics and attribute distribution of fracture-vug structures is critical in development geology.

Generally, to model a fracture-vug carbonate reservoir in 3D geological mode faces the following challenges:

1. It is difficult to describe the 3D characteristics of a fracture-vug reservoir due to its complicated distribution and high heterogeneity.
2. The conventional “porous” reservoir characterization method for clastic reservoirs is not suitable for fracture-vug reservoirs due to big difference among caverns, fractures, and vugs in them.
3. Fracture-vug reservoirs may be developed through tectonism combined with karstification, which is neither depositional as for clastic rock nor structural stress as for pure fractured reservoirs, therefore it is difficult to build a mathematical model.

This chapter has chosen the fracture-vug carbonate reservoir in the test area in the Tahe Oilfield as a prototype model to illustrate the pore space, introduce the 3D geological modeling methods, and characterize the 3D structure and attribute distribution of fracture-vug reservoirs.

3.1 Identification of fracture-vug reservoir

After multistage tectonism, karstification superimposing modification, and hydrocarbon accumulation, various caverns, vugs, large-scale fractures, and microfractures are coexistent, resulting in significantly different pore space and highly heterogeneous fracture-vug reservoirs. A combination of well and seismic data is required to improve the description of fracture-vug reservoirs in different scales, which is the basis for 3D geological modeling of such a reservoir.

3.1.1 Pore space

Studies on drilling, core, well logging, and production performance data indicates that pore space in fracture-vug carbonate reservoirs can be classified into three types: cavern, vug, and fracture. Vugs and fractures play an important role in pore

and flow space, and can act as the important pore space and major flow channels for formation fluids. Without essential reservoir properties, the matrix can only act as interlayers or barriers to separate and block pore space.

3.1.1.1 Matrix

The matrix is the pore network system composed of matrix pores connected by microfractures, ultramicrofractures, or poro throats cut by the fracture system, and with an aperture less than or equal to $10\ \mu\text{m}$ (Zhang et al., 1996). The matrix mainly represents a reservoir interval containing less-developed solution pores, vugs, and fractures. In order to reveal the characteristics of the fracture-vug reservoir matrix in the Tahe Oilfield, a total of 50 core samples were recovered from nine wells in seven blocks (these samples cover the whole oilfield from north to south, and thus are regionally representative) and were analyzed using a variety of technological means, such as porosity-permeability analysis, apparent observation, computed tomography (CT), cast slice, nuclear magnetic resonance (NMR), and rate-controlled mercury injection.

The distribution of the core permeability and porosity (Fig. 3.1) indicates that the permeability of the 50 cores are ultra-low (extreme-low), less than $10.0 \times 10^{-3}\ \mu\text{m}^2$: 47 cores have ultra-low permeability of less than $1.0 \times 10^{-3}\ \mu\text{m}^2$, accounting for 94% of total cores; three cores have extreme-low permeability of more than $1.0 \times 10^{-3}\ \mu\text{m}^2$ and less than $10.0 \times 10^{-3}\ \mu\text{m}^2$, accounting for 6% of total cores; eight cores have porosity of more than 2.0% (lower limit of porosity), accounting for 16.0% of total cores; and 23 cores have porosity of less than 1.0%, accounting for 46% of total cores. The test result suggests that the matrix system in the fracture-vug carbonate reservoirs in the Tahe Oilfield can be classified into ultra-low (extreme-low) permeability and extreme-low porosity reservoirs, which is considered to be almost ineffective.

Apparent observation (Fig. 3.2) indicates that the matrix recovered from the fracture-vug reservoir in the Tahe Oilfield has no obvious pores but contains abundant network-like microfractures, particularly in block 4 where a 5-cm-long core sample contains 5–20 visible microfractures on the surface, of which 8–16 are most concentrated. Core samples recovered from the other six blocks share similar

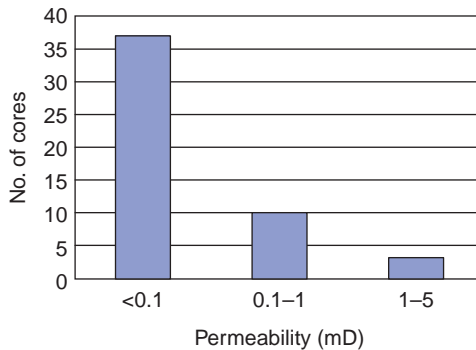


Figure 3.1 Core permeability distribution.

developments, showing 5–10 microfractures concentrated. Sixty-four percent of the fractures have an aperture of less than 0.1 mm, and 33% more than 1 mm but are highly filled. It is concluded that the microfractures are well-developed but highly filled in the matrix of the carbonate reservoirs in the Tahe Oilfield.

CT scanning analysis (Fig. 3.3) indicates that no obvious pores but microfractures are found in the cores, and the microfractures in the cores are very different from those observed on the surface in distribution features. In conclusion, the microfractures in the matrix of the fracture-vug reservoir in the Tahe Oilfield exhibit three types of typical distributions:

1. Less developed and highly filled microfractures which present weak microfracture features on CT photographs. This type of matrix has a very low permeability.
2. Relatively wider microfractures distributed locally but not abundant. This type of matrix is relatively permeable.
3. Well-developed microfractures. This type of matrix has a good permeability. Obviously, the permeability is subject to the development of the microfractures in the matrix core. Well-developed microfractures deliver high permeability, and poorly developed microfractures deliver low permeability.



Figure 3.2 Fractures observed on the cores.

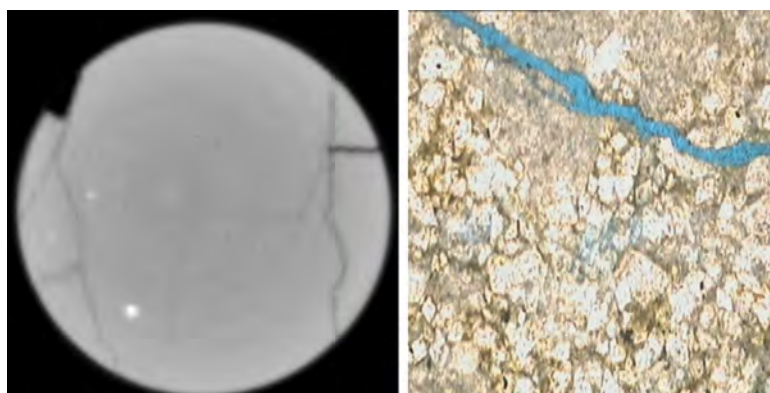


Figure 3.3 CT scanning photo.

Cast slice analysis (Fig. 3.4) confirms there are very few intergranular and solution pores distributed locally in the cores. These pores are isolated and poorly connected with each other. Microfractures, however, are quite visible, and are essentially network-like and relatively well-developed. It can be concluded that the very few isolated pores cannot act as effective permeable space in the matrix, but it is the well-developed microfractures that contribute to the permeability of the matrix.

NMR T2 spectrum was used to analyze occurrence state of the fluids in the pores and quantitatively estimate reservoir prediction parameters such as movable water saturation and bound water saturation. Average fluid saturation calculated from the test result is 30.17% (Fig. 3.5). Movable water stays mainly in microfractures.

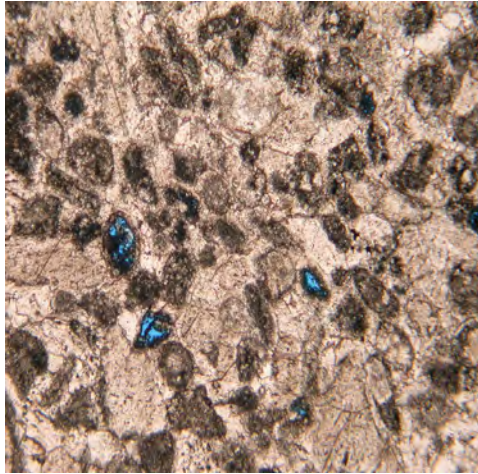


Figure 3.4 Cast slice.

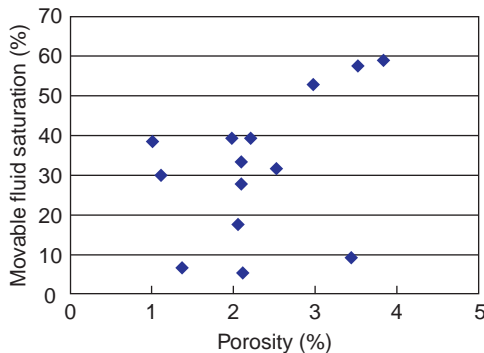


Figure 3.5 Movable fluid saturation distribution in the carbonate matrix in the Tahe Oilfield.

Local cores contain fluid but it is less moveable. It can be concluded that the microfractures and fine fractures developed in the cores are spaces for moveable fluid.

The rate-controlled mercury injection method was used to analyze the pore structure for quantitatively determining reservoir pores and throats, and their distribution of different sizes, which in turn more clearly characterize microscopic pore structure. The test concluded that the cores recovered in the Tahe Oilfield contained very few throats and had extreme-low permeability (Fig. 3.6). That is to say, there are no pores and throats for containing fluid in the matrix; unlike conventional clastic rock, the microfractures provide the primary reservoir space and flow channels in the matrix.

3.1.1.2 Caverns

Caverns of more than 200 mm diameter are important reservoirs and flow spaces in fracture-vug carbonate oil reservoirs (Fig. 3.7). They differ in size, shape and spatial distribution (Archie, 1952; Choquette and Prey, 1970; Lucia, 1983; Yuzhu, 2008).

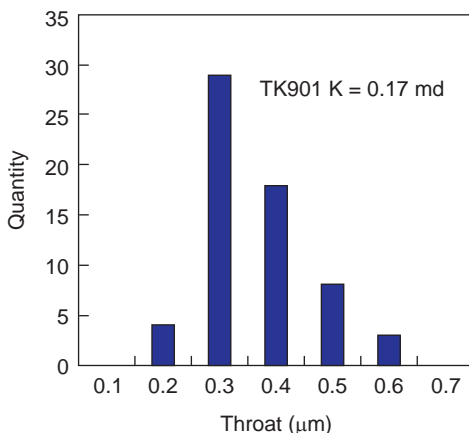


Figure 3.6 Throat development (histogram) in the carbonate matrix in the Tahe Oilfield.

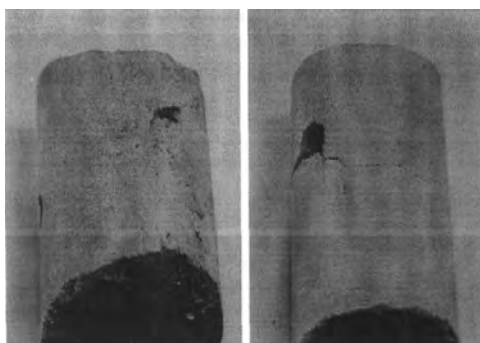


Figure 3.7 Photos of full-diameter cores recovered from the solution-pore reservoir in the Tahe Oilfield.

Caverns are defined as large vugs of more than 10 m in diameter, which are recognizable by existing geophysical techniques and can be characterized using deterministic modeling methods. Caverns usually result in drilling break, lost circulation, and well kick. They represent primary production layers.

Interpretation of 75 wells by drilling, well logging and core data indicates that 48 wells were drilled into caverns, accounting for 64% of total wells in the study area. The average height of the cavern is 10 m. Seventy-five percent of wells were acidized and fractured for production. The minimum cavern is 1 m. Forty-three caverns are 10 m high; 11 are 10–20 m high; 9 are more than 20 m high (Table 3.1).

Core data revealed a 20-m-high fully filled cavern (5535–5555 m, Well T615). Well logging data identified a 72-m-high cavern (5586–5658 m, Well TK409). Development performance data confirms that the Ordovician carbonate reservoir in the Tahe region is so special that caverns and vugs are the primary and fractures are the secondary reservoir spaces in the fracture-vug oil reservoir while the matrix cannot act as a reservoir.

3.1.1.3 Vugs

Vugs are defined to have a diameter of less than 200 mm, which are usually recognizable using conventional well logging, imaging logging, and core data. In the Tahe Oilfield, for example, cores recovered from the 5367.5- to 5376.6-m interval of Well T401 have an average porosity of 2.67%, and contain well-developed network-like fractures and small vugs which are filled with oil. Core samples recovered from the 5391.37- to 5397.83-m interval of Well TK407 contain abundant oil-filled dissolved pores, with a pore density ranging from 3.5 to 8.5 per 10 cm², and multiple oil-filled high-angle structural fractures. Although large vugs and caverns were not found in this interval, blowout occurred while drilling, reflecting a good reservoir performance. Core samples recovered from the 5457.38- to 5478.67-m interval of Well S65 are rich in microfractures and small vugs filled with brown oil.

3.1.1.4 Fractures

Fractures are widely developed reservoir space and important flow channels in carbonate reservoirs, where they exhibit extremely active hydrocarbon show. Fractures can be identified using conventional well logging, imaging logging, and core data.

Table 3.1 Height statistics of different types of caverns in the fourth block, the Tahe Oilfield

Type of cavern	Number of caverns	Minimum height (m)	Well example	Maximum height (m)	Well example	Average height (m)
Filled	25	1	TK422	72	TK409	13.3
Partially filled	15	1	T416	26	TK464	6.1
Unfilled	27	1	TK486	30	TK471X	8.7

Fracture development level and morphology

In the study area, structural, structural dissolved and diagenetic pressolved fractures (stylolites) have been developed, but bedding or plane fractures are fewer. Karst fractures were formed during weathering and dissolution periods. They are open, highly filled but ineffective. Diagenetic fractures involve pressolved stylolites and pressure fractures developed during the middle-deep buried stage, among which the meandering dissolved fractures formed through pressure-erosion along original stylolites are very effective. Fluorescence slice statistics indicate that the structural and structural dissolved fractures exhibit high percentages of hydrocarbon show, but the stylolites have better hydrocarbon show. The fractures enable effective vugs to be connective and allow them to become important flow channels. By average aperture, the fractures are defined as small (0.01–1 mm aperture), middle (1.0–10 mm aperture), and large (more than 10 mm aperture); by filled degree, the fractures are open or filled. Open fractures are effective, while the effectiveness of filled fractures is subject to fillers and filling mode. Fracture shape reflects its bending degree. A structural fracture commonly presents a regular shape with a comparably flat and straight fracture surface.

From the point of fracture identification, the seismically recognizable fracture system is called the large-scale fracture system which can be simulated by a deterministic model, and the fracture system that is unrecognizable by seismic data but recognizable by well logging and core data is called the microscale fracture system which should be simulated by a stochastic model.

Dynamic indicator of fractures

Core observation, CT, and cast slice provide direct ways to observe fracture development inside and outside a core (Figs. 3.2, 3.3, and 3.4). The flow pressure curve indicates that the test pressure on a fracture-vug carbonate core fluctuates. Specifically, more developed microfractures make the test pressure fluctuate more at a steady state; especially when there are open fractures, the test pressure changes fiercely (Fig. 3.8), and rapid pressure drops may be seen, indicating that the

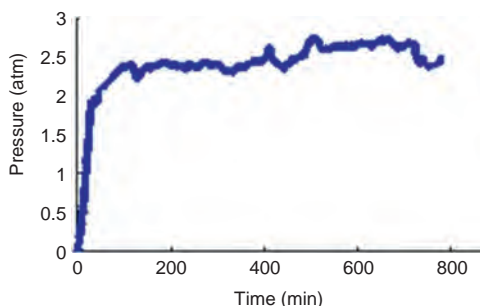


Figure 3.8 The flow curve of 13–34/55(1) core from Well T901.

fracture is highly flow-conductive, and therefore requires a low pressure difference. A carbonate core may share a similar flow image with a sandstone core in the case where fractures are either absent or largely filled. The core flow curve provides the measurement of the development and connection of internal fractures. Quicker fluctuation means well-developed fractures; stronger fluctuation (large amplitude) means more open fractures.

3.1.2 Single-well identification of fracture-vug reservoirs

Based on the identification accuracy provided by oilfield data, reservoir space in the fracture-vug carbonate reservoir can be divided into four types: cavern, vug, large-scale fracture, and microscale fracture which form three types of reservoir: cavernous, vug, and fractured reservoirs. Table 3.2 lists how to identify these reservoirs by well logging and drilling data.

3.1.2.1 Cavernous reservoirs

A cavern is an ideal reservoir space for hydrocarbons and is classified as a Class I reservoir in well logging interpretation results. This type of reservoir typically yields a high initial production and maintains a long and stable production period. Examples are the Lower Ordovician reservoirs drilled in S48, T401, T402, and TK407 wells in the Tahe Oilfield. Providing a high initial productivity for a long and stable period, this Class I reservoir is considered to be one of the important reservoirs in the Ordovician carbonate oil reservoir in the Tahe region. Using the single-well core, well logging, imaging logging, acidizing, fracturing, and testing data, the cavernous reservoirs covering 75 single wells are further divided into three types: unfilled, partially filled (or semi-filled), and filled, depending on the filling degree of the caverns. It is noted that unfilled and semi-filled caverns are relatively defined due to different scales and the accuracy of the data used.

Coring recovery rate is low in cavernous intervals (contains unfilled and partially filled caverns), therefore such intervals often lack core data. Caverns and fractures usually result in drilling break and lost circulation during drilling operations, and well logging data were acquired only from a small proportion of wells, making it difficult to identify this type of reservoir in single wells. The basis for identifying the filling degree of cavernous reservoir is as follows:

Unfilled caverns exhibit: (1) drilling break, lost circulation and low drilling time (less than 10 min/m, Fig. 3.9); (2) evident enlarged boreholes; (3) low resistivity, usually less than $20 \Omega \cdot \text{m}$; (4) high apparent porosity on porosity log; (5) low natural gamma logging (GR) (Fig. 3.10), less than 20 API (the numerical unit of natural gamma logging, it is a relative value defined by the American Petroleum Institute); and (6) thick and continuous dark-colored patterns on formation micro-scanner image logging (FMI) (Fig. 3.10). Evident drilling break and lost circulation were recorded in 22 wells in the fourth block of the Tahe Oilfield.

Table 3.2 Well logging response and drilling indicator of the Ordovician fracture-vug reservoir in the Tahe Oilfield

Reservoir space		Drilling indicator	Core	Borehole diameter (in.)	GR (API)	KTH (API)	RD, RS* ($\Omega \cdot m$)	DEN* (g/cm^3)	AC* ($\mu s/ft$)	CN (%)	FMI	Seismic indicator
Cavern	Unfilled	Drilling break, lost circulation, drilling time <10 min/m	Failed	Particularly evident enlargement	< 20	< 20	RD < 20	Very low	Very high	Very high	A thick interval of dark-colored image	Bead-like pattern
	Partially filled	Slight lost circulation, drilling time >5 min/m	Failed	Comparatively evident enlargement	20 ~ 60	Obviously less than GR	RD < 20	Very low	Very high	Very high	Evidently light-colored matrix image in caverns	Bead-like pattern
	Filled	No lost circulation, drilling time >5 min/m	Filling property recognizable	Minor enlargement	> 60	Close to GR	RD < 20	Very low	Very high	Very high	Fully or partially dark-colored image in caverns	Bead-like pattern
Fracture and vug		No drilling break, no lost circulation, drilling time >10 min/m	Visible microscale fractures and vugs	Minor enlargement	< 15	< 15	RD20–200, RD > RS	Obviously higher than matrix	Obviously higher than matrix	Obviously higher than matrix	Obvious strap-shaped and subcircular, dark-colored image	Chaotic and weak reflection
Fracture		No drilling break, no lost circulation, drilling time >10 min/m	Visible microscale fractures	Basically no enlargement	< 15	< 15	RD100 ~ 1000, RD > RS, with evident “dual-track” feature	Close to matrix	Close to matrix	Close to matrix	Obvious strap-shaped, dark-colored image	Chaotic and weak reflection

*RD: deep lateral resistivity logging; RS: shallow lateral resistivity logging; DEN: density logging; AC: acoustic logging.

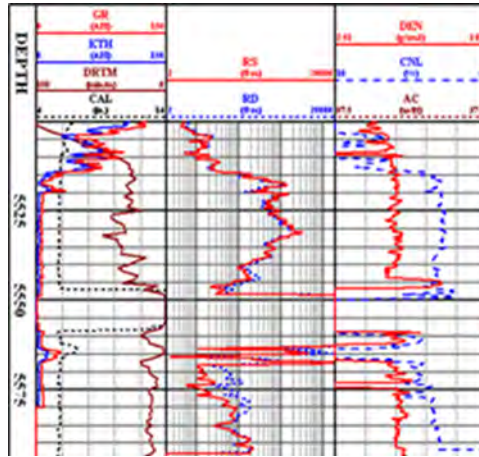


Figure 3.9 Unfilled caverns on Well TK471X log.

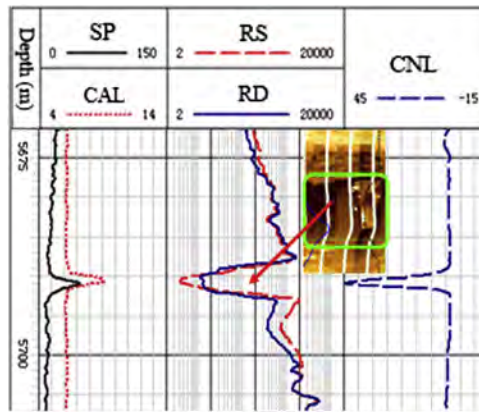


Figure 3.10 Unfilled caverns on Well T701 log.

Compared with unfilled caverns, partially filled caverns exhibit: (1) higher drilling time (Fig. 3.11); (2) seldom drilling breaks or lost circulation; (3) less enlarged boreholes; and (4) higher GR (Fig. 3.12), 20–60 API. High uranium content and low potassium and thorium contents were recorded on GR spectrometry for caverns filled with sand and mud (Fig. 3.13).

Filled caverns, in contrast to partially filled ones, exhibits: (1) almost constant borehole diameter; and (2) higher GR (Fig. 3.12), more than 60 API. High potassium and thorium contents were recorded on GR spectrometry for caverns filled with sand and mud, like in Well T403 and TK 409 (Figs. 3.14 and 3.15).

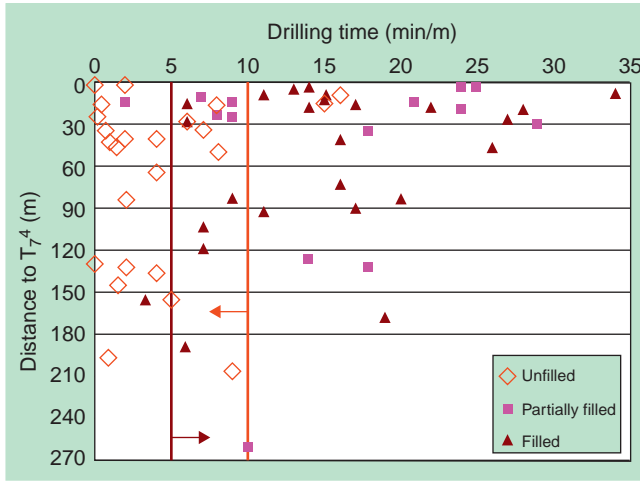


Figure 3.11 Drilling time log for different types of caverns.

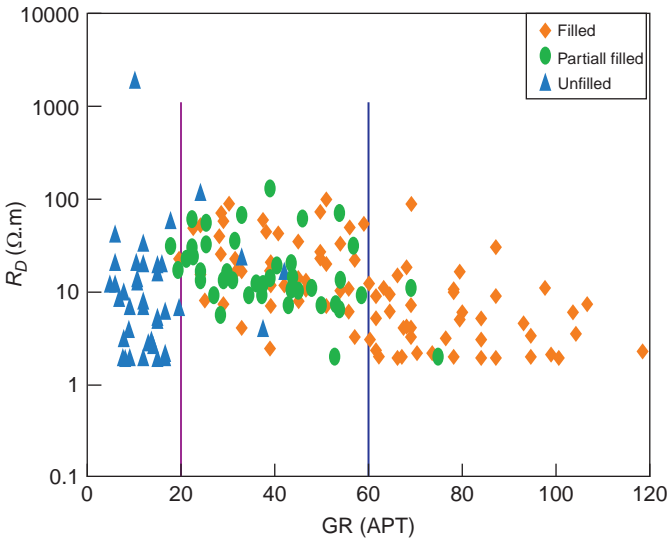


Figure 3.12 GR log for different types of caverns.

3.1.2.2 Vug reservoirs

Vug reservoirs contain secondary pores, vugs, and matrix pores. Vugs consist of solution pores and caves. Vug reservoirs deliver a generic performance showing on well logs such as: (1) a low resistivity, 20–200 $\Omega \cdot RD$, and a positive difference of RD to RS on the resistivity log; (2) significant increase on AC and CNL

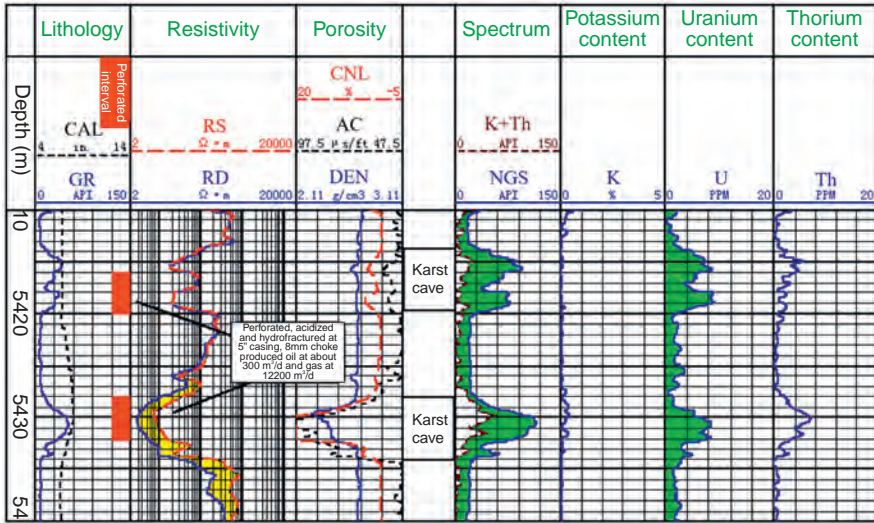


Figure 3.13 Conventional log of Well TK404, 5410–5440 m, Ordovician.

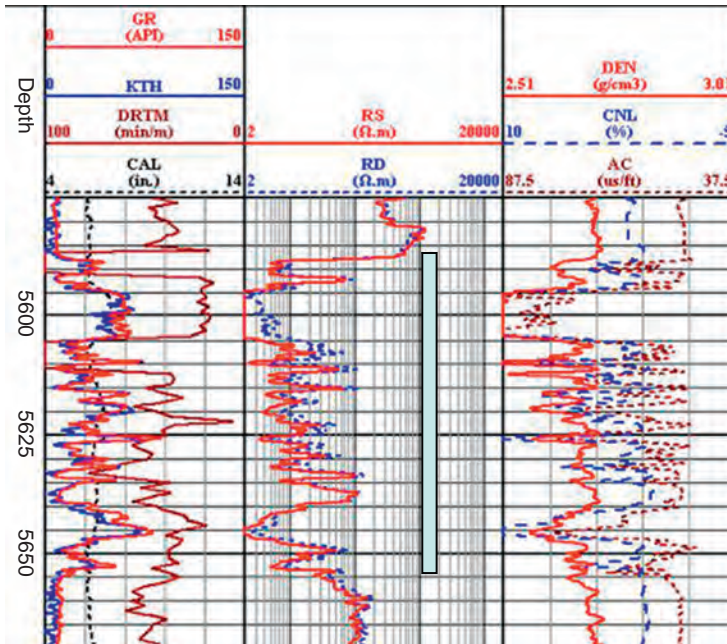


Figure 3.14 Log of Well T403 showing filled caverns.

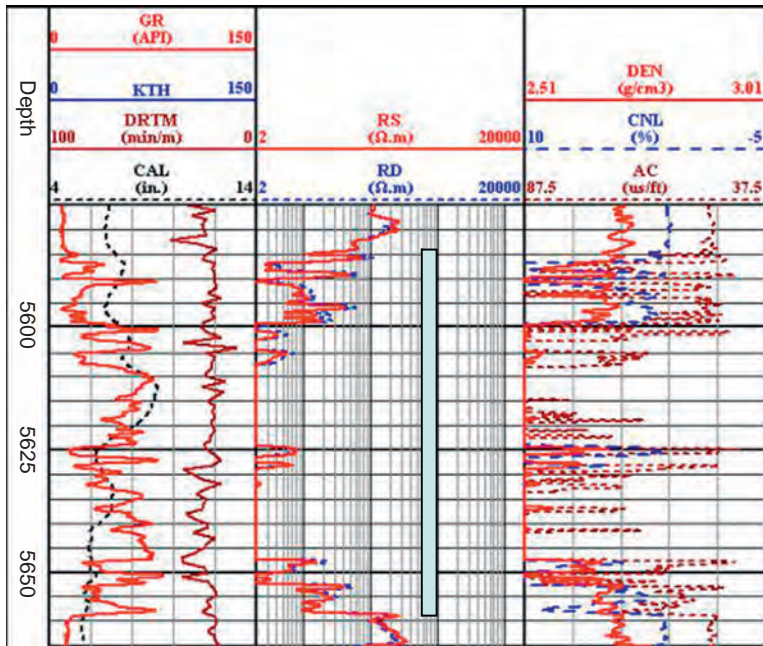


Figure 3.15 Filled caverns on Well TK409 log.

(compared to matrix), decrease on DEN, $AC > 51 \mu\text{s}/\text{ft}$, $DEN < 2.68 \text{ g}/\text{cm}^3$, and $CNL < 2\%$; (3) slightly enlarged caliber, 6.3"; and (4) low GR, less than 15API (Liqiang, 2009; Liangxiao and Yong, 1994).

3.1.2.3 Large-scale fracture reservoirs

Large-scale fracture can be obtained by seismic data interpretation. Ant cube attributes extracted from seismic data provide large-scale fracture and fault information.

1. Fault interpretation

Artificial fault interpretation is based on regional geological rules and seismic section features, and by considering fault markers on seismic section and fault complex law. Faults determined in this way are highly reliable.

2. Fault tracking

Compared with artificial fault interpretation, automatic fault interpretation by ant-tracking method delivers more precise results, not only for interpretation of large-scale fractures, but also for lower-order microscale fractures, even for fracture systems (Xin, 2010).

Variance cube and ant-tracking are two effective methods that are so far available for identifying faults, fractures, and discontinuous formation change. First the variance cube technique preprocesses original seismic data to enhance the spatial discontinuity. Then the ant-tracking technique identifies and tracks the discontinuous traces that meet the preset condition for the fracture in the variance cube, and extracts the ant attribute cube. With fault system information from artificial fault interpretation, fractures can be picked automatically from the ant attribute cube in different fracture systems.

3. Integrated interpretation

Artificial seismic interpretation is used to identify large faults, while the ant-tracking method is used to reveal and characterize small faults. To enhance the precision and reliability of fault interpretation, interactively, artificial faults and ant-tracked faults are often compared and analyzed on their matching one by one.

3.1.2.4 *Microscale fracture reservoir*

Interpretation of microscale fractures mainly relies on core and well logging data. Deep lateral resistivity logging and imaging logging are considered to be effective in identifying microscale fractures which show the following features on well logs.

1. Deep lateral resistivity ranging from 100 to 1000 $\Omega \cdot$, there is an evident positive difference between deep and shallow lateral resistivity logs ($RD > RS$), and the reservoir interval exhibits an evident “dual-track” phenomenon on these two logs.
2. Porosity log changes slightly, similar to matrix.
3. Caliper log remains constant or changes slightly.
4. GR value is low, less than 15API, similar to matrix.
5. FMI shows a dark-colored sinusoidal form.
6. Stoneley wave exhibits strong attenuation.

3.1.3 *Cross-well identification of fracture-vug reservoirs*

Cross-well identification of fracture-vug reservoirs mainly relies on high-resolution 3D seismic techniques, involving seismic reflection features, wave impedance inversion and seismic attribute cube (Guangfu, 2008; Lifeng et al., 2009; Chunyuan et al., 2007; Yang, 2012; Gehua et al., 2006; Han Dong et al., 2014).

3.1.3.1 *Identification of fracture-vug reservoir by seismic reflection feature*

There is a correlation between seismic reflection and fracture-vug reservoirs. Forward modeling results indicates that the seismic reflection features of a fracture-vug carbonate reservoir can be influenced by many factors including its shape, scale, complex form, and distance from the Ordovician weathering surface. Based on systematic analysis of seismic reflection features and corresponding development features of fracture-vug reservoirs, reflection

features are divided into four classes, nine subclasses, and 20 types, as listed in [Table 3.3](#).

1. Classification of seismic reflection features

a. Bead-like reflection (I)

Bead-like reflection is from below T_7^4 . Depending on the intensity and position, bead-like reflections are subdivided into four subclasses: surface weak + internal bead-like reflection (I1), surface strong + internal bead-like reflection (I2), overall bead-like reflection (I3), and deep bead-like reflection (I4). Every subclass includes several types.

b. Weak reflection (II)

On seismic time migration sections, seismic reflections from Yijianfang and Yingshan formations seem predominantly weaker than those from surrounding layers, which are continuous and strong; therefore they are defined as weak reflections. Depending on the intensity of the reflection energy from T_7^4 top, weak reflection is subdivided into surface weak + internal weak reflection (II1) and surface strong + internal weak reflection (II2). Every subclass includes several types.

c. Strong reflection (III)

On seismic time migration sections, seismic reflections from the internal Yijianfang and Yingshan formations are strong locally, and are thus defined as strong reflections. Depending on the intensity of the reflection energy from T_7^4 top, strong reflection is subdivided into three subclasses: surface weak + internal strong reflection (III1), surface strong + internal strong reflection (III2), and chaotic strong reflection (III3). Every subclass includes several types.

d. Atypical reflection (IV)

On seismic time migration sections, seismic reflections from the internal Yijianfang and Yingshan formations are similar to those from surrounding structures, and very different from classes I, II, and III above. This class of seismic reflection is defined as atypical reflection (IV) which is subdivided into two subclasses: monadnock fold + atypical reflection feature (IV1) and no monadnock fold + atypical reflection feature (IV2). Every subclass includes several types.

2. Relationship between seismic reflection feature and production

Four hundred and eighty-five wells drilled into the Ordovician oil reservoir in the Tahe Oilfield have been studied to determine the relationship between seismic reflection features and production ([Fig. 3.6](#)). Of these wells, bead-like reflection features were recorded in 276 wells, strong reflection features were recorded in 102 wells, weak reflection features were recorded in 86 wells, and the other 21 wells showed atypical reflection features.

Cumulative production illustrates that the wells showing bead-like reflection features yielded the highest production of 9.166million tons, those showing strong reflection feature yielded 5.5415million tons, those showing weak reflection feature yielded 3.236million tons, and the other showing atypical reflection feature yielded 46,700 tons ([Fig. 3.16](#)).

Single-well average cumulative production proves that the wells showing chaotic strong reflection features yielded the highest average cumulative production of 80,500 tons/well, those showing surface weak + internal weak reflection features yielded 46,200 tons/well, and those showing surface weak + internal bead-like reflection features yielded 434,00 tons/well ([Fig. 3.17](#)).

3. Relationship between reflection features and high-productivity wells

One hundred and ninety-three production wells producing from the Ordovician reservoirs in the Tahe Oilfield have yielded cumulative production of over 20,000 t/well. Reflection feature analysis on these reservoirs ([Table 3.4](#)) indicates that 25% of them

Table 3.3 Classification of seismic reflection features for carbonate fracture-vug reservoir in the Tahe Oilfield

Class	Subclass	Type
Bead-like reflection (I)	Surface weak + bead-like reflection (I1)	Monadnock fold + surface weak + internal bead-like reflection (I11) No monadnock fold + surface weak + internal bead-like reflection (I12)
	Surface strong + bead-like reflection (I2)	Monadnock fold + surface strong + internal bead-like reflection (I21) No monadnock fold + surface strong + internal bead-like reflection (I22)
	Overall bead-like reflection (I3)	Monadnock fold + overall bead-like reflection (I31) No monadnock fold + overall bead-like reflection (I32)
	Deep bead-like reflection (I4)	Monadnock fold + deep bead-like reflection (I41) No monadnock fold + deep bead-like reflection (I42)
Weak reflection (II)	Surface weak + internal weak reflection (II1)	Monadnock fold + surface weak + internal weak reflection (II11) No monadnock fold + surface weak + internal weak reflection (II12)
	Surface strong + internal weak reflection (II2)	Monadnock fold + surface strong + internal weak reflection (II21) No monadnock fold + surface strong + internal weak reflection (II22)
Strong reflection (III)	Surface weak + internal strong reflection (III1)	Monadnock fold + surface weak + internal strong reflection (III11) No monadnock fold + surface weak + internal strong reflection (III12)
	Surface strong + internal strong reflection (III2)	Monadnock fold + surface strong + internal strong reflection (III21) No monadnock fold + surface strong + internal strong reflection (III22)
	Chaotic strong reflection (III3)	Monadnock fold + chaotic strong reflection (III31) No monadnock fold + chaotic strong reflection (III32)
Atypical reflection (IV)		Monadnock fold + atypical reflection (IV1) No monadnock fold + atypical reflection (IV2)

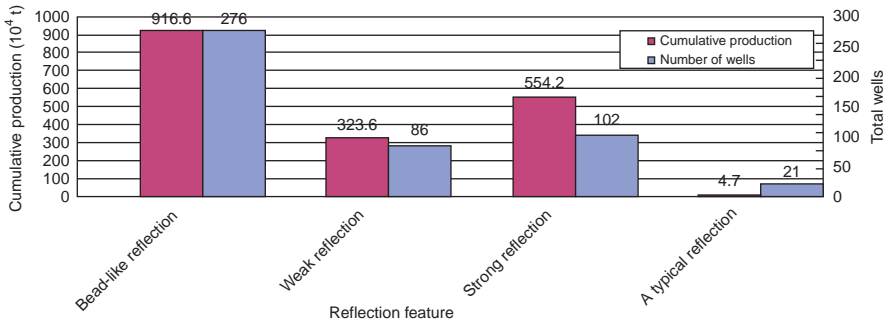


Figure 3.16 Reflection feature versus cumulative production.

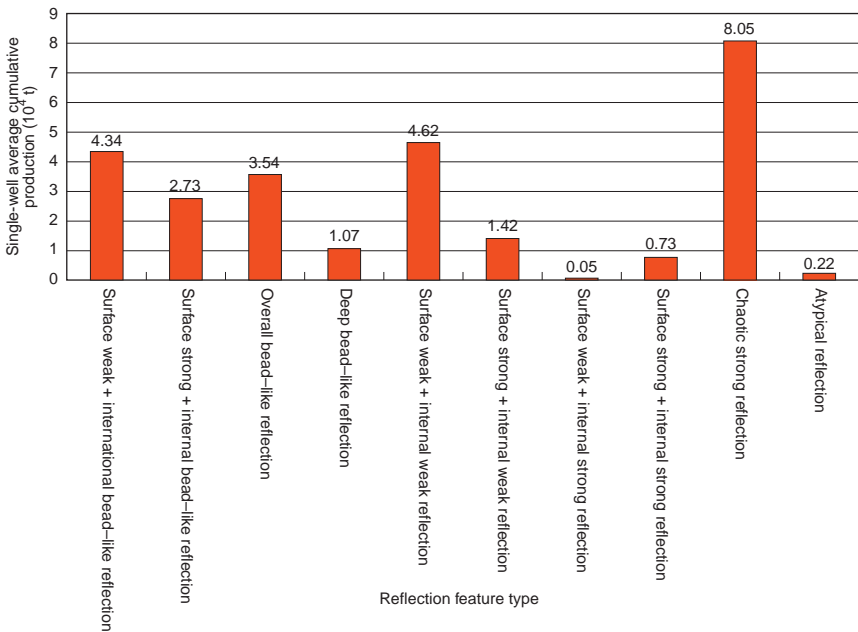


Figure 3.17 Reflection features versus single-well average cumulative production.

correspond to chaotic strong reflections, implying that this class of reflection feature is related to developed fractures and vugs; 13.5% of the reservoirs show bead-like reflection features, and 23.8% show surface weak + internal bead-like reflection features, implying these two types of reservoirs contain well-developed fractures and vugs; 8.8% show surface weak + internal weak reflections, implying this type of reservoir contains certain developed fractures and vugs; reservoirs showing atypical reflections, surface strong + internal weak reflections, or surface strong + internal strong reflections are less than 4%, implying absent fractures and vugs in them.

Table 3.4 Statistics of reflection feature versus high-productivity wells (individual cumulative production >20,000 tons)

Reflection feature	Surface weak + internal bead-like reflection	Surface strong + internal bead-like reflection	Overall bead-like reflection	Deep bead-like reflection	Surface weak + internal weak reflection	Surface strong + internal weak reflection	Surface weak + internal strong reflection	Surface strong + internal strong reflection	Chaotic strong reflection	Atypical reflection
Number of wells	46	37	26	6	17	7	0	3	50	1
Proportion (%)	23.8	19.2	13.5	3.1	8.8	3.6	0.0	1.6	25.9	0.5
Individual average production (10 ⁴ t)	9.1	5.77	7.18	3.94	16.1	3.22	0	4.3	10.4	4.2

3.1.3.2 *Identification of fracture-vug reservoir by wave impedance inversion*

1. High-resolution seismic inversion

3D geological modeling of a fracture-vug reservoir is based on high-resolution seismic wave impedance cube. The combination of geostatistical methods and seismic inversion allows for stochastic inversion of complicated and heterogeneous fracture-vug reservoirs using well logging, well testing, geologic and seismic data based on the spatial correlation on their own and with each other (e.g., well logging and seismic data), to ensure that reservoir descriptions approach towards geostatistical and seismic inversion results.

2. Analysis and evaluation of single-well inversion precision

In order to analyze and evaluate the precision and reliability of high-resolution seismic inversion, a statistical comparison between vugs/caves development and seismic inversion results was carried out on 48 wells in the Tahe Oilfield, suggesting a consistency of 47%.

3. Identification range analysis of vugs and caves

Of 75 wells (counted by wellhead) drilled in the fourth block of the Tahe Oilfield, 48 wells or 64% were drilled into 67 vugs, of which 40.3% were unfilled, 22.4% partially filled, and 37.3% filled. After analyzing the correspondence of the wave impedance to the identified vugs in the target layers, and studying the possible vug distribution on the wave impedance log, the probabilistic distribution function of the wave impedance and the vug reservoirs in different karst belts has been built.

Unfilled vug reservoirs commonly exhibit chaotic or blank reflection features, with a low impedance value derived from inversion, which is approximately less than $1.48 \times 10^7 \text{ kg/m}^3 \cdot \text{m/s}$; partially filled or fully filled vug reservoirs commonly exhibit “bead-like” or chaotic reflection features, with a low impedance value, which is approximately less than $1.60 \times 10^7 \text{ kg/m}^3 \cdot \text{m/s}$. Vug-fracture reservoirs contain abundant pores, vugs, and fractures, and are classified as vug carbonate reservoirs exhibiting blank-chaotic reflections on seismic section and with a moderate impedance value sometimes close to that of the limestone matrix, about $1.65 \times 10^7 \text{ kg/m}^3 \cdot \text{m/s}$; a fracture reservoir exhibits weak reflection on seismic section, with a moderate impedance value similar to that of a vug-fracture reservoir, and the impedance contrast between it and the limestone matrix depends on fracture development.

3.1.3.3 *Identification of fracture-vug reservoir by seismic attribute volume*

Seismic data contain rich reservoir geologic information. Seismic reservoir prediction has become an important measure for oil & gas reservoir identification and monitoring. With advances in seismic data acquisition, processing, and interpretation, attribute analysis has become a powerful tool to perceive features associated with an oil/gas reservoir. However, it is increasingly clear that seismic attributes computed using individual techniques, to some extent, can only reflect a certain geologic phenomenon and development feature, and each seismic attribute has its advantages and limitations for objective characterization. The limitations

result in noncomprehensive characterization. Moreover, a reservoir feature predicted by single data fails to solve the ambiguity of seismic information and cannot achieve the comprehensive characterization of a geologic target.

The most effective method for solving the ambiguity and the noncomprehensiveness is the integrated application of multiple data, that is to predict reservoirs with various reflection features using multiple parameters. Extraction and selection of seismic information related to geological property are critical to improving prediction success, combined with proper data fusion techniques, to optimize multiple attributes for reducing redundant information, integrating complementary information, and capturing collaborative information.

Conventional seismic attribute analysis and prediction involves target horizon interpretation, attribute extraction, quantitative prediction of reservoir parameters, and analysis and evaluation of promising reservoirs during which superposed validation, analysis, and judgment is often conducted. For fracture-vug reservoirs under development, they must be described by normalized and quantitative parameters from various seismic responses. This can be done through optimization and integrated analysis of multiple seismic attributes.

A fundamental workflow for optimization and fusion of multiattribute volume for a target fracture-vug reservoir is shown in [Fig. 3.18](#).

1. Seismic attribute extraction

Seismic attribute is a mathematical representation of changes in seismic velocity, amplitude, and frequency in response to spatial variation of reservoir physical properties and infilling fluid properties. Seismic attribute is the characterizable and quantifiable seismic feature, and the seismic characteristic value for describing formation structure, lithology, physical properties and other information. When the characteristic value reflecting a change in reservoir or fluid properties is large enough, seismic data will change on waveform, energy, frequency and phase geometrically, kinematically, dynamically, or statistically.

3D seismic data contains abundant structure and lithology information of subsurface media. With proper feature extraction and analysis methods, information related to a fracture-vug carbonate reservoir can be selected from a 3D seismic data cube. This helps define the fracture-vug development belt in a carbonate reservoir and understand its distribution feature.

Based on the geophysical response feature analysis of the fracture-vug bodies recorded in the test area in the Tahe Oilfield, 10 attribute volumes were extracted: average curvature, maximum positive curvature, minimum negative curvature, dip, azimuth, strong amplitude cluster, high-precision amplitude variation, discontinuity, attenuation gradient, and wave impedance derived from full-frequency band inversion.

2. Sensitive seismic attribute analysis

The purpose of quantitative attribute analysis is to convert numerical seismic attributes to reservoir features. The most important consideration in seismic attribute calibration is determination and identification of attributes that have geological and physical significances and stable statistical features.

Seismic attribute selection is to find a single seismic attribute or seismic attribute group that is the most sensitive and has the least number of attributes to the solution using

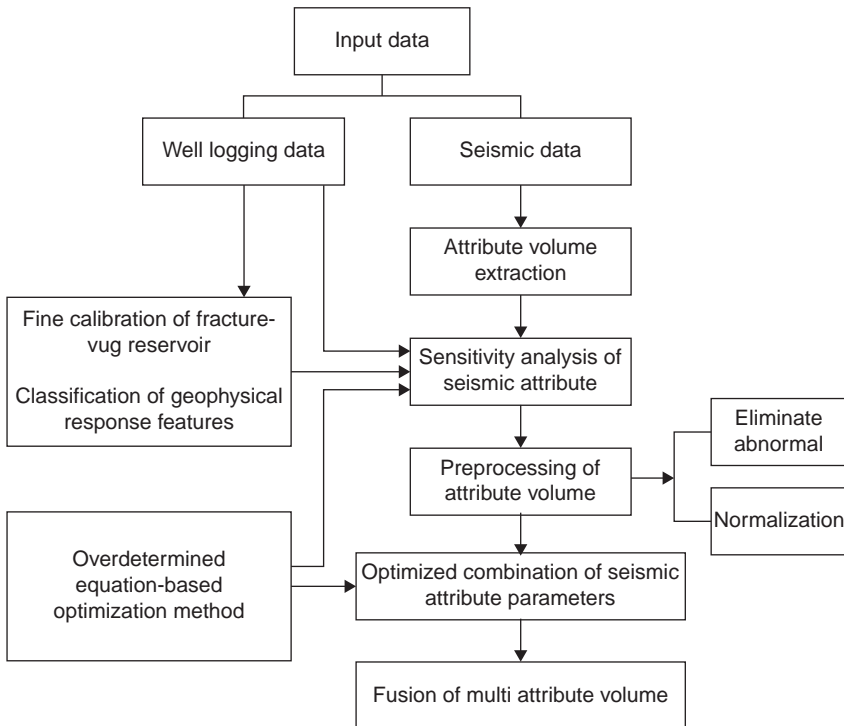


Figure 3.18 The workflow for optimization and fusion of multiattribute volume.

a priori knowledge or a mathematical method to enhance the precision of reservoir prediction and the effectiveness of seismic-attribute-related seismic data processing and interpretation. Attribute optimization is the important step to enhance the precision of reservoir parameter prediction. Usually, attribute optimization involves sensitivity analysis and multiple attributes optimization.

A least-squares-based reservoir expectation optimization technique may be applied to build a large-scale over-determined equation using linear combination of effective attributes at well points and the expectation of drilled reservoir to calculate the least squares solution, analyze the sensitivity of objective assignment of the calculated weight coefficient over seismic attribute (this process can also be realized using main principal component analysis), build a connection between attributes and objective prediction parameters, and attain the objective of attribute optimization.

a. Attribute weight coefficient optimization method based on the least squares solution

For the attribute volumes of the target area, such as imp, attenuation gradient of seismic signal (ATN), curvature, amp_var, eig, dip, azi, and so on, an output is derived from linear combination and combination coefficient can be obtained with the least-squares method.

If there is an n -dimensional vector x^* , and $A^T A x^* = A^T b$, x^* is the least squares solution of $Ax = b$.

The weight coefficient is calculated by the following steps:

- i. calculate all attributes (imp, ATN, curvature, amp_var, eig, dip, azi and strong amplitude cluster) in the target area;
 - ii. extract the center traces of every attribute within the effective radius centered on the well point in the target area, and then calculate the values of the seismic traces within the vertical horizon of vugs or fractures and calculate their average (average value of multiple traces);
 - iii. normalize the attribute values on each boundary of the center traces;
 - iv. If the b on the right side represents the expectation of fracture-vug body prediction, the equation is an over-determined equation set, and solve the resulting normalized equation set to obtain the least-squares solution x ; and
 - v. Assign the least squares solution x to the attribute value as its weight coefficient.
- b. Attribute selection

Comprehensive evaluation of seismic attribute is mainly based on the effectiveness, consistency, and correlation of fracture-vug body prediction and parameter statistics of near borehole reservoir interval by weighting average. Then the distribution of the reservoir parameters is analyzed to select some highly correlative attributes, and eliminate the lowly correlative ones or similar in performance in combination with fine reservoir calibration result, to select the optimum attributes.

Over-determined equation was used to calculate the weight coefficients of eight seismic attributes (Table 3.5). These coefficients reflect the contribution of the attributes to reservoir development; that is, the correlation to reservoir prediction effectiveness. Table 3.5 reveals the insignificant correlation of curvature, dip, and azimuth to reservoir prediction effectiveness. Therefore, it seems reasonable to remove them and retain the other five attributes (impedance, attenuation gradient, amplitude variation, discontinuity, and amplitude cluster) that may provide an effective reflection of fracture-vug information.

Seismic response feature analysis of fracture-vug reservoirs has confirmed that the reservoir near the weathering surface exhibits “weak amplitude, high discontinuity, and low impedance,” and internal fracture-vug reservoirs show “strong amplitude, high amplitude variation, high discontinuity, strong attenuation, and low impedance” on seismic sections. These features are consistent with the attributes provided by the attribute weight coefficient optimization method, which are the most effective to reflect the fracture-vug body. This demonstrates the effectiveness of this method.

In conclusion, it is possible to select attributes using a least-squares method. But our concern is how to select a combination of attributes that are optimum. Since there are only five selected attributes, the exhaustive search algorithm is applicable. In this way, a variety of combination cases were tested, including a combination of five, four, three,

Table 3.5 Seismic attributes’ weight coefficients influencing the effectiveness of fracture-vug body prediction

Attribute	imp	ATN	Curveness	Amp_var	eig	dip	azi	amp_cluster
Weight coefficient	0.27	0.14	0.08	0.12	0.18	0.05	0.04	0.12

and two attributes, respectively, to select a combination that contains the least and the most sensitive (most effective or most representative) attributes to the solution and yields minimum error. Study implies that the combination of impedance, attenuation gradient, and discontinuity attributes is optimum (Table 3.6 and Fig. 3.19), and helps to enhance the connectivity of seismic reservoir prediction in 3D space.

A total of 118 vertical wells have been drilled in the high-resolution 3D single-fold area around Well S48 in the Tahe Oilfield, of which 66 were drilled into caves. Calibration with drilling data indicates that the impedance value reflecting these caves is less than $1.6 \times 10^7 \text{ kg/m}^3 \cdot \text{m/s}$, and impedance prediction results match perfectly and basically with drilling results in 50 wells but poorly in 16 wells (76% matching); the attenuation gradient (slope value) reflecting these caves is less than -0.2 , and attenuation prediction results match perfectly and basically with drilling results in 41 wells but poorly in 25 wells (about 62.1% matching).

Table 3.6 Weight coefficients assigned to the optimum attribute combination for the high-resolution 3D area around Well S48

Attribute	imp	ATN	eig
Weight coefficient	0.602	0.194	0.204

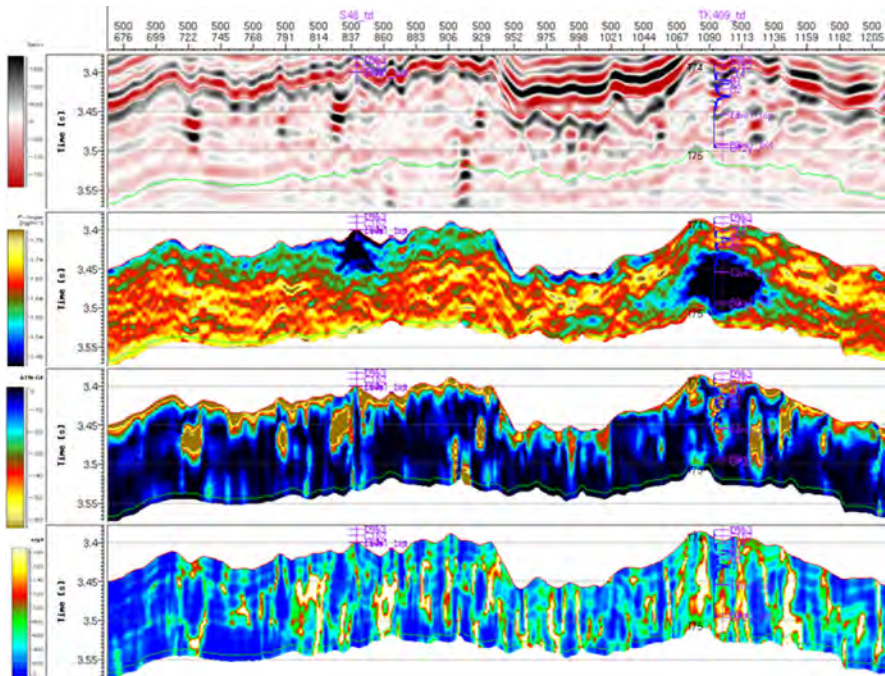


Figure 3.19 Sensitive attribute sections derived from Inline500. From top to bottom: seismic section, impedance section, attenuation section, and discontinuity section.

3. Preprocessing of seismic attributes

Before integrating, preprocessing of seismic attribute volumes is required, since there are many seismic attributes available for reservoir prediction, they may be greatly different in dimension and magnitude so that local anomalies are usually concealed in regional backgrounds, and some singular values may exist.

a. Removing singular values

In a large time window (40 ms) near the target layer, compute the average or maximum/minimum attribute to determine whether or not a singular value exists in a seismic data volume. Spot-like and iron plate-like features (shown by almost a color code) present on the seismic attribute map mean singular values in the seismic data volume, which should be removed or cut off before using the seismic data.

b. Nondimensionalization

Different seismic attributes have different physical significances and dimensions. To ensure the equivalent effectiveness and sequence of all parameters, nondimensionalization of original data is required. Firstly, initialize all data, that is, all data in a sequence will be divided by the first data to get the data in the new sequence, which are multiples of the first data. Secondly, mean all data, that is, all data in a sequence will be divided by the mean of this sequence to get the data in the new sequence, which are multiples of this mean.

c. Data standardization

Different attributes have different ranges, and different attribute volumes may vary widely in numerical magnitude (Fig. 3.20). In order to avoid the unequal-weighted scenario and to ensure a reasonable correlation in subsequent processing, seismic attribute standardization must be conducted.

There are a variety of methods available to standardize the observed sample data: total standardization, maximum standardization, norm standardization, center standardization, standard deviation standardization, range standardization, and range regularization. Based on the characteristics of seismic attribute parameters, standard deviation standardization methods were utilized to provide a normalization processing of seismic attribute parameters. The standard deviation standardization is defined as:

$$x_{ij}' = \frac{x_{ij} - \bar{x}_i}{S_i}$$

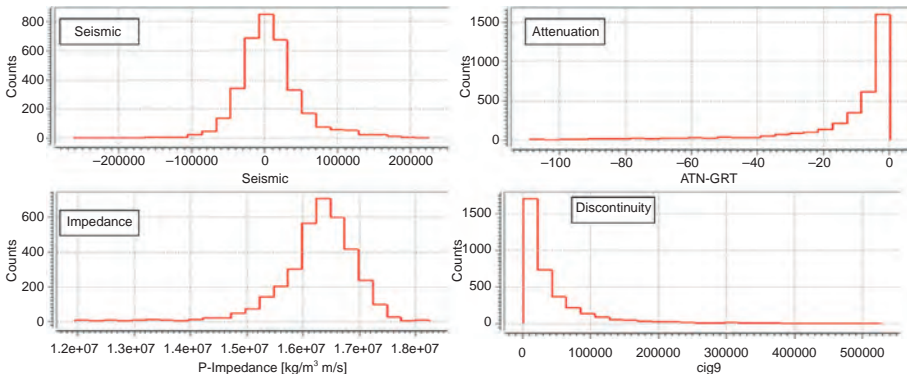


Figure 3.20 Attribute distribution histogram on Inline500 section.

where $i = 1, 2, \dots, m; j = 1, 2, \dots, n$;

$$s_i = \left[\frac{1}{n-1} \sum_{j=1}^n (x_{ij} - \bar{x}_i)^2 \right]^{\frac{1}{2}}$$

where $\bar{x}_i = \frac{1}{n} \sum_{j=1}^n x_{ij}$.

In this equation, n is data length; and if x_{ij} represents a matrix, x_{ij}' is the resulting data matrix of standard deviation standardization.

4. Fusion of multiple attribute volumes

More useful information can be derived from optimized combination of multiple attributes while reducing their dimensions. Integration of characteristic fields reduces prediction ambiguity. It is possible to take advantage of multiinformation integration to enhance the effectiveness of the entire system.

a. Feature fusion

Seismic records and seismic attributes are the comprehensive responses from subsurface geology. Reservoir information is hidden in such seismic records and seismic attributes, but is too weak to be visible. It is essential to utilize a mathematical transformation method or set a related parameter threshold to highlight the useful portion and suppress the noise to obtain a more evident reservoir feature, and then use weight coefficients for the combination of optimum attributes to conduct fusion calculation using the following equation:

$$\text{Fusion result} = 0.602 \times \text{imp} + 0.194 \times \text{eig} + 0.204 \times \text{ANT} \quad (3.1)$$

where imp is impedance, eig is discontinuity, and ATN is attenuation gradient.

An example of feature fusion volume based on Eq. (3.1) is shown in Fig. 3.21. Calibration by drilled reservoirs found that this fusion volume was highly sensitive to discontinuity data, but failed to play the role of inversion impedance and attenuation in defining reservoir thickness.

b. Normalization fusion

Since all parameters of attenuation gradient attributes are negative, the role of attenuation attributes in fracture-vug reservoir prediction cannot be represented by the

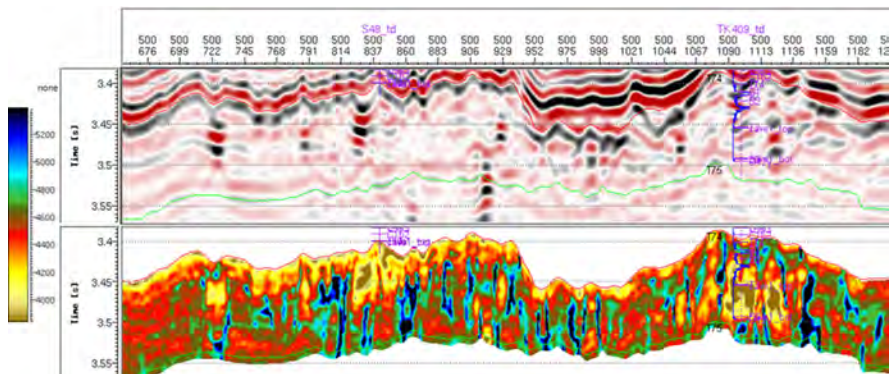


Figure 3.21 Multiattribute fusion section of Inline500.

feature fusion discussed above. To solve the issue, all values of attenuation, impedance, and discontinuity attributes should be normalized to 0–1 (Fig. 3.22), then weight coefficients should be used for the combination of optimum attributes to calculate the fusion result using the following equation:

$$\text{Fusion result} = 0.602 \times \text{imp} + 0.194 \times \text{eig} + 0.204 \times \text{ANT} \quad (3.2)$$

where imp is impedance, eig is discontinuity, and ATN is attenuation gradient.

An example of normalization fusion using Eq. (3.2) is shown in Fig. 3.23.

c. Combination fusion

Re-calibration by drilled reservoirs reveals that, compared with feature fusion, normalization fusion offers a significantly enhanced reservoir prediction precision. However, a layering feature is quite evident on the section, due to the significant magnitude of weight derived from inversion, which is inconsistent with the geologic rule that governs the development of a carbonate fracture-vug reservoir. For this reason, it was determined to fuse the attributes sensitive to prediction of a cave-vug reservoir first and then the attributes sensitive to prediction of a fracture reservoir, as shown in Fig. 3.24.

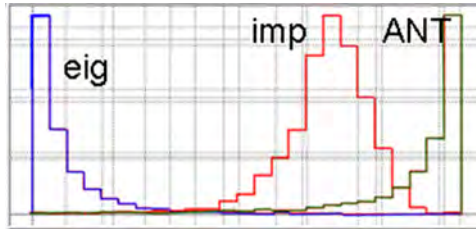


Figure 3.22 Normalized attribute distribution histogram of Inline500.

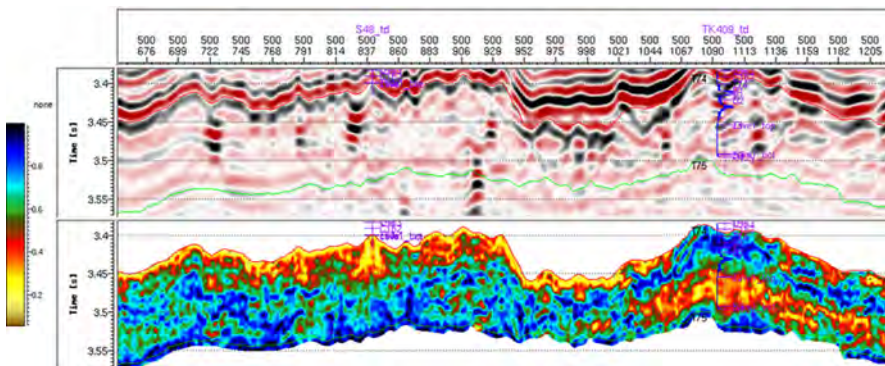


Figure 3.23 Multiattribute normalized fusion section of Inline500 (Top: seismic section; bottom: normalized fusion section).

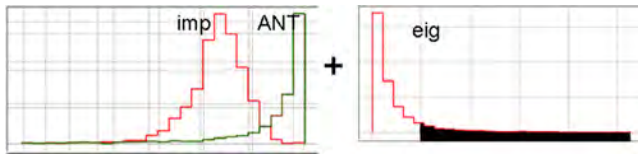


Figure 3.24 Combination fusion of attributes of Inline500.

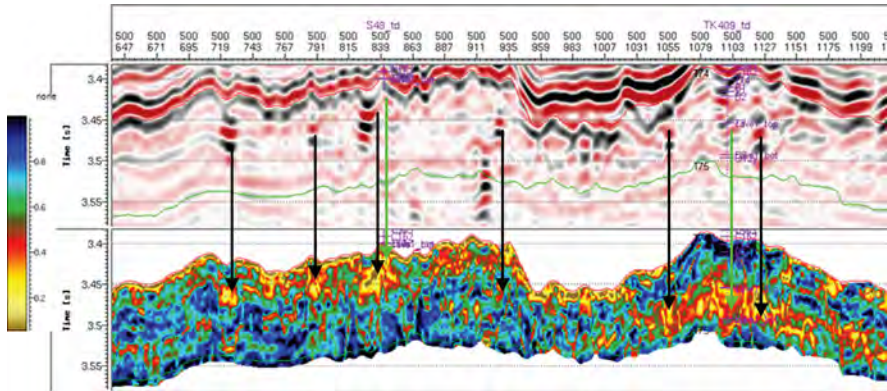


Figure 3.25 Multiattribute combination fusion section of Inline500.

Firstly, normalization fusion of the impedance and frequency attenuation gradient sensitive to prediction of a cave-vug reservoir was finished:

$$Attr_com_1 = 0.6033 \times imp + 0.3967 \times ANT$$

Secondly, feature fusion of the discontinuity sensitive to prediction of a fracture reservoir was carried out:

$$Attr_com_2 = 0.5055 \times Attr_com_1 + 0.4945 \times eig$$

An example of the fusion result is shown in Fig. 3.25.

The fusion section indicates that combination fusion inherits the capacity of defining the overall outline of fracture-vug reservoir interval and dividing the reservoir interval in the vertical direction from impedance, and holds the component of attenuation attribute that is sensitive to strong and short reflection and is capable of depicting the overall outline. Compared with feature fusion and normalization fusion, data volume derived from combination fusion possesses the capacity of discontinuity in detecting the lateral break and defining the boundary, as well as characterizing the high-frequency information that unequally progressively changes inside the reservoir. Correlation of the majority of drilled reservoir intervals over the whole region confirms that this fusion method offers a comparatively good matching to drilling results, enables a reasonable identification of a reservoir in

vertical and lateral directions, represents the areal and spatial distribution that matches well with the present-day structure and palaeogeomorphology, and yields a boundary that basically corresponds to the present-day and ancient trench and water channel, thereby providing comprehensive data for further 3D characterization and depiction of a fracture-vug body.

3.1.4 Distribution law of a fracture-vug reservoir

The Ordovician fracture-vug reservoir in the Tahe Oilfield developed primarily during the early period of Hercynian movement (about hundreds of millions years ago) in a naked weathering environment, and was then superimposed and modified by burial karstification during multiple tectonic movements, resulting in a quite complex spatial distribution pattern (Yuzhu, 2008).

1. Clear plane partition and longitudinal zonation of fracture-vug bodies

Based on 3D high-resolution seismic data and drilling data from 140 wells in the work area, and considering the thickness data of Class I and II reservoirs after sectional line interpretation and correlation, amplitude variation (primary) at different depths (with 10 ms interval), planar variation on seismic coherency section (secondary) and structural, geomorphologic and paleo-drainage maps of Top T_7^4 , vugs drilled in each well were calibrated using drilling, mud logging, well logging and production data and sections were compared following the method of point-line-plane and flattening the “dual-peak” limestone top (C_{1b}) in the Lower Carboniferous Bachu Formation. The correlation results indicate that the vugs exhibit evident layered distribution on a regional scale in the vertical direction and zoning distribution in the plane direction. Vertically, the cave interval can be divided into three segments (Fig. 3.26) from the top of the cave interval to T_7^4 , and there is an evident segmentation at 60 m.

2. Shallow well-developed caves 60 m below the weathering crust unconformity.

Based on static and dynamic data, a total of 132 caves have been drilled in 62 wells in the fourth block. Sixty-eight percent of them are 0–60 m, 26% are 60–150 m, and 6% are

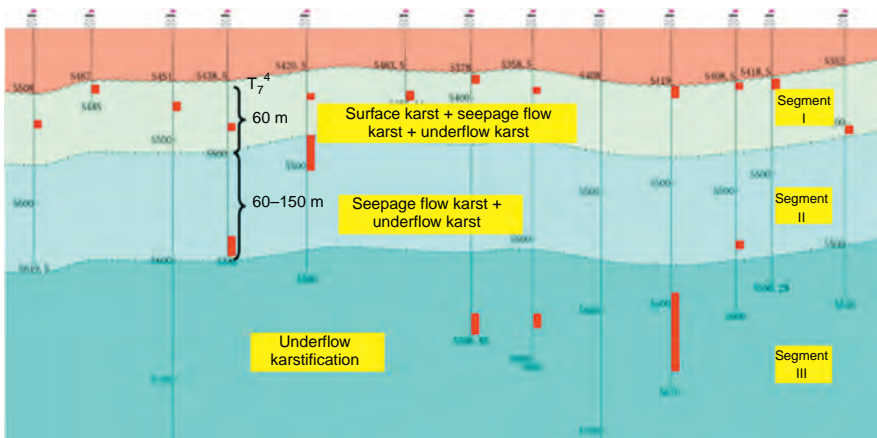


Figure 3.26 A sketch diagram showing vertical segmentation of the Ordovician karst reservoir in the 4th block, the Tahe Oilfield.

Table 3.7 Caves distribution in different intervals

Distance to T_7^4 (m)	Cave thickness (m)	Number of caves	Number of unfilled caves	Number of partially filled caves	Filled caves
0–60	710.04	90	63	12	15
60–150	347.39	34	25	2	7
>150	145.87	8	4	1	3
Total	1203.3	132	92	15	25

more than 150 m from the T_7^4 weathering layer. The cumulative thickness of the caves in a well is 1203.3 m. Ninety caves with a cumulative thickness of 710.04 m and 59% of total thickness have been drilled from 0 to 60 m to the weathering layer. Thirty-four caves with a cumulative thickness of 347.39 m and 29% of total thickness have been drilled from 60 to 150 m to the weathering surface. Eight caves with a cumulative thickness of 145.87 m and 12% of total thickness have been drilled over 150 m to the weathering layer. These data confirm that caves are mostly developed from 0 to 60 m under the weathering layer (Table 3.7).

3.2 Characterization of fracture-vug unit

A fracture-vug unit refers to a fracture-vug body with uniform pressure and hydrodynamic systems that resulted from collapse and fill modification of a fracture-vug system. A fracture-vug unit is connective internally, but externally isolated by a relatively tight or impermeable dissolved interface or sealing fault. A fracture-vug unit must be interconnective in a uniform pressure system, and has uniform oil–water contact and fluid properties. In this sense, a fracture-vug unit is an independent reservoir which is the fundamental unit for developing a fracture-vug reservoir (Fangzheng and Zhilin, 2008; Zhilin, 2012).

To divide fracture-vug units, first use borehole core, imaging log, well log, drilling, and mud log data to identify downhole intervals containing caverns, solution pores, vugs, and fractures. Second, use seismic reflection features and attributes to identify cross-well caverns and fractures. Finally, integrate geological, seismic, and production performance data to define the formation unit containing caverns, vugs, and fractures (Ximing et al., 2007; Hongbo, 2010; Jianjun et al., 2009; Zhihai et al., 2007).

3.2.1 Division of a fracture-vug unit

The boundary of a fracture-vug unit is identified by wave impedance inversion and analysis of waveform and seismic amplitude variation, and optimized and verified by production performance data.

1. How to divide a fracture-vug unit

Following the development rule of a fracture-vug reservoir, use dynamic and static data and correlative analysis of adjacent wells to divide a fracture-vug unit.

Laterally, wells drilled into the same fracture-vug unit usually share similar seismic amplitude variations or seismic waveforms within the same third-order karstic geomorphology unit, have similar fluid properties and relatively consistent pressure change, and show cross-well interference in production.

Vertically, production layers in the same fracture-vug unit (producing interval) are connective downhole or among wells, directly or through fractures, without thick and tight barriers to isolate them. Therefore there is no evident difference in their production performance.

2. How to define the boundary of a fracture-vug unit

The boundary of a fracture-vug unit can be defined using geological, seismic, well testing and production performance data based on the following points.

- a. The reservoir is surrounded by relatively tight or impermeable barrier beds.
- b. Quantitative analysis (e.g., seismic waveform or frequency analysis) shows the presence of a boundary, and amplitude variation maps illustrate the elliptical, bead-like and strap-shaped amplitude anomalies.
- c. Pressure change and fluid properties vary greatly among adjacent wells.
- d. Well testing data show the presence of an impermeable boundary.

3. Division of fracture-vug unit in the fourth block of the Tahe Oilfield

Cross-well connectivity analysis was conducted for 73 wells using production performance and static data. As a result, 20 fracture-vug units have been identified, of which six (30%) are cross-well units and 14 (70%) are single-well units.

3.2.2 Karst facies pattern

According to the structural element distribution features for typical fracture-vug units in the Ordovician reservoir in the Tahe Oilfield, two facies patterns were determined to model the fracture-vug unit, including fracture-water table dual control pattern and water table-dominated pattern.

1. Fracture-water table dual control mode

Vugs evolution starts with microscale fissures, then dissolved fracture, dissolved channels, and finally vugs. Statistics in the study area in the Tahe Oilfield demonstrate that the majority of drilling break and lost circulation events occurred in the proximity of fractures and about 86% of vug intervals more than 9 m thick are present in and around large-scale fractures. Developed vugs often share the same strike with these fractures. Vugs tend to form where multiple groups of fractures intersect, with common drilling break and lost circulation events recorded, such as in the S48 unit. This clearly reflects the “fault-controlled” feature. Modern karstification studies suggests that the intensity of a karstification is closely related to paleogeomorphology. There is a unique water table under every paleogeomorphologic condition. Water table is usually controlled by structural uplift and subsidence, as well as sea level change. Formation of large-scale karst channels is possible above and below a water table. Therefore, the water table is closely related to the development of karst channels. S48 unit is presently situated at a relatively higher structural part in response to the structural uplifting that occurred in the northern part of the Tahe region, and the fluctuation in water table allows for formation of multiple layers of caves. In addition, double-layered karst channels have been observed while dissecting the S48 unit.

It is determined through an integrated analysis that the development of the internal structure of the S48 unit is controlled primarily by fracture and water table, called fracture and water table dual control pattern (Fig. 3.27).

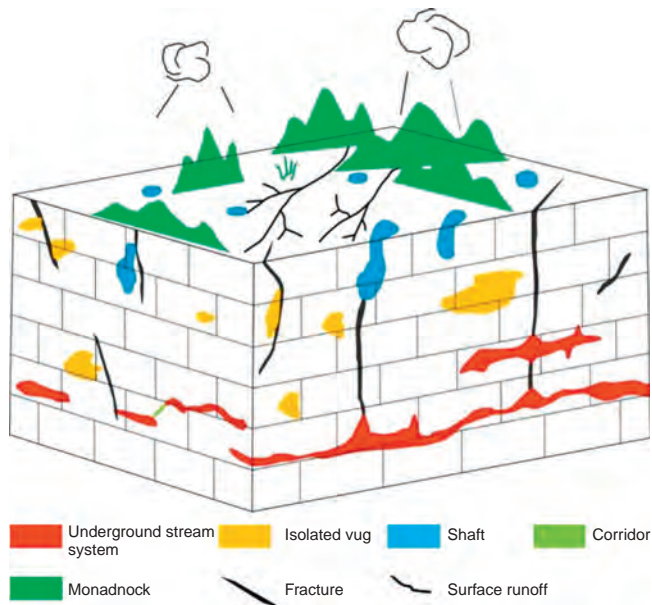


Figure 3.27 Development pattern inside fracture-vug reservoir.

2. Water table-dominated pattern

On a karst slope, near-surface and flowing karst zones have been denudated entirely, channels formed in runoff zones were uplifted to the surface so that the distribution of cavernous reservoirs were controlled primarily by the water table. In response to the repeatedly changing water table, new underground channels might be formed in the runoff dissolution zone by downcutting of the channel system and then connecting with preexisting underground channels, possibly resulting in multilayer caves. On the other hand, shafts developed in near-surface karst zones have virtually vanished.

T615 unit is a typical example. This unit is situated on a less fractured karst slope, and the distribution of cavernous reservoirs is controlled primarily by water tables. Vertically, a runoff dissolution zone has been developed in the T615 unit, and the repeatedly changing water table produced multilayer caves, making the runoff zone thicker and thicker, the flowing zone not well preserved, pipe cave and isolated cave developed (primarily pipe caves), but shaft cave vanished.

Channels in a runoff dissolution zone may be single or network distribution (Fig. 3.28).

Due to the repeatedly changing water table, multilayer caves might be developed in a runoff dissolution zone on a karst slope. Near-surface and flowing karst zones might be entirely denudated as a result of structural uplifting. The channels developed in runoff zones were uplifted to the surface. Shafts developed in near-surface karst zones almost vanished.

3.2.3 Characterization of a typical fracture-vug unit

For example, S48 is the largest fracture-vug unit of the Ordovician oil reservoir in the Tahe Oilfield, which is a folded erosion unit in origin and is structurally situated

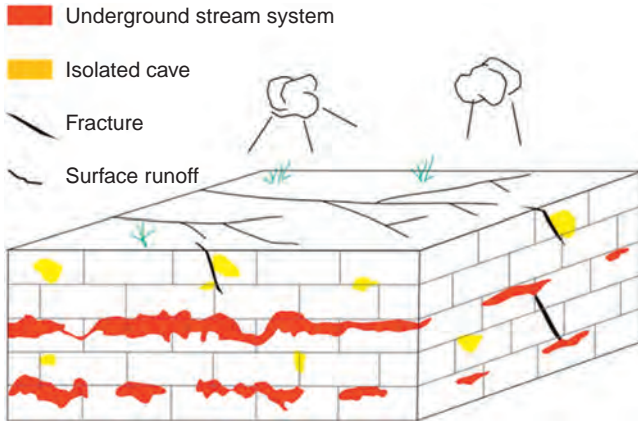


Figure 3.28 Section diagram showing main control mode of water table in the T615 unit.

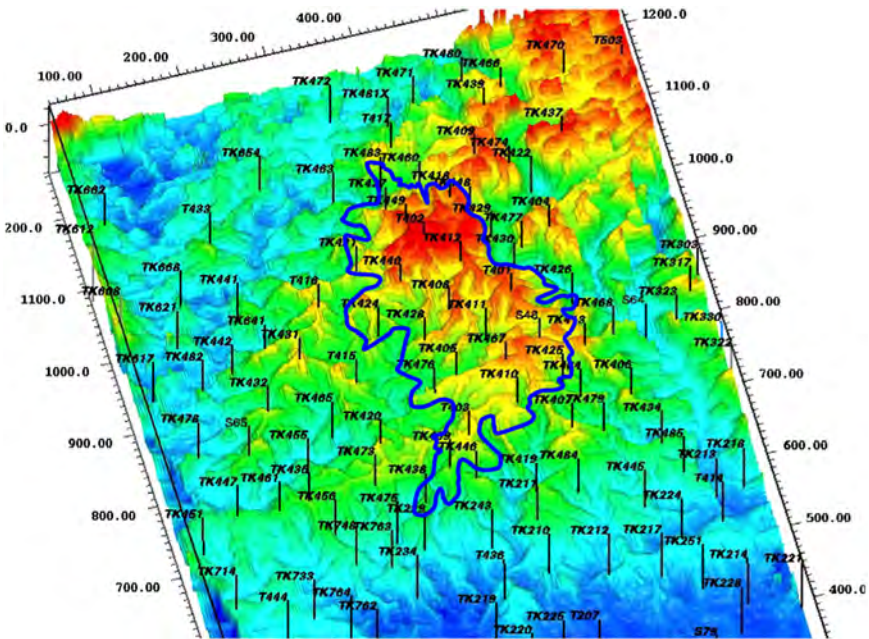


Figure 3.29 The paleogeomorphology of S48 unit during the Early Hercynian.

onto the axis of an anticline in the southern segment of the Akekule bulge. The S48 unit is located at the most favorable position where reservoirs are very developed and on the high part of the karst paleogeomorphology developed during the early Hercynian (Figs. 3.29 and 3.30). As a result, reservoirs in this unit have been well-developed and contain abundant oil and gas.

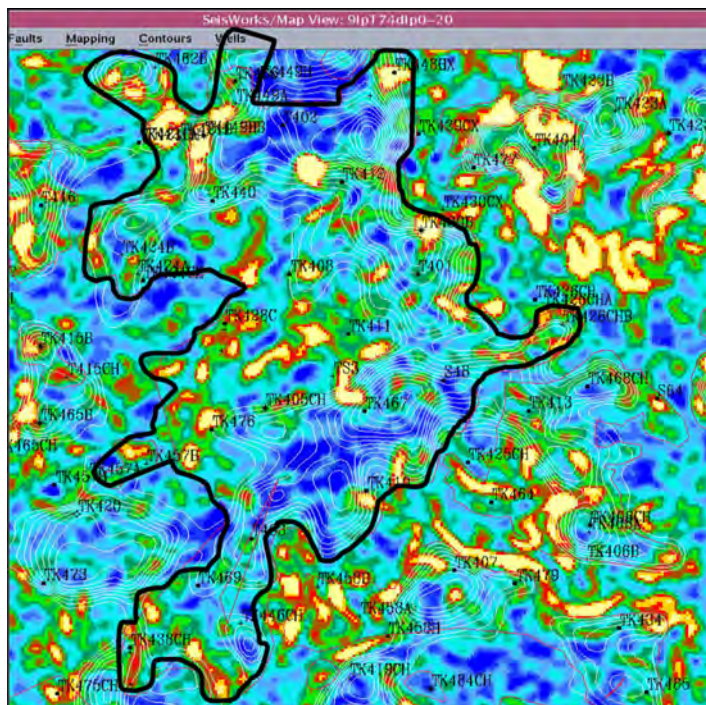


Figure 3.30 The overlapping section of amplitude variation over fold of S48 unit.

Following vug development rules, and using seismic, well logging, core, and production performance data, downhole reservoirs were divided into cavernous, vug, and fracture reservoirs, and filling materials and degree were identified. RMS amplitude and wave impedance attributes that match perfectly with single-well division results were selected for characterizing the distribution features of these caves, vugs, and fractures on single-well, impedance, and RMS amplitude sections, to comprehensively describe the reservoir type in this unit. It has been known that the S48 unit is the largest monadnock at the highest structural axis in the Tahe Oilfield and covers 17.07 km², where there are 36 faults (2.11 faults/km²), 39 NE, NNE and NW large fractures, eight underground stream vugs, 50 isolated vugs, and 23 shaft vugs (Fig. 3.31). Twelve wells have drilled into these vugs, amount to 41% of the overall vugs and an average of 3.9 m vugs drilled in a well. The amplitude variation on the unit boundary is 75. The elevation difference on T₇⁴ ranges from 50 to 120 m. The trend surface ranges from 0 to 95 m (Figs. 3.29 and 3.30).

Taking the divided fracture-vug unit as the reserve calculation unit, and using high pressure physical property (PVT) data and the closed constant-volume elastic driven material balance equation, we calculated the OOIP of the S48 unit to be 2609×10^4 t. Comprehensive evaluation suggests that the S48 unit has a good dynamic and static connectivity. By the end of November 2009, 29 wells had been drilled and put into

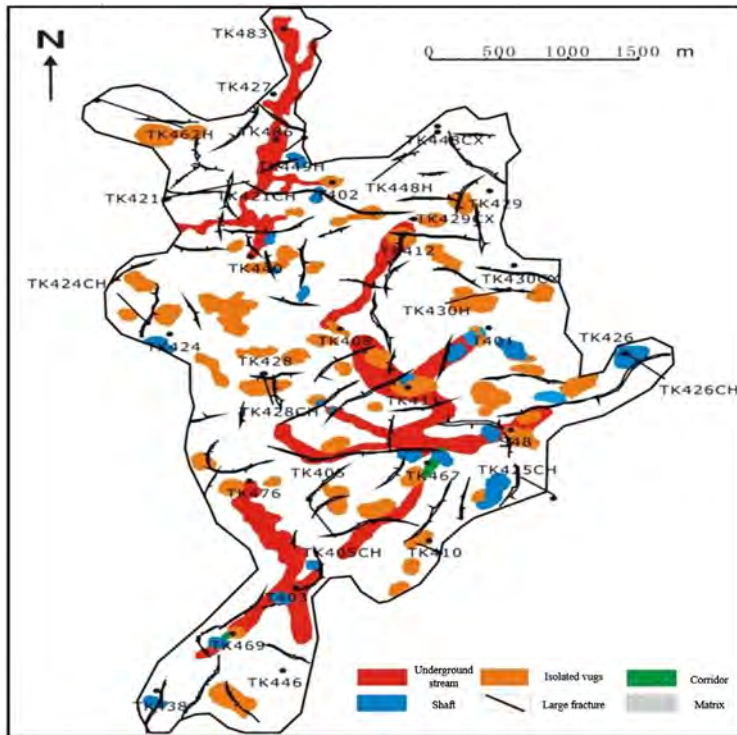


Figure 3.31 Fractures and vugs distribution in the S48 unit.

production in the S48 unit. The S48 unit delivered 148 t/day of liquid per well during initial production, 4.63 million tons of cumulative oil and 6.12 million tons of cumulative liquid.

3.3 3D modeling of a fracture-vug reservoir

There are essential distinctions between fracture-vug carbonate reservoirs and clastic and other carbonate reservoirs. Since carbonate fracture-vug reservoirs contain vugs, fractures, and solution pores, a conventional clastic reservoir model is not suitable for it (Min et al., 2008; Huiting et al., 2004). Taking the fracture-vug carbonate reservoir in the fourth block of the Tahe Oilfield as the prototype and the vertical Ordovician karst segmenting model as the base, we can build a model in two steps. The first step is to build deterministic discrete distribution models for caverns and large-scale fractures with constraints of their scales and other conditions and using seismic identification and characterization results, and then build a stochastic model for vugs and a discrete model for microscale fractures with constraints of karst facies and based on the development probabilistic volumes of

vugs and cross-well fractures and through multiattribute simulation. The second step is to integrate these four models into a 3D discrete distribution model using the collocated conditional assignment algorithm (Jiagen et al., 2012, 2013; Xiangyang et al., 2013, 2014; Yuming et al., 2012; Xinbian et al., 2012; Xiaoqiang et al., 2013; Zhao et al., 2011).

3.3.1 Designing a 3D model grid

Designing a 3D model grid is the first step in building the discrete and the attribute parameter models of a fracture-vug reservoir. This is to illustrate the layer distribution of a fracture-vug reservoir in a 3D grid.

Based on reservoir geologic and seismic study results, the Ordovician formation can be vertically divided into three karst segments (i.e., Segments I, II, and III) which may be treated as three layers. According to the well location and considering the reservoir heterogeneity in the test area, a deterministic model was built, in which lateral grid size is 25×25 m and vertical grid spacing is 2 m (Fig. 3.32).

3.3.2 Building a 3D caverns model

Using the results of 3D seismic data identification and characterization, the dynamic and static production data and the inversion result of high-resolution seismic and logging data, and based on geologic models of wells and sections, the spatial distribution features of a fracture-vug reservoir can be defined, then based on which and with the constraints of the karst facies pattern, a deterministic 3D distribution model can be built for caverns in a carbonate reservoir.

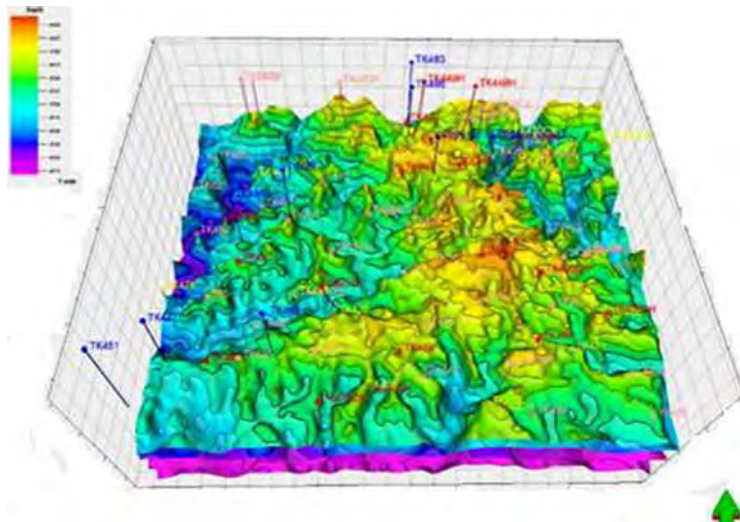


Figure 3.32 3D visualization of a paleo-buried hill on the top of the Ordovician formation.

In the fourth block, a 3D fusion volume of impedance and seismic attribute can be produced after combined well-seismic impedance inversion and multiattribute fusion. After the 3D fusion volume is calibrated using core, well logging, and production performance data, the impedance cutoff can be used to define the caverns in the 3D wave impedance volume. The values for defining unfilled, partially filled, and fully filled caverns mentioned above are used to characterize the distribution of these kinds of caverns in 3D space. As noted before, vertically three karst segments have been divided, so a deterministic 3D distribution model can be built for these caverns (Fig. 3.33).

1. Segment I

In the 4th block of the Tahe Oilfield, Segment I has been interpreted as the important section containing three filling types of caverns, especially in TK471x–T402–T408–S48–TK407. It is the primary oil reservoir, surrounding which the caverns are highly filled (Fig. 3.34).

2. Segment II

In Segment II, caverns have been developed well, and mainly include unfilled and filled caverns, so this segment is also the primary oil reservoir in the fourth block of the Tahe Oilfield. An unfilled reservoir was found in some intervals such as S65 and TK455, and an SN filled zone was found in the central area, such as T403 (Fig. 3.35).

3. Segment III

In Segment III, caverns are obviously reduced, with only unfilled and filled caves in the model. The primary caverns developed in TK427 were found in this segment (Fig. 3.36).

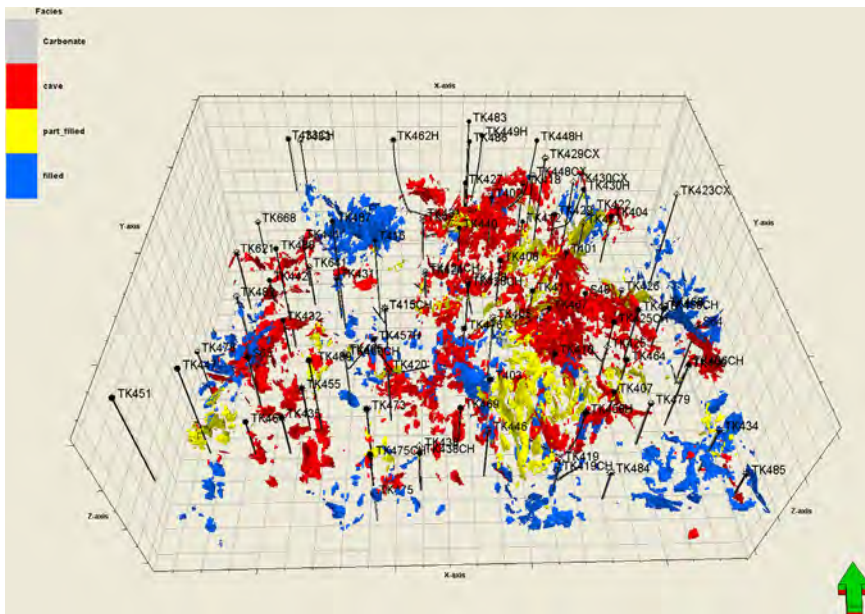


Figure 3.33 Caverns distribution model in the fourth block of the Tahe Oilfield.

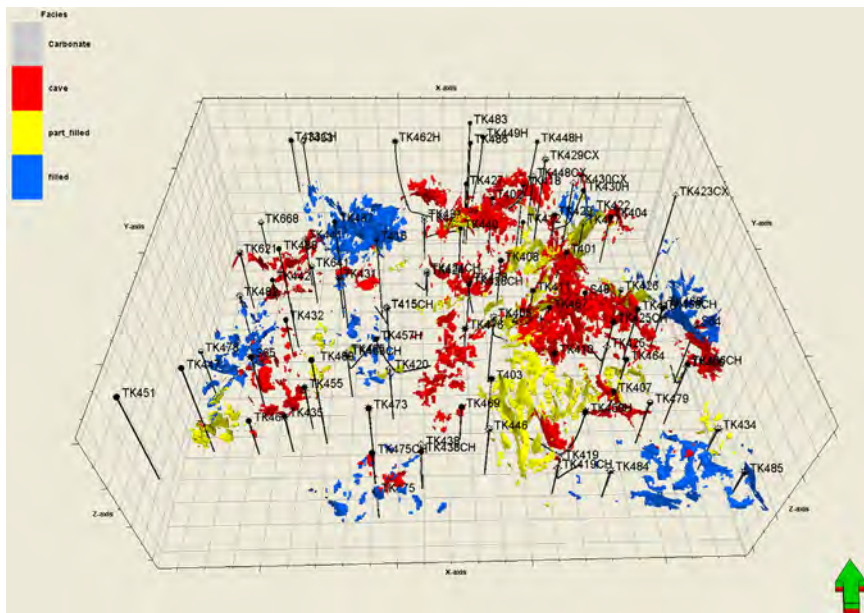


Figure 3.34 Caverns distribution model of Segment I.

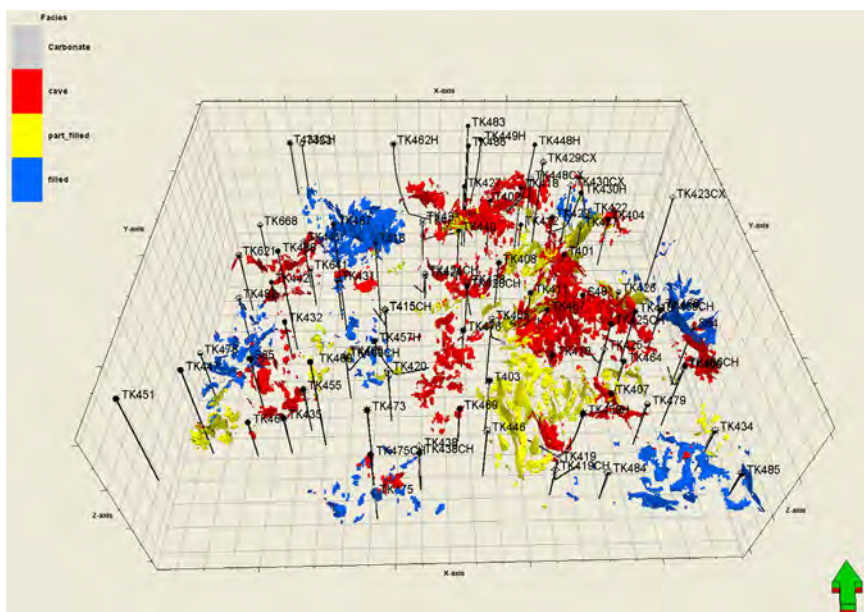


Figure 3.35 Caverns distribution model of Segment II.

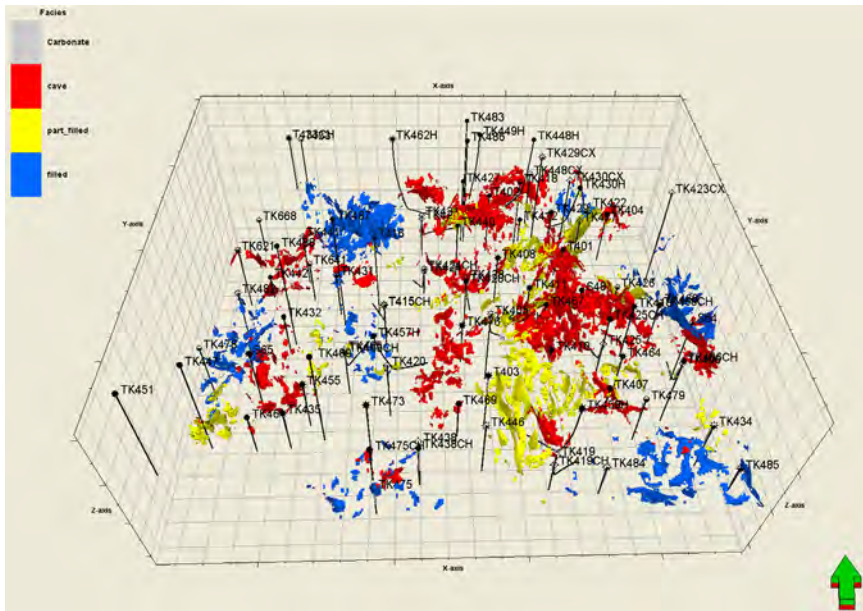


Figure 3.36 Caverns distribution model of Segment III.

3.3.3 Build a 3D vug model

Single well vugs can be identified using core, well logging, and production performance data. However for cross-well vugs with complicated structures, their distributions and accurate locations can only be predicted by geostatistical stochastic simulation.

Generally, vug distribution in the 3D space can be delineated with the constraints of vertical and lateral probabilistic development of caves identified using seismic data and using multiattribute simulation.

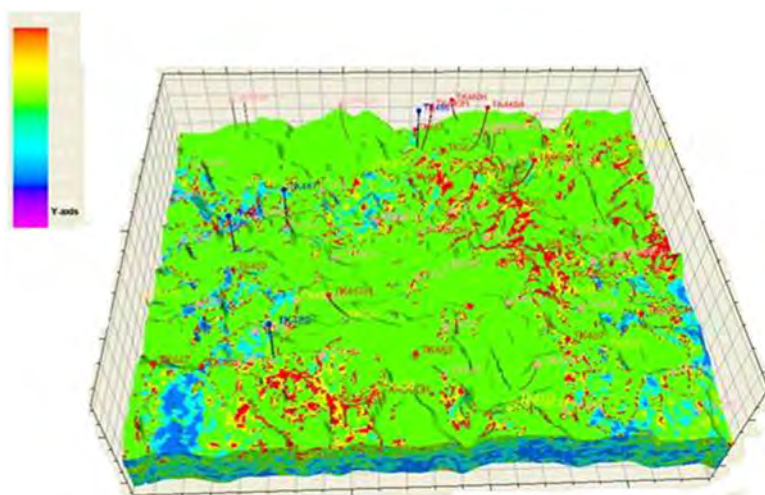
A sequential indicator simulation algorithm is often used to simulate the spatial distribution of vugs. Sequential indicator simulation is applicable to stochastic simulation of discrete variables and discretized continuous variables. This method provides a series of thresholds, instead of assuming that original samples follow a normal distribution, and yields a determination of distribution of stochastic variables by estimating the probability that a variable or discretized continuous variable is lower than a threshold. This method, in essence, is a sequential simulation that performs indicator kriging to calculate the cumulative condition distribution function (ccdf) showing the features including indicator transform, indicator kriging, and sequential simulation algorithms for variables.

In the fourth block of the Tahe Oilfield, based on the vertical three karst segments and the lateral fracture-vug unit, a 3D vug model can be built.

1. Use the probability volume of cavern development to constrain the spatial distribution of vugs Based on the 3D wave impedance inversion results, statistical inversion results and distribution of single-well caves (Table 3.8), the threshold for caverns is set to

Table 3.8 Statistics of inversion results and distribution of single-well caverns

Impedance ($\text{kg/m}^3 \times \text{m/s}$)	Matrix probability	Cavern probability
10,000–10,500	0.8	0.2
10,500–11,000	0.5	0.5
11,000–11,500	0.4	0.6
11,500–11,600	0.55	0.45
11,600–12,100	0.65	0.35
12,100–12,800	0.8	0.2
12,800–13,100	0.5	0.5
13,100–13,800	0.6	0.4
13,800–14,600	0.7	0.3
14,600–15,800	0.75	0.25
15,800–16,100	0.8	0.2
16,100–16,800	0.85	0.15
16,800–17,100	0.9	0.1

**Figure 3.37** Probability volume of cavern development.

15,600 $\text{kg/m}^3 \cdot \text{m/s}$, representing a low impedance. The probabilistic volume of the spatial distribution of caverns can be calculated using single-well development probability in different inversion ranges (Fig. 3.37).

2. Simulate the spatial distribution of vugs

Taking single-well vug distribution as conditional data, run data analysis on real single-well vug distribution data to get the variogram value (Table 3.9 and Fig. 3.38). Then with the cross-well constraints of the probability volume of cave development, and geostatistical sequential indicator simulation method, simulate the 3D vug distribution. Fig. 3.39 shows the 3D model of vug distribution in the fourth block of the Tahe Oilfield.

Table 3.9 Variogram data of vugs distribution

Segment	Type	Principal range (m)	Secondary range (m)	Vertical range (m)	Principal direction
I	Matrix	1500	1215.9	50	NW
	Unfilled vugs	1186.1	1079.8	100	NW
	Semi-filled vugs	806	783.4	100	NW
	Filled vugs	1861.2	1692.7	100	NW
II	Matrix	1484	1410.2	50	NW
	Unfilled vugs	1178	1059	100	NW
	Semi-filled vugs	812	779.2	100	NW
	Filled vugs	1163.1	1026.2	100	NW
III	Matrix	1515.2	1234.1	50	NW
	Unfilled vugs	1172.2	1067.2	50	NW
	Semi-filled vugs	807.3	782.4	50	NW
	Filled vugs	1892.2	1578.5	100	NW

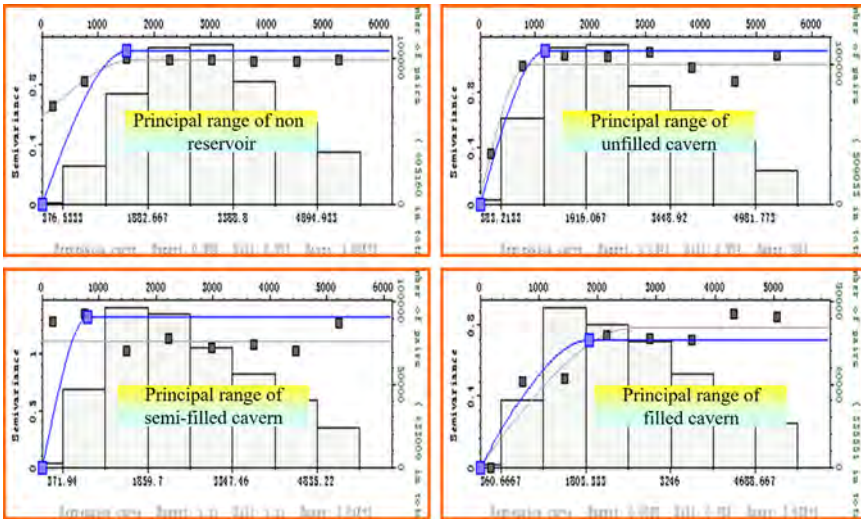


Figure 3.38 Variogram structure of Segment I.

3.3.4 Build a large-scale fracture model

Characterization of large-scale fracture is based on 3D seismic data interpretation and seismic attribute extraction. The distribution model of large-scale fracture in 3D space can be built using the deterministic modeling method (Xin, 2010).

The information on large-scale faults and fractures can be picked in a human-computer interactive manner using seismic coherence cube, seismic “ant

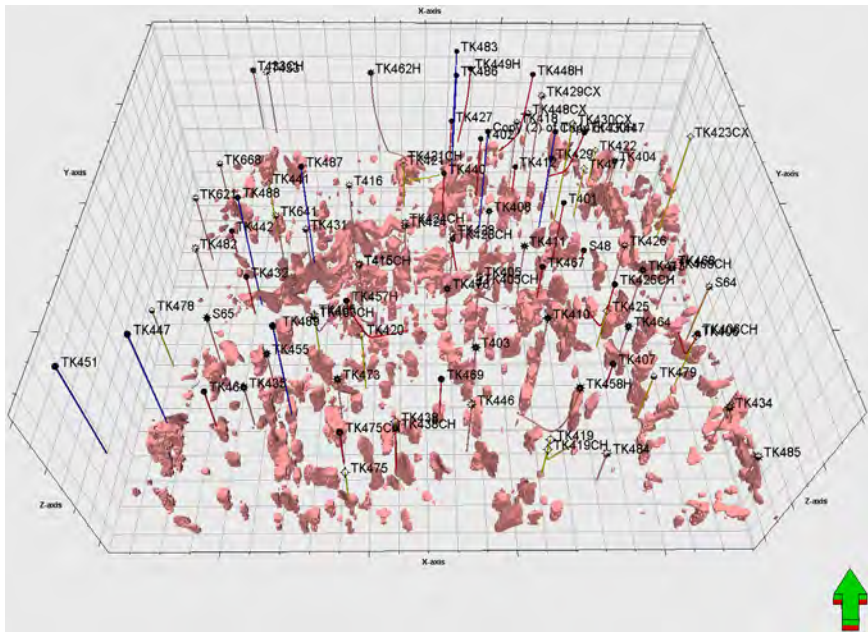


Figure 3.39 Vugs distribution model in the fourth block of the Tahe Oilfield.

cube,” and fracture-related seismic edge detection attributes, and the large-scale discrete fracture model can be created by groups in all azimuths.

There are abundant faults (about 400 faults) in the fourth block of the Tahe Oilfield, all of which are reverse faults with small fault throw and short extension (Fig. 3.40). According to seismic data interpretation, the maximum fault throw is 60 m and the minimum is 5 m; and the fault extension generally ranges from 1.0 to 1.5 km, with a maximum of 3.3 km. A statistics of fault strike indicates that there are roughly three fault development zones, and faults strike is dominated by NE–SW, followed by nearly SN.

Based on a filtering processing of seismic data, extraction of the fracture attribute volume from the edge detection attribute is possible. As shown on the fracture distribution map (Fig. 3.41), fractures are generally closely spaced and small in scale, forming multiple systems, and fracture systems exhibit a chessboard-like distribution; and the northeastern well blocks exhibit a higher fracture density than the southwestern well blocks. Vertically, fracture density varies over layers (Fig. 3.42): in the upper segment (from T74 to 60 m below), fractures are relatively widely spaced and commonly present in the northern well blocks; in the middle segment (from 60 to 150 m below T74), fractures are most closely spaced, and the eastern well blocks exhibit a higher fracture density than the western well blocks; and compared with the middle segment, the lower segment (from 150 to 240 m below T74) exhibits a lower fracture density, which is relatively higher in the eastern and southern well blocks.

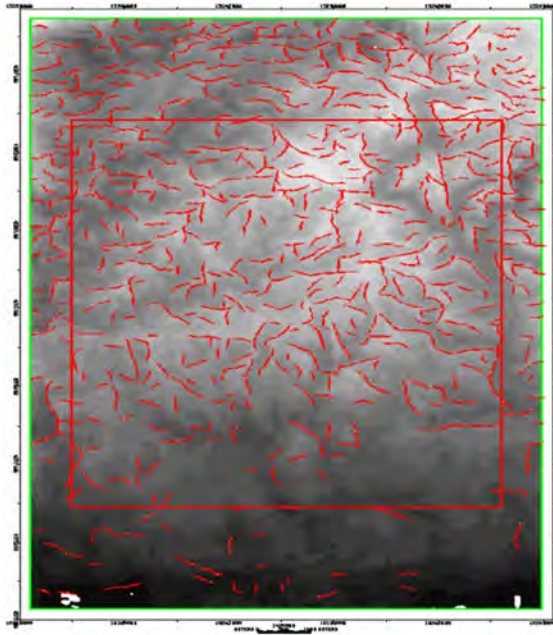


Figure 3.40 Iso-depth section of T74, S48 well block.

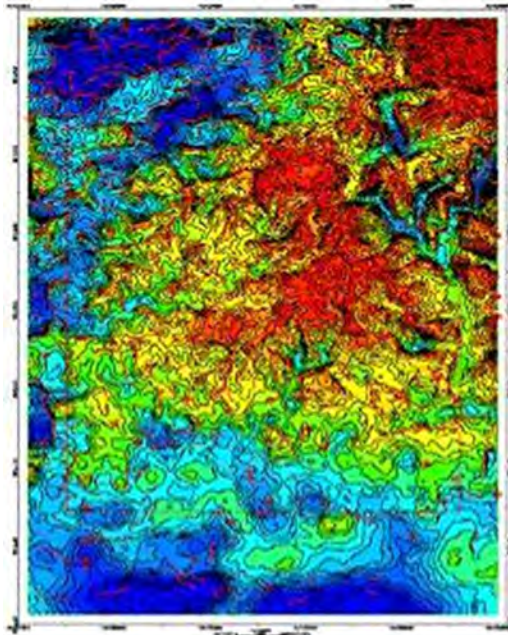


Figure 3.41 Fracture distribution of T74, S48 well block.

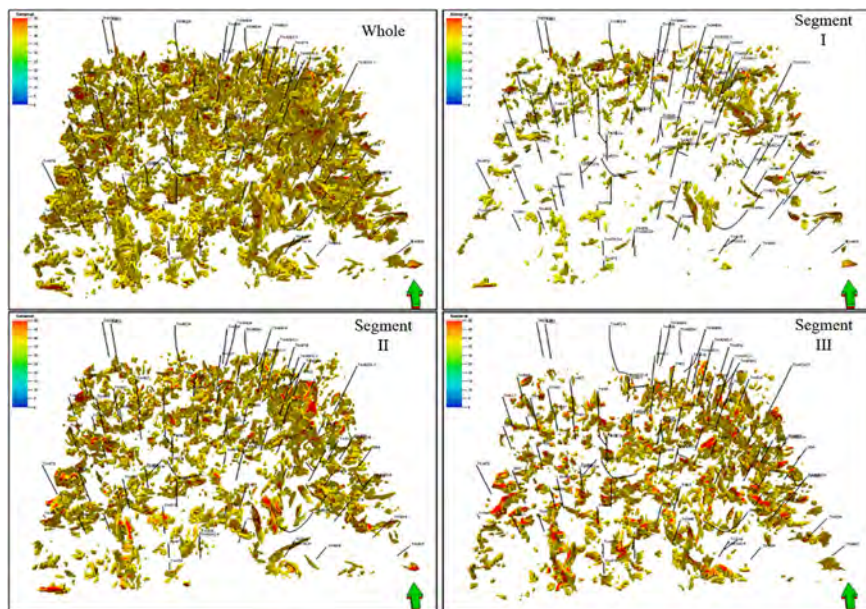


Figure 3.42 3D perspective of fracture detection result.

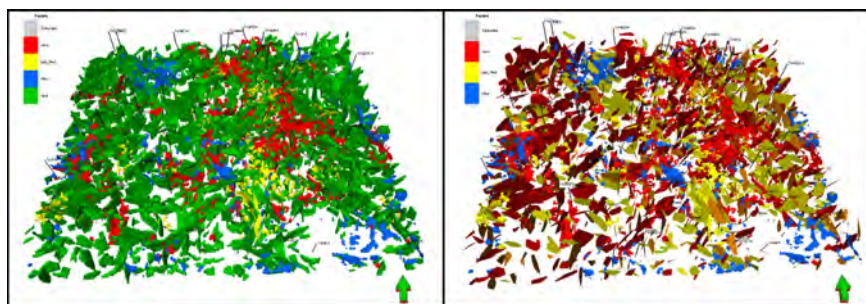


Figure 3.43 Tracking results of the fracture network in the fourth block of the Tahe Oilfield.

The characteristics of the fracture system in the test area were obtained using the integrated 3D seismic interpretation result and “ant-tracking” technique, and then the fracture distribution model of the fourth block of the Tahe Oilfield was created using the deterministic modeling method (Fig. 3.43). Fig. 3.44 shows the distribution of major fractures in the S48 unit.

3.3.5 Build a microscale discrete fracture network model

On the basis of single-well fracture model and under the constraint of fracture development density volume and distance to fracture, a 3D discrete model of the microscale fracture network can be built using the stochastic simulation method.

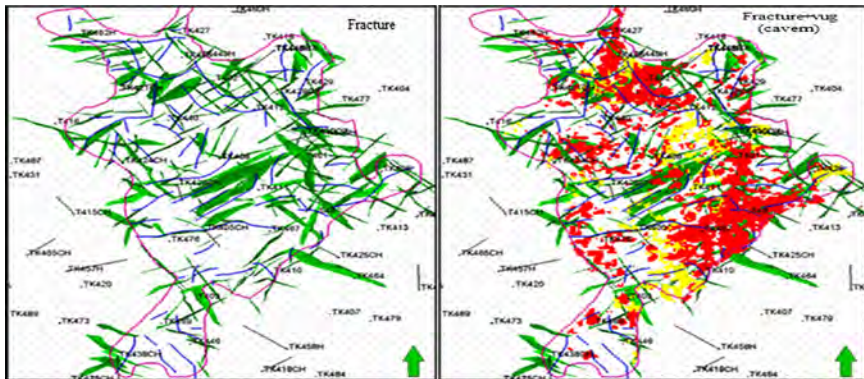


Figure 3.44 Tracking results of fracture network in the S48 unit.

It is possible to identify single-well microscale fractures using imaging log, core, and conventional well log data. Imaging log provides information on fracture development density, fracture occurrence, and aperture. Core and conventional well log data can be used to estimate fracture development density. With available data of regional stress field and fracture distribution, it is possible to macroscopically analyze the fracture development rule and then use this rule to constrain microscale fracture simulation.

Fracture interpretation from the imaging logs of five wells drilled in the fourth block of the Tahe Oilfield were used to calibrate the conventional well logging features. BP neural network technique and conventional well logging features were used to identify fracture facies. Conventional well logs were used to interpret the fracture density in each well (Fig. 3.45). Then, under the constraints of the fracture density and the distance to the nearest fracture, a microscale fracture density model was created by groups in all azimuths. Next the microscale fracture network model was built under the constraints of the microscale fracture density model.

1. Microscale fracture density model

The multicovariate sequential Gaussian simulation can be used to create the microscale fracture density model in any azimuth.

There are two covariates involved in high-angle fracture simulations: the distance to the nearest fracture in any azimuth and the fracture density in any azimuth extracted from fracture detection. Fracture density-constrained simulation provides an opportunity to simulate low-angle fractures. In practice, azimuth-variant variogram that shares the same azimuth with the fracture groups is used to control the simulation process to ensure the consistency of fracture density and related fracture distribution in a group.

Microscale fracture density in the three segments has the following distribution (Fig. 3.46): the upper segment (segment I) has relatively low fracture density; the middle and lower segments share the same fracture density; fracture density distribution varies laterally in each segment; fracture density in the upper segment tends to decrease from north to south, but that in the middle and lower segments is evenly distributed.

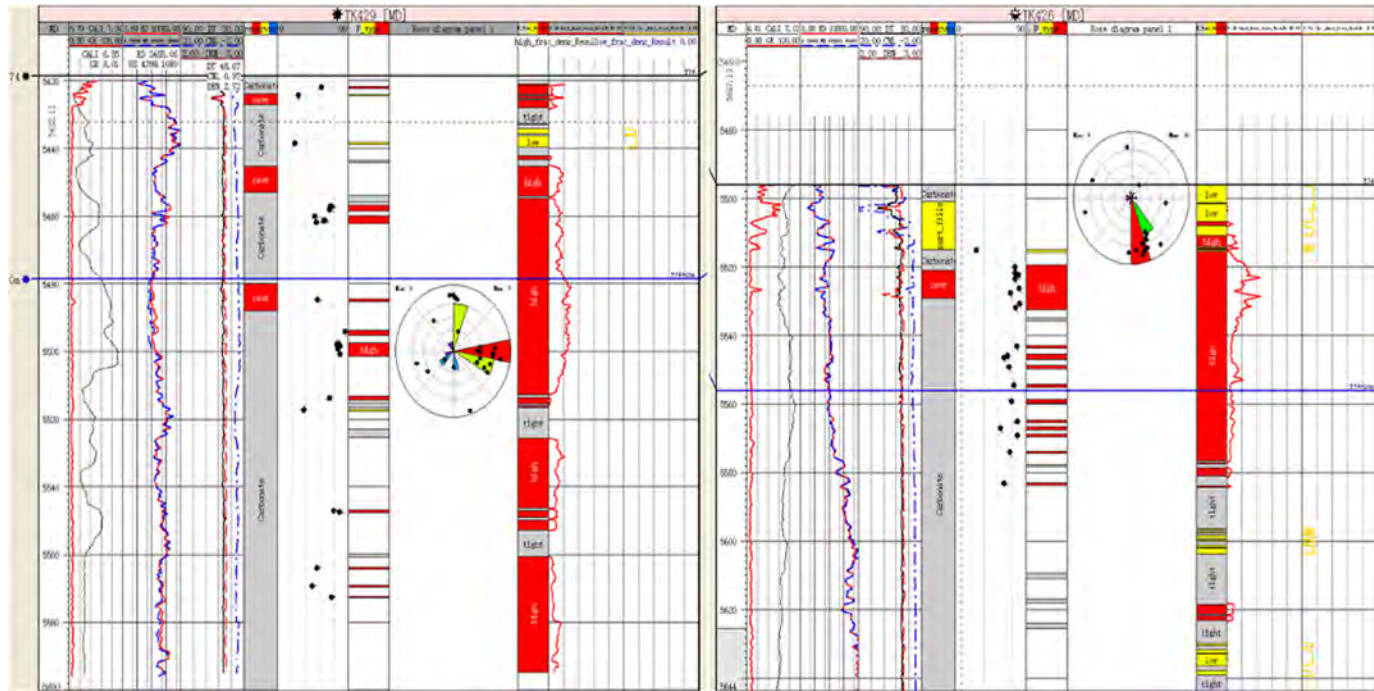


Figure 3.45 Final results of fracture facies identification and fracture density interpretation from a conventional well log.

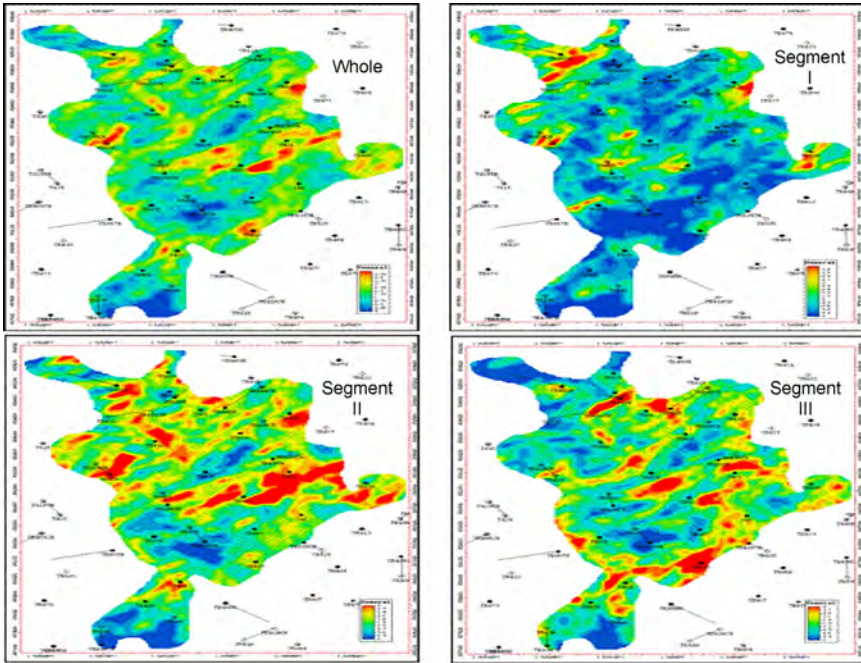


Figure 3.46 Distribution of fracture density in the three segments in the S48 unit.

2. Microscale fracture network model

Generally, length and height required to build a fracture network model are unknown (unless there is available outcrop data). This is the case in the test area where the empirical values of these two parameters are at meter level. However, the empirical length and height can be modified and fit by overall fracture porosity and permeability, especially in this area where the fracture density is too large to model on computer at meter level, so an equivalent transformation by increasing the fracture scale while reducing the fracture density was used in the real modeling process (Fig. 3.47).

In addition, considering spatially oval-shaped fractures, a flat hexagonal fracture shape was used, which may be more reasonable than the rectangular shape used commonly.

Because the microscale fracture density is very large, it is difficult to study their distribution rule based on a fracture network model. In order to perform qualitative analysis, the fracture density was sparsed (Fig. 3.48). Fig. 3.49 shows that the microscale fracture network matches well with the microscale fracture density and azimuth. In general, NE fractures are richest, followed by SN fractures, and next are NW fractures, demonstrating the consistency with the statistical results of well data. The fracture network model provides the basis for calculating equivalent fracture porosity and permeability.

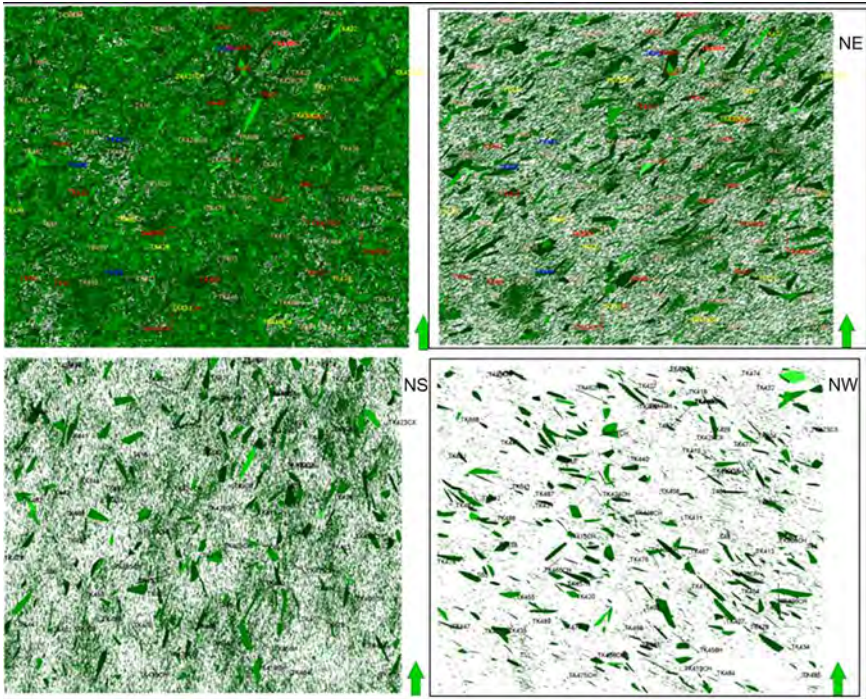


Figure 3.47 Microscale fracture network distribution model of the fourth block of the Tahe Oilfield.

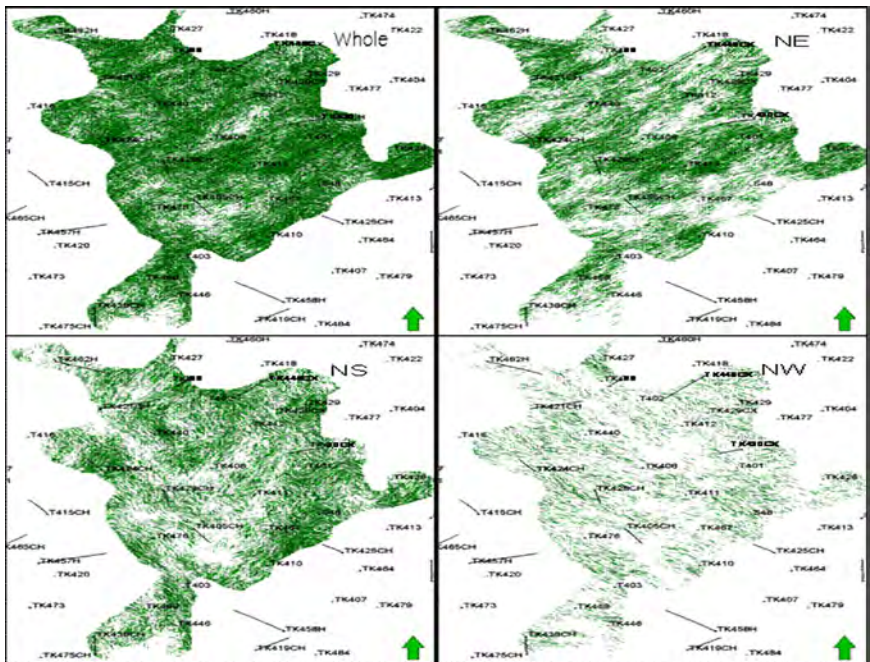


Figure 3.48 Microscale fracture network distribution model of the S48 unit.

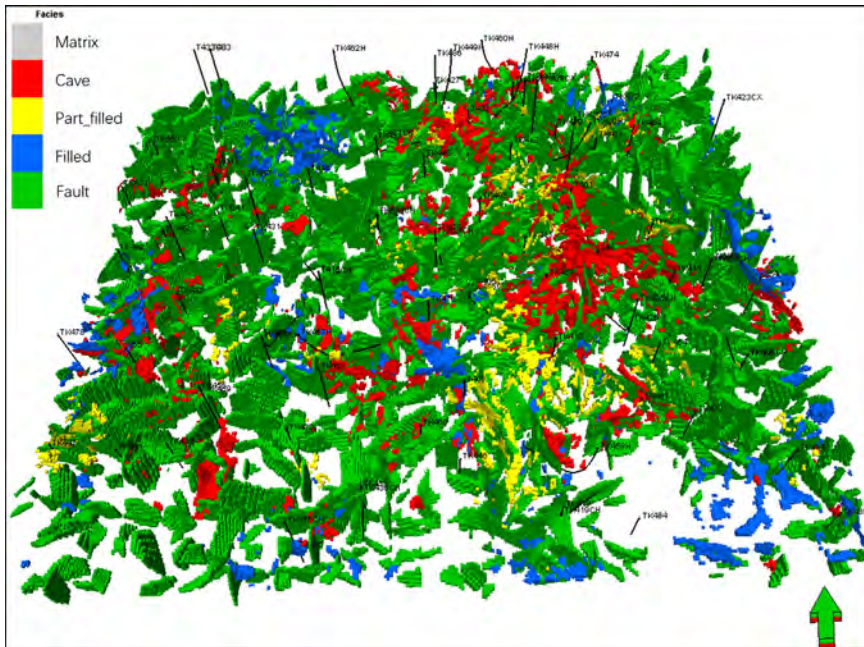


Figure 3.49 An 3D fused model of the fracture-vug reservoir in the fourth block, the Tahe Oilfield.

3.3.6 Fusion of discrete distribution models of fracture-vug carbonate reservoirs

Strictly following single well conditions and the development pattern and combination rule of fractures and vugs, and using the collocated conditional assignment algorithm, the four discrete models of caverns, vugs, large-scale fractures, and microscale fractures built above were integrated to create a multiscale 3D discrete distribution model of a fracture-vug reservoir (Figs. 3.49 and 3.50).

$$\text{DCFN}[x, y, z|(i)] = F\{I_{\text{cave}}, I_{\text{fault}}, I_{\text{vug}}, I_{\text{fracture}}(x, y, z)|(vug \text{ type})\}$$

where $I_{\text{cave}}(x, y, z)$ is cave index; $I_{\text{fault}}(x, y, z)$ is fault index; $I_{\text{vug}}(x, y, z)$ is vug index; $I_{\text{fracture}}(x, y, z)$ is fracture index.

3.4 Attribute parameter modeling of a fracture-vug carbonate reservoir

Conventional physical properties such as porosity, permeability, and saturation for characterizing clastic rocks are applicable to microscale vug and fracture reservoirs, but inapplicable for cavernous reservoirs. So new concepts, “void content,” “fluid

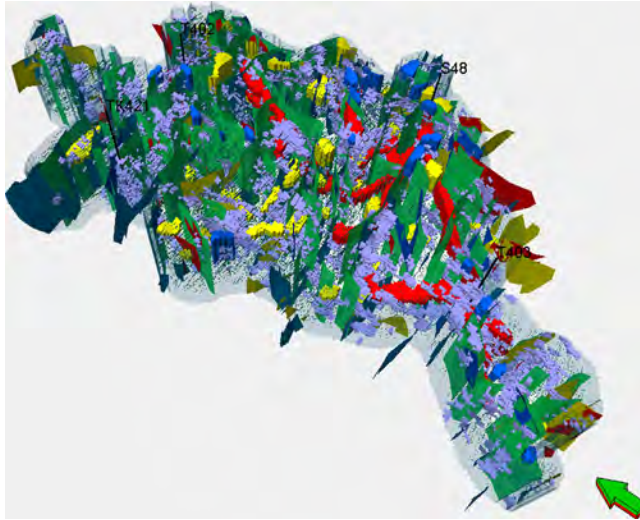


Figure 3.50 An 3D fused geological model of the S48 unit.

filling degree,” and “effective cavern volume,” were proposed to describe such reservoirs (Zhang et al., 1996). The attribute parameter model of a fracture-vug body can be built with special “facies-controlling” constraints and based on single-well interpretation.

3.4.1 Attribute parameters

3.4.1.1 Attribute parameters for caverns

It is proposed to use void content, fluid filling degree and effective cavern volume to describe cavernous reservoirs.

1. Void content

Void content is the space percent (%) of the pores, fractures, vugs, and caverns in a reservoir unit compared to the whole reservoir unit.

a. Use drilling data to estimate void content

In the case where drilling break, lost circulation, and borehole enlargement on caliper log are recorded while drilling, void content of this cavernous reservoir can be estimated with the following equation:

$$R_{fd} = \frac{\sum d}{\sum H}$$

where R_{fd} is the void content of caverns, %; $\sum d$ is the total thickness (m) of drilled intervals where drilling break and lost circulation occur; $\sum H$ is the total thickness (m) of drilled target layers.

- b. Use drilling and production performance data to estimate void content
 - i. In the case of no qualified well logging data recorded, full drilling break and lost circulation occurring while drilling, and the well is put into production without any measures, void content can be estimated using drilling and production performance data.
 - ii. For a Class I well (cumulative production exceeding 150,000 t), the void content is set to 50%–60% for cavernous intervals; for a Class II well (cumulative production ranging from 45,000 to 150,000 t), the void content is 40% by cavern type or 30% by cumulative liquid production; for a Class III well (cumulative production less than 45,000 t), the void content is 20% (15% if caverns are partially filled).
 - iii. In the case of the well drilled into partially filled caverns, drilling break and lost circulation occurring, and available well logging data (about 51 wells showing such phenomena in the test area), the void content of the interval where drilling break and lost circulation occurred can be calculated based on the statistics of compensated neutron formation porosity and weighted average of thickness.
- 2. Fluid filling degree

Fluid filling degree is the volume percent of the fluids charged in the fractures and caverns in a cavernous reservoir to the whole cavernous reservoir. For an oil reservoir, oil filling degree is the volume percent of the crude oil to the whole oil reservoir. If a cavern above the oil–water contact resulted in drilling break and lost circulation and was put into production without any measure, oil filling degree could be set to 100%.

3. Effective fracture and cavern volume

Effective fracture and cavern volume refers to the volume of the connective caverns and fractures in a fracture-cavernous carbonate reservoir, which can be calculated by one of the following methods:

- a. use a 3D geological model to calculate effective fracture and cavern volume;
- b. the volume of a fracture-cavernous unit multiplies its void content (R_{fd}), i.e.,

$$V_{fd} = V_{\text{bulk}} \times R_{fd}$$

where V_{fd} is the volume of the effective fractures and caverns in the fracture-cavernous reservoir, m^3 ; R_{fd} is the void content (%) of the reservoir; V_{bulk} means the total volume of the reservoir, m^3 .

3.4.1.2 Attribute parameters for vugs

Conventional porosity, permeability, and saturation can be used to describe vugs. Vugs usually result in partly drilling break and lost circulation, indicate vug and pore response on well logs, and show shale- or breccia-filling features on well logs and mud logs. The physical properties of a vug reservoir can be calculated based on well logs.

1. Porosity

A vug reservoir has a relatively low porosity which can be calculated using the crossplot of density and neutron logs:

$$\Phi_D = \frac{\text{DEN} - \text{DG}}{\text{DF} - \text{DG}} - \text{SH} \times \frac{\text{DSH} - \text{DG}}{\text{DF} - \text{DG}}$$

$$\Phi_T = \frac{\Phi_N^2 + \Phi_D^2}{2}$$

where SH is the shale content; DEN is the rock density (g/cm^3); DG is the matrix density (g/cm^3); DF is the pore fluid density (g/cm^3); DSH is the shale density (g/cm^3); Φ_N is the neutron porosity (%); Φ_D is the density porosity (%); and Φ_T is the total porosity (%).

2. Permeability

The seepage flow rule of a vug reservoir follows the Darcy law. Conventional well logs are used to calculate the permeability based the porosity–permeability relationship.

3. Oil saturation

Oil saturation of a vug reservoir is calculated using the Archie equation:

$$S_w = \left(\frac{abR_w}{\Phi^m R_t} \right)^{\frac{1}{n}}$$

$$S_{ohi} = 1 - S_w$$

where m is the cementation index; n is the saturation index; R_w is the formation water resistivity ($\Omega \cdot \text{m}$); Φ is the rock porosity; R_t is the formation resistivity ($\Omega \cdot \text{m}$); a , b are lithology factors; and S_w is the formation water saturation (%).

According to an experimental lithologic-electric analysis of core samples recovered from the Ordovician oil reservoir in the Tahe Oilfield, it is determined that $a = 3$, $b = 1.09$, $m = 1.34$, and $n = 3.63$. In the light of formation water data and formation temperature in the Tahe Oilfield, a $0.01\text{-}\Omega \cdot \text{m}$ formation water resistivity is used for saturation calculation.

3.4.1.3 Attribute parameters for fractures

Conventional porosity, permeability, and saturation can be used to describe fractures.

1. Porosity

Porosity of fractures is calculated based on deep and shallow lateral resistivity data.

The following empirical equations are applicable to the Tahe Oilfield:

a. Identification of fracture condition:

$$Y = \frac{Rd - Rs}{\sqrt{(Rd \times Rs)}}$$

where Rd and Rs are deep and shallow lateral resistivity ($\Omega \cdot \text{m}$), respectively; Y is a dimensionless determination index.

$Y > 0.1$ means high-angle fractures; $0.1 \geq Y \geq 0$ means heterotropic fractures; $Y < 0$ means low-angle fractures.

b. Interpretation model of fracture porosity:

$$\Phi = \left(\frac{A_1}{Rs} + \frac{A_2}{Rs} + A_3 \right) \times R_{mf}$$

where Φ_f is fracture porosity (%); R_{mf} is the resistivity ($\Omega \cdot \text{m}$) of mud filtrate at formation temperature; A_1 , A_2 , and A_3 are constants, depending on fracture condition Y .

Table 3.10 lists the constants.

Table 3.10 The constants for fracture porosity interpretation model

Fracture condition	Y	A_1	A_2	A_3
Low-angle fracture	$Y < 0$	- 0.992417	1.97247	0.000318291
Heterotropic fracture	$0 \leq Y \leq 0.1$	7.6332	20.36451	0.00093177
High-angle fracture	$Y > 0.1$	8.522532	- 8.242788	0.00071236

2. Permeability

Fracture permeability depends on fracture occurrence. Generally fracture occurrence can be classified into three types:

a. Single-group fracture system

A single horizontal or vertical fracture on a single strike direction is treated as a single-group fracture system, for which the fracture permeability interpretation model is:

$$K_f = 8.5 \times 10^{-4} d^2 \Phi_f$$

b. Multigroup fracture system

The multigroup fracture system is similar to the matchstick case, for which the fracture permeability interpretation model is:

$$K_f = 4.24 \times 10^{-4} d^2 \Phi_f$$

c. Network fracture system

The network fracture system involves criss-crossed fractures, for which the fracture permeability interpretation model is:

$$K_f = 4.24 \times 10^{-4} d^2 \Phi_f$$

where d is the fracture width, Φ_f is the fracture porosity, and K_f is the fracture permeability.

3. Oil saturation

According to global experiences, oil saturation of fracture (Sof) is 90%.

3.4.2 Attribute parameter modeling method

A carbonate fracture-vug reservoir has a complicated flow mechanism involving seepage flow and nonseepage flow such as pipe flow, therefore different attribute parameters are required and should be modeled in 3D for the reservoirs containing different types of space.

1. Algorithm for attribute parameter modeling

A sequential Gaussian simulation method is used as the simulation algorithm.

Gaussian random field is the most classic stochastic function. The most significant characteristic of this model is that random variables follow the Gaussian distribution (normal distribution). Therefore, it is possible to use the simple kriging to calculate the

ccdf for Gaussian simulation. The normality of ccdf enables a significant simplification of the entire simulation process. As a result, a series of sequentially determined ccdf can be simplified to a series of kriging equation sets. Of course, most geological data do not follow the symmetric Gaussian distribution. In practice, it is possible to conduct a normal transform of regionalized variables (e.g., porosity and permeability) (transforming them into Gaussian distribution) for simulation and then convert the simulation results to regionalized variables.

There are a variety of algorithms available for Gaussian simulation, such as the sequential simulation, error simulation, and probability field simulation. In practice, the sequential simulation method is often used; that is, the sequential Gaussian simulation.

Sequential Gaussian simulation is a stochastic simulation method that yields the spatial distribution of continuous variables using Gaussian probability theory and sequential simulation algorithms. The simulation process runs sequentially from one pixel to another. In addition to original data, all simulated data are considered when defining the conditional data for calculating the ccdf of a pixel. The simulation realization can be obtained by stochastically extracting quantile from ccdf.

Input parameters of sequential Gaussian simulation include variable statistical parameters (e.g., mean and standard deviation), variogram parameters (e.g., range and nugget effect), and conditional data. Input of 3D facies model is required for the facies-controlled modeling, and the related variable statistical parameters and variogram parameters must be input for each facies.

2. Parameter modeling of caverns

When dealing with caverns, it is natural to determine the “void content” and “fluid filling degree” on single wells on the basis of the statistics of drilling break, lost circulation, and single well production and the parameter calculating method. Under the constraint of the cavern model, the void content distribution model of the caverns in the test area can be created using the sequential Gaussian simulation methods (Fig. 3.51).

Interpretation of well logging and testing data allows us to create a single-well permeability model. With the void content volume acting as a major constraint, the permeability distribution model of the cavern in the fourth block of the Tahe Oilfield can be created using the sequential Gaussian simulation method, in combination with well testing interpretation (Fig. 3.52).

3. Parameter modeling of vugs

Conventional porosity, permeability, and saturation parameters remain applicable to model vugs where fluid flow follows the Darcy Law. From well logging data porosity, permeability and oil saturation values can be calculated, and then the three parameters can be modeled using the sequential Gaussian simulation method and under the constraint of the 3D vug model.

4. Parameter modeling of fractures

A 3D discrete fracture network model (DFN) is obtained by integrating the large-scale and the microscale fracture models. Based on it, models of porosity, permeability, and oil saturation of discrete fractures can be created using geometric equivalence methods.

Because of the anisotropy of permeability models, the dominant permeability, i.e., the maximum permeability in three directions, should be calculated to create a comprehensive permeability model.

The comprehensive permeability model (Fig. 3.53) reveals that faults and large-scale fractures contribute more to permeability, followed by intensive microscale fractures.

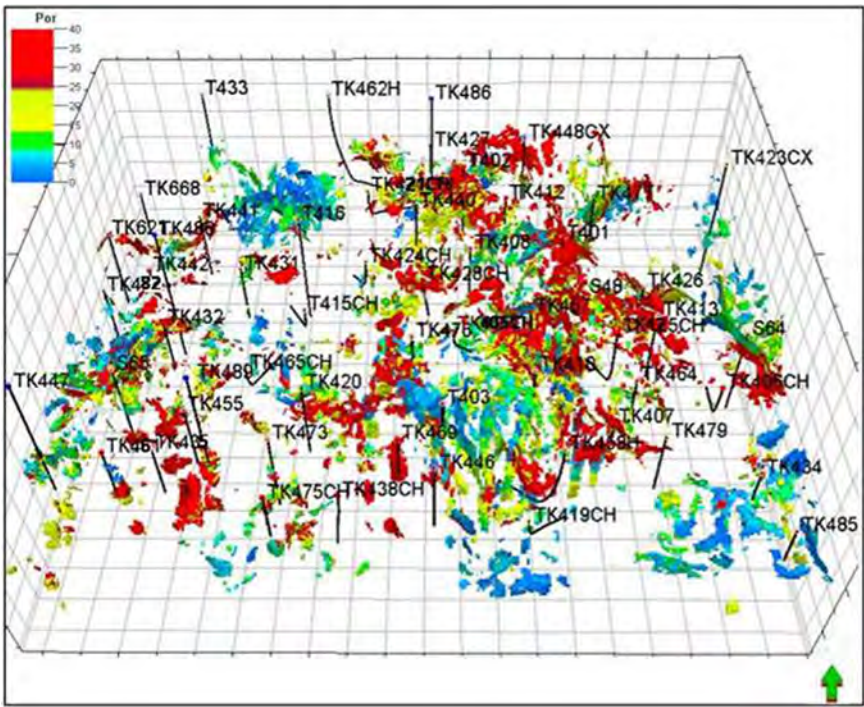


Figure 3.51 3D void content distribution model of the caverns in the prepared block of the Tahe Oilfield.

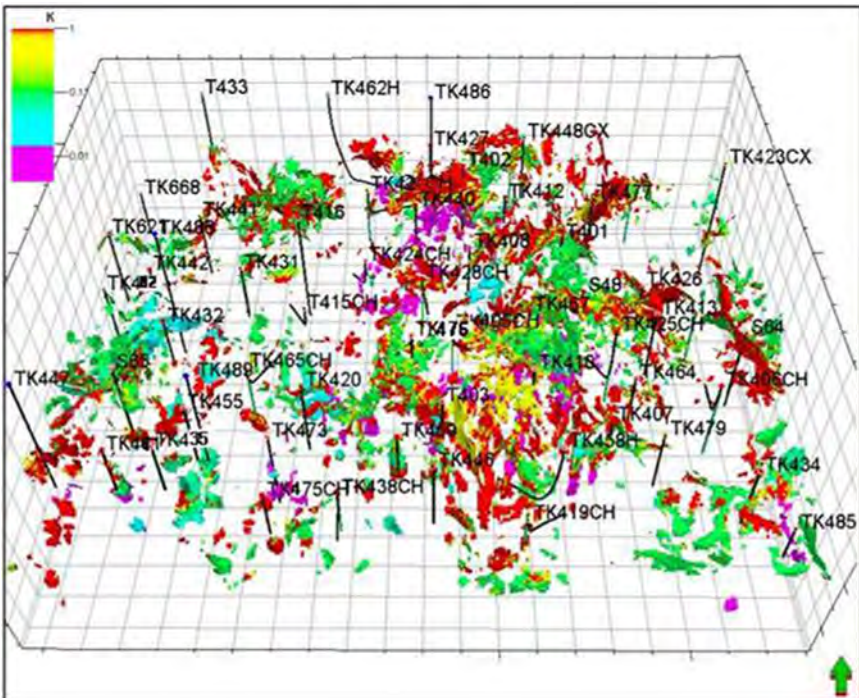


Figure 3.52 3D permeability distribution model of the caverns in the prepared block of the Tahe Oilfield.

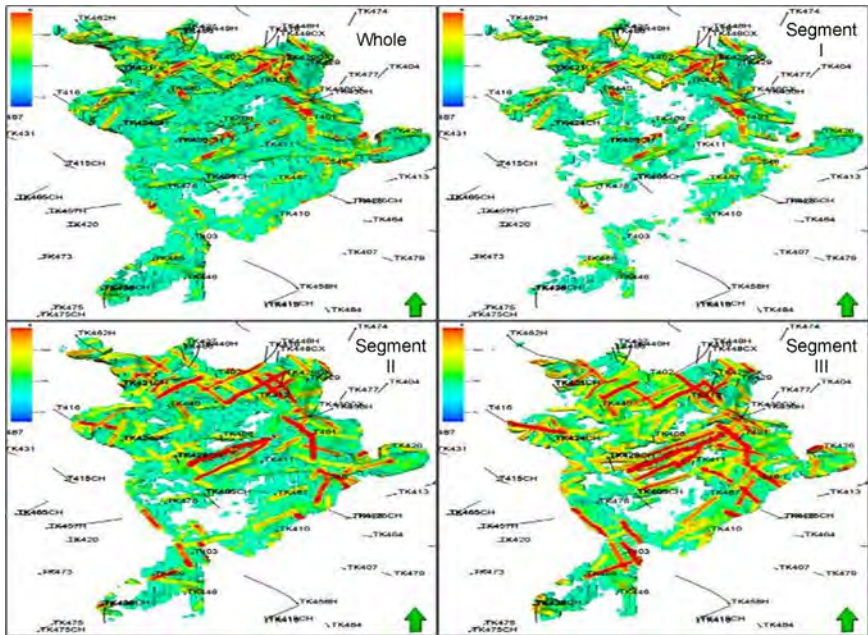


Figure 3.53 3D permeability distribution models of the S48 unit.

3.5 Verification and application

Fracture-vug carbonate reservoirs are highly heterogeneous. 3D geologic models have been built to simulate reservoir space distribution at different scales (caverns, vugs, and fractures) and verified to be effective by drilled well and production data. Application of these models is encouraging, especially in profile control of production wells, sidetracking and water-flooding development.

3.5.1 Verification by drilled well

TK446CH, a newly drilled sidetracking horizontal well, was selected to verify cavern/vug distribution, porosity, and permeability models using the production performance data. This well in the initial period produced oil at 71 tons/day, with no water production, and in the later period produced oil at 32 tons/day, with 14% water content. In general, real production data match well with model results (Fig. 3.54).

3.5.2 Verification by production data

1. Verification of the cavern/vug model by production data
The geologic model of the S48 unit was verified by loading production data. The verification result shows a consistency between the model and the production data.

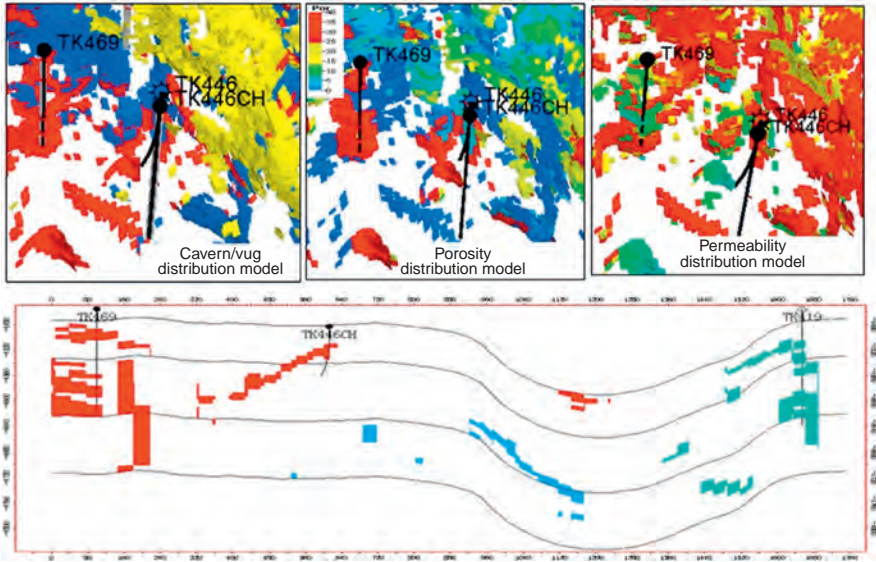


Figure 3.54 The 3D geologic model of Well TK446CH.

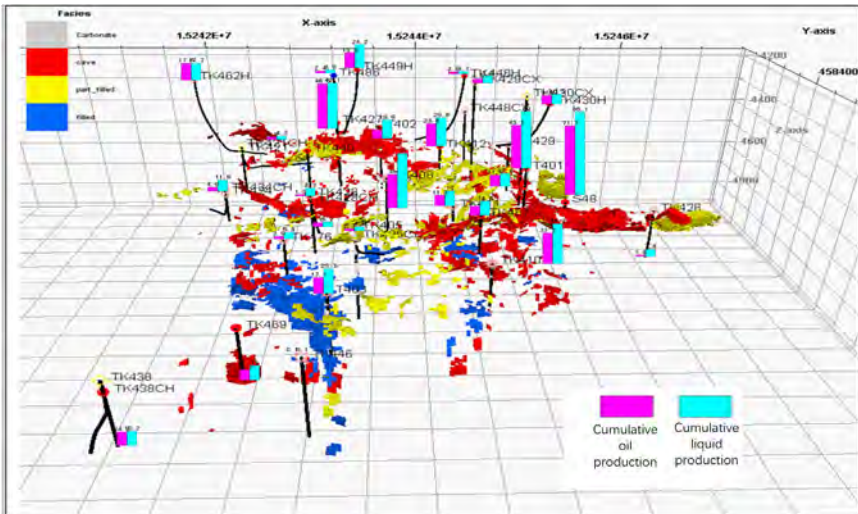


Figure 3.55 Overlapping of caverns/vugs distribution on cumulative production in the S48 unit.

- a. Caverns/vugs are distributed primarily in the northern and eastern parts of the S48 unit, but highly filled in the TK403 well block.
- b. Production wells drilled into the interval containing well-developed caverns/vugs in the model delivered high initial and cumulative productivity (Fig. 3.55).

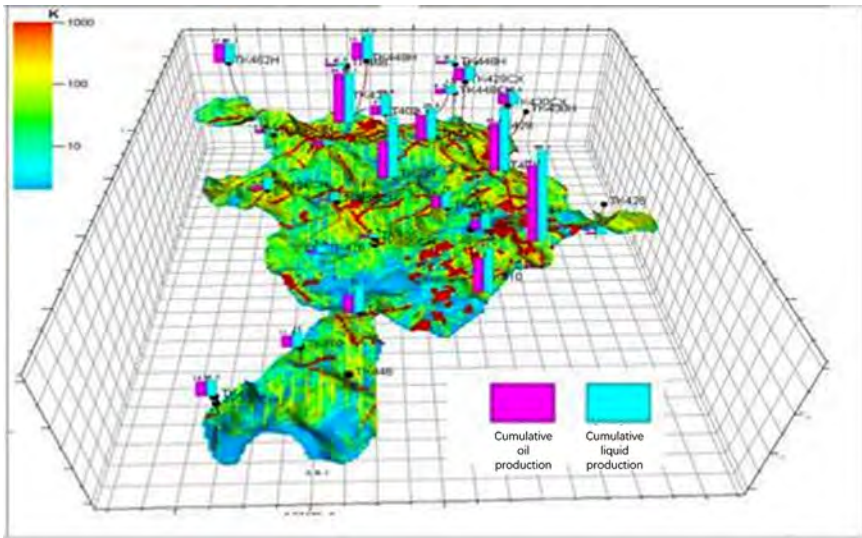


Figure 3.56 Overlapping of permeability distribution on cumulative production in the S48 unit.

2. Verification of the fracture model by production data

The dominant permeability under the S48 well block is NE, which is consistent with the fracture development direction (Fig. 3.56). The permeability model slice 60 m below T_7^4 (i.e., Segment I) indicates that the permeability is higher in the northern part than those in other parts; the permeability model slice 150 m below T_7^4 (i.e., Segment II) indicates that the permeability is higher in the northern, western, and locally eastern parts than those in other parts; and the permeability model slice 150 m below T_7^4 (i.e., Segment III) indicates that the deeply buried reservoirs commonly exhibit a relatively poor permeability.

Production data reveal that high-permeability play zones and intervals have high productivities and relatively long and stable production periods.

3.5.3 Verification by performance data

The connectivity model was verified by injection-production, tracer, and production performance data based on the evaluation of connectivity classification in the S48 unit.

The advancing velocity of the tracker waterline can be used to quantitatively evaluate the cross-well connectivity based on the following criteria: the connectivity is Class I if the advancing velocity exceeds 250 m/day; Class II if the velocity ranges from 100 to 250 m/day; and Class III if the velocity is less than 100 m/day.

In the fourth block of the Tahe Oilfield, 16 well groups are classified as Class I and 12 as Class II. The connectivity generally trends NE–SW, which is consistent with the strike of structural fractures formed during the Early Hercynian.

The permeability simulation result of the S48 unit (Fig. 3.57A) indicates that, on the fracture-vug connectivity model obtained by a cut-off of 300 mD (Fig. 3.57B), intensive fracture systems provide good connection among scattered cavern/vug systems, which is consistent with the understanding of the connective relation from production performance data and the distribution of caverns, vugs, and fractures shown on the reservoir section (Fig. 3.58).

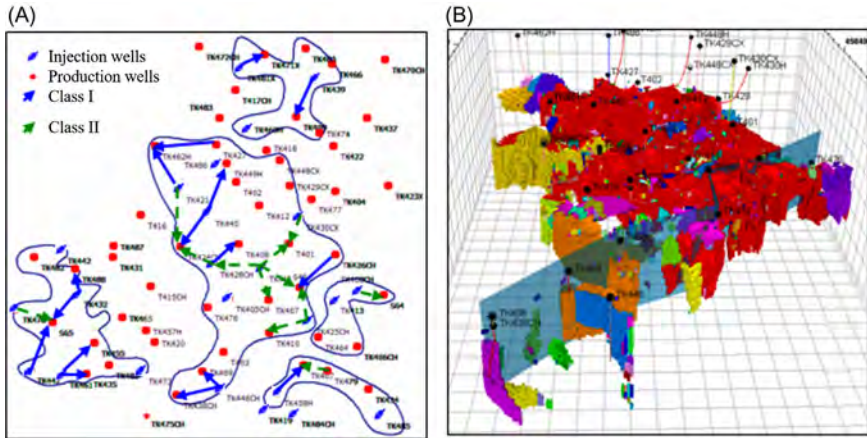


Figure 3.57 Dynamic verification of connectivity in the prepared block. (A) Classification of connectivity; (B) 3D distribution model of connectivity.

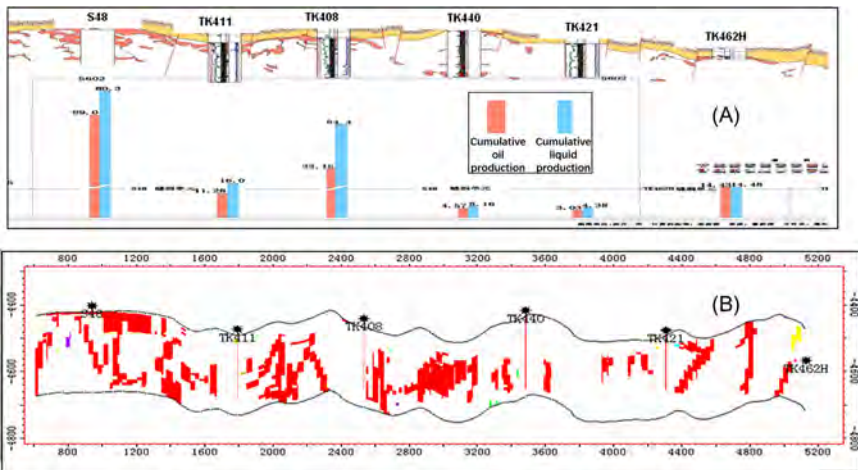


Figure 3.58 Cross-well sections: (A) cavern/vug section across S48–TK411–TK408–TK440–TK421–TK462H; (B) permeability connectivity section across S48–TK411–TK408–TK440–TK421–TK462H).

3.5.4 Application of geologic model

The 3D geological models for characterizing the 3D geometric pattern and attribute distributions of different types of reservoirs (Figs. 3.59 and 3.60) have been applied for reserves calculation and reservoir numerical simulation in the fourth block of the Tahe Oilfield.

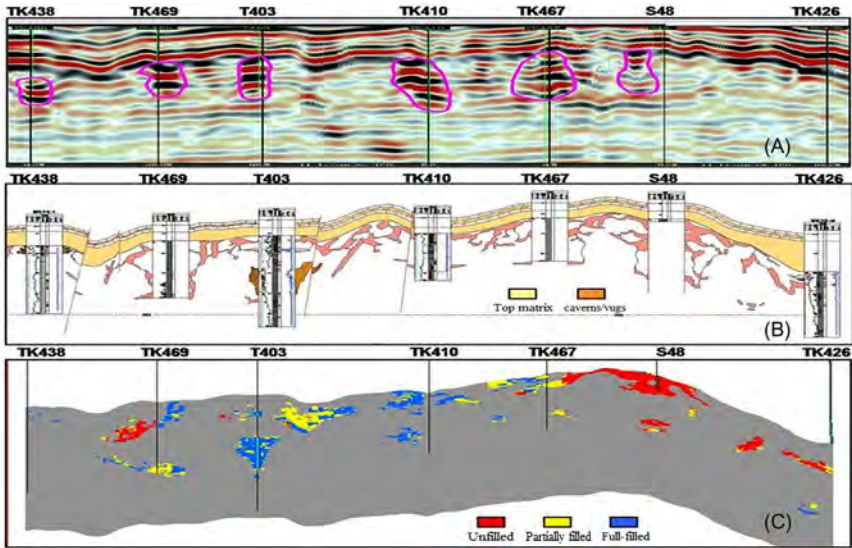


Figure 3.59 Cross-well section across TK438–TK469–T403–TK410–TK467–S48–TK426. (A) The section of fracture-vugs reservoir from seismic reflection (B) The section of fracture-vug reservoir from multi-well interpretation (C) The section of fracture-vug reservoir from 3D model.

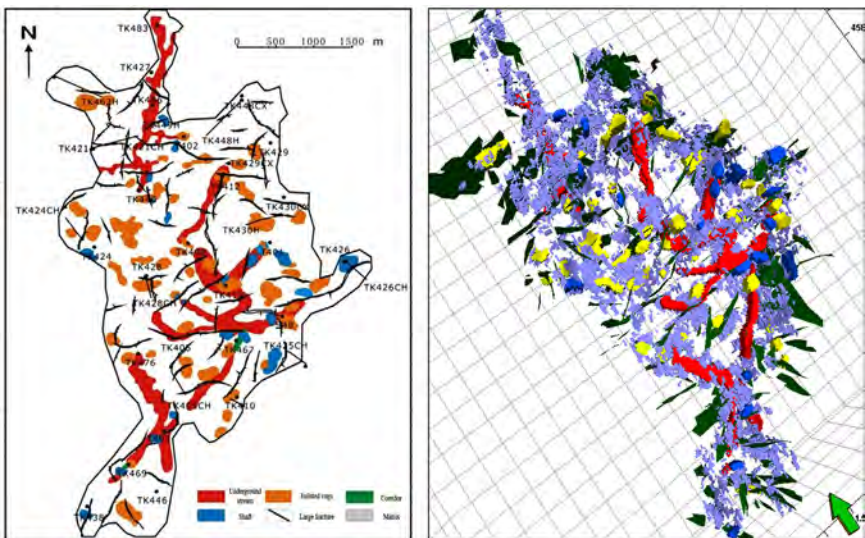


Figure 3.60 Models of S48 unit. Left, planar model; right, 3D model.

In addition, the 3D geologic models provide the base for development and implementation of stimulation measures, such as infilling wells and sidetracking in existing wells.

Developed fracture intervals predicted by the 3D geologic model provide the base for making acidizing and fracturing stimulation plans. For example, because Well T402 produced intermittently due to high water cut, Segment III to 5602 m was drilled. After the entire borehole was stimulated by acidizing treatment, water-flooding effectiveness was recorded in Well TK448CX.

Fluid flow law in fracture-vug carbonate reservoir

4

The Complicated distribution of fracture and vug systems in fracture-vug carbonate reservoirs result in large differences in fluid flow channels, complex characteristics and mechanisms. In addition to fluid flow in the matrix, there are also one-dimensional pipe flow, 2D flow in fracture, 3D free flow in unfilled (or semi-filled) vugs, and the transfer flow between the matrix, fracture, and vugs in fracture-vug carbonate reservoir (Yang, 2006; Jun and Zisheng, 2007; Zhongchun et al., 2009). It is necessary to have a clear understanding of the law of fluid flow in fracture-vug carbonate reservoir and the mechanism of the transfer flow between the matrix, fracture, and vug because these are the theoretical basis for scientifically and efficiently developing the fracture-vug carbonate reservoir and improving the oil recovery.

4.1 Design of physical modeling experiment for fracture-vug media

To study the fluid flow mechanisms in fracture-vug medium, physical models and physical modeling experimental systems are required. In this section, the similarity criteria for developing the physical model is established firstly, and then, various typical fracture-vug models are built based on the proposed criteria. Finally, an equipment for physical modeling is designed, which can be used to conduct the experiment to study the mechanism of fluid flow in fracture-vug carbonate reservoir.

4.1.1 *Fundamental principles and similarity criteria*

Primary reservoir space in the Tahe carbonate reservoir is composed of vugs and fractures. Microscale fractures in matrix have a very low permeability, so they contribute little to seepage flow and are not the main flow channels in developing the carbonate reservoir. In fact, fractures are the main channels through which fluids in vugs can flow to a wellbore. In this sense, in the Tahe carbonate reservoir, vugs and fractures act as the main reservoir spaces and flow channels, and comparatively the contribution of matrix to fluid storage and flow capacity can be negligible (Xia, 1993).

4.1.1.1 *Fundamental principles*

Physical modeling study provides a method where a model of the physical system to be studied is first built, and then the physical laws of the system are analyzed based

on the model. The model used in physical modeling research is the prototype of the real physical system, both of which are similar in physical properties, but different in their dimensions; i.e., the model is the result of zooming in or out of the real system.

1. Similarity laws

The fundamental principle of physical modeling is similarity theory (Ting, 1995), which involves three similarity laws:

First similarity law: the similarity criteria possessed by similar phenomena are equal in numerical values.

Second similarity law: supposing that a physical phenomenon is composed of n different physical quantities, among which, k physical quantities are independent, the other $n-k$ physical quantities are not, then the formula representing the physical phenomenon can also be completely expressed by $n-k$ dimensionless quantities N_1, N_2, \dots, N_{n-k} , and N_1, N_2, \dots, N_{n-k} are similarity criteria.

Third similarity law: if the single value conditions among phenomena are similar and the similarity criteria composed of these single value conditions are equal in numerical values, these phenomena are similar. The single value conditions include the following factors: geometric properties of the system, properties of media having a great effect on the studied object, parameters of other objects, and initial conditions and boundary conditions of the system, etc.

2. Additional conditions

When using similarity theory to solve practical technical problems, there are four additional conditions as follows:

Additional condition 1: for two composite systems composed of multiple systems, if the corresponding single systems are similar, i.e., the corresponding single units in them are similar and the corresponding boundary conditions of the single systems are similar too, the two composite systems are similar.

Additional condition 2: the similarity conditions suitable for a linear system can be applied in a nonlinear system as long as the relative characteristics of the corresponding nonlinear parameters are coincident.

Additional condition 3: the similarity conditions suitable for isotropic and homogeneous systems can also be applied in anisotropic and heterogeneous systems as long as the associated anisotropy and heterogeneity of the two systems are the same.

Additional condition 4: the physical processes of systems with geometric dissimilarities can be similar, and every point in the system space can find a completely matching point in the space of its similar system.

These additional conditions play an important role in modeling a physical system. In other words, as long as every unit and their interconnection in the system can be accurately modeled, the resulting composite system can be accurately modeled too.

3. Similarity criteria and determination methods

Similarity criteria are important parts in similarity theory; they are nondimensional and used to indicate the relation among physical quantities in some physical phenomena. The methods for determining similarity criteria include dimensional analysis and equation analysis (inclusive of similarity conversion, integral analogy, etc.), which can be used to obtain similarity criteria for physical modeling based on the analysis of basic process (Junjie, 2005).

4.1.1.2 Similarity criteria

Based on similarity theory, the basic requirements for the physical model to be similar to the prototype should meet the three similarity laws. Accordingly, the

scaling model and the field prototype should be similar in geometric, fluid, and petrophysical parameters, as well as in their initial and boundary conditions. However, for a fracture-vug reservoir, complicated structure and challenging production make it impracticable to fully model any derived similarity criteria on the physical model. During physical modeling, it is essential to analyze specific and solve major problems of the oil reservoirs, to determine and realize the similarity criteria that play leading and decisive roles in the modeling, and neglect the secondary similarity criteria. This may truly reflect the fluid flow pattern to some extent.

The study on the fluid flow mechanism in fracture-vug reservoirs focuses on the effects of fractures and vugs on single-phase and oil–water two-phase flow laws in the reservoir, so the physical quantities related to the distribution of fractures and vugs in the reservoirs are the main elements taken into account when selecting characteristic quantities and determining similarity criteria. However, the study on the flow law inside the reservoir medium focuses on single-phase flow law in different types of fracture-vug media, so the physical quantities related to the distribution of fractures and vugs and flow resistance are the main elements that should be taken into account when selecting characteristic quantities and determining similarity criteria.

1. Selection of characteristic quantities

The purpose of selecting characteristic quantities is to keep the system unchanged when the proportion of the system model to its prototype changes. In most cases, the basis for selecting characteristic quantities is to be able to present the best physical property matching within the range of interest. Based on the objectives and contents of flow mechanism study and production practices of fracture-vug reservoirs, the characteristic quantities were selected as follows.

- a. The characteristic quantity of porosity equals the fracture porosity ϕ_f of reservoir.
- b. The characteristic quantity of time is the time t when the first displacement starts.
- c. The characteristic quantity of saturation is the movable oil saturation when the first displacement starts.

$$\Delta S = 1 - S_{or} - S_{wc}$$

- d. The characteristic quantity of length is set to be the net thickness of the reservoir, L .
- e. The characteristic quantity of permeability is set to be the absolute permeability of the reservoir, k .
- f. The characteristic quantity of pressure equals the maximum drawdown pressure, i.e., the difference between the maximum and the minimum pressure predictions.

$$\Delta P = P_{\max} - P_{\min}$$

It is not necessary to take the exact values values. However, if the values are taken properly, the best results will be obtained when matching the model with the prototype for physical properties. Therefore, the minimum pressure is taken as the reference.

- g. The characteristic quantity of density equals the density of oil, ρ_o .
- h. The characteristic quantity of viscosity equals the dynamic viscosity of oil, μ_o .
- i. The characteristic quantity of acceleration is the acceleration of gravity, g .
- j. The characteristic quantity of fluid flow rate is the flow rate of oil. Q_o .

2. Determination of similarity criteria

Nine similarity criteria were summarized for modeling the flow mechanism in the fracture-vug reservoir in the Tahe Oilfield (Table 4.1). They are the most simplified, and can meet the prerequisite that key elements and mechanisms must be similar, and the objectives of the study on fluid flow mechanism.

In Table 4.1, n_f is fracture density (also called fracture frequency or fracture line density), referring to the number of fractures within a unit length perpendicular to the fracture strike; n_v is vug density, referring to the number of vugs within an unit area; k_f and k_m represent the permeability of fracture and matrix, respectively; C is connectivity, representing the complexity of fracture-vug structure; δ represents the filled degree of vugs; and L_f is fracture length.

Neither capillary force nor matrix permeability and porosity were taken into account in developing the similarity criteria listed in Table 4.1. If the matrix has larger permeability and porosity, it means that it has storage and seepage capacity, the reservoir should be treated as a fracture-pore reservoir. The permeability of a fracture-vug reservoir is usually very large, so the capillary force can be negligible compared with the viscous force or gravity. In a pore reservoir, because inertia resistance is generally much smaller than viscous resistance, the contribution of inertia force are not a studied. However, in a fracture-vug reservoir, an almost impermeable matrix decreases the seeping area greatly, and increases the seepage flow rate, and even damages the linear resistance law, so the effect of inertia force should be studied. Similarity criterion 2 is used to study the effect of inertia force.

Table 4.1 Nine similarity criteria for modeling the flow mechanism in the fracture-vug reservoir in the Tahe Oilfield

SN	Similarity criterion	Physical significance
1	$\frac{P}{\rho g L}$	Pressure to gravity ratio
2	$\frac{\rho v L}{\mu}$	Inertia resistance to viscous resistance ratio, similar to the Reynolds number
3	$\frac{k}{L^2}$	Ratio of the flow rate flowing through microscale fractures to that through large-scale fractures
4	$\frac{\rho g k}{\mu v}$	Effect of gravity
5	$\frac{n_f b}{n_v d L}$	Effect of the size and density of fractures and vugs
6	$\frac{C \phi_f}{\phi_v}$	Effect of the porosity and connectivity of fractures and vugs
7	$\frac{Q t}{\rho L^3}$	Fluid flow rate
8	$\delta \phi$	Ratio of filled pore volume to total pore volume
9	$\frac{k_f w}{L_f k_m}$	Relative conductivity of fracture (to matrix)

The parameters of an indoor experimental model were defined in accordance with the similarity criteria in Table 4.1 and the parameters of field prototype. During the experiment, the parameters could be adjusted to meet similarity requirements according to the specific model and the experimental objectives. Table 4.2 lists the typical model parameters used in the experiment.

4.1.2 Physical modeling experiment design

4.1.2.1 Selecting experiment materials

1. Model matrix materials

It is impracticable to meet all similarity criteria by selecting appropriate experimental materials. To achieve the research objectives and cover the characteristics of the fracture-vug reservoir, and make the experiment convenient to conduct, lucite and marble were selected as the experimental model materials. During selection, the wettability (Table 4.3) of the real reservoir was considered, but the matrix permeability was ignored.

2. Model fluids

Fluids used in the experiment mainly consist of oil and water. Since flow mechanism is the primary objective, tap water and aviation kerosene were selected for the convenience and requirements of the physical modeling experiment. The viscosity–temperature curves of the oil and water used in the experiment are shown in Fig. 4.1.

The viscosity–temperature curve-fitting equations of the oil and water used in the experiment at 10.00–40.00°C are listed as follows respectively,

Table 4.2 Typical model and field parameters

	Field parameter	Model parameter
Injection–production differential pressure	2–12 MPa	Adjustable
Vug diameter	0.2–500 cm	0.2–5 cm
Flow rate	0.15–1.5 m/d	Adjustable
Viscosity	2–100 MPa·s	1–2 MPa·s
Fracture aperture	0.1–2 mm	0.05–0.5 mm
Fracture density	5–50 fractures/m	10–100 fractures/m
Injection rate	20–1000 m ³ /d	Adjustable

Table 4.3 Core wettability used in the experiment

SN	Well	Core	Oil-wet index	Water-wet index	Relative wetting index	Wettability
1	T402	8-8/41	0.97	0.86	−0.11	Slightly oil wet
2		8-17/41	0.98	0.81	−0.17	Slightly oil wet
3		8-28/41	0.94	0.81	−0.13	Slightly oil wet
4		8-29/41	0.97	0.85	−0.12	Slightly oil wet
5	T427	7-10/50	0.96	0.85	−0.11	Slightly oil wet
6	S64	2-56/60	0.93	0.89	−0.04	Neutral

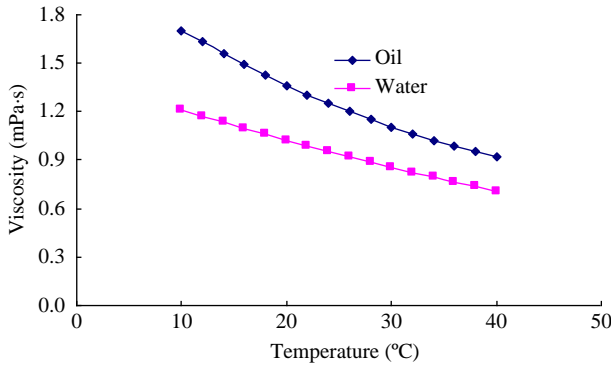


Figure 4.1 Viscosity–temperature curves of oil and water used in the experiment.

$$\mu_o = 0.0004T^2 - 0.046T + 2.1244 \quad (4.1)$$

$$\mu_w = 0.0001T^2 - 0.0218T + 1.4195 \quad (4.2)$$

where, the units of temperature and viscosity are °C and MPa · s, respectively.

4.1.2.2 Building experiment models

2D and 3D physical models involving various fracture-vug complexes and filling degrees were designed to ensure detailed understanding of the effect of the size, density, and connectivity of fractures and vugs on the flow mechanism in the fracture-vug system. Controllable fracture-vug shapes and sizes and precise models (as precise as 0.1 mm) laid a foundation for quantitative evaluation of reservoir development mechanisms.

1. Large-scale fracture-vug models

Based on existing geologic outcrop and 3D geological models, some 3D fracture-vug models, including single fracture-vug model, complex fracture-vug model, unfilled vug model, semi-filled vug model, fully filled vug model, planar fracture-vug model, and sectional fracture-vug model are built. The visualized (lucite) single vug model with different filling degrees, the fracture connected vug model, and the fracture connected underground river model are shown in Fig. 4.2. The physical model with heterogeneous fractures and vugs, and some 2D and 3D fracture-vug storage model are shown in Fig. 4.3 and Fig. 4.4, respectively.

These models can be applied to conduct quantitative studies on fluid flow. Design and building of fractures and vugs are precise to within 0.1 mm (Fig. 4.5). Shapes and sizes of fractures and vugs, such as vug shape and fracture aperture, are controllable (Fig. 4.6).

2. Fractured models

Three key technologies were applied in building fractured models:

- a. fracture construction technology—fractures were constructed by padding slices between lucite (marble) plates;
- b. fracture aperture control technique—fracture apertures were controlled by different number of layers of special superhard stainless-steel slices (as small as 20 μm);

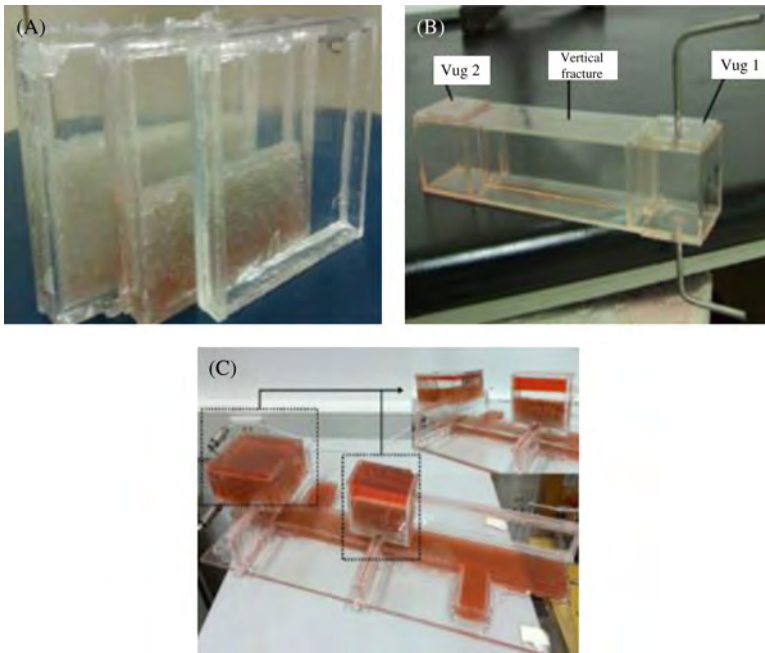


Figure 4.2 Large-scale fracture-vug reservoir models. (A) Single vug models filled at different degrees; (B) complex fracture-vug combination model; (C) interconnective fracture-underground stream model.

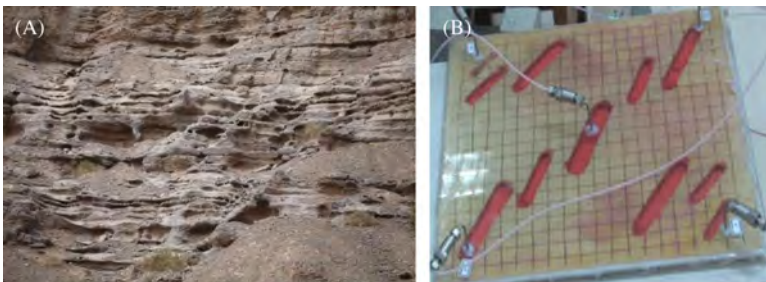


Figure 4.3 Physical model of heterogeneous fracture-vug reservoir. (A) Fracture-vug distribution on the outcrop section; (B) physical model of heterogeneous fracture-vug distribution.

- c. roughness control technique—special marble plates with different finish levels were applied to control the roughness of the models.

Using these techniques, and combining with the purpose of the study, some fracture models are designed as shown in Fig. 4.7.

3. Fracture-vug models

Three key technologies were applied in building fracture-vug models:

- a. vug creation technique—the vugs in the fracture-vug models were created by making $\frac{1}{4}$ circles at marble corners firstly and then piecing four marble plates together;

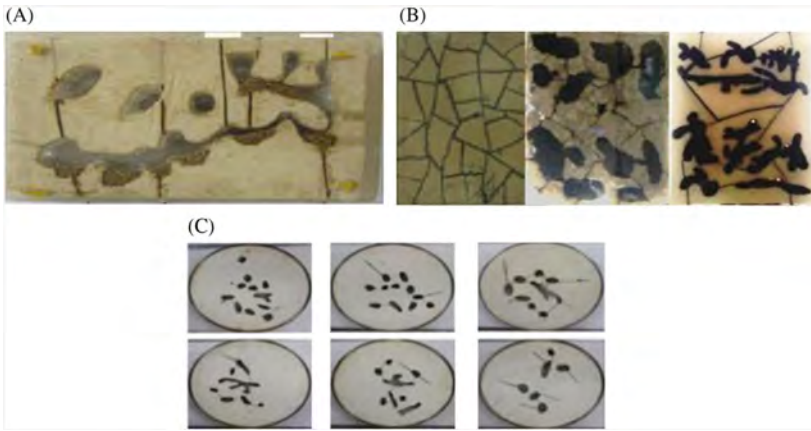


Figure 4.4 2D and 3D physical models of fracture-vug reservoirs. (A) Sectional fracture-vug model; (B) planar fracture-vug model; (C) slices of 3D fracture-vug model.

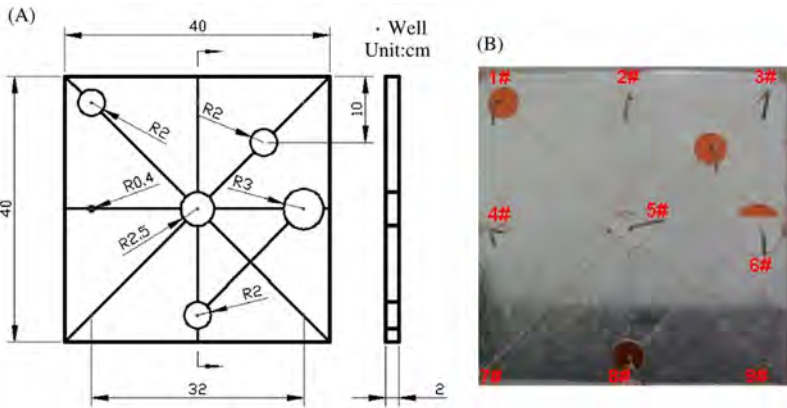


Figure 4.5 High accuracy physical models of fracture-vug reservoir. (A) CAD-designed model; (B) laser cut and processed model.

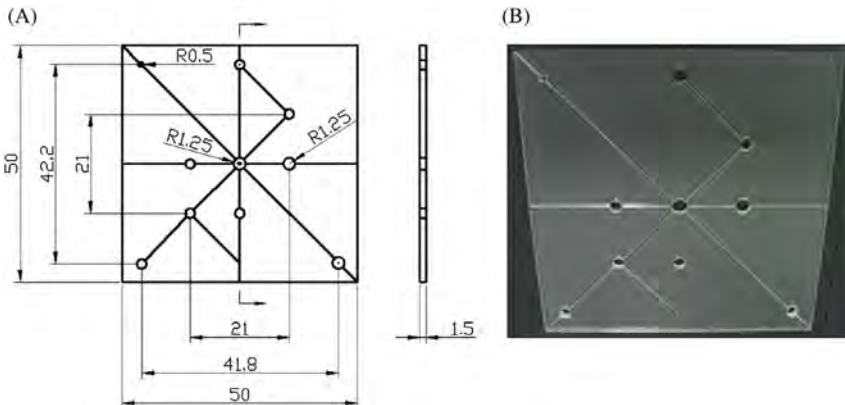


Figure 4.6 Physical models of fracture-vug reservoirs at different scales. (A) CAD-designed model with different sizes of vugs; (B) laser cut and processed model.

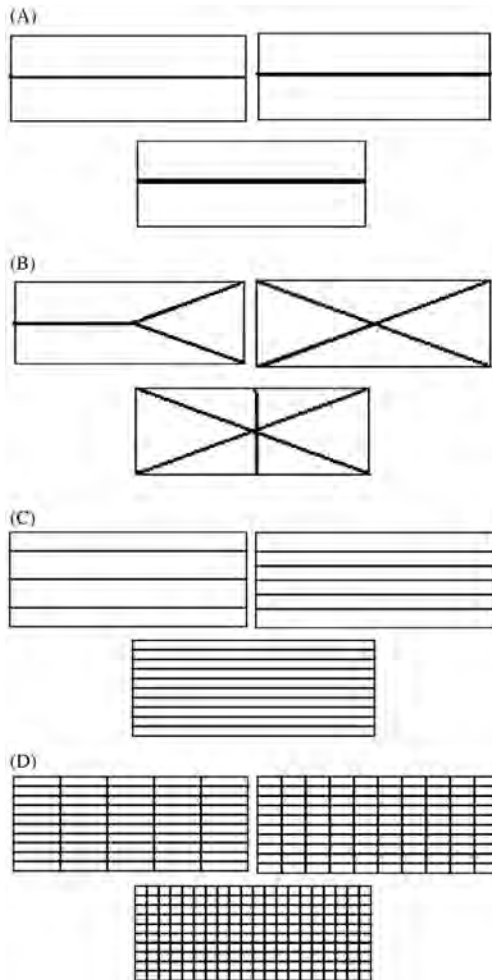


Figure 4.7 Fractured models. (A) Fractured models with different fracture apertures; (B) fractured models with different connection modes; (C) fractured models with different densities; (D) fractured models with different orthogonal networks.

- b. vug control technique—different types of vugs were formed by making hemispheroid or any other geometry at the marble plates;
- c. multifracture-vug model building technique—the model formed by many fractures and vugs is built by several lucite (marble) plates with many slice paddings.

The fracture-vug models (Fig. 4.8) were built using these techniques for our experimental program.

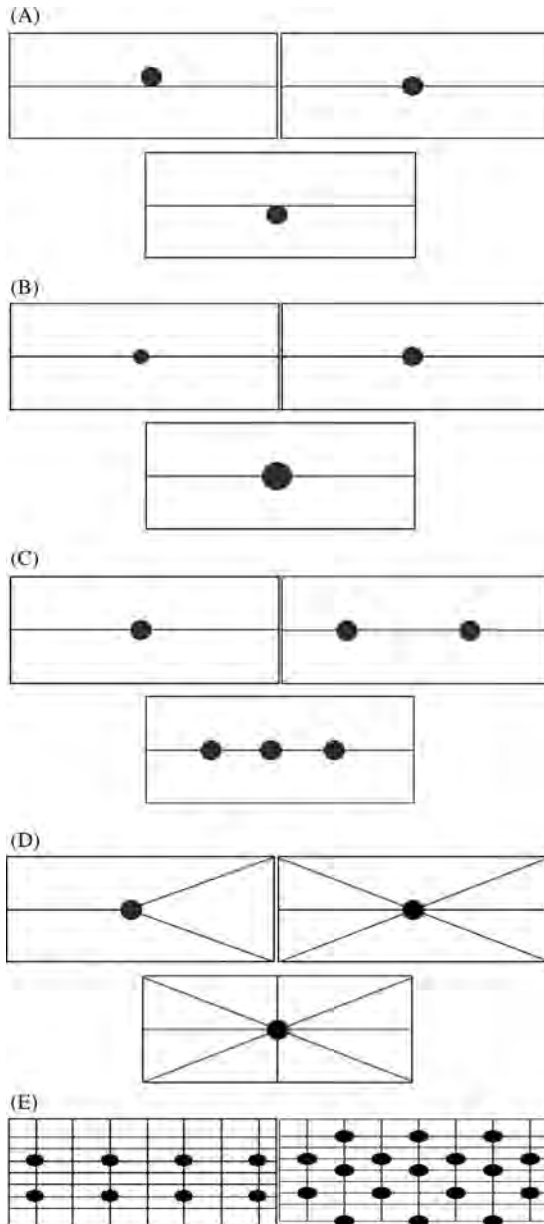


Figure 4.8 Fracture-vug models. (A) Fracture-vug models with vug at different locations; (B) Fracture-vug models with different vug diameters; (C) fracture-vug models with different vug densities; (D) fracture-vug models with different connection modes; (E) fracture-vug models with different orthogonal networks.

4.1.2.3 Physical modeling experiment system

A macroscopic physical modeling experimental apparatus was designed and constructed to conduct the physical modeling experiment on fracture-vug type media (Fig. 4.9). The modular apparatus is composed of nine modules: High temperature high pressure (HTHP) core holder (Fig. 4.10), overburden pressure control module (MP-I multipurpose hydraulic pump), fluid delivery module (advection pump and precise crossflow pump), vacuum-pumping system (vacuum pump and liquid storage bottle), liquid storage module (2-L and 5-L piston type intermediate containers), pressure metering module (differential and confining pressure sensors), temperature control module (thermostat), outlet metering module (oil, gas, and water triphase gauge)

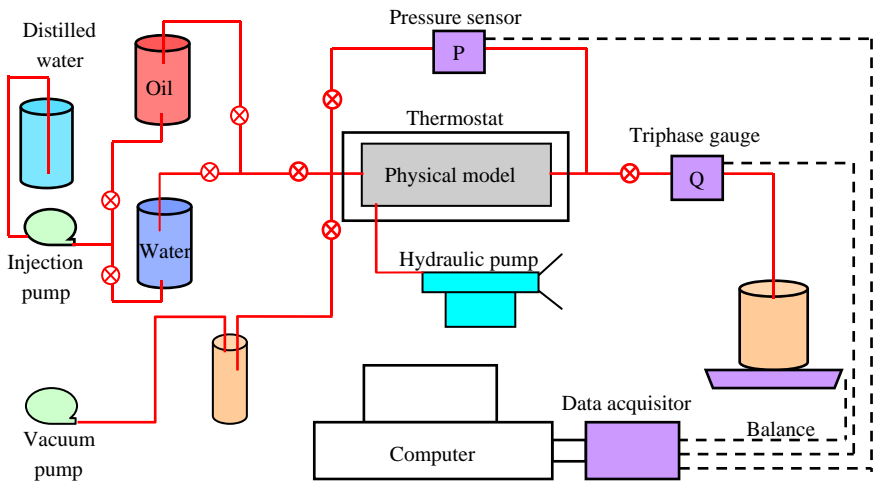


Figure 4.9 Sketch map of physical modeling experiment system.

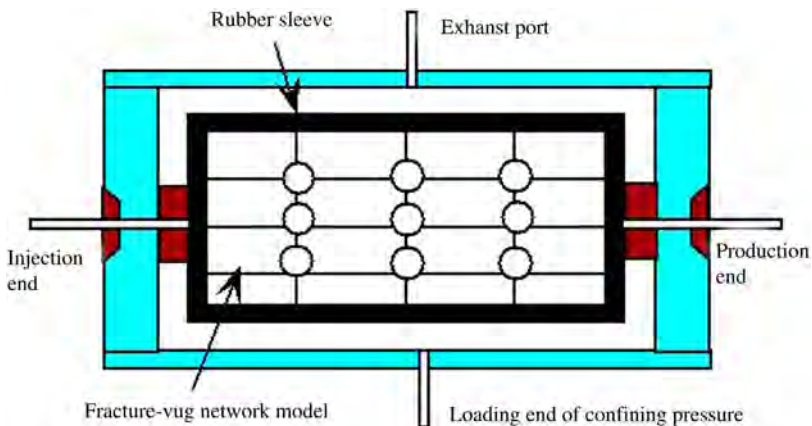


Figure 4.10 HTHP core holder.

and electronic balance), and computer-based data acquisition, processing and control module. If the pressure is below 40 MPa and the temperature is lower than 150°C, it will automatically conduct the experiment at a measured flow rate up to 0.01 mL/min.

As the most important part, the HTHP core holder can relatively truly simulate underground formation conditions in the laboratory. The HTHP core holder, which is the effective amplification of a conventional 1D small core holder, is very suitable for HTHP physical modeling. In addition, an end effect elimination method—set a buffer at the model inlet and outlet, respectively—was used to keep the experimental fluids flowing uniformly into the model.

4.2 Single-phase flow law in a fracture-vug medium

The fluid flow in fracture-vug type media is determined by the special hydrodynamic mechanisms which refer to the mechanical essentials deciding fluid flow pattern and law, or how various forces affect fluid flow patterns and laws, involving mode of action, degree of action, and conversion condition of flow law, etc. Based on flow tests, this section illustrates the complicated fluid flow patterns (including N–S unrestricted flow in unfilled vugs, Darcy flow in filled vugs and caves, and high velocity non-Darcy flow in fractures), establishes flow equations, concludes flow features and conversion conditions, plots critical flow rate curves, and analyzes dynamic flow mechanisms in fracture-vug reservoirs. To ensure similar fluid flow law in the experimental models and the prototype, the similarity criterion—Forchheimer number—is used to characterize the interacting relation between inertia force and viscous force. Forchheimer number reflects the interacting degree between inertia force and viscous force. Its critical value is the converting condition under which flow law changes.

4.2.1 Single-phase flow experiments

4.2.1.1 On unfilled vug models

The one-phase fluid flow experiment based on unfilled vug models is designed to analyze the flow law in a reservoir consisting of large-scale unfilled vugs. Physical experiments letting bottom water channel into the vugs through the fractures in the experiment model demonstrate that the vugs provide large-scale flowing space where the inertia force effect cannot be neglected in the fluid flow motion—a free flow resulting from inertia force, gravity, pressure, and viscous force, can be expressed by N–S equation instead of the Darcy law (Fig. 4.11).

N–S equation is used as a numerical equation:

$$\begin{cases} \rho \frac{\partial \vec{v}}{\partial t} - \nabla \cdot \mu(\nabla \vec{v} + (\nabla \vec{v})^T) + \rho \vec{v} \cdot \nabla \vec{v} + \nabla p = \rho \vec{g} \\ \nabla \cdot \vec{v} = 0 \end{cases}$$

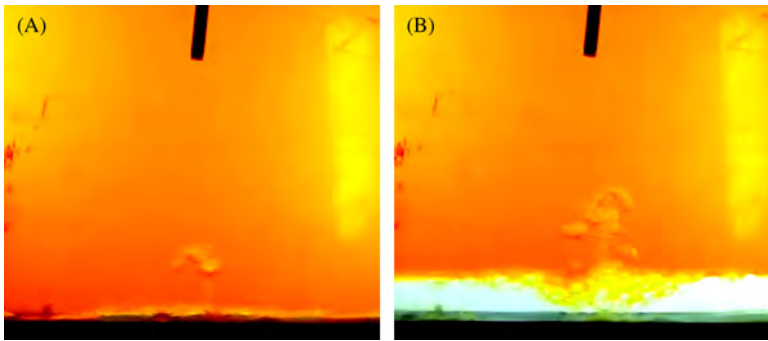


Figure 4.11 Experiment of bottom water channeling into vugs through fractures. Bottom water channeling into unfilled vugs at the early stage (A) and the late stage (B).

Initial conditions: to solve the pressure distribution problem, the pressure function should meet the following condition,

$$\lim_{t \rightarrow 0} p(x, t) = p_0(x)$$

where, $p_0(x)$ is the pressure distribution at initial stage, it is a given function; if $p_0(x) = \text{const}$, the initial pressure is homogeneous.

4.2.1.2 On fractured models

1. Single-phase flow curve based on a fracture network model

Single-phase fluid flow experiments based on fracture network models study the effects of fracture aperture, roughness, density and connectivity, and orthogonal fracture networks on the single-phase flow law in fractured media. Using physical models with different fracture network systems, single-phase flow curves were set up (Fig. 4.12), showing the flow features in fractured models.

On the curve in Fig. 4.12, C stands for connectivity, a parameter expressing the complexity of fracture systems, and is calculated by Eq. (4.3):

$$C = \text{branchnumber} - \text{nodenumber} + 1 \quad (4.3)$$

For example $C = 20, 9-0-1$, where the first number (9) represents the number of horizontal fractures parallel to the flow direction, the second number (0) represents the number of vertical fractures parallel to the flow direction, and the third number (1) is the number of vertical fractures perpendicular to the flow direction, if the node number is 9 and the branch number is 28, the fracture connectivity in the model is $C = 20$.

As shown in Fig. 4.12, the seepage velocity–pressure gradient curves are straight only at the initial stage; as seepage velocities increase steadily, these curves gradually bend towards the pressure gradient axis, exhibiting nonseepage flow features.

2. The relation between model-based permeability and fracture network connectivity in the linear flow region

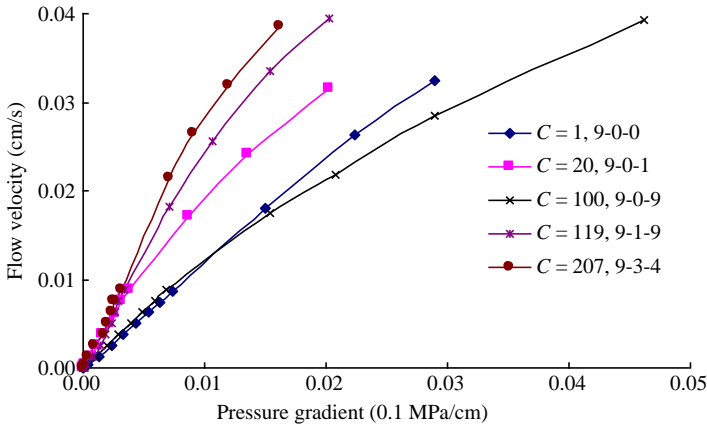


Figure 4.12 Pressure gradient versus seepage velocity.

The single-phase flow curves demonstrate that when seepage velocity is low, seepage velocity and pressure gradient meet Darcy’s law:

$$v = -\frac{k dp}{\mu dx} \tag{4.4}$$

When C (connectivity) = 1, it is the case of single fracture where the flow law is applicable for discrete fractures. The fitted empirical relation of model-based permeability k , fracture aperture b and relative fracture roughness is expressed by Eq. (4.5):

$$k = \frac{b^3}{12H} \left[\frac{1}{1 + 12 \left(\frac{e}{b}\right)^{10}} \right] \tag{4.5}$$

When $C > 1$, the whole fracture system is regarded as a continuous medium, the fitted empirical relation of model-based permeability k , fracture aperture b , fracture connectivity C ($C > 1$) and relative fracture roughness is expressed by Eq. (4.6):

$$k = \frac{nb^3}{12H} \left[\frac{1}{1 + 12 \left(\frac{e}{b}\right)^{10}} \right] [20(1 - C^{-0.015})] \tag{4.6}$$

where, b , e , and H are in μm , and k is in μm^2 .

4.2.1.3 On fracture-vug models

1. Single-phase flow curve based on a fracture-vug model

Based on the results of fractured model, single-phase fluid flow experiments analyze the location of vugs, diameter, connectivity and density and orthogonal fracture-vug networks on the one-phase flow laws in a fracture-vug medium. Next we take the fracture-vug models with different vug densities as examples to explain one-phase flow curves.

Vug density refers to the number of vugs on a unit flow area. Models with a single fracture each were designed to analyze the effect of vug density on the flow law in a fracture-vug medium. The models' parameters are that fracture aperture = 200 μm, vug diameter = 10 mm, depth = 10 mm, and vug density = 0–50 vugs/m². The seepage velocity–pressure gradient curves based on different vug densities were built (Fig. 4.13).

As shown in Fig. 4.13, the single-phase flow curves based on the fracture-vug models are straight only at the initial stage; as seepage velocities increase steadily, these curves gradually bend towards the pressure gradient axis, exhibiting non-Darcy flow features.

2. The relation between model-based permeability and vug density in the linear flow region

In the linear flow region, the permeability increases with the increasing of vug density, their fitting curve is shown as in Fig. 4.14, and their relation can be expressed by Eq. (4.7):

$$k_{fvs} = k_{fs} \frac{1}{1 - 0.0075n_v} \tag{4.7}$$

where, k_{fvs} and k_{fs} represent the permeability of fracture-vug system and fracture system, respectively, in μm²; n_v stands for vug density, in vug(s)/m².

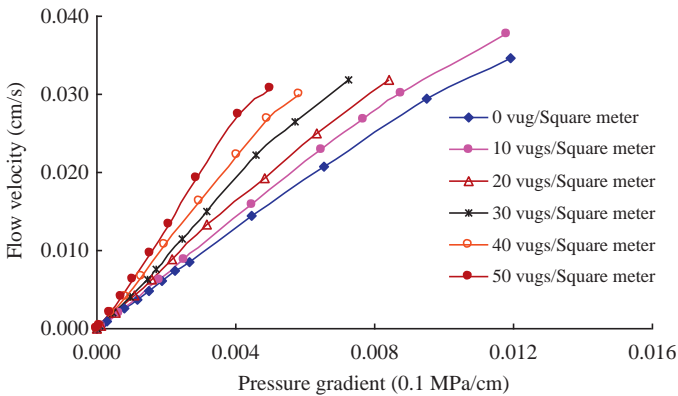


Figure 4.13 Pressure gradient versus seepage velocity.

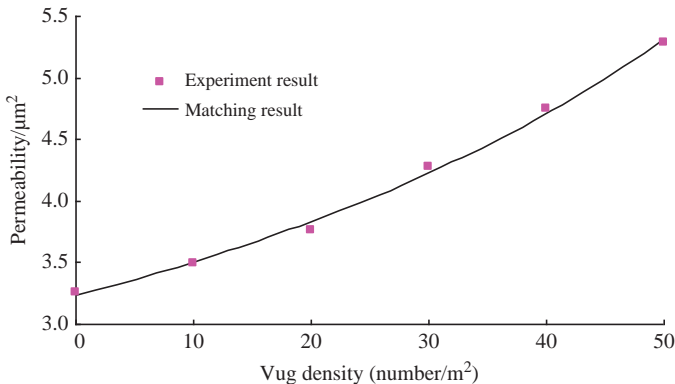


Figure 4.14 Permeability–vug-density relation based on a fracture-vug model (experiment and fitted values).

4.2.2 Single-phase flow pattern and conversion conditions

The one-phase flow curves based on different fracture-vug models shows that when seepage velocity increases to a certain value, the flow pattern changes from linear to non-Darcy flow. For field application, the criteria for discriminating the flow pattern conversion was determined, and then based on which, the critical velocity equation was established to analyze the conversion condition of the flow pattern in the fracture-vug network.

4.2.2.1 Discrimination of flow pattern

1. Discrimination criteria

Darcy's law is the basic rule to describe seepage flow. The 1D Darcy's equation can be expressed as:

$$-\frac{dp}{dx} = \frac{\mu v}{k} \quad (4.8)$$

where, p is pressure, 0.1 MPa; x is flow direction, cm; μ is fluid viscosity, mPa·s; v is Darcy velocity, cm/s; and k is medium permeability, μm^2 .

At a high seepage velocity, inertia resistance cannot be neglected, the fluid motion equation can be expressed by the Forchheimer Eq. (4.9):

$$-\frac{dp}{dx} = \frac{\mu v}{k} + \beta \rho v^2 \quad (4.9)$$

where, β is non-Darcy coefficient, 1/cm; and ρ is fluid density, g/cm^3 .

In particular, when the connectivity $C=1$, it is the case of a single fracture, and the flow pattern can be applied in the discrete fracture system. The experimental results show that within the real production pressure gradient in the Tahe oilfield, when the fracture aperture is smaller than 300 μm , the fluid flow pattern basically coincides with Eq. (4.8); when the fracture aperture is larger than 300 μm , if Eq. (4.8) is used to describe the fluid flow pattern, a large deviation would occur, indicating that inertia force can no longer be neglected, and the fluid flow pattern should be described by Eq. (4.9).

In the Forchheimer Eq. (4.9), the left side is total pressure gradient, the first and second items on the right side are pressure gradients required to overcome viscous resistance and inertia resistance, respectively. The ratio of inertia resistance pressure gradient to viscous resistance pressure gradient $k\beta\rho v/\mu$ is the Forchheimer number (Fo)—the discrimination criterion of flow patterns:

$$Fo = \frac{k\beta\rho v}{\mu} \quad (4.10)$$

Apparently, the Forchheimer number has the same physical significance as the Reynolds number—both of them represent the inertia resistance to viscous resistance ratio. The Forchheimer number has a clear definition, rational physical significance, and extensive applicability, thus all parameters in Eq. (4.10) are clear and deterministic. It is evident that as long as permeability and non-Darcy coefficient are determined by experiment or empirical equation, the Forchheimer number can be applied in all types of media.

Therefore, the Forchheimer number is selected as the discrimination criterion of flow patterns in the fracture-vug type media.

2. Determination of critical Forchheimer number

The cause to determine the critical Forchheimer number is that the critical values, at which non-Darcy flow starts, obtained from new and existing discrimination criteria, are different. A known critical value will help researchers determine whether flow patterns include non-Darcy flow in a porous medium.

For a porous medium, the relation curve of resistance coefficient and Reynolds number and that of pressure gradient and seepage velocity are usually used to analyze the initial point from which linear Darcy's flow law changes to non-Darcy's flow law, and nonlinear phenomena. However, the critical point determined by this method is usually inaccurate, which is especially more serious in fracture-vug reservoirs, therefore, the Forchheimer number is introduced.

The non-Darcy effect parameter E is defined as the ratio of pressure gradient overcoming inertia resistance to total pressure gradient. According to the Forchheimer Eq. (4.9), we get

$$E = \frac{\beta \rho v^2}{-\frac{dp}{dx}} \quad (4.11)$$

Using Eq. (4.9) to replace $-(dp/dx)$ in Eq. (4.11), and incorporating Eq. (4.10), we get

$$E = \frac{Fo}{1 + Fo} \quad (4.12)$$

There is a direct relationship between the Forchheimer number and the non-Darcy effect (an error resulting from the neglect of non-Darcy flow).

Considering the relationship between the Forchheimer number and the non-Darcy effect (Eq. (4.12)), assuming E_c represents the critical value of non-Darcy effect, we get the critical Forchheimer number Fo_c as

$$Fo_c = \frac{E_c}{1 - E_c} \quad (4.13)$$

Eq. (4.13) allows researchers to select the critical Forchheimer number according to the problem studied. For instance, if the non-Darcy flow effect is restricted at 10%, the critical Forchheimer number Fo_c can be obtained by Eq. (4.13) as 0.11.

3. Establishment of critical velocity equation

As the concept of the Forchheimer number is relatively abstract, it is not applicable in the oilfield. Supposing that the seepage velocity is the critical velocity when the flow pattern converts from the Darcy flow into a non-Darcy flow, a critical velocity equation expressing the flow pattern conversion in the fracture-vug type media can be established based on the Forchheimer number.

The non-Darcy coefficient β in the definitional equation of the Forchheimer number Eq. (4.10) meets the following relation:

$$\beta = \frac{a}{k^m \phi^n} \quad (4.14)$$

where, a , m , and n can be determined through single-phase flow experiments.

When Eq. (4.14) is substituted in Eq. (4.10), we get:

$$Fo = \frac{a}{k^{m-1} \phi^n} \frac{\rho v}{\mu} \quad (4.15)$$

Combined with Eqs. (4.13) and (4.15), the equation of critical velocity in fracture-vug type media is obtained as

$$v_c = \frac{\mu Fo_c}{\rho k \beta} = \frac{k^{m-1} \phi^n}{a} \frac{E_c}{1 - E_c} \frac{\mu}{\rho} \quad (4.16)$$

The coefficients a , m , and n in the equation can be determined through single-phase flow experiments.

With known critical velocity at which the non-Darcy flow starts, the maximum output of non-Darcy flow pattern can be ascertained based on field production data,

$$Q_c = 2\pi R_w h v_c \quad (4.17)$$

where, Q_c is maximum output; R_w is oil well radius; and h represents perforated thickness. Supposing that an oil well radius is 10 cm, the perforated thickness is 3.7–14.9 m, the critical velocity is 0.025 cm/s, and the degassed crude density is 0.97 t/m³, the maximum output of the oil well is 48.7–202.1 t/day when the non-Darcy flow occurs.

4.2.2.2 Features of flow pattern conversion

For the typical fracture-vug network models used in the study, the coefficients a , m , and n in Eq. (4.16) are provided by the single-phase flow experimental data (Table 4.4), the non-Darcy effect error depends on specific study objectives, the fluid viscosity and density are the fluid properties from the oilfield, and the permeability and porosity are subject to the fracture-vug network medium used in the study.

To analyze the one-phase flow pattern conversion features and establish the critical velocity type curves suitable for the fracture-vug medium, we used the fluid properties in the Tahe Oilfield (Table 4.5) to calculate the critical velocity.

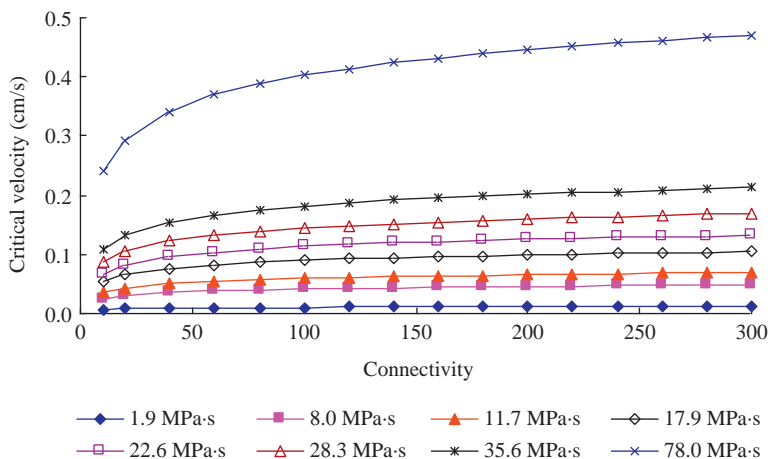
Based on the characteristics of fracture-vug reservoirs and the experimental objectives, the non-Darcy effect error E_c was restricted below 5%, then the critical Forchheimer number Fo_c was calculated as 0.053 using Eq. (4.13); after the parameters k , ϕ , a , b , and c corresponding to different fracture-vug models have been substituted in the critical velocity calculation Eq. (4.16), the critical velocity variation rules in different fracture-vug reservoirs were obtained. In the following paragraphs, different fracture network models and fracture-vug models with

Table 4.4 Non-Darcy coefficients

Fracture-vug model	a	m	n
Different fracture networks	8.054	1.758	-1.369×10^{-14}
Different vug densities	7804	6.906	-3.445×10^{-13}

Table 4.5 Fluid properties in the Tahe Oilfield

Well	TK313	S65	S67	TK442	S74	TK409	TK631	TK404
Viscosity (mPa·s)	1.9	8.0	11.7	17.9	22.6	28.3	35.6	78.0
Density (g/cm ³)	0.90	0.95	0.97	0.98	0.98	0.96	0.96	0.95

**Figure 4.15** Critical velocity versus fracture connectivity.

different vug densities are taken as examples to show the critical velocity variation characteristics in the fracture-vug networks at the time of flow pattern conversion.

1. Critical velocity characteristics in different fracture network models

Supposing that in the fracture-vug type media, the fracture aperture is 100 μm , the average embossed height of fracture surface e is 40 μm , and the fracture connectivity ranges from 10 to 300, when the permeability Eq. (4.6) and the coefficients (Table 4.3) are substituted in the critical velocity calculation Eq. (4.16), the relation curves of critical velocity variation with the change of connectivity are obtained (Fig. 4.15).

As shown in Fig. 4.15, the variation of critical velocity at which non-Darcy flow occurs in the fracture network system has such an overall trend that the critical velocity increases with the increase of fracture connectivity and fluid viscosity, and the critical velocity exhibits a concave downward shape with the increase in fracture connectivity.

The analysis of Eq. (4.15) and the coefficients in it show that the porosity exponent c is a constant approaching zero in the model with different fracture connectivities; when the fluid properties are certain, the variation in critical velocity depends on the variation of k^{m-1} . It is known from the empirical relation of permeability in fracture network model (Eq. (4.3)) that k^{m-1} increases with the increase in fracture connectivity; therefore, the critical velocity increases with the increase in fracture connectivity.

2. The characteristics of critical velocity in the fracture-vug reservoir with different fracture density

Supposing that in the fracture-vug network, the fracture aperture is $200\ \mu\text{m}$, the vug density ranges from 0 to $50\ \text{vug(s)/m}^2$, and the average embossed height of fracture surface e is $40\ \mu\text{m}$, when the permeability Eq. (4.6) and the coefficients (Table 4.3) are substituted in the critical velocity calculation Eq. (4.16), the relation curves of critical velocity variation with the change in vug density are obtained (Fig. 4.16).

As shown in Fig. 4.16, the variation in critical velocity at which non-Darcy flow occurs in the different vug density system has such an overall trend that the critical velocity exhibits a concave upward shape that increases with the increasing vug of density, and increases with the increasing of viscosity.

The analysis of Eq. (4.15) and the coefficients in it shows that the porosity exponent c is a constant approaching zero in the model with different vug densities; when the fluid properties are certain, the variation in critical velocity depends on the variation of k^{m-1} . It is known from the empirical permeability relation based on the models with different vug densities (Eq. (4.6)) that k^{m-1} increases with the increase in vug density; accordingly, the critical velocity increases with the increase in vug density.

In general, single-phase fluid flowing in the fracture-vug network system meets the linear seepage law at low seepage velocity, but the non-Darcy law at a high seepage velocity when the seepage flow curve bends towards the pressure gradient axis. In the scope of the experimental study, the critical velocity at which the single-phase flow pattern converts increases with the increase in model parameters (connectivity, vug density, microlitic percentage, etc.) and fluid viscosity. When the fluid flow velocity is lower than the critical velocity in the fracture-vug network, the viscous resistance plays a dominant role and the effect of inertia resistance is negligible in the course of fluid flow, the flow conforms to Darcy's law; on the contrary, when the fluid flow velocity is higher than the critical velocity, the effect of inertia resistance cannot be neglected in the course of fluid flow, and the flow conforms to the non-Darcy flow pattern. The major factor deciding the conversion is the effect of inertia resistance on the course of fluid flow. The permeability is very large and the viscous resistance is relatively small in large fracture and vug, the driving pressure differential required at conventional flow rate is very small, and the

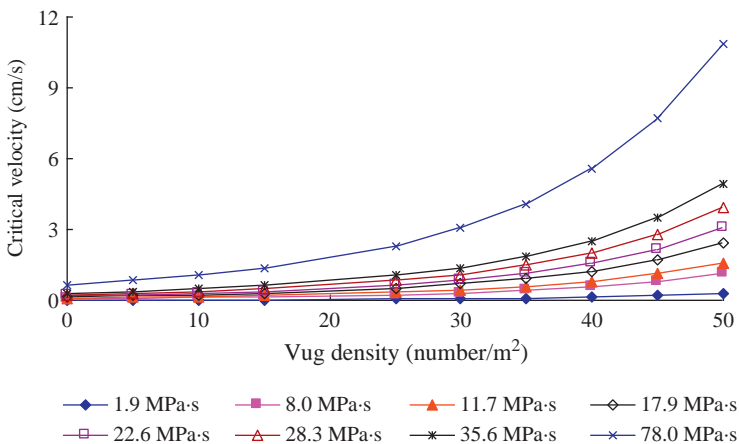


Figure 4.16 Critical velocity versus vug density.

inertia force cannot be neglected. The well inflow is contraction flow in an actual oil reservoir; the nearer to the wellbore the higher the flow rate and the more prominent the inertia resistance.

4.3 Two-phase flow law in fracture-vug medium

The study on the oil–water two-phase flow law in fracture-vug type media is a significant advance on the basis of single-phase flow law. Systematic oil–water two-phase flow experiments on different models demonstrate the flow features, develop the relative permeability curves, discriminate the flow pattern conversion features, and set up the flow motion equation in fracture-vug type media.

4.3.1 Two-phase flow patterns

From the aforesaid analysis, for single-phase flow, the general equation of non-Darcy coefficient can be written as

$$\beta = \frac{a}{k^b \phi^c} \quad (4.18)$$

where, k and ϕ represent the permeability and porosity of fracture-vug media, respectively. When two-phase fluids flow simultaneously in a fracture-vug medium, the k and ϕ in Eq. (4.18) are the effective permeability k_{eff} and the effective pore volume fraction ϕ_{eff} of a fluid, respectively,

$$\begin{cases} k_{eff} = kk_{ri} \\ \phi_{eff} = \phi S_i \end{cases} \quad i = w, o \quad (4.19)$$

After Eq. (4.19) has been substituted in Eq. (4.18), the expression of non-Darcy coefficient β_i in the biphasic fluid flow system is obtained as

$$\beta_i = \beta \beta_{ri} = \frac{a}{(kk_{ri})^b (\phi S_i)^c} \quad i = w, o \quad (4.20)$$

In a single-phase flow system, the critical flow velocity equation v_c is expressed as

$$v_c = \frac{\mu F o_c}{\rho k \beta} = \frac{\mu F o_c}{\rho \frac{a}{k^{b-1} \phi^c}} \quad (4.21)$$

Replacing the permeability k and the non-Darcy coefficient β in Eq. (4.21) with the effective permeability and the non-Darcy coefficient β_i of two-phase flow, we get

$$v_{ic} = \frac{\mu_i F o_c}{\rho_i k_{eff} \beta_i} = \frac{\mu_i F o_c}{\rho_i k k_{ri} \frac{a}{(k k_{ri})^b (\phi S_i)^c}} \quad i = w, o \quad (4.22)$$

Rearranging Eq. (4.22), we get

$$v_{ic} = \frac{\mu_i F_{Oc}}{a} \cdot k_{ri}^{b-1} S_i^c \quad i = w, o \quad (4.23)$$

$$\rho_i \overline{k^{b-1} \phi^c}$$

Obviously, the critical velocity conversion in a two-phase flow pattern is related to fluid properties (density and viscosity), medium properties (permeability and porosity) and Forchheimer number, as well as relative permeability and water saturation. Compared with the one-phase critical velocity, the two-phase critical velocity mainly depends on $k_{ri}^{b-1} S_i^c$. During the study, we designed models that differed in fracture aperture, roughness, density and connectivity, and orthogonal fracture network to analyze the two-phase flow law in fractured media.

4.3.2 Oil–water two-phase flow experiment

4.3.2.1 On unfilled vug models

In large unfilled vugs, because flowing resistance is small, multiphase turbulence occurs easily, especially when fluids flow from fractures into vugs or near the wellbore. In the study, the Level Set method was used to model the two-phase flow patterns (Fig. 4.17).

The basic idea of the Level Set method is to set the dynamic interface to the zero isosurface of function φ . At time t , the zero isosurface of φ is determined by computing the φ value within the computing domain, so as to trace the dynamic interface.

The mathematical model for two-phase flow modeling in a vug model is:

$$\begin{cases} \rho \frac{\partial \vec{v}}{\partial t} + \rho(\vec{v} \cdot \nabla) \vec{v} = \nabla \cdot \left[-p \vec{I} + \eta(\nabla \vec{v} + \nabla \vec{v}^T) \right] + \vec{F}_g + \vec{F}_{st} + \vec{F} \\ \nabla \cdot \vec{v} = 0 \\ \frac{\partial \phi}{\partial t} + \vec{v} \cdot \nabla \phi = 0 \end{cases} \quad (4.24)$$

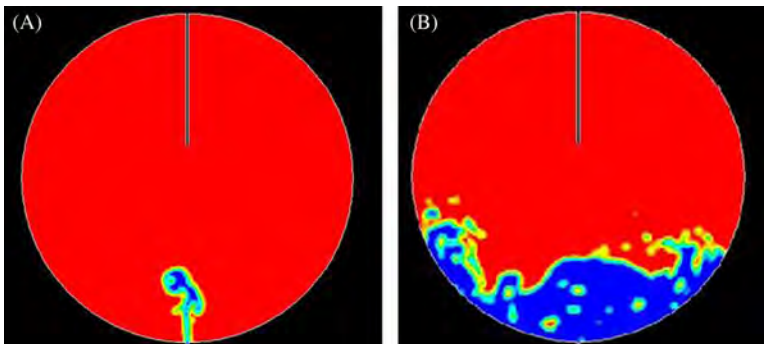


Figure 4.17 Oil–water flow patterns when bottom water entering vugs through fractures. Bottom water entering vugs through fractures at the initial stage (A) and the late stage (B).

where,

$$F_g \text{ is gravity, } \vec{F}_g = \rho \vec{g} \tag{4.25}$$

\vec{F}_{st} is interfacial tension,

$$\vec{F}_{st}(\vec{x}) = \sigma k(\vec{x}_\Gamma) \hat{n}(\vec{x}_\Gamma) = \sigma \left(\nabla \cdot \frac{\nabla \phi}{|\nabla \phi|} \right) \nabla \phi \tag{4.26}$$

$\phi(\vec{x}, t)$ is always the symbolic distance from point \vec{x} to interface $\Gamma(t)$,

$$\phi(\vec{x}, t) = \begin{cases} d(\vec{x}, \Gamma(t)) & \vec{x} \in \Omega_1(t) \\ 0 & \vec{x} \in \Gamma(t) \\ -d(\vec{x}, \Gamma(t)) & \vec{x} \in \Omega_2(t) \end{cases} \tag{4.27}$$

4.3.2.2 On fractured models

Now we take fracture network models as examples to show the two-phase flow features in fractured media. During the study, six physical models with different fracture networks were designed, with connectivity ranging from 1 to 207. The experimental measurements of recovery and injected pore volume based on different fracture networks textures are illustrated in Fig. 4.18 where the numbers “X-X-X” represent the structure of the fracture networks—the first number represents the number of horizontal fractures parallel to the flow direction, the second and the third represent the number of vertical fractures parallel and perpendicular to the flow direction, respectively.

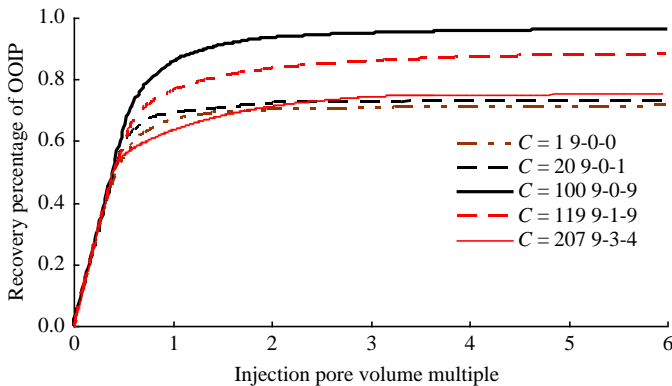


Figure 4.18 Recovery versus pore volume injected.

According to the curves shown in Fig. 4.18, when the connectivity is smaller than 100, the ultimate recovery of water-displaced oil increases with the increase in connectivity, but when the connectivity is larger than 100, the ultimate recovery reduces with the increase in connectivity. This demonstrates that in a simple fracture network, large connectivity and more flow channels parallel to the flow direction are favorable for improvement of displacement efficiency. On the contrary in a complicated fracture network, larger connectivity and more complicated network result in low displacement efficiency. The analysis of the model structures reveal that the increase in vertical fractures at the flow direction reduces the recovery factor, indicating that such vertical fractures aggravate water channeling, but the increase in vertical fractures orthogonal to the flow direction increases the recovery factor, indicating that such vertical fractures make the fractures at the flow direction more connective and the flow in them more consistent.

The relationship between water cut and recovery was also studied. On the water cut- recovery curves shown in Fig. 4.19, the typical behaviors of the water cut are sudden jump, slow ascent, and stepped rise, which are consistent with the actual water cut variation in Block 4 of the Tahe Oilfield. When the connectivity $C = 1$, stepped rise occurs, reflecting that water firstly breaks through along a limited flow channel and then gradually sweeps. When $C = 207$, a sudden jump occurs where transverse, longitudinal and vertical fractures are abundant and connective, and the water/oil front can keep good consistency in the course of water advancing. In other situations, the water cut patterns are similar, showing slow water breakthrough. In addition, all curves (Fig. 4.19) fluctuate at the high water cut stage, possibly influenced by the structure of the fracture network, and the fluid flow changes in the transverse and longitudinal fractures where the crude oil in the fractures at the flow direction has been produced at the low water cut stage, while some crude oil in the fractures orthogonal to the flow direction was produced by exchanging with the fluid in the fractures parallel to the flow direction at the high water cut stage.

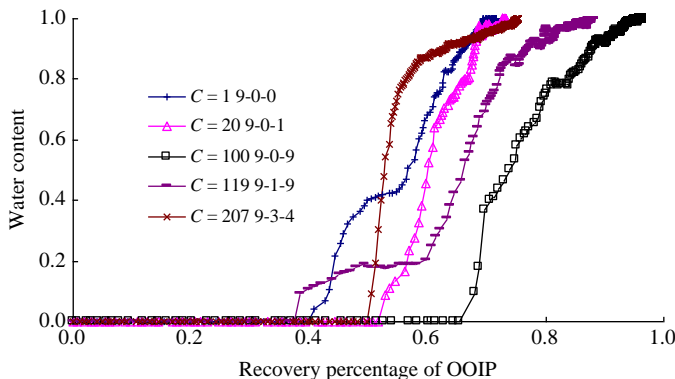


Figure 4.19 Water cut versus recovery.

4.3.2.3 On fracture-vug models

Two-phase flow experiments on fracture-vug models are based on the results of fractured models. They focus on the effects of vug location, diameter, connectivity and density, and orthogonal fracture-vug networks on the two-phase flow patterns in fracture-vug media. Here we take fracture-vug models with different vug densities as examples to analyze the two-phase flow features in such models.

Experimental study of water displacing oil was conducted on the models with a single fracture and different vug densities (0–50 vug(s)/m²). The relationship between measured recovery and pore volume injected was analyzed and plotted (Fig. 4.20).

In general, in the models with a single fracture and multiple vugs, the ultimate recovery of water displacing oil tends to reduce as vug density increases. Table 4.6 lists the ultimate water displacing oil recovery at different vug densities.

The measured water cut changes with the measured recovery at different vug densities (Fig. 4.21).

In the models with a single fracture and multiple vugs, water free recovery tends to be long when vug density is low (Fig. 4.21). For example when injection rate is 130 mL/min and vug density is 0, water free recovery can be up to 63.29%; however, when vug density is 50 vugs/m², water free recovery is only 49.18%.

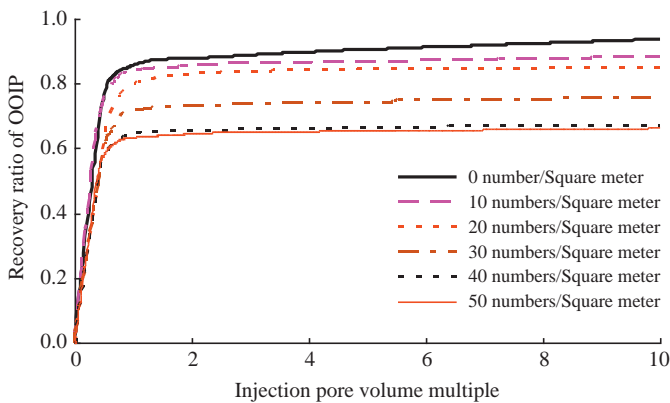


Figure 4.20 Recovery versus pore volume injected.

Table 4.6 Ultimate recovery of water displacing oil at different vug densities

Vug density (vug(s)/m ²)	0	10	20	30	40	50
Ultimate recovery (%)	93.74	88.34	85.24	75.57	67.14	66.32

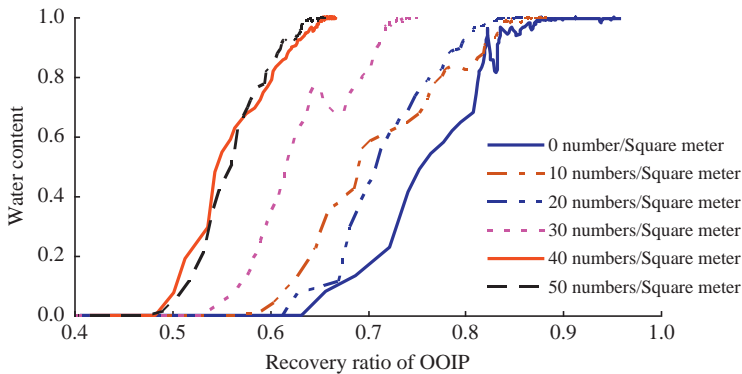


Figure 4.21 Water cut versus recovery.

4.3.3 Oil–water two-phase flow features

A relative permeability curve reflects the relationship between relative permeability and water saturation in pure viscous flow conditions (i.e., in the linear flow region). It is the comprehensive reflection of oil and water seepage flow characteristics in porous media, and is widely used to analyze reservoir pore texture variation, oil and water saturation distribution and flow characteristics, to compute oil displacement efficiency and recovery ratio, to estimate irreducible water saturation and residual oil saturation, and to determine and predict development trend. In fracture-vug reservoirs, fluids flow follows a N–S flow law in unfilled caverns and vugs (refer to Section 4.2). The oil–water interface tracking method can be used to analyze the oil–water two-phase flow features. However, this method is very computationally expensive for the fracture-vug system, and as a result, relative permeability curves as equivalent processing methods will be used to solve the two-phase flow problem in such reservoirs.

In the study, aviation kerosene and tap water were selected as working fluids to conduct water displacing oil experiments in different fracture-vug models at a displacement velocity of 80 mL/min. Relative permeability curves were concluded and analyzed.

4.3.3.1 Relative permeability curves based on fractured models

Relative permeability curves based on fractured models with different fracture apertures, densities, and network systems were measured and analyzed.

1. Relative permeability curves—effect of fracture aperture

Water displacing oil experiments were conducted based on the models with different fracture apertures (Fig. 4.7A). The measured relative permeability curves (Fig. 4.22) show that:

- a. As fracture aperture increases, the relative permeability curves of water gradually change from concave to straight line, possibly resulting from early water breakthrough under small fracture apertures at the same injection flow rate.

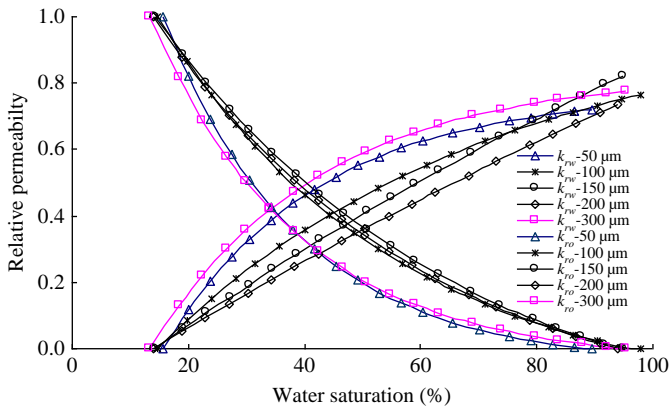


Figure 4.22 Relative permeability curves under different fracture apertures.

- b. In the two-phase flowing area, the sum of oil and water relative permeabilities is less than 1. However, as fracture aperture increases, the isoperm point gradually moves right, and a relatively regular trade-off between oil phase and water phase is set up—oil relative permeability declines deceleratingly, but water relative permeability increases deceleratingly.
 - c. Compared with porous medium, the sum of oil and water relative permeabilities changes little (slightly less than 1) in the two-phase flowing area. This means that flow resistance changes little in the process of displacement, and the Jamin effect resulting from pore texture complexity in porous medium would not occur.
 - d. As fracture aperture increases, irreducible water saturation reduces; the smaller the fracture aperture, the more slowly the water relative permeability increases with the increase of water saturation; and at late waterflood stage, the gentler the fracture aperture, the poorer the water injection capacity, and the lower the water relative permeability in the place where there is residual oil. This indicates that as water saturation increases, the smaller the fracture aperture, more easily the discrete phase can occur in the oil phase, and water phase movement is thus hindered to some extent.
2. Relative permeability curves—effect of fracture density

Water displacing oil experiments were conducted based on the models with different fracture densities (Fig. 4.7C). The following conclusions can be summarized according to the measured relative permeability curves (Figs. 4.22 and 4.23 where the legend provides fracture density ranging from 45 fractures/m to 95 fractures/m).

- a. All relative permeability curves of water are in concave shape, possibly resulting from early breakthrough. The higher the fracture density the deeper the concave shape becomes.
- b. In the two-phase flowing area, the sum of oil and water relative permeabilities is less than 1. A relatively regular trade-off between oil phase and water phase is set up—oil relative permeability declines deceleratingly, but water relative permeability increases deceleratingly. Compared with porous medium, the sum of oil and water relative

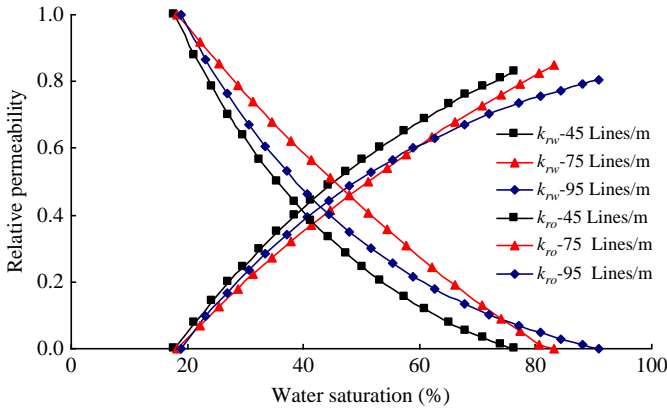


Figure 4.23 Relative permeability curves under different fracture density.

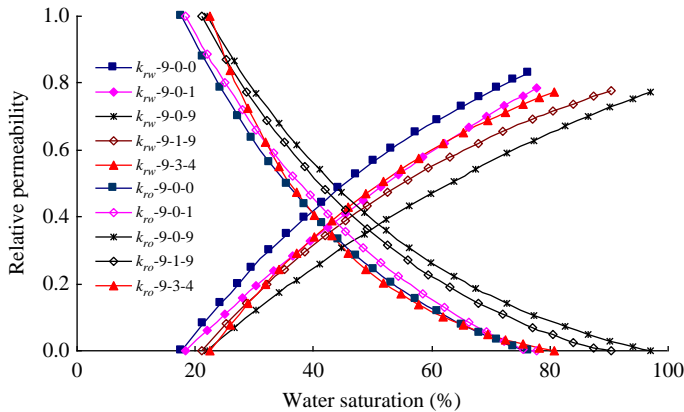


Figure 4.24 Relative permeability curves in different fracture networks.

permeabilities changes little (slightly less than 1) in the two-phase flowing area. This means that flow resistance changes little in the process of displacement, and the Jamin effect resulting from pore texture complexity in porous medium would not occur.

3. Relative permeability curves—effect of fracture network

Experiments were performed on the models with different fracture networks (Fig. 4.7D). The following points can be concluded according to the relative permeability curves (Fig. 4.24 where the numbers “X-X-X” represent information of the fracture network—the first number represents the number of horizontal fractures parallel to the flow direction, the second and the third numbers represent the number of vertical fractures parallel and perpendicular to the flow direction, respectively):

- a. All relative permeability curves of water are in concave shape. The reasons may be as follows: The vertical fractures can make horizontal fractures connective and from the gravitational differentiation of oil and water in vertical fractures, and thus injected water easily breaks through at the bottoms of vertical fractures at the early stage.

- b. When the model structure is “9-0-X”—the number of fractures parallel to the flow direction is equal, but the number of vertical fractures perpendicular to the flow direction is unequal, as the number of fractures perpendicular to the flow direction increases, residual oil saturation reduces, two-phase flowing area enlarges, and the saturation at the isoperm point increases.

When the model structure is “9-X-9”—the number of horizontal fractures parallel to the flow direction is equal to the number of vertical fractures perpendicular to the flow direction, residual oil saturation increases with the increase of the number of vertical fractures parallel to the flow direction, two-phase flowing area reduces, and the saturation at the isoperm point reduces. This may be a result of increasing residual oil in the upper part of the model after gravitational differentiation of oil and water in vertical fractures.

4.3.3.2 Relative permeability curves based on fracture-vug models

Relative permeability curves based on fracture-vug models were analyzed in terms of vug location and density and microlitic percentage.

1. Relative permeability curve-effect of vug location

Three kinds of vug distribution models—vug center locates above, right on (symmetrically), and below fracture line, respectively (Fig. 4.8A)—were built to study the influence of vug location on relative permeability curves. Analysis of the relative permeability curves (Fig. 4.25) measured shows that:

- a. According to shape, all relative permeability curves of water are in concave shape. The below level of the concave on the relative permeability curve from the model with vug center slightly higher than the fracture line is maximum because only a small portion of oil in the vug was swept out, and injected water easily broke through in horizontal fractures at the early stage; in the high water cut phase saturation section, the increasing rate of water phase permeability becomes smaller and smaller, and its curve tends to be flat. The ultimate water phase relative permeability maximizes at the place where there is residual oil.

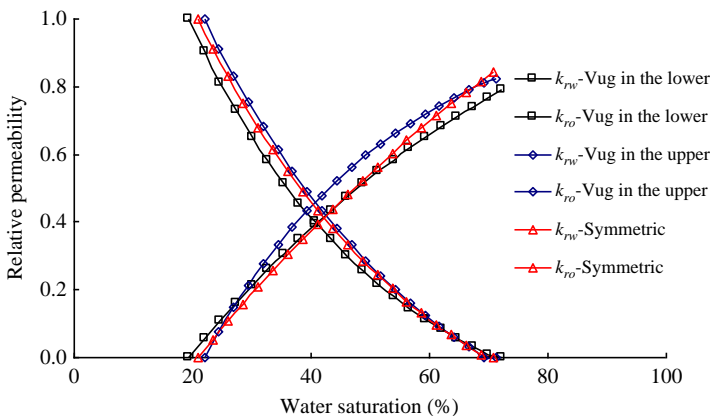


Figure 4.25 Relative permeability curves influenced by vug location.

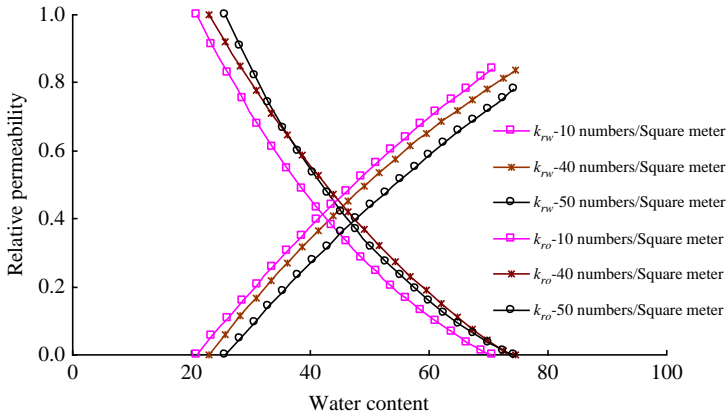


Figure 4.26 Relative permeability curves influenced by vug density.

- b. The existence of vug increases residual oil saturation; when vug center is higher than fracture line, the increase of residual oil saturation is maximum. The major factor affecting oil/water distribution and retention in the vug is gravity, i.e., the effect of the different densities of oil and water.
2. Relative permeability curves-effect of vug density

Models with different vug densities (10–50 vugs/m²) were used to study the influence of vug density on relative permeability curves. Analysis of the relative permeability curves measured (Fig. 4.26) shows that:

 - a. According to shape, all relative permeability curves of water are in concave shape, but the curvature is small, similar to the line.
 - b. As vug density increases, residual oil saturation increases, two-phase flowing area reduces, and the isoperm point shifts slightly. This may be the result of gravitational differentiation of oil and water in vugs. The oil above the fracture in the vug cannot be withdrawn and becomes residual oil; the larger the vug density, the more residual oil left, resulting in increasing residual oil saturation.
3. Relative permeability curves-effect of miarolitic percentage

Miarolitic percentage refers to the percentage of vug volume in all pore volume in the rock. Multifracture and multimiarolitic models were built to study the influence of miarolitic percentage on relative permeability curves. The models used have fracture aperture of 100 μm , vug diameter of 20 mm, vug depth of 40 mm, and miarolitic percentage to total porosity ratio (φ_v/φ) of 0%–67.7%. Analysis of the relation between oil and water relative permeability and water saturation (Fig. 4.27) shows that:

 - a. The relative permeability curves of water are in concave shape; the larger the miarolitic percentage, the larger the curvature of relative permeability curves is; in the high water cut phase saturation section, the increasing rate of water-phase permeability becomes smaller and smaller, and its curve tends to be flat.
 - b. The water relative permeability is maximum in the place where there is residual oil; furthermore, when a horizontal line is drawn from the isoperm points, two relative permeability curves basically exhibit a symmetric trend.
 - c. As miarolitic percentage increases, residual oil saturation increases, two-phase flowing area reduces, and the isoperm point shifts slightly. This may be because the larger miarolitic percentage causes more oil left in the upper part of vugs after waterflooding.

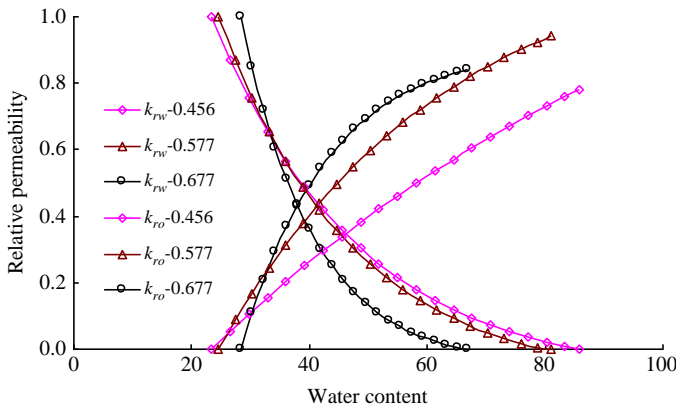


Figure 4.27 Relative permeability curves influenced by microlitic percentage.

Analysis of relative permeability curves related to fracture-vug type media provides the following conclusions:

1. In fracture-vug type media, fluids flow in a large space, so the effect of capillary force is limitative on two-phase flow pattern. In the Tahe Oilfield, the wettability of the Ordovician carbonate rock is close to neutral, so capillary force effect is weaker and can be completely neglected.
2. In large fractures and vugs, the permeability is very large and the viscous resistance is relatively small, the horizontal driving pressure difference required at conventional flow rate is very small. For large vugs, its vertical scale is large, and gravity action cannot be neglected, but for fractures, gravity effect can be neglected in horizontal fractures, but not in vertical fractures.

According to the Eq. (4.23), considering $X_i = k_{ri}^{b-1} S_i^c$ $i = w, o$, relative permeability and saturation set to 0-1, and known coefficients in Eq. (4.23) from Table 4.7, the critical velocity characteristics related to two-phase flow pattern conversion in fracture-vug models can be described. Here we take a 9-3-4 fracture network system ($C = 207, 10 \text{ vugs/m}^2$) for example to analyze how X_i changes with saturation (Figs. 4.28 and 4.29).

As shown in Table 4.7 and Figs. 4.28 and 4.29:

1. $X_i = k_{ri}^{b-1} < 1.0$ means that in fracture-vug models, the critical velocity of oil phase (or water phase) in the two-phase flow pattern is smaller than that in the one-phase flow pattern;
2. X_w increases with water saturation, whereas X_o reduces with water saturation, indicating that the critical velocity of the water phase increases with water saturation, but the critical velocity of the oil phase reduces with water saturation.

It can be summarized that in fracture-vug media, the critical velocity of every phase is not fixed in a two-phase flow pattern, but is variable depending on relative permeability $k_{r,i}$ and water saturation S_w . In the oilfield application, studies on the two-phase flow pattern should be based on the geological characteristics of the fracture-vug system in the actual reservoir and appropriate relative permeability curves.

Table 4.7 Coefficients of critical velocity equation

Model name	<i>a</i>	<i>b</i>	<i>c</i>	<i>b-1</i>	X_w	X_o
Fracture network	8.054	1.758	-1.369×10^{-14}	0.758	<1.0	<1.0
Vug density	7804	6.906	-3.445×10^{-13}	5.906	<1.0	<1.0

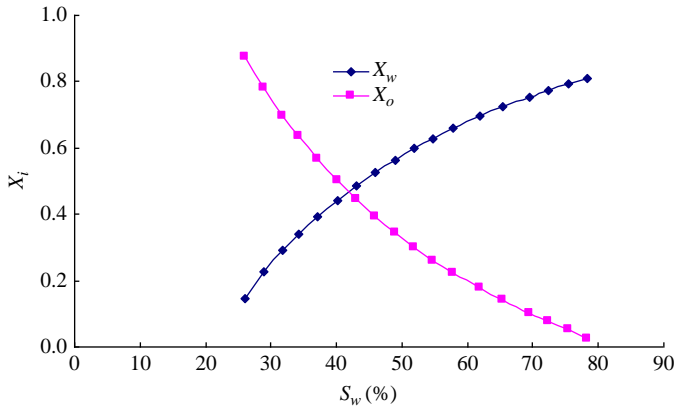


Figure 4.28 X_i versus saturation in the fracture network model with $C = 207$.

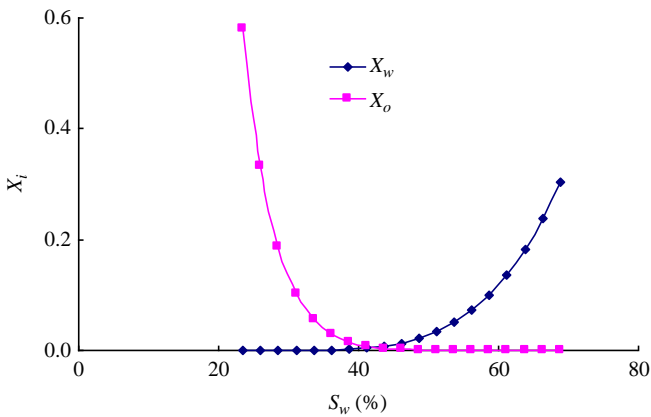


Figure 4.29 X_i versus saturation in the fracture-vug model with vug density of 10 vugs/m².

4.4 Fluid flow law among different systems in fracture-vug media

Fracture-vug carbonate reservoirs consist of various media in different combinations, among which fluid exchange always occur. Studies on fluid flow laws among different media should be carried out to provide theoretical evidences for numerical simulation and dynamic prediction of fracture-vug carbonate reservoirs. This section analyzes fluid flow laws, patterns, and features occurring among different media in fracture-vug reservoir based on experiments and typical mathematical models.

4.4.1 Flow law between fracture and matrix

4.4.1.1 Experimental design and methodology

Physical property parameters of lab cores

Fractures are extensively developed in fracture-vug carbonate reservoirs. Cores from the Tahe Oilfield where fractures are well developed can realistically reflect the characteristics of the oilfield fracture-vug reservoirs and are the best media to study the fluid flow law between matrix and fracture. In our experiment, two typical carbonate cores were selected to conduct crossflow pressure experiments: core 1-1 contains microscale fractures, core 2–5 contains wider fractures, both of them have high permeability. Results of variable confining pressure displacement experiments on the cores have been analyzed and compared to understand the displacement pressure variation during fluid crossflow between fracture and matrix.

Experimental method and workflow

1. Vacuate and saturate core with formation water at high pressure, and then put the saturated core in a core holder.
2. Put the core holder in a 70°C thermostat, and connect it to a high pressure displacement system and an automatic recording system.
3. Add confining pressure on the core to 5 MPa, and select an appropriate velocity, generally about 0.1 mL/min, to apply long constant flow displacement in the core.
4. Add the confining pressure to 10 MPa and continue to perform displacement after the pressure becomes stable.
5. Repeat the process until the confining pressure up to 25 MPa, terminate the displacement.

In the course of the experiment, the automatic recording system can continuously record the injection pressure—the shortest recording interval may be 1 second. This ensures the continuous monitoring of the crossflow between the matrix and the fracture in the core, and achieves the experimental objectives. The experiment workflow is shown in [Fig. 4.30](#).

4.4.1.2 Experimental results and analyses

The displacement pressure–time curves ([Fig. 4.31](#)) demonstrate that at 5 MPa confining pressure, the pressure in core 1-1 fluctuates, showing a crossflow at

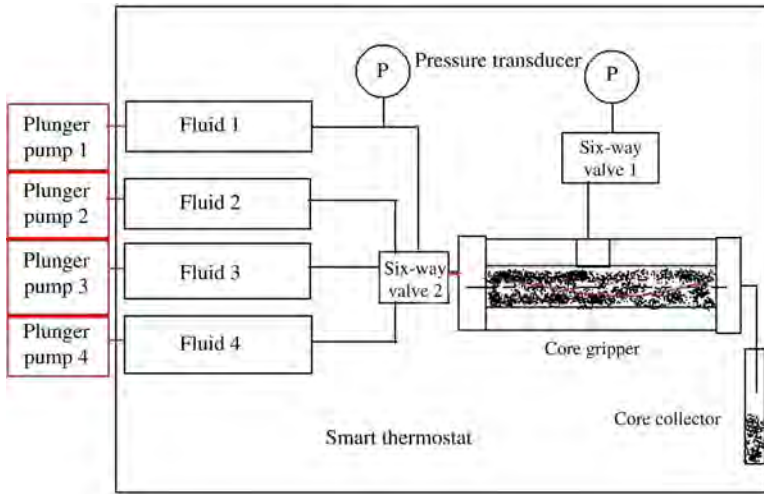


Figure 4.30 Experiment workflow.

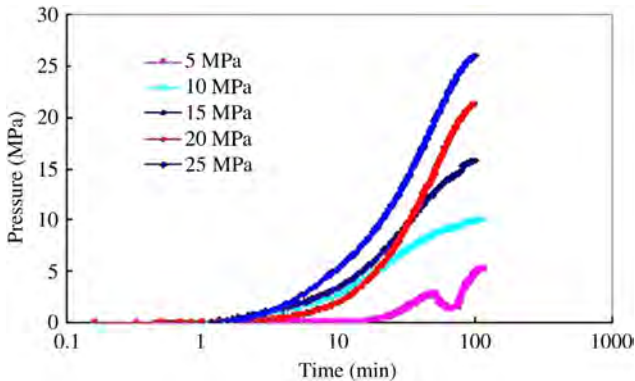


Figure 4.31 Displacement pressure versus time on core 1-1.

about 2.5 MPa between the fracture and the matrix; however, when the confining pressure is increased to 10 MPa or higher, the displacement pressure exhibits a straight climbing trend, and crossflow no longer occurs. This may be the result of higher effective stress on the fracture face, which forces microscale fractures to close.

The displacement pressure–time curves (Fig. 4.32) demonstrate that the displacement pressure curve on core 2–5 keeps fluctuating at any experimental confining pressure, showing that crossflow exists in the whole experiment process, regardless of how much confining pressure is applied. There always exists a crossflow pressure, but its size changes with the confining pressure applied. The smaller the confining pressure is, the smaller the crossflow pressure is, and vice versa.

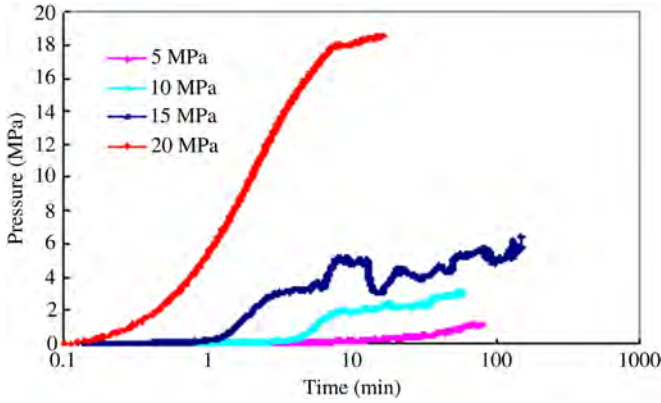


Figure 4.32 Displacement pressure versus time on core 2-5.

In general, because the permeability contrast between the fracture and the matrix in core 2–5 is very small, crossflow coefficient is large, and crossflow occurs more easily.

4.4.1.3 Mathematical model and calculation

1. Mathematical model

Based on the differential equation of dual-medium seepage flow, with the assumption that flow state is at pseudosteady state, the definite solution of crossflow between matrix and fracture can be expressed as:

$$\frac{\partial^2 P_{fD}}{\partial x_D^2} + \lambda(P_{mD} - P_{fD}) = \omega_f \frac{\partial P_{fD}}{\partial t_D} \quad (4.28)$$

$$\lambda(P_{fD} - P_{mD}) = \omega_m \frac{\partial P_{mD}}{\partial t_D} \quad (4.29)$$

$$P_{mD}(t_D = 0) = P_{fD}(t_D = 0) = 0 \quad (4.30)$$

$$P_{mD}(x_D = L_D) = P_{fD}(x_D = L_D) = 0 \quad (4.31)$$

$$\lim_{x \rightarrow 0} \frac{\partial P_{fD}}{\partial x} = -1 \quad (4.32)$$

In zero dimension, it is defined as:

$$P_{fD} = \frac{\Delta P_f k_f \sqrt{A}}{q\mu}, P_{mD} = \frac{\Delta P_m k_m \sqrt{A}}{q\mu}, \mu_m = \mu_f = \mu; x_D = \frac{x}{\sqrt{A}}, L_D = \frac{L}{\sqrt{A}}$$

$$t_D = \frac{k_f t}{(\Phi\mu C_t)_{mf} A}, \omega_f = \frac{(\Phi\mu C)_f}{(\Phi\mu C)_{mf}}, \omega_m = \frac{(\Phi\mu C)_m}{(\Phi\mu C)_{m+f}}, \lambda = \frac{\alpha k_m A}{K_f}; \omega_f + \omega_m = 1$$

where, k_m , Φ_m , μ_m , C_m , and ω_m represent the permeability, porosity, viscosity, compressibility and storativity of matrix, respectively; k_f , Φ_f , μ_f , C_f , and ω_f represent the permeability, porosity, viscosity, compressibility, and storativity of fracture, respectively; λ is crossflow coefficient; q is flow rate; t is time; α is shape factor; A is cross-section area; and x and L are dual-medium sizes.

Conduct Laplace transform to the aforesaid equations; then, combined with definite conditions, the Laplace domain space solution is reached as:

$$\bar{P}_{fD}(s) = \frac{1}{s\sqrt{sf(s)}} \frac{\sinh\left[(L_D - x_D)\sqrt{sf(s)}\right]}{\cosh(L_D\sqrt{sf(s)})} \tag{4.33}$$

$$f(s) = \frac{\omega_f(1 - \omega_f)s + \lambda}{(1 - \omega_f)s + \lambda} \tag{4.34}$$

The Stehfest method is the universal method for Laplace numerical inversion; by means of programing and numerical calculation, the relationship between pressure with time can be plotted.

2. Effect of storativity ratio

When the characteristic parameters of fracture-matrix dual-continuum reservoir are $L_D = 8.8$, $x_D = 0.7$, $\lambda = 0.05$, and $\omega = 1, 0.1, 0.01, 0.001$, and 0.0001 , the semilog plots (Fig. 4.33) calculated by software shows that variation in storativity ratio ω has a very large effect on the occurrence time of crossflow: ω determines the distance between early and late straight segments and mainly affects the transitional section of the pressure curve; lower ω value results in premature occurrence of transitional section; but when ω approaches 1, the early straight segment approaches the late straight segment, and the transitional section tends to disappear, at this time, the curve shape is the same as that of uni-medium.

3. Effect of crossflow coefficient

When the characteristic parameters are $L_D = 8.8$, $x_D = 0.7$, $\omega = 0.01$ and $\lambda = 1, 0.5, 0.1, 0.05$, and 0.01 , the semilog plots (Fig. 4.34) calculated by software show that the variation in crossflow time λ has a very great effect on the value of crossflow pressure: the value of λ determines the occurrence height of the transitional section; the smaller

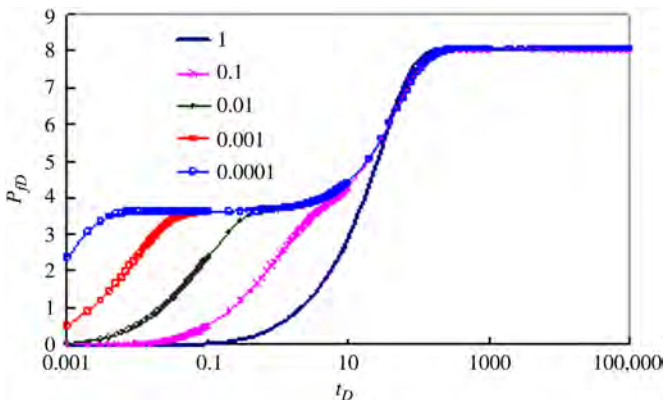


Figure 4.33 Effect of storativity ratio on displacement pressure curve.

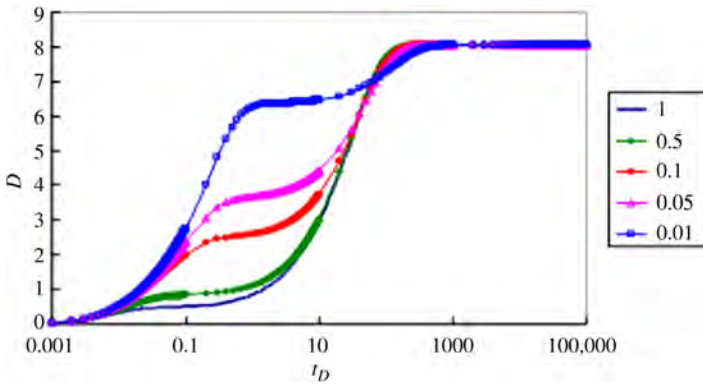


Figure 4.34 Effect of crossflow coefficient on displacement pressure.

the λ value, the higher the transitional section on the coordinate diagram is, i.e., the larger the pressure difference required to flow across the matrix and fracture.

In the course of the development of a fracture-matrix dual-continuum reservoir, the effective stress of rock is everchanging, which has certain effects on pore texture; in turn the change in pore texture tends to result in a change in rock permeability and porosity, i.e., the porosity and permeability of the reservoir are pressure sensitive. In a dual-continuum core, because its porosity and permeability are apparently affected by effective stress, and storativity and crossflow coefficient are directly determined by porosity and permeability, the change in effective stress can directly affect the seepage flow law, crossflow occurrence time and pressure magnitude in the core. This phenomenon is quite obvious in the physical modeling experiment of the crossflow pressure test.

In conclusion, as effective stress increases, the crossflow platform shifts towards the upper left, indicating that increasing effective stress causes fractures become narrower, decreases the storativity ratios and crossflow coefficients, then increases the crossflow pressure and make the crossflow platform appears earlier and becomes longer. All of which are almost identical to the numerical simulation results.

4.4.1.4 Crossflow law at pseudosteady state

When fractures are relatively developed in one direction in a reservoir, i.e., they are distributed layer by layer or row by row, the matrix shapes in layer or massive structure, as shown in Fig. 4.35, the thickness of the layered matrix block is $2L$.

According to symmetry, a half of the matrix block (Fig. 4.35) was taken for study. At pseudosteady linear flow condition, the pseudopressure in the matrix block changes with time and space as follows:

$$\frac{\partial p}{\partial t} = f(t) \tag{4.35}$$

$$\frac{\partial p}{\partial y} = -\frac{y q_o \mu}{2L k_m A} \tag{4.36}$$

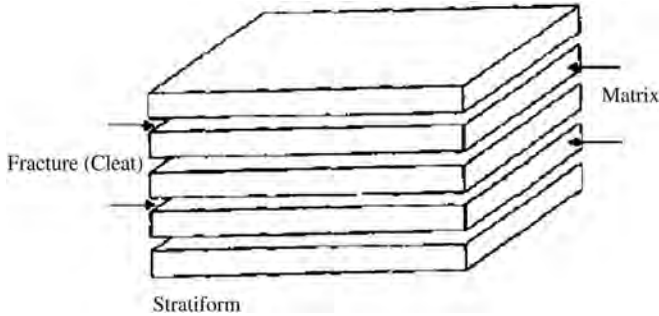


Figure 4.35 Sketch map of layered matrix block.

Integrate Eq. (4.36), we get:

$$p|_{y=y} - p|_{y=L} = \frac{q_o \mu (L^2 - y^2)}{4Lk_m A} \quad (4.37)$$

Integrate Eq. (4.37) from 0 to L , then, taking the average, we get:

$$\bar{p} - p|_{y=L} = \frac{q_o \mu L}{6k_m A} \quad (4.38)$$

As is known from the matrix block shape:

$$\bar{p} = p_m \quad p|_{y=L} = p_f \quad (4.39)$$

Substitute Eq. (4.39) in Eq. (4.38), we get:

$$q_o = \frac{6k_m(p_m - p_f)}{\mu L} \quad (4.40)$$

4.4.2 Flow law between matrix and vug

4.4.2.1 Flow law between matrix and vug

1. Physical model

A vug drilled by an oil well must be surrounded by matrix which has a certain flow capacity, like the sketch of a vug-matrix reservoir in Fig. 4.36, where r_c is vug radius, r_e is boundary radius, k means matrix permeability, φ means porosity, h means reservoir thickness, reservoir has a finite closed boundary.

2. Mathematical model

The mathematical model is built based on the following assumptions: (1) circular closed boundary; (2) fluid flow following the Darcy's law at the moment of seepage flow in matrix body; (3) isothermal flow; (4) minor compressible fluid and rock

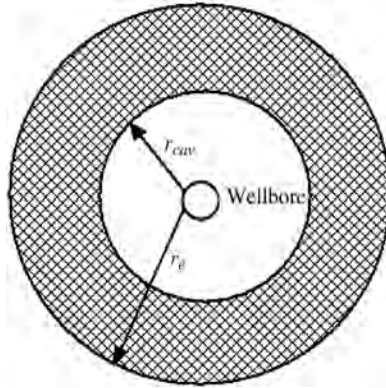


Figure 4.36 Sketch map of vug-matrix reservoir.

(C_L denotes fluid compressibility, C_s denotes rock compressibility); (5) constant production pressure; and (6) negligible flow resistance between wellbore and vug which is treated as enlarged wellbore. The seepage flow equation set is:

$$\text{Control equation: } \frac{\partial^2 p}{\partial r^2} + \frac{1}{r} \frac{\partial p}{\partial r} = \frac{1}{\eta} \frac{\partial p}{\partial t} \quad r_c \leq r \leq r_e \quad (4.41)$$

$$\text{Initial condition: } p|_{t=0} = p_i \quad (4.42)$$

$$\text{Closed outer boundary: } \left. \frac{\partial p}{\partial r} \right|_{r=r_e} = 0 \quad (4.43)$$

$$\text{Constant rate condition: } \left. \frac{2\pi r h k \partial p}{\mu \partial r} \right|_{r=r_c} - \pi r_c^2 h C_L \left. \frac{\partial p}{\partial t} \right|_{r=r_c} = q B_o \quad (4.44)$$

where η is transmissivity, cm^2/s ; p_i is initial reservoir pressure, 0.1 MPa; k is matrix permeability, μm^2 .

3. Crossflow at pseudosteady state

At pseudosteady state, the pressure in the matrix block changes with time and space as follows:

$$\frac{2\pi r h k \partial p}{\mu \partial r} = \frac{r_e^2 - r^2}{r_e^2 - r_c^2} q_o \quad (4.45)$$

Integrate Eq. (4.45), we get:

$$\frac{2\pi h k}{\mu} (p|_{r=r} - p|_{r=r_c}) = \left(\frac{r_e^2}{r_e^2 - r_c^2} \ln \frac{r}{r_c} - \frac{r^2 - r_c^2}{2(r_e^2 - r_c^2)} \right) q_o \quad (4.46)$$

Integrate Eq. (4.46), then, taking the average, we get:

$$\frac{2\pi h k}{\mu} (\bar{p} - p|_{r=r_c}) = \left(\frac{r_e^2}{r_e^2 - r_c^2} \left(\frac{r_e^2}{(r_e^2 - r_c^2)} \ln \frac{r_e}{r_c} - \frac{1}{2} \right) - \frac{(r_e^2 + r_c^2)}{4(r_e^2 - r_c^2)} + \frac{r_c^2}{2(r_e^2 - r_c^2)} \right) q_o \quad (4.47)$$

As is known from the matrix block shape:

$$\bar{p} = p_m \quad p|_{r=r_c} = p_c \quad (4.48)$$

By combining Eq. (4.47) with Eq. (4.48), we get:

$$q_o = \frac{2\pi kh(p_m - p_c)}{\mu \left(\frac{r_e^2}{r_e^2 - r_c^2} \left(\frac{r_e^2}{(r_e^2 - r_c^2)} \ln \frac{r_e}{r_c} - \frac{1}{2} \right) - \frac{(r_e^2 + r_c^2)}{4(r_e^2 - r_c^2)} + \frac{r_c^2}{2(r_e^2 - r_c^2)} \right)} \quad (4.49)$$

4. Influential factors to matrix crossflow

Assuming that vug radius is 80 m, well control radius is 320 m, both reservoir thickness and vug height are 50 m, oil compressibility is 0.001 MPa^{-1} , oil viscosity is $22.5 \text{ MPa} \cdot \text{s}$, and total compressibility is $5 \times 10^{-5} \text{ MPa}^{-1}$, we analyze the effect of matrix permeability and bottom hole flow rate on crossflow rate and bottom hole pressure.

Analysis of the curves (Fig. 4.37) demonstrates that crossflow rate increases with time; when matrix permeability is lower than 0.5 MPa , bottom hole pressure drop is less than 12 MPa , crossflow rate does not exceed 10% of bottom hole flow rate (when bottom hole inflow rate is $100 \text{ m}^3/\text{day}$, crossflow rate does not exceed $10 \text{ m}^3/\text{day}$); in this case matrix crossflow fluid has little effect on the production of the vug-matrix reservoir, it is negligible, and the reservoir can be treated as an isolated-vug reservoir (Fig. 4.38).

As shown in the curves (Fig. 4.39), the smaller the daily fluid rate is, the larger the cumulative crossflow rate at the same cumulative fluid production is, and the greater the contribution of matrix crossflow fluid to the production of matrix-vug type reservoir is; when the matrix permeability is small, the cumulative crossflow rate is smaller than the cumulative fluid production, and the crossflow has little effect on the production as a whole. In conclusion, when matrix permeability is low, it may be ineffective to enhance production by reducing daily fluid rate (Fig. 4.40).

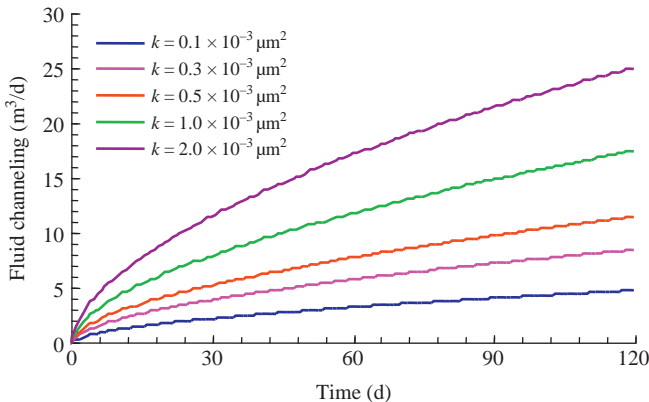


Figure 4.37 Crossflow rates at different matrix permeabilities.

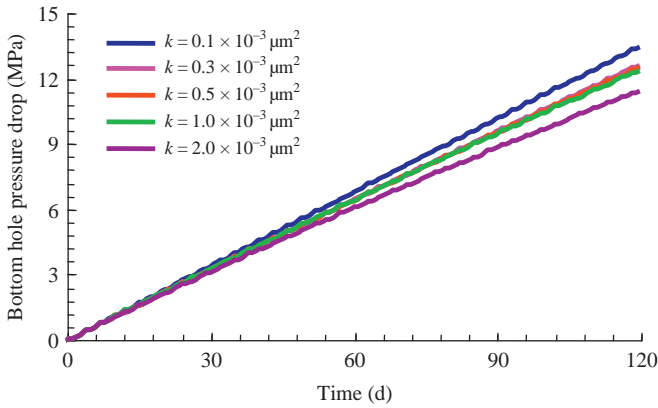


Figure 4.38 Bottom hole pressure drops at different matrix permeabilities.

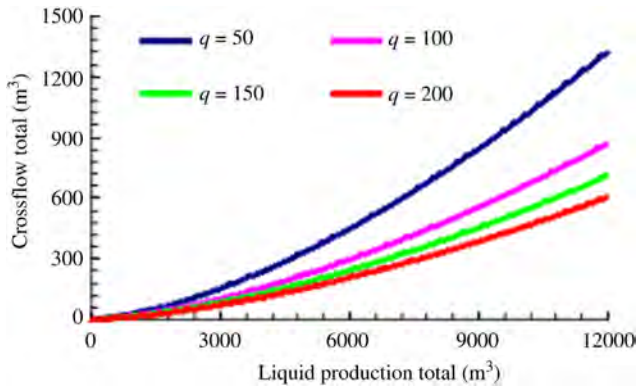


Figure 4.39 Cumulative crossflow rate versus cumulative fluid production.

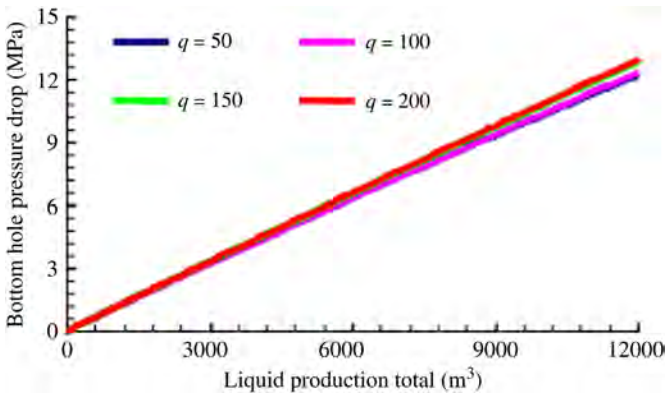


Figure 4.40 Bottom hole pressure drop versus cumulative fluid production.

4.4.2.2 Flow law between filler and vug

1. Physical model

A vug drilled by an oil well is filled with some filler on the bottom, as shown in the sketch in Fig. 4.41. Supposing V is vug cavity volume, h is filler thickness, A is cross-section area, porosity is φ , permeability is k , initial pressure is P_i , total compressibility is C_t , and vug compressibility is negligible, we build a physical model.

2. Flow modeling test

Model materials include an intermediate container with diameter $d_1 = 10$ cm and volume $V = 1000$ mL to model vug cavity, and full diameter ($d_2 = 10$ cm) cores (saturated with formation water) with different permeabilities, lengths and porosities. Several models were built with different fillers and filling degrees. Flow laws between filler and vug were modeled based on these models and the parameters in Table 4.8.

The pressure-time curve of vugs and core boundary were plotted based on measured pressure drop data. The examples in Figs. 4.42 and 4.43 are the results based on $0.098 \times 10^{-3} \mu\text{m}^2$ core permeability, 48.5% filling degree, 13.4% filler porosity, and 1 mL/min flow rate.

Modeling results indicate that if the pore volume is relatively small and the flow rate is constant, vug pressure changes linearly with time, the pressures on the core end and in the vug exhibit “scissors difference” at the early stage; poorer filling medium conductivity, higher filling degree and faster suction rate result in more significant pressure “scissors difference”; however, when the filling medium flow capacity is stronger



Figure 4.41 Sketch map of vug-filling type reservoir.

Table 4.8 Modeling parameters

SN	Filling degree (%)	Filler porosity (%)	Gas survey permeability ($\times 10^{-3} \mu\text{m}^2$)	Flow rate (mL/min)	Pore volume (mL)
1	48.5	15.9	1.42	1 ~ 10	149.7
2	61.1	15.9	1.42	1 ~ 10	249.7
3	61.1	13.4	0.098	1 ~ 10	210.5
4	48.5	13.4	0.098	1 ~ 10	126.2

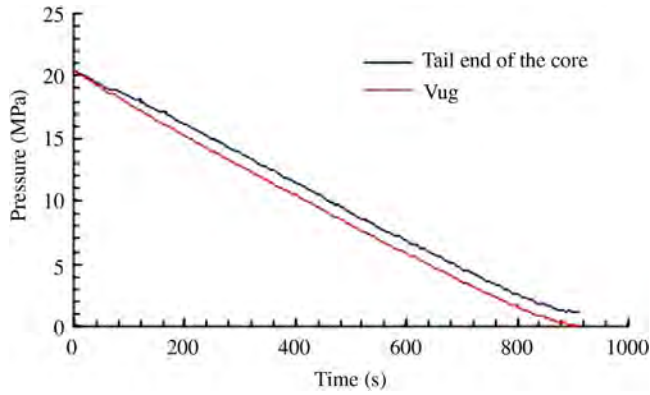


Figure 4.42 Pressure–time curve.

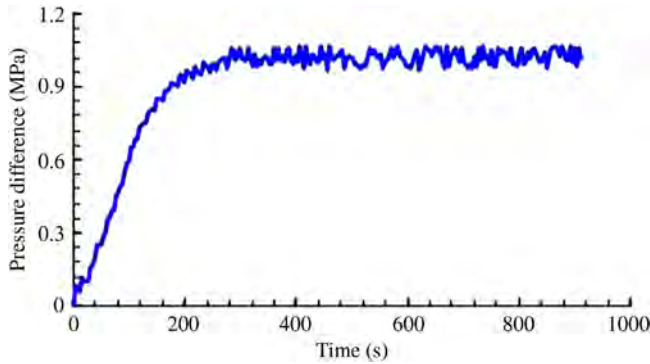


Figure 4.43 Pressure difference-time curve.

and the fluid entry volume is relatively small, the pressure difference between two sides of the filling medium quickly becomes stable the pressure difference between two sides of the filling medium quickly becomes stable.

3. Mathematical model

Assume that a reservoir in which the vugs are filled, filling medium thickness is h , porosity is φ , permeability is k , vug cavity volume is V , vug cross-section is A ; oil compressibility is C_o , oil viscosity is μ , oil volume factor is B_o ; and flow resistance from vug into wellbore is negligible, the mathematical model can be expressed by,

$$\text{Control equation: } \frac{\partial^2 p}{\partial x^2} = \frac{1}{\eta} \frac{\partial p}{\partial t} \tag{4.50}$$

$$\text{Initial condition: } p(t = 0) = p_i \tag{4.51}$$

$$\text{Boundary condition: } \left. \frac{\partial p}{\partial x} \right|_{x=L} = 0 \tag{4.52}$$

$$\left. \frac{Ak}{\mu} \frac{\partial p}{\partial x} \right|_{x=0} - VC_L \left. \frac{\partial p}{\partial t} \right|_{x=0} = qB_o \tag{4.53}$$

Eqs. (4.50)–(4.53) constitute jointly the control equations and initial boundary conditions of a filled-vug-type reservoir which was assumed to produce in a constant production rate. On the left side of Eq. (4.53), the first item means the indirect delivery volume from crossflow, the second item is the elastic storage of vug cavity.

4. Crossflow from filler to vug at pseudosteady state

When fluid flow occurs at pseudosteady state, pressure distribution in the filling medium meets the following relation:

$$\frac{\pi r_c^2 k}{\mu} \frac{\partial p}{\partial z} = \frac{L-z}{L} q_o \quad (4.54)$$

Integrate Eq. (4.54), we get:

$$\frac{\pi r_c^2 k}{\mu} (p|_{z=z} - p|_{z=0}) = \left(z - \frac{z^2}{2L} \right) q_o \quad (4.55)$$

Integrate Eq. (4.55), then, taking the average, we get:

$$\frac{\pi r_c^2 k}{\mu} (\bar{p} - p|_{z=0}) = \frac{Lq_o}{3} \quad (4.56)$$

As is known from the filling medium shape:

$$\bar{p} = p_m \quad p|_{r=r_c} = p_c \quad (4.57)$$

By combining Eq.(4.56) with Eq. (4.57), we get:

$$q_o = \frac{3k\pi r_c^2 (p_m - p_c)}{\mu L} \quad (4.58)$$

4.4.3 Flow law in different fracture-vug combinations

Fluid flow from vugs to wellbore through fractures, and fluid in vugs far away from wellbore flows into fractures that are directly connected with wellbore through fractures. These are universal phenomena of fluid flow in fracture-vug reservoirs (Yingjie et al., 2004). It is of great significance to understand the development rules in fracture-vug reservoirs by studying fluid flow laws between vugs and fractures. Generally fluid flow between fractures and vugs involves the following scenarios: (1) single vug–near-vug fracture; (2) double vugs (an oil well drilled into the major vug and fractures near the major vug); and (3) multiple fractures and vugs.

4.4.3.1 Flow law in single-vug–near-vug fracture (high dip) medium

Here we only analyze the case where an well drills into high-dipped fracture(s) near a vug, and there is no supply from the outer boundary of the vug (Fig. 4.37). The

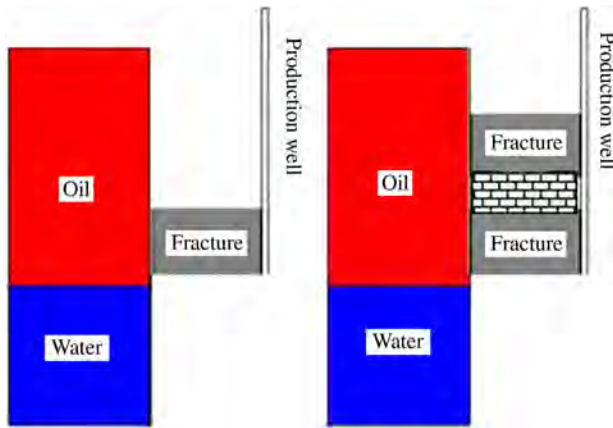


Figure 4.44 Sketches of one-vug-one fracture (left) and one vug-two fractures (right).

interfacial tension between oil and water is negligible because of the remarkable space in vug and fracture, oil–water contact is believed to be a horizontal plane, and the uplift of oil–water contact in the vug mainly relies on the elastic expansion energy of fluid and rock (mainly considering elastic energy in the study). In the study, two cases including one-vug–one-fracture and one-vug–two-fractures were analyzed (Fig. 4.44).

1. Basic flow law

a. Physical modeling experiment

A core with diameter of 2.50 cm, length of 5.00 cm, and permeability of $0.24 \times 10^{-3} \mu\text{m}^2$ was selected. The modeling experiment was carried out on the core and the permeability of the core connecting the vug was changed to analyze the conductivity of the fracture.

The pressure-time curve of vug matches well with the production rate-time curve of well in a simple exponential manner (Fig. 4.45).

b. Mathematical model

Based on the material balance equation of closed elastic drive in a nonsaturated reservoir, the cumulative oil production is:

$$N_p = \frac{NB_{oi}C_i(p_i - \bar{p}(t))}{B_o} \quad (4.59)$$

Vug's daily rate is:

$$q_{cavity} = \frac{w^3h}{12\mu l} (\bar{p}(t) - p_{wf}) \quad (4.60)$$

Integrate Eq. (4.59), then, substitute the initial condition into this equation, the pressure drop in the vug is derived as:

$$\bar{p}(t) - p_{wf} = (p_i - p_{wf})e^{-\frac{w^3h}{12\mu l} \cdot \frac{B_o}{NB_{oi}C_i} t} \quad (4.61)$$

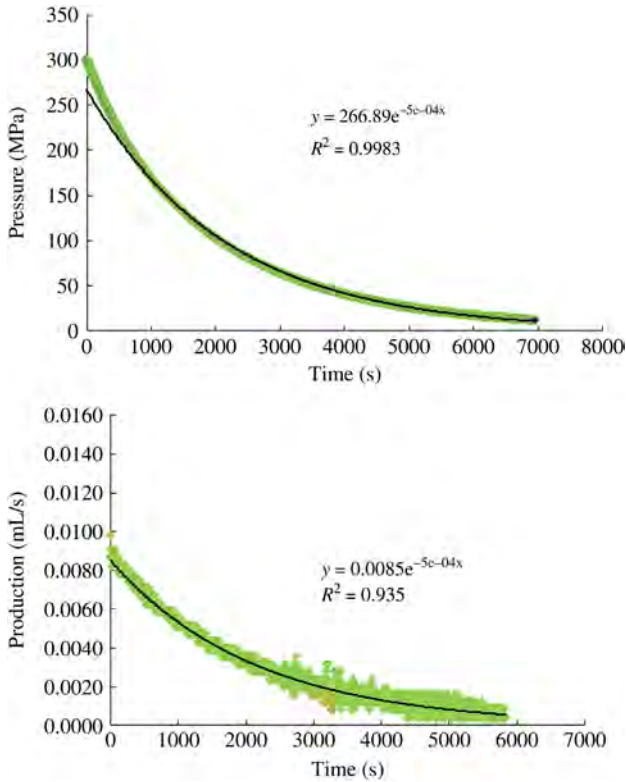


Figure 4.45 Test results at core permeability of $0.24 \times 10^{-3} \mu\text{m}^2$.

Substitute Eq. (4.61) in Eq. (4.60), the variation rule of vug output is derived as:

$$q_{\text{cavity}} = \frac{w^3 h}{12\mu l} (p_i - p_{wf}) e^{-\frac{w^3 h}{12\mu l} \cdot \frac{B_o}{NB_{oi} C_t} t} \quad (4.62)$$

Comparison between the theoretical model and the experimental result proves that they coincide with each other: both pressure and output show simple exponential decline variation with time, and the decline exponent is related to the fracture conductivity.

2. Water cut variation

a. Water cut variation in the one-vug–one-fracture model

In this case where a well drill into a near-vug high-dipped fracture. The oil-water contact in the vug is far below the fracture before water breakthrough, the production well only produces oil. Based on the law of elasticity, the production of oil is:

$$qB_o = -C_o V_o(t) \frac{\partial p_c(t)}{\partial t} - C_w V_w(t) \frac{\partial p_c(t)}{\partial t} \quad (4.63)$$

The volume expansion relation of the water phase in the vug is:

$$\frac{\partial V_w(t)}{\partial t} = -C_w V_w(t) \frac{\partial p_c(t)}{\partial t} \quad (4.64)$$

From Eq. (4.64), the oil–water contact expression is derived as:

$$X(t) = \frac{V_w(0)}{A} e^{-C_w(p_c(t)-p_i)} \quad (4.65)$$

where, $X(t)$ is the height from the oil–water contact to the fracture bottom, m.

Combine the first order approximation of Eq. (4.65) with Eq. (4.63) and solve this equation, the height difference of oil–water contact in the vug is written as:

$$\Delta X(t) = \frac{V_w(0)}{A} \frac{qtB_o C_w}{(V_o(0)C_o + V_w(0)C_w)} \quad (4.66)$$

where, $\Delta X(t)$ is the rise of the oil–water contact, m.

From the above equation, the oil–water contact in the vug rises proportionally with time at a constant production rate and before water breakthrough, and the slope is related to the vug radius, oil and water volume in the vug, and oil and water compressibility.

After breakthrough, the oil–water contact in the vug will rise over the bottom of the high-dipped fracture, and at this stage, both oil and water will be produced:

$$q = \frac{q_o}{B_o} + \frac{q_w}{B_w} \quad (4.67)$$

Based on the law of elasticity, we get

$$q_o + q_w = -(C_o V_o(t) + C_w V_w(t)) \frac{\partial p_c(t)}{\partial t} \quad (4.68)$$

The water phase volume in the vug meets the following relation

$$\frac{\partial V_w(t)}{\partial t} = -C_w V_w(t) \frac{\partial p_c(t)}{\partial t} - q_w(t) \quad (4.69)$$

The oil–water contact rises following the relation below:

$$\frac{\partial X(t)}{\partial t} = -C_w \frac{V_w(t)}{A} \frac{\partial p_c(t)}{\partial t} - \frac{q_w(t)}{A} \quad (4.70)$$

Eqs. (4.67)–(4.70), i.e., the differential equations for crossflow after the oil–water contact rises over the fracture bottom, can be solved after discretization by difference.

By combining Eq. (4.69) with Eq. (4.70), we get

$$A \frac{\partial h_w}{\partial t} = \frac{(q_o + q_w)h_w C_w}{(H - h_w)C_o + h_w C_w} - q_w \quad (4.71)$$

When the energy is sufficient in the vug, water breakthrough just occurs and a little water is produced, the right of Eq. (4.71) can be written as:

$$RHS = \frac{(q_o + q_w)h_w C_w}{(H - h_w)C_o + h_w C_w} - q_w > 0 \quad (4.72)$$

Eq. (4.72) indicates that after water breakthrough, the oil–water contact will keep rising.

After water breakthrough for a long time, if only water is produced, then:

$$RHS = \frac{(q_o + q_w)h_w C_w}{(H - h_w)C_o + h_w C_w} - q_w < 0 \quad (4.73)$$

According to the Roll's law, oil and water production meet the following relation at a time during production:

$$RHS = \frac{(q_o + q_w)h_w C_w}{(H - h_w)C_o + h_w C_w} - q_w = 0 \quad (4.74)$$

Eq. (4.74) indicates that in the course of production, oil–water contact will be stable, as well as oil production, water production, and water cut. The water cut during stable production is:

$$\eta = \frac{B_o C_w V_w}{B_o C_w V_w + B_w C_o V_o} \quad (4.75)$$

where, η is stable water cut; V_w is water phase volume in the vug at stable water cut; V_o is oil phase volume in the vug at stable water cut.

Oil–water contact and water cut in the vug at different oil–water ratios (Figs. 4.46 and 4.47):

b. Water cut variation in the one-vug–two-fractures model

Prior to water breakthrough in an oil well drilled into a one-vug–two fractures reservoir, the oil–water contact is below the fracture bottom, and the fluid flow

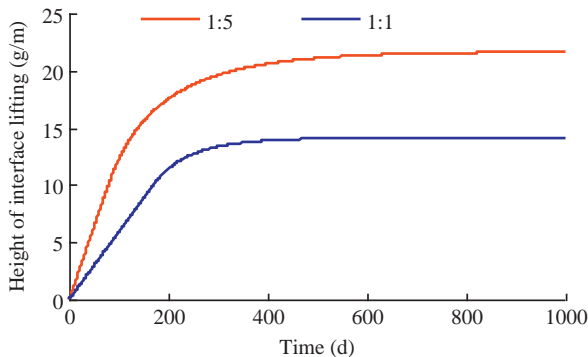


Figure 4.46 Rising oil–water contact in the vug.

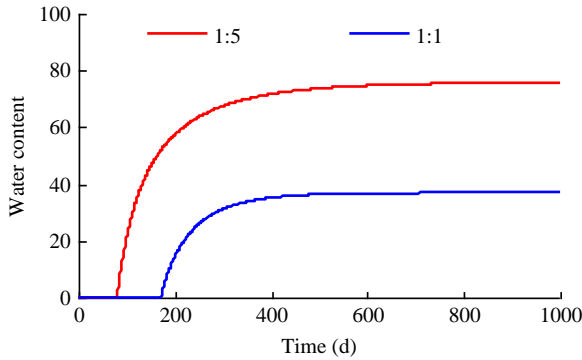


Figure 4.47 Water cut in the vug.

equation is similar to that in one-vug–one-fracture model. The breakthrough time equation of water is derived as:

$$t_o = \frac{[V_o(0)C_o + V_w(0)C_w] AL}{V_w(0)C_w qB_o} \tag{4.76}$$

After water breakthrough, the oil–water contact and water cut variation are related to the relative fluid flowability in lower and upper fractures and relative elastic energy of oil and water in the vug.

- i. The elastic energy of water is relatively small, and the fluid flowability in the lower fracture is relatively strong

Because the elastic energy of water is relatively small, and the fluid flowability in the lower fracture is relatively strong, the oil–water contact is finally stabilized on a point in the lower fracture; in this case, after water breakthrough, the flow features in the one-vug–two-fractures model are the same as those in the one-vug–one-fracture model.

- ii. The elastic energy of water is relatively large, and the fluid flowability in the lower fracture is relatively weak

Because the elastic energy of water is relatively large, and the fluid flowability in the lower fracture is relatively weak, when the oil–water contact rises to the top of the lower fracture, the water expansion rate is faster than the water production rate, the oil–water contact will still go on rising, and a temporary water cut stable stage will occur, and at this time, the water cut is expressed as Eq. (4.71); after the oil–water contact has risen to the bottom of the upper fracture, the water cut starts to rise again and finally is stabilized, and at this time, the water cut is expressed as Eq. (4.72); the water cut exhibits stepped variation in the whole process, as shown in Fig. 4.48.

$$f_{w1} = \frac{\frac{k_1 w_1 h_1}{\mu_w} B_o}{\frac{k_1 w_1 h_1}{\mu_w} B_o + \frac{k_2 w_2 h_2}{\mu_o} B_w} \tag{4.77}$$

$$f_{w2} = \frac{B_o C_w V_w}{B_o C_w V_w + B_w C_o V_o} \tag{4.78}$$

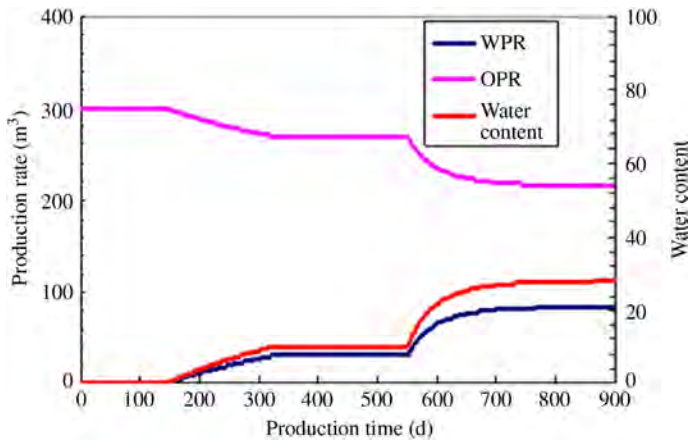


Figure 4.48 Water cut change in the one-vug–two-fractures model.

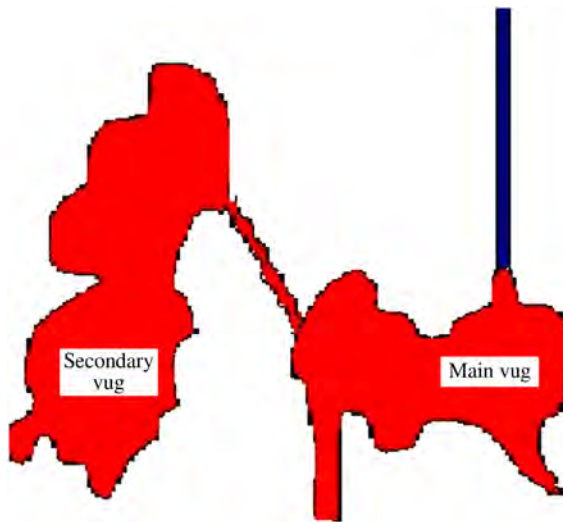


Figure 4.49 Sketch map of double-vug reservoir where a vug is drilled.

4.4.3.2 Flow law in double-vug medium

1. Flow law in the double-vug model where the primary vug is drilled

The double-vug reservoir contains two vugs connecting through a fracture (vug-fracture-vug structure). The vug drilled into by a well is called the primary vug. The secondary vug connects with the primary through a fracture. The sketch of a double-vug reservoir is given in Fig. 4.49.

a. Physical modeling experiment

Cores with diameter of 2.50 cm, length of 5.00 cm, and permeability of $14 \times 10^{-3} \mu\text{m}^2$, $0.24 \times 10^{-3} \mu\text{m}^2$, and $0.0454 \times 10^{-3} \mu\text{m}^2$, respectively were selected

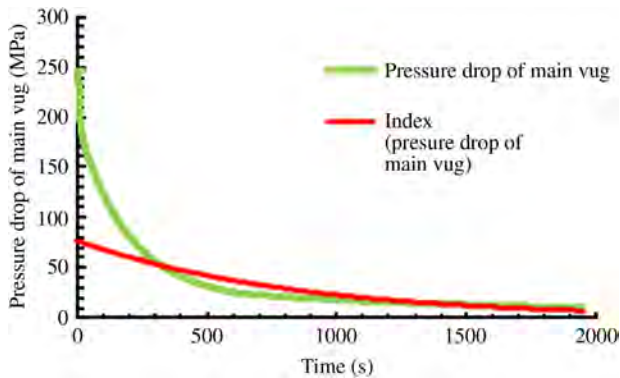


Figure 4.50 Primary vug pressure curve.

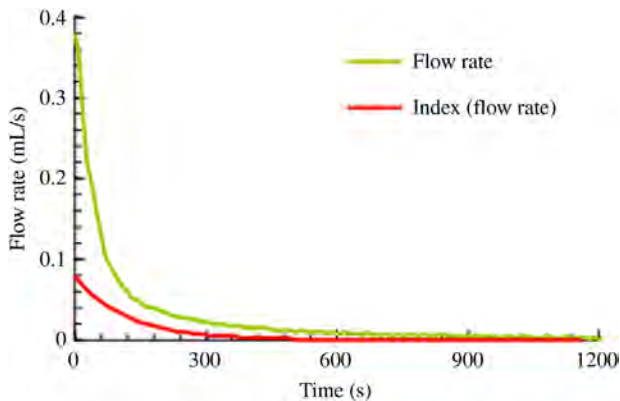


Figure 4.51 Well flow rate curve.

to conduct experiments, and different conductivities of fracture(s) between vugs were modeled by changing the permeability of cores connecting the vugs.

Comparisons between the primary vug pressure–time and the well flow rate–time curves and their exponential function curves (at core permeability of $0.24 \times 10^{-3} \mu\text{m}^2$) (Figs. 4.50 and 4.51) indicate that at the early stage, the primary vug pressure is high but declines quickly, and at the late stage, the primary vug pressure is low but declines slowly; similarly at the early stage, the well flow rate is high but declines fast, and at the late stage, the well flow rate is low but declines slowly.

In the case that the vug in the single-vug model is identical to the primary vug in volume, in the vug-fracture-vug model, these vugs' pressure variations were compared (Fig. 4.52). It is proved that the vug pressure in the single-vug model meets the exponential decline law, but the pressure in the primary vug does not, exhibiting such a phenomenon as where the pressure is high but declines fast at the early stage and low but declines slowly at the late stage; in production variation, the two types of reservoir are similar.

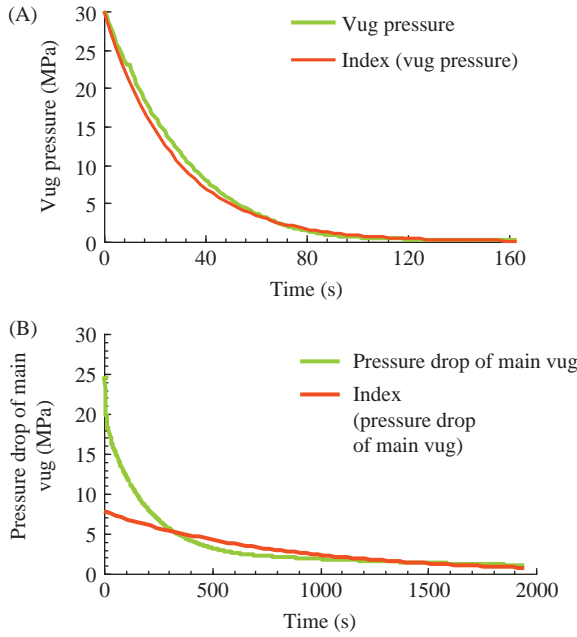


Figure 4.52 Vug pressure in single-vug model (A) and primary vug pressure in vug-fracture-vug model (in volume, the vug in (A) is similar to the primary vug in (B)). (A) single-vug; (B) double-vug.

b. Mathematical model

Supposing that the fluid in vugs is minor compressible at a constant C_L , the primary and secondary vugs are different equipotential bodies, production is carried out at a constant bottom hole pressure, and the effect of elastic storage and release of the fluid in fracture and wellbore are negligible, then, based on the law of elasticity:

$$q = -V_1 C_L \frac{\partial p_1}{\partial t} - V_2 C_L \frac{\partial p_2}{\partial t} \quad (4.79)$$

where, V_1 is primary vug volume; V_2 is secondary vug volume; p_2 is relative pressure in the secondary vug.

According to flow law between vug and fracture, we get:

$$\frac{\pi r_w^4}{4\mu L_1} \left(\frac{V_2 C_L \mu L}{KA} \frac{\partial p_2}{\partial t} + p_2 \right) = -V_1 C_L \frac{\partial}{\partial t} \left(\frac{V_2 C_L \mu L}{kA} \frac{\partial p_2}{\partial t} + p_2 \right) - V_2 C_L \frac{\partial p_2}{\partial t} \quad (4.80)$$

The solution of Eq. (4.80) is

$$p_2(t) = \beta_1 e^{-\lambda_1 t} + \beta_2 e^{-\lambda_2 t} \quad (4.81)$$

where,

$$\lambda_{1,2} = \frac{-b \pm \sqrt{b^2 - 4ac}}{2a}; \quad a = \frac{V_2 C_L V_1 C_L \mu L}{KA}; \quad b = V_1 C_L + V_2 C_L + \frac{\alpha V_2 C_L \mu L}{KA}; \quad c = \frac{\pi r_w^4}{4\mu L}$$

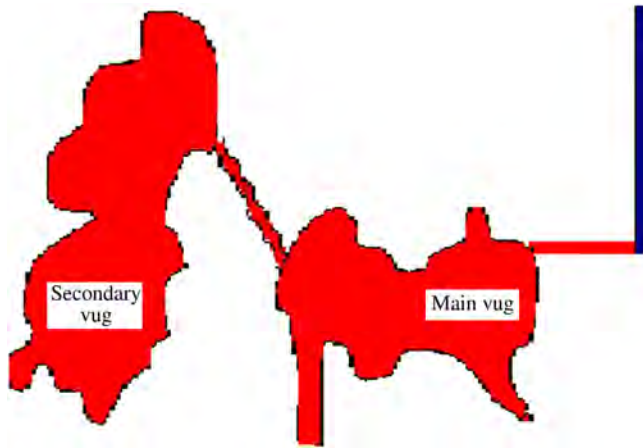


Figure 4.53 Double-vug model sketch—a well drilled into the fracture near a vug.

Substitute Eq. (4.81) in Eq. (4.80), the equations for variation of primary vug relative pressure and well flow rate with time are derived as:

$$p_1 = \beta_3 e^{-\lambda_1 t} + \beta_4 e^{-\lambda_2 t} \quad (4.82)$$

$$q = \beta_5 e^{-\lambda_1 t} + \beta_6 e^{-\lambda_2 t} \quad (4.83)$$

where constant coefficients $\beta_1 \sim \beta_6$ are reached based on initial conditions. According to Eqs. (4.82) and (4.83), the relative pressure in the primary vug and the well flow rate change with time in a double exponential mode.

2. Flow law in the double-vug model where fractures near the primary vug are drilled

In the double-vug reservoir, it is the case that a well drills into the fracture near a vug which connects to other vugs through fractures, as in the sketch in Fig. 4.53. The vug near the fracture drilled is called the primary vug, and the other is called secondary vug.

a. Physical modeling experiment

In the experiment, fractured cores with diameter of 2.5 cm, length of 5.0 cm, and permeability of $0.78 \times 10^{-3} \mu\text{m}^2$ and $9.06 \times 10^{-3} \mu\text{m}^2$, respectively, were used to model the reservoir fractures, and the flow law in vug-fracture reservoirs under different formation pressures and fracture-vug combinations were modeled by changing fracture permeability, vug size, and initial vug pressure.

As shown by the curves in Figs. 4.54 and 4.55, stronger conductivity of the fracture connecting the well to the primary vug delivers larger flow rate at an early production stage, but makes the primary vug pressure decline faster; when the conductivity of the fracture connecting the well to the primary vug is relatively strong and that connecting the primary to the secondary vugs is relatively weak, the flow rate is large but declines fast at the early stage and small (but declines slowly) at the late stage; when the conductivity of the fracture connecting the well to the primary vug is relatively weak and that connecting the primary vug to the secondary vug is relatively strong, both the flow rate and the primary vug pressure exhibit an exponential decline with production time.

The differential pressure between the primary and secondary vugs exhibits a trend of increasing first and reducing afterwards; the poorer the conductivity between the

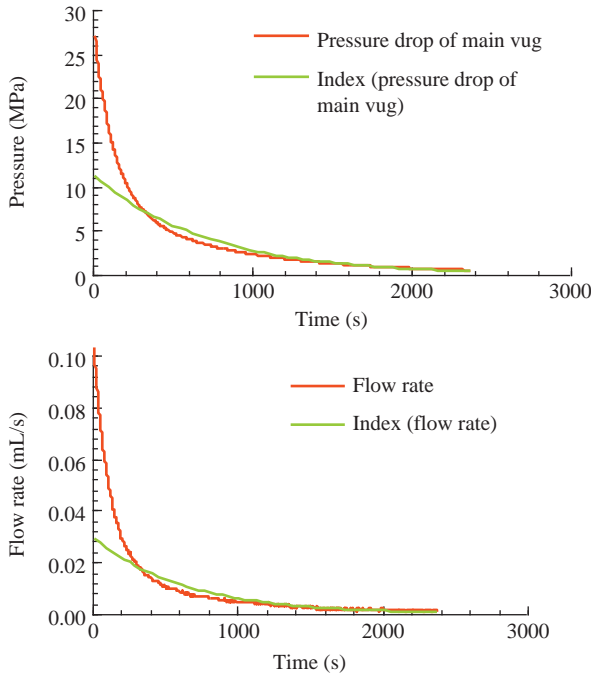


Figure 4.54 Primary vug pressure and well flow rate curves under $0.78 \times 10^{-3} \mu\text{m}^2$ to $9.06 \times 10^{-3} \mu\text{m}^2$ combination.

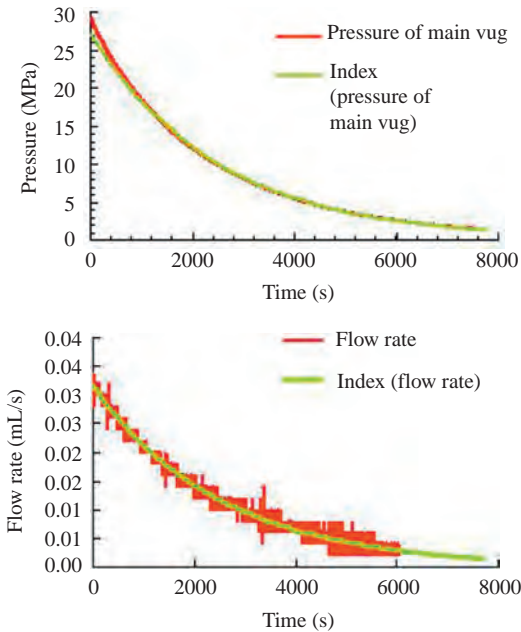


Figure 4.55 Primary vug pressure and well flow rate curves under $9.06 \times 10^{-3} \mu\text{m}^2$ to $0.78 \times 10^{-3} \mu\text{m}^2$ combination.

two vugs, the larger the differential pressure between them is; when the conductivity becomes stronger, the differential pressure is always small, in this case the two vugs are equivalent to one vug.

Comparison of the cumulative fluid production curve and the total drawdown curve of the primary vug indicates that when the conductivity of the fracture between the primary vug and the wellbore is poor and that connecting the primary vug to the secondary vug is strong, there is a linear relation between cumulative fluid production and total drawdown, like the characteristics of the single-vug reservoir; when the conductivity of the fracture between the primary vug and the wellbore is strong and that connecting the primary and secondary vugs is weak, the linear relation is no longer maintained.

b. Mathematical model

Supposing that the fluid in the vug is slightly compressible at constant C_L , and the primary and secondary vugs are different equipotential bodies, based on the fluid flow law between the primary vug and the fracture, the flow rate is:

$$q = \frac{k_1 A_1 p_1}{\mu L_1} \quad (4.84)$$

where, p_1 is relative pressure in the primary vug; k_1 is permeability of the fracture drilled; L_1 is length of the fracture drilled.

The elastic energy in the wellbore and the fracture is negligible, based on the law of elasticity, the flow rate is:

$$q = -V_1 C_L \frac{\partial p_1}{\partial t} - V_2 C_L \frac{\partial p_2}{\partial t} \quad (4.85)$$

where, V_1 is primary vug volume; V_2 is secondary vug volume; p_2 is relative pressure in the secondary vug.

Combined with the Darcy's law, the flow equation is derived as:

$$\frac{k_1 A_1 \left(\frac{\mu L_2}{k_2 A_2} V_2 C_L \frac{\partial p_2}{\partial t} + p_2 \right)}{\mu L_1} = -V_1 C_L \frac{\partial \left(\frac{\mu L_2}{k_2 A_2} V_2 C_L \frac{\partial p_2}{\partial t} + p_2 \right)}{\partial t} - V_2 C_L \frac{\partial p_2}{\partial t} \quad (4.86)$$

The solution of Eq. (4.86) is

$$p_2 = \beta_1 e^{-\lambda_1 t} + \beta_2 e^{-\lambda_2 t} \quad (4.87)$$

where,

$$\lambda_{1,2} = \frac{-b \pm \sqrt{b^2 - 4ac}}{2a}; a = \frac{V_2 C_L V_1 C_L \mu L_2}{k_2 A_2}; b = V_1 C_L + V_2 C_L + V_2 C_L \frac{k_1 A_1 L_2}{k_2 A_2 L_1}; c = \frac{k_1 A_1}{\mu L_1}$$

Substitute Eq. (4.87) in Eq. (4.85), the equations for variation of the primary vug relative pressure and the well flow rate with time are derived as:

$$p_1 = \beta_3 e^{-\lambda_1 t} + \beta_4 e^{-\lambda_2 t} \quad (4.88)$$

$$q(t) = \beta_5 e^{-\lambda_1 t} + \beta_6 e^{-\lambda_2 t} \quad (4.89)$$

where constant coefficients $\beta_1 \sim \beta_6$ are calculated based on initial conditions. As is known from Eqs. (4.88) and (4.89), the relative pressure in the primary and secondary vugs and the well flow rate exhibit double-exponential variation with time.

4.4.3.3 Flow law in multifracture and multivug medium

According to the flow laws in the single-vug-fracture and the double-vug-fracture models, both bottom hole pressure and production decline in an exponential mode—simple exponential decline in single-vug structure, and double-exponential decline in double-vug structure. Whether fracture or vug is drilled depends on the term of fracture conductivity in β and λ expressions. Based on the pressure superposition principle, the fluid flow law in a multifracture and multivug model meets:

$$q = \sum_{i=1}^N A_i e^{-\beta_i t} \quad (4.90)$$

$$P_1 = \sum_{i=1}^N B_i e^{-\beta_i t} \quad (4.91)$$

4.5 Applications and numerical experimental study

To validate the model study results have been applied in a typical fracture-vug reservoir. In addition, numerical simulation study on fracture-vug media has been conducted for the sake of making up for the deficiency of the physical modeling experiment in model complexity and test amount and opening a broader research space.

4.5.1 Application

From the above, fluids in a fracture-vug reservoir show a coupling flow of unrestricted flow and seepage flow. The coupling flow equation is:

$$\frac{\partial \rho \mathbf{u}}{\partial t} + \nabla \cdot (\rho \mathbf{u} \mathbf{u}) = -\nabla p - \nabla \cdot \boldsymbol{\tau} + \rho \mathbf{g} + \mathbf{f}_\delta - \left(\frac{\mu}{k} + \frac{C_o \rho}{2} |\mathbf{u}| \right) \mathbf{u}$$

where, \mathbf{f}_δ is superficial tension, ρ is fluid density, \mathbf{u} is flow velocity, $\boldsymbol{\tau}$ is shearing stress, t is time, μ is viscosity, k is permeability, p is pressure, \mathbf{g} is the acceleration of gravity, and C_o is compressibility.

The first half of the equation is the N–S equation, and the second half is the non-Darcy flow equation. When medium is unfilled vug, the N–S equation is adopted. When the medium is fracture and vug combination or fracture, the non-Darcy flow equation is adopted.

4.5.1.1 Production characteristics in isolated vug reservoirs

Take Well T207 in the Tahe Oilfield as an example. This well had been in a flowing state from 18 September 2002 to 15 August 2005, during which time a 6-mm choke, then a 5-mm choke, and then a 4-mm choke were used. Production time at a 6 mm choke was short. When the 5-mm choke was used, the tubing pressure and production rate dropped quickly, so it was replaced with a 4-mm choke which slackened the production decline. By 31 December 2007, 83,777 m³ oil and 16,401 m³ water had been produced in total; specifically, when a 4 mm choke was used for flow production, the cumulative well fluid and the tubing pressure satisfactorily met the linear relation (Fig. 4.56); in such a way, every time the tubing head pressure dropped by 1.00 MPa, about 6000 m³ fluid could be produced, and the elastic production rate was 0.60×10^4 m³/MPa.

During the flow production using 4-mm choke for 3 years, both daily oil rate and tubing pressure of Well T207 exhibited an exponential decline with time (Fig. 4.57), and the daily oil rate dropped from 120 m³/day to 15 m³/day. It was estimated that theoretical flow production using 4-mm choke would be 7514 m³ more oil from the well.

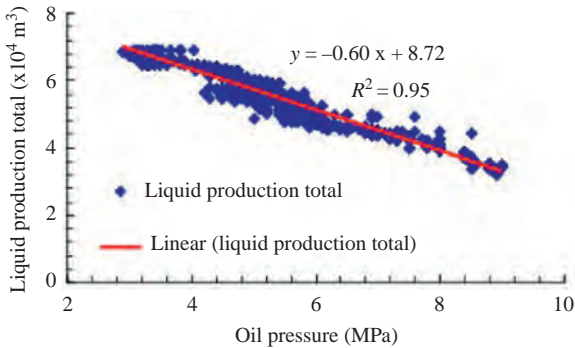


Figure 4.56 Tubing pressure versus cumulative fluid of well T207.

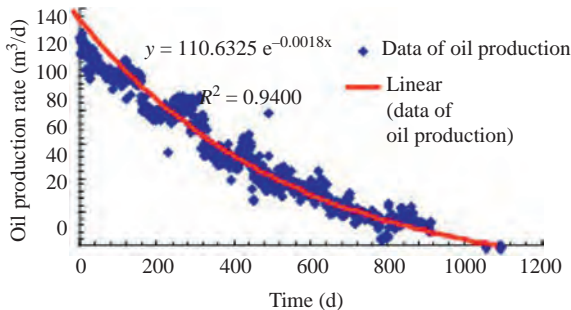


Figure 4.57 Daily oil rate curve of well T207.

In conclusion, the production equation and pressure drawdown equation and cumulative fluid–total pressure drawdown relation curve obtained from the isolated vug reservoir model at the condition of constant pressure production match well with field production performance, so they can be applied for production performance analysis and guiding the development of the isolated-vug reservoir.

4.5.1.2 Production characteristics in a near-vug fracture reservoir

In the reservoir containing large-scale vug (cavity) and near-vug fractures, water cut variation is typical, as has been found in some wells in the Tarim Basin. Here we take some wells as examples to analyze water cut variation in reservoirs containing single near-vug fracture and multiple near-vug fractures, respectively.

1. Single near-vug fracture

The reservoir of a well was believed to be a fracture-vug reservoir by well log interpretation. This well was put into production on 10 September 2006 and delivered an initial oil flow rate of 30 t/day at the early stage, but its water-free oil and gas producing period only lasted 228 days at 20 t/day. After water breakthrough, water cut rose fast (intermittent shut-in had ever been implemented, but it failed to take effect) and was finally stabilized at about 80% (Fig. 4.58: the production performance). On 10 July 2008, the well was shut in due to high water cut (water cut reached 90% after reopening). Because the water cut variation in the well is similar to the theoretical curve of the water cut variation in the high-dipped fracture model analyzed above, considering the well log interpretation results, the well might drill into the fracture near a vug.

2. Multiple near-vug fractures

The productivity of a well has been dropping since being put into production in April 2007. At the initial stage, the monthly average decline rate reached 18% (Fig. 4.59). After producing for 9 months, the daily oil rate dropped from 150 m³ to less than 30 m³, and the tubing pressure dropped from 30 MPa to 13 MPa. After shut in for half a year, the tubing pressure was only restored to 20 MPa, and the daily oil rate increased to 60 m³ but dropped quickly. The production performance (Fig. 4.59) indicates that the reserve controlled by the well is relatively small, and the supply capacity of the peripheral reservoir is limited.

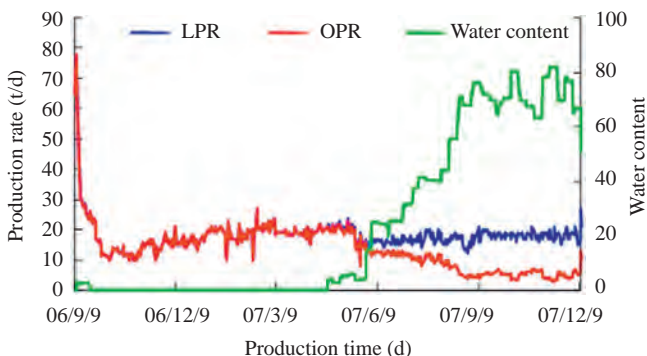


Figure 4.58 Production performance of a well drilling into fractures near a vug.

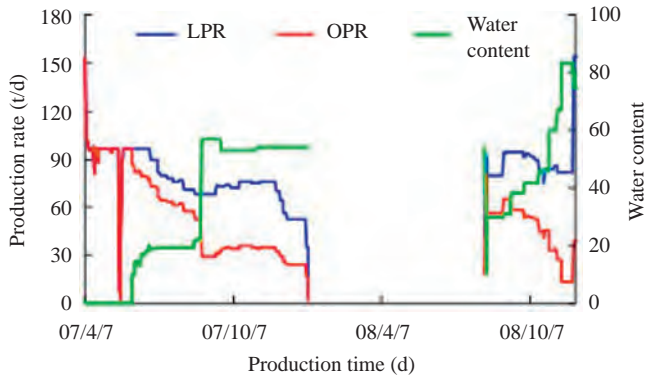


Figure 4.59 Production performance of a well drilling into multiple fractures near a vug.

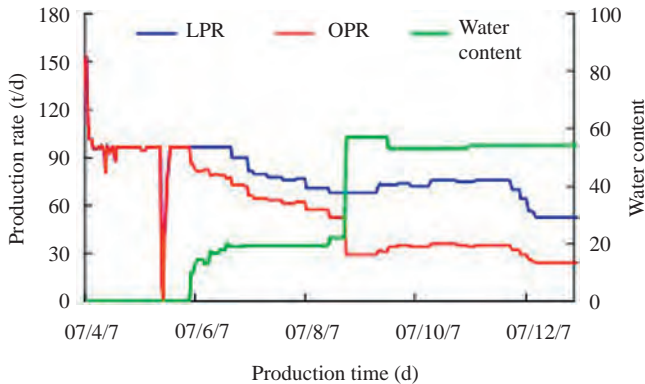


Figure 4.60 Water cut and fluid rate of a well drilling into multiple fractures near a vug.

The water cut variation of the well (Fig. 4.60) is consistent with that found in the model where fracture is drilled near a vug (like the model of double fractures), changing in a stepped manner. It may be concluded that the well is drilled into the fractures near a vug in a fracture-vug reservoir. This conclusion has been confirmed by the well log interpretation results.

4.5.1.3 Production characteristics in vug-fracture-vug reservoir

By 31 December 2008, a well put into production on 25 June 2006 produced a total of $10,378 \text{ m}^3$ oil, with a little water (10.51 m^3 water in total) and without any gas. During this period, the well was shut in four times due to low productivity, but the productivity decline was not well controlled, and the daily oil rate dropped from initially $160 \text{ m}^3/\text{day}$ to $10 \text{ m}^3/\text{day}$ (see the production performance in Figs. 4.61 and 4.62).

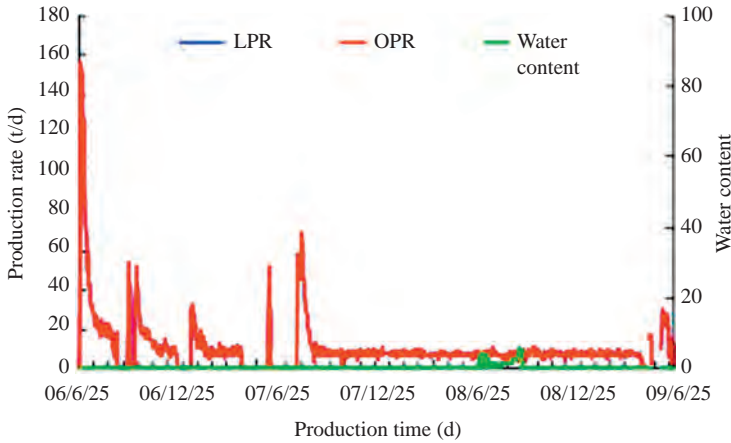


Figure 4.61 Daily fluid rate versus time.

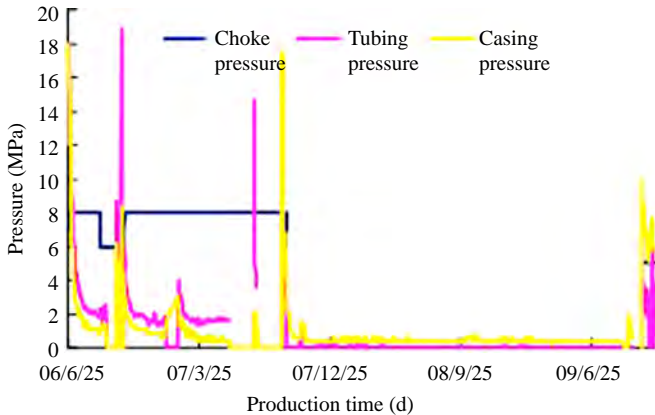


Figure 4.62 Tubing pressure and casing pressure versus time.

As shown in Figs. 4.61 and 4.62, the daily oil flow rate, tubing pressure, and casing pressure of the well dropped quickly at the early stage, but as the production went on, the decline rate gradually became slow. When the well was put into production again after shut in, the daily oil flow rate, tubing pressure, and casing pressure were restored to some extent, but they dropped again before long. Analysis of the reproduction data after every shut-in indicates that during reproduction, the daily oil flow rate and the casing pressure change with time in double exponential law (Figs. 4.63 and 4.64).

Based on the reproduction characteristics of the well after every shut-in, it is preliminarily determined that the well might be drilled into a multifracture and multivug reservoir where the conductivity of the fractures connecting to vugs is weak.

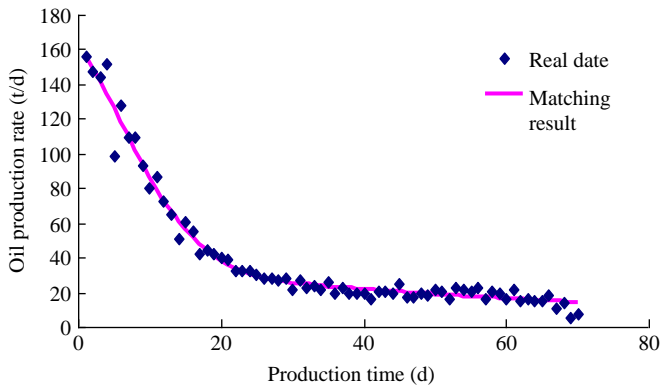


Figure 4.63 Daily oil flow rate fitting curve.

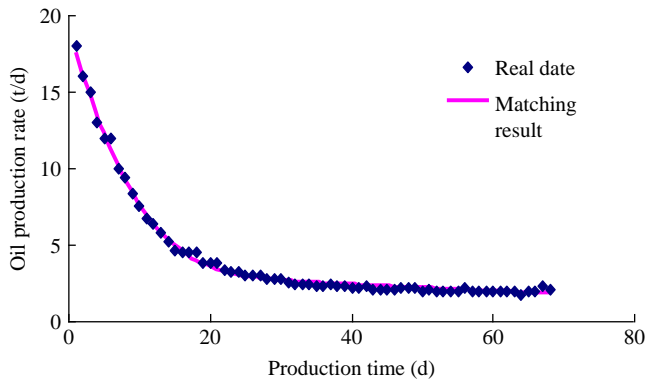


Figure 4.64 Casing pressure fitting curve.

4.5.2 Numerical experimental study

Limited by lab modeling conditions and technology, model complexity, test amount and flow regime, visualization of physical modeling experiments are restricted largely because of the lab modeling conditions and technology, therefore, it is necessary to carry out numerical experiments to supplement physical modeling of fracture-vug reservoirs.

4.5.2.1 One-phase flow regime in fracture-vug medium

To study the effect of vug diameter on one-phase flow regime in a fracture-vug model, a single-phase flow finite-element numerical simulation study was conducted on the single-fracture-vug model whose vug diameter is 5–15 mm, vug center is symmetric, and fracture aperture is 2 mm. The fluid was injected into the right inlet at 0.001 m/s and produced from the left outlet of the single-fracture-vug model (Fig. 4.65).

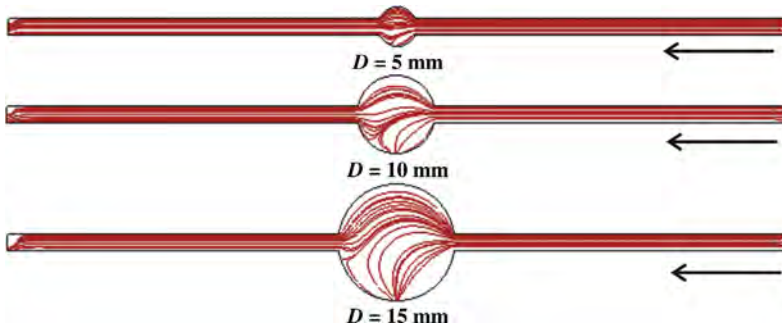


Figure 4.65 Flow regime in different vug diameter models.

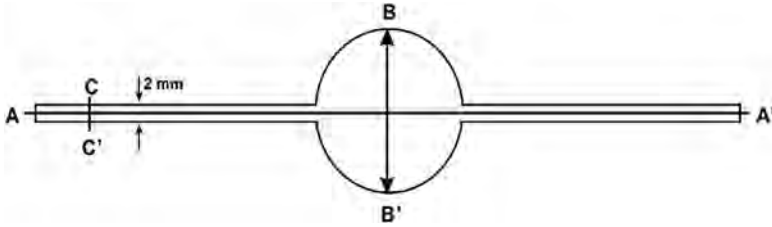


Figure 4.66 Location for taking values.

As shown in Fig. 4.65, the smaller the vug diameter, the smaller the bending of the streamline in the model towards the vug bottom, i.e., the smaller the effect of gravity on the flow regime in the vug.

To study the pressure characteristics in the flow direction in the model, the pressure values on the axial line (AA' in Fig. 4.66) parallel to the flow direction in the model were selected, and then relevant data were calculated in the pressure and location semilog coordinate system, as shown in Fig. 4.67.

As shown in Fig. 4.67, on the same horizontal axial line, the pressure variation is very small in the vug; at the same flow rate, the larger the vug diameter, the smaller the differential pressure between two ends of the model is, indicating the vug is favorable for fluid flow in the fracture-vug model.

To study the characteristics of the flow rate distribution perpendicular to the fracture direction in the vug, the flow rate data on the vertical axis (BB' in Fig. 4.66) were selected, where point B is at the vug top, point B' is at the vug bottom. Then the relevant data were figured out in the flow rate and location semilog coordinate system (Fig. 4.68). Due to the action of gravity, the flow rate distribution in the vug is no longer symmetric to axis AA'; the larger the vug diameter, the larger the effect of gravity on the flow rate in the vug is, and the larger the flow rate at the bottom of the vug.

To study the characteristics of the flow rate distribution perpendicular to the fracture direction inside the fracture, the flow rate data were selected in the place perpendicular to the flow direction (CC' in Fig. 4.66), where point C is at the top of

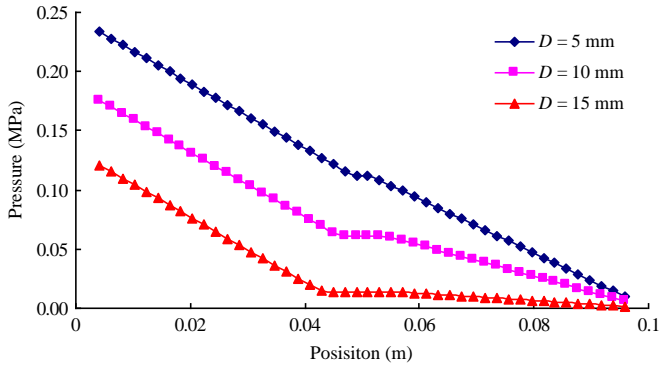


Figure 4.67 Pressure–location relation in the models with different vug diameters (AA’).

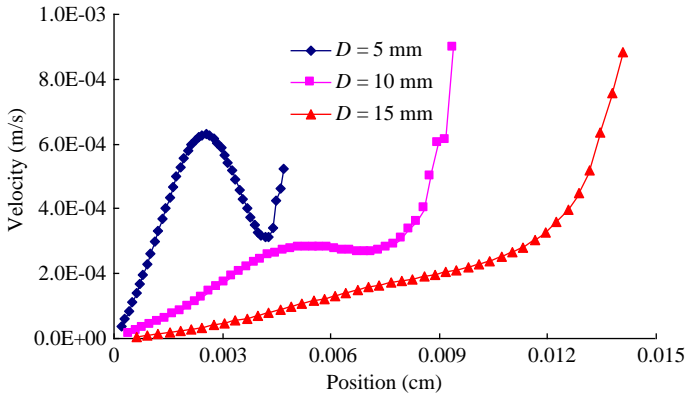


Figure 4.68 Flow rate and location relation in the vug (BB’).

the fracture, and point C’ is at the bottom of the fracture. Then, the relevant data were calculated in the flow rate and location semilog coordinate system (Fig. 4.69). As is observed in the figure, the flow rate distribution inside the fracture is symmetric to axis AA’, i.e., the gravity action is basically negligible in the fracture; the flow rate is the highest at the central position of the fracture (i.e., cross-point of axis AA’ and line CC’); at the same injection rate and at the same value-taking position, the flow rate values inside the fracture in the models with different vug diameters are equal, free from the effect of vug diameters.

4.5.2.2 Two-phase flow regime in fracture-vug medium

The water displacing oil process was simulated in four models with symmetric vugs of diameter ranging from 5 to 20 mm and fracture aperture of 2 mm, and at a mL/min injection rate. The interfaces were obtained at two-phase flow state for these models (Fig. 4.70).

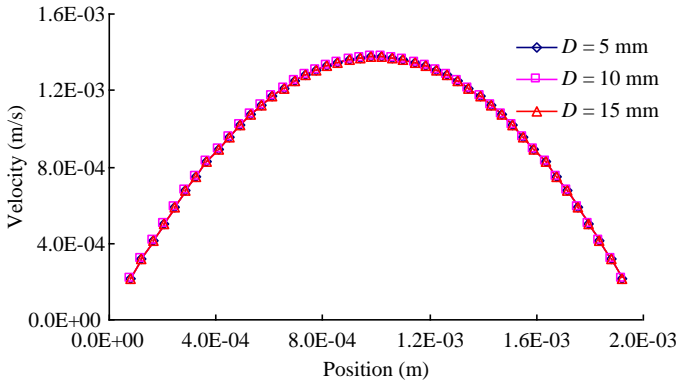


Figure 4.69 The relation between flow rate and vug location in the fracture (CC').

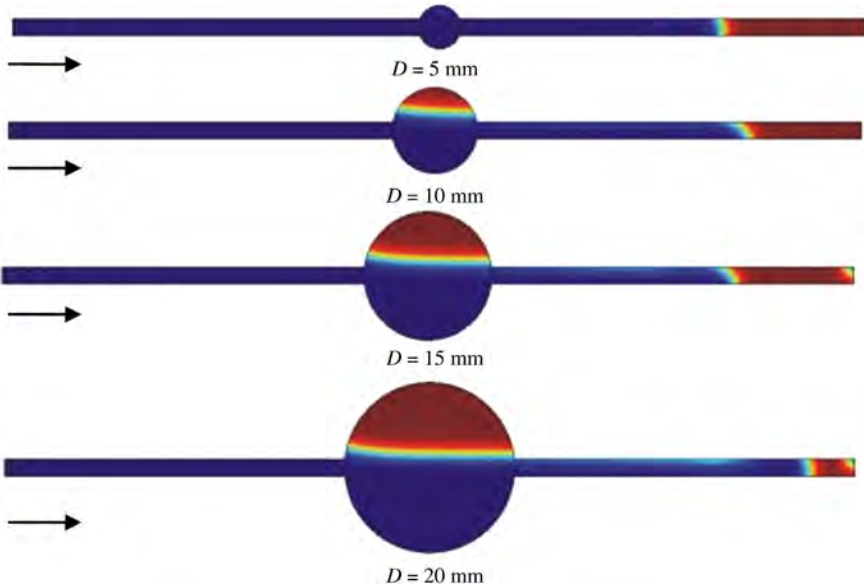


Figure 4.70 Biphasic dynamic interface in fracture-vug models.

As shown in Fig. 4.70, the water displacing oil in the fracture is a piston-like displacement, and the arc oil–water contact uniformly advances towards the exit; whereas in the vug, the contact is nearly a horizontal plane. After water enters the vug, it rapidly settles down to the bottom of the vug; as more water is injected continuously, the contact rises slowly, which does not stop until the fracture and vug juncture is submerged.

The recovery reflects the production status of oil in place of an oilfield, and it is a key indicator used to judge the development of the oilfield. The relation curve of recovery with injection pore volume was plotted (Fig. 4.71).

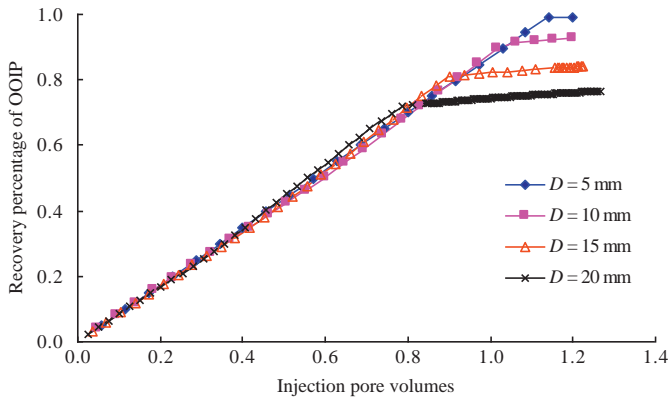


Figure 4.71 Recovery (%) versus injection pore volume.

As shown in Fig. 4.71, the ultimate recovery reduces with the increase of vug diameter; for instance, the ultimate recovery for the model with a 5-mm vug is up to 98.9%, but is only 76.6% from the model with a 20-mm vug. Because the vug is the main reservoir space in the models, the ultimate recovery depends on the oil recovery of the vug. The residual oil refers to the oil in the upper part of the vug that cannot be recovered after the fracture and vug juncture has been submerged by the oil–water contact. The larger the vug diameter, the more residual oil there is in the upper part of the vug, and the lower the ultimate recovery of the model is.

The injection–production differential pressure refers to the bottom hole pressure difference between water injector and oil producer, and it reflects the strength of oil displacement energy: the larger the pressure difference, the stronger the water displacing oil power is.

At an injection rate of 2 mL/min, the relationship between injection–production differential pressure and injection pore volume were built based on the models with different vugs (Fig. 4.72).

Figure 4.72 illustrate that the differential pressure between two ends of the model sweeps down gradually, and when the injected water is same, pressure difference is negatively correlated with vug diameter. As introduced in the single phase flow simulation, the flow resistance in the vug is very small, the pressure drawdown in the fracture-vug model mainly occurs in the fracture. Since the total length of the model is given, if the vug diameter increases, the fracture length must reduce, resulting in the decrease in the differential pressure.

For the example of vug diameter $D = 20$ mm, which means the characteristics of differential pressure changing with injection pore volume at a 2 mL/min injection rate was analyzed (Fig. 4.73), which shows that the differential pressure tends to decline on the whole, including five phases: prevug declining (A), in-vug stable (B), out-vug jumping (C), postvug declining (D) and postflooding constant (E) phases.

Let L represents the length of total flow path, L_i , $i = w, o$ represents the flow path length of water phase or oil phase, ρ_i , $i = w, o$ represents the fluid density of

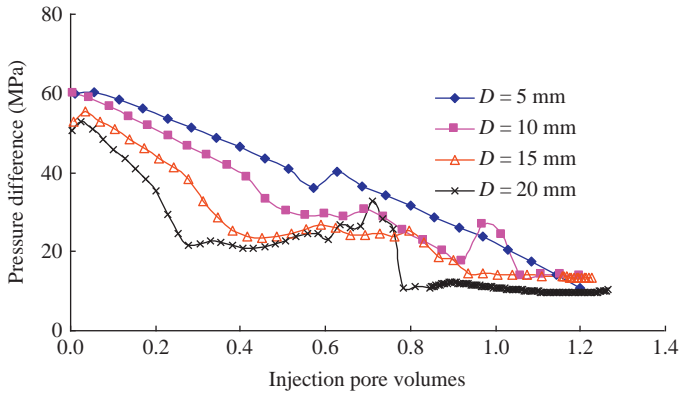


Figure 4.72 Injection–production differential pressure changes with injection pore volume.

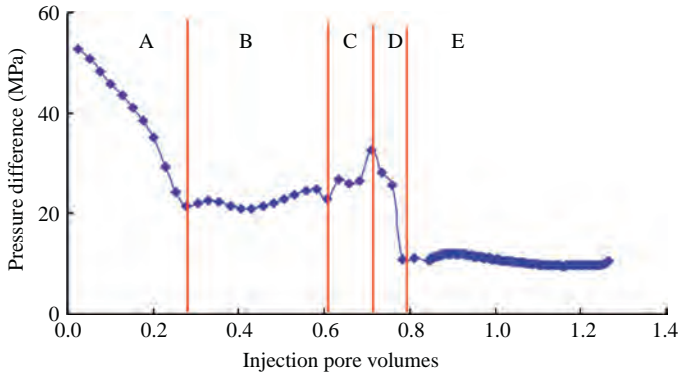


Figure 4.73 Differential pressure changes with injection pore volume ($D = 20$ mm model).

water phase or oil phase, and μ_i , $i = w, o$ represents the density of water phase or oil phase, referring to numerical calculation conditions, then

$$L_w + L_o = L; \mu_w < \mu_o; \rho_w > \rho_o \tag{4.92}$$

According to the numerical results, turbulence did not occur in a state of oil and water two-phase flow in the fracture-vug model. In addition, the fracture is represented by a 2-mm (diameter) circular pipe in the model, whereas the vug is represented by a 20-mm (inner diameter) sphere, where the fluid flow state is similar to that in the circular pipe in hydromechanics. Therefore, the circular pipe laminar flow frictional head loss Eq. (4.93) in hydromechanics can be used to analyze the pressure variation in the model:

$$h_f = \frac{32\mu Lv}{\rho g D^2} \tag{4.93}$$

where, D is the circular pipe diameter; h_f is the frictional head loss (corresponding to injection–production differential pressure). Therefore, at oil and water two-phase flow state, the head loss can be expressed as

$$h_{fi} = \frac{32\mu_i L_i v_i}{\rho_i g D_i^2}, \quad i = w, o \quad (4.94)$$

Analyzing Eq. (4.94), it is known that when oil and water flow through the circular pipes with the same diameter and length at the same flow rate, the head loss of the oil phase is larger than that of water phase. When oil and water flow simultaneously in the fracture-vug model, the head loss can be expressed as:

$$H_f = \frac{32\mu_w L_w v_w}{\rho_w g D_w^2} + \frac{32\mu_o L_o v_o}{\rho_o g D_o^2} \quad (4.95)$$

Next, Eq. (4.95) can be used to describe the pressure variation for different phases in the fracture-vug model.

1. Prevg declining differential pressure (Phase A): the oil–water contact is located in the fracture in front of the vug, and it gradually advances (Fig. 4.74).

In the course of flow,

$$v_w = v_o, \quad D_w = D_o, \quad L_o > L_w \quad (4.96)$$

The flow path of oil phase L_o gradually reduces, the flow path of water phase L_w gradually increases, and the oil and water two-phase flow path has the same rangeability. As is known from the above analysis, under the same conditions, the frictional head loss at the time of water phase flow is smaller than that at the time of oil phase flow, therefore, in this phase, the head loss reduced by oil phase flow is larger than that increased by water phase flow. Then as the oil–water contact advances in the fracture in front of the vug, the injection–production differential pressure gradually reduces.

2. In-vug stable differential pressure (Phase B): the oil–water contact advances upward horizontally in the vug (Fig. 4.75).

In the course of flow,

$$v_w = v_o, \quad D_w = D_o \quad (4.97)$$

The flow parameters of oil and water phases vary slowly, and the rangeability of oil and water two-phase frictional head loss is small, therefore, the overall head loss variation is relatively stable, in other words, the injection–production differential pressure is stable.



Figure 4.74 Prevg declining differential pressure.

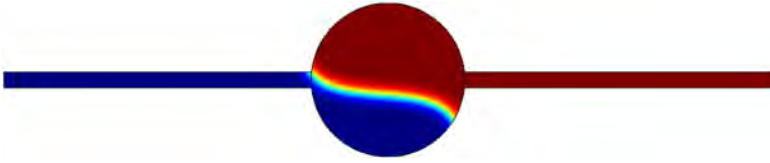


Figure 4.75 In-vug differential pressure smooth phase.

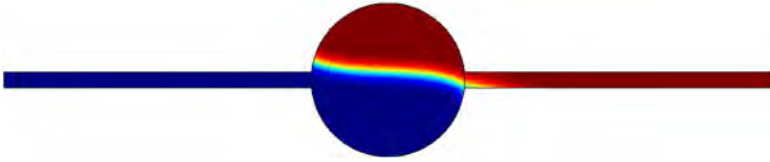


Figure 4.76 Out-vug jumping differential pressure.

3. Out-vug jumping differential pressure (Phase C): the oil–water contact is higher than the interface of vug and fracture behind it and starts to advance toward the fracture; such flow is the same as the variable-area flow in hydromechanics (Fig. 4.76). For a phase, the continuity equation is,

$$\rho_i v_{i1} \pi \left(\frac{D_{i1}}{2} \right)^2 = \rho_i v_{i2} \pi \left(\frac{D_{i2}}{2} \right)^2, \quad i = w, o \quad (4.98)$$

where, D_{i1} and D_{i2} represent the pipe diameters of current and next slot, respectively, then, the current flow rate is expressed as:

$$v_{i2} = \left(\frac{D_{i1}}{D_{i2}} \right)^2 v_{i1}, \quad i = w, o \quad (4.99)$$

As time goes on, the flow cross-section of one phase gradually reduces, and its flow rate v_i gradually increases. From the frictional head loss Eq. (4.99), for a phase, when the flow path length is fixed, the pipe diameter D_i reduces, the flow rate v_i increases, then, its frictional head loss increases, and the total frictional head loss H_f also increases, i.e., the injection–production differential pressure increases.

4. Postvug declining differential pressure phase (Phase D): the oil–water contact has completely entered the fracture behind the vug (Fig. 4.77).

In the course of flow,

$$v_w = v_o, \quad D_w = D_o, \quad L_o < L_w \quad (4.100)$$

The flow path of oil phase L_o gradually reduces, the flow path of water phase L_w gradually increases, and the oil and water two-phase flow path has the same rangeability. However, because under the same conditions, the frictional head loss at the time of water phase flow is smaller than that at the time of oil phase flow, in this phase, the head loss reduced by oil phase flow is larger than that increased by water phase flow. Therefore, as the oil-water contact advances in the fracture behind the vug, the injection–production differential pressure gradually reduces.

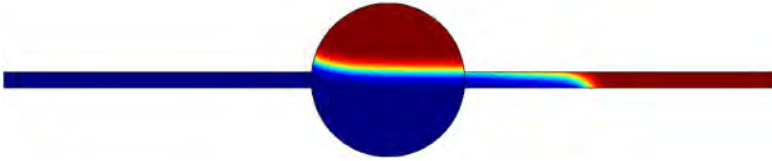


Figure 4.77 Postvug declining differential pressure.



Figure 4.78 Postflooding constant differential pressure.

5. Postflooding constant differential pressure (Phase E): besides the residual oil in the upper part of the vug, no oil can be produced out of the fracture-vug model, one-phase (water phase) flow occupies the model, and its frictional head loss remains unchanged (Fig. 4.78).

The numerical experiment shows that the effect of gravity is apparent in the fracture-vug model with larger vug diameter; on the same horizontal plane, pressure variation is small in the vug; at the same flow rate, the larger the vug diameter, the smaller the differential pressure between two ends of the model, meaning the vug is favorable for fluid flow; in the fracture, water displaces oil like a piston, showing as an arc oil–water contact uniformly advancing; residual oil—the oil left in the upper part of the vug after the oil–water contact surpassed the interface between the fracture and the vug—cannot be produced.

Numerical simulation of a fracture-vug carbonate reservoir

Symbols and units

Symbol	Parameter	International unit
V	Volume	m^3
φ	Porosity	Dimensionless
S_β	Saturation of β phase	Dimensionless
ρ	Density	kg/m^3
u	Rate	m/s
q	Oil yield	m^3/s
t	Time	s
p	Pressure	Mpa
k	Permeability	D
μ	Viscosity	cP
g	Acceleration of gravity	m^2/s
k_r	Relative permeability	Dimensionless
D	Depth	m
λ_B	Pressure gradient	MPa/m
x	Distance	m
b	Fracture aperture	m
r	Radius of circular pipe	m
d	Diameter of circular pipe	m
w	Fracture gap	m
β	Equivalent non-Darcy fow coefficient	m^{-1}
σ	Surface tension of fluid	N/m
F_v	Unit volumetric tension of fluid	N/m^3
α_β	Volumetric fraction	Dimensionless
κ	Mean curvature	$1 m^{-1}$
T	Temperature	$^\circ C$
τ	Fluid shear stress	N/m^2
V	Volume	m^3
M	Mass	kg
Q	Source-sink term	m^3/s
Γ	Diffusion coefficient	Dimensionless
C_2	Inertial resistance coefficient	Dimensionless
S	Skin factor	Dimensionless
C	Storage of wellbore	m^3/MPa
p_{wf}	Well flowing pressure	MPa
r_w	Radius of wellbore	m
h	Formation thickness	m
V_w	Volume of wellbore	m^3

Nomenclature

Subscripts

o	oil
w	water
G	gas
β	phase
D	dimensionless

Superscripts

n	current time
$n + 1$	next time

Abbreviations

E	extensive quantity
Ω	spatial zone
D	spatial zone
M	matrix
F	fracture
e	intensive quantity of E
H	M , F , and V , respectively
x_0	center of mass of a volume
L_1	limit of solution pore
L_2	limit of fracture
L_3	limit of vug
REV	representative element volume
n	unit vector perpendicular to surface
A_{ij}	area of the interface between units i and j
η_i	collection of unit j connecting to cavern i
R	residual error
ξ	random physical quantity
ψ	clipper
γ_{ij}	conductivity coefficient
Φ	fluid potential

A fracture-vug carbonate oil reservoir has a complex structure and different reservoir types and fluid flow mechanisms so that current numerical simulation methods and technology are unsuitable. Our study task and objectives on numerical simulation included establishment of a fluid flow mathematical model, obtainment of a numerical simulation solution, and development of numerical simulator.

Current numerical simulation methods are mainly suitable for porous and continuous reservoirs based on the continuity equation and the Darcy flow equation. Fracture-vug reservoirs contain not only fractures and vugs where fluid flow shows seepage characteristics, but also caverns where fluid flow shows free flowing-characteristics; therefore, multiphase coupling calculation for this complex fracture-vug

medium faces great difficulties. Based on the theory of coupling of continuous and discrete media, this chapter describes how to build a dynamic mathematical model and develop a numerical solution for equivalent multimediu and coupling models, and finally verifies the accuracy of the methods and models obtained.

5.1 Mathematical model

The mathematical model is fundamental to reservoir numerical simulation, which refers to the equations using mathematical language to describe the flow mechanics and physical chemistry phenomena of water/gas/oil in a reservoir. To solve the complexity of a fracture-vug carbonate reservoir, and meet the requirements of calculation speed and accuracy, two mathematical models were built: an equivalent multimediu mathematical model based on the matured dual-medium theory and expanded to cover multiphase flow in large karst caves (caverns), high-speed non-Darcy flow, N–S flow and other complex inter-medium channelling; and a coupling reservoir mathematical model based on the N–S flow equation and expanded to coupling flow of multiphase vug and seepage flows.

5.1.1 *Mathematical model for an equivalent multimediu reservoir*

5.1.1.1 *Equivalent multiple medium*

Since the 1960s, studies on fluid flow law and numerical simulation in dual-medium have made great progress. Barenblatt et al. proposed a dual-porosity model which assumes that the matrix is segmented by the fracture network, and they form a spatially superimposed isotropic continuity where fluid channeling will occur between two systems. The fracture system has high permeability but low reservoir capacity, while the matrix system shows high capacity but low permeability (Barenblatt et al., 1960). Warren and Root updated the Barenblatt model. In the new model, the reservoir capacity of the fracture system is not neglected, and it is assumed that homogenous, orthogonal, and interconnective fracture networks have been developed in the matrix system, which are distributed at equal intervals and the primary flowing axial is parallel to the fracture group on any azimuth (Warren and Root, 1963). Based on these assumptions, the Warren–Root model can provide parameters of fracture and matrix systems and the anisotropy of orthogonal systems can be taken into account. To accurately describe fluid exchange between fracture and matrix systems, Kazemi put forward an exchanging function related to pressure and pressure gradient (Kazemi, 1969). In addition, based on the Barenblatt model, Hill and Thomas proposed a dual-permeability model which not only considers the reservoir capability of matrix system but also the fluid flow in the matrix system (Hill and Thomas, 1985). These researches form a complete dual-medium theory.

Based on the dual-medium concept, different triple-medium models were developed (Closemann, 1975; Wu and Ge, 1983; Abdassah and Ershaghis, 1986;

Bai et al., 1933; Wu and Liu, 2004; Kang, 2006). Among these models the multi-medium model built by Pruess and Narasimhan (1985) assumes media are correlated and continuous; the triple-medium model for one-phase flow, built by Liu et al. (2003) and Camacho-Velazquez et al. (2005), incorporates the influence of vug on flow law in matrix by adding porosity into matrix. Wu and Liu (2004) and Kang (2006) consider a fracture-vug reservoir as a triple-medium system composed of matrix, fracture, and vug, and based on which different combinations of the three systems were proposed. However, all the multimediuim models are based on dual-medium theory, namely, all of them treat the fracture system as the primary flow channel and the matrix and vug systems are the primary reservoir space so that such issues as multiphase flow in a vug system, multimediuim. multiphase. high-speed, non-Darcy flow and gravity differentiation of multiphase fluids in large caves (caverns) are still unresolved.

In the Tahe oilfield, fracture-vug reservoirs (Figs. 5.1 and 5.2) consist of fractures, solution pores, vugs, and matrix (Zhang, 1999). These vugs and solution pores vary in shape and size (several millimeters to meters in diameter). Flow laws in them are different, involving seepage flow (Darcy flow and non-Darcy flow), one-dimensional (1D) pipe flow, 2D flow on fracture surface, 3D “vug flow” in unfilled vugs (caverns), and fluid exchange among different types of pore spaces.



Figure 5.1 Outcrop photo 1.



Figure 5.2 Outcrop photo 2.

5.1.1.2 Multimediuim representative elementary volume

REV refers to the minimum volume of a rock body where some nature does not vary with volume. In the study on fluid flow in rock bodies, REV is the basic unit to study continuous medium, and the prerequisite for applying mechanics research methods in continuous media. Only if there are permeable REVs can the permeability tensor be defined. By now, the study on REV in single porosity medium has made achievements, while for the complex fracture-vug medium, most studies were focused on the existence of REV, but little on division of REV.

Supposing in the fracture-vug medium, there is a volume $\Omega(x_0)$, x_0 is the particle of the volume $\Omega(x_0)$, E is the extensive quantity (mass, pore space, fluid mass per unit time, etc.), e is the intensive quantity (density, porosity, mass flux, etc.). $E(\Omega(x_0))$ represents the extensive quantity of $\Omega(x_0)$ and $e(x)$ represents the intensive quantity in location x , if the limit value does exist, then,

$$e(x_0) = \lim_{\Omega(x_0) \rightarrow \Omega_0(x_0)} \left(\frac{E(\Omega(x_0))}{\Omega(x_0)} \right) \tag{5.1}$$

and the variation of $E(\Omega(x))$ near x_0 is smooth, the limit value of $e(x)$ is

$$e(x_0) = \lim_{x \rightarrow x_0} e(x) \tag{5.2}$$

Thus, $\Omega_0(x_0)$ is called the REV of the complex medium, and the methodology of continuous medium is valid (Fig. 5.3).

In the scope of study, if the REV above exists, then the single porous medium method can be applied to study the complex medium.

In fact, because there are different types of pores which vary greatly in size and where multiphase fluids flow following different laws in a complex reservoir, single

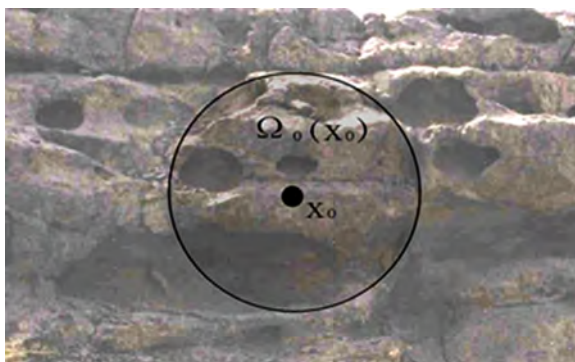


Figure 5.3 Schematic of a REV.

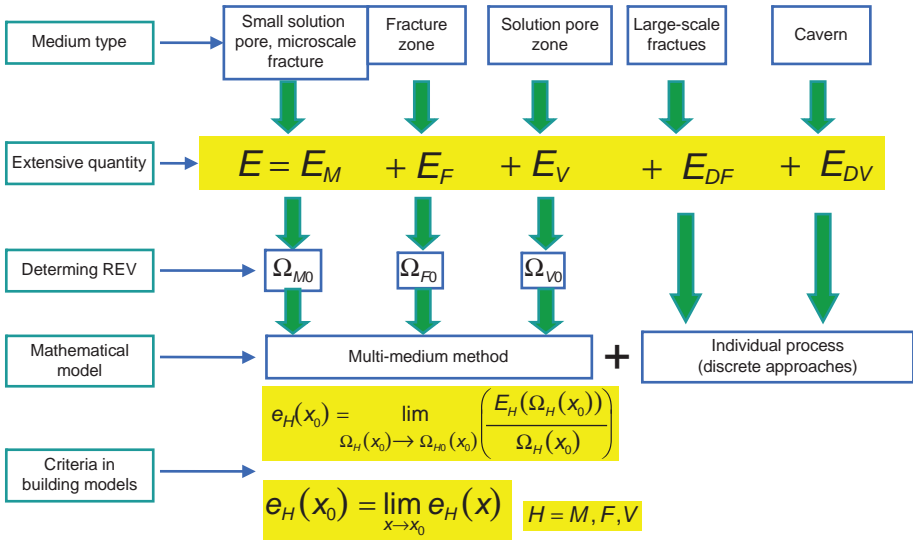


Figure 5.4 Schematic of multiple REV of the complex medium

REV may not exist in the scope of the study, so a multiple REV concept should be proposed (Fig. 5.4).

By space, divide the extensive quantity E of volume V in the complex medium into two parts, Ω and D :

$$E = E_\Omega + E_D \tag{5.3}$$

where E_Ω is the extensive quantity of space Ω ; E_D is the extensive quantity of space D ; $W = \Omega \cup D$. Space D is composed of m sets of nonintersective subdomain D_j , E_{D_j} is the extensive quantity of D_j .

$$E_D = \sum_{j=1}^m E_{D_j} \tag{5.4}$$

The space Ω is composed of three intersective subdomains Ω_H . Assuming H is M , F , and V , respectively, $E_{H=M,F,V}$ is the extensive quantity of M , F , and V , respectively, then,

$$E_\Omega = E_M + E_F + E_V \tag{5.5}$$

If in the scope of the study, the REV of intensive quantity e related to the extensive quantity E in the complex medium is not existent, the method of continuous medium is inapplicable.

If the validation of Eqs. (5.3)–(5.5) can be achieved through certain division, and it satisfies the following equations:

$$e_H(x_0) = \lim_{\Omega_H(x_0) \rightarrow \Omega_{H0}(x_0)} \left(\frac{E_H(\Omega_H(x_0))}{\Omega_H(x_0)} \right), \quad H = M, F, V \tag{5.6}$$

$$e_H(x_0) = \lim_{x \rightarrow x_0} e_H(x), \quad H = M, F, V \tag{5.7}$$

the REV of intensive quantity e_H corresponding to extensive quantity E_H exists, and the method of continuous medium is inapplicable. Eqs. (5.3)–(5.5) are the fundamental principles for building the multimedium model of a complex medium reservoir.

How to build the mathematical model of the complex medium:

1. set the scale limits of solution pores, fractures and vugs to be L_1, L_2, L_3 , respectively, and $L_1 < L_2 < L_3$;
2. divide the complex medium into three zones: microscale ($L < L_1$), middle scale ($L_1 \leq L < L_3$) and large scale ($L_3 < L$) according to the size (L) of the fractures and vugs in the medium (Fig. 5.5);
3. divide the middle-scale zone into three media: matrix M ($L < L_1$), fracture F ($L_1 \leq L < L_2$), and vug V ($L_2 \leq L < L_3$);
4. use a single porous medium model to simulate the microscale zone, and identify whether there is a REV_{micro} according to Eqs. (5.1) and (5.2). If not, go back to Step 1 and change the limit L_1 ;
5. use a multimedium model to simulate the middle-scale zone and identify REV_M (matrix), REV_F (fracture), and REV_V (vug) according to Eqs. (5.3)–(5.5). If they do not exist, then go back to Step 1 and adjust L_2 and L_3 ;
6. use a single porous medium model to simulate the large-scale zone. Now with the results from Steps 4 and 5, the numerical model for the complex medium should have been built.

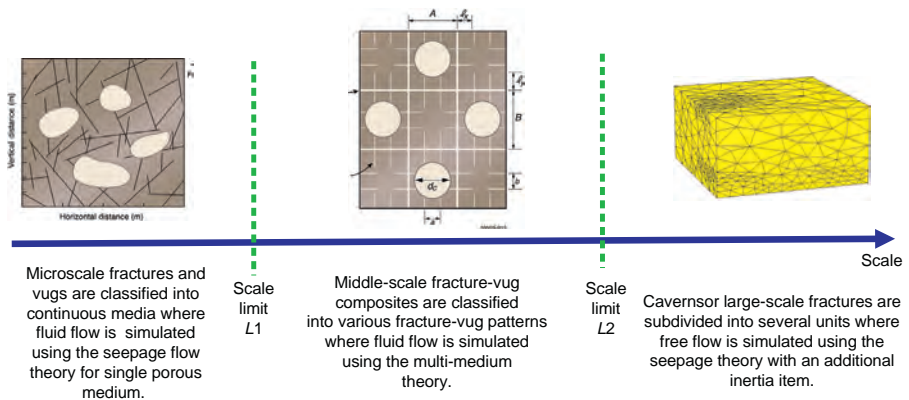


Figure 5.5 Division of study scale in the complex medium.

5.1.1.3 Equation of mass conservation of equivalent multimediuim reservoir

The model assumes that fluid flow is an isothermal process, and the medium contains oil, gas, and water three-phase fluid. In the reservoir, the oil component is completely in the oil phase, the water component is completely in the water phase, and the gas component is not only in the gas phase as free gas but also in the oil phase as dissolved gas. In the porous medium zone, affected by pressure, gravity, and capillary pressure, every phase flows following Darcy's law, but fluid flow in intra-vug and inter-vug is non-Darcy flow or pipe flow. The equation of mass conservation is used to describe the flow law of three phases in the medium containing pores, fractures, and vugs:

For the gas phase:

$$\frac{\partial}{\partial t} [\phi(S_o \bar{\rho}_{dg} + S_g \rho_g)] = -\nabla \cdot (\bar{\rho}_{dg} \vec{u}_o + \rho_g \vec{u}_g) + q_g \quad (5.8)$$

For the water phase:

$$\frac{\partial}{\partial t} (\phi S_w \rho_w) = -\nabla \cdot (\rho_w \vec{u}_w) + q_w \quad (5.9)$$

For the oil phase:

$$\frac{\partial}{\partial t} (\phi S_o \bar{\rho}_o) = -\nabla \cdot (\bar{\rho}_o \vec{u}_o) + q_o \quad (5.10)$$

where if β phase fluid ($\beta = g$ (gas), or w (water), or o (oil)) flows following Darcy's law, the flow rate is defined as the following:

$$\mathbf{u}_\beta = -\frac{k k_{r\beta}}{\mu_\beta} (\nabla p_\beta - \rho_\beta \mathbf{g} \nabla D) \quad (5.11)$$

In Eqs. (5.8)–(5.11), ρ_β is the density of β phase in oil reservoir conditions; $\bar{\rho}_o$ is the density of degassed crude oil in oil reservoir conditions; $\bar{\rho}_{dg}$ is the density of dissolved gas in oil reservoir conditions; ϕ is the effective porosity of the oil layer; μ_β is the viscosity of β phase; μ_β is the saturation of β phase; p_β is the pressure of β phase; S_β is the yield or injection per unit volume of β phase at oil reservoir condition; g is the acceleration of gravity; k is the absolute permeability of oil layers; $k_{r\beta}$ is the relative permeability of β phase; and D is reservoir depth.

As the controlling equation of triple-phase mass conservation, constraint and constitutive equations need to be added to Eqs. (5.8), (5.9), and (5.10); namely, to express the second-order variables and parameters as the function of basic primary mechanic variables. Capillary pressure and relative permeability can frequently be expressed as a function of fluid saturation; the density and viscosity of oil, gas, and water can be expressed as a function of fluid pressure.

In a multimediuim numerical model, complex medium is divided into several blocks in the spatial domain. Each block is comprised of unit vug (V), unit fracture (F), and unit matrix (M) (Fig. 5.6). The multiphase flow occurring in each block is described by the fluid flow among V , F , and M ; the multiphase fluid flow between blocks i and j is described by the flow between V_i and V_j , and that between F_i and F_j . The fluid flow between different units can be considered as seepage or pipe flow, Darcy or non-Darcy flow.

The flow law in a fracture-vug carbonate reservoir is complex (Fig. 5.7), involving seepage flow (Darcy flow, high-speed non-Darcy flow), 1D pipe flow,

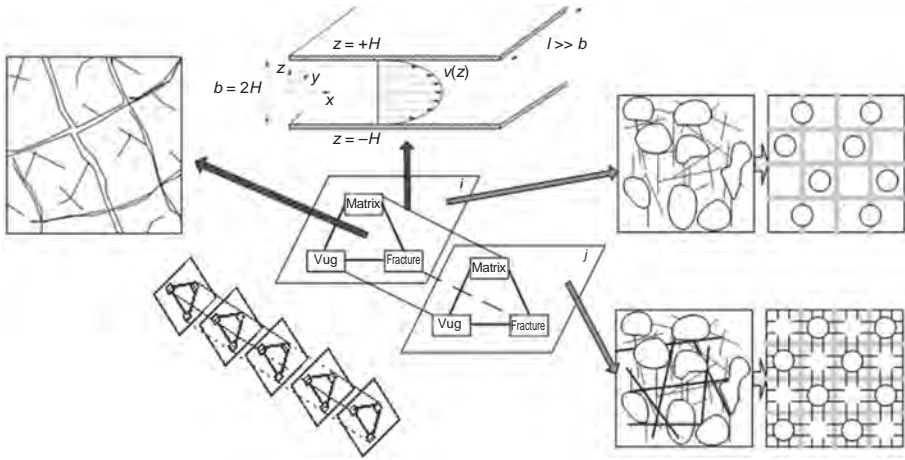


Figure 5.6 Fluid flow inside block and among blocks in a multimediuim model.

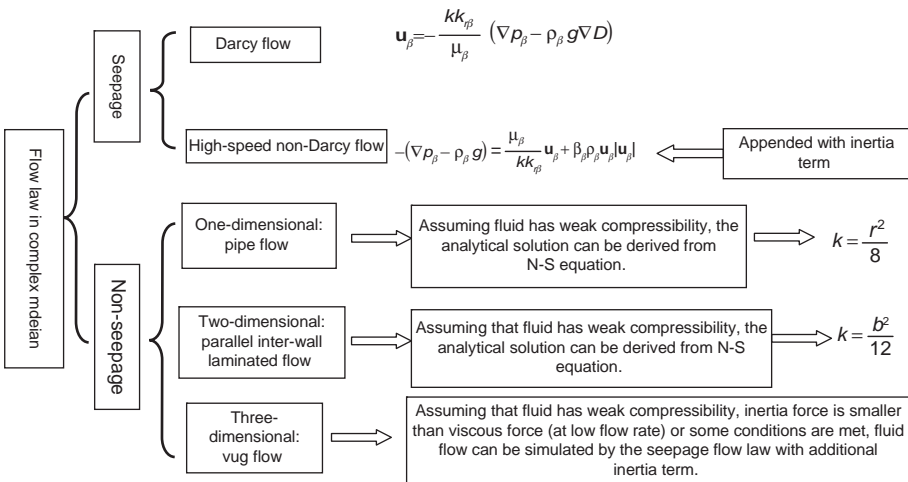


Figure 5.7 Flow simulation methods in a multimediuim model.

2D flow on fracture plane, and 3D “vug flow” in the unfilled vugs (Fig. 5.7). The flow in a channeling of a reservoir unit is described in Section 5.1.1.4.

5.1.1.4 Pipe flow, fracture flow, and high-speed Darcy flow

Let us consider the 2D stable flow in the narrow space between two parallel straight walls. Assuming that the flow is laminated and the fluid is minor compressible, based on the N–S equation, we can derive:

$$-\nabla p + \mu \nabla^2 u_x = 0 \quad (5.12)$$

where p is the fluid pressure, and μ is the viscosity.

The flow rate through unit width between the straight walls in unit time is given by:

$$q = \int_{-b}^b u_x dy = -\frac{b^3}{12\mu} \frac{dp}{dx} \quad (5.13)$$

where b is the distance between two parallel straight walls.

Likewise, the flow rate under pipe flow conditions in unit time can be derived:

$$q = \int_0^R 2\pi r u_x dr = -\frac{\pi r^4}{8\mu} \frac{dp}{dx} \quad (5.14)$$

where r is the radius of pipe.

Comparison of Eqs. (5.13) and (5.14) with Darcy’s law indicates that Darcy’s law is still effective for pipe flow and inter-parallel-wall flow. Eqs. (5.13) and (5.14) are, respectively, equivalent to the cases of permeability $k = \frac{b^2}{12}$ and $k = \frac{r^2}{8}$ in Darcy’s law.

For 1D pipe flow and 2D fracture flow, the multimedium numerical model above is applicable. The flow simulation between units can be calculated according to the following expressions.

For 1D pipe flow:

$$\gamma_{ij} = \frac{\pi r^4}{8(d_i + d_j)} \quad (5.15)$$

For 2D fracture flow:

$$\gamma_{ij} = \frac{wb^3}{12(d_i + d_j)} \quad (5.16)$$

where w is the aperture of fracture, b is the width of fracture, and r is the radius of pipe.

Darcy's law of multiphase fluid in porous medium is:

$$\mathbf{u}_\beta = -\frac{kk_{r\beta}}{\mu_\beta}(\nabla p_\beta - \rho_\beta \mathbf{g} \nabla D) \quad (5.17)$$

For multiphase 1D pipe flow and 2D fracture flow, Eq. (5.17) is:

$$\mathbf{u}_\beta = -\frac{kS_\beta}{\mu_\beta}(\nabla p_\beta - \rho_\beta \mathbf{g} \nabla D) \quad (5.18)$$

The fluidity can be calculated according to the following expression:

$$\lambda_{\beta,ij+1/2} = \left(\frac{\rho_\beta S_\beta}{\mu_\beta} \right)_{ij+1/2} \quad (5.19)$$

With the increase of flow rate in 1D pipe flow and 2D fracture flow, the assumption of laminated flow will not be valid and turbulent flow will occur. The Forchheimer law of high-speed non-Darcy flow is used to describe one-phase fluid in porous medium:

$$-\nabla p = \frac{\mu}{k} u + \beta \rho u^2 \quad (5.20)$$

where β is the coefficient of equivalent non-Darcy flow in m^{-1} .

Let us combine Eq. (5.17) with Eq. (5.20), then the Forchheimer law of one-phase high-speed non-Darcy flow is extended to solve the problem of multiphase high-speed non-Darcy flow (Evans and Evans, 1988):

$$-\left(\nabla p_\beta - \rho_\beta \mathbf{g}\right) = \frac{\mu_\beta}{kk_{r\beta}} \mathbf{u}_\beta + \beta_\beta \rho_\beta \mathbf{u}_\beta |\mathbf{u}_\beta| \quad (5.21)$$

where β_β is the coefficient of equivalent non-Darcy flow for fluid β under multiphase condition, and the unit is m^{-1} .

5.1.1.5 Multiphase vug (cave) flow

First we consider one-phase vug flow. According to the law of conservation of mass, the continuous equation of one-phase flow is derived:

$$\frac{\partial \rho}{\partial t} + \nabla \cdot (\rho \mathbf{u}) = 0 \quad (5.22)$$

where ρ is the density of fluid, \mathbf{u} is flow rate.

According to the law of conservation of momentum, the flow equation is derived:

$$\frac{\partial(\rho\mathbf{u})}{\partial t} + \nabla \cdot (\rho\mathbf{u}\mathbf{u}) = \nabla \cdot \boldsymbol{\sigma} + \mathbf{F}_v \quad (5.23)$$

where $\boldsymbol{\sigma}$ is the stress of fluid, \mathbf{F}_v is the force per volume in flow field;

From Eqs. (5.22) and (5.23), it is derived that:

$$\rho \frac{\partial \mathbf{u}}{\partial t} + \rho(\nabla \cdot \mathbf{u})\mathbf{u} = \nabla \cdot \boldsymbol{\sigma} + \mathbf{F}_v \quad (5.24)$$

In Eq. (5.24), the term of resistance caused by filling is appended to:

$$\rho \frac{\partial \mathbf{u}}{\partial t} + \rho(\nabla \cdot \mathbf{u})\mathbf{u} = \nabla \cdot \boldsymbol{\sigma} + \mathbf{F}_v - \frac{\mu}{k} \mathbf{u} \quad (5.25)$$

where μ is the viscosity, and k is the permeability.

Assuming the fluid is compressible, and then we have:

$$\rho \frac{\partial \mathbf{u}}{\partial t} + \rho \left(\nabla \cdot \left(\frac{\mathbf{u}^2}{2} \right) - \mathbf{u} \times (\nabla \times \mathbf{u}) \right) = -\nabla p + \mathbf{F}_v + \mu \nabla^2 \mathbf{u} - \frac{\mu}{k} \mathbf{u} \quad (5.26)$$

Considering the stable flow with no eddy, then we derive:

$$-(\nabla p - \mathbf{F}_v) = \frac{\mu}{k} \mathbf{u} + \left(\frac{\rho}{2} \nabla \mathbf{u}^2 - \mu \nabla^2 \mathbf{u} \right) \quad (5.27)$$

If Eq. (5.28) is valid,

$$\left(\frac{\rho}{2} \nabla \mathbf{u}^2 - \mu \nabla^2 \mathbf{u} \right) \approx \beta \rho \mathbf{u} |\mathbf{u}| \quad (5.28)$$

then the flow Eq. (5.24) can be simplified as Eq. (5.29):

$$-(\nabla p - \mathbf{F}_v) = \frac{\mu}{k} \mathbf{u} + \beta \rho \mathbf{u} |\mathbf{u}| \quad (5.29)$$

Eq. (5.29) is identical to the Forchheimer law of high-speed non-Darcy flow, where β is the coefficient of non-Darcy flow.

It can be seen that, if the condition of Eq. (5.28) is met, then the Forchheimer law of 3D high-speed non-Darcy flow can be employed to approximately simulate vug flow.

For the multiphase case, the dual-flow model is used to describe the flow in a vug. Two types of immiscible fluids are different components. Each of them is considered as a continuous medium filled in the flow field, on which any point is simultaneously occupied by two components which interact with each other.

According to the law of conservation of mass, the continuous equation of β phase ($\beta = o$ (oil), or $\beta = w$ (water)) can be derived:

$$\frac{\partial \alpha_\beta \rho_\beta}{\partial t} + \nabla \cdot (\alpha_\beta \rho_\beta \mathbf{u}_\beta) = 0 \quad (5.30)$$

where α_β is the volume fraction of β phase, ρ_β is the density of β phase, \mathbf{u}_β is the flow rate of β phase.

According to the law of conservation of momentum, the equation of motion of β phase can be derived:

$$\frac{\partial}{\partial t} (\alpha_\beta \rho_\beta \mathbf{u}_\beta) + \nabla \cdot (\alpha_\beta \rho_\beta \mathbf{u}_\beta \mathbf{u}_\beta) = -\alpha_\beta \nabla \cdot \boldsymbol{\sigma} + \alpha_\beta \mathbf{F}_v - \sum_l \alpha_\beta \mathbf{F}_{\beta l} \quad (5.31)$$

where $\boldsymbol{\sigma}$ is the stress of fluid, \mathbf{F}_v is the force per volume on fluid field, \mathbf{F}_β is the force applied on β phase by another phase, and can be expressed as the function of the relative flow rate of β phase ($\mathbf{u}_\beta - \mathbf{u}_\gamma$) (to another phase):

$$\mathbf{F}_\beta = f(\mathbf{u}_\beta - \mathbf{u}_\gamma) \quad (5.32)$$

The volume fractions of all phases have relations as follows:

$$\sum \alpha_\beta = 1 \quad (5.33)$$

After adding the term of resistance caused by fillers to Eq. (5.31), we can derive:

$$\frac{\partial}{\partial t} (\alpha_\beta \rho_\beta \mathbf{u}_\beta) + \nabla \cdot (\alpha_\beta \rho_\beta \mathbf{u}_\beta \mathbf{u}_\beta) = -\alpha_\beta \nabla \cdot \boldsymbol{\sigma} + \alpha_\beta \mathbf{F}_v - \sum_l \alpha_\beta \mathbf{F}_{\beta l} - \frac{\mu_\beta}{kk_{r\beta}} \mathbf{u}_\beta \quad (5.34)$$

Similarly as for one-phase flow, assuming fluid is compressible and at stable state with eddy, if the following expression is valid,

$$\left(\frac{\alpha_\beta \rho_\beta}{2} \nabla u_\beta^2 - \mu_\beta \nabla^2 \mathbf{u}_\beta \right) \approx \beta_\beta \rho_\beta \mathbf{u}_\beta |\mathbf{u}_\beta| \quad (5.35)$$

then the flow Eq. (5.34) can be simplified as Eq. (5.36):

$$-(\nabla \alpha_\beta \rho_\beta - \alpha_\beta \mathbf{F}_{v\beta}) = \frac{\mu_\beta}{kk_{r\beta}} \mathbf{u}_\beta + \beta_\beta \rho_\beta \mathbf{u}_\beta |\mathbf{u}_\beta| \quad (5.36)$$

where μ_β is the viscosity of β phase fluid.

It is concluded that multiphase vug flow can be approximately simulated by introducing the seepage law with an additional inertia term (the Forchheimer law of

3D high-speed non-Darcy flow) on the prerequisite that the condition of Eq. (5.35) must be valid.

5.1.1.6 Fluid flow interface in caverns

Eq. (5.34) can be used to describe the multiphase flow in caverns. For minor compressible fluid:

$$\begin{aligned} \alpha_\beta \rho_\beta \frac{\partial \mathbf{u}_\beta}{\partial t} + \alpha_\beta \rho_\beta \left(\nabla \left(\frac{u_\beta^2}{2} \right) - \mathbf{u}_\beta \times (\nabla \times \mathbf{u}_\beta) \right) \\ = -\alpha_\beta \nabla p + \alpha_\beta \mathbf{F}_v + \alpha_\beta \mu_\beta \nabla^2 \mathbf{u}_\beta - \sum_l \alpha_\beta F_{\beta l} - \frac{\mu_\beta}{kk_{r\beta}} \mathbf{u}_\beta \end{aligned} \quad (5.37)$$

At a stable flow state without eddies, the flow rate gradient and the variance of flow rate with time is small enough to satisfy the following expressions:

$$\begin{aligned} \alpha_\beta \rho_\beta \frac{\partial \mathbf{u}_\beta}{\partial t} + \alpha_\beta \rho_\beta \left(\nabla \left(\frac{u_\beta^2}{2} \right) - \mathbf{u}_\beta \times (\nabla \times \mathbf{u}_\beta) \right) \\ = \alpha_\beta \mu_\beta \nabla^2 \mathbf{u}_\beta - \sum_l \alpha_\beta F_{\beta l} - \frac{\mu_\beta}{kk_{r\beta}} \mathbf{u}_\beta \end{aligned} \quad (5.38)$$

then the expression can be approximated as:

$$\nabla p - \rho_\beta \mathbf{g} = \mathbf{0} \quad (5.39)$$

Eq. (5.39) means that the immiscible multiphase fluid in caverns is in a static equilibrium and gravity separation state.

The fluid flow resistance in caverns is far smaller than that in the surrounding porous medium zone. If it is reasonable that the immiscible multiphase fluid can reach equilibrium instantaneously and separate by gravity, in the time step of the fluid flow in the porous-medium zone, the fluid flow rate gradient and variation with time is small enough to ensure that Eq. (5.39) is valid.

5.1.2 Coupling mathematical reservoir model

To accurately simulate the fluid flow in vugs and fractures and the coupling flow among vugs, fractures, and matrix in a fracture-vug reservoir, a mathematical model for simulating the coupling flow of immiscible water–oil two-phase fluid in multiple zones has been established based on the basic equation of continuous mechanics and coupling of N–S and seepage flows. In the model the flow on

medium interface is considered as a jumping continuity, and each fluid is identified by an indicator function.

5.1.2.1 Continuity equation

For each phase, the continuity equation is:

$$\frac{\partial(S_w\rho_w)}{\partial t} + \nabla \cdot (S_w\rho_w\mathbf{u}) = 0 \quad (5.40)$$

$$\frac{\partial(1-S_w)\rho_o}{\partial t} + \nabla \cdot ((1-S_w)\rho_o\mathbf{u}) = 0 \quad (5.41)$$

where ρ_o is the density of oil and water, ρ_w is the density of water, \mathbf{u} is the seepage rate, S_w is the saturation of water phase.

The continuity equation indicates that the mass of fluid within an enclosed zone can only be changed by the flow through the boundary of the zone, namely the boundary mass flux which is defined as the flow through unit area in unit time.

Let us define density ρ as:

$$\rho = S_w\rho_w + (1-S_w)\rho_o \quad (5.42)$$

Thereby we can derive:

$$\frac{\partial\rho}{\partial t} + \nabla \cdot (\rho\mathbf{u}) = 0 \quad (5.43)$$

The indicator function is defined as the volume fraction S of β phase fluid:

$$S_\beta(x, t) = \frac{\text{Volume of } \beta \text{ phase fluid}}{\text{Total volume of controlling body}} \quad (5.44)$$

$$S_\beta(x, t) = \begin{cases} 1 & (x, t) \text{ In } \beta \text{ phase} \\ 0 & (x, t) \text{ In other phases} \\ 0 < S_\beta < 1 & (x, t) \text{ In water and oil transitional zone} \end{cases} \quad (5.45)$$

The indicator function in the whole zone is continuously derivable. This not only guarantees the continuity of physical properties in the model, but also it can be applied to the formula for calculating interface curvature.

It can be derived from Eq. (5.43):

$$\frac{\partial\rho}{\partial t} + \mathbf{u} \cdot \nabla\rho + \rho\nabla \cdot \mathbf{u} = 0 \quad (5.46)$$

$$\nabla \cdot \mathbf{u} = -\frac{1}{\rho} \left(\frac{\partial\rho}{\partial t} + \mathbf{u} \cdot \nabla\rho \right) = -\frac{D\ln\rho}{Dt} \quad (5.47)$$

5.1.2.2 Momentum equation

$$\frac{\partial \rho \mathbf{u}}{\partial t} + \nabla \cdot (\rho \mathbf{u} \mathbf{u}) = -\nabla p - \nabla \cdot \boldsymbol{\tau} + \rho \mathbf{g} + \mathbf{f}_\delta - \left(\frac{\mu}{k} + \frac{C_o \rho}{2} |\mathbf{u}| \right) \mathbf{u} \quad (5.48)$$

where \mathbf{f}_δ is surface tension, ρ is fluid density, \mathbf{u} is flow rate, $\boldsymbol{\tau}$ is shear stress, t is time, μ is viscosity, k is permeability, p is pressure, \mathbf{g} is acceleration of gravity, C_o is compression coefficient.

By the continuous surface force model (CSF) and combined with the volume of fluid (VOF) model, it can be derived that:

$$\mathbf{f}_\delta = \int \delta(\mathbf{x} - \mathbf{x}_f) \sigma \kappa \mathbf{n} ds \quad (5.49)$$

In the expression, κ is mean interface curvature, σ is surface tension coefficient, \mathbf{n} is unit vector perpendicular to the surface, $\delta(\mathbf{x} - \mathbf{x}_f)$ is the Dirac function, \mathbf{x}_f is the instantaneous location of interface, ds is the area of interface.

The expressions of \mathbf{n} and κ are, respectively, the following:

$$\mathbf{n} = \frac{\nabla S_w}{|\nabla S_w|} \quad (5.50)$$

$$\kappa = -\nabla \cdot \left(\frac{\nabla S_w}{|\nabla S_w|} \right) \quad (5.51)$$

The gradient of S_w , always from oil phase to water phase, is a continuous function, and always zero on any location outside transitional zone.

Therefore, the term of the Dirac function is equivalent to it:

$$\nabla S_w = \int \delta(\mathbf{x} - \mathbf{x}_f) \mathbf{n} ds \quad (5.52)$$

Thus,

$$\mathbf{f}_\delta = \sigma \kappa \nabla S_w \quad (5.53)$$

This is the consecutive interface model proposed by Brackbill. It contains two features: it defines the indicator function, by which the boundary normal is defined; it assumes that the pressure on the interface originates from the transition zone of the indicator function because it is 0 or 1, and its gradient is 0 outside the transition zone, so the pressure term does not exist. The smoothness of distribution of force on the interface is similar to that of indicator functions. The value and direction of numerical integration for the force are equivalent to that of true surface tension.

Where $\kappa > 0$ means water phase on the concave of the interface, $\kappa < 0$ means oil phase on the concave of the interface. $\kappa \nabla S$ always points to the concave of the interface.

In a fracture-vug reservoir, some zones contain fluid only (vugs), others are composed of porous medium. Since the last term in the equation of momentum means the effect of porous medium on fluid, it is not required in the equation of momentum for full fluid zones (vugs).

5.1.2.3 Equation of state

For the isothermal and compressible model, its equation of state describes the effect of pressure on density.

Compressible coefficient is defined as:

$$C_T = -\frac{1}{V} \left(\frac{\partial V}{\partial p} \right)_T = \frac{1}{\rho} \left(\frac{\partial \rho}{\partial p} \right)_T \quad (5.54)$$

where C_T is compressible coefficient, V is fluid volume of, p is pressure, ρ is fluid density.

5.1.2.4 Equation of indicator function

From Eq. (5.40), we get

$$\frac{\partial S_w \rho_w}{\partial t} + \nabla \cdot (S \rho_w \mathbf{u}) = 0 \quad (5.55)$$

After derivation, we get

$$\frac{\partial S_w}{\partial t} + \mathbf{u} \cdot \nabla S_w = S_w (1 - S_w) \frac{Dp}{Dt} \left(\frac{C_o}{\rho_o} - \frac{C_w}{\rho_w} \right) \quad (5.56)$$

Eq. (5.56) is the transfer equation of the indicator function for minor compressible fluid, where S_w is water saturation, \mathbf{u} is flow rate, p is pressure, ρ_o is the density of oil, ρ_w is the density of water, C_o is the compressible coefficient of oil, and C_w is the compressible coefficient of water.

5.1.2.5 Mathematical model

$$\frac{\partial \rho}{\partial t} + \nabla \cdot (\rho \mathbf{u}) = 0$$

$$\frac{\partial \rho \mathbf{u}}{\partial t} + \nabla \cdot (\rho \mathbf{u} \mathbf{u}) = -\nabla p - \nabla \cdot \boldsymbol{\tau} + \rho \mathbf{g} - \sigma \nabla \cdot \left(\frac{\nabla S}{|\nabla S|} \right) \nabla S - \left(\frac{\mu}{\alpha} + \frac{C_o \rho}{2} |\mathbf{u}| \right) \mathbf{u}$$

$$\frac{\partial S_w}{\partial t} + \mathbf{u} \cdot \nabla S_w = S_w (1 - S_w) \frac{Dp}{Dt} \left(\frac{C_o}{\rho_o} - \frac{C_w}{\rho_w} \right)$$

(5.57)

$$\rho = S_w \rho_w + (1 - S_w) \rho_o \quad (5.58)$$

$$\tau = -\mu(\nabla \mathbf{u} + (\nabla \mathbf{u})^T) + \frac{2}{3} \mu(\nabla \cdot \mathbf{u}) \delta \quad (5.59)$$

$$\mu = S_w \mu_w + (1 - S_w) \mu_o \quad (5.60)$$

where p is pressure, ρ is the density of fluid, ρ_0 is reference density; ρ_o is the density of oil, ρ_w is the density of water, C is linear coefficient equal to the reciprocal of squared sound velocity, S_w is water saturation, \mathbf{u} is flow rate; μ_o is the viscosity of oil, μ_w is viscosity of water, τ is shear stress, σ is surface tensional coefficient.

5.1.2.6 Boundary conditions

In addition to the differential equations for flow control, initial and boundary conditions are used to define flow boundary. For unsteady flow simulation, any variable should be given an initial value before calculation, namely, each variable should have a start calculation point on all the grids so that it is possible to calculate the variance of the field variable with time on the time step. This is called initial conditions. Boundary conditions include Dirichlet boundary conditions (specify boundary values), Neumann boundary conditions (specify boundary gradient) and Couchy boundary conditions (mixed boundary conditions, maybe suitable for porous medium with a semi-permeable boundary).

5.2 Numerical solution to fracture-vug reservoir model

The following procedures were performed to get a numerical solution: (1) converted partial differential equations into differential equations by discretion processing; (2) linearized nonlinear coefficient term to get linear algebraic equations; (3) solved the linear equations to obtain the distribution and variation of unknowns (pressure, saturation, component, etc.). Based on the equivalent multimediuim model, Darcy flow, non-Darcy flow, and vug flow were simulated and solved. Both models were solved using the finite differential volume method.

5.2.1 Numerical solution based on equivalent multimediuim model

5.2.1.1 Numerical simulation of Darcy flow

It is known that no matter fluids flow inside a reservoir block or among blocks, in fact they flow among vug, matrix, and fracture units. Such multiphase flow follows the following conditions:

$$-\text{div}(\rho_\beta \mathbf{u}_\beta) + q_\beta = \frac{\partial}{\partial t} (\phi \rho_\beta S_\beta) \quad \beta = o, w, g \quad (5.61)$$

After numerical integration by infinite volume method (V is volume, A is area), we get,

$$-\int_V \text{div}(\rho_\beta \mathbf{u}_\beta) dV + q_\beta V = V \frac{\partial}{\partial t} (\phi \rho_\beta S_\beta) \tag{5.62}$$

According to Gauss theorem,

$$-\int_V \text{div}(\rho_\beta \mathbf{u}_\beta) dV = -\int_A \rho_\beta (\mathbf{u}_\beta \cdot \mathbf{n}) dA = \int_A \rho_\beta (\mathbf{u}_\beta \cdot (-\mathbf{n})) dA = \sum F_{\beta,ij} \tag{5.63}$$

As shown in Fig. 5.8, the mass flow of β phase between unit i and j is $F_{\beta,ij}$.

After space discretion by employing the infinite volume method, and time discretion by differentiating to the next order, we get the equation in unit i :

$$[(M_\beta)_i^{n+1} - (M_\beta)_i^n] \frac{V_i}{\Delta t} = \sum_{j \in \eta_i} F_{\beta,ij}^{n+1} + Q_{\beta i}^{n+1} \tag{5.64}$$

where M is the mass of β phase, the superscript n represents a previous moment, the superscript $n + 1$ represents the current time, V_i is the volume of unit i (matrix, fracture, or vug), Δt is the time step, η_i is the collection of unit j connecting to unit i , $F_{\beta,ij}$ is the mass flow term for β phase between unit i and unit j , $Q_{\beta i}$ is the source-sink term for β phase in unit i .

For Darcy flow, the flow term $F_{\beta,ij}$ between units i and j in multiple medium is expressed as follows:

$$\begin{aligned} F_{\beta,ij} &= A_{ij} \left(\frac{\rho_\beta k k_{r\beta}}{\mu_\beta} \right)_{ij+1/2} \frac{[(P_{\beta j} - \rho_{\beta,ij+1/2} g D_j) - (P_{\beta i} - \rho_{\beta,ij+1/2} g D_i)]}{d_i + d_j} \\ &= \left(\frac{\rho_\beta k_{r\beta}}{\mu_\beta} \right)_{ij+1/2} \left(\frac{A_{ij} k_{ij+1/2}}{d_i + d_j} \right) [(P_{\beta i} - \rho_{\beta,ij+1/2} g D_j) - (P_{\beta i} - \rho_{\beta,ij+1/2} g D_i)] \\ &= \lambda_{\beta,ij+1/2} \gamma_{ij} [\Phi_{\beta j} - \Phi_{\beta i}] \end{aligned} \tag{5.65}$$

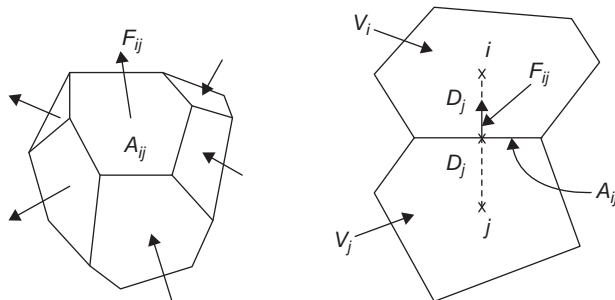


Figure 5.8 Flow of fluid between units.

where $\lambda_{\beta,ij+1/2}$ is the flow rate of β phase,

$$\lambda_{\beta,ij+1/2} = \left(\frac{\rho_{\beta} k_{r\beta}}{\mu_{\beta}} \right)_{ij+1/2} \tag{5.66}$$

Here the subscript $ij + 1/2$ represents the weighted average of property parameters in unit i and j ; $k_{r\beta}$ is the relative permeability of β phase. In Eq. (5.65), γ_{ij} is conductivity coefficient calculated by the infinite differentiating method as:

$$\gamma_{ij} = \frac{A_{ij} k_{ij+1/2}}{d_i + d_j} \tag{5.67}$$

where A_{ij} is the interface area between units i and j ; d_i is the distance from the central point of unit i to the interface between units i and j ; $k_{ij+1/2}$ is the mean absolute permeability along the connected location between units i and j . The flow potential in Eq. (5.65) is:

$$\Phi_{\beta i} = P_{\beta i} - \rho_{\beta,ij+1/2} g D_i \tag{5.68}$$

where D_i is the depth of unit i center; the sources/sinks of unit i are defined as follows:

$$Q_{\beta i} = q_{\beta i} V_i \tag{5.69}$$

In the multimedium numerical model, the complex medium has been divided into several blocks. Each block is composed of three units V , F , and M , representing vug unit, fracture unit, and matrix unit, respectively. According to the geometrical distribution of the vug, fracture, and matrix in the complex medium, several distribution patterns inside a block were summarized (Figs. 5.9–5.12).

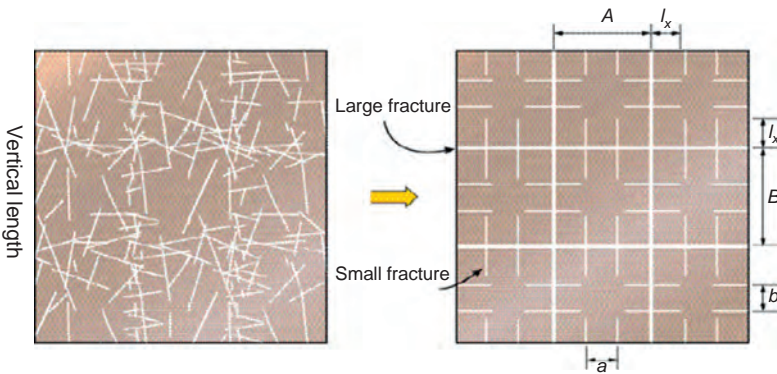


Figure 5.9 Unit pattern A inside block.

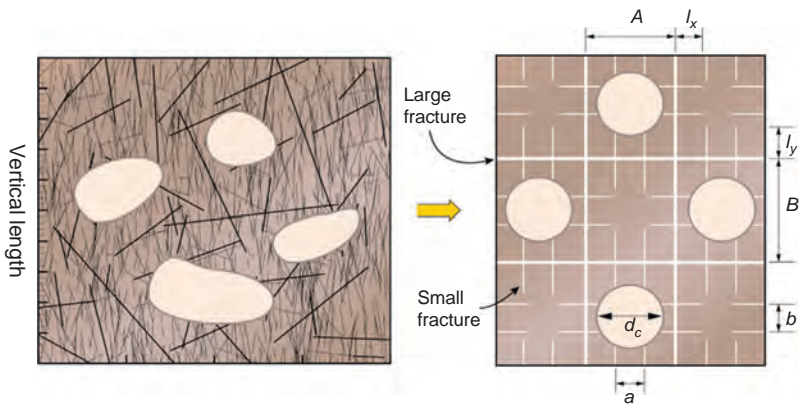


Figure 5.10 Unit pattern B inside block.

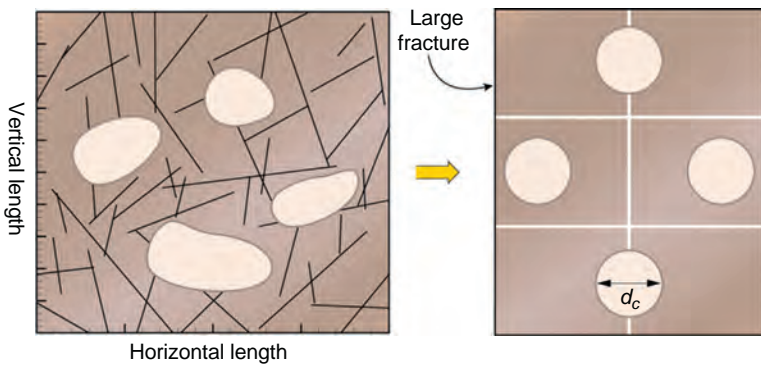


Figure 5.11 Unit pattern C inside block.

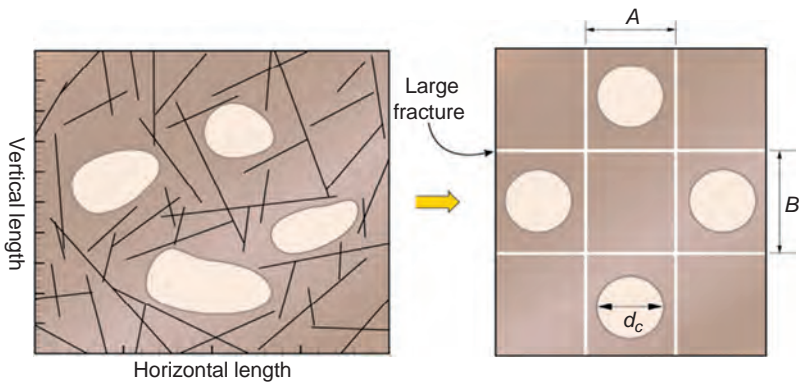


Figure 5.12 Unit pattern D inside block.

For any distribution pattern, the flow term can be calculated by Eq. (5.65). The conductivity coefficient in Eq. (5.67) can be calculated according to the distribution pattern.

For the flow between fracture and matrix:

$$\gamma_{FM} = \frac{A_{FM}k_M}{l_{FM}} \quad (5.70)$$

where A_{FM} is the connective area between F (fracture unit) and M (matrix unit), k_M is the absolute permeability of matrix, l_{FM} is the feature flow distance between F and M .

For the flow between fracture and vug:

$$\gamma_{FV} = \frac{A_{FV}k_V}{l_{FV}} \quad (5.71)$$

where A_{FV} is the connective area between F (fracture unit) and V (vug unit); l_{FV} is the feature flow distance between F and V ; k_v is the absolute permeability of V , equal to the permeability of small fractures connecting vugs and fractures. For isolated vugs, there is no need to calculate the flow between fractures and vugs.

For the flow between vugs and matrix:

$$\gamma_{VM} = \frac{A_{VM}k_M}{l_{VM}} \quad (5.72)$$

where A_{VM} is the connective area between V and M , l_{VM} is the feature flow distance between M and V .

Table 5.1 lists the formula for calculating the feature distance according to the distribution patterns inside block.

5.2.1.2 Numerical simulation of high-speed non-Darcy flow

Equivalent non-Darcy flow coefficient and relative permeability should be the function of fluid properties such as saturation and pressure gradient:

$$\gamma_\beta = \gamma_\beta(S_\beta, k_{r\beta}, \nabla p_\beta) \quad (5.73)$$

$$k_{r\beta} = k_{r\beta}(S_\beta, \nabla p_\beta) \quad (5.74)$$

For one-phase high-speed non-Darcy flow in porous medium, Tek et al. (1962) suggested using the following formula to calculate equivalent non-Darcy flow coefficient:

$$\gamma = \frac{C_\beta}{k^{\frac{3}{2}}\phi^{\frac{3}{2}}} \quad (5.75)$$

where C_β is the parameter related to solid phase and fluid properties.

Table 5.1 Feature distance calculation

Fracture system	Matrix scale (distribution pattern) (m)	Feature distance (m) between fracture and matrix	Feature distance (m) between fracture and vug	Feature distance ^a (m) between vug and matrix	Feature distance ^b (m) between fracture and matrix
1D	A	$l_{FM} = A/6$	$l_{FV} = l_x$	$l_{VM} = a/6$	$l_{VM} = (A - d_c)/2$
2D	A, B	$l_{FM} = AB/4(A + B)$	$l_{FV} = \frac{l_x + l_y}{2}$	$l_{VM} = ab/4(a + b)$	$l_{VM} = \frac{A + B - 2d_c}{4}$
3D	A, B, C	$l_{FM} = 3ABC/10/(AB + BC + CA)$	$l_{FV} = \frac{l_x + l_y + l_z}{3}$	$l_{VM} = 3abc/10/(ab + bc + ca)$	$l_{VM} = \frac{A + B + C - 3d_c}{6}$

Note: A , B and C are the matrix scales in x , y , and z directions, respectively.

^aThe feature distance between vug and matrix means vug and matrix connect to each other by small fractures, a , b and c are the fracture interval distances in x , y , and z directions, respectively.

^bfeature distance between vug and matrix means the distance between vug and fracture.

Accordingly, expand Eq. (5.75) to multiphase high-speed non-Darcy flow:

$$\gamma_{\beta} = \frac{C_{\beta}}{(kk_{r\beta})^{\frac{5}{2}}(\phi(S_{\beta} - S_{\beta r}))^{\frac{3}{2}}} \quad (5.76)$$

where $S_{\beta r}$ is the residual saturation of fluid β in porous medium.

For high-speed non-Darcy flow in a multimedial numerical model, the flow term $F_{\beta,ij}$ connecting unit i to unit j is:

$$F_{\beta} = \frac{A_{ij}}{2(k\beta_{\beta})_{ij+1/2}} \left\{ -\frac{1}{\bar{\lambda}_{\beta}} + \left[\left(\frac{1}{\bar{\lambda}_{\beta}} \right)^2 - \bar{\gamma}_{ij}(\Phi_{\beta j} - \Phi_{\beta i}) \right]^{1/2} \right\} \quad (5.77)$$

where

$$\text{Coefficient of fluidity: } \bar{\lambda}_{\beta} = \frac{k_{r\beta}}{\mu_{\beta}} \quad (5.78)$$

$$\text{Conductivity coefficient: } \bar{\gamma}_{ij} = \frac{4(k^2\rho_{\beta}\beta_{\beta})_{ij+1/2}}{d_i + d_j} \quad (5.79)$$

5.2.1.3 Numerical simulation of cavern flow

In adopting the above-mentioned approximation calculation method to calculate the multiphase flow caverns, the discrete form of the equation of conservation of mass is still valid.

$$[(M_{\beta})_i^{n+1} - (M_{\beta})_i^n] \frac{V_i}{\Delta t} = \sum_{j \in \eta_i} F_{\beta,ij}^{n+1} + Q_{\beta i}^{n+1} \quad (5.80)$$

where M is the mass of β phase, superscript n represents the previous moment, superscript $n + 1$ indicates the current moment, V_i is the volume of cavern i , Δt is time step, η_i is the collection of unit j connecting to cavern i , $F_{\beta,ij}$ is the mass flow term of β phase between cavern i and unit j , $Q_{\beta i}$ is the source-sink term of β phase in cavern i .

For Darcy flow, the flow term $F_{\beta,ij}$ in Eq. (5.80) can be expressed as follows:

$$F_{\beta,ij} = \lambda_{\beta,ij+1/2} \gamma_{ij} [\Phi_{\beta j} - \Phi_{\beta i}] \quad (5.81)$$

Here subscript $I, j + 1/2$ indicates the weight average of property parameters for caverns i and j ; $k_{r\beta}$ is the relative permeability of β phase in unit j .

The conductivity coefficient γ_{ij} in Eq. (5.81) is:

$$\gamma_{ij} = \frac{A_{ij}k_j}{d_j} \quad (5.82)$$

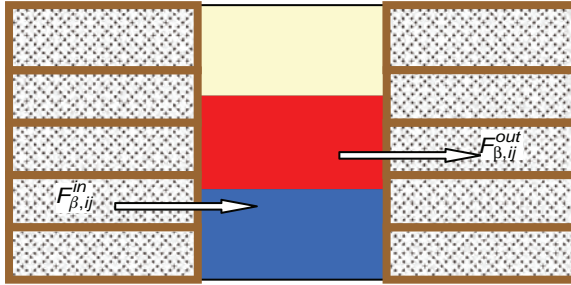


Figure 5.13 Flow terms in a cavern.

where A_{ij} is the interfacial area between cavern i and j ; d_j is the distance from the center of unit j to the interface between cavern i and unit j .

The flow potential in Eq. (5.80) is:

$$\Phi_{\beta i} = p_{\beta i} - \rho_{\beta,ij+1/2} g D_i \tag{5.83}$$

where D_i is the depth of the unit center; the source/sink point of unit i is defined as follows:

$$Q_{\beta i} = q_{\beta i} V_i \tag{5.84}$$

In order to achieve the assumption of instantaneous equilibrium and gravity separation in caverns by programming in numerical modeling procedures, we need to distinguish the flow term of units connecting to caverns as the free inflow zone term $F_{\beta,ij}^{in}$ and the free outflow zone term $F_{\beta,ij}^{out}$.

The inflow term $F_{\beta,ij}^{in}$ is calculated using the original formula. The outflow term $F_{\beta,ij}^{out}$ is calculated by modifying relative permeability $k_{r\beta}$ according to the gravity separation of different phases and the vertical location of connective porous medium units (Fig. 5.13).

5.2.1.4 Full-implicit algorithm

The Newton–Raphson method is used to solve the nonlinearity of multiphase flow in multiple media. In the case of oil–gas–water three-phase flow, the equations are:

Gas:

$$\begin{aligned} & \left\{ \left[\phi S_o \bar{\rho}_{dg} + \phi S_g \rho_g \right]_i^{n+1} - \left[S_o \bar{\rho}_{dg} + \phi S_g \rho_g \right]_i^n \right\} \frac{V_i}{\Delta t} \\ & = \sum_{j \in \eta_i} (\bar{\rho}_{dg} \lambda_o)_{ij+1/2}^{n+1} \gamma_{ij} \left[\Phi_{oj}^{n+1} - \Phi_{oi}^{n+1} \right] + \sum_{j \in \eta_i} (\rho_g \lambda_g)_{ij+1/2}^{n+1} \gamma_{ij} \left[\Phi_{gj}^{n+1} - \Phi_{gi}^{n+1} \right] + Q_{gi}^{n+1} \end{aligned} \tag{5.85}$$

Water:

$$\left\{ [\phi S_w \rho_w]_i^{n+1} - [\phi S_w \rho_w]_i^n \right\} \frac{V_i}{\Delta t} = \sum_{j \in \eta_i} (\rho_w \lambda_w)_{ij+1/2}^{n+1} \gamma_{ij} [\Phi_{wj}^{n+1} - \Phi_{wi}^{n+1}] + Q_{wi}^{n+1} \quad (5.86)$$

Oil:

$$\left\{ [\phi S_o \bar{\rho}_o]_i^{n+1} - [\phi S_o \bar{\rho}_o]_i^n \right\} \frac{V_i}{\Delta t} = \sum_{j \in \eta_i} (\bar{\rho}_o \lambda_o)_{ij+1/2}^{n+1} \gamma_{ij} [\Phi_{oj}^{n+1} - \Phi_{oi}^{n+1}] + Q_{oi}^{n+1} \quad (5.87)$$

where n represents the current time, $n + 1$ represents the next time needed to solve, V_i is the volume of unit i , Δt is time step, η_i contains the collection in unit i and the neighboring unit j .

$$\begin{aligned} R_i^{g,n+1} &= \left\{ [\phi S_o \bar{\rho}_{dg} + \phi S_g \rho_g]_i^{n+1} - [\phi S_o \bar{\rho}_{dg} + \phi S_g \rho_g]_i^n \right\} \frac{V_i}{\Delta t} \\ &\quad - \sum_{j \in \eta_i} (\bar{\rho}_{dg} \lambda_o)_{ij+1/2}^m \gamma_{ij} [\Phi_{oj}^{n+1} - \Phi_{oi}^{n+1}] \\ &\quad - \sum_{j \in \eta_i} (\rho_g \lambda_g)_{ij+1/2}^m \gamma_{ij} [\Phi_{gj}^{n+1} - \Phi_{gi}^{n+1}] - Q_{gi}^{n+1} = 0 \end{aligned} \quad (5.88)$$

$$\begin{aligned} R_i^{w,n+1} &= \left\{ [\phi S_\beta \rho_w]_i^{n+1} - [\phi S_w \rho_w]_i^n \right\} \frac{V_i}{\Delta t} \\ &\quad - \sum_{j \in \eta_i} (\rho_w \lambda_w)_{ij+1/2}^m \gamma_{ij} [\Phi_{wj}^{n+1} - \Phi_{wi}^{n+1}] - Q_{wi}^{n+1} = 0 \end{aligned} \quad (5.89)$$

$$\begin{aligned} R_i^{o,n+1} &= \left\{ [\phi S_o \bar{\rho}_o]_i^{n+1} - [\phi S_o \bar{\rho}_o]_i^n \right\} \frac{V_i}{\Delta t} \\ &\quad - \sum_{j \in \eta_i} (\bar{\rho}_o \lambda_o)_{ij+1/2}^m \gamma_{ij} [\Phi_{oj}^{n+1} - \Phi_{oi}^{n+1}] - Q_{oi}^{n+1} = 0 \end{aligned} \quad (5.90)$$

Eqs. (5.88)–(5.90) can be simplified as:

$$R_i^{\beta,n+1}(x_{k,p+1}) = 0 \quad (5.91)$$

where x_k represents primary variables: oil pressure, oil saturation, saturation pressure, or gas saturation. The third variable depends on the phase condition in the reservoir unit. If there is no free gas, the unit is not saturated and oil reservoir pressure is larger than bubble point pressure, saturation pressure p_s is considered as the third primary variable. If there is free gas, the unit is saturated and oil reservoir pressure is smaller than bubble point pressure, gas saturation S_g is considered as the third primary variable.

To conduct Taylor expansion of Eq. (5.91):

$$\begin{aligned}
 R_i^{\beta,n+1}(x_{k,p+1}) &= R_i^{\beta,n+1}(x_{k,p}) + \sum_k \left. \frac{\partial R_i^{\beta,n+1}}{\partial x_k} \right|_p (x_{k,p+1} - x_{k,p}) + \dots \\
 &\approx R_i^{\beta,n+1}(x_{k,p}) + \sum_k \left. \frac{\partial R_i^{\beta,n+1}}{\partial x_k} \right|_p (x_{k,p+1} - x_{k,p}) \\
 &= 0
 \end{aligned}
 \tag{5.92}$$

From Eq. (5.92), the iterative formula of the Newton–Raphson method is derived:

$$\sum_k \left. \frac{\partial R_i^{\beta,n+1}}{\partial x_k} \right|_p (x_{k,p+1} - x_{k,p}) = -R_i^{\beta,n+1}(x_{k,p})
 \tag{5.93}$$

Or it can be written in the form of a matrix:

$$\mathbf{J} \cdot \Delta \mathbf{x} = \mathbf{R}
 \tag{5.94}$$

where $J_{ni} = - \sum \frac{\partial R_n^{\beta,n+1}(x_{i,p})}{\partial x_i}$, $\Delta x_{i,p+1} = x_{i,p+1} - x_{i,p}$, $R_n = R_n^{\beta,p+1}(x_{i,p})$

5.2.1.5 Solution of linear equations

The iterative formula of Eq. (5.93) in the Newton–Raphson method can be summarized as the solution of the following linear equations.

$$\mathbf{Ax} = \mathbf{b}
 \tag{5.95}$$

Due to the large size of an actual oil reservoir, the order of linear equations will be very high; the calculation efficiency of direct solution is very low, thus it is necessary to adopt the contemporary iterative method for the solution.

Supposing the coefficient matrix of Eq. (5.95) is a real symmetric positive definite matrix, construct quadratic function,

$$f(\mathbf{x}) = \frac{1}{2} \mathbf{x}^T \mathbf{Ax} - \mathbf{b}^T \mathbf{x}
 \tag{5.96}$$

We can derive,

$$\nabla f(\mathbf{x}) = \mathbf{Ax} - \mathbf{b}
 \tag{5.97}$$

Since matrix \mathbf{A} is a symmetric positive definite matrix, Eq. (5.96) has a unique minimum point; thereby the equations of Eq. (5.95) should have a unique solution (set as \mathbf{x}^*). It is indicated from Eq. (5.97) that the solution of Eq. (5.95) linear equations is equivalent to the minimum value of the quadratic function $f(\mathbf{x})$.

Set $\mathbf{x}^{(k)}$ is an approximation of \mathbf{x}^* , the process of iteration is to find $\mathbf{x}^{(k+1)}$ with smaller target function value starting from $\mathbf{x}^{(k)}$ in the direction of $\mathbf{d}^{(k)}$, thus making $\mathbf{x}^{(k+1)}$ much closer to the minimum point \mathbf{x}^* .

From Eq. (5.96), we can derive:

$$f(\mathbf{x}^{(k+1)}) = f(\mathbf{x}^{(k)} + \alpha_k \mathbf{d}^{(k)}) \quad (5.98)$$

The value of α_k should ensure Eq. (5.98) takes the minimum, so we can derive:

$$\alpha_k = \frac{(\mathbf{r}^{(k)})^T \mathbf{d}^{(k)}}{(\mathbf{d}^{(k)})^T \mathbf{A} \mathbf{d}^{(k)}} \quad (5.99)$$

where $\mathbf{r}^{(k)}$ is the residual error of approximate $\mathbf{x}^{(k)}$:

$$\mathbf{r}^{(k)} = \mathbf{b} - \mathbf{A} \mathbf{x}^{(k)} = -\nabla f(\mathbf{x}^{(k)}) \quad (5.100)$$

In the conjugate gradient method, the searching direction $\mathbf{d}^{(k+1)}$ takes the combination of negative $\mathbf{r}^{(k+1)}$ and previous searching direction $\mathbf{d}^{(k)}$;

$$\mathbf{d}^{(k+1)} = \mathbf{r}^{(k+1)} + \beta_k \mathbf{d}^{(k)}$$

And it requires that $\mathbf{d}^{(k)}$ and $\mathbf{d}^{(k+1)}$ is conjugated with respect to \mathbf{A} , we can derive:

$$\beta_k = -\frac{(\mathbf{r}^{(k+1)})^T \mathbf{d}^{(k)}}{(\mathbf{d}^{(k)})^T \mathbf{A} \mathbf{d}^{(k)}} \quad (5.101)$$

This is the conjugate gradient method which, with given $\mathbf{x}^{(0)}$, is used to calculate the residual error and searching direction. The calculation process will be repeated until the calculation accuracy is satisfied.

The conjugate gradient method requires that the coefficient matrix is symmetric positive definite. However, it is usually not a symmetric positive definite matrix in reservoir modeling calculation. The asymmetry is mainly caused by taking the upstream weight for the relative permeability in the interface when calculating the flow term between units. Therefore, on the basis of conjugate gradient method, the target function is required to be taken as follows:

$$f(\mathbf{x}) = (\|\mathbf{r}\|_2)^2 = \mathbf{r} \cdot \mathbf{r} \quad (5.102)$$

This is the Orthomin method, in which α_k and β_k are calculated as follows:

$$\alpha_k = \frac{(\mathbf{r}^{(k)})^T \mathbf{A} \mathbf{d}^{(k)}}{(\mathbf{A} \mathbf{d}^{(k)})^T \mathbf{A} \mathbf{d}^{(k)}} \quad (5.103)$$

$$\beta_k = -\frac{(\mathbf{A} \mathbf{r}^{(k+1)})^T \mathbf{A} \mathbf{d}^{(k)}}{(\mathbf{A} \mathbf{d}^{(k)})^T \mathbf{A} \mathbf{d}^{(k)}} \quad (5.104)$$

The convergence rates of the conjugate gradient method and the Orthomin method based on the conjugate gradient method depend on the condition number of the coefficient matrix. In order to speed up the convergence, we need to conduct pretreatment on Eq. (5.95) as follows, thus making \mathbf{AP}^{-1} show better condition number than \mathbf{A} :

$$\mathbf{Ap}^{-1} \mathbf{px} = \mathbf{b} \quad (5.105)$$

or

$$\mathbf{Ap}^{-1} \mathbf{y} = \mathbf{b} \quad (5.106)$$

where $\mathbf{y} = \mathbf{Px}$, the pretreatment matrix $\mathbf{y} = \mathbf{Px}$ can be derived from the incomplete LU factorization.

For Eq. (5.105) after pretreatment, the Orthomin method is adopted, thus we can derive the following calculating process:

First preestimate $\mathbf{x}^{(0)}$, and then calculate $\mathbf{r}^{(0)} = \mathbf{b} - \mathbf{Ax}^{(0)}$, finally solve $\mathbf{pd}^{(0)} = \mathbf{r}^{(0)}$. Repeat the following process until getting the accuracy requirement ($k = 0, 1, 2, 3 \dots$):

$$\mathbf{g} = \mathbf{Ad}^{(k)} \quad (5.107)$$

$$\delta^{(k)} = (\mathbf{g}^{(k)})^T \mathbf{g}^{(k)} \quad (5.108)$$

$$\alpha_k = \frac{(\mathbf{r}^{(k)})^T \mathbf{g}^{(k)}}{\delta^{(k)}} \quad (5.109)$$

$$\mathbf{x}^{(k+1)} = \mathbf{x}^{(k)} + \alpha_k \mathbf{d}^{(k)} \quad (5.110)$$

$$\mathbf{r}^{(k+1)} = \mathbf{r}^{(k)} - \alpha_k \mathbf{g}^{(k)} \quad (5.111)$$

To solve

$$\mathbf{Ph}^{(k+1)} = \mathbf{r}^{(k+1)} \quad (5.112)$$

$$\mathbf{b}_j^{(k)} = -\frac{(\mathbf{Ah}^{(k+1)})^T \mathbf{g}^{(j)}}{\delta^{(j)}}, \quad (j = 0, 1, 2, 3 \dots k) \quad (5.113)$$

$$\mathbf{d}^{(k+1)} = \mathbf{h}^{(k+1)} + \sum_{j=0}^k (\mathbf{b}_j^{(k)})^T \mathbf{d}^{(j)}$$

5.2.2 Numerical solution based on the coupling model

Considering the geometry irregularities of a fracture-vug reservoir, the finite volume method (FVM) based on unstructured grids was adopted to discrete the controlling

equation. Equation discretion is to convert one or multifarious differential equations into linear equations. By solving the linear equations, the value of specified position in temporal-spatial state is obtained. The numerical solutions are approximate, and the accuracy depends on the quality of discretion, and errors come mainly from three aspects: (1) approximate or idealized mathematical models for describing physical phenomena, (2) approximate discretion method, and (3) approximate iterative method.

Discretion process includes discretion of the solution zone and that of equations. The discretion of the solution zone produces numerical description of the solution zone, which includes the location of solution point and boundary description. The space to discrete is divided into finite zones, namely controlling volume or volumetric grid. For transient problems, time is divided into finite time step.

The FVM contains the following properties: (1) the basic physical quantities, such as mass and momentum, are conserve in the controlling bodies because the method is based on the integral form of controlling equations. (2) The coordinate system is a Cartesian coordinate system, and this method is applicable to the steady-state and transient calculations. (3) The controlling body is a polyhedron, and the number of adjacent cells is variable, so the overall grid is an arbitrary unstructured one. All variables share the same controlling body, which is called collocated grid arrangement. (4) Partial differential equations are solved by an isolation method, namely, an equation is solved each time, and the explicit approach is used to deal with the coupling among equations.

5.2.2.1 Finite volume discretion in solution domain

Similar to the finite element and the finite difference method, it also requires to discretion of the solution domain is also required, dividing them into discrete grids of finite size. Therefore, the calculation grids required to solve the controlling equation are produced, meanwhile, the temporal-spatial solution is determined. This process can be divided into two parts, namely temporal discretion and spatial discretion.

The discretion of time is to designate the size of time step. The spatial discretion needs to divide the space into controlling bodies, which fill the calculation domain and do not overlap.

Let us set calculation point a , located in the center of the controlling body, namely:

$$\int_{V_a} (\mathbf{x} - \mathbf{x}_a) dV = 0 \quad (5.114)$$

The mesh is divided into two groups: the inner surface and the boundary surface, and the boundary surface overlaps with the external surface. The surface vector \mathbf{S}_f is defined as the grid from low index to high index, which is perpendicular to the surface. And its value is equal to the area of the surface.

5.2.2.2 Discretion of transfer equation

For any physical quantity ξ , the transfer equation can be written as:

$$\frac{\partial \rho \xi}{\partial t} + \nabla \cdot (\rho u \xi) - \nabla \cdot (\rho \Gamma_{\xi} \nabla \xi) = S_{\xi}(\xi) \quad (5.115)$$

Taking ξ as different variables and diffusion coefficients and source terms as appropriate expression, the continuity equation and momentum and energy equations, etc., will be obtained. Therefore Eq. (5.115) is called the universal transfer equation, representing the conservation relationship of each variable in the transfer of fluids. When $\xi = 1$, $\Gamma = 0$, $S_{\xi}(\xi) = 0$, Eq. (5.115) is a continuity equation; when $\xi = u$, $\Gamma = \mu$, Eq. (5.115) is a momentum equation.

The key procedure of the FVM is to conduct integration on the controlling differential Eq. (5.115) within the controlling volume V_p , namely,

$$\frac{\partial}{\partial t} \int_{V_a} \rho \xi dV + \int_{V_a} \nabla \cdot (\rho u \xi) dV - \int_{V_a} \nabla \cdot (\rho \Gamma_{\xi} \nabla \xi) dV = \int_{V_a} S_{\xi}(\xi) dV \quad (5.116)$$

Since the diffusion term is the second derivative of ξ , to ensure consistency, the order number of discretion in the finite volume must be equal to or greater than the order of the equation.

The accuracy of the discretion method depends on the assumed varying function $\xi = \xi(x, t)$ in the temporal-spatial location close to point a . In order to obtain the calculating method of second-order accuracy, this variance must be linear spatially and temporally, namely assuming that:

$$\xi(x) = \xi_a + (\mathbf{x} - \mathbf{x}_a) \cdot (\nabla \xi)_a \quad (5.117)$$

$$\xi(t + \Delta t) = \xi^t + \Delta t \cdot \left(\frac{\partial \xi}{\partial t} \right)^t \quad (5.118)$$

where

$$\xi_a = \xi(\mathbf{x}_a) \quad (5.119)$$

$$\xi^t = \xi(t) \quad (5.120)$$

The Taylor series indicate that the above-mentioned extension is second-order accuracy.

1. Discretion of spatial term

According to Gauss's law

$$\int_V \nabla \cdot \mathbf{a} dV = \int_{\partial V} dS \cdot \mathbf{a} \quad (5.121)$$

$$\int_V \nabla \phi dV = \int_{\partial V} d\mathbf{S} \phi \quad (5.122)$$

$$\int_V \nabla \mathbf{a} dV = \int_{\partial V} d\mathbf{S} \mathbf{a} \quad (5.123)$$

In the above expression, ∂V is the closed plane which contained V , and $d\mathbf{S}$ is the infinitesimal bin in outward normal direction.

Taking into account the variation of ξ in the control body of a ;

$$\begin{aligned} \int_{V_a} \xi(x) dV &= \int_{V_a} [\xi_a + (\mathbf{x} - \mathbf{x}_a) \cdot (\nabla \xi)_a] dV \\ &= \xi_a \int_{V_a} dV + \left[\int_{V_a} (\mathbf{x} - \mathbf{x}_a) dV \right] \cdot (\nabla \xi)_a \\ &= \xi_a V_a \end{aligned} \quad (5.124)$$

In the expression, V_a is the volume of the grid; since a is located in the center of the controlling body, the integral of the second term in the equation is zero.

For the divergence operator, since the control body is surrounded by planar polygons, we can conduct the following conversion:

$$\begin{aligned} \int_V \nabla \cdot \mathbf{a} dV &= \int_{\partial V} d\mathbf{S} \cdot \mathbf{a} \\ &= \sum_f \left(\int_f d\mathbf{S} \cdot \mathbf{a} \right) \end{aligned} \quad (5.125)$$

From linear assumption:

$$\begin{aligned} \int_f d\mathbf{S} \cdot \mathbf{a} &= \left(\int_f d\mathbf{S} \right) \cdot \mathbf{a}_f + \left[\int_f d\mathbf{S} (\mathbf{x} - \mathbf{x}_f) \right] \cdot (\nabla \mathbf{a})_f \\ &= \mathbf{S} \cdot \mathbf{a}_f \end{aligned} \quad (5.126)$$

It can be derived from the integration:

$$(\nabla \cdot \mathbf{a}) V_a = \sum_f \mathbf{S} \cdot \mathbf{a}_f \quad (5.127)$$

where subscript f indicates that the value of variables at the center of the surface, \mathbf{S} is the surface vector in outward normal direction.

Next we will conduct spatial discretion on convective, diffusion, and source terms in the transfer equation.

a. Spatial discretion of convective term

Discretion of convective term is conducted by Eq. (5.127),

$$\begin{aligned} \int_{V_a} \nabla \cdot (\rho u \xi) dV &= \sum_f \mathbf{S} \cdot (\rho u \xi)_f \\ &= \sum_f \mathbf{S} \cdot (\rho u)_f \xi_f \\ &= \sum_f F \xi_f \end{aligned} \quad (5.128)$$

In the expression, F is the mass flux across the surface, namely;

$$F = S \cdot (\rho u)_f \tag{5.129}$$

In the expression, ξ_f represents the value of ξ on the surface, and this value is obtained by convection differential format from the value of volumetric grid.

b. Convection differential format

Convection differential format determines how to obtain values on the surface from volumetric values.

Let us assume that ξ varies linearly between two points a and b , thus the values on the surface are:

$$\xi_f = (1 - f_x)\xi_a + f_x\xi_b \tag{5.130}$$

where f_x is defined as the ratio of \overline{fa} to \overline{Pb} .

$$f_x = \frac{\overline{fa}}{\overline{Pb}} \tag{5.131}$$

The differential format used in Eq. (5.130) is the central differential (CD), which is a second-order format. However, for the problems dominated by convection, the boundness principle of solution is violated due to the production of nonphysical oscillation.

The format entitled to ensure boundness is the upwind differential (UD) format; the surface is subject to the direction of flow:

$$\xi_f = \begin{cases} \xi_f = \xi_a & F \geq 0 \\ \xi_f = \xi_b & F < 0 \end{cases} \tag{5.132}$$

This format ensures solution boundness, but at the expense of solution accuracy. By introducing numerical errors and reducing the order number of discretion, the final solution may be distorted.

The hybrid differential format is the combination of CD and UD:

$$\xi_f = (1 - \gamma)(\xi_f)_{UD} + \gamma(\xi_f)_{CD} \tag{5.133}$$

In Eq. (5.133), γ is the blending factor.

In fact, the format that meets both the requirements of accuracy and boundness must not be linear.

c. Discretion of diffusion term

Use the same method to solve the diffusion term:

$$\begin{aligned} \int_{V_a} \nabla \cdot (\rho \Gamma_\xi \nabla \xi) dV &= \sum_f S \cdot (\rho \Gamma_\xi \nabla \xi)_f \\ &= \sum_f (\rho \Gamma_\xi)_f S \cdot (\nabla \xi)_f \end{aligned} \tag{5.134}$$

d is the vector directing from a to b . When vector d is parallel to S , it can be expressed as follows:

$$S \cdot (\nabla \xi)_f = |S| \frac{\xi_b - \xi_a}{|d|} \tag{5.135}$$

In the Eq. (5.135), the gradient of ξ is calculated using the values of two volumes sharing the surface, or the gradient value in the volume center:

$$(\nabla\xi)_a = \frac{1}{V_a} \sum_f S\xi_f \quad (5.136)$$

After performing differential treatment, we get:

$$(\nabla\xi)_f = f_x(\nabla\xi)_a + (1 - f_x)(\nabla\xi)_b \quad (5.137)$$

And then perform dot product with S . More calculation units are used in Eq. (5.137), so its truncation error is much larger. Eq. (5.135) is not suitable for non-orthogonal grid.

For this reason, $S \cdot (\nabla\xi)_f$ is divided into two parts:

$$S \cdot (\nabla\xi)_f = \underbrace{\Delta \cdot (\nabla\xi)_f}_{\text{正交}} + \underbrace{k \cdot (\nabla\xi)_f}_{\text{非正交}} \quad (5.138)$$

where Δ and k meet the following expression:

$$S = \Delta + k \quad (5.139)$$

Let Δ be parallel to d to use Eq. (5.135) in the orthogonal part, and restrict the inaccurate method the nonorthogonal part. The construction methods of S are different: the first is the minimum correcting method which makes the nonorthogonal corrected items as small as possible.

$$\Delta = \frac{d \cdot S}{d \cdot d} d \quad (5.140)$$

When the nonorthogonality of grids increases, the contribution of ξ_a and ξ_b decreases.

The second is the orthogonal correcting method, which remains the contribution of ξ_a and ξ_b unchanged regardless of the orthogonality conditions, therefore it is defined as:

$$\Delta = \frac{d}{|d|} |S| \quad (5.141)$$

The third is the overly-loose method where the contribution of ξ_a and ξ_b increases when the nonorthogonality increases, it is defined as:

$$\Delta = \frac{d}{d \cdot S} |S|^2 \quad (5.142)$$

The diffusion term in the differential equation meets the boundness of ϕ . However, only in the orthogonal grid can this property be maintained. When the grid shows high

nonorthogonality, the nonorthogonal correcting can potentially increase the possibility of boundness violation. If the nonorthogonal amendment is abandoned, the accuracy of discretion will be affected. Therefore, the selection of method is dependent on the tradeoff between solution accuracy and stability. The ultimate expression formats for the three methods mentioned above are the same:

$$\mathbf{S} \cdot (\nabla \xi)_f = |\Delta| \frac{\xi_b - \xi_a}{|d|} + \mathbf{k} \cdot (\nabla \xi)_f \quad (5.143)$$

d. Discretion of source term

Apart from the diffusion term, convection term, and time term in the transfer equation, other terms can be included in the source term. The FVM generally conducts the treatment of linearization on the source term:

$$S_\xi(\xi) = S_u + S_p \xi \quad (5.144)$$

In the expression, S_u and S_p may depend on ξ . From Eq. (5.124), we can derive:

$$\int_{V_a} S_\xi(\xi) dV = S_u V_a + S_p V_a \xi_a \quad (5.145)$$

The advantage of linearization is particularly prominent in conducting implicit calculation.

2. Discretion of time term

For Eq. (5.116),

$$\frac{\partial}{\partial t} \int_{V_a} \rho \xi dV + \int_{V_a} \nabla \cdot (\rho u \xi) dV - \int_{V_a} \nabla \cdot (\rho \Gamma_\xi \nabla \xi) dV = \int_{V_a} S_\xi(\xi) dV \quad (5.146)$$

Substituting Eqs. (5.124), (5.128), (5.143), and (5.145), assuming that the controlling bodies do not vary with time, Eq. (5.116) is written as:

$$\frac{\partial}{\partial t} (\rho_a \xi_a V_a) = - \sum_f F \xi_f + \sum_f (\rho \Gamma_\xi)_f \mathbf{S} \cdot (\nabla \xi)_f + S_u V_a + S_p V_a \xi_a \quad (5.147)$$

For simplification, Eq. (5.147) can be expressed as:

$$\frac{\partial}{\partial t} (\rho_a \xi_a V_a) = M(t) \quad (5.148)$$

The discretion of time can be performed using different methods. The first is the Euler explicit, in which the surface value of ξ and $\nabla \xi$ is dependent on the field in the previous time interval. And the linear part of the source term also depends on the field in the previous time interval. Therefore, it can be expressed as:

$$\frac{\rho_a^n \xi_a^n - \rho_a^o \xi_a^o}{\Delta t} V_a = M(t^o) \quad (5.149)$$

The new ξ_a can be obtained from direct calculation without solving linear equations. The disadvantage of this method is the constraint of the Courant number. The Courant number is defined as:

$$C_o = \frac{\mathbf{v}_f \cdot \mathbf{d}}{\Delta t} \quad (5.150)$$

where v_f is the interpolation speed of surface f . If the C_o number is greater than 1, the explicit format will be unstable, thereby constraining the selection of time step.

The second method is the Euler implicit, the time term in the format is the same as that in the first method. The surface value can be expressed by the volumetric grid values, therefore:

$$\frac{\rho_a^n \xi_a^n - \rho_a^o \xi_a^o}{\Delta t} V_a = M(t^n) \quad (5.151)$$

This format is first-order, unlike explicit, and the equations are established in this method:

$$\mathbf{a}_a \xi_a^n + \sum_b \mathbf{a}_b \xi_b^n = R_a \quad (5.152)$$

The coupling of variables is stronger than the explicit, even if the C_o number is violated, the system still maintains stable. And the boundness of solution can be maintained.

The third method is the Crank–Nicholson format, the discretion of time is the same as that in the previous methods and the surface value is the mean of old value and new value:

$$\frac{\rho_a^n \xi_a^n - \rho_a^o \xi_a^o}{\Delta t} V_a = \frac{1}{2} [M(t^o) + M(t^n)] \quad (5.153)$$

This format is second-order and unconditionally stable in time, but is not bounded.

The fourth method is backward differential format, which is second-order in time. But it ignores the variance of surface value with time, namely expressed by the new volumetric values.

$$\frac{\frac{3}{2} \rho_a^n \xi_a^n - 2 \rho_a^o \xi_a^o + \frac{1}{2} \rho_a^\infty \xi_a^\infty}{\Delta t} V_a = M(t^n) \quad (5.154)$$

3. Treatment of boundary conditions

To obtain discretion form for the transfer equation, the key is to determine the value on surface f and its perpendicular gradient, namely ξ_f and $\mathbf{S} \cdot (\nabla \xi)_f$. The previous analysis describes how to obtain these values in the inner surface. For the surface located on the boundary, its values can be obtained from boundary conditions.

Vector \mathbf{d} is the vector connecting the volume grid center to surface grid center, and \mathbf{d}_n is the component of \mathbf{d} which is parallel to the normal direction of the surface, then:

$$\mathbf{d}_n = \frac{\mathbf{d} \cdot \mathbf{S}}{|\mathbf{S}|} \frac{\mathbf{S}}{|\mathbf{S}|} \quad (5.155)$$

a. Constant boundary conditions

The ξ value on the boundary surface is designated as $\xi = \xi_c$ which is considered in the discretion of the convection and diffusion term on the boundary surface. From Eq. (5.128), the convection term is

$$\int_{V_a} \nabla \cdot (\rho u \xi) dV = \sum_f F \xi_f \quad (5.156)$$

As the value on the boundary surface is ξ known as ξ_c , on the surface the term is $F_c \xi_c$, where F_c is the surface flux.

From Eq. (5.134), the diffusion term is,

$$\int_{V_a} \nabla \cdot (\rho \Gamma_\xi \nabla \xi) dV = \sum_f (\rho \Gamma_\xi)_f \mathbf{S} \cdot (\nabla \xi)_f \tag{5.157}$$

The vertical gradient on the surface is given by surface value and volume center value:

$$\mathbf{S} \cdot (\nabla \xi)_c = |\mathbf{S}| \frac{\xi_c - \xi_a}{|\mathbf{d}|} \tag{5.158}$$

b. Boundary condition with constant gradient

In this boundary condition, the dot product of gradient and outward unit normal vector is designated.

$$\left(\frac{\mathbf{S}}{|\mathbf{S}|} \cdot \nabla \xi \right)_c = g_c \tag{5.159}$$

For the convection term, the surface values are obtained from the calculation of values in the volumetric center and designated gradient:

$$\begin{aligned} \xi_c &= \xi_a + \mathbf{d}_n \cdot (\nabla \xi)_c \\ &= \xi_a + |\mathbf{d}_n| g_c \end{aligned} \tag{5.160}$$

For the diffusion term, the dot product of surface vector and $(\nabla \xi)_c$ is known, namely,

$$|\mathbf{S}| g_c \tag{5.161}$$

This term is:

$$\rho \Gamma_\xi |\mathbf{S}| g_c$$

Since \mathbf{d}_n does not direct to the center of the interface, the calculation of surface integral under the constant gradient boundary condition is only first-order accuracy.

4. The accuracy and boundness of convection differential format

Since no method can guarantee both solution accuracy and boundness, two solutions were proposed in this paper, including the total variation diminishing (TVD) method and the normalized variation analysis (NVA) method.

a. TVD differential format

Define total variation $TV(\xi^n)$ as:

$$TV(\xi^n) = \sum_f |\xi_b^n - \xi_a^n| \tag{5.162}$$

where a and b are the central points in the volumetric grids sharing surface f . In each step, the TVD format satisfies the following:

$$TV(\xi^{n+1}) \leq TV(\xi^n) \tag{5.163}$$

The condition of Eq. (5.163) is used in high-order flux format, however, it is written as the sum of first-order boundness differential format (UD) and constrained Gauss correction, namely:

$$\xi_f = (\xi)_{UD} + \psi[(\xi)_{HO} - (\xi)_{UD}] \quad (5.164)$$

In Eq. (5.164), $(\xi)_{HO}$ is the surface value of high-order format, ψ is the clipper. The clipper is the function of ξ sequential gradient:

$$r = \frac{\xi_C - \xi_U}{\xi_D - \xi_C} \quad (5.165)$$

Therefore:

$$\psi = \psi(r) \quad (5.166)$$

The U , C , and D points are the upper, middle, and lower points, respectively, in the flow direction of surface f .

The clipper satisfies the TVD condition under the following conditions:

$$0 \leq \left(\frac{\psi(r)}{r}, \psi(r) \right) \leq 2 \quad (5.167)$$

The accuracy of this differential format is higher than the first-order, but will not result in solution oscillation in the conventional second-order accuracy.

b. NVA method

Define the normalized variables as,

$$\tilde{\xi} = \frac{\xi - \xi_U}{\xi_D - \xi_U} \quad (5.168)$$

From the normalized expression of the surface values, get

$$\tilde{\xi}_f = f(\tilde{\xi}_C) \quad (5.169)$$

To ensure boundness:

$$0 \leq \tilde{\xi}_C \leq 1 \quad (5.170)$$

$\tilde{\xi}_f$ is the function of $\tilde{\xi}_C$, it should satisfy the following:

- i. If $0 \leq \tilde{\xi}_C \leq 1$, then $\tilde{\xi}_C \leq \tilde{\xi}_f \leq 1$;
- ii. If $\tilde{\xi}_C \leq 0$ or $\tilde{\xi}_C > 1$, then $\tilde{\xi}_f = \tilde{\xi}_C$

The NVA method is used in the unstructured grid system.

In the NVA method, the upper point U is used to define $\tilde{\xi}_C$. In an unstructured grid system, it is difficult to confirm the point, so gradient information is used to calculate $\tilde{\xi}_C$.

$$\tilde{\xi}_C = \frac{\xi_C - \xi_f^-}{\xi_f^+ - \xi_f^-} = 1 - \frac{\xi_f^+ - \xi_C}{\xi_f^+ - \xi_f^-} \quad (5.171)$$

The expression of $\xi_f^+ - \xi_C$ is:

$$\begin{aligned} \xi_f^+ - \xi_C &= f_x(\xi_D - \xi_C) \\ &= f_x \frac{\xi_D - \xi_C}{x_D - x_C} (x_D - x_C) \\ &= f_x(\nabla\xi)_f \cdot \hat{\mathbf{d}}(x_D - x_C) \end{aligned} \quad (5.172)$$

where $\hat{\mathbf{d}}$ is unit vector:

$$\hat{\mathbf{d}} = \frac{\mathbf{d}}{|\mathbf{d}|} \quad (5.173)$$

$\xi_f^+ - \xi_f^-$ can be converted using the following method:

$$\begin{aligned} \xi_f^+ - \xi_f^- &= \frac{\xi_f^+ - \xi_f^-}{x_f^+ - x_f^-} (x_f^+ - x_f^-) \\ &= (\nabla\xi)_C \cdot \hat{\mathbf{d}}(x_f^+ - x_f^-) \end{aligned} \quad (5.174)$$

Therefore:

$$\begin{aligned} \tilde{\xi}_C &= 1 - \frac{\xi_f^+ - \xi_C}{\xi_f^+ - \xi_f^-} \\ &= 1 - \frac{f_x(\nabla\xi)_f \cdot \hat{\mathbf{d}}(x_D - x_C)}{(\nabla\xi)_C \cdot \hat{\mathbf{d}}(x_f^+ - x_f^-)} \end{aligned} \quad (5.175)$$

As C is the center point of grids, then it comes to the following relations:

$$\frac{x_f^+ - x_f^-}{x_D - x_C} = 2 \frac{x_f^+ - x_C}{x_D - x_C} = 2f_x \quad (5.176)$$

We can derive from above expression:

$$\tilde{\xi}_C = 1 - \frac{(\nabla\xi)_f \cdot \mathbf{d}}{2(\nabla\xi)_C \cdot \mathbf{d}} \quad (5.177)$$

It is not necessary to use the upper point U in Eq. (5.177).

Before applying the NVA method, we should define the range of $\tilde{\xi}_C$, and set up the function relationship between $\tilde{\xi}_f$ and $\tilde{\xi}_C$ in the range of $0 \leq \tilde{\xi}_C \leq 1$.

In the range of $0 \leq \tilde{\xi}_C \leq 1$, the CD-based hybrid format is used to achieve numerical target, such as accuracy, or the UD-based hybrid format is used to identify the interface, combining with the compressed format.

The zone to be corrected is in the range of $0 \leq \tilde{\xi}_C \leq 1$. Usually the linear mixed factors are used:

$$\gamma = \frac{\tilde{\xi}_C}{\beta_m} \quad (5.178)$$

It guarantees the continuity of format variation, preventing the convergence problems caused by format mutations.

5.2.2.3 Discretion of momentum equation

Discretion of universal transfer equation has been described above. For the special numerical model built for the fracture-vug reservoir in the Tahe Oilfield, it is necessary to introduce the discretion of momentum equation.

Without consideration of the impact of porous medium, the momentum equation is:

$$\frac{\partial \rho \mathbf{u}}{\partial t} + \nabla \cdot (\rho \mathbf{u} \mathbf{u}) = -\nabla p - \nabla \cdot \boldsymbol{\tau} + \rho \mathbf{g} - \sigma \nabla \left(\frac{\nabla S}{|\nabla S|} \right) \nabla S \quad (5.179)$$

The shear term in this expression can be written as:

$$\nabla \cdot \boldsymbol{\tau} = -\nabla \cdot (\mu \nabla \mathbf{u}) - \nabla \mathbf{u} \cdot \nabla \mu - \mu \nabla (\nabla \cdot \mathbf{u}) - \nabla \left(\frac{2}{3} \mu (\nabla \cdot \mathbf{u}) \right) \quad (5.180)$$

The latter two terms are the gradient of speed discretion, which can be neglected when density does not vary with space greatly.

$$\frac{\partial \rho \mathbf{u}}{\partial t} + \nabla \cdot (\rho \mathbf{u} \mathbf{u}) - \nabla \cdot (\mu \nabla \mathbf{u}) - \nabla \mathbf{u} \cdot \nabla \mu = -\nabla p + \rho \mathbf{g} - \sigma \nabla \cdot \left(\frac{\nabla S}{|\nabla S|} \right) \nabla S \quad (5.181)$$

To obtain the pressure equation, we conduct semi-discretion (with pressure term reserved) on Eq. (5.181). The expression gives the integral form of the momentum equation:

$$\begin{aligned} & \frac{\partial}{\partial t} \int_{V_a} \rho \mathbf{u} dV + \int_{V_a} \nabla \cdot (\rho \mathbf{u} \mathbf{u}) dV - \int_{V_a} \nabla \cdot (\mu \nabla \mathbf{u}) dV - \int_{V_a} \nabla \mu \cdot (\nabla \mathbf{u}) dV \\ & = \int_{V_a} \left(-\nabla p + \rho \mathbf{g} - \sigma \nabla \cdot \left(\frac{\nabla S}{|\nabla S|} \right) \right) dV \end{aligned} \tag{5.182}$$

After conducting implicit discretion on each term on the left side of Eq. (5.182), the coefficient matrix of algebraic equations is obtained. The diagonal quantity is a_a for the matrix, and positive value of the product between nondiagonal terms and speed is $\mathbf{H}(\mathbf{u})$.

To conduct explicit discretion (∇p is reserved, in Eq. (5.186)) on each term on the right of Eq. (5.182), and the explicitly discreted term can be viewed as the product of the integral term of the central point in unit body and the volume of unit body, namely,

$$\int_{V_a} \left(\rho \mathbf{g} - \sigma \nabla \cdot \left(\frac{\nabla S}{|\nabla S|} \right) \right) dV = \left(\rho \mathbf{g} - \sigma \nabla \cdot \left(\frac{\nabla S}{|\nabla S|} \right) \right)_a V_a \tag{5.183}$$

The subscript P of the implicit discretion term disappears in the expression below.

$$\mathbf{u}_a = \frac{\mathbf{H}(\mathbf{u})}{a_a} + \frac{1}{a_a} \left(-\nabla p + \rho \mathbf{g} - \sigma \nabla \cdot \left(\frac{\nabla S}{|\nabla S|} \right) \nabla S \right) \tag{5.184}$$

And we define:

$$\mathbf{u}^* = \frac{\mathbf{H}(\mathbf{u})}{a_a} + \frac{1}{a_a} \left(\rho \mathbf{g} - \sigma \nabla \cdot \left(\frac{\nabla S}{|\nabla S|} \right) \nabla S \right) \tag{5.185}$$

Then,

$$\mathbf{u}_a = \mathbf{u}^* - \frac{1}{a_a} \nabla p \tag{5.186}$$

It is derived from continuous equations:

$$\frac{\partial \rho}{\partial t} + \mathbf{u} \nabla \rho + \rho \nabla \cdot \mathbf{u} = 0 \tag{5.187}$$

$$\frac{D\rho}{Dt} + \rho \nabla \cdot \mathbf{u} = 0 \quad (5.188)$$

$$\frac{Dp}{Dt} \frac{\partial \rho}{\partial p} + \rho \nabla \cdot \mathbf{u} = 0 \quad (5.189)$$

$$\left(\frac{\partial p}{\partial t} + \mathbf{u} \cdot \nabla p \right) \frac{\partial \rho}{\partial p} + \rho \nabla \cdot \mathbf{u} = 0 \quad (5.190)$$

$$\left(\frac{\partial p}{\partial t} + \mathbf{u} \cdot \nabla p \right) \frac{1}{\rho} \frac{\partial \rho}{\partial p} + \nabla \cdot \mathbf{u} = 0 \quad (5.191)$$

From above expressions:

$$\left(\frac{\partial p}{\partial t} + \mathbf{u} \cdot \nabla p \right) \frac{1}{\rho} \frac{\partial \rho}{\partial p} + \nabla \cdot \left(\mathbf{u}^* - \frac{1}{a_p} \nabla p \right) = 0 \quad (5.192)$$

$$\left(\frac{\partial p}{\partial t} + \nabla \cdot (\mathbf{u}p) - p \nabla \cdot \mathbf{u} \right) \frac{C}{\rho} - \frac{1}{a_a} \nabla^2 p + \nabla \cdot \mathbf{u}^* = 0 \quad (5.193)$$

Eq. (5.193) is the pressure equation to solve, where the \mathbf{u}^* can be obtained from Eq. (5.185). Since other terms include pressure, the implicit discretion should be conducted. Solve the equations to get the pressure in this iteration.

As we know, there are multiple zones which show varying properties. After finishing the discretion of momentum equation for all fluid on all zones, it is time to consider the effect of the porous medium on the porous medium zone.

To model porous medium, generally we add a source term to the standard flow equations. This term includes two parts: viscous loss term (Darcy term) and inertial loss term.

$$\mathbf{Q} = - \left(\mathbf{D} \mu \mathbf{u} + \mathbf{C} \frac{1}{2} \rho |\mathbf{u}| \mathbf{u} \right) \quad (5.194)$$

where \mathbf{Q} is source term, D and C are tensors, \mathbf{D} is the coefficient of viscous loss (Darcy term), \mathbf{C} is the coefficient of inertial loss. In isotropic porous medium, the source term can be expressed as:

$$\mathbf{S} = - \left(\frac{\mu}{k} \mathbf{u} + C_2 \frac{1}{2} \rho |\mathbf{u}| \mathbf{u} \right) \quad (5.195)$$

where k is permeability, and C_2 is the coefficient of inertial resistance.

When setting these tensors, first set the major axis of them, then their diagonal components. For isotropic medium, set their diagonal values to be the same, namely, spherical tensors.

To process the porous medium term, first define individual porous medium zones, each of them is deemed as a collection of volumetric grids, and then set the coefficients of viscous loss term (Darcy term) and inertial loss term in each porous medium zone. Porous medium term can be added implicitly and explicitly. Implicit addition is to add the porous term to the left side of the matrix equation. As the term only correlates with the grids of the current zone and shows no correlation with adjacent grids, only the diagonal terms will be affected. The diagonal values in the matrix are expressed by tensors. In this way, the left side of the equation is expressed as the product of diagonal matrix tensor and speed vector. And the right side is expressed as the aggregation of the contribution of source term and negative nondiagonal. After adding pressure contribution to the right and conducting inversion on the tensors of diagonal matrix and transferring it to the right side of the equations, the new speed prediction will be achieved. Explicit addition is to add the diagonal component of porous medium term to the left side of the matrix equation and the nondiagonal component of porous medium term is added to the right side of the equation, thus solving new speed equations.

The differences between implicit and explicit methods lie in the treatment of porous medium term. During implicit treatment, all components of porous medium term are transferred to the left side of the equation, while during explicit treatment, only the diagonal components are transferred to the left side of the equation. In solving the speed prediction value, implicit treatment is equivalent to the Gauss–Seidel iteration, while it is a complete solution in explicit treatment. As a conclusion, if the anisotropic properties of porous medium are prominent, it is better to use implicit method; if the porous medium is isotropic, it is better to use the explicit method; for less prominent anisotropic porous medium, explicit treatment is suggested.

5.2.2.4 *Coupling solution of pressure–velocity equations*

By now, discretization processing of all equations has been described. Next we will introduce how to get the coupling solution of the pressure–velocity equation. For minor compressible two-phase flow, we use the standard pressure implicit with splitting of operator (PISO) algorithm as follows:

1. Initialize all variables.
2. To calculate the turbulence, calculate fluid viscosity according to the speed and density of the field in the previous time interval.
3. Calculate the Courant number, and adjust the step as needed.
4. Solve the S equation using the volumetric flux and density field in the previous time interval.
5. Solve the continuity equation using the mass flux in the previous time interval. The actual mass flux is unknown, it is an approximation of the new density field in the previous time interval.
6. Conduct momentum prediction. The actual pressure value is unknown, so use the pressure field in previous time interval. Momentum prediction provides an approximation of new speed field.
7. Solve the pressure equation to get new speed field, volumetric flux field, and density field.
8. Go back to step (2).

5.2.2.5 Solution to linear equations

After discretion of algebraic Eq. (5.152):

$$\mathbf{a}_a \xi_a^n + \sum_b \mathbf{a}_b \xi_b^n = R_a \quad (5.196)$$

Two methods can be used to solve linear equations: direct and iterative solutions. The direct solution is obtained by finite algebraic calculation. The iterative method is to get the real solution by iterative calculation based on a given initial value until solution error is within the allowable range. For the direction solution, the number of calculations increases with the number of equations in a squared manner. As a result, to solve large equations, the number of calculations would be very large. Comparatively, the iterative solution seems more economical.

In order to ensure convergence of the iterative solver, it generally requires a diagonally dominant matrix. For a matrix, if the diagonal quantity is equal to the nondiagonal quantity, then it is called diagonally equal. To reach a diagonally dominant matrix, every row must meet the requirement of $|a_a| > \sum_n |a_b|$. For the discretion of the linear part of the source term, the source term is less than zero, thus increasing the diagonal dominance.

The boundness principle of Algebraic equations indicates that the diagonally equal matrix with positive coefficient matrix can guarantee the boundness of solution. Among them, only the employment of upwind format can guarantee that they are diagonally equal for convection term, and other formats will generate a diagonally negative term. To conduct CD on uniform grids, if the diagonal coefficient is zero, then the solving difficulty increases. The diffusion term can only guarantee diagonally equality for orthogonal matrix and the correction of the nonorthogonal can result in a negative coefficient. The time term increases the diagonal coefficient and matrix source term, thus increasing the diagonal dominance. However the boundness principle is obtained without considering the matrix source term, so it is difficult to distinguish the influence of time term on boundness. From this point, only time and negative source terms can increase the diagonal dominance of the matrix.

Conjugate gradient is adopted during solving the matrix using iterative method. It guarantees obtaining a real solution under the condition that iterative times are less or equal to the equation number. Convergent speed depends on the distribution of matrix eigenvalues, which may be improved by preliminary treatment by using the incomplete Cholesky method (ICCG) for symmetrical matrix, the Bi-CGSTAB method for nonsymmetrical matrix, or currently the AMG algebraic multigrid method to speed up the solving process.

5.3 Validation of numerical simulation method

Based on the numerical simulation methods above, two software systems have been developed: *KarstSim* for numerical simulation of an equivalent multimedimum

fracture-vug carbonate reservoir and *CaveSim* for numerical simulation of coupling multiphase flow. These mathematical models, numerical solutions, and software systems have been validated by analytical solution, physical experiment, actual fracture-vug reservoirs, and similar software.

5.3.1 Validation of equivalent multimedial numerical simulation

5.3.1.1 Numerical simulation

In order to verify the correctness of the numerical model of multimedial Darcy flow, the analytical solution of triple-medium radial flow was calculated and compared with the numerical solution. This validates that the numerical simulation method for the equivalent multimedial reservoir is correct.

Based on the assumption of triple medium, a mathematical model for radial flow in a finite or infinite reservoir was established and the analytic solution in Laplace space was obtained with consideration of wellbore storage and skin effect.

The model is based on following assumptions:

1. The reservoir has uniform thickness and impermeable top and bottom limits.
2. Fluids flow to the wellbore from formation system as a radial flow, and vugs and matrix connect to the wellbore through fractures.
3. All rock properties, such as permeability, porosity, and initial compressibility are constant in continuous medium.
4. One-phase isothermal fluid with minor compressibility and constant viscosity.
5. Quasi steady flow between fractures and matrix ($F-M$), and between vugs and matrix ($V-M$).

Control equation:

Fluid flow between fractures:

$$\frac{k_F}{\mu} \frac{1}{r} \left(r \frac{\partial P_F}{\partial r} \right) - \phi_M C_M \frac{\partial P_M}{\partial t} - \phi_V C_V \frac{\partial P_V}{\partial t} = \phi_F C_F \frac{\partial P_F}{\partial t} \quad (5.197)$$

Fluid flow between fracture and vug:

$$\phi_V C_V \frac{\partial P_V}{\partial t} = \frac{\alpha_{FV} k_V}{\mu} (P_F - P_V) + \frac{\alpha_{VM} k_M}{\mu} (P_M - P_V) \quad (5.198)$$

Fluid flow between fracture and matrix:

$$\phi_M C_M \frac{\partial P_M}{\partial t} = \frac{\alpha_{FM} k_M}{\mu} (P_F - P_M) + \frac{\alpha_{VM} k_M}{\mu} (P_V - P_M) \quad (5.199)$$

Where the subscript F means fracture, M means matrix and V means vug; P , ϕ , C , and k , respectively, denote pressure, initial porosity, effective compression

coefficient and permeability; μ is fluid viscosity; α_{FV} , α_{FM} , and α_{VM} are channeling coefficients between fracture and vug, between fracture and matrix and between vug and matrix, respectively. They have the relation as follows:

$$\alpha_{FM} = \alpha_{VM} = \alpha \quad (5.200)$$

The channeling coefficient between fracture and vug is:

$$\alpha_{FV} = \frac{A_{FV}}{l_{FV}} \quad (5.201)$$

where A_{FV} is the total area connective between fracture and vug in unit volume (m^2/m^3), l_{FV} is the feature length which is defined as:

$$l_{FV} = l_f/2 \quad (5.202)$$

where l_f is the average length of small fractures connecting vugs with large fractures.

Initial and boundary conditions:

Assuming that the initial formation pressure P_i of the three media is uniformly distributed, then:

$$P_F(r, 0) = P_V(r, 0) = P_M(r, 0) = P_i \quad (5.203)$$

For infinite radial flow, the pressure is constant on the outer boundary:

$$P_F(r = \infty, t) = P_i \quad (5.204)$$

For finite radial flow, the outer boundary (radius = r_e) must meet the following two conditions:

1. Constant boundary condition:

$$P_F(r = r_e, t) = P_i \quad (5.205)$$

2. Closed outer boundary condition:

$$\frac{\partial P(r = r_e, t)}{\partial r} = 0 \quad (5.206)$$

The boundary condition of wellbore ($r = r_w$) is determined by volume flow and affected by wellbore storage effect and skin effect.

$$P_{wf} = \left[P_F - S r_w \frac{\partial P_F}{\partial r} \right]_{r=r_w} \quad (5.207)$$

$$-C \frac{\partial P_{wf}}{\partial t} + \frac{2\pi r_w k_F h}{\mu} \frac{\partial P_F}{\partial r}(r_w, t) = q \tag{5.208}$$

where S is skin factor, C is wellbore storage coefficient (a dimensionless constant), P_{wf} is bottom flow pressure, r_w is wellbore radius, h is formation thickness. C is defined as:

$$C = V_w c_L \tag{5.209}$$

where V_w is wellbore volume, c_L is the compressibility coefficient of fluid and liquid in the wellbore. After introducing dimensionless $P_D(r_D, t_D)$, radius r_D , and time,

$$P_D(r_D, t_D) = \frac{2\pi k_F h}{\mu q} (P_i - P(r, t)) \tag{5.210}$$

$$r_D = \frac{r}{r_w} \tag{5.211}$$

$$t_D = \frac{t}{[\mu r_w^2 (\phi_F C_F + \phi_V C_V + \phi_M C_M) / k_F]} \tag{5.212}$$

According to the controlling Eqs. (5.197)–(5.199), and the boundary condition Eqs. (5.204)–(5.208), we get:

$$\omega_F \frac{\partial P_{DF}}{\partial t_D} - \frac{1}{r_D} \frac{\partial}{\partial r_D} \left(r_D \frac{\partial P_{DF}}{\partial r_D} \right) - \lambda_{FV} (P_{DV} - P_{DF}) - \lambda_{FM} (P_{DM} - P_{DF}) = 0 \tag{5.213}$$

$$\omega_V \frac{\partial P_{DV}}{\partial t_D} + \lambda_{FV} (P_{DV} - P_{DF}) + \lambda_{VM} (P_{DV} - P_{DM}) = 0 \tag{5.214}$$

$$\omega_M \frac{\partial P_{DM}}{\partial t_D} + \lambda_{FM} (P_{DM} - P_{DF}) + \lambda_{VM} (P_{DM} - P_{DV}) = 0 \tag{5.215}$$

The definitions of ω and λ are listed in Table 5.2.

Initial conditions:

$$P_{DF}(r_D, 0) = P_{DV}(r_D, 0) = P_{DM}(r_D, 0) = 0 \tag{5.216}$$

Outer boundary conditions:

$$P_{DF}(\infty, t_D) = 0 \tag{5.217}$$

$$P_{DF}(r_D = r_e / r_w = r_{eD}, t_D) \tag{5.218}$$

$$\left. \frac{\partial P_{DF}}{\partial r} \right|_{r_D=r_{eD}} = 0 \tag{5.219}$$

Table 5.2 Dimensionless parameters and variables for radial flow simulation in triple-medium reservoir

Parameter	Definition
Dimensionless time	$t_D = \frac{k_F t}{\mu r_w^2 (\phi_M C_M + \phi_V C_V + \phi_F C_F)}$
Dimensionless radius	$r_D = \frac{r}{r_w}$
Dimensionless pressure	$P_D = \frac{P_i - P_F(r, t)}{\frac{q \mu}{2\pi k_F h}}$
Channeling coefficient between fracture and matrix	$\lambda_{FM} = \frac{\alpha_{FM} r_w^2 k_M}{k_F}$
Channeling coefficient between fracture and vug	$\lambda_{FV} = \frac{\alpha_{FV} r_w^2 k_V}{k_F}$
Channeling coefficient between vug and matrix	$\lambda_{VM} = \frac{\alpha_{VM} r_w^2 k_M}{k_F}$
Storage coefficient of fracture	$\omega_F = \frac{\phi_F C_F}{\phi_M C_M + \phi_V C_V + \phi_F C_F}$
Storage coefficient of vug	$\omega_V = \frac{\phi_V C_V}{\phi_M C_M + \phi_V C_V + \phi_F C_F}$
Storage coefficient of matrix	$\omega_M = \frac{\phi_M C_M}{\phi_M C_M + \phi_V C_V + \phi_F C_F}$
Variables based on the above parameters:	
$A_1 = A_0 + \frac{\lambda_{FM} + \lambda_{FV}}{2\omega_F} + \left[\left(A_0 + \frac{\lambda_{FM} + \lambda_{FV}}{2\omega_F} \right)^2 - \frac{B_0}{\omega_F} \right]^{1/2}$	
$A_2 = A_0 + \frac{\lambda_{FM} + \lambda_{FV}}{2\omega_F} - \left[\left(A_0 + \frac{\lambda_{FM} + \lambda_{FV}}{2\omega_F} \right)^2 - \frac{B_0}{\omega_F} \right]^{1/2}$	
$B_1 = A_0 + (A_0^2 - B_0)^{1/2}$	
$B_2 = A_0 - (A_0^2 - B_0)^{1/2}$	
$A_0 = \frac{1}{2} \left[\frac{\lambda_{FM}}{\omega_M} + \frac{\lambda_{FV}}{\omega_V} + \left(\frac{1}{\omega_M} + \frac{1}{\omega_V} \right) \lambda_{VM} \right]$	
$B_0 = \frac{\lambda_{FM} \lambda_{FV} + (\lambda_{FM} + \lambda_{FV}) \lambda_{VM}}{\omega_M \omega_V}$	

Inner boundary conditions:

$$P_{Dwf} = \left[P_{DF} - S \frac{\partial P_{DF}}{\partial r_D} \right]_{r_D=1} \quad (5.220)$$

$$C_D \frac{\partial P_{Dwf}}{\partial t_D} - \left(\frac{\partial P_{DF}}{\partial r_D} \right)_{r_D=1} = 1 \quad (5.221)$$

where

$$P_{Dwf} = \frac{2\pi k_F h}{\mu q} (P_i - P_{wf}) \quad (5.222)$$

Dimensionless wellbore storage coefficient,

$$C_D = \frac{C}{2\pi(\phi_F c_F + \phi_{FCF} + \phi_{FCF}) h r_w^2} \quad (5.223)$$

The solution in Laplace space:

After Laplace transfer, we can derive

$$\omega_F s \bar{P}_{DF} - \frac{1}{r_D} \frac{\partial}{\partial r_D} \left(r_D \frac{\partial \bar{P}_{DF}}{\partial r_D} \right) - \lambda_{FV} (\bar{P}_{DV} - \bar{P}_{DF}) - \lambda_{FM} (\bar{P}_{DM} - \bar{P}_{DF}) = 0 \quad (5.224)$$

$$\omega_V s \bar{P}_{DV} + \lambda_{FV} (\bar{P}_{DV} - \bar{P}_{DF}) + \lambda_{VM} (\bar{P}_{DV} - \bar{P}_{DM}) = 0 \quad (5.225)$$

$$\omega_M s \bar{P}_{DM} + \lambda_{FM} (\bar{P}_{DM} - \bar{P}_{DF}) + \lambda_{VM} (\bar{P}_{DM} - \bar{P}_{DV}) = 0 \quad (5.226)$$

$$\bar{P}_{DF}(r_D = \infty, s) = 0 \quad (5.227)$$

$$\bar{P}_{DF}(r_D = r_{eD}, s) = 0, \quad (5.228)$$

$$\left. \frac{dP_{DF}}{dr} \right|_{r_D=r_{eD}} = 0 \quad (5.229)$$

Inner boundary conditions:

$$\bar{P}_{Dwf} = \left[\bar{P}_{DF} - S \frac{d\bar{P}_{DF}}{dr_D} \right]_{r_D=1} \quad (5.230)$$

$$C_D s \bar{P}_{Dwf} - \left(\frac{d\bar{P}_{DF}}{dr_D} \right)_{r_D=1} = \frac{1}{s} \quad (5.231)$$

where \bar{P}_{DF} , \bar{P}_{DV} , \bar{P}_{DM} , and \bar{P}_{Dwf} are, respectively, the transfer function of P_{DF} , P_{DV} , P_{DM} , and P_{Dwf} in Laplace space; S is the variable of Laplace transfer. Substitute matrix Eq. (5.225) and vug Eq. (5.226) to fracture Eq. (5.224), and we get:

$$\frac{1}{r_D} \frac{\partial}{\partial r_D} \left(r_D \frac{\partial \bar{P}_{DF}}{\partial r_D} \right) - sf(s) \bar{P}_{DF} = 0 \quad (5.232)$$

where

$$f(s) = \omega_F + \frac{(\lambda_{FV} + \lambda_{FM})s + \frac{1 - \omega_F}{\omega_V \omega_M} [\lambda_{FV} \lambda_{FM} + (\lambda_{FV} + \lambda_{FM}) \lambda_{VM}]}{s^2 + \left[\frac{\lambda_{FV}}{\omega_V} + \frac{\lambda_{FM}}{\omega_M} + \left(\frac{1}{\omega_V} + \frac{1}{\omega_M} \right) \lambda_{VM} \right] s + \frac{\lambda_{FV} \lambda_{FM} + (\lambda_{FV} + \lambda_{FM}) \lambda_{VM}}{\omega_V \omega_M}} \quad (5.233)$$

The general solution of Eq. (5.233) is:

$$\bar{P}_{DF} = C_0 K_0 \left(\sqrt{sf(s)} r_D \right) + D_0 I_0 \left(\sqrt{sf(s)} r_D \right) \quad (5.234)$$

where K_0 and I_0 are zero-order Bessel functions with first-class and second-class correctness, respectively.

1. Infinite reservoir:

After substituting the analytical solution to the boundary Eqs. (5.227), (5.230), and (5.231), we can derive:

$$\bar{P}_{DF} = \frac{K_0 \left(\sqrt{sf(s)} r_D \right)}{s \left\{ \sqrt{sf(s)} K_1 \left(\sqrt{sf(s)} \right) + C_D s \left[K_0 \left(\sqrt{sf(s)} \right) + S \sqrt{sf(s)} K_1 \left(\sqrt{sf(s)} \right) \right] \right\}} \quad (5.235)$$

$$\bar{P}_{Dwf} = \frac{K_0 \left(\sqrt{sf(s)} r_D \right) + S \sqrt{sf(s)} K_1 \left(\sqrt{sf(s)} \right)}{s \left\{ \sqrt{sf(s)} K_1 \left(\sqrt{sf(s)} \right) + C_D s \left[K_0 \left(\sqrt{sf(s)} \right) + S \sqrt{sf(s)} K_1 \left(\sqrt{sf(s)} \right) \right] \right\}} \quad (5.236)$$

2. Finite reservoir with closed outer boundary:

After substituting the analytical solution to the boundary Eqs. (5.228), (5.230), and (5.231), we can derive:

$$\bar{P}_{DF} = \frac{\left\{ I_0 \left(\sqrt{sf(s)} r_D \right) K_1 \left(\sqrt{sf(s)} r_{eD} \right) + I_1 \left(\sqrt{sf(s)} r_{eD} \right) K_0 \left(\sqrt{sf(s)} r_D \right) \right\}}{C_D s^2 \left\{ Y - S \sqrt{sf(s)} X \right\} - s \sqrt{sf(s)} X} \quad (5.237)$$

$$\begin{aligned} \bar{P}_{Dwf} = & \frac{\left\{ I_0 \left(\sqrt{sf(s)} \right) K_1 \left(\sqrt{sf(s)} r_{eD} \right) + I_1 \left(\sqrt{sf(s)} r_{eD} \right) K_0 \left(\sqrt{sf(s)} \right) \right\}}{C_D s^2 \left\{ Y - S \sqrt{sf(s)} X \right\} - s \sqrt{sf(s)} X} \\ & \times \frac{S \sqrt{sf(s)} \left\{ I_0 \left(\sqrt{sf(s)} \right) K_1 \left(\sqrt{sf(s)} r_{eD} \right) + I_1 \left(\sqrt{sf(s)} r_{eD} \right) K_1 \left(\sqrt{sf(s)} \right) \right\}}{C_D s^2 \left\{ Y - S \sqrt{sf(s)} X \right\} - s \sqrt{sf(s)} X} \end{aligned} \quad (5.238)$$

where

$$X = I_1(\sqrt{sf(s)})K_1(\sqrt{sf(s)r_{eD}}) - I_1(\sqrt{sf(s)r_{eD}})K_1(\sqrt{sf(s)}) \tag{5.239}$$

$$Y = I_0(\sqrt{sf(s)})K_1(\sqrt{sf(s)r_{eD}}) - I_1(\sqrt{sf(s)r_{eD}})K_0(\sqrt{sf(s)}) \tag{5.240}$$

3. Finite reservoir with closed boundary and constant pressure. In the case of closed boundary with constant pressure and no well storage effect and skin effect, we can derive:

$$\bar{P}_{Dwf} = \frac{\{K_0(\sqrt{sf(s)r_D})I_0(\sqrt{sf(s)r_{eD}}) - K_0(\sqrt{sf(s)r_{eD}})I_0(\sqrt{sf(s)r_D})\}}{s\sqrt{sf(s)}[I_0(\sqrt{sf(s)r_{eD}})K_1(\sqrt{sf(s)}) + I_1(\sqrt{sf(s)})K_0(\sqrt{sf(s)r_{eD}})]} \tag{5.241}$$

The solution of Eq. (5.241) indicates that fluid flow in continuous triple medium can be described by five dimensionless parameters including two ω 's and three λ 's (see Table 5.2), of which two λ 's are independent.

In order to verify the multimedium numerical simulation program, we conducted numerical modeling on radial flow on a triple-medium model using the parameters in Table 5.3. The simulation results show that the numerical solution is consistent with the analytical solution (Fig. 5.14).

Table 5.3 Parameters for simulating radial flow in triple-medium reservoir

Parameter	Value	Unit
Matrix porosity	0.263	Dimensionless
Fracture porosity	0.001	Dimensionless
Vug porosity	0.01	Dimensionless
Fracture interval	5	m
Small fracture interval	1.6	m
Feature length of fracture	3.472	m
Contact between fracture–matrix/–vug per unit rock	0.61	m ²
Density of groundwater	1000	kg/m ³
Viscosity of groundwater	1 × 10 ⁻³	Pa · s
Matrix permeability	1.572 × 10 ⁻⁴	D
Permeability of small fractures	1.383 × 10 ⁻¹	D
Permeability of small fracture and vug	1.383 × 10 ⁻²	D
Water yield	100	m ³ /d
Compressibility coefficients of fracture, vug, and matrix	1.0 × 10 ⁻³	MPa ⁻¹
Wellbore radius	0.1	m
Formation thickness	20	m

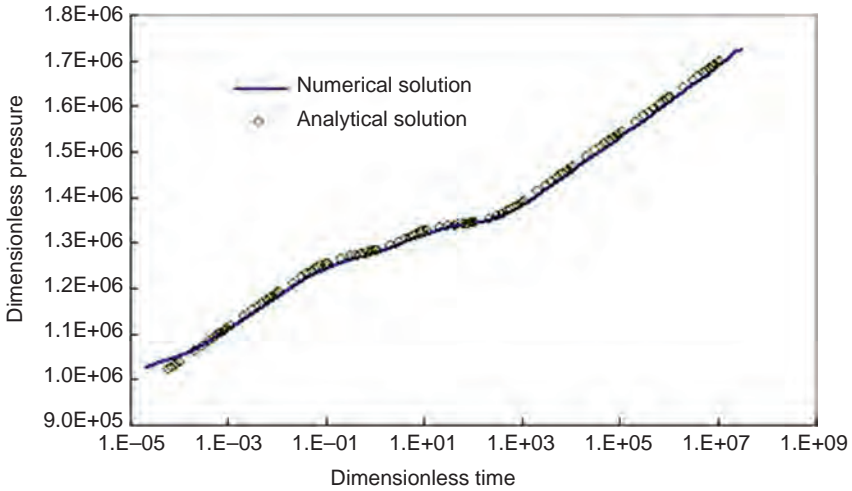


Figure 5.14 Analytical solution versus numerical solution for radial flow in a triple-medium reservoir.

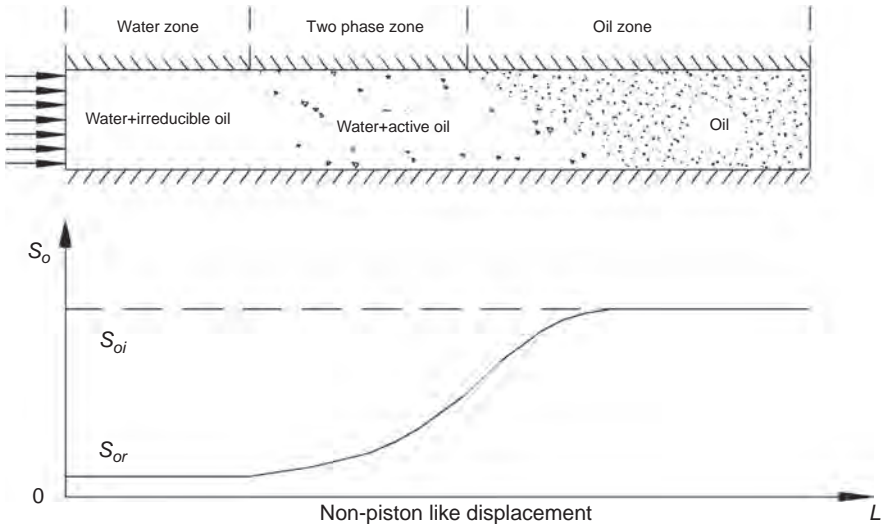


Figure 5.15 Schematic of two-phase non-Darcy flow in porous medium

5.3.1.2 Simulation of high-speed non-Darcy flow

In order to verify the correctness of the numerical model, first we derived the solution under the condition of two-phase high-speed non-Darcy flow (Fig. 5.15) in 1D porous medium. When injection volume is constant, the displacement front at certain saturation can be calculated from the analytical solution.

Table 5.4 lists the simulation parameters. Fig. 5.16 shows the relative permeability curve. Fig. 5.17 shows the equivalent non-Darcy flow coefficient. At varying injection rate, the saturation distribution of wetting phase is shown as in Fig. 5.18 after injecting for 10 hours. At varying high-speed non-Darcy flow coefficient, the water saturation distribution is shown as in Fig. 5.19 after injecting 0.36 m³.

The simulation results show that for 1D two-phase high-speed non-Darcy flow, all the relative permeability curves, high-speed non-Darcy flow parameters and

Table 5.4 Simulation parameters for two-phase high-speed non-Darcy flow in 1D porous medium

Parameters	Value	Unit
Effective porosity (ϕ)	0.30	Dimensionless
Matrix permeability (k_m)	1×10^{-3}	D
Density of wetting phase (ρ_w)	1000	kg/m ³
Viscosity of wetting phase (μ_w)	1	cP
Density of nonwetting phase (ρ_n)	800	kg/m ³
Viscosity of nonwetting phase (μ_n)	1	cP
Non-Darcy flow factor (C_β)	3.2×10^{-9}	m ³ /2
Injection rate (q)	1×10^{-4}	m ³ /s
Azimuth (α)	0	Degrees

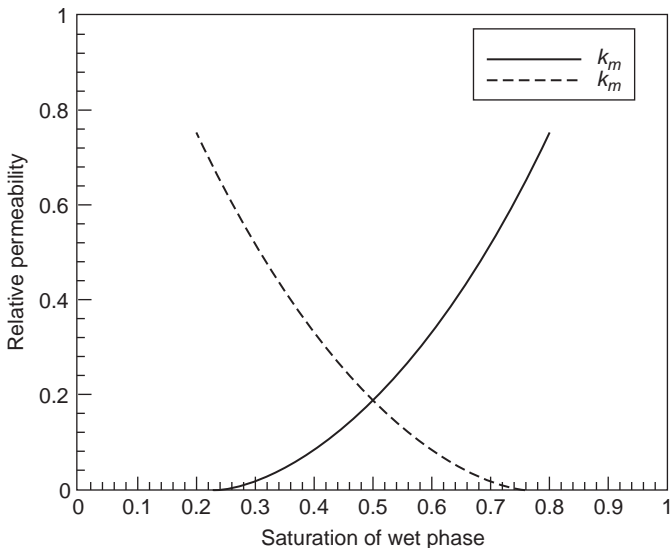


Figure 5.16 Relative permeability curve.

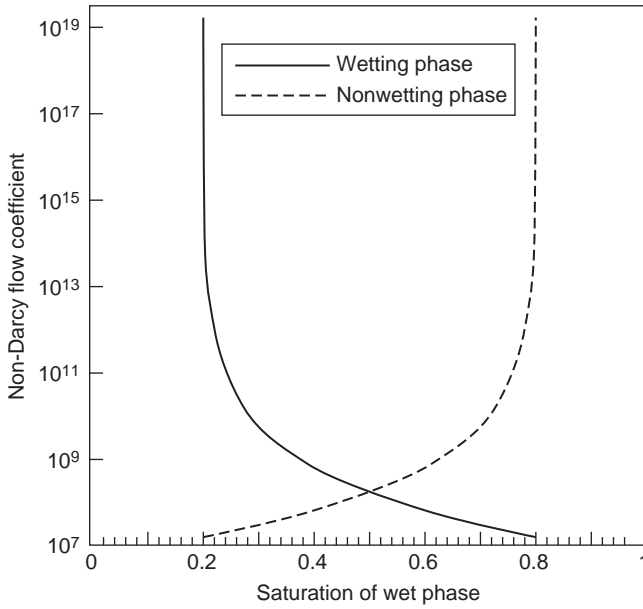


Figure 5.17 High-speed non-Darcy flow coefficient.

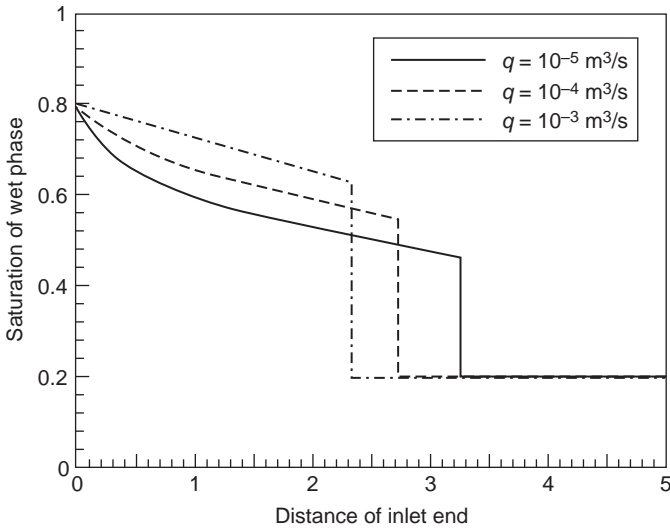


Figure 5.18 Wetting-phase saturation 10 h after injection.

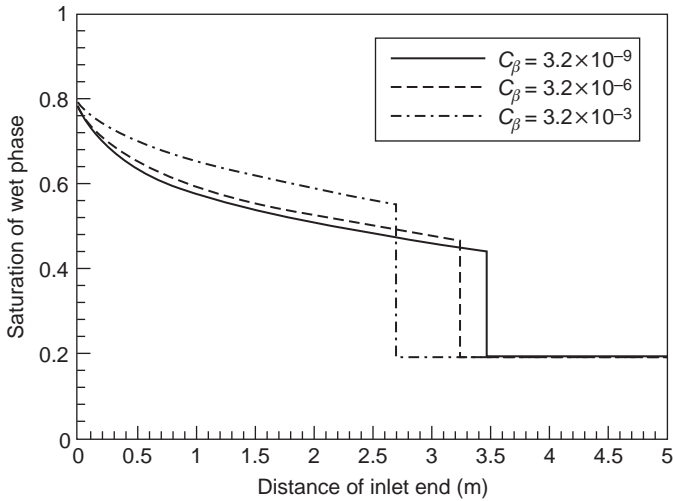


Figure 5.19 Wetting-phase saturation after injecting water of 0.36 m^3 .

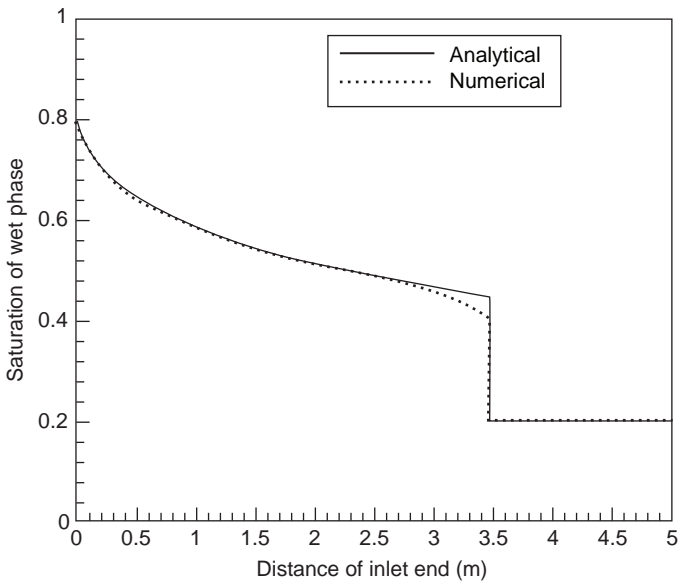


Figure 5.20 Water-phase saturation (10 h after injection).

injection rate have an impact on the displacement front and saturation distribution. The contrast between numerical solution and analytical solution of water saturation distribution is present in Fig. 5.20. The simulations have a high degree of agreement, verifying the accuracy of the numerical simulation and procedures.



Figure 5.21 Physical experimental modeling of fracture-vug reservoir.

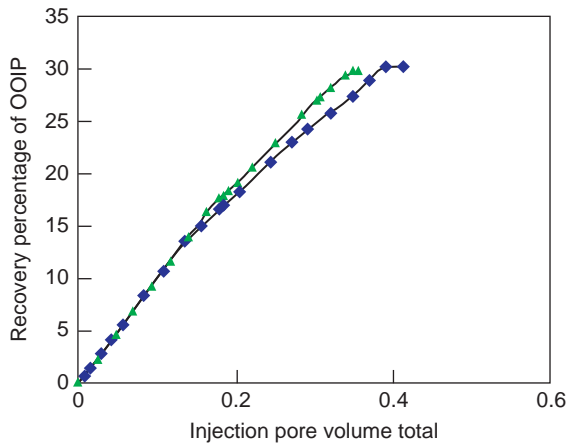


Figure 5.22 Contrast between physical experiment and numerical modeling results.

5.3.1.3 Physical experiment on a plate fracture-vug model

Physical experiment conducted on a plate fracture-vug model (Southwest Petroleum University) was used to verify the accuracy of the simulation results. The fracture-vug model is 90 cm long, 50 cm wide, and 8 cm thick (Fig. 5.21). The crude oil used has density of 0.8433 g/mL and viscosity of 8.36 cp. The experiment was performed at an injection rate of 0.45 L/min.

Comparison of the numerical simulation with the experimental results (Fig. 5.22) shows that the injection and the recovery curves are consistent by 92.5%. The saturation distributions (Figs. 5.23 and 5.24) verify that the numerical simulation method is accurate and applicable.

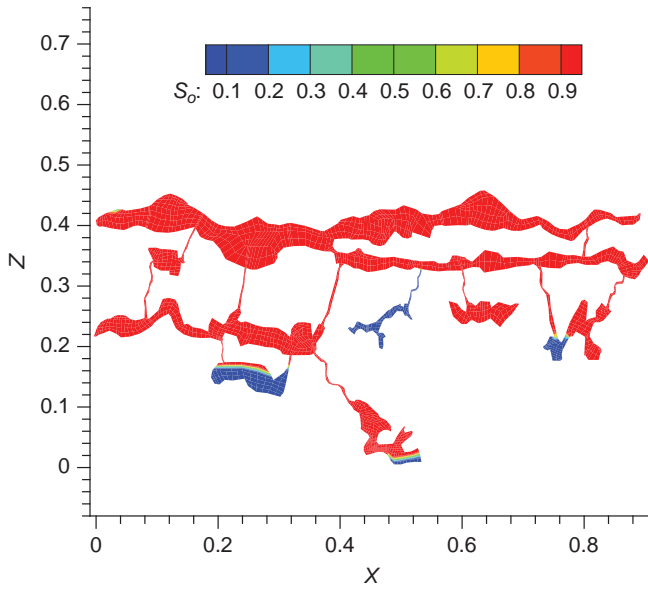


Figure 5.23 Initial saturation distribution by numerical modeling.

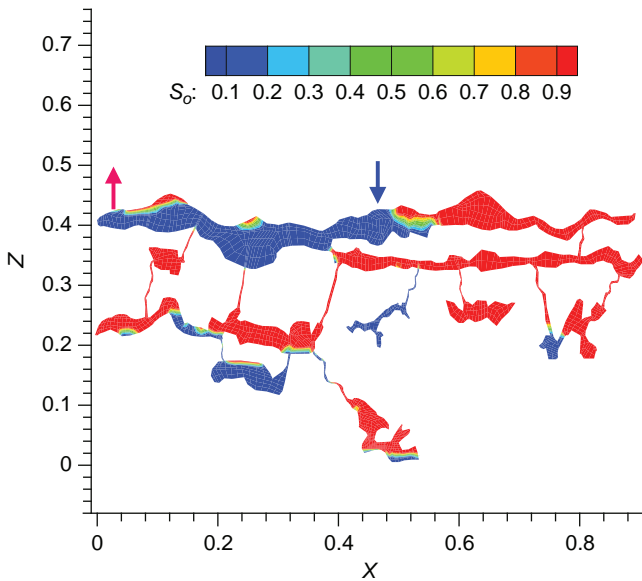


Figure 5.24 Calculated saturation distribution by numerical modeling.

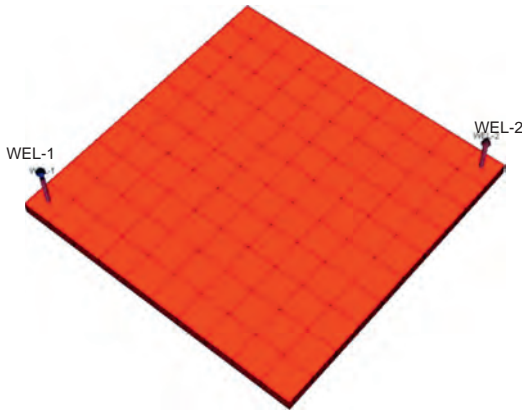


Figure 5.25 Single-medium model.

5.3.1.4 Comparison of KarstSim with similar software based on single-medium model

KarstSim, the software developed by SINOPEC for simulating an equivalent multi-medium fracture-vug reservoir, has been compared with ECLIPSE, the popular numerical simulation software, based on a single-medium model which was introduced as the standard testing example 1 in paper SPE18741. Injection and recovery were analyzed and compared in these two simulations.

The single-medium model including oil-water two-phase fluid is divided into 500 grids ($10 \times 10 \times 5$) (Fig. 5.25), with the step of 14.22 m in both the X and Y directions, and 1.22 m in the Z direction, the permeability of 15.79 mD in X , Y , and Z directions, respectively, the porosity of 0.2 and the top depth of 1.0 m.

The model involves an injection well (Well 1) and a production well (Well 2). Well 1 injects water at $1.67 \text{ m}^3/\text{day}$. Well 2 produces at a constant bottom hole pressure (Fig. 5.26).

After 70 years' simulation, both the pressure and the oil saturation fields provided by two software system are very similar, and their injection–recovery curves match well. This verifies that these two software systems deliver consistent simulation results on the single-medium model.

5.3.1.5 Comparison of KarstSim with similar software based on dual-medium model

KarstSim has been compared with ECLIPSE based on a dual-medium model which was introduced as the standard testing example 6 in paper SPE18741. Injection and recovery relationship, pressure, and saturation distribution fields of different layers were analyzed and compared in these two simulators.

The dual-medium including uniform oil–water two phase fluid is divided into 500 grids ($10 \times 10 \times 5$), with the step of 14.22 m in both the X and Y directions, and 1.22 m in the Z direction, the matrix permeability of 1.572 mD in X , Y and Z

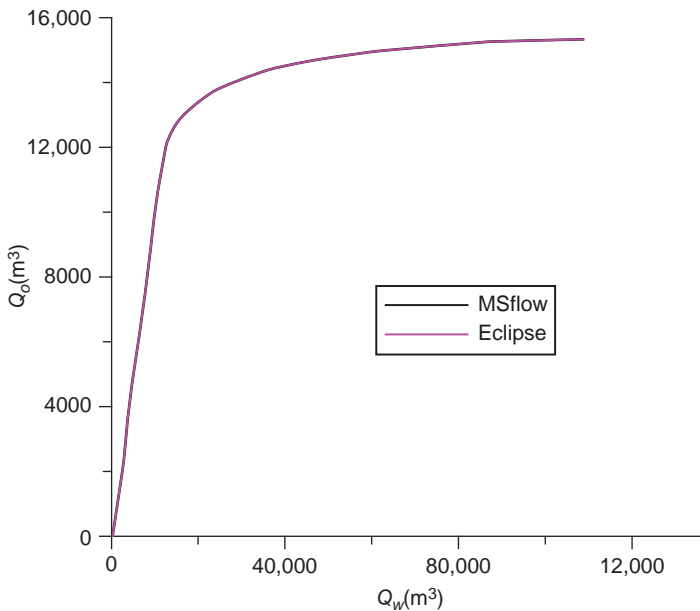


Figure 5.26 Injection versus recovery.

directions, respectively, the fracture permeability of 138.3 mD, the matrix porosity of 0.263, the fracture porosity of 0.0005, and similar fluid and high-pressure petrophysical properties.

The model involves an injection well (Well 1) and a production well (Well 2). Well 1 injects water at 1.669 m³/day. Well 2 produces at a constant bottom hole pressure.

After 70 years' simulation, both the pressure and the oil saturation fields provided by the two software systems are very similar (Figs. 5.27 and 5.28), and their injection–recovery curves almost match with each other (Fig. 5.29). This verifies that these two software systems deliver consistent simulation results on the dual-medium model. The deviation occurring in the transition period of the fitting curves may be because Eclipse used a 1D shape coefficient while Karstism used a 3D shape coefficient which seems more reasonable.

5.3.2 Validation of coupling numerical modeling method

5.3.2.1 Physical experiment modeling of fluid flow in filled vugs

In order to verify the numerical simulation method for fluid flow in filled vugs, a water displacing oil experiment was conducted and CaveSim (the coupling numerical simulation software) was used to simulate the experiment.

The physical experiment model is 600 mm long, 200 mm wide, and 20 mm high. In its center a vug, 70 mm long, 200 mm wide, and 20 mm thick, is located and

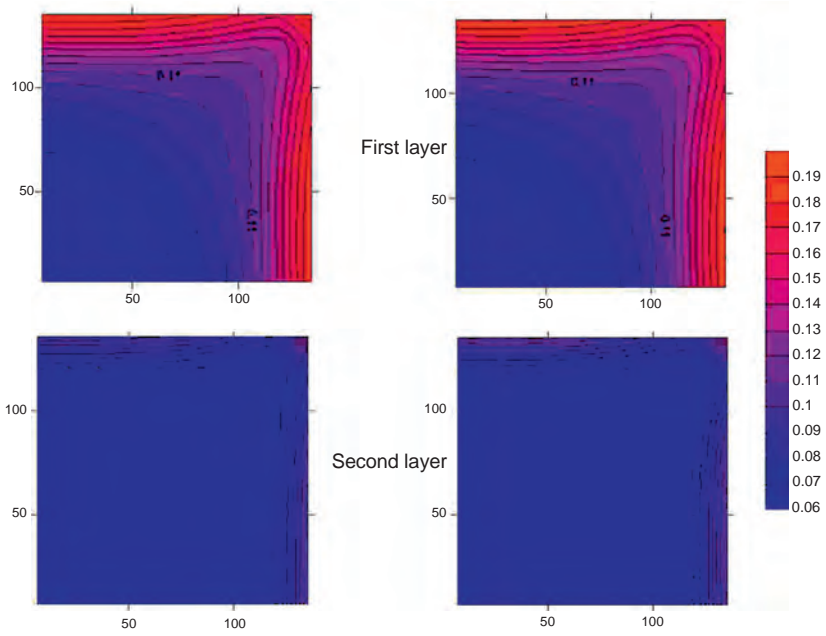


Figure 5.27 Distribution of oil saturation field.

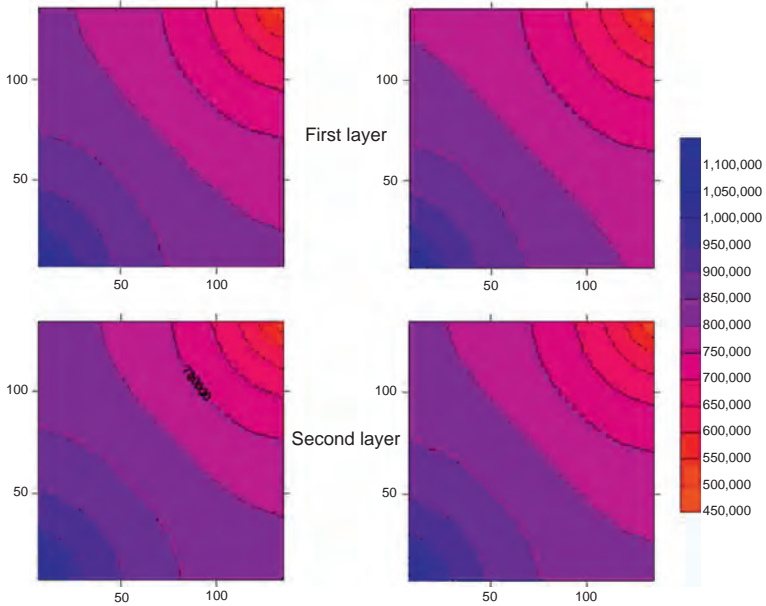


Figure 5.28 Distribution of pressure field.

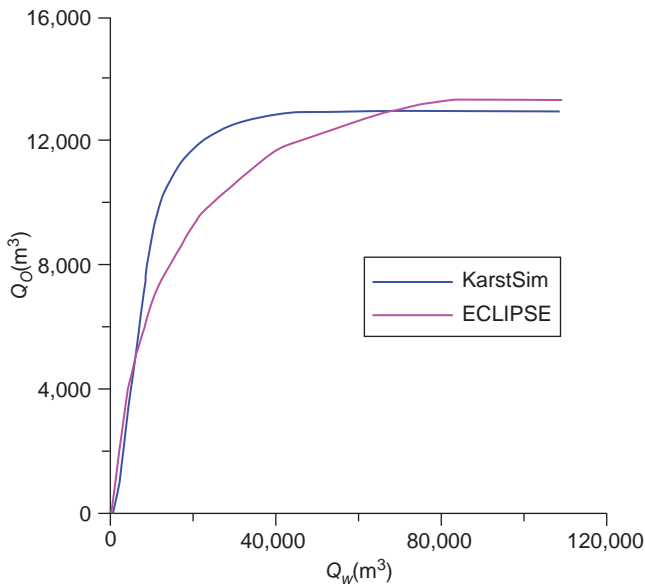


Figure 5.29 Injection versus recovery.

filled with gravel on both sides. Water is injected in the upper right inlet and flows out of the upper left outlet. Both of them have an inner diameter of 2.5 mm. Gravels filled into the model are white marbles with a grain size of 3 mm on the right side, and 5 mm on the left side. The total filling volume is 2.36 L, 1.25 L of which is pore volume. The average porosity is 52.97%.

The density of the simulated oil and water is 0.738 g/mL and 1.00 g/mL, respectively. Oil-soluble capsanthin was taken as the oil colorant and water-soluble green was taken as the water colorant. The horizontal water displacing oil experiment was conducted at an injection rate of 0.45 L/min.

In the experiment process, water injected into the 3-mm-grain-size marble first gradually extended from top down and then ascended when it reached the bottom. Water in the vug displaced oil upwardly and horizontally. Right water–oil contact is triangular or trapezium coning and left water–oil contact is rectangular coning. At the 60th second, lateral sweeping volume was 0.216 L, then after 60 seconds, water gradually ascended to display oil (Fig. 5.30). The remaining oil was mainly distributed in the top part of the side of the vug. The final oil displacement efficiency is 92.1%.

Similar to the experiment model, the numerical model was designed such that a vug was in the center, two sides were filled with white marbles (the right side has porosity of 45.8% and the left 47.7%), and there were 2.5-mm inner diameter inlet and outlet. The modeling and the experimental results match well (Fig. 5.31), during which the right oil–water contact represented triangular coning initially, the oil–water contact in the vug was horizontal, and the left oil–water contact was consistent with the oil–water contact in the vug, displacing oil horizontally and upwardly. The

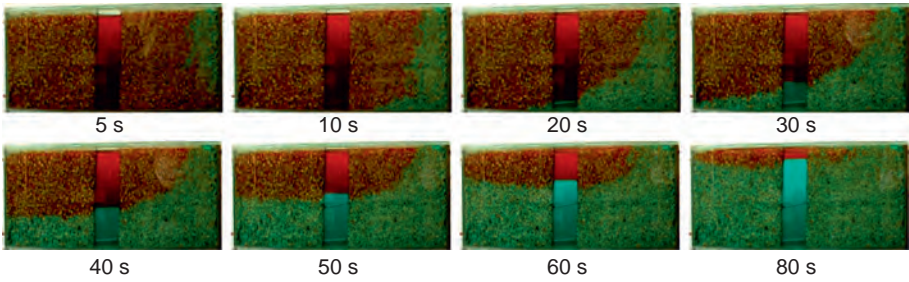


Figure 5.30 Physical modeling of water displacing oil process.

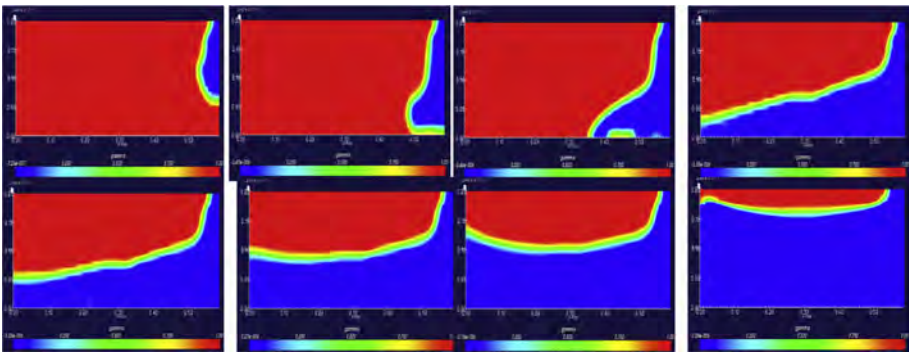


Figure 5.31 Numerical simulation of water displacing oil process.

remaining oil was mainly distributed in the top part of the sides of the vug. The utmost oil displacement efficiency is 92.1%, and the fitting ratio is 99.0%.

5.3.2.2 Two-phase numerical simulation in large caves (caverns)

In order to verify the calculation accuracy of water coning in two-phase flow in large caves/caverns, the physical experiments of two-phase flow in large caves/caverns were conducted. The model used has a length $L = 3600$ mm, a width $k = 130$ mm, and a height $h = 800$ mm (Fig. 5.32). The outlet from which oil is displaced is 127 mm long and 130 mm wide. The density of the oil used is 960 kg/m^3 . The density of the water used is 1140 kg/m^3 . The viscosity of the oil is $0.001 \text{ kg/m} \cdot \text{s}$. Before conducting the experiment, the model was completely filled with oil and kept in a stationary state.

The purpose of the experiment is to simulate the oil recovery process from the well drilled into caverns, focusing on water coning process and variance of water–oil contact to provide a fundamental physical model for numerical simulation. The experiment demonstrated that water coning interface was formed in the oil recovery process due to density difference between oil and water (Fig. 5.33) with the starting angle of coning at about 12 degrees and then gradually reducing.

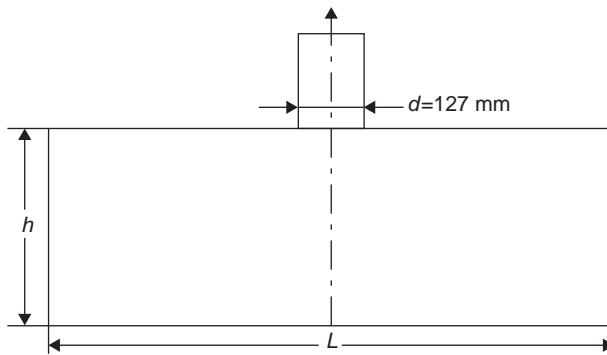


Figure 5.32 Schematic of water coning modeling experiments in caverns.

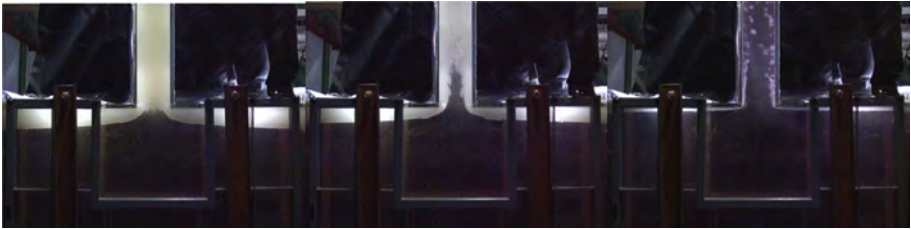


Figure 5.33 Physical modeling of water coning of two-phase flow in caverns.

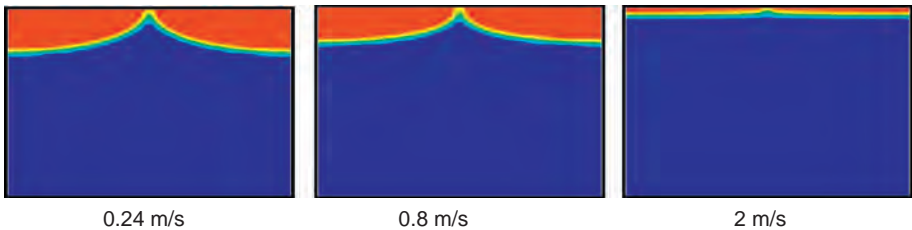


Figure 5.34 Saturation distribution of numerical simulation of water coning of two-phase flow in caverns.

The remaining oil was left mainly in the top of both sides of the well. The ultimate recovery is 90.8%.

The numerical model was designed to be consistent with the physical model (Fig. 5.34). The simulation result matches well with that of the experiment, showing consistent saturation variation, the ultimate recovery up to 92.7%, and good coincidence between them.

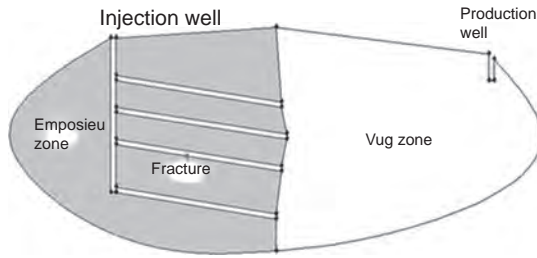


Figure 5.35 The design of a cave-fracture-vug model.

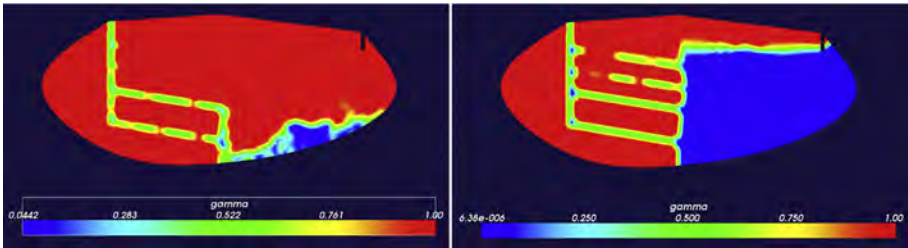


Figure 5.36 Saturation distribution at in different times in the in cave-fracture-vug reservoir model.

5.3.2.3 Injection-recovery simulation in a cave-fracture-vug model

In order to verify the calculation accuracy for complex medium, a conceptual cave-fracture-vug reservoir model was designed based on the prototype of a collapsed cavern where in the middle-lower part, there are residual unfilled caves surrounded by many fractures which extend outward at low angles and among which are vugs. We took half of the numerical model as the conceptual model where the right part was designed to be vugs and the left part was matrix system and there were four fractures (Fig. 5.35).

Boundary conditions: in the right cave zone there is an injection well connecting to the left part through fractures; in the vug zone, there is an oil well where the vugs are completely filled with oil at initial state (Fig. 5.36). The cave is 100 m wide and 45 m high and has a 1-m-wide inlet. The experiment was conducted at an injection rate of 5 m/s using the oil with density of 960 kg/m³ and viscosity of 20 cP, and the water with density of 1140 kg/m³ and viscosity of 1 cP. The injection–recovery simulation reflected the characteristics of oil and water two-phase flow in a cave-fracture-vug reservoir.

5.3.3 Numerical modeling on S48 fracture-vug unit

The equivalent multimedium numerical simulator was applied to simulate the reservoir pressure, saturation, and production performance of the S48 fracture-vug unit based on a 3D geological model and inputting high-pressure physical properties of

reservoir fluid. The simulation result is consistent with the oil yield and water saturation in real oil wells. This proves that the simulator is correct and applicable.

5.3.3.1 General description of S48

S48 is the largest fracture-vug unit in the Tahe Oilfield, which covers a proven oil-bearing area of 11.82 km². Put into production in 1997, the reservoir unit produced the highest daily oil yield in September 2000 – daily oil yield up to 2268 t. Before water flooding, the average daily oil yield is 252 t, total water saturation is 1.34%, annual oil yield is 74.97×10^4 t, and oil recovery is up to 2.54%. In July 2005, water flooding experiments in the unit were conducted. In the initial water flooding stage, oil increase was obvious and daily oil yield increased to 663 t.

The 3D geological model was divided into 362,700 grids: 155 in the *X* direction and 156 in the *Y* direction, and 15 layers in *Z* (vertical) direction. See the parameters of the S48 unit (Table 5.5).

5.3.3.2 Production history fitting in S48

The original formation pressure in S48 is 59 MPa, indicating the reservoir has certain natural energy. Before injecting water, the formation pressure decreased to 50.5 Mpa. After injecting water, the formation pressure recovered to 52.1 Mpa. The historical fitting proves that the calculated formation pressure is consistent with the measured pressure by over 91% (Fig. 5.37), and matches well with the variance of actual formation pressure.

From May 1999 to December 2000, S48 entered the overall development stage when the daily fluid yield was 2822 m³, the oil yield was 2578 t, and the water cut was 5.6%. In September 2000, oil production reached the peak—the unit produced oil at 2268 t/day, the average oil per well was 252 t/day, the water cut was 1.34%, and the annual oil reached up to 74.97×10^4 t. From January 2001 to December 2001, oil production reduced quickly – the daily fluid yield reduced to 2239 m³, the daily oil production reduced to 1318 m³, the water cut increased by 18.0%–43.1%,

Table 5.5 Basic parameters of the S48 fracture-vug unit

Parameter	Value	Parameter	Value
Formation oil saturation pressure	20.20 MPa	Density of formation oil	860.40 kg/m ³
Formation saturation pressure difference	38.80 MPa	Density of surface oil	948.20 kg/m ³
Compressibility coefficient of formation oil	$1.11 \times 10^{-3} \text{ MPa}^{-1}$	Oil/gas ratio	66.00 m ³ /m ³
Viscosity of formation oil	21.70 cP	Oil-water contact	5600.00 m
Original formation pressure	59.00 MPa	Average density of formation water	1140.00 kg/m ³

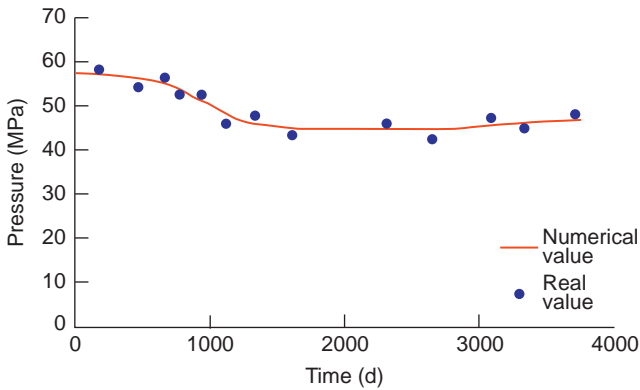


Figure 5.37 Average pressure fitting in the whole area.

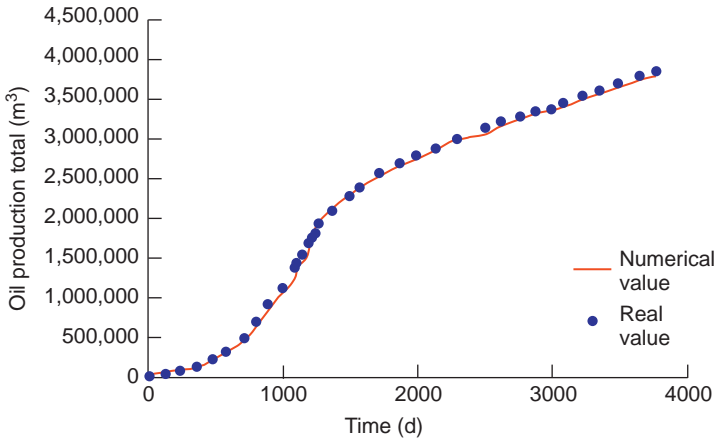


Figure 5.38 Cumulative oil yield fitting result of the S48 unit.

and the natural decline rate was 51.60%. Water injection was conducted from July 2005–10 during which the daily oil production increased to 663 t. The numerical simulation result fits well with the actual production—similar cumulative oil yield and 91%—consistent water cut (Figs. 5.38 and 5.39).

A total of 25 wells (including side drilling wells and deviated wells) in the S48 reservoir unit were fitted. The overall fitting percentage for a single well is 84.6%. Fig. 5.40 shows the fitting result of the cumulative oil yield and water cut of Well S48. Fig. 5.41 shows the fitting result of the cumulative oil yield and water cut of TK142.

After injecting water, oil saturation in the S48 fracture-vug unit changes significantly and the remaining oil is mainly distributed in (Figs. 5.42 and 5.43): (1) the higher part in local fracture-vug bodies not controlled by wells near the weathering crust; (2) unswept area; (3) the area around the seriously flooded well which

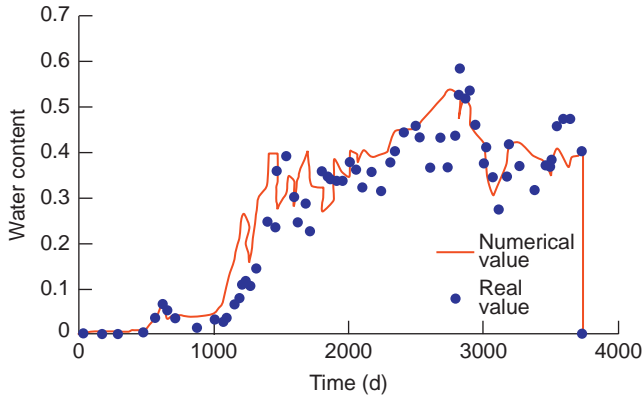


Figure 5.39 Water saturation fitting result of the S48 unit.

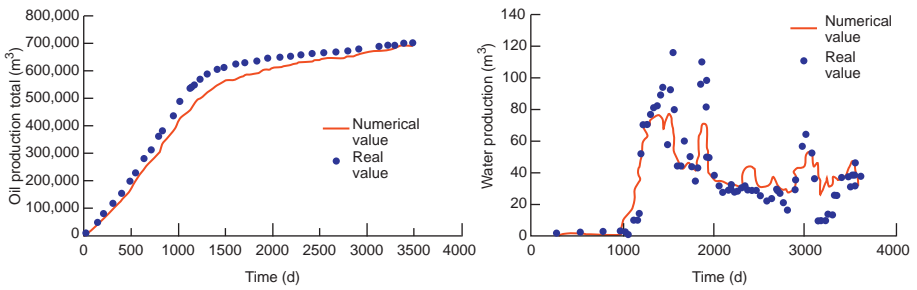


Figure 5.40 Fitting result of the cumulative oil yield and water yield of Well S48.

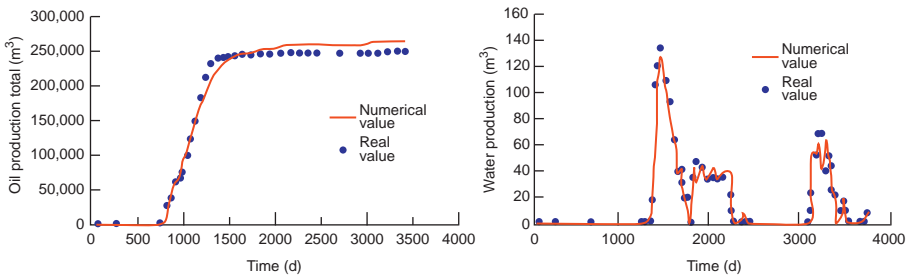


Figure 5.41 Fitting result of the cumulative oil yield and water yield of Well TK412.

produced higher initial production; (4) the area around plane fracture where water channeling occurred; (5) the area around the favorable flow channel in the fracture-vug reservoir between injection and production wells; (6) the sealed zone in local tight bodies (refer to the local higher part in the lower layer).

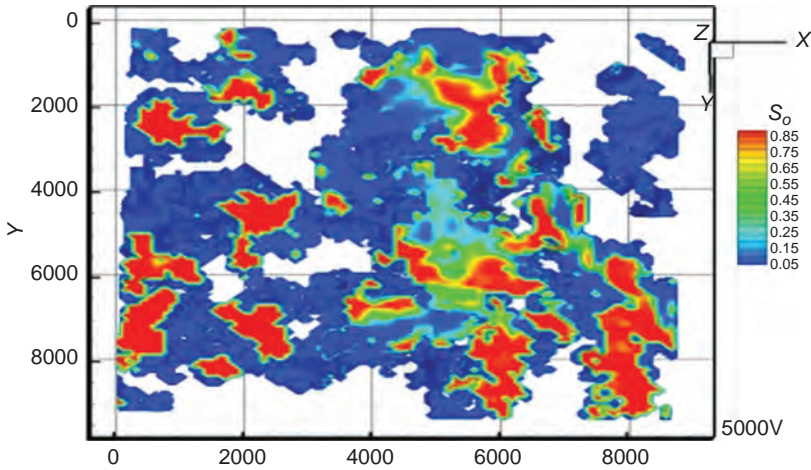


Figure 5.42 The top view of the residual oil distribution in the S48 unit.

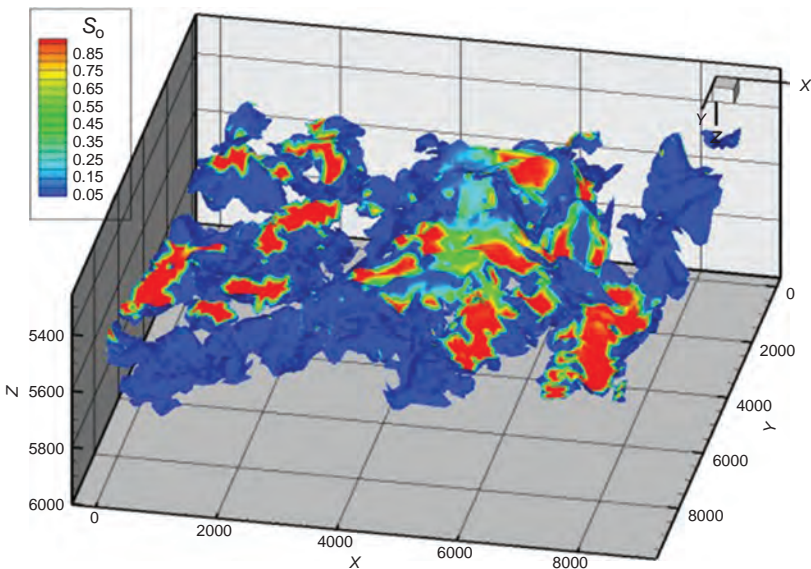


Figure 5.43 The stereogram of the residual oil distribution in the S48 unit.

5.3.3.3 Functions of the numerical simulation software

The numerical simulation software can process reservoir parameters before and after simulation (Fig. 5.43), display different types of reservoirs for the diversity of the fracture-vug reservoir (Fig. 5.44), and show profiles in different manners (Figs. 5.45 and 5.46).

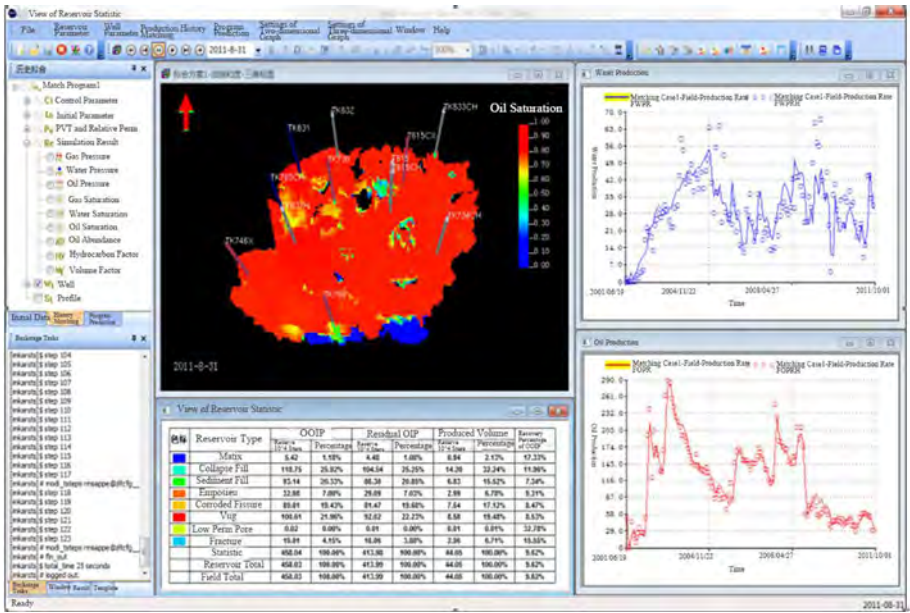


Figure 5.44 Pre- and post-processing windows.

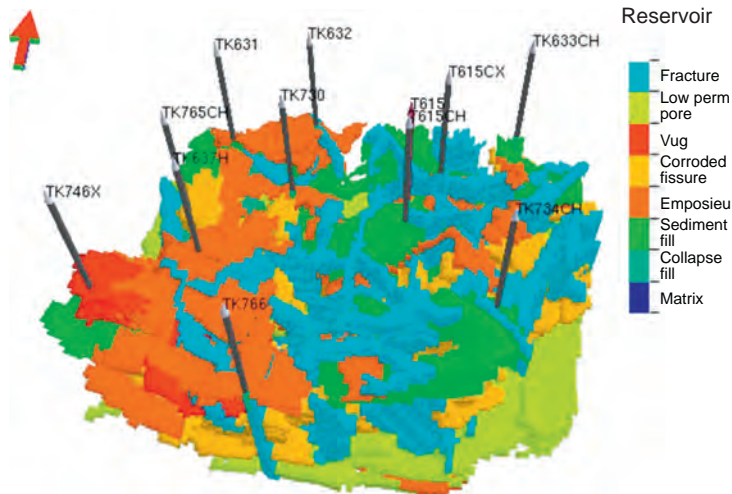


Figure 5.45 Display reservoir in multiple manners.

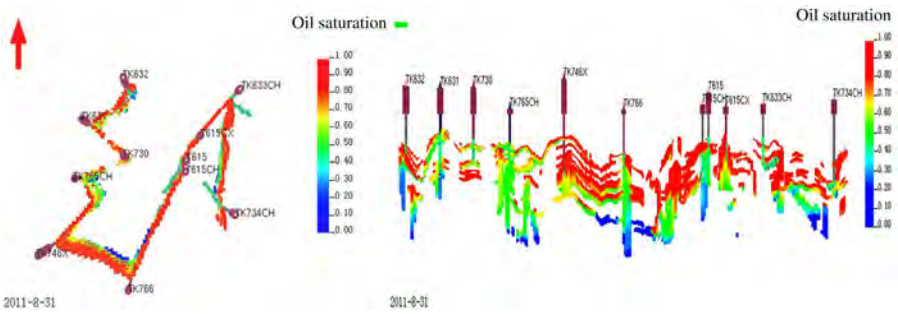


Figure 5.46 Display sections in multiple modes.

Development technology for fracture-cavern carbonate reservoirs

6

During the initial production stage, the fracture-cavern reservoir of the Tahe Oil Field suffered from low drilling success rates, low recovery, and rapid production decline. The lack of mature development technology resulted in generally poor development potential for this type of reservoir. Recently, our research projects supported by the National Basic Research Program of China (973 Program) have succeeded in developing new technologies involving natural energy, water injection, and gas injection.

The development of fracture-cavern carbonate reservoirs can be classified into two categories, one being the development with natural energy, and the other with artificially supplemented energy. Natural energy consists mainly of elastic energy of reservoir fluid and rock, as well as the energy of edge and bottom water. As a result of the discontinuous fractures and caverns, the limited amount of natural energy, and the economically determined wide spacing of usually deep production wells for this type reservoir, the oil extraction ratio is generally low (about 10% for the Tahe Oil Field) and confined to near-borehole regions when relying on natural energy alone. Artificial energy supplements often come in two forms, waterflooding and gas flooding. Waterflooding can effectively displace inter-well residual oil, increase oil production and recovery ratios (currently 3%–5% in the Tahe Oil Field). However, fracture-cavern reservoirs commonly have complex spatial distribution patterns and, consequently, waterflooding may produce only small sweep areas and water channeling. Complex spatial configurations between a fracture-cavern system and production wells may result in attic residual oil being left at the tops of caves, which can be effectively displaced by a gas cap generated from gas flooding.

6.1 Performance analysis techniques for fracture-cavern reservoirs

After an oil field is put into development, the understanding of production characteristics and variation pattern of the reservoir is the key to achieving effective development and production. Multiscaled reservoir bodies and diverse fluid flow patterns in a carbonate fracture-cavern reservoir result in complex performance and variation patterns of production. In this study, the production variations, water-cut, and energy characteristics in different types of reservoir bodies have been

examined, and a theoretical well testing model has been built for coupled percolation and free flow in a triple-porosity medium.

6.1.1 Variation characteristics and prediction model for individual well production

There are many types of reservoir bodies in a fracture-cavern reservoir, and wells penetrating different types of reservoir bodies can have quite different production performance characteristics.

6.1.1.1 Variation characteristics of individual well production

Most of the oil wells that penetrate cavern-type reservoir bodies or connect with large caves through stimulation measures (e.g., acid fracturing) produce through natural flow, with a high initial production rate, a prolonged water-free oil recovery period, and a relatively long period of stable production, but they also have a rapid decrease in production after entering the decline stage. Oil wells penetrating fracture-cavern reservoir bodies have the potential of natural flow, with moderate to high initial production, a short water-free oil recovery period, a moderate duration of stable production, and a relatively long period of reduced production during the decline stage. In general, oil wells penetrating fracture-cavern or fractured reservoir bodies are put into production using artificial lift, characterized by insufficient energy and low production, without a period of stable production (Figs. 6.1–6.3, Table 6.1).

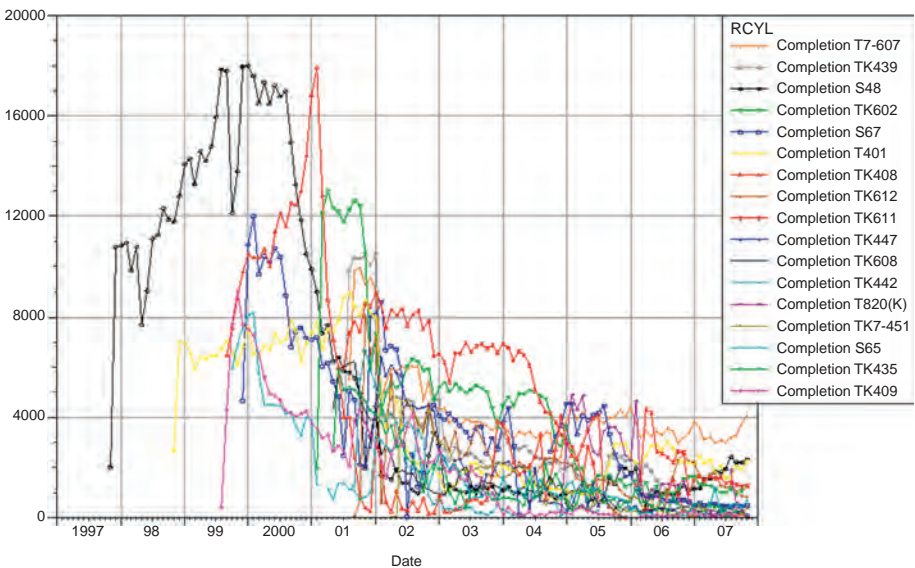


Figure 6.1 Production curve of oil wells penetrating the cavern reservoir body.

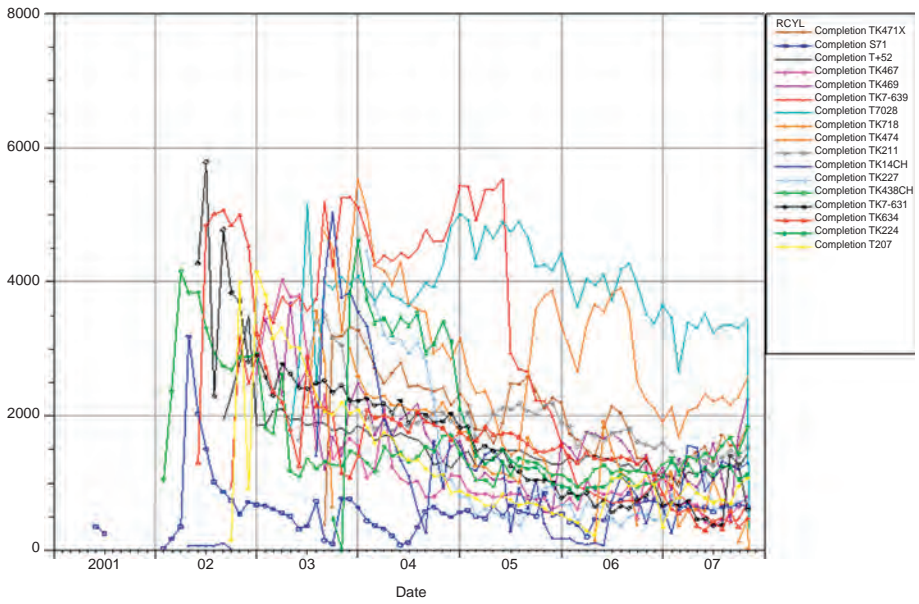


Figure 6.2 Production curve of oil wells penetrating the fracture-cavern reservoir body.

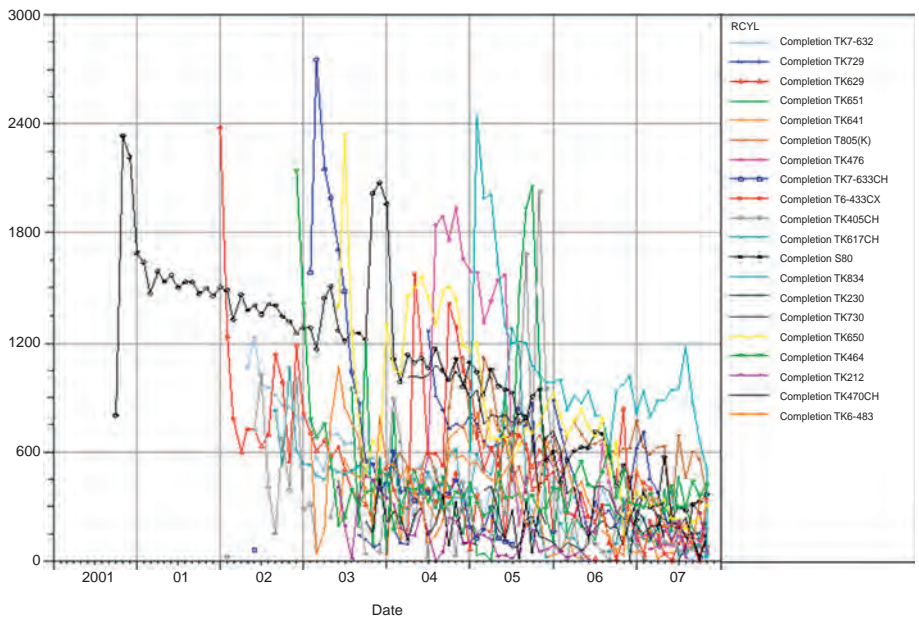


Figure 6.3 Production curve of oil wells penetrating the fracture-cavern or fractured reservoir body.

Table 6.1 Performance of individual wells penetrating different types of reservoir bodies in the Tahe Oil Field

Type of penetrated reservoir bodies	Performance characteristics			
		Maximum	Minimum	Average
Cavern reservoir body	Initial production (t/d)	378.60	104.36	225.59
	Water free oil production period (d)	1391	178	875.04
	Period of stable production (d)	1440	314	948.3
Fracture-cavern reservoir body	Initial production (t/d)	354.87	34.96	137.44
	Water free oil production period (d)	1168	0	265.5
	Period of stable production (d)	2700	60	627.94
Fracture-cavern or fractured reservoir body	Initial production (t/d)	280.2	0	36.61
	Water free oil production period (d)	736	0	47.64
	Period of stable production (d)	0	0	0

6.1.1.2 Prediction model for individual well production

Production prediction models for different types of wells have been built through statistical analysis of production well data.

The production decline of oil wells penetrating a cavern-type reservoir body or connecting with large caves through stimulation measures (e.g., acid fracturing) fits an exponential decline pattern, with a monthly decline rate of 0.028. The fitted production decline equation is:

$$q = q_i e^{-0.028t} \quad (6.1)$$

According to the relationship between production and cumulative production in exponential decline, the prediction model for cumulative oil production in the decline period is:

$$N_p = \frac{q_i - q}{0.028} \quad (6.2)$$

where q is the monthly oil production, t/month; q_i is the initial monthly oil production, t/month; N_p is the cumulative oil production in the decline period, t .

The production decline of oil wells penetrating a fracture-cavern reservoir body also fits an exponential decline pattern, with a monthly decline rate of 0.019. The fitted production decline equation is:

$$q = q_i e^{-0.019t} \quad (6.3)$$

According to the relationship between production and cumulative production in exponential decline, the prediction model of cumulative oil production in the decline period is:

$$N_p = \frac{q_i - q}{0.019} \quad (6.4)$$

The production decline of oil wells penetrating fracture-cavern or fractured reservoir bodies fits a harmonic decline pattern, with an initial monthly decline rate of 0.028. The fitted production decline equation is:

$$q = \frac{q_i}{1 + 0.028t} \quad (6.5)$$

According to the relationship between production and cumulative production in harmonic decline, the prediction model for cumulative oil production in the decline period is:

$$N_p = \frac{q_i}{0.028} \ln \frac{q_i}{q} \quad (6.6)$$

6.1.2 Evaluation of natural energy in fracture-cavern reservoir

There are mainly two types of natural energy in fracture-cavern reservoirs, one being the elastic expansion energy corresponding to elastic drive mostly during the initial development period, and the other the edge and bottom water energy outside of the reservoir from the elastic water drive.

6.1.2.1 Comprehensive evaluation index of natural energy – D_{pr}

D_{pr} is the average formation pressure drawdown when 1% of the geological reserve has been extracted:

$$D_{pr} = \frac{\Delta PN}{100N_p} \quad (6.7)$$

where N is the original oil in place (OOIP), $\times 10^4$ t; N_p is the cumulative oil production, $\times 10^4$ t; ΔP is average formation pressure drawdown, MPa.

D_{pr} is used for comprehensive evaluation of natural energy. A lower D_{pr} value indicates more sufficient natural energy.

6.1.2.2 Evaluation index of elastic energy – elastic productivity

Elastic productivity is the recovered volume of oil due to elasticity, measured by the product of extracted reserves, initial volume factor and total compressibility coefficient, when the pressure in a fracture-cavern unit drops by 1 MPa:

$$\text{Elastic productivity} = NB_{oi}C_t \quad (6.8)$$

where B_{oi} is the volume factor of oil, and C_t is the total compressibility, MPa^{-1} .

Elastic productivity is used to evaluate the elastic energy of a reservoir and a greater elastic productivity value implies a higher level of elastic energy sufficiency and a higher elastic recovery.

To evaluate the elastic energy in the Tahe Oil Field, the following criteria are used:

- A fracture-cavern unit with low elastic energy has an elastic productivity of less than $2 \times 10^4 \text{ m}^3/\text{MPa}$;
- A fracture-cavern unit with a moderate amount of elastic energy has an elastic productivity between 2×10^4 and $10 \times 10^4 \text{ m}^3/\text{MPa}$;
- A fracture-cave unit with sufficient elastic energy has an elastic productivity greater than $10 \times 10^4 \text{ m}^3/\text{MPa}$.

With formation pressure about 60 MPa, bubble pressure about 20 MPa, and total compressibility of $1.25 \times 10^{-3} \text{ MPa}^{-1}$, the Tahe Oil Field has a theoretical elastic recovery of 4%–6%. However, the actual pressure drawdown in the Tahe Oil Field is lower than 5 MPa and, consequently, the actual elastic recovery rate is very low (less than 1%).

6.1.2.3 Evaluation index for edge and bottom water energy – N_{pr}

N_{pr} is a dimensionless measure of elastic production, expressed as the ratio of cumulative production and elastic production:

$$N_{pr} = \frac{N_p B_o}{N B_{oi} C_i (P_i - \bar{P})} \quad (6.9)$$

where P_i is the initial formation pressure, MPa; \bar{P} is the current average formation pressure, MPa.

N_{pr} reflects the energy of natural water, and higher N_{pr} values imply a greater degree of energy sufficiency of natural water.

In terms of natural water energy, the elastic energy of fracture-cave reservoir in the Tahe Oilfield is classified into four types:

- Units with sufficient natural water energy: $N_{pr} \geq 30.0$;
- Units with relatively sufficient natural water energy: $8.0 \leq N_{pr} < 30.0$;
- Units with a moderate amount of natural water energy: $2.5 \leq N_{pr} < 8.0$;
- Units with insufficient natural water energy: $N_{pr} < 2.5$.

During the production period driven by natural energy in the Tahe Oil Field, the formation pressure drawdown does not exceed 5 MPa; units with sufficient natural water energy, relatively sufficient energy, moderate energy, and insufficient energy will have a recovery rate of over 18%, between 4% and 18%, between 1% and 4%, and less than 1%, respectively.

Evaluation of the natural water energy in the Tahe Oil Field shows that the proportions of reserve units with sufficient energy, relatively sufficient energy, moderate energy and insufficient energy are 48%, 31%, 12% and 9%, respectively.

Therefore, the theoretical recovery driven by natural water energy in the Tahe Oil Field is approximately 12%.

6.1.3 Numerical well testing model and interpretations for fracture-cavern reservoirs

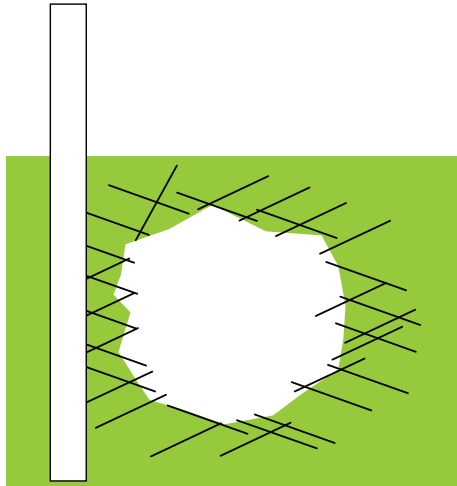
Well testing aims to determine the producing capacity and reservoir parameters of a well. Well testing models include analytical well testing models and numerical well testing models, with the former reflecting reservoir parameters of uniform reservoirs and the latter delineating reservoir parameters of anisotropic reservoirs. Conventional analytical well testing and numerical well testing models are not applicable to the Tahe Oil Field because of the multiscale and discontinuous characteristics of its fracture-cavern reservoir. Through our research coupling flow in medium with pores, fractures and caverns of various scales, two types of numerical well testing models – the triple-porosity model and the coupled percolation-free flow model – have been built to tackle well testing issues, including fracture-cavern multiscale medium, different production variations, and multiphase flow. When the reservoir medium is continuous, the triple-porosity numerical model is used for interpretation, which is applicable to oil wells where fractures are connected with caverns. When there are large-scale fractures and caverns in the reservoir medium, the coupled percolation-free flow model is used for interpretation, an approach applicable to oil wells that directly penetrate caverns.

For fracture-cavern reservoirs, well testing comprises interpretation of both conventional parameters (such as borehole storage coefficient, skin factor, fracture or cavern permeability, coefficient of crossflow from matrix to cavern, coefficient of crossflow from fractures to caverns, elastic storativity ratio of rock and elastic storativity ratio of caverns) and other parameters such as cavern size, spatial relationships of caverns and wells, and fracture width and density.

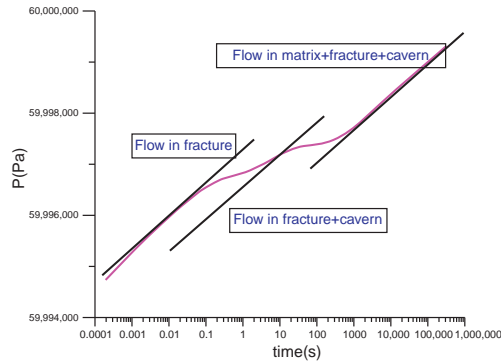
6.1.3.1 Numerical well testing based on triple-porosity medium

1. Percolation pattern from numerical well testing based on single-phase flow in triple-porosity medium

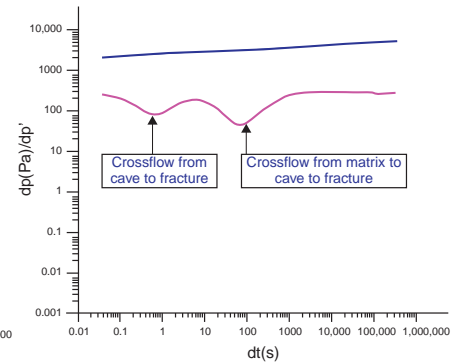
When an oil well penetrates fractures connected with caverns, as shown in [Fig. 6.4A](#), the single-phase flow pattern in a triple-porosity medium obtained by numerical well testing can be summarized as follows. After shut-in, the well pressure in the fracture system recovers first, but the pressure in the matrix and cavern system remains unchanged, resulting in a pressure difference between the fracture-cavern system and the pore-fracture system. When the pressure difference is small, there is only crossflow from fractures to caverns, and the pressure recovery becomes slower, generating the first sag on the derivative curve; thereafter, with further increase in the pressure difference, a crossflow from matrix to fractures and caverns occurs, causing further slow-down in pressure recovery and generating the second sag on the derivative curve. Finally, the pressure in the matrix, fracture, and cave system reaches an equilibrium, corresponding to a linear rise in the semi-log curve, which depicts the characteristics of the entire system, as shown in [Fig. 6.4B and C](#).



(A)



(B)



(C)

Figure 6.4 Analysis of percolation pattern in triple-porosity medium. (A) Concept model (B) Pressure curve (C) Pressure derivative curve.

Several factors can affect well testing responses, including cavern permeability, fracture permeability, cavern porosity, fracture porosity, matrix porosity, fracture spacing, characteristic length of fracture, formation pressure, skin factor, and borehole storage coefficient.

2. Well testing responses for complex geological models

Complex models include fault model, production variation model and composite model. These three models have different well-testing responses in accordance with the triple-porosity single-phase flow numerical well-testing theory.

a. Production variation model

In general, the analytical method of well testing is based on the assumption of constant production, which is difficult to find in actual situations, whereas numerical well testing can deal with variable production wells. Based on the well-testing theory for fracture-cavern reservoirs, the pressure response (Fig. 6.5) to a stepwise production variation (Fig. 6.6) demonstrates that the production variations do not affect the responses of the theoretical well testing curve to a triple-porosity medium model

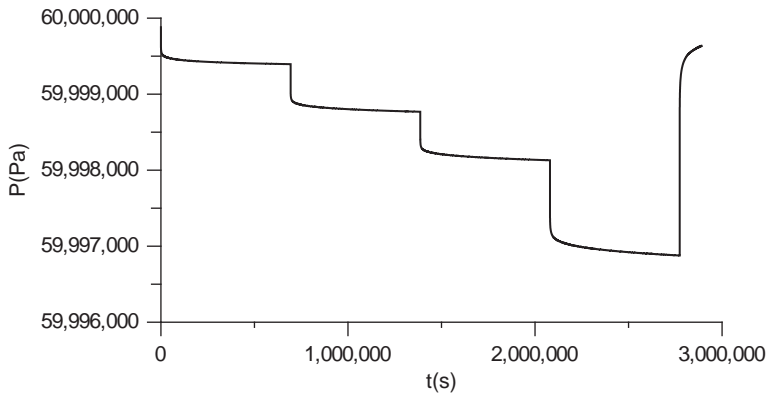


Figure 6.5 Pressure history from numerical simulation with production variation model.

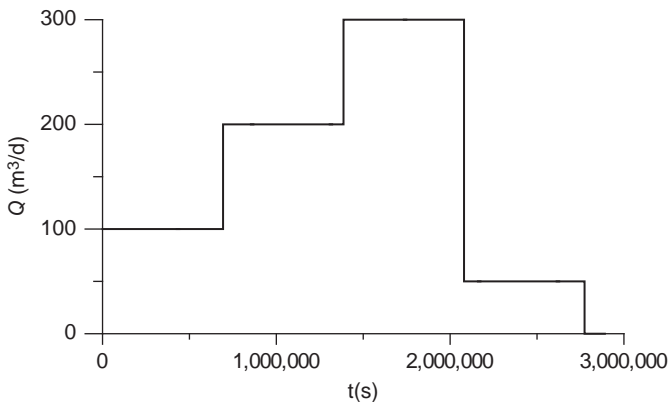


Figure 6.6 Expansion view of production history from production variation model.

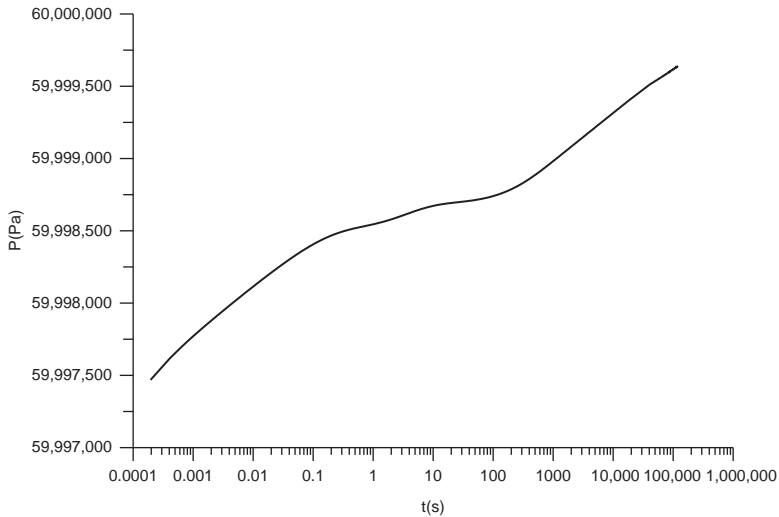


Figure 6.7 Semi-log plot of pressure build-up from production variation model.

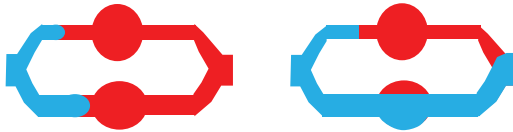


Figure 6.8 Waterflooding displacement sketch of fracture-cave reservoirs.

(Fig. 6.7) because the semi-log pressure build-up curve still shows three straight-line segments and two transitional segments, which are the fundamental characteristics of the triple-porosity well testing curve.

b. Linear fault model

The design of this model is based on closed square blocks of strata. The effects of constant pressure boundary, the presence of a single fault or double faults on theoretical well testing curves are described by positioning the well at the center, on the edge, or in the corner of the square. Each square block of strata is $1050 \times 1050 \times 20$ m, in a $21 \times 21 \times 4$ grid along X , Y , and Z axes, respectively. The model uses a block-centered grid, with permeability values of $0.1572 \times 10^{-3} \mu\text{m}^2$, $1383 \times 10^{-3} \mu\text{m}^2$ and $13.83 \times 10^{-3} \mu\text{m}^2$ in three respective directions. The pressure drawdown curve and pressure build-up curve are shown in Figs. 6.8 and 6.9, respectively. It can be observed that when the well is located in the center of the square block, the curve demonstrates the effect of closed square block boundary; when the well is located on the edge, the curve shows the effect of double faults, similar to that of a closed boundary of a circular-shaped stratal formation. When the well is located in the corner, the curve shows the effect of a single fault.

Radial grid is applicable to the study of stratal formation characteristics around a single well and circular boundary, whereas block centered grid can be used to investigate multiwell interference well testing, in addition to the description of relatively complex formational conditions (Figs. 6.10 and 6.11).

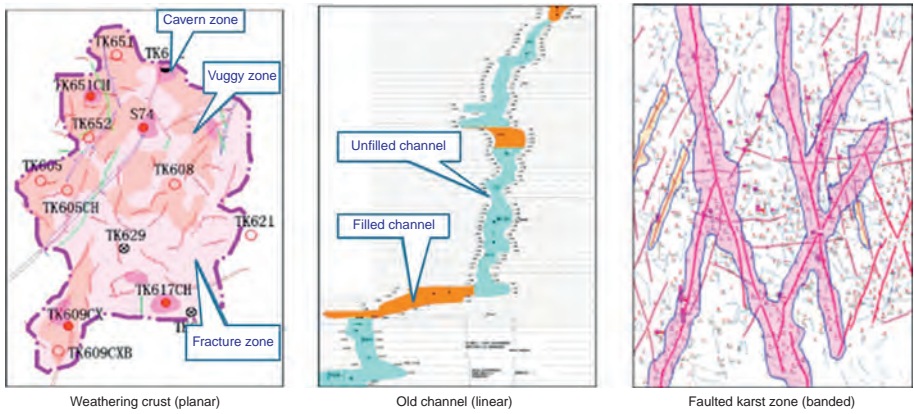


Figure 6.9 Distribution characteristics of three types of typical fracture-cave reservoir bodies.

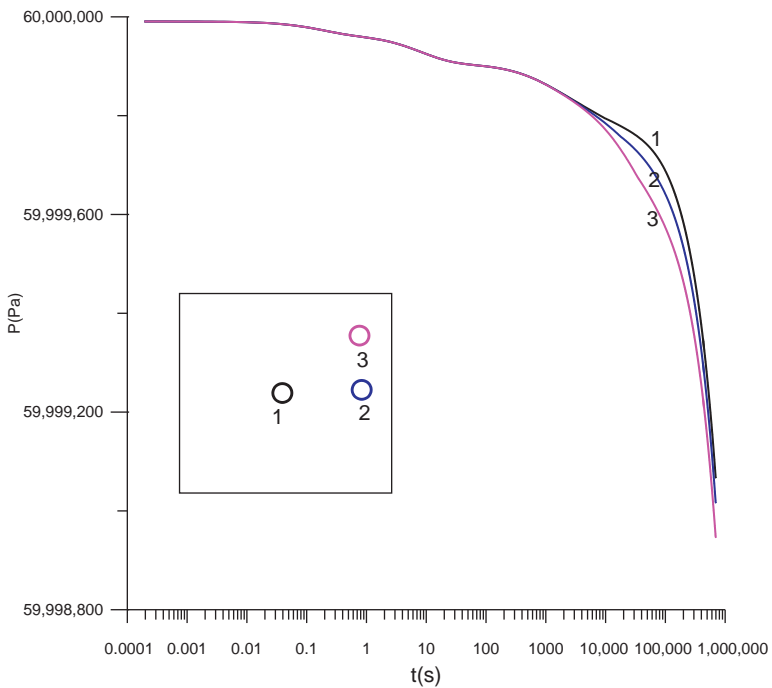


Figure 6.10 Comparison of pressure drawdown curves with well in different positions in a closed stratal formation.

c. Composite reservoir model

In terms of fracture permeability, the late segment of a semi-log pressure drawdown curve will show a drop if the composite reservoir lithology deteriorates, but it will show a rise if the composite reservoir lithology improves (Fig. 6.12). The late

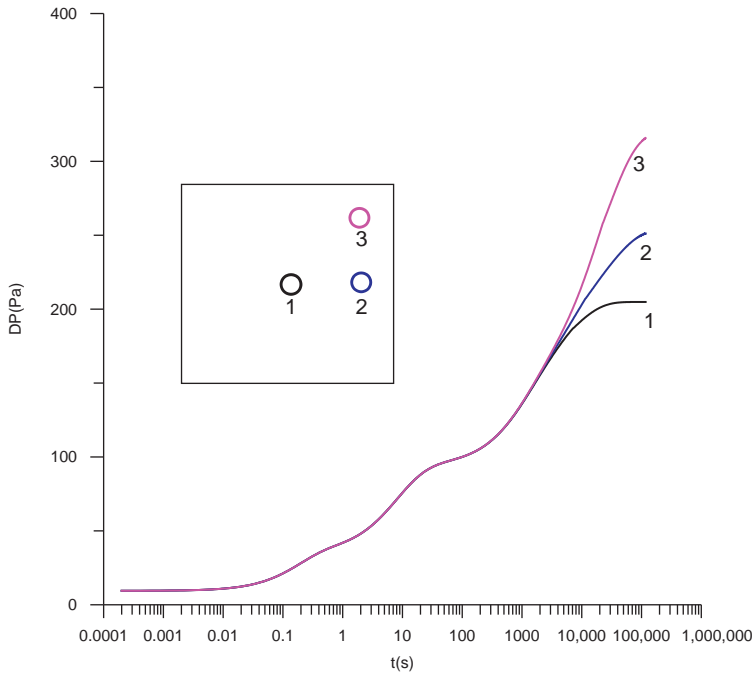


Figure 6.11 Comparison of pressure buildup curves with well in different positions in a closed stratal formation.

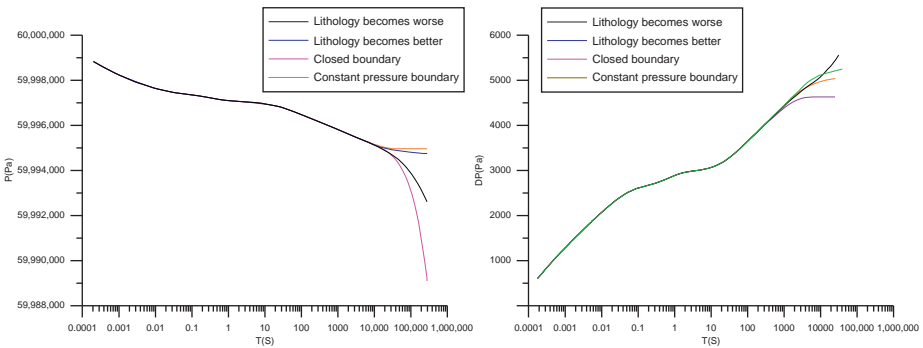


Figure 6.12 Comparison of pressure drawdown and pressure build-up curves of composite reservoir and uniform reservoir with closed or constant pressure boundary.

segment of a semi-log pressure build-up curve will show a rise if the composite reservoir lithology worsens, but it will become flat if the composite reservoir lithology ameliorates.

In actual well testing interpretations, the curve of a reservoir with significant lithology deterioration has similar characteristics to that of a reservoir with a closed boundary, whereas the curve of a reservoir with significant lithology improvement shows

similar characteristics to that of a reservoir with constant pressure boundary. Thus, the geological information should be taken into consideration for achieving a reliable interpretation.

3. Inversion of single-phase numerical well testing in triple-porosity medium

Based on the existing knowledge of a reservoir, the closest well testing parameter combination is selected, and more actualistic formation parameters are obtained through well testing inversion.

a. Theoretical basis for solving inversed well testing problems with automatic fitting technique: Gauss–Newton Method (GNM)

The GNM used in geophysical inversion can achieve the best fit between the theoretical curve and the actual curve under some constraints. This method is applicable to rebuilding a fast optimization of the multiparameter complex model, with good stability and high resolution.

The relationship between the model parameter vector and observation data vector is assumed to be:

$$D\vec{m} = \vec{d} \quad (6.10)$$

where D = forward operator; \vec{m} = model parameter vector; \vec{d} = response of real model (observation data vector).

In general, D is nonlinear and should be linearized first. The Taylor series expansion of Eq. (6.10) is

$$\vec{d} = D\vec{m}_0 + A\Delta\vec{m} \quad (6.11)$$

Let $\vec{d}_0 = D\vec{m}_0$, then

$$\Delta\vec{d} = A\Delta\vec{m} \quad (6.12)$$

The equation above is the fundamental tool for inversion, in which A is the Jacobian matrix, and

$$A = \frac{\partial D}{\partial \vec{m}} \quad (6.13)$$

$$\text{That is } A_{ij} = \frac{\partial d_{ij}}{\partial m_i} \quad (6.14)$$

In well testing interpretation, Eq. (6.12) is overdetermined and cannot be solved directly. Instead, the minimum variance method is generally used.

The objective function is assumed to be:

$$E = (d_{obs} - d)^T (d_{obs} - d) \quad (6.15)$$

Eq. (6.12) is substituted into Eq. (6.16), and set the derivative of E with respect to the correction of model parameters to 0, then

$$A^T A \Delta\vec{m} = A^T \Delta d_{obs} \quad (6.16)$$

Δd_{obs} in Eqs. (6.15) and (6.16) is the difference between the observation value and the forward calculation value of the initial model, which is known. Therefore, the correction of model parameters, $\Delta \vec{m}$, can be calculated, then

$$\vec{m} = \vec{m}_0 + \Delta \vec{m} \tag{6.17}$$

The process above is repeated for the corrected model, until the given convergence condition is met.

b. Automatic fitting method for well testing curves

The parameter perturbation method is used to solve a Jacobian matrix in order to calibrate theoretical well testing curves. Based on the existing inversion result, \vec{m}_k , the elements of \vec{m}_k are randomly perturbed to obtain the n th time forward modeling result. The difference between this resultant value and \vec{m}_k is divided by the perturbation item. Then

$$A_{ij} = \frac{\partial d_j^i}{\partial m_i} = \frac{d_j^i - d_j^{m_k}}{\Delta m_i}, i = 1, \dots, n; j = 1, \dots, m \tag{6.18}$$

$$A_k = (A_{ij})_{n \times m}$$

When calculating the theoretical well testing curve, the time intervals are selected according to the requirement on the convergence property of the forward modeling calculation. During inversion calculation, the time intervals of forwarding are designed according to the requirement on convergence, and samples are taken by interpolation of observed time points. A set of forward response data is obtained with the time points identical to that of observation data, which is then used to calculate the objective function in inversion and to fit observed data. For a specific problem under study, the theoretically calculated value is interpolated in logarithmic coordinates and the sampling data are used for inversion.

c. Inversion examples

Fracture permeability, cavern permeability, initial formation pressure, skin factor, and borehole storage coefficient are used as unknown parameters and inversely simulated simultaneously. The curves fit well (Fig. 6.13), but the cavern permeability and borehole storage coefficient have poor interpretation accuracy (Table 6.2).

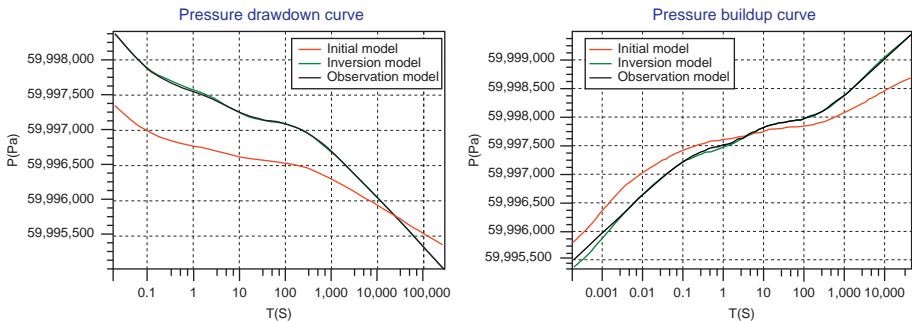
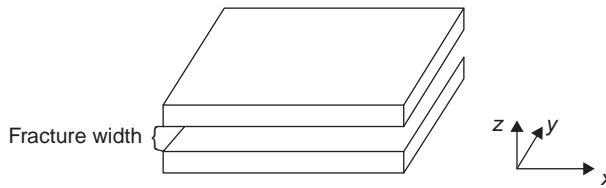


Figure 6.13 Result curves of simultaneous inversion of five parameters.

Table 6.2 Results from simultaneous inversion of five parameters

Parameter	Initial model	Inversion result	Actual model
Fracture permeability k_F (m ²)	2.383×10^{-13}	$1.3998595 \times 10^{-13}$	1.383×10^{-13}
Cave permeability (small fracture permeability), k_V (m ²)	1.000×10^{-14}	2.2548×10^{-14}	1.383×10^{-14}
Initial formation pressure, PI (Pa)	50,000,000	59,999,990.7239	60,000,000
Skin factor	2	0.100045	0
Borehole storage coefficient (m ³ /MPa)	2.812E-6	1.3368E-6	2.812E-7

**Figure 6.14** Schematic diagram of fracture plane model.

4. Numerical well testing model and well testing responses for fractured reservoirs with large fractures and caverns

If there are large caverns or fractures in a reservoir, fracture or cavern grids are defined in the model and the system is considered a single-porosity medium. The shape of the grid is determined according to the specific shape of fractures and caverns.

For large fractures, the fracture plane model is used, as shown in Fig. 6.14. Let the fracture width be W , and the fracture permeability is:

$$K_{x,y} = W^2/12, K_z = 0 \quad (6.19)$$

The conductivity factor between the fracture and other grids is calculated using the following equation:

$$\gamma_{ij} = \frac{A_{ij} k_{ij+1/2}}{d_i + d_j} \quad (6.20)$$

where A_{ij} is the area of the interface sharing by unit i and unit j ; d_i is the distance from the center of unit i to the interface of unit i and unit j ; d_j is the distance from the center of unit j to the interface of unit i and unit j ; $k_{ij+1/2}$ is average absolute permeability along the connection of unit i and unit j ; D_i is the depth of the center of unit i .

The fracture volume can be calculated according to fracture width, fracture length, and fracture height. For large caverns, an entire cavern is assumed to be an equipotential body, which is achieved by setting the distance from the cavern to the interface of the

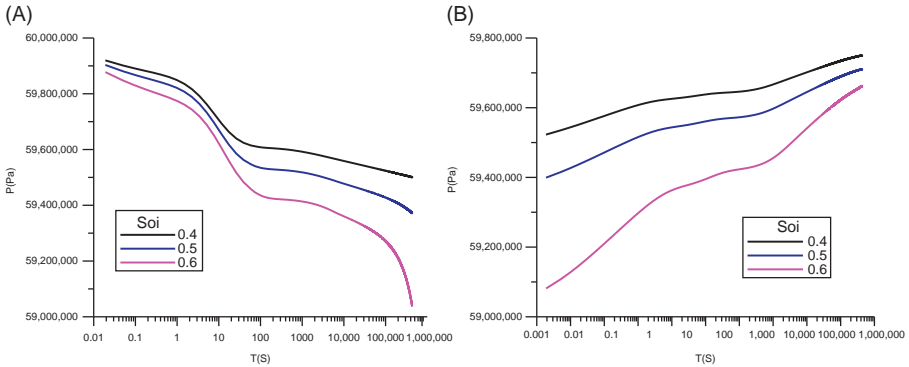


Figure 6.15 Well testing curves at different initial saturation values. (A) Drawdown curve; (B) pressure build-up curve.

adjacent grid, D_i , at 0, whereas the permeability of the cavern can be any finite value, and the cavern volume is calculated according to its spatial shape. After the treatment, the shape, position, and permeability of the large fracture can be accurately determined.

5. Response characteristics of two-phase flow in triple-porosity medium through numerical well testing

For fracture-cavern reservoirs, water breakthrough occurs after a short period of production in some wells, but immediately after well opening in some others. Thus, the oil–water two-phase flow is more prevalent because developed fractures are most likely connected with the edge and bottom water. Oil and water production in a two-phase flow are dependent on oil and water viscosity, relative permeability and capillary pressure. A two-phase flow differs from a single-phase flow. Therefore, if the single phase-flow well testing method is used to analyze two-phase flows, errors in formation parameter prediction will become inevitable. As a result, the absolute fit of two-phase flow well testing with formation flow includes not only bottom hole pressure during well opening and well shut-in, but also oil and water production curves.

Fig. 6.15 shows the pressure drawdown, pressure build-up and production variation curves under such conditions as oil–water two-phase flow, constant liquid production, and different initial oil saturation levels. The figure demonstrates that the pressure drawdown and pressure build-up curves in a two-phase flow change with initial oil and water saturation.

To calculate the parameters using the triple-porosity oil–water two-phase flow well testing curves, the following two steps are involved. First, the formation permeability, relative permeability, oil–water viscosity and capillary pressure curves are adjusted to fit oil–water production curves, and the pressure build-up curve is changed at the same time. Second, the parameter series determined by single-phase well testing are adjusted to fit the pressure build-up curve, with a spontaneous fit for the pressure drawdown curve, while the production curve does not change. The entire process is equivalent to a parameter calculation process with history fitting within a single well range.

6.1.3.2 Coupled flow well testing model and analytical method

In the numerical well testing model based on a multiporosity medium, caverns act as reservoir space for fluid or channels, providing liquid directly to the borehole,

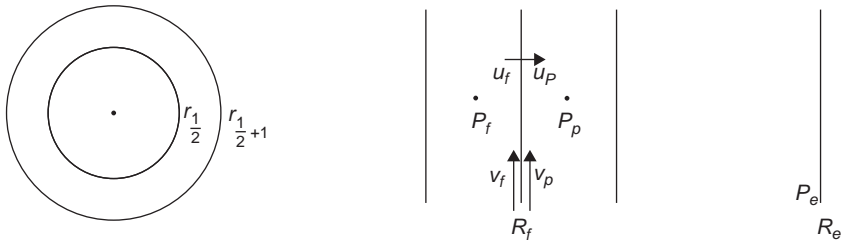


Figure 6.16 Schematics of coupled flow well testing.

where the fluid flow conforms to Darcy's Law in the same manner as for matrix and fractures. Regardless of their size and continuity, caverns are treated as a multiporosity medium. In actual oil wells that directly penetrate caverns, however, the cavern fluid flow pattern deviates significantly from Darcy's Law. Hence, fluid percolation characteristics in matrix and fractures and fluid hydrodynamic properties in caverns should be considered together, so as to better reflect flow characteristics of fluid in fracture-cavern reservoirs. On this basis, a mathematical well testing model is built, and a well testing analytical method is developed.

1. Mathematical model of coupled flow well testing

In Fig. 6.16, the axisymmetrical circular area contains a cavern at radius R_f from the borehole. The region from the borehole to the cavern is referred to as the free flow zone, and beyond this radius is the percolation zone with a closed outer boundary. In the percolation zone, the fluid is regarded as being slightly compressible, whereas the fluid in the free flow zone is regarded as being incompressible. In the production period, the flow rate is a constant, q .

In the percolation zone, the slightly compressible fluid is assumed, thus:

$$\nabla P_P = -\frac{\mu}{K} V_P \quad (6.21)$$

$$\nabla^2 P_P = \frac{\phi\mu C_t}{K} \frac{\partial P}{\partial t} \quad (6.22)$$

In the free flow zone, the incompressible fluid is also assumed, thus:

$$\rho \frac{dV_f}{dt} = -\nabla P_f + \mu \nabla^2 V_f \quad (6.21)$$

$$\nabla \cdot V_f = 0 \quad (6.22)$$

For the outer boundary, closed boundary, and percolation zone:

$$\frac{\partial P_P}{\partial r} = 0 \quad (6.23)$$

For the inner boundary and free flow region, the flow rate is q in the producing period and 0 in the pressure build-up period.

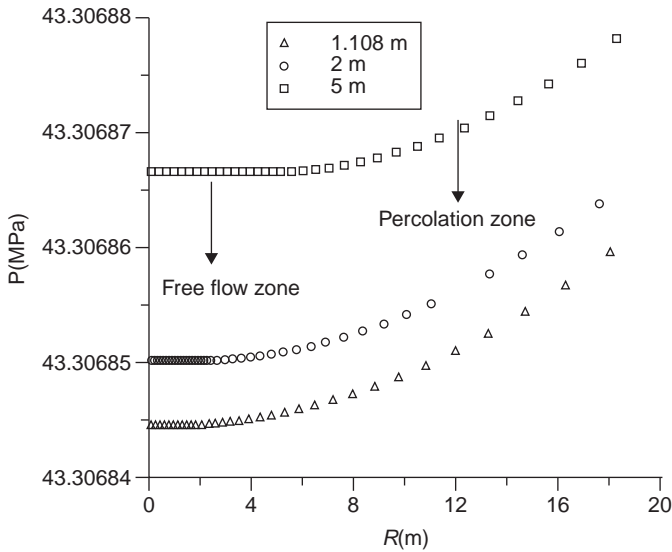


Figure 6.17 Comparison of pressure drawdown around caverns of different sizes (with closed boundary).

$$V_f 2\pi r_w h = q \quad (6.24)$$

$$P_w = P_f|_{r=r_w} \quad (6.25)$$

The initial condition is

$$P(r, 0) = P_i \quad (6.26)$$

2. Numerical well testing plot

a. Flow pattern of coupled flow model

Fig. 6.17 shows the comparison of pressure drawdown distribution around caverns of different diameters with a closed boundary and constant pressure boundary. It can be seen that the pressure in the caverns has negligible variations compared with that in the percolation zone and can be considered an equipotential body, because the pressure in the center well point of the cavern zone is simply the pressure on the boundary of the percolation zone plus a drawdown inversely proportional to the distance. This implies that the pressure drawdown will essentially reflect the condition on the edge of the cavern if a pressure drawdown test is conducted in a cavern-penetrating well.

The analysis revealed three features for the flow pattern of coupled flow model:

- i. The pressure drops slowly in the free flow zone from the cavern edge to borehole, and the cavern can be regarded as an equipotential body.
 - ii. The presence of a cavern is equivalent to the expansion of borehole radius. The larger the cavern diameter, the larger the equivalent borehole radius.
 - iii. The pressure drop shown in the drawdown test in cavern-penetrating wells is actually the pressure drawdown on the edge of caverns.
- b. Percolation and free flow coupled flow model for dual-porosity and triple-porosity medium: a case study

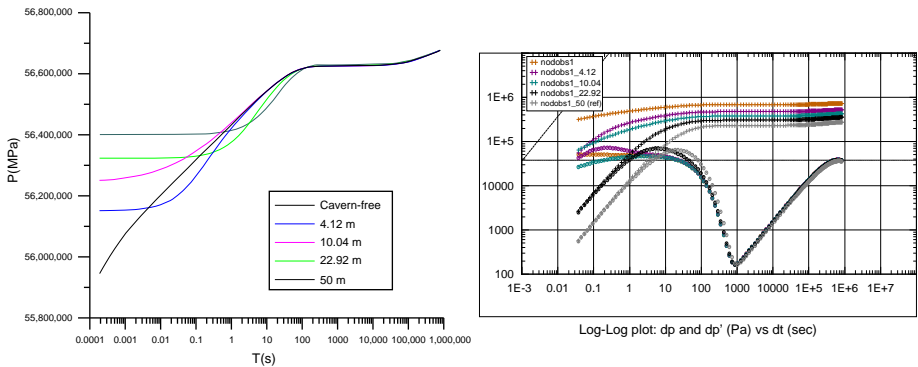


Figure 6.18 Comparison of pressure drawdown and pressure build-up curves obtained from dual-porosity percolation and free flow coupled model.

Fig. 6.18 shows the comparison of pressure drawdown and pressure build-up curves obtained from the dual-porosity percolation and free flow coupled model for different cavern sizes. It can be seen that the curves largely retain the overall characteristics of dual-porosity flow with increase in cave diameter, and the pressure build-up curve trends upwards with the increase in cavern size, although there is a flat initial stage. On the derivative curve, its intersection point with the pressure difference curve moves towards the right as the cavern diameter increases. Through inversed calculation, the diameter of a cavern in the free flow zone and its corresponding flow parameters of the percolation zone can be obtained.

6.1.3.3 Interpretation of testing data from fracture-cavern carbonate reservoirs of the Tahe Oil Field

The parameters for well testing interpretation of fracture-cavern reservoirs include not only conventional well testing parameters, such as borehole storage coefficient, skin factor, fracture or cave permeability, coefficient of crossflow from matrix to cavern, coefficient of crossflow from fracture to cavern, elastic storativity ratio of rock and elastic storativity ratio of caverns, but also cavern size, cavern-well spatial relationships, as well as fracture width and density. The established well testing model and interpretation method for fracture-cavern reservoirs have been used to reevaluate or interpret well testing data from 48 wells in the Tahe Oil Field, including quantitative interpretation of 40 wells and qualitative evaluation of eight wells.

Among the 40 wells quantitatively analyzed, 29 wells were interpreted using the conventional well testing model, and 11 wells using the well testing model and method newly developed in this study. In terms of geological concept and flow pattern, some well testing curves do not fit well with those derived using the conventional well testing model, but the fit is improved with the newly developed method (triple-porosity numerical well testing model), which confirms that the new method (percolation-free flow coupled model and double-phase flow model) can better depict the fluid flow characteristics of fracture-cavern reservoirs (Table 6.3).

Table 6.3 Statistics of logging interpretation and evaluation results of wells in Tahe Oil field

	Well testing model		Interpreted or evaluated wells	Well no.
New method	Triple-porosity numerical well testing model		6	TK444, TK608, TK313, T702B, TK631 and S65 TK313, S48, TK609 and TK630 TK634
	Percolation-free flow coupled model		4	
	Multiple-porosity two phase flow model		1	
Conventional method	Borehole storage + skin or infinite conductivity fracture	Homogeneous reservoir	6	TK651, TK413, TK630, TK632, S113 and T207 TK625, TK452, S7201, TP12CX, S106_3, T740, TK442, TK723, T705, T213 and S117 TK404, TK409, S106, S112, TK461, TK460H, S112_1, TK609, TK629, S74, S67, S48 and TK607 T706, T115, TK447 and TK743
		Radial composite reservoir	11	
		Dual-porosity reservoir	12	
		Multilayer (multiple fracture-cavern system) reservoir	4	

6.2 Waterflooding development technology for fracture-cavern oil reservoirs

Waterflooding is an important development technique for oilfields. As the fracture-cavern oil reservoir is characterized by a multiscale discontinuous medium, its development mechanisms and technology are significantly different from those for conventional clastic oil reservoirs that has a continuous porous medium.

6.2.1 Waterflooding development mechanisms for fracture-cavern oil reservoirs

Oil reservoir development involves three fundamental components, formation energy (pressure difference), injected medium displacement (water and gas displacement), and proper well grid and production parameters (reserve control and high-efficiency oil exploitation). The oil recovery factor is dependent on the well grid control coefficient, sweep efficiency and oil displacement efficiency.

$$E_{\text{oilfield}} = E_P \cdot E_V \cdot E_D$$

Based on the three fundamental development components, four dimensionless numbers have been derived to depict the various matching relationships between production wells and fractures and caverns, to evaluate waterflooding displacement effectiveness and to demonstrate waterflooding displacement mechanisms.

6.2.1.1 Recovery mechanisms of production wells in a cavern zone

When injected into a cavern, water displaces oil from the bottom to the top through oil–gas gravity segregation, with a high degree of waterflooding efficiency (Fig. 6.19).

The sweep efficiency of water-floored caverns is determined by the water cone number, which is the ratio of driving force to gravity ($\frac{\nabla p}{\Delta \rho g}$). In an unfilled cavern, gravity is dominant, so that the number approaches 0, and water cone cannot be generated easily. In filled caverns, the closer the water cone number is to 0, the

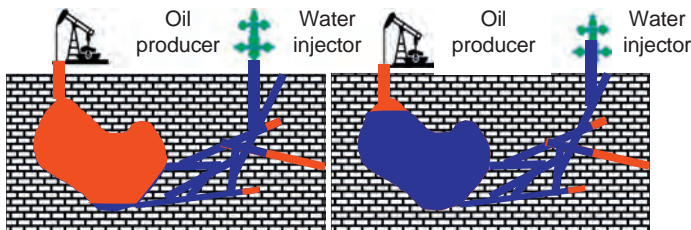


Figure 6.19 Sketch of waterflooding in the cave.

smaller the water cone number, and the higher the sweep efficiency. Thus, the key to high-efficiency development of filled caverns is to properly control the water cone number.

The waterflooding displacement efficiency of filled caverns is determined by the oil–water displacement number, which is the ratio of capillary force to gravity ($\frac{P_c}{\Delta\rho gh}$). The critical displacement number is 1 for caverns with oil-wetted fill: the smaller the number, the more significant the role played by gravity, and the higher the displacement efficiency. For caverns with water-wetted fill, the number is less than 1: both capillary force and gravity are the driving forces of displacement, and oil displacement efficiency is high.

6.2.1.2 Recovery mechanisms for production wells in fractured zone

The displacement of oil by water in fractures is affected mainly by fracture aperture and angle. The viscous force and capillary force vary inversely with the fracture aperture: the larger the fracture aperture, the smaller the viscous and capillary forces. The effect of gravity varies with the fracture angle: the larger the fracture dip, the more likely the injected water breaks through along the bottom under the effect of gravity.

The model with two parallel connected fracture-cavern combinations is built with the following parameters: the fracture length of L , the upper fracture aperture r_1 , the lower fracture aperture of r_2 , and the ratio $r_1 < r_2$. Water is injected from the left end and the pressure difference between the two ends is $P_A - P_B$. Thus, the velocity difference generated in two fractures due to different fracture apertures is:

$$v_{r2} - v_{r1} = (r_2^2 - r_1^2) \frac{P_A - P_B}{12[\mu_w x + \mu_o(L - x)]} \quad (6.27)$$

It can be seen from Eq. (6.27) that when capillary force is ignored, the velocity in the large fracture is higher than in the small fracture, and there is still oil in the small fracture when water in the large fracture reaches the distal end.

When capillary force is effective, whether the oil can be displaced depends on not only the pressure difference, but also on the capillary force. If the fracture is oil-wetted, the capillary force, which resists waterflooding, must be overcome by an artificial pressure difference. In water-wetted fractures, however, capillary force is the driving force for waterflooding.

The sweep efficiency of fracture-cavern combinations is determined by the equilibrium displacement number.

Areal displacement number is defined as the ratio of areal flow velocity in different directions without considering well spacing differences, and is calculated with the formula $\frac{k_2 \Delta p_2 L_1^2}{k_1 \Delta p_1 L_2^2}$. The sweep efficiency reaches the optimum when this number reaches 1.

The vertical equilibrium displacement number is the ratio of horizontal velocity to vertical velocity without considering the effect of variable reservoir thicknesses, and is calculated using the formula $\frac{\Delta\rho g k_z L^2}{\Delta p k_x h}$. In the process of waterflooding, it is necessary to make full use of gravity segregation to maintain the vertical equilibrium displacement number above 1, so as to prevent premature water breakthrough in oil producing wells.

6.2.1.3 Factors influencing development effectiveness and development countermeasures

The analysis based on practical oilfield development and laboratory experiments show that the effectiveness of waterflooding displacement is affected mainly by the following four factors and, therefore, corresponding countermeasures for improving the effectiveness have been developed.

1. Types of reservoir bodies

Different types of reservoir bodies correspond to notably different development effectiveness. Cavern reservoir bodies are characterized by large reserve, sufficient energy, and high productivity, whereas fractured reservoir bodies typically have small reserve, rapid decline and short service life. Therefore, cavern reservoir bodies should be regarded as the major development targets and oil-production wells should be drilled into caverns as far as possible.

2. Spatial relationships between oil-producing wells and caverns

The oil recovery factor is directly affected by the location (high or low) of oil-producing wells relative to caverns. The oil in a cavern can be completely extracted when the producing well is drilled into its top. When the wells are drilled into the bottom of a cavern, however, the oil at its top cannot be extracted, forming attic residual oil. Hence, the best attempt should be made to aim oil-producing wells at the high positions of caverns.

3. Spatial relationships between injection and production wells

Fracture-cavern reservoir bodies have a discrete distribution and, therefore, the effectiveness of their waterflooding development is greatly affected by the spatial relationships between oil-producing wells and water injectors. When producing wells are positioned high and water injectors are low, the extraction effectiveness will be good, with a high degree of waterflooding displacement efficiency due to gravity segregation. Otherwise, the extraction effectiveness will be low. When producing wells are located at the cavern zone and water injectors at the fracture zone, the extraction effectiveness will be good, with a highly efficient waterflooding displacement because the injected water was negligibly affected by fracture aperture and angle, and can displace the oil evenly. Without this spatial arrangement, the development effectiveness will be poor because the injected water tends to channel along fractures. When designing waterflooding development patterns, therefore, it is imperative to follow the principle of "water injectors positioned low and oil producing wells high; water injectors in the fracture zone and producing wells in the cavern zone," in accordance with the spatial configurations of fracture-cavern reservoir bodies.

4. Natural energy

Small fracture-cavern units (mostly with only one well drilled) usually have insufficient natural energy and will encounter rapid decline in energy and liquid production, and

even failure of oil production during recovery. Larger fracture-cavern units (i.e., large enough for deploying an injection-production well grid) with a moderate amount of natural energy will experience gradual energy decrease in the course of production, edge and bottom water channeling, and decline in oil production rate. Therefore, it is necessary to supplement reservoir energy by injecting water or gas to increase the recovery rate.

6.2.2 Waterflooding development technology

Fracture-cavern reservoirs are different from layered sandstone oil reservoirs and, therefore, their well grid deployment and parameter design are necessarily different from those of clastic oil reservoirs. The relative positions of injection versus production wells, the timing and modes of water injection, and production/injection parameters have been optimized by means of field tests, laboratory experiments, and numerical reservoir simulation.

6.2.2.1 Spatially structured well grid

For waterflooding development, the spatially structured well grid should be built according to the distribution characteristics of fractures and caverns. A spatially structured well grid refers to the well configuration that is properly deployed based on the fracture-cavern systems in terms of the morphology, size, interconnection and spatial distribution of fractures and caverns within a fracture-cavern oil reservoir unit.

The deployment principles of spatially structured well grids are as follows.

1. In terms of structural planes, the well grid design should follow the principle of water injectors positioned low and oil producing wells high, and water injectors in the fracture zones and producing wells in the cavern/cavity zones. The injection/production well grids should be connected bi-directionally or multidirectionally as much as possible, so as to make full use of the displacement of injected water.
2. Vertically, the heterogeneity of fracture-cavern distribution should be taken into full consideration. It is necessary to carry out segmented water injection based on the development characteristics of tight intervals so as to improve vertical oil displacement efficiency.
3. Injection-production well grids should be designed according to the types of reservoir bodies.
 - a. For units dominated by weathering crusts, the reservoir bodies tend to be connected multidirectionally. Therefore, the injection and production well grid should be on irregular planes, deployed according to the principle of water injectors positioned low and producing wells high, and water injectors in the fracture zones and producing wells in the cavern/cavity zones.
 - b. In old channel-dominated units, reservoir bodies are distributed and developed along underground rivers. Therefore, the injection/production wells should be deployed in a linear pattern along the underground channel, with oil producers at the main channels and water injectors along the edges.
 - c. For units dominated by a faulted karst zone, reservoir bodies are distributed along the fault. Therefore, linear injection-production patterns shall be deployed according to the width of fracture opening, with oil producing wells arranged in the cavern zones and water injectors in the fracture zones (Fig. 6.20).

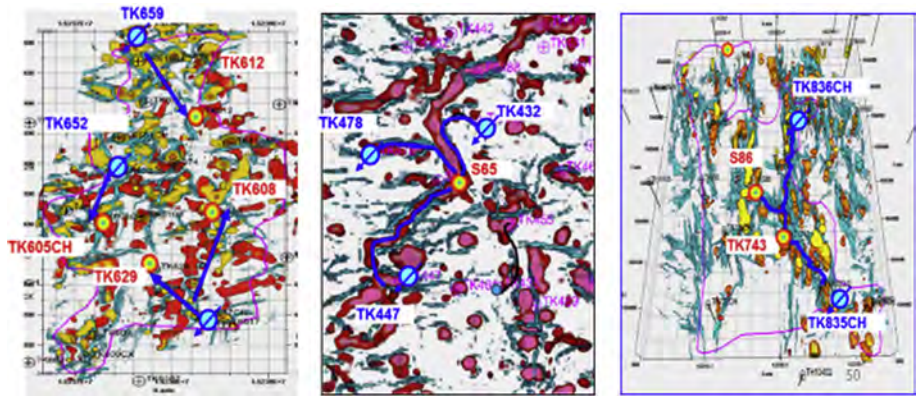


Figure 6.20 Configurations of well grids for weathering crust, old channel, and faulted karst units.

6.2.2.2 Water injection timing

In this study, the sensitivity of reservoir parameters that influence water injection timing was analyzed using numerical simulation; the rate of reserve recovery when water cut of oil producing wells is up to 98% has been calculated; and a relationship between water injection timing and geological factors has been established. The factors considered include fracture/cavern reserve ratio (indicating the degree of cavern filling), average fracture permeability, fracture permeability contrast, water body multiple, and oil–water viscosity ratio.

1. Weathering crust

For weathering crust reservoir bodies, the fracture permeability contrast and water body multiple values are dominant main controlling factors, whereas the fracture permeability and fracture/cavern reserve ratio are nondominant main controlling factors; and the effect of oil–water viscosity ratio is nonsignificant. Permeability contrast is in logarithmic relationship with water injection timing, as is the water body multiple value (Fig. 6.21).

The mathematical model of water injection timing in weathering crusts is expressed as:

$$\exp\left(\frac{T-b}{a}\right) = \frac{1}{DW} \frac{R_{fc}}{\ln K} \quad (6.28)$$

where T is the water injection timing (water cut), R_{fc} is the fracture/cave reserve ratio, D is the fracture permeability contrast, K is the fracture permeability (mD), W is the water body multiple, and a , and b are regression constants ($a = 3.4878$, $b = 88.819$).

2. Faulted karst body

For faulted karst bodies, the water body multiple value and fracture permeability contrast are the dominant main controlling factors, whereas the fracture permeability is a nondominant main controlling factor; and the effect of fracture/cavern reserve ratio and oil–water viscosity ratio are nonsignificant. Permeability contrast is in logarithmic relationship with water injection timing, as is the water body multiple value with water injection timing (Fig. 6.22).

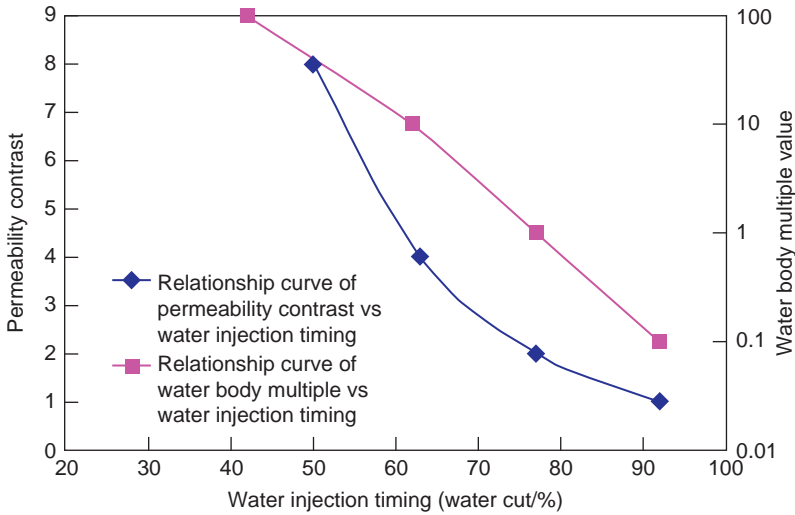


Figure 6.21 Single factor analysis on master prominent factors of weathering crust.

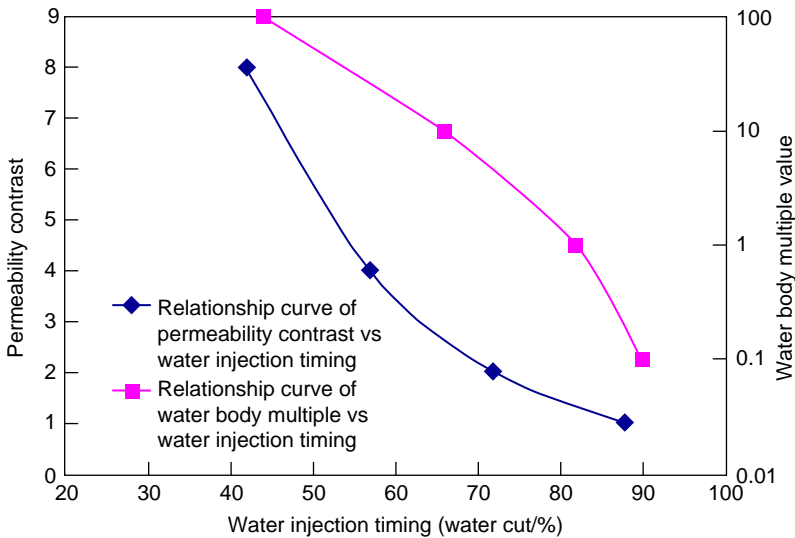


Figure 6.22 Single factor analysis on master prominent factors of faulted karst bodies.

The mathematical model for water injection timing in faulted karst bodies is expressed as:

$$\exp\left(\frac{T - b}{a}\right) = \frac{1}{DWK} \tag{6.29}$$

where T is the water injection timing (water cut), R_{fc} is the fracture/cave reserve ratio, D is the fracture permeability contrast, K is the fracture permeability (mD), W is the water body multiple, and a and b are the regression constants ($a = 4.175$, $b = 93.841$).

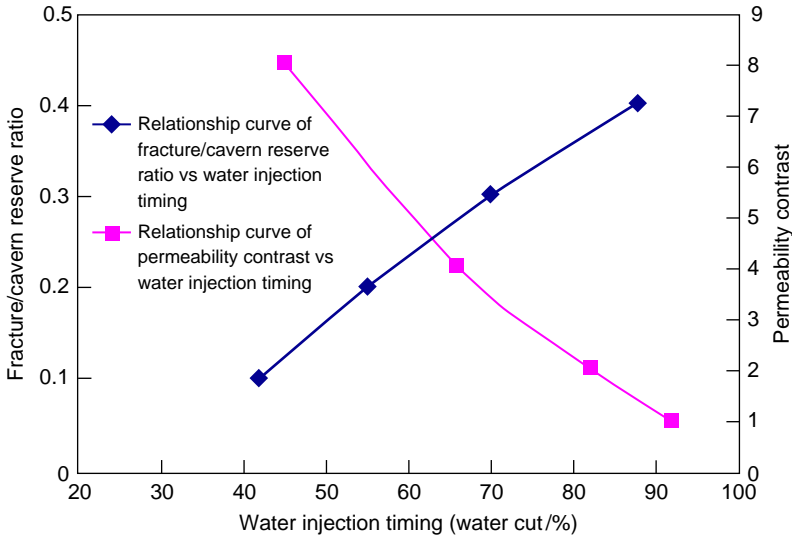


Figure 6.23 Single factor analysis on master prominent factors of underground rivers.

3. Underground river

For underground reservoir bodies, the fracture permeability contrast and fracture/cavern reserve ratio are dominant main controlling factors, whereas the fracture permeability and oil–water viscosity ratio are nondominant main controlling factors; and the effect of water body multiple is nonsignificant. Permeability contrast is in exponential relationship with water injection timing, as is fracture/cavern reserve ratio with water injection timing (Fig. 6.23).

The mathematical model for water injection timing in underground rivers is expressed as:

$$\ln T = a + b \frac{R_{fc} \mu_{ow}}{e^D \ln K} \quad (6.30)$$

where T is the water injection timing (water cut), R_{fc} is the fracture/cave reserve ratio, D is the fracture permeability contrast, K is the fracture permeability (mD), W is the water body multiple, and a , b are regression constants ($a = 3.9127$, $b = 0.3405$).

6.2.2.3 Water injection mode

The ultimate rate of reserve recovery via different water injection modes was calculated using numerical simulation to determine the optimal water injection mode for different geological settings. The results in this study show that at the early stage of waterflooding development, the interwell communication relationship will be ascertained further by injecting a tracer and by considering the production/injection well response characteristics. Water injection will proceed at a moderate rate and through cyclic water injection. After the breakthrough of injected water, diverted water injection, profile control, and water plugging can be used to increase the sweep volume and improve waterflooding displacement efficiency.

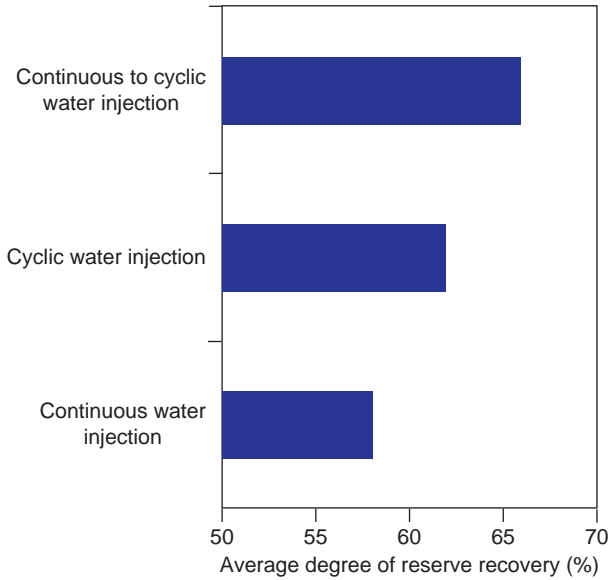


Figure 6.24 Comparison of average degree of reserve recovery of weathering crust with different water injection modes.

1. Weathering crust

The optimal water injection mode for weathering crust reservoir bodies is continuous water injection at the early stage, and subsequently by cyclic water injection after water breakthrough (Fig. 6.24).

2. Faulted karst body

For faulted karst bodies, cyclic water injection is the optimal mode (Fig. 6.25).

3. Underground river

The optimal water injection mode for underground river reservoir bodies is continuous water injection at the early stage, subsequently switching to cyclic water injection after water breakthrough (Fig. 6.26).

6.2.2.4 Optimization of injection/production parameters

In this study, the injection/production parameters were optimized by means of numerical reservoir simulations and optimization control algorithm so as to determine the optimal working system. The optimization of injection/production parameters is a closed loop optimization process. The oilfield working system is modified after production optimization, then the established reservoir model is modified and updated in real time based on the newly measured production data, and a new process of oil reservoir production optimization is followed. In the course of oil reservoir development, a closed loop optimization is formulated in the sequence of matching—optimization—re-matching—re-optimization, so that the benefit of oil reservoir development and production is ultimately maximized (Fig. 6.27).

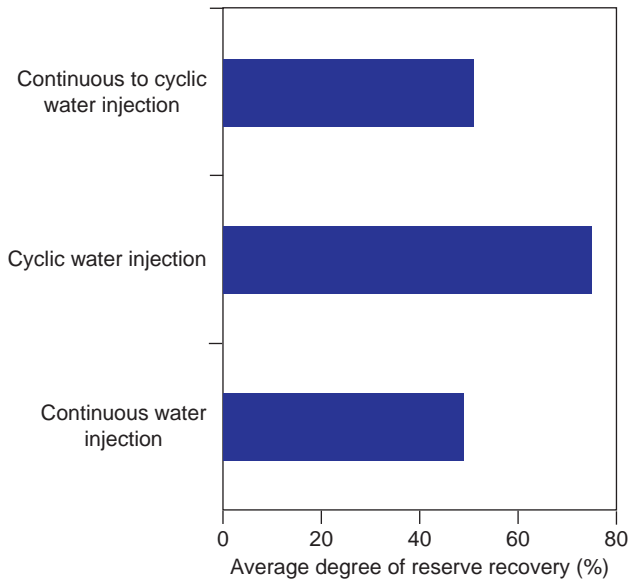


Figure 6.25 Comparison of average degree of reserve recovery of faulted karst body with different water injection modes.

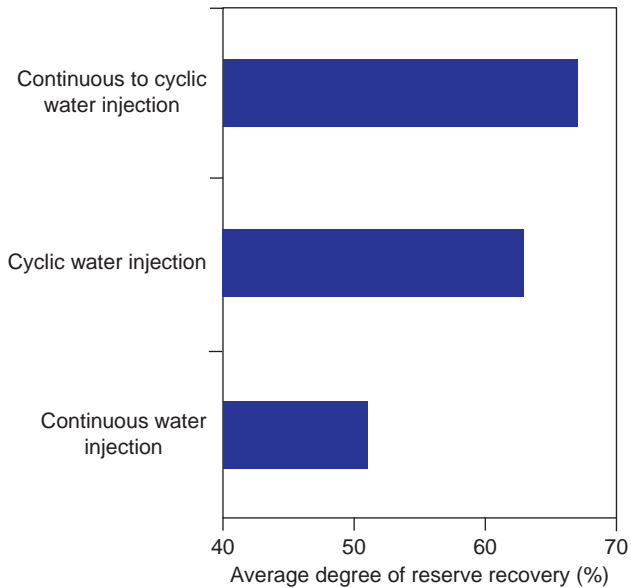


Figure 6.26 Comparison of average degree of reserve recovery of underground river with different water injection modes.

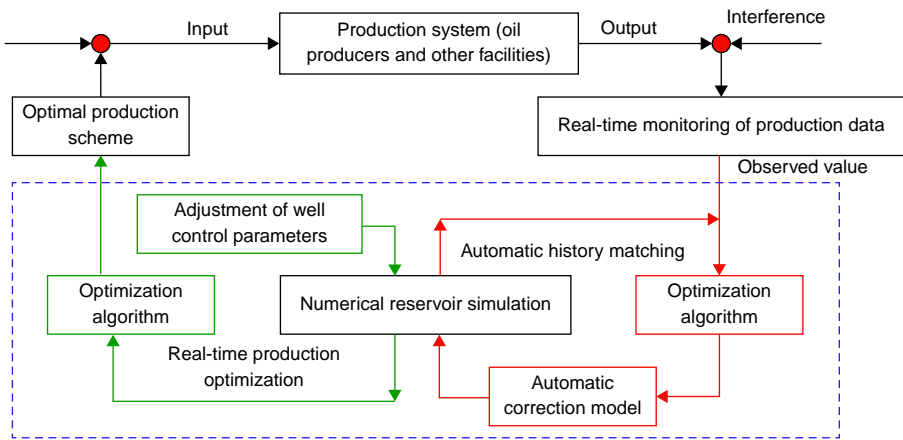


Figure 6.27 Closed loop of oil reservoir production optimization.

A performance index function is developed based on field situations. The adoption of different performance indices results in different optimal control. With a continuous increase in oilfield water cut, the production cost increases gradually and the economic benefit decreases, making it necessary to optimize the development scheme. Reservoir development and production optimization and control technology can solve these problems, reducing the time for oilfield development scheme design and decision-making by 75%. Accordingly, under the prerequisite of reducing production cost as far as possible, water fingering is slowed down and oil production is increased, resulting in better water production control and oil production stabilization for the production block.

The oil reservoir development and production system were depicted using a three-dimensional triple-phase simulator, and its economic benefit of waterflooding development is evaluated by taking the net present value (NPV) during the production as the performance index function, as expressed below:

$$J(u) = \sum_{n=1}^L \left[\sum_{j=1}^{N_p} (r_o q_{o,j}^n - r_w q_{w,j}^n) - \sum_{i=1}^{N_I} r_{wi} q_{wi,i}^n \right] \frac{\Delta t^n}{(1+b)^{t^n}} \quad (6.31)$$

where, J is the performance index function to be optimized; L is the total control step; N_p and N_I are total oil producers and total water injectors, respectively; r_o , r_w , r_{wi} are oil price, water production cost price and water injection price (\$/STB), respectively; $q_{o,j}^n$, $q_{w,j}^n$, $q_{wi,i}^n$ are the average oil production rate of no. j producer at the moment of n , average water production rate of no. j producer at the moment of n , and average water injection rate of no. i injector at the moment of n (STB/day); b is the average average annual interest rate (%); Δt^n is the simulated computation time step at the moment of n (day); t^n is the cumulative computation time at the moment of n (years); u is the vector of the N_u dimension control variable.

The elements of control variable u reflect the working systems of each well at each control time step (e.g., bottom-hole flowing pressure (BHP) and flow rate), and N_u is obviously the product of control well quantity multiplied by total control time step L . If it is assumed that the liquid production rate of two oil producers is adjusted every 6 months with an initial rate of 100 STB/day and total control steps of 10, the initial control variable is $u = [100, 100, \dots, 100]^T$ with $N_u = 20$.

Under the given conditions of initial geological model, the NPV J corresponding to the control variable u can be calculated by means of numerical reservoir simulation. While in the calculation of J , both oil production rate $q_{o,j}^n$ and water production rate $q_{w,j}^n$ are also related to the state variables of the oil reservoir (e.g., pressure and saturation). Therefore, J can be taken as a function of control variable u , state variable y and initial geological model m , and is expressed as follows:

$$J = J(u, y, m) \quad (6.32)$$

where m is the vector comprising geological parameters of the reservoir model grid (e.g., porosity and permeability), and y is the vector consisting of state parameters of the reservoir model grid (e.g., pressure and saturation). In the process of reservoir production optimization, only the control variable u related to the wells can be operated, and the state variable y of the oil reservoir system cannot be controlled directly, but the control variable, as an external factor, influences the operation state of the reservoir production system via the state variable, and hence affects the results of performance index J . In addition, well operation in actual production should be restricted to a given degree, i.e., the control variable must satisfy some constraints that are dominantly linear or nonlinear, such as equality, inequality, and boundary constraints. The typical equality constraint, such as the liquid production rate or injection rate of the whole block, will be a given value; the liquid production rate and the injection rate of the block are confined by operating capacity of oilfield equipment, and thus they generally require an inequality constraint. Boundary constraint is the most common constraint form, and mainly focuses on well production limit. In order to control the flow rate of oil and gas wells, the lower limit is generally set at 0 (shut-in). In terms of the constraint of the BHP of oil wells, the lower pressure limit will generally be higher than the bubble point pressure, or an appropriate value should be set to inhibit bottom water coning. For the borehole basal pressure of water wells, the upper pressure limit will be lower than the formation fracture pressure.

Based on the performance index function and constraints mentioned above, the optimal mathematical control model for oil reservoir production is established as follows:

$$\text{Max } J = J(u, y, m) \quad (6.33)$$

S.t.

$$e_i(u, y, m) = 0, \quad i = 1, 2, \dots, n_e$$

$$c_j(u, y, m) \leq 0, j = 1, 2, \dots, n_c$$

$$u_k^{low} \leq u_k \leq u_k^{up}, k = 1, 2, \dots, N_u$$

where u_k^{low} and u_k^{up} are the upper and lower limits of no. k control variable u_k , and $e_i(u, y, m)$ and $c_j(u, y, m) < 0$ are the equality and inequality constraints, respectively. It can be seen that the reservoir production optimization is to calculate the maximum performance index J and its corresponding optimal control variable u^* while the control variable satisfies all constraints.

Case study: Unit 74 is located at the northern structural axis of Block 6 in the Tahe Oil Field and its geological model is shown in Fig. 6.28. In total, there are 12 oil and water wells in the oil reservoir. The inversion parameters of the model included porosity, permeability, and oil-water relative permeability curves. Cumulative oil production, cumulative liquid production, and cumulative water injection of wells and block were the dynamic indices to be matched, and their history matchings were performed using the parameter dimension reduction method and the ensemble smoother multiple data assimilation (ES-MDA) method, respectively. Furthermore, multimodel robust production optimization was carried out on the basis of the matched reservoir model with the daily liquid production of oil producers and the daily water injection of water injectors as the optimization parameters. The working system was optimized once a year for 10 years. The NPV iteration results are shown in Fig. 6.29.

The cumulative oil production and water cut curves of the block before and after optimization are shown in Fig. 6.30, and the working system of each well before and after optimization are shown in Fig. 6.31. The production proration increases in

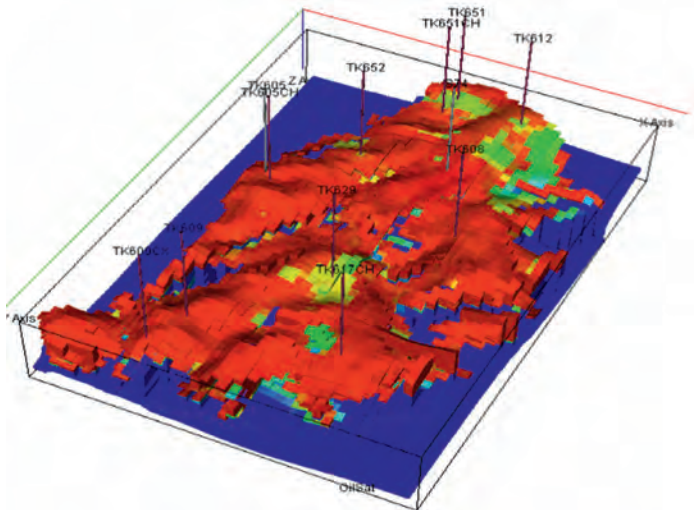


Figure 6.28 3D model of the oil reservoir.

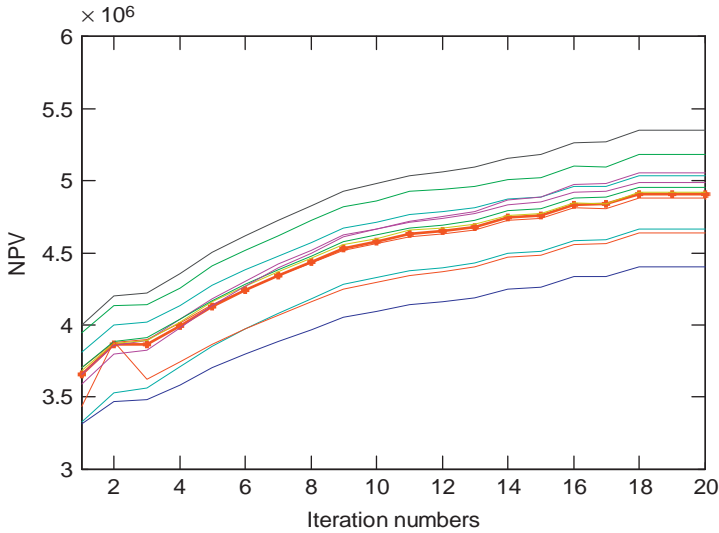


Figure 6.29 NPV iteration optimization results.

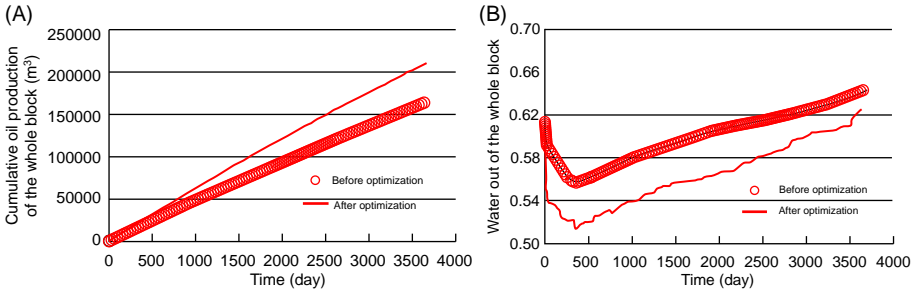


Figure 6.30 Cumulative oil production and water cut of the whole block before and after optimization. (A) Oil production optimization; (B) water production optimization.

Well TK608 and TK612, but decreases in Well TK652. It can be seen that the cumulative oil production increases by $43 \times 10^3 \text{ m}^3$ and water cut drops by 2.3% after optimization.

6.2.3 Evaluation of waterflooding effectiveness

6.2.3.1 Technical evaluation index system

In order to evaluate the effectiveness of waterflooding in oil reservoirs with a continuous porous medium, fractional flow curves are plotted according to Darcy’s Law, and then the indices (e.g., flood front distribution, water cut escalating rate and recovery factor) are calculated. In the multiscale discontinuous medium of fracture-cavern oil reservoirs, however, multiple flow patterns (e.g., free flow and

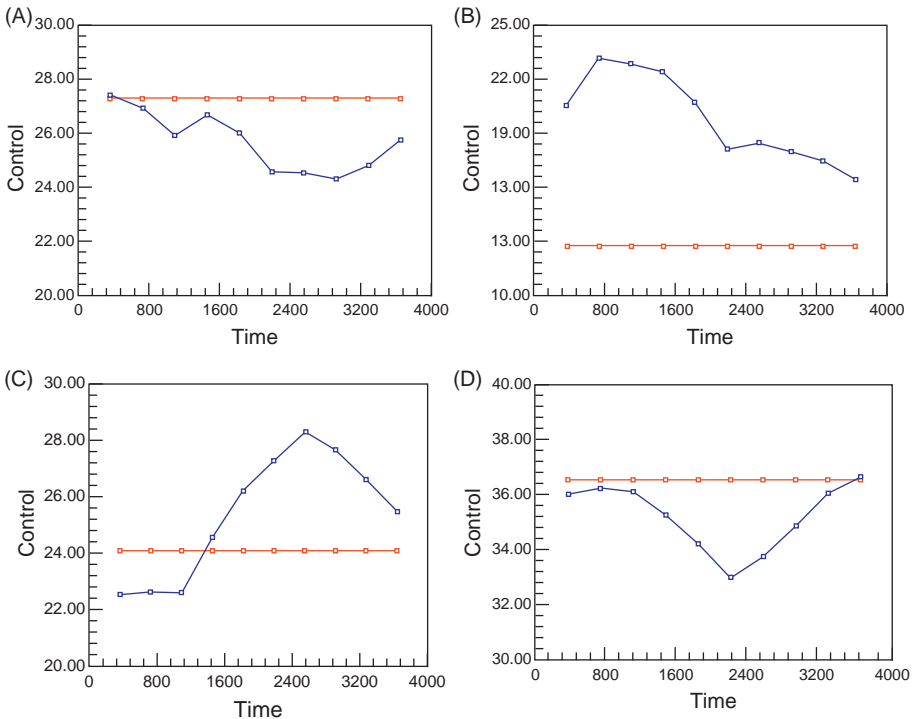


Figure 6.31 Optimization results of individual-well injection/production parameters, (A) TK605CH; (B) TK608; (C) TK612; (D) TK629.

percolation) coexist (see Section 4.5 of Chapter 4: Fluid flow law in a fracture-vug carbonate reservoir) and, therefore, it becomes necessary to carry out simulation and calculations using new numerical simulation technologies (described in Chapter 5: Numerical simulation of a fracture-vug carbonate reservoir) to evaluate the waterflooding effectiveness. Spatial structure patterns in the field are different from one another, so that the numerical simulation is restricted by time efficiency. Therefore, the following field indices are also used for evaluating the development effectiveness.

- Oil incremental index: (1) interim oil increment; (2) ultimate oil increment;
- Degree of resource utilization: (3) ultimate recovery factor; (4) enhanced oil recovery (EOR) rate;
- Water cut variation: (5) water cut decline rate;
- Energy utilization: (6) degree of reservoir pressure maintenance and build-up rate;
- Economy: (7) water–oil displacement rate.

6.2.3.2 Overall evaluation methods for fracture-cavern units

The effectiveness of waterflooding development for fracture-cavern oil reservoirs will be evaluated primarily on the basis of well clusters from the following aspects.

1. **Connectivity.** The connectivity and the degree of connection between producing wells and water injectors will be determined based on injection/production response characteristics (pressure, production rate, and water cut variation) and tracer test. The presence of relatively large caverns may add difficulty for detecting the tracers. Therefore, the results of log interpretations and 3D geological modeling may be needed to determine whether two wells are connected, as well as the manner of their connection.
2. **Response.** The indices mentioned above are used for response analysis and they are calculated using the following methods of calculation.
 - a. Method based on natural depletion of recoverable reserves. The recoverable reserves during the natural depletion phase are predicted using production decline curves, such as exponential, harmonic, hyperbolic, and attenuation decline curves.
 - b. Method based on interim oil increment. The oil increment following the start of response is calculated. The ultimate oil increment of waterflooding development is determined based on predicted ultimate recoverable reserves.
 - c. Method based on OOIP. Based on geological modeling, OOIP is estimated using the material balance method and volumetric method jointly.
 - d. Method based on ultimate recoverable reserves. The ultimate recoverable reserves are predicted by means of the numerical simulation method, decline method, or waterflooding characteristic curve method. The ratio of ultimate recoverable reserves to OOIP is the ultimate recovery factor.
 - e. Method based on water–oil displacement rate. Water–oil displacement rate is the ratio of cumulative oil increment from waterflooding to cumulative water injection volume, reflecting the benefit of waterflooding development.

6.2.4 Analysis of field waterflooding development results

By the end of 2014, waterflooding development had been conducted for 82 fracture-cavern oil reservoir units in the Tahe Oil Field, with a cumulative oil increment of 4.13×10^6 t and a recovery factor increase of 4%.

1. Reservoir energy boost

The reservoir pressure of five water injection units in the Ordovician oil reservoirs, Block Tahe 4, has recovered again to various degrees (Table 6.4).

2. Increase in oil production rate and slowdown of natural decline rate

Among 39 production wells in five water injection units, 23 wells have seen responses 6 months after waterflooding, accounting for 59.0% of all the production wells. Among the 23 wells, seven wells have experienced an energy boost, and 16 wells have experienced a displacement response. Their natural decline rate has decreased variously between 6.86% and 25.35%, by an average of 16.27% (Table 6.5).

3. Drop in water cut

After the waterflooding responses, the composite water cut of all units has dropped to various degrees. The overall water cut of five units has dropped by 24.4%, from 54.8% to 30.4% at the early stage of the response; water cut escalating rate at the early stage of water injection has dropped to various degrees, by 9.55% on average (Table 6.6).

4. Increase in recovery factor

The five water injection units had various increases in recovery factor, between 1.7% and 10.6%, with an average of 7.98%, and a recoverable reserve increment of 422.85×10^4 t, demonstrating remarkable waterflooding results (Table 6.7).

Table 6.4 Reservoir pressure of multiwell fracture-cavern units in Block Tahe 4 before and after water injection (by 31 December 2014)

Unit	Reservoir pressure before water injection (MPa)	Current reservoir pressure (MPa)	Difference between current reservoir pressure and reservoir pressure before water injection (MPa)
S48	57.2	57.8	0.6
S64	54.7	55.8	1.56
S65	54.6	58.8	2.80
TK407	56.7	57.3	0.39
TK409	56.20	58.4	1.40
Average	55.88	57.62	1.74

Table 6.5 Decline rate of fracture-cave units in Block Tahe 4 before and after water injection (by 31 December 2014)

Unit	Annual decline rate before water injection (%)	Decline rate at the early stage of water injection response (%)	Difference (%)
S48	28.88	12.05	16.83
S64	33.1	25.29	7.81
S65	29.14	22.28	6.86
TK407	32.54	8.06	24.48
TK409	37.15	11.8	25.35
Average	32.16	15.90	16.27

Table 6.6 Statistics on water cut escalating rate of water injection units in Block Tahe 4 (by 31 December 2014)

Unit	Water cut escalating rate before water injection (%)	Water cut escalating rate at the early stage of water injection response (%)	Decline rate of water cut escalating rate (%)
S48	35.09	4.3	35.64
S64	15.0	7.7	15.12
S65	40.06	15.06	38.66
TK407	16.8	11.7	20.4
TK409	30.71	8.5	32.51
Average	16.57	7.02	9.55

The application of the above waterflooding development technology in fracture-cavern oil reservoirs have achieved good development results. This demonstrates that waterflooding is effective for increasing the recovery factor of fracture-cavern oil reservoirs. In the Tahe Oil Field, however, water injectors are mostly converted

Table 6.7 Recovery factor and recoverable reserves of water injection units in Block Tahe 4 before and after water injection (by 31 December 2014)

Unit	Recoverable reserves (10 ⁴ t)			Recovery factor (%)		
	Before water injection	After water injection	Difference	Before water injection	After water injection	Difference
S48	467	814.8	347.8	14.16	24.71	10.55
S65	104.6	118.7	14.1	12.61	14.30	1.70
S64	28.3	31.95	3.65	10.32	11.65	1.33
TK407	42.1	57.6	15.5	14.01	19.16	5.16
TK409	87.9	129.7	41.8	14.70	21.70	6.99
Total	729.9	1152.75	422.85	13.77	21.75	7.98

from shut-in/stripped wells, and injection/production well grids are incomplete. Thus, the recovery factor showed a relatively low rate of increase, and there is still room to enhance the recovery factor through waterflooding optimization.

6.3 Nitrogen injection EOR technology for fracture-cavern reservoirs

After natural depletion and waterflooding, there is still a substantial amount of residual oil in fracture-cavern reservoirs because of the complex fracture-cavern structures, in which attic oil at the top of caverns is one of the main sources of residual oil. Nitrogen injection EOR technology has been developed to tap this type of residual oil.

6.3.1 Formation mechanism and distribution pattern of residual oil in fracture-cavern reservoirs

Because of the large differences in fractures and caverns, fracture-cavern reservoirs differ widely in two-phase flow performance, vertical and horizontal displacement scheme, and occurrence and distribution pattern of residual oil.

After bottom waterflooding, a considerable amount of oil still remains in the fracture-cavern reservoir, and this oil source has variable occurrences and distribution patterns as a result of different fracture and cavern combination patterns and production systems.

There are mainly six types of residual oil in fracture-cavern reservoirs: attic oil, oil beyond high-conductivity channels, oil filling the porous medium, residual oil on the surface of fractures and caverns, residual oil due to poor connectivity and low energy, and oil not controlled by wells (Fig. 6.32 and 6.33).

Characteristics of residual oil distribution in the fracture-cavern model after bottom waterflooding are listed in Table 6.8.

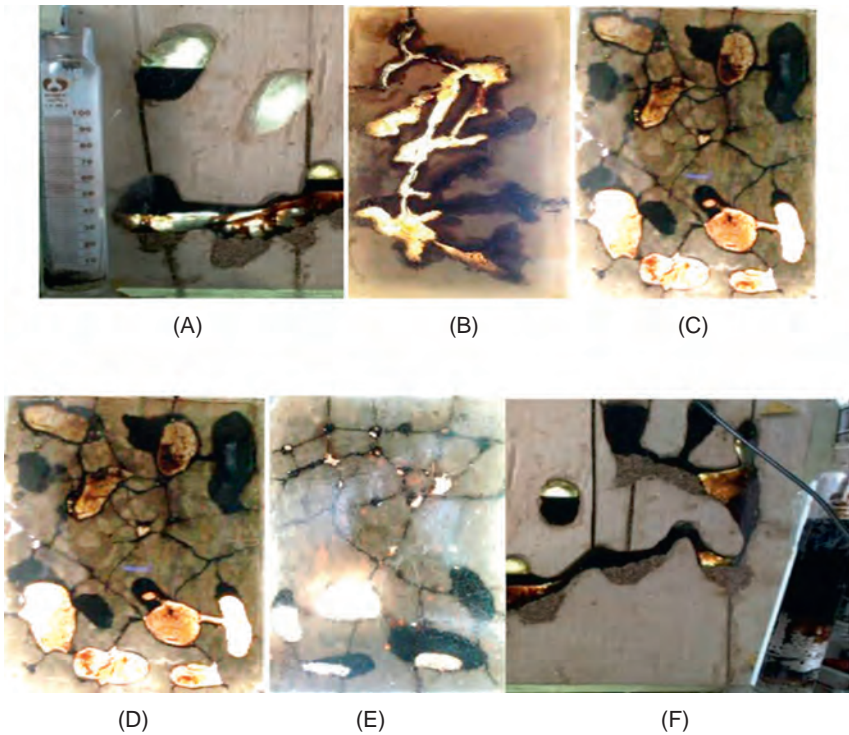


Figure 6.32 Main types of residual oil in fracture-cavern reservoirs. (A) Attic oil; (B) oil beyond high-conductivity channels; (C) residual oil on the surface of fracture and cavern (D) residual oil due to poor connectivity and energy; (E) oil filling the porous medium; (F) oil not controlled by well.

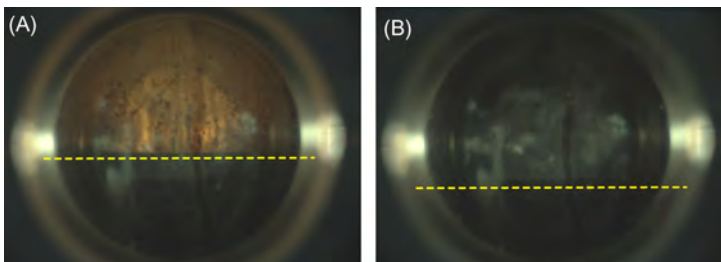


Figure 6.33 N₂ (A) and CO₂ (B) Properties experiment at 125°C, 60MPa.

The residual oil of six fracture-cavern units in the Tahe Oil Field has been studied through numerical simulation, and it shows that attic oil and oil not controlled by well are the main types of residual oil in these fracture-cavern reservoirs, and also the targets for EOR (Table 6.9).

Nitrogen injection EOR technology has been developed to tap attic oil after waterflooding. Nitrogen is an inert gas, with low density and high compressibility.

Table 6.8 Main types of residual oil and their origins after waterflooding

Type of residual oil	Formation mechanism	Key controlling factors	Position
Oil on the top of cave (attic oil)	Fracture & cave contact relationship	Trap structure on top of cave	Upside of cave
Residual oil beyond the high-conductivity channels	Big difference in flow resistance	The pressure difference and intensity between injection and production	The cave with transverse cracks or big displacement resistance
Residual oil in porous filling medium	Pore structural heterogeneity, capillary force and interfacial tension	Filling degree, permeability	Inner pore at filling position
Residual oil at the surface of fractures & caves	Rock wettability and oil	Rock surface wettability	Surface of fractures and caves
Residual oil due to poor connectivity and low energy	Fracture-cave outside the flow field, big difference in flow resistance in adjacent fracture-cave systems	Position of injectors and producers, formation energy	Caves and fractures outside the control of the flow field
Oil not controlled by well	Dissolution cavities and caves of poor connectivity, low coordination number of 1 in general	Position of injectors and producers	Boundary of fracture and cave units

After injection into the fracture-cavern units, it will form a gas cap at the top of the fracture-cavern units due to gravity differentiation, replenishing reservoir energy, and displacing the residual oil at the cave top. This makes nitrogen injection an effective technique to enhance oil recovery.

6.3.2 EOR technology by nitrogen injection for single wells

Oil recovery enhancement by nitrogen injection in single wells involves multiple cycles of nitrogen gas injection during and/or after the late stage of waterflooding.

6.3.2.1 EOR mechanism of gas injection in single wells

1. Displacement by gravity differentiation

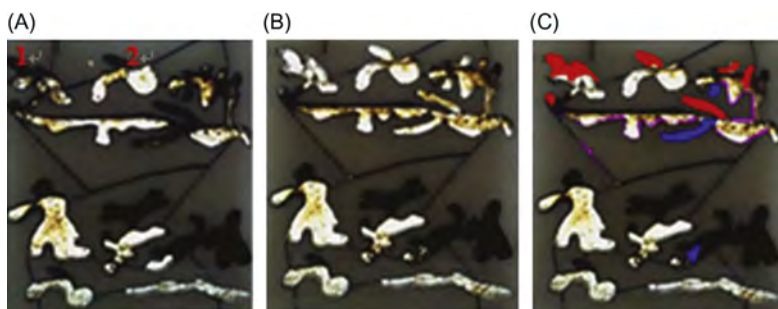
Pressure-volume-temperature (PVT) experiment shows that both N_2 and CO_2 are in gas state under the reservoir conditions of the Tahe Oil Field (125°C, 60 MPa), obvious in gas-oil contact, and in immiscible displacement state. The difference is that the

Table 6.9 Reserves of different types of residual oil in typical fracture-cave units of Tahe Oil Field

Fracture-cavern unit	Original oil in place (10 ⁴ t)	Type and proportion of residual oil								Geological reserves of residual oil (10 ⁴ t)
		Oil not controlled by well		Attic oil		Residual oil by energy shortage and pore		Residual oil beyond the high-conductivity channels		
		Reserves (10 ⁴ t)	Proportion (%)	Reserves (10 ⁴ t)	Proportion (%)	Reserves (10 ⁴ t)	Proportion (%)	Reserves (10 ⁴ t)	Proportion (%)	
S48	2829	379.4	15.82	778.4	32.46	649.5	27.09	590.7	24.63	2398
T7-607	1235.5	213.8	19.73	390.6	36.05	244.6	22.57	234.5	21.64	1083.5
S66	579.5	67.5	13.54	245.2	49.20	96.1	19.28	89.6	17.98	498.4
S74	513.4	124.5	28.54	85.2	19.53	138.8	31.81	87.8	20.12	436.3
T615	425.9	118.8	32.06	118.3	31.93	77.7	20.97	55.73	15.04	370.5
S80	2273	391	20.56	866	45.53	315	16.56	330	17.35	1902

Table 6.10 Comparison of N₂ and CO₂ properties under conditions of Tahe reservoir (125°C, 60 MPa)

Type	N ₂	CO ₂
Property		
Density (kg/m ³)	65.0	812.0
Viscosity (MPa · s)	0.032	0.075
Compressibility factor (dimensionless)	1.75	0.79
Solubility in crude oil (%)	2.8	53.0

**Figure 6.34** Comparison of residual oil activation by nitrogen injection. (A) Oil distribution after flooding; (B) oil distribution after gas injection; (C) comparative analysis

nitrogen–oil (Tahe Oil Field) contact is clearer than CO₂–oil contact (Tahe Oil Field) because CO₂ extracts the light components from crude oil, making the gas darker, but the oil–gas contact still exists in the CO₂–oil system.

N₂ and CO₂ differ significantly in property (Table 6.10). At the same temperature and pressure, N₂, with much lower density and solubility than CO₂, is more likely to form a gas cap due to gravity differentiation, and displace the attic oil. Moreover, N₂ has a higher compressibility coefficient and expansibility than CO₂, making an ideal elastic driving force.

2. Changes in the flow field after waterflooding

During the gas cap drive process, the injected gas changes the pressure distribution in the oil and water seepage space after bottom waterflooding, thus altering the flow field, and activating some residual oil that cannot be displaced by bottom water. The physical simulation experiment below shows that, with the injection of N₂, the attic oil inside the cavern directly above the injection well is displaced first (see Fig. 6.34). Next, driven by the injected gas, the oil in cavern no. 1 migrates into cavern no. 2, carrying the attic oil to the well head, driven by the bottom water. With the effect of bottom water pressure and conduit formed by waterflooding, the injected gas cannot sweep across all the caverns, thus emphasizing the need to enhance the swept volume of injected gas.

The oil recovery was enhanced by about 15.43% via gas injection after waterflooding: the incremental oil thus recovered includes 79.72% attic oil, 24.86% residual oil beyond high-conductivity channels, and 0.85% oil slick. The attic oil is mainly displaced by oil and gas gravity segregation, and the residual oil beyond high-conductivity channels by changing the direction of water flow.

Table 6.11 Comparison of working fluid level and oil pressure before and after N₂ injection

Well no.	Working fluid level before gas injection (m)	Working fluid level after gas injection (m)	Oil pressure before gas injection (MPa)	Oil pressure after gas injection (MPa)
TH12110	1096	0	2.36	18
TH12503	2347	75	0.42	14.5
T415CH	576	0	2.7	12
TK672	2589	0	0.8	8.5
TK675X	401	200	0.7	1.6
T702B	114	0	0.48	8.7

3. Replenishment of formation energy

The pressure distribution around the borehole was calculated by numerical simulation, demonstrating that the hole-bottom pressure and formation energy increased after gas injection. In addition, the production performance of gas injection wells shows an increase in working fluid level and oil pressure/casing pressure (Table 6.11), indicating a boost of formation energy through gas injection.

6.3.2.2 Factors controlling the effectiveness of N₂ injection in single wells

A number of factors influence the effectiveness of gas injection in a single well, including reservoir body type, reservoir body size, degree of filling, bottom water energy, spatial relationship between well and reservoir body, etc. All these controlling factors have been analyzed by numerical simulation to determine the main factors that influence the effectiveness of gas injection in a single well.

1. Reserve scale

Reserve scale has a relatively strong influence on the effectiveness of gas injection in cavern reservoirs. Reservoir bodies of different sizes have different production characteristics after gas injection (Figure 6.35).

A reservoir body with a large reserve has a more effective production cycle, slower decline, delayed gas breakthrough, and a lower gas–oil ratio. A reservoir body with a small reserve has less effective production cycles, early gas breakthrough immediately after well opening, and a lower oil increment per cycle.

2. Degree of filling

The degree of filling has a strong influence on the effectiveness of gas injection. Unfilled reservoir bodies correspond to a highly effective gas injection and more economic injection cycles. Partially filled reservoir bodies show a fairly good gas-injection effectiveness, with recovered residual oil in two parts: the bottom residual oil driven by water, and the upper residual oil driven by gas injection. Because of its high diffusion

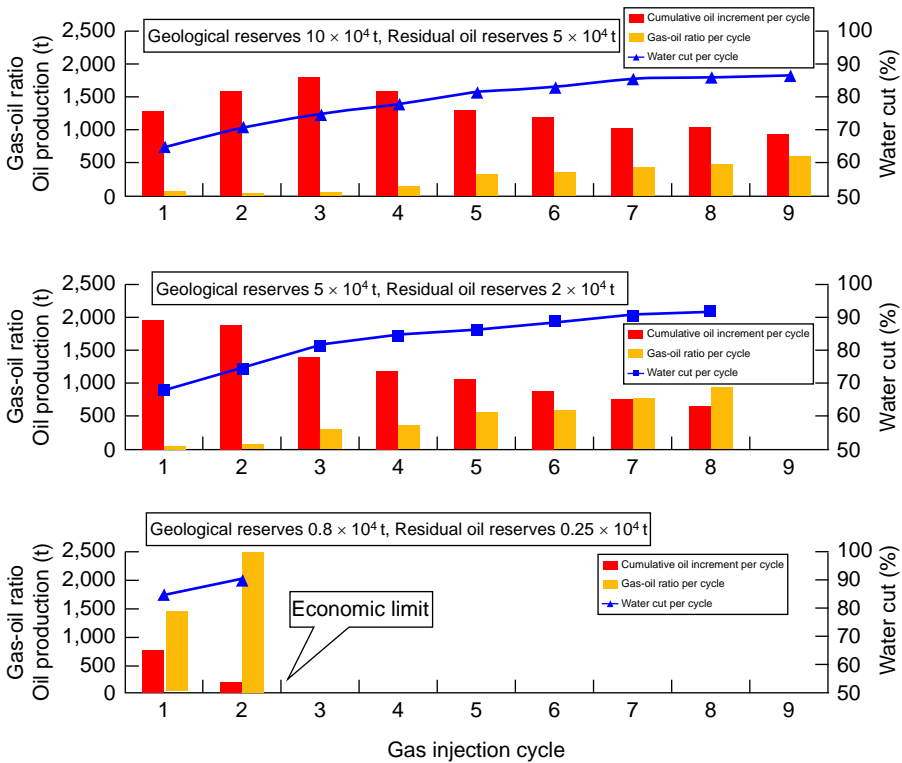


Figure 6.35 Period production status of cave reservoir bodies of different reserve scale.

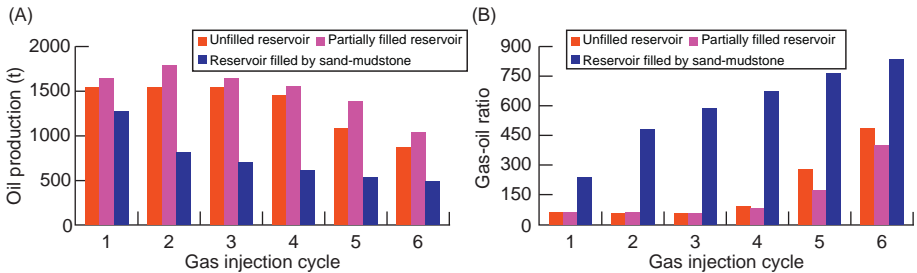


Figure 6.36 Comparison of gas injection effect in reservoirs of different degrees of filling. (A) Comparison of oil production cycles; (B) Gas–oil ratio per cycle.

resistance to gas, fully filled reservoir bodies experience a longer period of gas–liquid differentiation, gas stalling around the bottom of well, early gas breakthrough, high produced gas to oil ratio (GOR), and high gas recovery percentage, mostly resulting in a poorly effective gas injection (Fig. 6.36).

3. Bottom water energy

The bottom water energy has a fairly strong influence. Reservoir bodies with a medium or large aquifer have a good gas injection effect, with higher oil production per

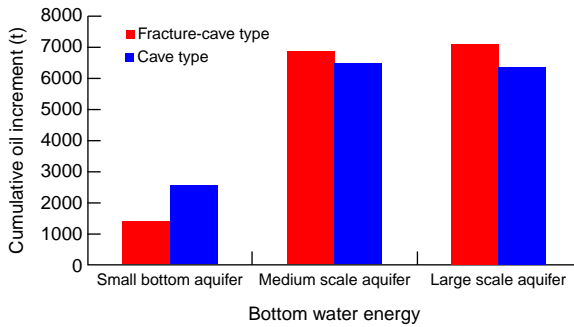


Figure 6.37 Comparison of cumulative oil increment in different types bottom aquifer.

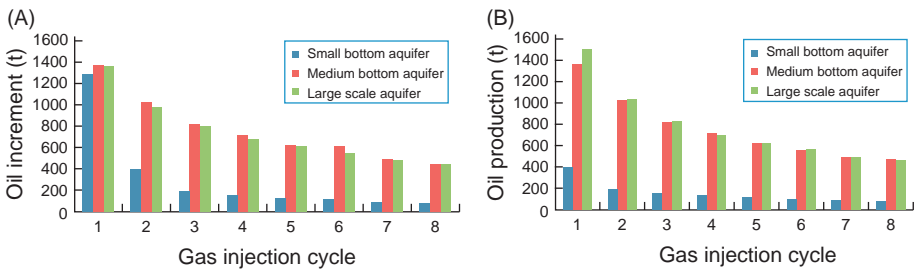


Figure 6.38 Comparison of cycle oil production in reservoir bodies with different scales of bottom water energy. (A) Cave reservoir body; (B) fracture-dissolved pore reservoir body.

cycle, slow production decline, and prolonged viable production cycle. Reservoir bodies with a small or weak bottom aquifer have a reduced gas injection effect. Fracture-cavern reservoir bodies have poorer gas injection effect than cavern reservoir bodies (Figs. 6.37 and 6.38).

4. Spatial configuration between well and reservoir body

When the oil well reaches the bottom of a reservoir body, it promotes more viable production cycles, and a lower gas–oil ratio and water cut. When the well penetrates to the top of a reservoir, it induces a rapid drop in oil production, fewer viable production cycles, early gas breakthrough, fast rise in gas–oil ratio, and poor gas injection effect (Fig. 6.39).

6.3.2.3 Well selection principles for gas injection in single well

Well selection criteria:

1. Unfilled and partially filled cave reservoir bodies are the primary choice, followed by fracture-cavern reservoir bodies.
2. A reservoir body drilled by a single well has a reasonable reserve scale, and economically recoverable residual oil.
3. Wells with production zones in the middle or lower part of a reservoir body should be selected first.
4. Wells with medium or strong energy levels should be selected in priority.

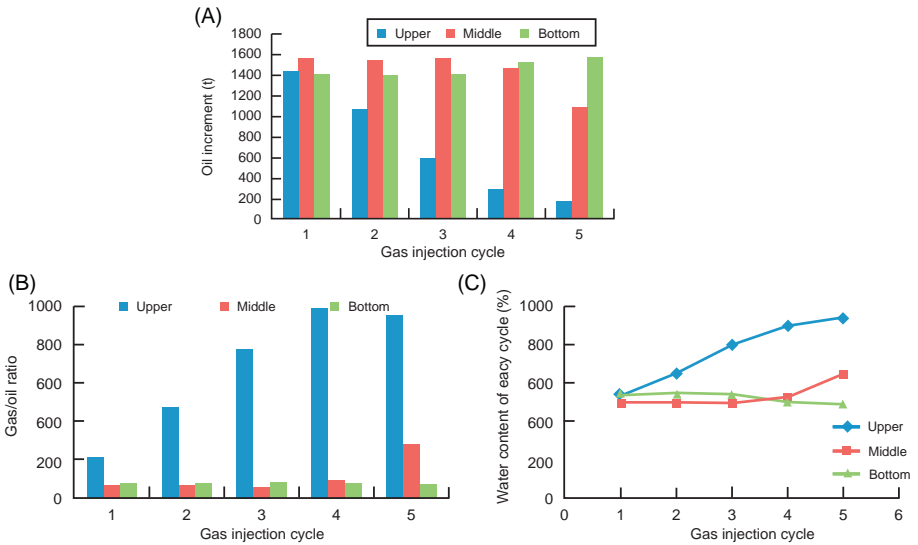


Figure 6.39 Comparison of gas injection effect at different configuration of well and reservoir. (A) Comparison of oil increment per cycle; (B) comparison of gas–oil ratio; (C) comparison of water cut in each cycle.

6.3.2.4 Optimization of gas injection parameters for single well

For attic oil in a fracture-cavern reservoir, injection-production parameters were analyzed under the following consistent conditions: a reserve of 50,000 t, large bottom aquifer, and an oil well drilled to the bottom of the attic oil reservoir. The controlling conditions for production are set at the maximum liquid production rate of 100 m³/day, and the maximum of 15 times of puff and huff. The calculation shows about 3,790,000 m³ liquid N₂ is needed to displace 10,000 m³ of tank oil.

1. Cyclic gas injection volume

The cyclic gas injection volume will influence the economically viable cumulative oil increment.

For the cavern reservoir body, under the premise of a consistent total gas injection volume, the smaller the gas injection volume in a cycle, the more gas injection cycles will be needed. By taking oil price and economic cost into consideration, the development effectiveness was evaluated by economic oil increment, which is the cumulative oil increment by gas injection minus the lower limit of economic oil increment. With increase in cyclic gas injection volume, economic oil increment increased, and reached a peak at the gas injection volume of about 1,500,000 m³, while the oil exchange ratio decreased (Figure 6.40).

For fracture-cavern reservoirs, the higher the gas injection volume per cycle, the higher the cumulative oil increment. When the gas injection volume is greater than 500,000 m³, the cumulative oil increment volume varies little. With increased gas injection volume per cycle, the oil exchange ratio decreases rapidly because of the slow gas diffusion rate, large

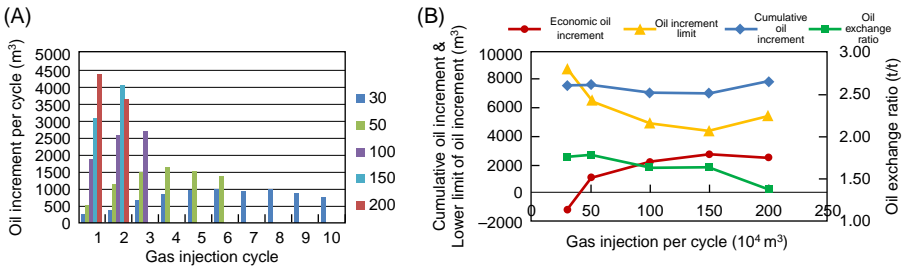


Figure 6.40 Influence of cycle gas injection volume on gas injection effect of cave reservoir body. (A) Comparison of oil increment cycles at different gas injection volumes per cycle; (B) comparison of economic oil increment and oil exchange ratio at different gas injection volume per cycle.

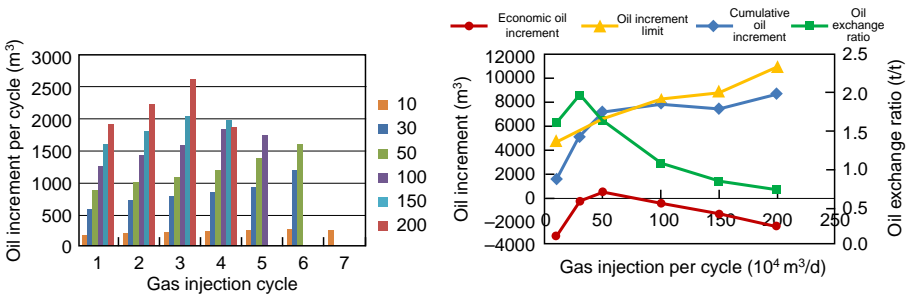


Figure 6.41 Influence of cycle gas injection volume on gas injection effect of fracture-cave reservoir body. (A) Comparison of single cycle oil increment at different gas injection volumes per cycle; (B) comparison of economic oil increment and oil exchange ratio at different gas injection volumes per cycle.

amount of recovery gas and low percentage of net injection. The cumulative oil increment becomes higher than the lower limit of economic oil increment only when the gas injection volume per cycle is about $500,000 \text{ m}^3$ (Fig. 6.41).

2. Gas injection rate

For different types of reservoir bodies, the gas injection rate has different effects on oil increment. For cavern reservoir bodies, the injected gas tends to diffuse rapidly, resulting in different gas injection rates having little influence on the gas injection effect for a single well (Fig. 6.42).

For a fracture-cavern reservoir, the gas diffusion rate tends to be slow and, therefore, rapid gas injection is not beneficial for generating a gas-cap drive; the lower the gas injection rate, the higher the oil exchange ratio (Fig. 6.43).

3. Well shut-in time

For an unfilled cavern reservoir body, the gas will quickly spread to the top of attic oil, and displace oil. Thus, the well shut-in time has little influence on the gas injection effectiveness for a cavern reservoir body. But a fracture-cavern reservoir body will require a long well shut-in time because of a slow gas diffusion rate (Figs. 6.44 and 6.45).

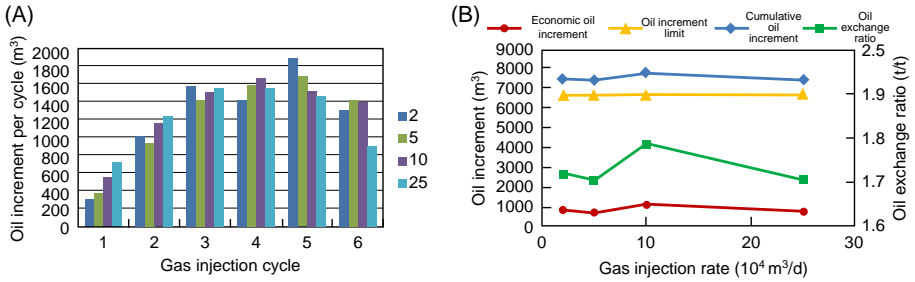


Figure 6.42 Influence of gas injection rate on gas injection effect of cave reservoir body. (A) Comparison of single cycle oil increment at different gas injection rates; (B) comparison of oil increment at different gas injection rates for cavern reservoir body.

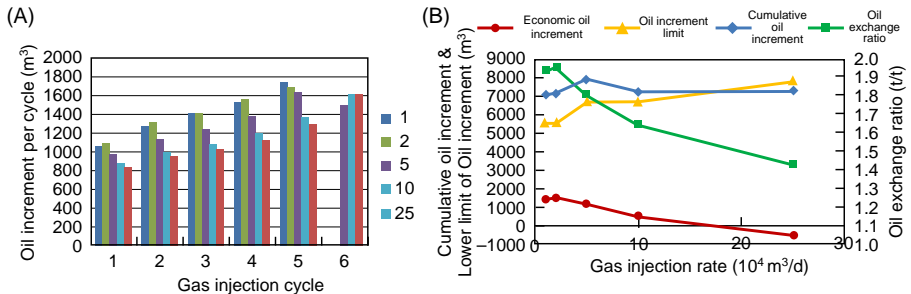


Figure 6.43 Influence of gas injection rate on gas injection effect of fracture-cave reservoir body. (A) Comparison of single cycle oil increment at different gas injection rate; (B) comparison of oil increment at different gas injection rate of fracture-cavern reservoir.

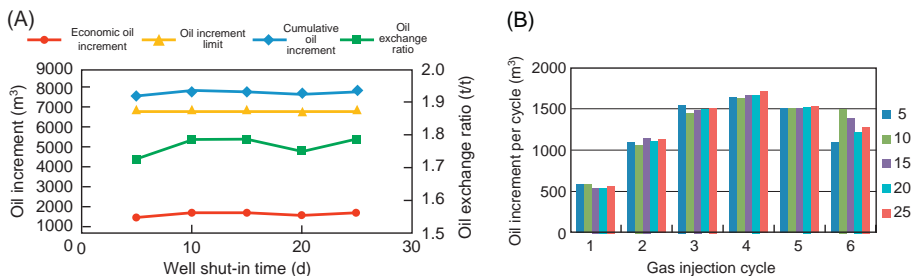


Figure 6.44 Influence of well shut-in time on gas injection effect of cave reservoir body. (A) Comparison of single cycle oil increment at different well shut-in time; (B) comparison of economic oil increment and oil exchange ratio at different well shut-in time.

4. Fluid producing intensity

For a cave reservoir body, the higher the fluid producing intensity, the higher the water cut, and the lower the cycle oil increment (Fig. 6.46). In this regard, a fracture-cavern reservoir will show a similar regularity to a cavern reservoir (Fig. 6.47).

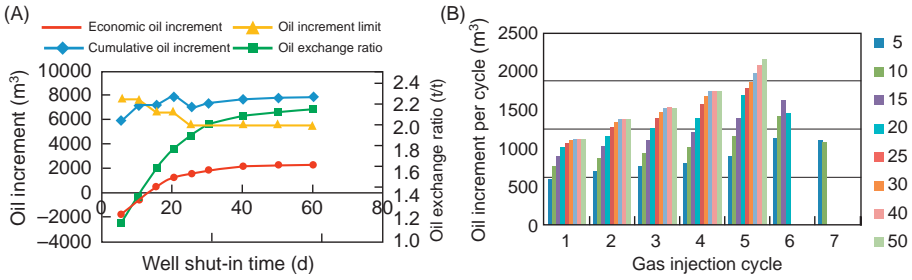


Figure 6.45 Influence of well shut-in time on gas injection effect of fracture-cave reservoir body. (A) Comparison of single cycle oil increment at different well shut-in time; (B) comparison of economic oil increment and oil exchange ratio at different well shut-in time.

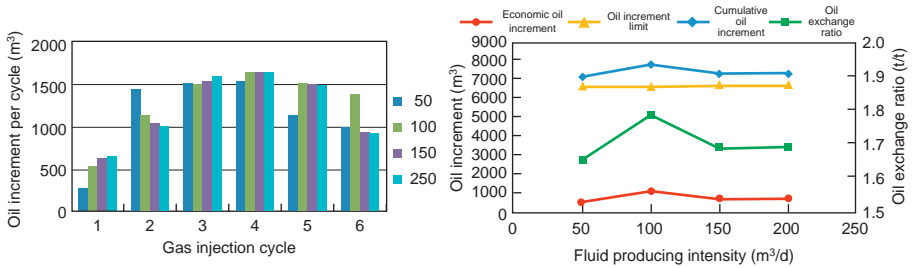


Figure 6.46 Influence of fluid producing intensity on gas injection effect of cave reservoir body (A) Comparison of single cycle oil increment at different fluid producing intensity (B) Comparison of economic oil increment and oil exchange ratio at different fluid producing intensity.

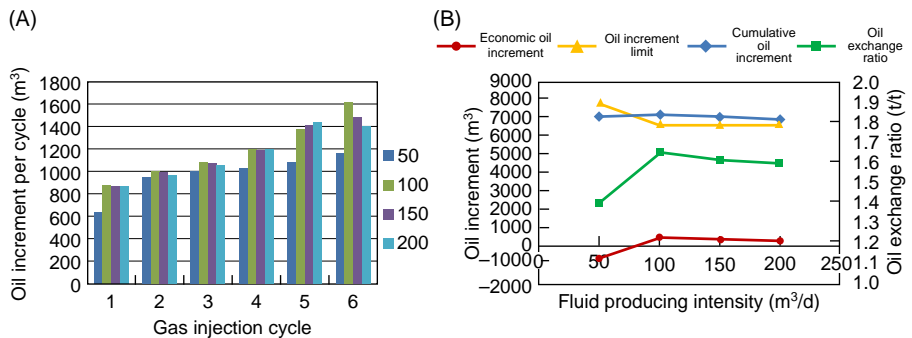


Figure 6.47 Influence of fluid producing intensity on gas injection effect of fracture-cave reservoir body. (A) Comparison of single cycle oil increment at different fluid producing intensity; (B) comparison of economic oil increment and oil exchange ratio at different fluid producing intensities.

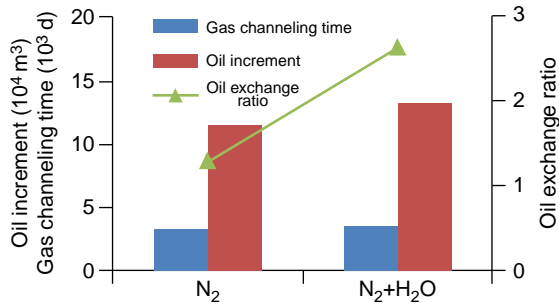


Figure 6.48 Selection of gas injection mode for different geological settings.

6.3.3 Gas injection EOR technology for fracture-cavern units

The gas injection development technology for fracture-cavern units uses horizontal displacement of N₂ to drive oil from fractures, caverns, and pores to wells, replenish formation energy, decrease the production decline caused by energy shortage, increase oil production, and enhance oil recovery. The key for this technology is controlling gas channeling and increasing gas swept volume.

Lab experiment and field application show that water and gas alternate injection (WAG) has a higher oil exchange ratio, later gas channeling time than pure gas injection (Fig. 6.48), and improved benefit, making WAG more suitable for this type of reservoir.

6.3.4 Analysis of gas injection effectiveness

The gas injection EOR technology has achieved satisfactory oil incremental levels in field applications. By December 2015, it has been applied in 234 wells/548 well-times in the Tahe Oil Field, with an oil increment of about 90.3×10^4 t.

6.3.4.1 Effectiveness of typical single well gas injection

Well TK404, with a total depth of 5612.7 m, was put into production on 22 March 2000, followed by waterflooding development on 12 September 2006, with a total water injection volume of 101,239 m³, and cumulative oil increment of about 32,078 m³ and cumulative liquid production of about 95,549 m³. A volume of 778 m³ of liquid nitrogen (equivalent to standard nitrogen of 50.4×10^4 m³, or underground volume of 1649.36 m³) was injected from 14 April to 17 April 2012. After shut-in for 10 days following gas injection, the well was opened to produce liquid from 27 April to 27 May 2012; after producing 1176 m³ of water, oil was exhausted. The well was blowing in the beginning, with a daily liquid production of

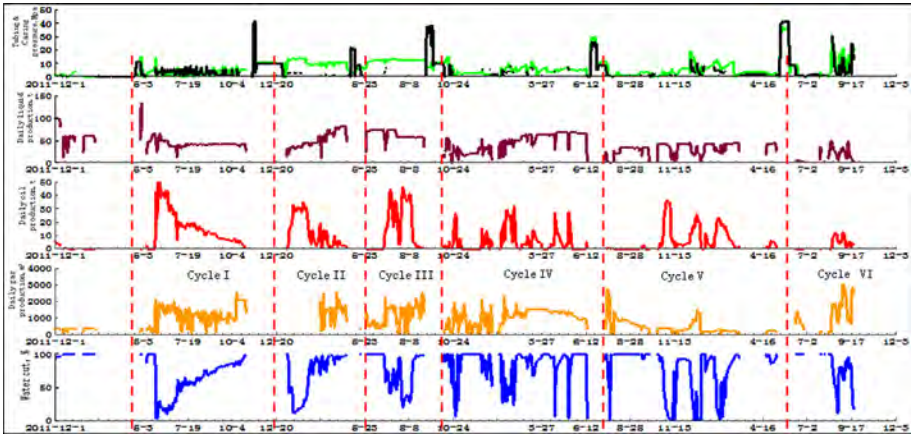


Figure 6.49 Production curve of Well 404 by gas injection.

44.4 m³, daily oil production of 43.11 t, and water cut of 2.9%. At that point, the well had gone through six cycles of gas injection, with five of the cycles evaluated, with a cumulative gas injection volume of 2,970,000 m³ and an oil increment of 8157 t (Fig. 6.49).

6.3.4.2 Effectiveness of typical well-cluster gas injection

The TK666 gas injection well cluster includes three production wells, Nos 667, 602, and 625, and one gas injection well, No. 666. Gas injection in Well No. 666 started on 11 February 2015, at an initial gas injection rate of 48,000 m³/day (138 m³/day), and water injection rate of 190 m³/day. After a cumulative gas of about 1,230,000 m³ (3534 m³) and water of 3493 m³ were injected, it began to generate responses on 17 March 2015.

Response characteristics: water cut decreased rapidly, working fluid level increased from 1035 m to wellhead. By then Well No. 666 had been injected about 2,760,000 m³ of N₂, and 7353 m³ of water, and produced about 618 tons of oil.

6.4 Horizontal well sidetracking and reservoir stimulation technologies for fracture-cavern oil reservoirs

It is difficult to identify and distinguish fracture-cavern carbonate oil reservoirs because of their multiscale and discontinuous distribution, and the precise identification of small-scale fracture-cavern bodies has an especially high level of uncertainty. As a result, some wells drilled are shut in because of their small reserve

control and short production cycle. In order to increase the production rate of reserves and the utilization ratio of production wells, it is necessary to develop and implement sidetracking and reservoir stimulation technologies.

6.4.1 Small-radius horizontal well sidetracking technology for fracture-cavern oil reservoirs

Sidetracking from long-closed, low-yield and low-efficiency wells can reach new reservoir bodies, and enhance well utilization ratio effectively.

In small-radius horizontal well sidetracking, deflection building is completed within a vertical range of ± 50 m and pretarget displacement of 60 m by using a high deflection rate and small curvature radius. This is followed by drilling a horizontal section, allowing the old hole to directionally communicate with adjacent fracture-cavern reservoir bodies.

6.4.1.1 Drilling string optimization technology for small-radius ultradeep sidetracked horizontal wells

Drilling string optimization for small-radius ultradeep horizontal wells should focus on reducing the drag and torque and reduce and hence the probability of fatigue failure of the drilling string when bottom hole assembly (BHA) drilling and deflection are controlled accurately. Therefore, the prediction and control of drag and torque is not only the key to, but also the difficult point in, the successful drilling of small-radius horizontal wells.

1. Drilling string drag and torque prediction model

An infinitesimal body AB with an arch length of ds is taken from the borehole axis coordinate and the force on it can be analyzed with A as the starting point (axis coordinate s) and B as the end point (axis coordinate $s + ds$), as shown in Fig. 6.50.

The drag can be calculated for full-stiffness drilling string of sidetracked horizontal wells using the following formula:

$$\left\{ \begin{array}{l} \frac{dT}{ds} + K \frac{dM_b}{ds} \pm \mu_a N - q_m k_f \cos \alpha = 0 \\ \frac{dM_t}{ds} = \mu_t R N \\ - \frac{d^2 M_b}{ds^2} + K \cdot T + \tau (\tau \cdot M_b + K \cdot M_t) + N_n - q_m K_f \cos \alpha \frac{K_a}{K} = 0 \\ - \frac{d(KM_b + \tau M_t)}{ds} - \tau \frac{dM_b}{ds} + N_b - q_m K_f \sin^2 \alpha \frac{K_\phi}{K} = 0 \\ N^2 = N_n^2 + N_b^2 \end{array} \right. \quad (6.34)$$

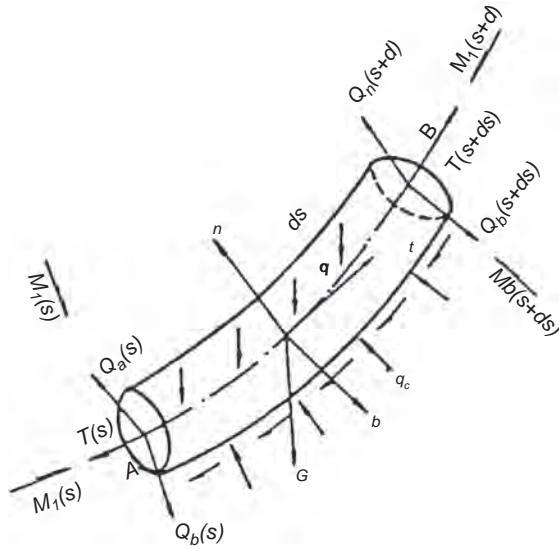


Figure 6.50 Force on the infinitesimal body of drilling string.

where

$$K = \left| \frac{d^2\vec{\gamma}}{ds^2} \right| = \sqrt{K_a^2 + K_\phi^2 \sin^2 \alpha}$$

$$K_\alpha = \frac{d\alpha}{ds}$$

$$K_\phi = \frac{d\phi}{ds}$$

$$K_f = 1 - \frac{\gamma_m}{\gamma_s}$$

$$N^2 = N^2_n + N^2_b$$

where K_α is the rate of deviation change, rad/m; K is the rate of direction change, rad/m; τ is the borehole torsion, rad/m; q_m is the weight per unit length of drilling string, N/m; M_b is the bending moment at infinitesimal section of drilling string, $N \cdot m$; N ; α is the deviation angle, rad; μ is the friction coefficient; M_t is the torque on drilling string, $N \cdot m$; dT is the axial force increment of drilling string, N ; T is the axial force at infinitesimal section, N ; R is the string radius; Q_n , Q_b are the shear forces at curvilinear coordinate S in the direction of principal normal and binormal, respectively, N ; N_n , N_b are the uniformly distributed contact forces in the direction of principal normal and binormal, respectively, N/m ; μ is the external radius of drilling string, “+” for up and “-” for down.

2. Drag and torque analysis and drilling string strength check on small-radius horizontal wells in Tahe Oil Field

There are mainly two types of sidetracked horizontal wells in the Tahe Oil Field: one was drilled with a $\Phi 88.9$ -mm drilling pipe inside a $\Phi 177.8$ -mm casing, and the other with a $\Phi 88.9$ -mm drill pipe + $\Phi 127$ -mm drill pipe inside a $\Phi 177.8$ -mm liner.

The calculation shows that in the case of pulling out of hole (POOH), neither the maximum wellhead hook load (1767.33 kN) nor the maximum torque (11.01 kN·m) is high, implying that the existing drilling rigs can meet the requirement. The wellhead axial load and torque in different cases, such as POOH, run in hole (RIH), slide drilling, rotary drilling, and back reaming horizontal sidetracking were calculated, showing that the safety coefficient of wellhead drilling string is higher than 1.8 when the horizontal well is drilled to the planned well depth, confirming that the drilling string is obviously safe.

6.4.1.2 Trajectory optimization technology for short-radius ultradeep sidetracked horizontal wells

The pay zones in Tahe Oil Field, at depths of 5600–6500 m, comprise yellow–gray, gray and light gray micrite and yellow–gray arenitic micrite. Casings of $\Phi 177.8$ mm in old wells are generally run to the weathering crust at the top of the Yijianfang Formation. The overlying Qiaerbake and Bachu formations are composed mainly of mudstone. For severely waterflooded old wells, it is necessary to avoid the waterflooded zones (120–150 m around old wells) and the wall collapse sections in the mudstone of the Qiaerbake and Bachu formations. For the old wells where water breakthrough is not too serious, direct sidetrack can be carried out from the open hole section of the pay zones. When sidetracking from the open hole section, however, the vertical distance between the sidetracking point and the target is small because the sidetracking point is located in the pay zone of the Yijianfang Formation. As a result, the borehole curvature of the sidetracked horizontal well is higher, generally greater than 20 degree/30 m.

When the horizontal displacement is 1000 m, the hook load and torque of slide drilling vary with borehole curvature. For open-hole sidetracked horizontal wells, the deflection rate is generally set in a range from 20 to 30°/30 m. The depth of the sidetracking point is determined with a single-arc deflection section according to the vertical depth of the target area and the selected deflection rate, and the sidetracking point should be lower than the $\Phi 177.8$ -mm casing shoe.

6.4.2 Reservoir stimulation technology for fracture-cavern oil reservoirs

Over 75% of the wells drilled in Ordovician carbonate oil reservoirs of the Tahe Oil Field have low or even null natural productivity. Therefore, reservoir stimulation must be carried out to create artificial fractures so as to communicate oil and gas reservoir space and improve oil well productivity. In the Tahe Oil Field, acid fracturing is currently one of the key technologies for Ordovician oil reservoir exploration and development.

The Tahe carbonate reservoirs are ultradeep, with high temperatures (140–160°C) and developed in fractures and caverns, leading to rapid acid-rock

reaction and serious acid fracturing fluid loss. Hence, the length of acid etched fractures is limited, making it difficult to produce multiple reservoir intervals efficiently in long open-holes. To tackle these issues, the acid fracturing fluid system with high temperature resistance, retardance and fluid loss control has been prepared, and a corresponding acid fracturing technology that can increase the fracture and cavern communication ratio has been developed. These have proven effective for increasing the productive construction rate and reserve extraction rate of oil wells.

6.4.2.1 Prefrac effect prediction technology

The mathematical models for prefrac effect prediction have been built on the basis of two mathematical methods, i.e., the partial correlation analysis and neural network, and the “acid fracturing effect decision system software” has been developed to eliminate the blindness in well and layer selection that was based on experience alone. This has laid a foundation for a transformation in well and layer selection for acid fracturing of fracture-cavern carbonate oil reservoirs from qualitative evaluation to quantitative prediction. Prefrac effect prediction of the development wells drilled since August 2007 reaches a coincidence rate of over 72%, and close to 80% in the main part.

6.4.2.2 Optimization and improvement of acid fracturing fluid

1. Evaluation and optimization of fracturing fluid for ultrahigh temperature

The existing fracturing fluid systems cannot meet the requirements on the acid fracturing stimulation of reservoirs at a temperature of 160°C, making it necessary to develop a fracturing fluid system for ultrahigh temperature.

Guar gum modification: The existing hydroxypropyl guar gum is modified by connecting carboxyl groups and stiff pyrrolidone groups to mannose chains, the network degree of gel is increased by introducing crosslinkable groups, and the stiff groups introduced can improve the temperature resistance of guar gum molecules.

Crosslinker preparation: A new type of zirconium-bearing organic boron is used as the crosslinker. The composite ligand is the mixture of ethyl-butyl propylene glycol, pentaerythrite, neopentyl glycol, and diethylene glycol methylene. The crosslinker can improve temperature resistance and shear resistance of the crosslinked gel considerably, thus satisfying requirements on acid fracturing stimulation of reservoirs with temperatures of 160°C.

Optimization and evaluation of thickener dosage: It is shown from a series of studies that the fluid viscosity corresponding to the shear of 170 s^{-1} is lower than $60 \text{ MPa} \cdot \text{s}$ when the guar gum content is over 0.45%. According to the acid fracturing requirement that the viscosity of base fluid in fracturing fluid be over $70 \text{ MPa} \cdot \text{s}$, the dosage of guar gum should be in the range of 0.5%–0.55%.

Performance evaluation of the crosslinker: With dosages of guar gum, clay stabilizer, foaming agent, bacteriacide and clean-up additive at 0.55%, 0.5%, 0.05%, 0.1% and 0.2%, respectively, the viscosity of base fluid was tested at pH values of 9, 10, 11, 12, and 13, buffered using sodium carbonate. Crosslinker of 0.5% ($A:B = 100:6$) was added into the base liquid at different pH values for crosslinking in the water bath of 70°C, and

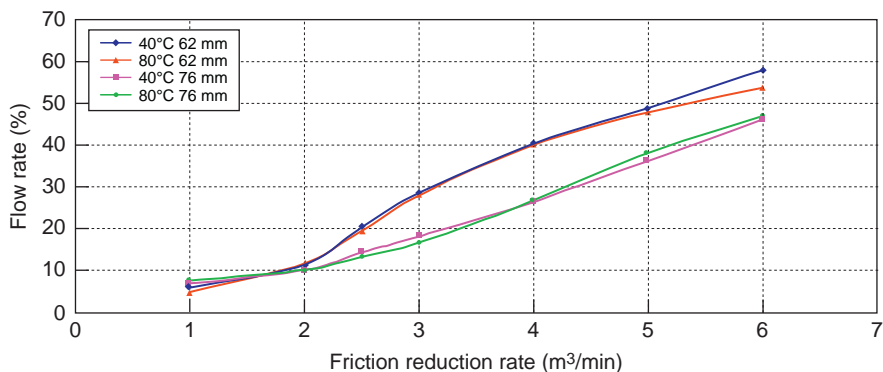


Figure 6.51 Friction reduction effect of the ultrahigh-temperature fracturing fluid.

then the gel was tested. The crosslinking time is 2–3 minutes when the pH of fracturing liquid is 10–11, and the crosslinking time is 2–3 minutes also when the crosslinking ratio is 0.4%–0.6%.

Based on mono-additive optimization evaluation, the high-temperature fracturing formula is as follows:

0.55% guar gum + 0.5% clay stabilizer + 0.1% bactericide + 0.25% clean-up additive (pH adjusted to 11).

Crosslinker A:B = 100:10, and crosslinker dosage 0.6%.

Evaluation of rheological property of high-temperature fracturing fluid: From high-temperature evaluation of the gel with an optimal crosslinking ratio 0.6% under conditions of 160°C and 170 s⁻¹, it can be shown that the viscosity of the ultrahigh temperature fracturing gel stays at 350 MPa·s after 60 minutes of shearing, and remains above 200 MPa·s after 120 minutes of continuous shearing. This confirms that this fracturing fluid system can satisfy the requirements of acid fracturing of reservoirs with temperature of 160°C.

Friction drag resistance: The rheological property of the fracturing fluid was evaluated using a multifunction circulation rheometer. The experimental results show that the friction reduction rate of the fracturing fluid increases with increase in flow rate, but decreases with increase in pipe diameter, and is negligibly affected by temperature. When the flow rate is 6 m³/min, the friction of the fracturing fluid along the pipe is 50% that of fresh water, indicating that the high-temperature guar gum fracturing fluid is satisfactory in terms of its friction reduction property and can effectively reduce the friction drag during acidification (Fig. 6.51).

Evaluation of core damage: This study shows that the degree of oil reservoir damage is 18%–16% after the invasion of fracturing fluid.

6.4.2.3 Fracture height control technology

The height of acid-induced fractures is affected jointly by in situ stress, mechanical parameters of the rock formation, property of the acid fracturing fluid, and the acid fracturing process. The in situ stress difference of acid fracturing intervals is the key factor controlling the fracture height propagation. In the Tahe Oil Field,

however, the carbonate reservoirs are vertically homogeneous in terms of lithology and in situ stress, so that the fractures hardly meet any barrier in the process of height propagation. If no measure is taken to control the vertical propagation of fractures, the lateral propagation of fractures will certainly be restricted and, eventually, the distance of acid-fracturing penetration will be reduced and the connection of fractures and caverns lowered significantly.

1. Fracture height control technology

Five fracture height control technologies have come to be used for the Tahe fracture-cavern carbonate reservoirs.

- a. Acid fracturing parameter optimization: Simulated optimization and field application in multiple wells demonstrated that upward acid fracturing intervals are generally less than 60 m. The acid fracturing fluid is composed of fracturing fluid (140–180 m³) and acidizing fluid (60–220 m³). During fluid injection, the flow rate of the fracturing fluid and acidizing fluid should be maintained below 4.5 m³/min and 6.0 m³/min, respectively.
- b. Fracture height control technology based on stepwise flow rate increase: Fractures are initialized at low flow rate so as to avoid unsteady propagation of fracture and loss control of fracture height. This study shows that, to some extent, the fracture height can be controlled by increasing the flow rate step by step at the early stage of fracturing, so that the length propagation of fractures is improved effectively.
- c. Perforation and acidizing pretreatment: Open hole completion is generally used in the Ordovician strata of the Tahe Oilfield. The reservoirs to be stimulated are mostly type II and III reservoirs of 30–50 m thick, with relatively few breaking points and high fracturing pressure, making the reservoirs difficult to fracture, or the fracture height hard to control once fractured. The perforation technology is applicable to extremely tight reservoirs or cement-damaged reservoirs near the borehole. Perforation can result in fracturing pressure drops by about 15 MPa. The acidizing pretreatment technology is suitable for intervals with some fractures near the borehole and the plugging removal of well intervals with significant damage caused by mud loss in the process of well drilling and completion, which can reduce the formation fracture pressure by about 10 MPa.
- d. Stimulation technology by creating fractures directly using acidizing fluid: The bottom water communication can be easily achieved if the stimulation technology of conventional fracturing fluid is applied in conjunction with modified acidizing fluid to the wells with bottom water and better oil and gas shows near the borehole in the area with relatively developed vertical fractures. In these types of wells, acid with variable viscosity can be used to create fractures, so that favorable reservoir bodies near the borehole can be stimulated and connected and the height propagation of fractures can be restricted.
- e. Fracture height control technology based on artificial barriers: With this technology, the separant (hollow fine powder and silts) is carried into fractures by the carrying fluid when the fractures develop to a certain scale after prepad fluid injection; the hollow fine powder will flow to the top of newly created fractures quickly through buoyancy, and the silts will precipitate at the bottom of the fractures via gravity, forming a low-permeability or impermeable artificial barrier, respectively, at the top and the bottom of fractures. Two materials are selected as artificial barriers according to the requirements on artificial barrier in accordance with the technical specifications of fracture height control and the principles of barrier material selection.

2. Filtration control technology

The analytical results on deep acid fracturing stimulation demonstrate that fluid filtration (including fracturing fluid and acidizing fluid) during acid fracturing of fracture-cavern carbonate reservoirs is affected jointly by the development of fractures and cavities, the viscosity of working fluid, the acid–rock reaction velocity, and the acid fracturing technology and process. The development of acid-dissolution wormholes can be inhibited through acid-dissolution retardation with slow acid–rock reaction rate, or by increasing the viscosity of acidizing fluid, or taking technical measures to reduce acid–rock reaction rate (e.g., multistage alternative acid fracturing).

6.4.2.4 Optimization and support of combined acid fracturing technology

1. Optimization of prepad acid fracturing technology

Stimulation of the remote reservoirs in the Tahe Oil Field requires an increase in prepad fluid volume to improve fracture penetration depth and achieve deep acid fracturing. Prepad acid fracturing with stronger adaptability has been a proven field application. Statistical data show that the consumption volume ratio of prepad fluid to acidizing fluid in the Tahe Oil Field was 1:1 during the 2003–06 period and in the range of 1:1.89–1:0.68 after 2008. This is because the reservoirs stimulated in recent years were poorer and more complicated, so that acid fracturing was optimized based on well and layer conditions and stimulation targets.

2. Combined acid and sand fracturing technology

a. Stimulation mechanism: For acid fracturing stimulation, proppant is not used and the flow conduit is provided by the acid etched fractures that tend to close under high stress. Fracturing stimulation technique using sand-bearing gel acid can combine the advantages of the two technologies in a dynamic manner to maximize the deep penetration of acidizing fluid and the high flow-conductivity of fractures.

b. Well and layer adaptability: Gel acid can significantly increase the dynamic fracture length because of its good proppant-carrying capacity and a viscosity of more than 60 MPa·s at reservoir temperature. For this technology, the principles for well and layer selection are as follows.

i. Fractured reservoirs, cavern-fractured reservoirs or wells with higher filtration.

ii. Layers and wells with effective reservoir bodies over 120 m away from the borehole and in need of deep stimulation.

iii. Wells with tight nearbore reservoirs and poorer oil and gas shows.

iv. Layers with no water layers 50 m above and below or medium and light oil zones.

c. Fracturing process

i. (1) Fracturing fluid + gel acid + gelling acid fracturing

Gel acid can significantly increase the distance of deep penetration because it has the same fracture creating property as the fracturing fluid. Quick break is favorable for flowback, so that gel breaker is added linearly at the late stage. In the borehole vicinity, the flow through fracture openings can be improved by applying closed acid fracturing with regular gelling acid.

ii. (2) Multistage alternative injection of gel acid + gelling acid

Multistage injection and acid fracturing can be fully achieved by injecting gel acid and gelling acid alternatively, solving the problem of acid nonresistance of guar fracturing fluid. In field applications, the gel acid with different pumping, rheological and

filtration properties can be prepared by varying the crosslinker portions according to different formation situations. Gel breaker and crosslinking acid are added simultaneously.

iii. (3) Fracturing using sand-bearing gel acid

Fracturing using sand-bearing gel acid can be applied to porous reservoirs with undeveloped fractures to increase the flow in acid-etched fractures after acid fracturing. Proppant is packed in acid etched fractures to prevent the fractures from closing, resulting in improved fracturing effectiveness.

3. Fracturing using combined clean diverting acid and conventional acid

The acidizing fluid tends to flow into high-permeability zones. This can result in significant fluid loss if the conventional acidizing fluid system is used for acid fracturing of strongly heterogeneous carbonate reservoirs, especially in wells with developed fractures near the borehole. Consequently, high-permeability layers are over-stimulated and it is much easier for the subsequent acidizing fluid to flow into high-permeability layers, whereas the low-permeability layers and severely damaged intervals that need stimulating will not be stimulated sufficiently.

a. Well and layer applicability: this technology is suitable for acidizing or acid-fracturing strongly heterogeneous reservoirs in open hole intervals to achieve effective full-hole stimulation, and for temporarily plugged acid fracturing with fracture height control in the well layers characterized by a limited span and abundant bottom water.

b. Implementation process

Single-stage injection: the design of fracturing using clean diverting acid is essentially the same as that of closed acid fracturing. After the acid-etched fractures are closed, a given amount of closed acid is injected to increase the flow through fracture openings.

Multistage injection: diverting acid + gelling acid/friction reducing acid can be injected alternatively in a combined multistage pattern according to the field requirements.

6.4.3 Application results of sidetracking and acid fracturing

In the demonstration area, horizontal sidetrack drilling was conducted for seven wells, involving an extractable reserve of 3975×10^3 t, and resulting in a recoverable reserve increment of 795×10^3 t, new production capacity of 7.39 t, and cumulative oil production of 152×10^3 t.

Moreover, acid fracturing stimulation has been carried out 20 times in 17 wells, with a new production capacity of 185×10^3 t, extracted reserves of 9520×10^3 t, a recoverable reserve increment of 1904×10^3 t, and an enhanced recovery factor of 3.0%. The input/output ratio of this project is 1:7.1.

References

- Abdassah, D., Ershaghis, I., 1986. Triple-porosity system for representing naturally fractured reservoirs. *SPE Form. Eval.* 1, 113–127.
- Al-Yahya, K., 1989. Velocity analysis by iterative profile migration. *Geophysics.* 54, 718–729.
- Archie, G.E., 1952. Classification of carbonate reservoir rocks and petrophysical considerations. *AAPG Bull.* 81, 712–733.
- Bai, M., Elsworth, D., Roegiers, J.C., 1993. Multiporosity/multipermeability approach to the simulation of naturally fractured reservoirs. *Water Resour. Res.* 29, 1621–1633.
- Bancroft, J.C., Geigerz, H.D., Margra, G.F., 1998. The equivalent offset method of prestack time migration. *Geophysics.* 63 (6), 2042–2053.
- Barenblatt, G.E., Zheltov, I.P., Kocina, 1960. Basic concepts in the theory of seepage of homogeneous liquids in fissured rocks. *Soviet J App Math Mech.* 24 (5), 1285–1303.
- Bar-Matthews, M., Avner, A., Kaufman, A., 1999. The Eastern Mediterranean paleoclimate as a reflection of regional events: Soreq cave, Israel”. *Earth Planet. Sci. Lett.* 166, 86–95.
- Bar-Matthews, M., Ayalon, A., Kaufman, A., 2000. Timing and hydrological conditions of Sapropel events in the Eastern Mediterranean, as evident from speleothems, Soreq Cave, Israel. *Chem. Geol.* 169, 146–156.
- Bin, Z., Jiagen, H., Yuming, L., 2011. 3D geological modeling of Ordovician carbonate karst cave reservoir in the Tahe Oilfield and its application. *J. Oil Gas Technol.* 33 (5), 12–16.
- Camacho-Velazquez, R., Vasquez-Cruz, M., Castrejon-Aivar, R., Arana-Ortiz, V., 2005. Pressure transient and decline-curve behavior in naturally fractured vuggy carbonate reservoirs. *SPE Reservoir Eval.* 8, 95–112.
- Choquette, P.W., Prey, L.C., 1970. Geologic nomenclature and classification of porosity in sedimentary carbonates. *AAPG Bull.* 54, 207–250.
- Chunfang, C., 1997. Study on fluid-rock interactions in the Tarim Basin. Geological Publishing House, Beijing.
- Chunyuan, L., Xiucheng, W., Shengfeng, X., et al., 2007. Overview of application of geophysical methods in carbonate reservoir prediction. *Prog. Geophys.* 22 (6), 1815–1822.
- Claerbout, J.F., 1985. *Imaging the Earth’s Interior.* Blackwell Scientific Publications.
- Closemann, P.J., 1975. The aquifer model for fissured fractured reservoir. *SPE Paper.* 385–398.
- Cooley, T., 2002. Engineering approaches to conditions created by a combination of karst and faulting at a hospital in Birmingham, Alabama (in Engineering and environmental impacts of karst). *Eng. Geol.* 65 (2–3), 197–204.
- Daoxian, Y. (Ed.), 1988. *Dictionary of karstology.* Geological Publishing House, Beijing.
- Daoxian, Y., Zaihua, L., Yushi, L., et al., 2002. *Dynamic system for Karst in China.* Geological Publishing House, Beijing.

- Dengfa, H., 2001. Structural evolution and hydrocarbon accumulation in the Tarim Basin. Geological Publishing House, Beijing.
- Doherty, S., Claerbout, J., 1974. Velocity analysis based on the wave equation. *SEP*. 1, 160–178.
- Dong, H., Xiangchun, Y., Xiangyang, H., et al., 2014. Application of post-stack seismic reservoir prediction in characterization of fracture-vug reservoir. *J. Oil Gas Technol.* 36 (9), 63–68.
- EЖOB et al., 1992. Vertical zoning of karst development (M. Yuezhi, Trans.): Selection of Translation Works for hydrological geology and engineering geology, 6: 30–35.
- Evans, E.V., Evans, R.D., 1988. Influence of an immobile or mobile saturation on non-Darcy compressible flow of real gases in propped fractures. *J. Pet. Technol.* 40 (10), 1343–1351.
- Fangzheng, J., Zhilin, D., 2008. Research and Practice of the Development of Carbonate Fracture-Vug Reservoir in the Tahe Oilfield. Petroleum Industry Press, Beijing.
- Gascoyne, M., 1992. Palaeoclimate determination from cave calcite deposits. *Quat. Sci. Rev.* 11, 609–632.
- Gehua, H., Lixin, Q., Zongjie, L., et al., 2006. Prediction technique of the Ordovician carbonate fracture-vug reservoir in the Tahe Oilfield. *Oil Gas Geol.* 27 (6), 860–870, 878.
- Genty, D.D., Baker, A., Massault, M., 2001. Dead carbon in stallagmites: Carbonate bedrock paleodissolution vs. ageing of soil organic matter: Implications for ^{13}C variations in speleothems. *Geochim. Cosmochim. Acta.* 20, 3443–3457.
- Guangfu, W., 2008. Integrated identification and prediction method of carbonate cavernous reservoir. *Acta Petrol. Sin.* 29 (1), 47–51.
- Hendy, C.H., Wilson, A.T., 1986. Palaeoclimatic data from speleothem. *Nature.* 216, 48–51.
- Hill, A.C., Thomas G.W., A new approach for simulating complex fractured reservoirs. In: SPE Middle East Oil Technical Conference and Exhibition, March 11–14, 1985.
- Hong, L., Guofeng, L., Bo, L., et al., 2009. The travel time calculation method via lateral derivative of velocity and its application in pre-stack time migration. *Geophys. Prospect. Petroleum.* 48 (1), 3–10.
- Hongbo, Z., 2010. Fracture-vug unit division for and development decision of the Ordovician oil reservoir in the Tahe Oilfield. *J. Oil Gas Technol.* 32 (2), 204–205.
- Huanzhang, L., 1990. Geochemistry study for inclusions. Geological Publishing House, Beijing.
- Huiting, Y., Tongwen, J., Qibin, Y., et al., 2004. A primary investigation of 3D geological modeling method for fracture-vug carbonate reservoir. *Daqing Pet. Geol. Oilfield Dev.* 23 (4), 11–16.
- Jiagen, H., Xiaoqiang, M., Xiangyang, H., et al., 2013. A few critical questions related to geological modeling of carbonate karst reservoir. *Geol. J. Chin. Univ.* 19 (1), 64–69.
- Jiagen, H., Xiaoqiang, M., Yuming, L., et al., 2012. Research on multi-class and multi-scale modeling method for fracture-vug carbonate reservoir: a case study from the Ordovician reservoir in the 4th block of the Tahe Oilfield. *Earth Sci. Front.* 19 (2), 59–66.
- Jianjun, H., Jiaduo, L., Xinbian, L., et al., 2009. Identification and division of fracture-vug unit in carbonate reservoir using forward modeling seismic attribute analysis. *Oil Geophys. Prospect.* 44 (4), 472–477.
- Jintao, W., 1987. Karst and carbonate in Guilin. Chongqing Publishing House, Sichuan.
- Jun, Y., Zisheng, W., 2007. Well Test Interpretation Theory and Method for Fracture-vug Carbonate Reservoir. China University of Petroleum Press, Dongying.
- Junjie, Y., 2005. Similarity Theory and Structural Model Test. Wuhan University of Technology Press, Wuhan.

- Junjie, Y., Chunying, X., Wei, W., 2010. A method and its application of scattered-wave image for low signal-to-noise seismic data. *J. China Coal Soc.* 35 (12), 2064–2067.
- Kang, Z.J., 2006. The seepage flow characteristics in the fracture-vug carbonate reservoir in the Tahe Oilfield. *Oil Gas Geol.* 26 (5), 634–640.
- Kazemi, H., Pressure transient analysis of naturally fractured reservoirs with uniform fracture distribution. In: SPE, pp. 451–462. Trans., AIME, 246, 1969.
- Liangxiao, Z., Yong, B., 1994. *Well-log Evaluation Technique for Carbonate Reservoir*. Petroleum Industry Press, Beijing.
- Lifeng, L., Zandong, S., Haijun, Y., et al., 2009. Optimization method for seismic attribute of fracture-vug carbonate reservoir and its application. *Oil Geophys. Prospect.* 44 (6), 747–754.
- Liqiang, S., 2009. *Well-log Evaluation Method of Carbonate Reservoir and Its Application*. Petroleum Industry Press, Beijing.
- Liu, J.C., Bodvarsson, G.S., Wu, Y.S., 2003. Analysis of pressure behavior in fractured lithophysal reservoirs. *J. Contam. Hydrol.* 62, 189–211.
- Lucia, F.J., 1983. Petrophysical parameters estimated from visual description of carbonate rocks: a field classification of carbonate pore space. *J. Pet. Technol.* 35, 629–637.
- Mangin, A., 1974. Contribution a l'etude hydrodynamique des aquifers karstiques. *Ann Speleol.* 29, 283–332.
- Margrave, G.F., and Ferguson, R.J. Wavefield extrapolation by nonstationary phase shift, in: *Depth Imaging of Foothills Seismic Data*. Soc. of Expl. Geophys., Tulsa, 1999, 122–131.
- Min, Z., Zhihong, K., Liujie, 2008. Modeling of fracture-vug carbonate reservoir and its application. *Xinjiang Pet. Geol.* 29 (3), 318–320.
- Mosher, C.C., Keho, T.H., Weglein, A.B., Foster, D.J., 1996. The impact of migration on AVO. *Geophysics.* 61, 1603–1615.
- Nowak E.J. Imhof M.G. Diffractor localization via weighted Radon Transforms. Expanded Abstr. 74th Annu. Int. SEG Meet., 2004, 2108–2111.
- Pech, A., Tsvankin, I., Grechka, V., 2003. Quartic moveout coefficient: 3D description and application to tilted TI media. *Geophysics.* 68, 1600–1610.
- Pestana, R., Stoffa, P.L., 2000. Plane wave Pre-stack time migration. In: *Expanded Abstracts, the 70th SEG annual international conference*. pp. 810–813.
- Price, N.J., Cosgrave, J.W., 1990. *Analysis of geological structures*. Cambridge University Press, Cambridge, England, p. 502.
- Pruess, K., Narasimhan, T.N., 1985. A practical method for modelling fluid and heat flow in fractured porous media. *SPE.* 25 (1), 14–26.
- Qidong, D., 2000. *Tectonic movements of the Tianshan Mountain*. Seismological Press, Beijing.
- Riyuan, X., Hongfeng, C., Shengzhang, Z., Bin, L., 2003. Methodology and significance of study of epikarst zones: Study for karst underground water and desertification in China. *Guangxi Science and Technology Press, Nanning*, pp. 141–147.
- Riyuan, X., Jiansheng, T., 2004. Features of mineral inclusions and performances as indicators for palaeokarst activities. *Acta Geosci. Sin.* 25 (3), 373–377.
- Riyuan, X., Jiansheng, T., Shengzhang, Z., Bin, L., 2006. Features of inclusions in filling materials of palaeokarst on northern edges of the Tarim Basin. *China Karst.* 25 (3), 246–249.
- Tek, M.R., Coats, K.H., Katz, D.L., 1962. The effect of turbulence on flow of natural gas through porous reservoirs. *J. Pet. Technol.* 225, 799–806.
- Ting, X., 1995. *Similarity Method and Its Application*. China Machine Press, Beijing.
- Tingyu, L., 2004. *Geochemistry Processes and Their Environmental Significance of Evolution of Stable Carbon Isotope in Karst Vug Systems*. Doctoral Dissertation. Graduate University of Chinese Academy of Sciences, Beijing.

- Warren, J.E., Root P.J., 1963. The behavior of naturally fractured reservoirs. In: SPE, pp. 245–255, Trans., AIME, 228.
- Weglein, A.B., 1999. Multiple attenuation: an overview of recent advances and the road ahead. *Leading Edge*. 18 (1), 40–44.
- Wei, W., JunJie, Y., XueWei, L., JunMeng, Z., Yun, W., Ying, H., 2007. Equivalent offset method and its application. *Chin. J. Geophys.* 50 (6), 1823–1830.
- Wu, Y.S., Ge, J.L., 1983. The transient flow in naturally fractured reservoirs with three porosity systems. *Acta Mech. Sin. Theor. Appl. Mech.* Beijing, China. 15 (1), 81–85.
- Wu, Y.-S., Liu, H.-H., 2004. A triple-continuum approach for modeling flow and transport processes in fractured rock. *J. Contam. Hydrol.* 73 (1–4), 145–179.
- Xia, C., 1993. Preliminary analysis on origin and storage performance of ordovician karst reservoir in ordos platform. *Carsol. Sin.* 12 (3), 261–272.
- Xiangyang, H., Xiangchun, Y., Jiagen, H., et al., 2014. Multi-scale karst facies-controlling modeling method for carbonate fracture-vug reservoir. *Acta Petrol. Sin.* 35 (2), 340–346.
- Xiangyang, H., Yang, L., Lianshun, Q., et al., 2013. 3D geological modeling method for carbonate fracture-vug reservoir: a case study from the Ordovician reservoir in the 4th block of the Tahe Oilfield. *Oil Gas Geol.* 34 (3), 383–387.
- Xiaoguang, T., et al., 1996. *Progresses in Petroleum Geology Studies in the Tarim Basin*. Beijing Science Press, Beijing.
- Xiaoqiang, M., Jiagen, H., Xiangyang, H., 2013. Discussion of 3D geological modeling of paleo-karst cave reservoir. *Geol. Rev.* 59 (2), 315–324.
- Ximing, Z., Jianguo, Z., Zongyu, L., et al., 2007. Characteristics and division of fracture-vug unit for carbonate fracture-vug reservoir in the Tahe Oilfield. *Mar. Origin Pet. Geol.* 12 (1), 21–24.
- Xin, Z., 2010. Application of ant tracking in automatic fault interpretation: a case study from the Fangheting structure, the Pinghu Oilfield. *Oil Geophys. Prospect.* 45 (2), 278–281.
- Xinbian, L., Min, Z., Xiangyang, H., et al., 2012. Research on 3D modeling method and technique of carbonate fracture-vug reservoir: a case study from the Ordovician fracture-vug reservoir in the Tahe Oilfield. *Pet. Geol. Exp.* 34 (2), 193–198.
- Xinjiang Institute of Geography and Chinese Academy of Science, 1986. *Evolution of the Tianshan Mountain*. Beijing Science Press, Beijing.
- Yang, J., 2006. Numerical simulation theory and methodology study of fracture-vug unit in fracture-vug carbonate reservoir.
- Yang, L., 2012. Identification and quantitative characterization of the Ordovician carbonate cavernous reservoir in the Tahe Oilfield. *J. Chin. Univ. Pet.* 36 (1), 1–7, (Edition of Natural Sciences).
- Yingjie, Z., Qiang, W., Jingxuan, Z., et al., 2004. Prediction on fracture distribution in Chenbei 30 buried hill Archeozoic fractured reservoir. *J. Chin. Univ. Mining Technol.* 33 (4), 433–437.
- Yubin, H., 1991. Hydrodynamic profiles and significance of evenly distributed thick limestone formations. *China Karst.* 10 (1), 1–12.
- Yuming, L., Jiagen, H., Xiangyang, H., et al., 2012. 3D modeling of paleo-karst reservoir body in the Tahe Oilfield. *J. Chin. Univ. Pet.* 36 (2), 34–38, Edition of Natural Sciences.
- Yuzhu, K., 2008. Characteristics of and hydrocarbon distribution in Paleozoic carbonate paleo-karst reservoir. *Nat. Gas Ind.* 28 (6), 1–12.
- Zhang, B.S., et al., 1996. *Development of Carbonate Buried Hill Oil Field*. Petroleum Industry Press, Beijing.

- Zhang, K., 1999. The development and geology application in the Tahe Oilfield. *Oil Gas Geol.* 20 (2), 120–124.
- Zhihai, C., Xujie, M., Guangtao, H., 2007. Research on division method for fracture-vug unit in fracture-vug carbonate oil reservoir. *Oil Gas Geol.* 28 (6), 847–855.
- Zhilin, D., 2012. *Development Technique for Fracture-Vug Carbonate Reservoir in the Tahe Oilfield*. Petroleum Industry Press, Beijing.
- Zhongchun, L., Jianglong, L., Chengyuan, L., Zhongliang, T., Ming, L., 2009. Experimental study on the effect of reservoir space type of fracture-vug reservoir on water cut of oil well. *Acta Pet. Sin.* 30 (2), 271–274.

Further Reading

- Aishan, L., Xingyao, Y., Fanchang, Z., Baoli, W., 2007. Application of prestack simultaneous AVA multi-parameter inversion in gas-bearing reservoir prediction. *Oil Geophys. Prospect.* 46 (1), 64–68.
- Bartana, A., Kosloff, D., Ravve, I., 2006. Discussion and Reply On Angle-domain common-image gathers by wavefield continuation methods. *Geophysics.* 71, X1–X4.
- Bin, Z., Jiagen, H., Yuming, L., et al., 2011a. A modeling method of carbonate fractured reservoir based on Marked Point Process Simulation. *Sci. Technol. Rev.* 29 (3), 39–43.
- Biondi and Chemingui: Transformation of 3-D prestack data by azimuth moveout (AMO): 1994.
- Biondi, B., Symes, W., 2004. Angle-domain common-image gathers for migration velocity analysis by wavefield-continuation imaging. *Geophysics.* 69, 1283–1298.
- Biondi, B., Tisserant, T., 2004. 3D angle-domain common-image gathers for migration velocity analysis. *Geophys. Prospect.* 52, 575–591.
- Biondi, B., Tisserant, T., Symes, W., 2003. Wavefield-continuation angle-domain common-image gathers for migration velocity analysis. In: *The 73rd SEG Annual International Conference*: pp. 2104–2107.
- Chao, H., Liangguo, D., 2009. Staggered-grid high-order finite-difference method in elastic wave simulation with variable grids and local time-steps. *Chin. J. Geophys.* 52 (11), 2870–2878.
- Chen, Y.M., et al., 1989. *Base of Reservoir Numerical Simulation*. China University of Petroleum Press, Dongying Shandong.
- Chen, X., Shuli, M., 2007. Hydrocarbon detection based on transient wavelet absorption. *Small Hydrocarbon Reservoirs.* 12 (2), 29–31.
- Chunyu, L., Shengwang, Z., Xiucheng, W., Shengfeng, X., 2010. Application of Seismic wave forward modeling in random media for carbonate reservoir prediction. *Geophys. Prospect. Pet.* 49 (2), 133–139.
- Desheng Y. Ordovician palaeokarst in Akekule Upheaval, Tarim Basin and the Tahe Oilfield. In: *Proceedings of the 2001 China National Conference of Sedimentology*.
- Dubrulle, A.A., 1983. Numerical methods for the migration of constant-offset sections in homogeneous and horizontally layered media. *Geophysics.* 48, 1195–1203.
- Ekren, B.O., Ursin, B., 1999. True-amplitude frequency-wavenumber constant-offset migration. *Geophysics.* 64, 915–924.
- Fang, W., Wenbin, C., Shichao, L., 2010. Application of RMS extraction technique in geological modeling of cave carbonate reservoir. *Geoscience.* 24 (2), 279–286, 293.
- Fanyi, L., Jianxin, W., Bangrang, D., 2009. Forward simulation of seismic response in carbonate caverns with varied lateral scale. *Geophys. Prospect. Pet.* 48 (6), 557–562.

- Ge, J.L. (Ed.), 2003. *Principles of Modern Reservoir Percolation Mechanics*. Petroleum Industry Press, Beijing.
- Heeremans, J.C., T.E.H. Esmail, C.P.J.W. van Kruijsdijk, Feasibility study of WAG injection in naturally fractured reservoirs. In: SPE-100034, Presented at the 2006 SPE/DOE Symposium on Improved Oil Recovery, Tulsa, OK, April 22–26, 2006.
- Hidajat, I., Mohanty, K.K., Flaum, M., Hirasaki, G., 2004. Study of vuggy carbonates using NMR and X-Ray CT scanning. *SPE Reservoir Eval. Eng.* 365–377.
- Huazhong, W., Bo, F., Haoran, R., 2009. Finite-difference pre-stack time migration of 2D offset plane wave. *Geophys. Prospect. Pet.* 48 (1), 11–19.
- Jianxin, W., Bangrang, D., 2007. Experimentally surveying influence of fractural density on P-wave propagating characters. *Oil Geophys. Prospect.* 42 (5), 554–559.
- Jianxin, W., Bangrang, D., Lihua, W., 2008. Seismic physical modeling for cavern reservoir. *Geophys. Prospect. Pet.* 47 (2), 156–160.
- Jun, Z., Chengwen, X., Bing, Y., 2011. Well log evaluation of the filling degree of the cavernous carbonate reservoir in the Lungu region. *Acta Petrol. Sin.* 32 (4), 605–610.
- Junfeng, W., Yao, Y., Liming, S., 2007. Analysis on seismic response of special cavernous structure of carbonate. *Oil Geophys. Prospect.* 42 (2), 180–185.
- Kang, Z.J., Wu, Y.S., Modeling multiphase flow in naturally fractured vuggy petroleum reservoirs. In: SPE 102356, 2006.
- Kazemi, H., 1979. Numerical simulation of water imbibition in fractured cores. *SPE.* 323–330.
- Komtime, A.M.A., Jianhua, Z., Yang, L., Fuping, Z., Yufei, G., 2008. Carbonate fractures and karstification. *Geol. Rev.* 4, 76–82.
- Kossack and Curpine, A methodology for simulation of vuggy and fractured reservoirs.
- Kostov, C., Biondi, B., 1987. Improved resolution of slantstacks using beam stacks, Expanded Abstracts. In: The 57th SEG annual international conference, pp. 792–794.
- Liangguo, D., Chao, H., Yuzhu, L., Qun, Z., 2010. Numerical simulation of seismic wave propagation in cave carbonate reservoir. *Geophys. Prospect. Pet.* 49 (2), 121–124.
- Liangjie, T., 1996. *Evolution and structural patterns of the Tarim Basin*. Geological Publishing House, Beijing.
- Lihua, W., Jianxin, W., Bangrang, D., 2008. Seismic response of karst cave physical model and analysis of its attributes. *Oil Geophys. Prospect.* 43 (3), 291–296.
- Lu, S., Tingchao, G., 2006. AVA-based fracture detection and application. *Small Hydrocarbon Reservoirs.* 11 (3), 15–18.
- Mackay, S., Abma, R., 1992. Imaging and velocity estimation with depth-focusing analysis. *Geophysics.* 57, 1608–1622.
- Mackay, S., Abma, R., 1993. Depth-focusing analysis using a wavefront-curvature criterion. *Geophysics.* 58, 1148–1156.
- Mitchell, A.R., Kelamis, P.G., 1990. Efficient tau-p hyperbolic velocity filtering. *Geophysics.* 55, 619–625.
- Mosher, C.C., Foster, D.J., Hassanzaddh, S., 1997. Common angle imaging with offset plane waves. In: Expanded Abstracts, the 67th SEG annual international conference, pp. 1379–1382.
- Nailing, X., Wei, X., Shusheng, G., Zhiming, H., Fansheng, B., HuiL, X., 2008. Preliminary study on flow mechanisms in fracture-vug carbonate reservoir. *Drill. Prod. Technol.* 31 (1), 63–65.
- Neidell, N.S., Neidell & Associates, 1997. Perceptions in seismic imaging Part 2: Reflective and diffractive contributions to seismic imaging 1 to 4. *Leading Edge.* 16 (8), 1121–1123.

- Pei, L., Shengwang, Z., Shouli, Q., Zhenfeng, L., 2010. Analysis on P-wave seismic response of vertical fractures. *Geophys. Prospect. Pet.* 49 (2), 125–132.
- Pengfei, X., Shixing, W., Shouli, Q., Hui, C., Jin'e, X., 2009. Analysis on the impact of dip on fracture density inversion. *Oil Geophys. Prospect.* 48 (6), 544–551.
- Pruess, K. GMINC-A mesh generator for flow simulations in fractured reservoirs. In: Report LBL-15227, Berkeley, CA: Lawrence Berkeley National Laboratory, 1983.
- Qiang, S., 2012. Oil and Water Biphasic Flow Patterns in Fracture-vug Media [m]. China University of Petroleum (East China), Qingdao, Shandong.
- Qun, Z., Shouli, Q., Shigui, X., Ming, Z., 2010. Study on the seismic response characteristics on the physical model of carbonate cave. *Geophys. Prospect. Pet.* 49 (4), 351–358.
- Results of the Application of Reservoir Numerical Simulation. CNPC. Petroleum industry press, 1996.
- Rickett, J., Sava, P., 2002. Offset and angle-domain common image-point gathers for shot-profile migration. *Geophysics.* 67, 883–889.
- Rivas-Gomez et al., 2001. Numerical simulation of oil displacement by water in a vuggy fractured porous medium. In: SPE-66386, presented at the SPE Reservoir Simulation Symposium, Houston, TX, February 11–14.
- Riyuan, X., 2001. Progresses in researches related to palaeokarst and karst in oil and gas fields. *China Karst.* 20 (1), 76.
- Riyuan, X., Shengzhang, Z., Bin, L., et al., 2011. Study on Patterns and Genesis of Ordovician Carbonate Fracture-Vug System in the Tarim Basin. Geological Publishing House, Beijing.
- Sava, P., Fomel, S., 2003. Angle-domain common-image gathers by wavefield continuation methods. *Geophysics.* 68, 1065–1074.
- Schultz, P.S., Claerbout, J.F., 1978. Velocity estimation and downward continuation by wavefront synthesis. *Geophysics.* 43, 691–714.
- Shengwang, Z., Shouli, Q., Xiucheng, W., Chunyuan, L., 2007. Numeric simulation by grid-various finite-difference elastic wave equation. *Oil Geophys. Prospect.* 42 (6), 634–639.
- Shengwang, Z., Shouli, Q., Xiucheng, W., Pei, L., 2010. To improve imaging resolution by mapping noise attenuation on CSP gathers. *Geophys. Prospect. Pet.* 49 (2), 107–114.
- Shengwang, Z., Xiucheng, W., Shouli, Q., Chunyuan, L., Kailong, W., 2008. Description of the carbonate karst reservoir with random media model. *Acta Geol. Sin.* 82 (3), 420–427.
- Shixing, W., Huilan, C., Wenfang, J., Yuhua, C., 2005. Seismic response and prediction of fracture-cavity system in carbonate reservoir: A case study in the Ka-1 field. *Geophys. Prospect. Pet.* 44 (5), 421–427.
- ShouLi, Q., Sheng-ang, Z., Qun, Z., Pei, L., 2012. Analysis of seismic reflection characters for carbonate Karst reservoir. *Chin. J. Geophys.* 55 (6), 2053–2061.
- ShouWei, L., Huazhong, W., JiuBing, C., Zaitian, M., 2008. Space-time-shift imaging condition and migration velocity analysis. *Chin. J. Geophys.* 51 (6), 1883–1891.
- Stoffa, P.L., Buhl, P., Diebold, J.B., Wenzel, F., 1981. Direct mapping of seismic data to the domain of intercept time and ray parameter. *Geophysics.* 46, 255–267.
- Tao, L., Jiagen, H., Lixin, C., Ke, M., Wenming, Y., Yue, D., 2015. Division and evaluation of fracture-vug unit of fracture-vug reservoir in Ha-601 well block, Halahatang Oilfield. *Xinjiang Pet. Geol.* 36 (4), 436–444.
- Tieman, H.J., 1997. Improving plane-wave decomposition and migration. *Geophysics.* 62, 1195–2205.
- Wu, Y.S., Haukwa, C., Bodvarsson, G.S., 1999. A site-scale model for fluid and heat flow in the unsaturated zone of Yucca Mountain, Nevada. *J. Contam. Hydrol.* 38 (1–3), 185–217.

- Wu, Y.S., 2000b. A virtual node method for handling wellbore boundary conditions in modeling multiphase flow in porous and fractured media. *Water Resour. Res.* 36 (3), 807–814.
- Wu, Y.S., Pruess, K., 1988. A multiple-porosity method for simulation of naturally fractured petroleum reservoirs. *SPE Reservoir Eng.* 3, 327–336.
- Xiangbin, Y., Luping, G., Shixing, W., 2007. Seismic response characteristics and prediction of carbonate rock fracture-vug systems in the Tarim Basin. *Oil Gas Geol.* 28 (6), 828–835.
- Xiaote, H., 2002. Development technology discussion of fracture-vug type carbonate reservoir. *Pet. Geol. Exp.* 24 (5), 446–451.
- Xiaotao, W., Zhenhua, H., Deji, H., 2006. Integrative detection of fractures by multiple methods based on confidence analysis. *Oil Geophys. Prospect.* 41 (2), 207–210.
- Xishuang, W., Huizhen, S., Jie, L., 1999. Numerical simulation for tectonic stress field in the Tarim Basin and its significance on hydrocarbon accumulation. *Seismic Geol.* 21 (3), 268–273.
- Xubin, C., Haitao, H., Yinben, Z., et al., 2000. Void type and its origin analysis of the Ordovician paleo-weathering crust reservoir in Tarim Basin. *Nat. Gas Explor. Dev.* 23 (1), 36–42.
- Yumei, W., Xianjun, M., Guoqiang, S., 2007. The application of the prestack seismic inversion technology in gas reservoir prediction. *Pet. Geophys.* 5 (2), 33–37.
- Yang, L., Zhihui, F., 2011. Development feature and distribution law of fracture-vug system in the Ordovician carbonate reservoir in the Tahe Oilfield. *Acta Petrol. Sin.* 32 (1), 101–106.
- Yang, L., 2013. Theory and method of the development of carbonate fracture-vug reservoir in the Tahe Oilfield. *Acta Pet. Sin.* 34 (1), 115–121.
- Yehua, S., Weiping, G., 2001. Preliminary study on natural fracture forming mechanisms in reservoir. *Pet. Geol. Exp.* 23 (4), 457.
- Zeng, H., Loucks, R.G., Janson, X., et al., 2011. Three-dimensional seismic geomorphology and analysis of the Ordovician paleokarst drainage system in the central Tabei Uplift, northern Tarim Basin western China. *AAPG Bull.* 95 (12), 2061–2083.
- Zhanguo, L., Jun, Y., Diansheng, W., et al., 2010. Experimental study on percolation characteristics in orthogonal fracture network. *J. Chin. Coal Soc.* 35 (4), 555–558.
- Zheng, Q., Yumin, Z., 1996. Pore types and features of the Lower Paleozoic carbonate in the Taikang uplift. *Henan Pet.* 10 (5), 1–5.
- Zhihai, C., Lanfang, T., Tielong, C., et al., 2007. Preliminary study on fluid flow issues in fracture-vug type carbonate reservoir. *West Chin. Pet. Geosci.* 3 (1), 94–99.
- Zhihong, L., Hailong, Z., Qun, Z., Hui, C., 2009. Study and materialization of new seismic physical model building materials. *Prog. Geophys.* 24 (2), 408–417.
- Zhijiang, K., Jianglong, L., Dongli, Z., et al., 2005. Percolation characteristics of Tahe fracture-vug type carbonate reservoir. *Oil Gas Geol.* 5 (1), 635–673.
- Zhiming, L., 1991. Compensating finite difference errors in 3-D migration and modeling. *Geophysics.* 56, 1650–1660.

Index

Note: Page numbers followed by “*f*” and “*t*” refer to figures and tables, respectively.

A

Acid and sand fracturing technology, 479–480
Acidizing fluid system, 480
Acidizing pretreatment technology, 478
Acoustic wave equation (VS&T), 124–125
Akekule bulge, 33, 48–51, 75, 253–254
Akekule salient, 7–8, 10, 13, 50, 98
Aki–Richards approximation, 193–194
Ancient formation thickness, calculating, 73–74
Angle-domain common-image gathers (ADCIGs), 160–163
Attribute parameter modeling method, 274–276
 algorithm for, 274–275
 of caverns, 275
 of fractures, 275–276
 of vugs, 275
Attribute parameters, 271–274
 for caverns, 271–272
 for fractures, 273–274
 for vugs, 272–273
Azimuth variant seismograms for a high-dip fracture model, 150*f*

B

Barenblatt model, 355
Bayes’ theorem, 194–195
Biot–Gassmann equation, 190–191, 194–195
Born approximation, 128–129
Boundary mass flux, 367

C

Carbonate fracture-vug system, development pattern of, 55–72
 dolomite system, 71–72
 fault-karst system, 66–68
 hall-like cave system, 61–64

 pipe network underground stream system, 56–60
 reef shoal system, 70
 shaft-like cave system, 64–65
 single-pipe underground stream system, 55
 solution cave system, 64
 solution fracture system, 68–70
 tectonic corridor underground stream system, 60–61
Carbonate reservoir space, 4
Carbonate rock properties and karstification, relationship between, 20–23
 mechanism of differential denudation, 23
 rock mineral composition and karstification, relationship between, 20–22
 rock texture and karstification, relationship between, 22
Carbonatite structure and fracture-vug system, relationship between, 23–24
Carbon–oxygen isotope characteristics of Ordovician karst fillings, 37–39
 in the outcrop area of the northern Tarim Basin, 36
 in the Tahe Oilfield region, 37–39, 38*t*
Carbon–oxygen stable isotope characteristics of the Ordovician karst fillings, 36
Cartesian coordinate system, 157–158, 382
Cave prediction, 171–175
 discontinuity detection, 173–175
 reflection configuration analysis, 171–173
 strong amplitude clustering, 173
Cavern flow, numerical simulation of, 376–377
Cavernous reservoirs, 230–232, 271–272
CaveSim, 396–397, 411

- Characteristics of fracture-vug reservoirs, 1–17
 fracture-cave reservoirs, 6
 fracture reservoirs, 5–6
 fracture-vug reservoirs, 6
 karstic reservoir space, classification
 criteria of, 1–4
 cave/cavern, 2–3
 fracture, 3–4
 primary pore, 2
 secondary pore, 2
 ordovician reservoirs in Tahe oilfield, 7–17
 formation lithology, 13
 karstification, 13–17
 tectonism and rifting, 7–12
- Characterization of fracture-vug unit, 251–256
 division, 251–252
 karst facies pattern, 252–253
 fracture-water table dual control mode, 252
 water table-dominated pattern, 253
 typical fracture-vug unit, 253–256
- Common-imaging-point (CIP) gathers, 164
 Common-scatter-point (CSP) gather, 167–170
- Composite reservoir model, 433–435
- Comprehensive description of fracture-vug units, 182–189
 logging and seismic responses, 182
 multiattribute optimization and fusion, 185–186
 nonlinear reconstruction of log curves, 183–184
 palaeogeomorphologic study, 186
 palaeogeomorphology-controlled sculpting, 186–187
 petrophysical properties inversion, 188–189
 well-controlled frequency-divided inversion, 185
- Compressible coefficient, 369
 Conductivity coefficient, 372, 374, 376–377
 Conjugate gradient method, 380–381
 Consecutive interface model, 368
 Constrained sparse spike inversion (CSSI), 188–189, 218–219
 Continuous surface force model (CSF), 368
- Couchy boundary conditions, 370
 Coupled flow well testing model, 438–441, 439*f*
 mathematical model of, 439–440
 numerical well testing plot, 440–441
 flow pattern of coupled flow model, 440
 percolation and free flow coupled flow model, 440–441
- Coupling numerical modeling method, validation of, 411–416
 injection-recovery simulation in cave-fracture-vug model, 416
 physical experiment modeling of fluid flow in filled vugs, 411–414
 two-phase numerical simulation in large caves (caverns), 414–415
- Courant number, 387–388
 Crank–Nicholson format, 387–388
 Crossflow coefficient, 318–319
 Crossflow law at pseudosteady state, 319–320
- D**
- Darcy flow, 294, 298–299, 302–303, 360, 438–441
 numerical simulation of, 370–374
 Depth focusing analysis (DFA), 160–161
 Development level and morphology of fractures, 229
 Devonian–Early Carboniferous period
 Hercynian tectonic movement in, 48–50
 Differential denudation, mechanism of, 23
 Diffraction imaging, improving resolution of, 167–171
 diffracted waves on CSP gathers, 169–170
 field data testing, 171
 mapping noise suppression, 170
 theoretical modeling, 171
 Dirac function, 368
 Dirichlet boundary conditions, 370
 Discontinuity detection, 173–175
 Distribution law of fracture-vug reservoir, 250–251
 Dolomite system, 71–72, 71*t*
 Double-vug medium, flow law in, 332–338

- Drilled well, verification by, 277
- Dual-flow model, 364
- Dual-permeability model, 355
- Dynamic indicator of fractures, 229–230
- E**
- ECLIPSE, 410–411
- Elastic wave equation, variable-grid finite difference using, 123–124
- En echelon-type fault-karst system, 67
- EOR technology, by nitrogen injection.
See Nitrogen injection EOR technology
- Epikarst zone, 24, 26, 29, 90–96, 112–113
- Equation of mass conservation of equivalent multimediuim reservoir, 360–362
- Equivalent multimediuim reservoir,
mathematical model for, 355–366
equation of mass conservation, 360–362
equivalent multiple medium, 355–356
fluid flow interface in caverns, 366
multimediuim representative elementary volume, 357–359
multiphase vug (cave) flow, 363–366
pipe flow, fracture flow, and high-speed Darcy flow, 362–363
- Erosiveness, 20, 21*t*, 26
- Euler explicit, 387–388
- Euler implicit, 387–388
- Exposed weathered karst in the Devonian–Early carboniferous period, 48–50
- F**
- Fault-karst system, 66–68, 67*f*, 68*t*
classification characteristics of, 9*t*
- Field waterflooding development results,
analysis of, 457–459
- 15-m cave identification, 202–204
- Filler and vug, flow law between, 324–326
crossflow from filler to vug at pseudosteady state, 326
flow modeling test, 324–325
mathematical model, 325–326
physical model, 324
- Filling characteristics, 111–114
in different geomorphologic units, 111–112
in the karst lake, 112
in the karst mound depression, 112
in the peak-cluster ridge valley, 112
in different karst belts, 112–113
in the epikarst zone, 112–113
in the runoff dissolution zone, 113
in the undercurrent dissolution zone, 113
in the vertical seepage dissolution zone, 113
in the same geomorphologic unit, 113–114
- Filling degree, 111, 114
- Filling materials, 106–110
chemical deposition, 108–109
collapsed deposition, 26–27
mechanical deposition, 106
weathered residual materials, 110
- Filling space, 110–111
enclosed space, 110–111
open space, 110
partially open/closed space, 110
- Filtration control technology, 479
- Finite volume method (FVM), 381–382, 387
- Flow simulation methods in multimediuim model, 361*f*
- Fluid detection, 190–196
based on prestack elastic inversion, 218–220
EI inversion, 218–219
LMR inversion, 219–220
fluid probabilistic analysis, 194–196, 195*f*
prestack fluid detection, 192–194
LMR inversion, 194
prestack elastic impedance inversion, 193–194
sensitivity analysis, 190–191
feasibility study, 191
fluid substitution, 190–191
petrophysical model, 190
- Fluid flow in filled vugs, physical experiment modeling of, 411–414
- Fluid flow interface in caverns, 366
- Fluid flow law, 283
applications, 338–351
isolated vug reservoirs, production characteristics in, 339–340

Fluid flow law (*Continued*)

- near-vug fracture reservoir, production characteristics in, 340–341
 - vug-fracture-vug reservoir, production characteristics in, 341–342
 - between filler and vug, 324–326
 - between fracture and matrix, 315–320
 - crossflow law at pseudosteady state, 319–320
 - experimental design and methodology, 315
 - experimental results and analyses, 315–317
 - mathematical model and calculation, 317–319
 - between matrix and vug, 320–326
 - in double-vug medium, 332–338
 - in multifracture and multivug medium, 338
 - numerical experimental study, 343–351
 - one-phase flow regime in fracture-vug medium, 343–345
 - two-phase flow regime in fracture-vug medium, 345–351
 - one-phase flow law, 294–303
 - experiments, 294–297
 - one-phase flow pattern and conversion conditions, 298–303
 - physical modeling experimental design, 283–294
 - building experiment models, 288–292
 - experiment system, 293–294
 - fundamental principles and similarity criteria, 283–284
 - materials selection, 287–288
 - similarity criteria, 284–287
 - in single-vug–near-vug fracture (high dip) medium, 326–331
 - two-phase flow law, 303–314
 - oil–water two-phase flow experiment, 304–307
 - oil–water two-phase flow features, 308–314
 - patterns, 303–304
- Fluid probabilistic analysis, 221
- based on AVO inversion, 194–196, 195*f*
 - workflow of, 195*f*
- Forchheimer number, 294, 298–300, 304
- Fracture-cavern carbonate reservoirs, development technology for, 423
- field waterflooding development results, analysis of, 457–459
- horizontal well sidetracking and reservoir stimulation technologies, 472–480
- application results of sidetracking and acid fracturing, 480
 - reservoir stimulation technology, 475–480
 - small-radius horizontal well sidetracking technology, 473–475
- nitrogen injection EOR technology, 459–472
- EOR technology by nitrogen injection for single wells, 461–470
- formation mechanism and distribution pattern of residual oil, 459–461
- gas injection effectiveness, analysis of, 471–472
- gas injection EOR technology, 471
- performance analysis techniques, 423–442
- coupled flow well testing model and analytical method, 438–441
 - evaluation of natural energy, 427–429
 - interpretation of testing data from fracture-cavern carbonate reservoirs of Tahe Oil Field, 441–442
 - numerical well testing based on triple-porosity medium, 429–438
 - variation characteristics and prediction model for individual well production, 424–427
- waterflooding development mechanisms, 443–446
- natural energy, 445–446
 - recovery mechanisms for production wells in fractured zone, 444–445
 - recovery mechanisms of production wells in cavern zone, 443–444
 - reservoir bodies, types of, 445
 - spatial relationships between injection and production wells, 445
 - spatial relationships between oil-producing wells and caverns, 445
- waterflooding development technology, 446–455

- optimization of injection/production parameters, 450–455
 - spatially structured well grid, 446
 - water injection mode, 449–450
 - water injection timing, 447–449
- waterflooding effectiveness, evaluation of, 455–457
- overall evaluation methods, 456–457
- technical evaluation index system, 455–456
- Fracture height control technology, 477–479
 - filtration control technology, 479
 - fracture height control technology, 478–479
- Fracture plane model, 437–438, 437*f*
- Fracture prediction, 175–176
 - based on P-wave AVO for TTI media, 180–181
 - model-based AVO inversion, 181
 - theoretical basis, 180–181
 - based on residual P-wave NMO for TTI media, 177–180
 - residual NMO for TTI media, 177–178
 - residual P-wave NMO for TTI media, fracture detection based on, 178–180
- curvature, 175–176
- neural networks, 176
- Fracture reservoirs, 5–6
 - large-scale, 235–236
 - microscale, 236
- Fracture system, 96–106
 - development characteristics, 99–106
 - different stages of fractures, 101
 - dip angle of fracture, 99
 - length of fracture, 99–100
 - strike of fracture, 101
 - forming mechanisms, 98–99
 - impact of regional structures, 98–99
 - reformation at later stages, 99
- Fracture-cave reservoirs, 6
- Fractured models, 288–289, 291*f*
 - fracture aperture control technique, 288
 - fracture construction technology, 288
 - fracture-vug reservoirs, 117
 - high accuracy physical models of, 290*f*
 - relative permeability curves based on, 308–311
 - roughness control technique, 288
 - 2D and 3D physical models of, 290*f*
- Fractures and karstification, relationship between, 11*f*
- Fracture-vug models, 289–292, 292*f*
- Fracturing using combined clean diverting acid and conventional acid, 480
- G**
- Gabor transform, 131
- Gas injection effectiveness, analysis of, 471–472
 - typical single well gas injection, 471–472
 - typical well-cluster gas injection, 472
- Gas injection EOR technology for fracture-cavern units, 471
- Gauss–Newton Method (GNM), 435–436
- Genesis identification method, combined, 74
- Geologic model
 - application of, 281–282
 - numerical simulation of, 142–144
- Geological structure and karstification, relationship between, 24
- Geophysical characterization of fracture-vug carbonate reservoirs, 117
 - comprehensive application of geophysical technology, 196–221
 - data quality and acquisition, 196–204
 - fracture-vug units prediction, 205–221
 - fluid detection, 190–196
 - fluid probabilistic analysis, 194–196, 195*f*
 - prestack fluid detection, 192–194
 - sensitivity analysis, 190–191
 - logging and seismic responses, 182
 - multiattribute optimization and fusion, 185–186
 - nonlinear reconstruction of log curves, 183–184
 - palaeogeomorphology-controlled sculpting, 186–187
 - petrophysical properties inversion, 188–189
 - prestack azimuthal anisotropy-based fracture detection, 177–181
 - based on P-wave AVO for TTI media, 180–181
 - based on residual P-wave NMO for TTI media, 177–180
 - reservoir prediction, 171–176

- Geophysical characterization of fracture-vug carbonate reservoirs (*Continued*)
- cave prediction, 171–175
 - fracture prediction, 175–176
 - seismic forward modeling, 117–127
 - numerical simulation, 122–127
 - physical modeling, 117–122
 - seismic imaging, 155–171
 - diffraction imaging, improving resolution of, 167–171
 - offset plane-wave finite-difference prestack time migration, 156–158
 - time-shift depth migration and velocity analysis in angle domain, 160–167
 - seismic responses, 128–155
 - of a complicated cave system, 140–144
 - of fractures, 145–153
 - of isolated caverns, 128–139
 - 3D fracture-vug model, physical simulation of, 153–155
 - well-controlled frequency-divided inversion, 185
- Geophysical technology, comprehensive application of, 196–221
- apparent volume estimation, 212
 - data quality and acquisition, 196–204
 - 15-m cave identification, discussions of, 202–204
 - high-density data processing, 201
 - high-density seismic acquisition, 196–200
 - detailed description, 211–212
 - fluid detection, 218–221
 - based on prestack elastic inversion, 218–220
 - fluid probability analysis, 221
 - fracture-vug units prediction, 205–211
 - poststack seismic attributes, 205–208
 - P-wave AVO-based fracture detection, 210–211
 - P-wave residual NMO-based fracture detection, 209
 - goodness of fit, 213–218
 - karst development and evolution in the early coverage of, 50–51
- Hercynian tectonic movement in Devonian–Early Carboniferous period, 48–50
- Heterogeneous fracture-vug reservoir, physical model of, 289*f*
- High-density data processing, 201
- High-density seismic acquisition, 196–200
 - azimuth, 200
 - bin size, 199
 - fold, 200
 - lateral resolution, 197–199
 - maximum offset, 200
 - recording geometry, 200
- High-speed non-Darcy flow, numerical simulation of, 374–376
- Horizontal well sidetracking and reservoir stimulation technologies, 472–480
 - application results of sidetracking and acid fracturing, 480
 - reservoir stimulation technology for fracture-cavern oil reservoirs, 475–480
 - combined acid and sand fracturing technology, 479–480
 - filtration control technology, 479
 - fracture height control technology, 478–479
 - fracturing using combined clean diverting acid and conventional acid, 480
 - optimization and improvement of acid fracturing fluid, 476–477
 - optimization of prepad acid fracturing technology, 479
 - prefrac effect prediction technology, 476
 - small-radius horizontal well sidetracking technology, 473–475
 - drag and torque analysis and drilling string strength check, 474–475
 - drilling string drag and torque prediction model, 473–474
 - trajectory optimization technology, 475
- HTHP core holder, 293–294, 293*f*
- H**
- Hall-like cave system, 61–64
 - development characteristics of, 63*t*
- Hercynian period, 50–51

I

- Incomplete Cholesky method (ICCG), 396
- Indicator function, 367
 - equation of, 369
- Individual well production, 424–427
 - prediction model for, 426–427
 - variation characteristics of, 424–425
- Injection–production differential pressure, 347, 348*f*
- Injection-recovery simulation in a cave-fracture-vug model, 416
- Interpenetrating polymer network (IPN), 118
- In-vug stable differential pressure, 349

K

- Karst development and evolution in the early coverage of Hercynian period, 50–51, 51*f*
- Karst dynamics, 18–19
 - conceptual model of, 19*f*
- Karst facies pattern, 252–253
 - fracture-water table dual control mode, 252
 - water table-dominated pattern, 253
- Karst palaeogeomorphology, 186, 187*f*
- Karstic reservoir space, classification criteria of, 1–4
 - cave/cavern, 2–3
 - fracture, 3–4
 - filling degree, classification by, 3
 - occurrence and configuration, classification by, 3–4
 - origin, classification by, 3
 - scale, classification by, 4
 - primary pore, 2
 - secondary pore, 2
- Karstification, 10–17, 47–55, 83–84
 - effect of topographic and geomorphic conditions on, 24–27
 - fractures and, relationship between, 11*f*
 - geological structure and, 24
 - layered karstification in the burial stage, 51–55
 - occurring in ancient anticline structures, 12
 - paleo-karstification process, 1, 4–5, 34–39
 - rock mineral composition and, 20–22
 - rock texture and, 22

- KarstSim, 396–397, 410–411
 - comparison with similar software based on dual-medium model, 410–411
 - based on single-medium model, 410
- Kirchhoff integral migration, 161*f*
- Kirchhoff prestack time migration, 156

L

- Laplace numerical inversion, 317–318
- Large-scale fracture reservoirs, 235–236
 - fault interpretation, 235
 - fault tracking, 235–236
 - integrated interpretation, 236
- Large-scale fracture-vug models, 288, 289*f*
- Level Set method, 304
- Linear fault model, 432

M

- Matrix and vug, flow law between, 320–323
 - crossflow at pseudosteady state, 321–322
 - influential factors to matrix crossflow, 322
 - mathematical model, 320–321
 - physical model, 320
- Matured dual-medium theory, 355
- Miarolitic percentage, 312, 313*f*
- Microscale fracture reservoir, 236
- Microscale fractures in matrix, 283
- Moldic method, 72–74
- Monte Carlo probabilistic model, 194–195
- Multifracture and multivug medium, flow law in, 338
- Multifracture-vug model building technique, 291–292
- Multimedial representative elementary volume, 357–359
- Multiphase vug (cave) flow, 363–366
- Multiple near-vug fractures, 340–341

N

- Neumann boundary conditions, 370
- Newton–Raphson method, 377, 379
- “9-0-X” (model structure), 311
- “9-X-9” (model structure), 311
- Nitrogen injection EOR technology, 459–472
 - formation mechanism and distribution pattern of residual oil in fracture-cavern reservoirs, 459–461

Nitrogen injection EOR technology

(Continued)

gas injection effectiveness, analysis of, 471–472

typical single well gas injection, effectiveness of, 471–472

typical well-cluster gas injection, effectiveness of, 472

gas injection EOR technology for fracture-cavern units, 471

for single wells, 461–470

EOR mechanism of gas injection, 461–464

factors controlling the effectiveness of N₂ injection, 464–466

optimization of gas injection parameters, 467–470

well selection principles for gas injection, 466

Non-Darcy coefficient, 298–300, 300*r*, 303

Non-Darcy effect parameter, 299

Normalized variation analysis (NVA)

method, 389–392

N–S equation, 294–295, 338

Numerical simulation of fracture-vug

carbonate reservoir, 353

coupling mathematical reservoir model, 366–370

boundary conditions, 370

continuity equation, 367

equation of indicator function, 369

equation of state, 369

mathematical model, 369–370

momentum equation, 368–369

coupling numerical modeling method, validation of, 411–416

injection-recovery simulation in a cave-fracture-vug model, 416

physical experiment modeling of fluid flow in filled vugs, 411–414

two-phase numerical simulation in large caves, 414–415

equivalent multimedial numerical

simulation, validation of, 397–411

comparison of KarstSim with similar software, 410–411

numerical simulation, 397–403

physical experiment on a plate fracture-vug model, 408–409

simulation of high-speed non-Darcy flow, 404–407

equivalent multimedial reservoir, mathematical model for, 355–366

equation of mass conservation, 360–362

equivalent multiple medium, 355–356

fluid flow interface in caverns, 366

multimedial representative elementary volume, 357–359

multiphase vug (cave) flow, 363–366

pipe flow, fracture flow, and high-speed Darcy flow, 362–363

numerical solution based on equivalent multimedial model, 370–381

cavern flow, numerical simulation of, 376–377

Darcy flow, numerical simulation of, 370–374

full-implicit algorithm, 377–379

high-speed non-Darcy flow, numerical simulation of, 374–376

solution of linear equations, 379–381

numerical solution based on the coupling model, 381–396

coupling solution of pressure–velocity equations, 395

discretion of momentum equation, 392–395

discretion of transfer equation, 383–392

finite volume discretion in solution domain, 382

solution to linear equations, 396

S48 fracture-vug unit, numerical modeling on, 416–420, 417*t*

functions of numerical simulation software, 420

general description, 417

production history fitting in S48, 417–419

O

Offset plane-wave finite-difference prestack time migration, 156–158

method testing, 160

3D offset plane-wave decomposition, 156–158

- 3D offset plane-wave migration, 158–160
- Offset-domain common-image gathers (ODCIGs), 162–164
- Oil–water two-phase flow experiment, 304–307
- on fractured models, 305–306
 - on fracture-vug models, 307
 - on unfilled vug models, 304–305
- Oil–water two-phase flow features, 308–314
- fractured models, relative permeability curves based on, 308–311
 - fracture-vug models, relative permeability curves based on, 311–314
- One-phase flow law, 294–303
- experiments, 294–297
 - on fractured models, 295–296
 - on fracture-vug models, 296–297
 - unfilled vug models, 294–295
- one-phase flow pattern and conversion conditions, 298–303
- discrimination of flow pattern, 298–300
 - features of flow pattern conversion, 300–303
- Optimization and improvement of acid fracturing fluid, 476–477
- Optimization of prepad acid fracturing technology, 479
- Ordovician carbonate fracture-vug system, classification of, 52*t*
- Ordovician carbonate rock, 30–32, 72
- Ordovician fracture-vug reservoir, 250–251
- Ordovician karst fillings
- carbon–oxygen isotope characteristics of, 37–39
 - carbon–oxygen stable isotope characteristics of, 36
- Ordovician palaeo-karst fillings
- features of filling inclusion in, in the outcrop region of the northern Tarim Basin, 39
 - features of inclusions in, in the Tahe Oilfield, 39–44
- Ordovician reservoirs, 4–5, 13, 230, 252–253
- Ordovician weathered crust in the Tarim Basin
- Index system for dividing secondary geomorphic types of, 75*t*
 - Index system for dividing tertiary geomorphic types of, 76*t*
- Ordovician reservoirs in the Tahe oilfield, development conditions of, 7–17
- formation lithology, 13
- karstification, 13–17
- tectonism and rifting, 7–12
- control of faults over fracture development, 10
 - relationship between faults and karstification, 10–12
 - relationship between fractures and vugs, 12
- Out-vug jumping differential pressure, 350
- P**
- Palaeogeomorphologic study, 186
- Palaeogeomorphology restoration, identification indexes for of Ordovician weathered crust in the Tarim Basin, 78*t*
- Palaeogeomorphology-controlled sculpting, 186–187
- Palaeo-karst, developmental and evolutionary mechanism of, 18–55
- formation condition and controlling factors, 20–30
- carbonate rock properties and karstification, relationship between, 20–23
 - carbonatite structure and fracture-vug system, relationship between, 23–24
 - effect of topographic and geomorphic conditions on karstification, 24–27
 - geological structure and karstification, relationship between, 24
 - underground hydrodynamic circulation and karst development, relationship between, 27–30
- karst dynamic mechanism, 18–19
- in the Tahe region, 30–55
- evolution features, 47–55
 - formation conditions and controlling factors, 31–34
 - geochemical characteristics, 34–47
 - geological background, 30–31
- Paleoclimate, 30

- Paleokarst geomorphic units, storage
 properties of, 88–89
 hill cluster ridge trough, 89
 hill cluster ridge valley, 89
 hill peak depression, 88–89
 intermontane basin, 89
 karst trough, 89
 peak cluster depression, 88
- Paleokarst geomorphology, combined
 identification of the genesis of,
 72–74
- Paleokarst geomorphology and development
 conditions
 of karst platform, 82–83
 Karst hill depressions, 82–83
 Karst troughs, 83
 peak cluster depressions, 82
 of lower karst gentle slopes, 85–87
 hill cluster valleys and peak cluster
 valleys, 87
 hill peak depressions, 85
 peak cluster depressions, 86
 peak cluster ridge troughs, 86–87
 of upper karst gentle slopes, 83–85
 hill cluster ridge troughs, 84–85
 hill cluster ridge valleys, 84
 hill peak depressions, 83–84
 karst troughz, 85
- Paleokarst geomorphology features and karst
 development conditions of karst
 intermountain basins, 87
- Paleo-karst in the Tahe region, 30–55
 evolution features, 47–55
 development and evolution of exposed
 weathered karst, 48–50
 development and evolution of
 Yijianfang Formation karst, 47–48
 karst development and evolution in the
 early coverage of Hercynian period,
 50–51
 layered karstification in the burial
 stage, 51–55
 formation conditions and controlling
 factors, 31–34
 formation structure, type of, 32–33
 geological structure, 33
 lithological feature, 31–32
 palaeogeomorphological conditions,
 33–34
 palaeo-hydrodynamic conditions, 34
 geochemical characteristics, 34–47
 carbon–oxygen isotope characteristics,
 36–39
 causes and environmental significance
 of carbon and oxygen isotope
 variation, 34–39
 paleo-karstification, indication of filling
 inclusions to, 39–44
 geological background, 30–31
 carbonate sequence and lithologies, 31
 paleoclimate, 30
 regional structure, 30–31
- Paleo-karstification, indication of filling
 inclusions to, 39–44
 features of filling inclusion in Ordovician
 palaeo-karst fillings in the outcrop
 region of the northern Tarim Basin,
 39
 features of inclusions in Ordovician
 palaeo-karst fillings in the Tahe
 Oilfield, 39–44
- Paleo-karstification process, 1, 4–5, 34–39
- Paleo-pipe-network underground stream
 system, 60*f*
- Performance analysis techniques for
 fracture-cavern reservoirs, 423–442
 evaluation of natural energy, 427–429
 comprehensive evaluation index of
 natural energy, 427
 evaluation index for edge and bottom
 water energy, 428–429
 evaluation index of elastic energy,
 427–428
 individual well production, 424–427
 prediction model for, 426–427
 variation characteristics of, 424–425
 numerical well testing model and
 interpretations, 429–442
 coupled flow well testing model and
 analytical method, 438–441
 interpretation of testing data from
 fracture-cavern carbonate reservoirs
 of Tahe Oil Field, 441–442
 numerical well testing based on triple-
 porosity medium, 429–438
- Performance data, verification by, 279–280
- Physical modeling experimental design,
 283–294

- building experiment models, 288–292
 - experiment system, 293–294
 - fundamental principles and similarity
 - criteria, 283–284
 - materials selection, 287–288
 - similarity criteria, 284–287
 - similarity laws, 284
 - Pipe network underground stream system, 56–60
 - Pipeline-network underground stream system, 60*f*
 - Plate fracture-vug model, physical experiment on, 408–409
 - Postflooding constant differential pressure, 351
 - Postvug declining differential pressure phase, 350
 - Pre-Carboniferous paleokarst geomorphy in the Tahe Oilfield
 - classification of, 79*t*
 - Prefrac effect prediction technology, 476
 - Prepad acid fracturing technology, optimization of, 479
 - Pressure–velocity equations, coupling solution of, 395
 - Prestack azimuthal anisotropy-based fracture detection, 177–181
 - P-wave AVO for TTI media, fracture prediction based on, 180–181
 - model-based AVO inversion, 181
 - theoretical basis, 180–181
 - residual NMO for TTI media, 177–178
 - residual P-wave NMO for TTI media, fracture detection based on, 178–180
 - Prestack fluid detection, 192–194
 - LMR inversion, 194
 - prestack elastic impedance inversion, 193–194
 - Prevug declining differential pressure, 349
 - Production data, verification by, 277–279
 - Production variation model, 431–432
 - Pseudosteady state, crossflow law at, 319–320
 - P-wave amplitude variations, 152–153
 - P-wave AVO-based fracture detection, 210–211
 - P-wave azimuthal anisotropy
 - in a fractured medium with varied fracture dips, 150–151
 - in a vertically fractured medium, 145–149
 - analysis of experimental results, 145–147
 - azimuthal AVO responses, 147–149
 - P-wave residual NMO-based fracture detection, 209
 - P-wave responses for varied fracture densities, 151–153
- Q**
- Quartic moveout coefficient, 177–178, 178*f*
- R**
- Random medium description, 123
 - Reef shoal system, 70, 70*t*
 - Reflection configuration analysis, 171–173
 - Representative elementary volume (REV), 357, 357*f*
 - Reservoir prediction, 171–176
 - cave prediction, 171–175
 - discontinuity detection, 173–175
 - reflection configuration analysis, 171–173
 - strong amplitude clustering, 173
 - fracture prediction, 175–176
 - curvature, 175–176
 - neural networks, 176
 - Reservoir stimulation technology for fracture-cavern oil reservoirs, 475–480
 - acid fracturing fluid, optimization and improvement of, 476–477
 - combined acid and sand fracturing technology, 479–480
 - fracture height control technology, 477–479
 - filtration control technology, 479
 - fracture height control technology, 478–479
 - fracturing using combined clean diverting acid and conventional acid, 480
 - prefrac effect prediction technology, 476
 - prepad acid fracturing technology, optimization of, 479
 - Residual oil
 - different types of, in typical fracture-cave units of Tahe Oil Field, 462*t*
 - main types of, after waterflooding, 461*t*

- Residual thickness method, 74
- Rock mineral composition and karstification, relationship between, 20–22
- Rock texture and karstification, relationship between, 22
- Runoff dissolution zone, 30, 253
- S**
- S48 fracture-vug unit, numerical modeling on, 416–420
- functions of numerical simulation software, 420
 - general description, 417
 - production history fitting in S48, 417–419
- Sandstone reservoir, fractured-vug reservoir versus, 5*t*
- Scattered seismic waves in a single cavern theoretical analysis of, 128–129
- Scissors difference, 324–325
- Seismic attribute volume, identification of fracture-vug reservoir by, 241–250
- fusion of multiple attribute volumes, 247–248
 - combination fusion, 248
 - feature fusion, 247
 - normalization fusion, 247–248
 - preprocessing of seismic attributes, 246–247
 - seismic attribute extraction, 242
 - sensitive seismic attribute analysis, 242–245
- Seismic forward modeling, 117–127
- numerical simulation, 122–127
 - random medium description, 123
 - staggered-grid high-order finite difference, 126–127
 - variable-grid finite difference, 123–124
 - variable-grid numerical simulation, 124–125
 - physical modeling, 117–122
 - experiments, 121–122
 - geologic features of physical models, 118
 - model materials and model making, 118–121
- Seismic imaging, 155–171
- diffraction imaging, improving resolution of, 167–171
 - diffracted waves on CSP gathers, 169–170
 - field data testing, 171
 - mapping noise suppression, 170
 - theoretical modeling, 171
 - offset plane-wave finite-difference
 - prestack time migration, 156–158
 - method testing, 160
 - 3D offset plane-wave decomposition, 156–158
 - 3D offset plane-wave migration, 158–160
 - time-shift depth migration and velocity analysis in angle domain, 160–167
 - imaging conditions for, 162–164
 - method testing, 167
 - velocity analysis workflow, 167
 - velocity update, 164–167
- Seismic reflection feature, 236–240
- classification of, 237
 - atypical reflection, 237
 - bead-like reflection, 237
 - strong reflection, 237
 - weak reflection, 237
 - reflection features and high-productivity wells, relationship between, 237–240
 - seismic reflection feature and production, relationship between, 237
- Seismic responses
- of cave group, 141–142
 - numerical simulation of actual geologic model, 142–144
 - of random caves, 140–141
- Seismic responses of fractures, 145–153
- P-wave azimuthal anisotropy
 - in a fractured medium with varied fracture dips, 150–151
 - in a vertically fractured medium, 145–149
 - P-wave responses for varied fracture densities, 151–153
- Seismic responses of single caves
- with different filling materials, 137–139
 - with varied geometries, 135–137
 - with varied sizes, 129–135
 - amplitude analysis, 131

- single-cave physical modeling
 - experiment, 132–135
 - single-cavern responses, 129–131
 - Sensitivity analysis, 190–191
 - feasibility study, 191
 - fluid substitution, 190–191
 - petrophysical model, 190
 - Sequential indicator simulation, 260
 - Shaft-like cave system, 64–65, 66*t*
 - Similarity criteria, determination of, 286
 - Similarity laws, 284
 - Similarity theory, 284–285
 - Single near-vug fracture, 340
 - Single-pipe underground stream system, 55, 56*f*
 - Single-square-root (SSR) approximate
 - expression, 160
 - Single-vug–near-vug fracture (high dip)
 - medium, flow law in, 326–331
 - basic flow law, 327–328
 - water cut variation, 328–331
 - SINOPEC, 410
 - Small-radius horizontal well sidetracking
 - technology, 473–475
 - drag and torque analysis and drilling
 - string strength check on, 474–475
 - drilling string drag and torque prediction
 - model, 473–474
 - trajectory optimization technology for, 475
 - Soluble rock, 20
 - Solution cave system, 64
 - Solution fracture system, 68–70
 - Spatially structured well grid, 446
 - Staggered-grid high-order finite difference, 126–127
 - Stehfest method, 317–318
 - Storativity ratio, 318
 - Strip-type fault-karst system, 67
 - Strong amplitude clustering, 173, 174*f*
- T**
- Tahe carbonate reservoirs, 283, 475–476
 - Tahe Oil Field, 315, 339, 356
 - interpretation of testing data from
 - fracture-cavern carbonate reservoirs
 - of, 441–442
 - Ordovician reservoirs in, development
 - conditions of, 7–17
 - formation lithology, 13
 - karstification, 13–17
 - tectonism and rifting, 7–12
 - Pre-Carboniferous paleokarst geomorphy
 - in, 79*t*
 - Tectonic corridor underground stream
 - system, 60–61
 - Tectonism, 7–13
 - Tectonism and rifting, 7–12
 - control of faults over fracture
 - development, 10
 - faults and karstification, relationship
 - between, 10–12
 - fractures and vugs, relationship between, 12
 - 3D fracture-vug model., 290*f*
 - physical simulation of, 153–155
 - 3D geological modeling of fracture-vug
 - carbonate reservoir, 223
 - application, 281–282
 - attribute parameter modeling method, 274–276
 - algorithm for, 274–275
 - of caverns, 275
 - of fractures, 275–276
 - of vugs, 275
 - attribute parameters, 271–274
 - for caverns, 271–272
 - for fractures, 273–274
 - for vugs, 272–273
 - building a 3D caverns model, 257–259
 - building a 3D vug model, 260–261
 - characterization of fracture-vug unit, 251–256
 - division of a fracture-vug unit, 251–252
 - karst facies pattern, 252–253
 - typical fracture-vug , characterization
 - of unit, 253–256
 - cross-well identification, 236–250
 - by seismic attribute volume, 241–250
 - by seismic reflection feature, 236–240
 - by wave impedance inversion, 241
 - designing a 3D model grid, 257
 - discrete distribution models, fusion of, 270
 - distribution law of fracture-vug reservoir, 250–251

- 3D geological modeling of fracture-vug carbonate reservoir (*Continued*)
- large-scale fracture model, building, 262–265
 - microscale discrete fracture network model, building, 265–269
 - pore space, 223–230
 - caverns, 227–228
 - fractures, 228–230
 - matrix, 224–227
 - vugs, 228
 - single-well identification, 230–236
 - cavernous reservoirs, 230–232
 - large-scale fracture reservoirs, 235–236
 - microscale fracture reservoir, 236
 - vug reservoirs, 233–235
 - verification
 - by drilled well, 277
 - by performance data, 279–280
 - by production data, 277–279
- 3D offset plane-wave decomposition, 156–158
- 3D offset plane-wave migration, 158–160
- Time-shift depth migration and velocity analysis in angle domain, 160–167
- imaging conditions for, 162–164
 - method testing, 167
 - velocity analysis workflow, 167
 - velocity update, 164–167
- Time-shift offset-domain common-image gathers (TSODCIGs), 163–164
- TK666 gas injection well cluster, 472
- Total variation diminishing (TVD) method, 389–392
- Triple-medium models, 355–356
- Triple-porosity medium, numerical well testing based on, 429–438
- for fractured reservoirs with large fractures and caverns, 437–438
- inversion of single-phase numerical well testing, 435–436
- automatic fitting method for well testing curves, 436
 - Gauss–Newton Method (GNM), 435–436
 - inversion examples, 436
- percolation pattern, 429–431
- response characteristics of two-phase flow in triple-porosity medium, 438
- well testing responses for complex geological models, 431–435
 - composite reservoir model, 433–435
 - linear fault model, 432
 - production variation model, 431–432
- Two-phase flow law, 303–314
- oil–water two-phase flow experiment, 304–307
 - on fractured models, 305–306
 - on fracture-vug models, 307
 - on unfilled vug models, 304–305
 - oil–water two-phase flow features, 308–314
 - relative permeability curves based on fractured models, 308–311
 - relative permeability curves based on fracture-vug models, 311–314
 - two-phase flow patterns, 303–304
- Two-phase numerical simulation in large caves (caverns), 414–415
- U**
- Undercurrent dissolution zone, 30
- Underground hydrodynamic circulation and karst development, relationship between, 27–30
- epikarst zone, 29
 - runoff dissolution zone, 30
 - undercurrent dissolution zone, 30
 - vertical percolation dissolution zone, 29–30
- Universal transfer equation, 383
- V**
- Variable grid and time-step (VGTS), 126–127
- Variable-grid finite difference using elastic wave equation, 123–124
- Variable-grid numerical simulation, 124–125
- Vertical distribution features of the fracture-vug system, 90–95
- Vertical percolation dissolution zone, 29–30
- Vertical zonation type in the Tahe Oilfield, 90
- VOF model, 368
- Vug control technique, 291
- Vug creation technique, 289–290

Vug density, 296–297

Vugs distribution model, 263*f*

W

Warren–Root model, 355

Water injection mode, 449–450

Water injection timing, 447–449

 faulted karst body, 447–448

 underground river, 449

 weathering crust, 447

Water table-dominated pattern, 253

Waterflooding development mechanisms for fracture-cavern oil reservoirs, 443–446

 factors influencing development effectiveness and development countermeasures, 445–446

 natural energy, 445–446

 spatial relationships between injection and production wells, 445

 spatial relationships between oil-producing wells and caverns, 445

 types of reservoir bodies, 445

 optimization of injection/production parameters, 450–455

 recovery mechanisms for production wells

 in cavern zone, 443–444

 in fractured zone, 444–445

 spatially structured well grid, 446

 water injection mode, 449–450

 water injection timing, 447–449

 faulted karst body, 447–448

 underground river, 449

 weathering crust, 447

Waterflooding effectiveness, evaluation of, 455–457

 overall evaluation methods for fracture-cavern units, 456–457

 technical evaluation index system, 455–456

Wave impedance inversion, identification of fracture-vug reservoir by, 241

Well T207, 339

Well testing responses for complex geological models, 431–435

 composite reservoir model, 433–435

 linear fault model, 432

 production variation model, 431–432

Y

Yijianfang Formation karst, development and evolution of, 47–48

Z

Zoeppritz equations, 128–129

Development Theories and Methods of Fracture-Vug Carbonate Reservoirs

Fracture-Vug carbonate reservoirs are difficult to characterize and develop due to their complex storage mechanisms and fluid flow patterns of hydrocarbons. Problems such as a rapid decline in production rates, low recovery factors, and poor sweeping efficiency arise for such reservoirs around the world. As a result, few fracture-Vug carbonate reservoirs have been developed successfully in the world. The Ordovician reservoir in the Tahe oilfield of China is the largest fracture-Vug reservoir in the world, and has an estimated oil reserves of up to 3 billion tons.

Development Theories and Methods of Fracture-Vug Carbonate Reservoirs explores the theories and methods for successful development of a fracture-Vug reservoir by presenting the developmental strategies used in the Tahe oilfield. Some of the theories and methods of developing the fracture-Vug reservoirs have been inspired by two national research projects in China: "Basic research on development of fracture-vug carbonate reservoirs" (2006–10) and "Basic research on production mechanism and oil recovery enhancement of fracture-vug carbonate reservoirs" (2011–15) supported by the National Basic Research Program of China. These theories and methods have facilitated the successful development of the fracture-Vug reservoir in the Tahe oilfield, providing effective technologies and inspirations to developing similar reservoirs everywhere.

Key Features

- Provides information on both theoretical developments and technological innovations
- Applies the modern karst formation characterization and the fracture-Vug hierarchical structure to geological investigations of fracture-Vug carbonate reservoirs
- Introduces the karst facies-controlling 3D geologic modelling of fracture-Vug reservoir formations
- Proposes the coupled-processing and equivalent multimedial numerical simulation methods of fracture-Vug reservoirs
- Presents development methodologies and techniques of water/gas flooding

Yang Li is the vice chief engineer of Sinopec Corp., an Academician of the Chinese Academy of Engineering, and is engaged in research of petroleum geology and oil/gas reservoir development. He served as the chief scientist for two projects "Basic research on development of fracture-Vug carbonate reservoirs" (2006–10) and "Basic research on production mechanism and oil recovery enhancement of fracture-vug carbonate reservoirs" (2011–15) supported by the National Basic Research Program of China (973 Program).



ACADEMIC PRESS

An imprint of Elsevier
elsevier.com/books-and-journals

ENERGY
ENVIRONMENTAL
ENGINEERING

ISBN 978-0-12-813246-3



9 780128 132463